THÈSE

Présentée pour obtenir le grade de

DOCTEUR DE
L'UNIVERSITÉ PARIS–EST

Domaine : Génie civil

Présentée par :

Qiang Zeng

Sujet de la thèse :

Poromechanical behavior of cement-based materials subjected to freeze-thaw actions with salts : modeling and experiments

Comportement poromécanique des matériaux cimentaires soumis au gel-dégel en présence de sels : modélisation et expérimentation

Soutenue à Champs-sur-Marne le 30 11 2011

Les membres du jury :

Prof. Berthaud Yves	UPMC	Rapporteur
Prof. Perrin Bernard	UPS Toulouse	Rapporteur
Prof. Azouni Aza	CNRS, U. Paris-Est	Examinatrice
Prof. Hulin Jean-Pierre	CNRS, UPMC	Examinateur
Dr. Fabbri Antonin	ENTPE	Examinateur
Dr. Zuber Bruno	Lafarge	Examinateur
Dr. Fen-Chong Teddy	IFSTTAR, U. Paris-Est	Directeur de thèse

Abstract

When subject to freezing/thawing cycles with or without deicing salt, cement-based materials can suffer severe damage, which raises the long term sustainability problem of concrete/mortar in cold regions. Leaving aside the precise fracture mechanics and damage processes in this kind of problem, this PhD deals with the physical and thermomechanical phenomena undergone by cohesive porous solids under freezing, with particular attention to the material properties arising from cement hydration and microstructure development. The present work revisits the poromechanics of freezing porous materials developed by Olivier Coussy. This gives the opportunity to add the effect of the bulk supercooling and of salt in the liquid saturating the porous space.

We measured the relation between depressed temperature at the end of bulk supercooling and salt concentration. We then obtained that the contact angle between ice and pore wall by heterogeneous nucleation decreases as salt concentration increases. We showed that the instantaneous dilation at the end of bulk supercooling is related to the pore structure because the latter determines the in-pore ice content.

Using the pore size distribution measured by mercury intrusion porosimetry, we estimated the ice saturation degree with temperature and NaCl solution at different concentration through the Gibbs-Thomson equation. We measured the deformation of saturated cement pastes. The poromechanical analyses show that the strains depend on the initial salt concentration and pore structure of our cement pastes.

By the same experimental approach on dried cement pastes, we concluded that the porosity (with or without air voids) has significant influence on the thermal expansion coefficient of our cement pastes. We also performed measurements on the deformation of saturated air entrained cement pastes. The results obtained by both experiments and poromechanical analyses under drained and undrained conditions showed that the initial saturation degree in air-voids has significant influence on the deformation curves with temperature.

Keywords: Cement-based materials, Poromechanics, Pore structure, Freeze-thaw, NaCl solution, Strain, Air-voids.

Résumé

Les matériaux cimentaires peuvent se détériorer grandement lorsqu'ils sont soumis à des cycles de gel/dégel avec ou sans sels de déverglaçage. Ceci peut porter atteinte à la durabilité à long terme des bétons/mortiers dans les régions aux hivers froids. Laissant de côté les processus d'endommagement et de rupture mécanique à l'œuvre dans de tels problèmes, ce mémoire de thèse est consacré aux phénomènes physiques et thermo-mécaniques accompagnant la solidification de l'eau dans des solides poreux cohésifs, avec une attention particulière aux "propriétés matériau" issues de l'hydratation du ciment et de l'évolution de la microstructure.

Ce travail reprend la poromécanique des milieux poreux partiellement gelés telle que développée par Olivier Coussy, tout en lui adjoignant une analyse de l'effet de la fin de la surfusion (en volume, hors contribution capillaire) et de la présence de sels dans le liquide saturant l'espace poreux.

Nous avons mesuré la température de fin de surfusion en fonction de la concentration en sel. Ceci nous permet ensuite de calculer l'angle de contact entre la glace et les parois des pores dans le cadre classique de la nucléation hétérogène : on trouve que cet angle diminue avec la concentration en sel. Nous montrons que la dilatation instantanée consécutive à la fin de la surfusion dépend de la structure poreuse puisque cette dernière détermine la teneur en glace dans l'espace poreux.

À l'aide de la distribution de tailles de pores estimée par porosimétrie par intrusion de mercure, nous estimons le degré de saturation en glace en fonction de la température et de la concentration initiale en sel via la relation de Gibbs-Thomson. Nous avons mesuré la déformation d'échantilllons de pâte de ciment saturée. L'analyse poromécanique montre que la déformation dépend de la concentration initiale en sel et de la structure poreuse des pâtes de ciment.

En utilisant la même approche expérimentale sur des pâtes de ciment sèches, nous trouvons que la porosité (avec ou sans vide d'air entraîné) influence significativement le coefficient d'expansion thermique du matériau. En ce qui concerne les pâtes de ciment saturées, les mesures expérimentales et l'approche poromécanique en condition drainée ou non-drainée montrent que le degré de saturation initiale en liquide des vides d'air entraîné a un impact important sur la déformation de l'échantillon avec la température.

Mots clefs : matériau cimentaire, poromécanique, structure poreuse, gel/dégel, solution NaCl, déformation, vide d'air.

Acknowledgements

I would like to gratefully and sincerely thank Teddy Fen-Chong, Kefei Li and Patrick Dangla. Without their invaluable guidance and support, this dissertation work would have never been accomplished. They have not only been advisors, but also mentors and friends to me. Their mentorship was and will be paramount in providing a well rounded experience for both the academic part of my career and other aspect of my life.

I would also like to thank the Kefei Li group at Tsinghua University, which provided me with a great source of help and support for the present work in China. In particular, I would like to thank Chunsheng Zhou, Xiaoyun Pang, Mingyong Luo and Jiuna Hu for their help and friendship. I would also like to thank the colleagues and engineers who work at the Institution of Construction and Building Materials, Department of Thermal Engineering and Chemical Engineering, Department of Material Science and Engineering at Tsinghua University. They provided great support for the experiments.

I offer my sincere regards to those friends and colleagues in Laboratoire Navier (UMR 8205 ENPC / IFSTTAR / CNRS) including Haifeng Yuan, Jiyun Shen, Rongwei Yang... They also help my life to be easier in France.

Special thanks are given to my wife Xiaqiu Wu and my son Yu Zeng. The encouragement, patience, support and unconditional love by her made me through the hard time. My little baby provided great fun for me. I also thank our parents, for their faith in me and unending encouragement and support to me.

Contents

List of Figures

List of Tables

Chapter 1

General introduction

Contents

1.1 Freezing issues in civil engineering

The cement-based materials are known as a sort of most used materials in all fields of civil affairs, even military affairs. In 2010, the world cement production is about 3.3 billion tons [58]. The durability of cement-based materials are of significant importance in serviceability and economic consideration. In addition, the requirements of environmental sustainability and energy efficiency confirm the importance of the durability of cement-based materials due to the large amount of energy consumption and carbon dioxide emission during their product processes.

The loss of serviceability in the sense of lack of durability can be attributed to many different reasons. Besides inappropriate design/curing/use, which are man made factors, the severe environment loadings, such as, corrosion of reinforcement induced by chloride ingress and carbonation, cracking induced by alkali-silica reaction and freeze-thaw, and deteriorations induced by salt crystallization, are important factors for durability problems of cement-based materials. This can bring about very high cost for reparation and maintenance. In USA, for instance, the financing gap for road, highway and bridge repairs and improvements, can be as high as 495 billion US dollars in 2009 [398].

Among these common reasons for durability problem of cement-based materials, the freeze-thaw can be one of the most important factors. Although the freeze-thaw deterioration, in France, is not as serious

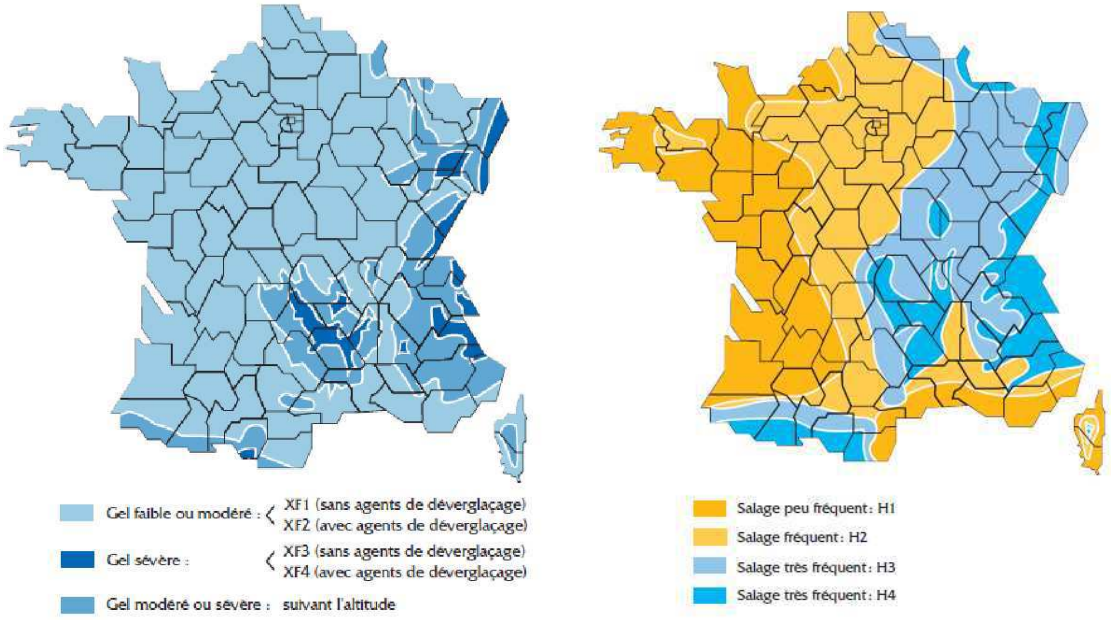

(a) (b)

Figure 1.1: The distribution of risks of frost deterioration (a) and frequency of salting (b) of concrete in France, source from [62].

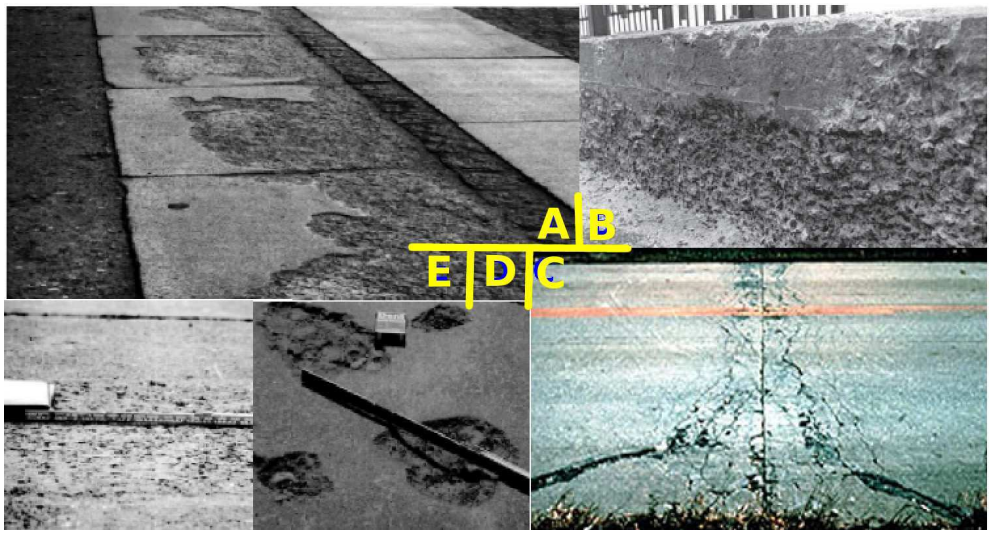

Figure 1.2: Various freeze-thaw damages observed in civil engineering. Figures (A,D,E) are adopted from Ronnings (2001) [328], figure (B) is adopted from Pigeon et al., (2003) [295], and figure (C) is adopted from [1].

as in northern countries, these phenomena can also be observed frequently, specially in some high-altitude alpine area [62]. Figure 1.1(a) shows the distributions of risks of frost damage of cement-based (concrete) constructions in France [62]. In addition, this durability problem is often worsened by a man made factor: the use of deicing salts. As shown in Figure 1.1(b), the salting is frequent in more than two thirds of the areas of France [62]. The original intention of using deicing salts , melting the sliding ice, is to increase serviceability of pavements, roads and/or bridge decks. The U.S. and Canada use approximately 15 million and 4-5 million tons of deicing salts each year, respectively [334]. However, both on-site and experimental observations confirm that the deicing salts can lead to serious deteriorations to cement-based constructions, the so-called frost scaling, see for instance (A), (D) and (E) in Figure 1.2. Scaling not only reduces the elegance but also brings about significant serviceable problems. For the reinforced concrete construction, which is usually acting as load-bearing structure, the surface layer (cover) is very important. The cover with alkali pore solution can provide a protective layer against the corrosion of reinforcement steels, and the chloride ions ingress and carbonation of cement-based materials of this layer, which can weaken and/or brake the electrochemical immunity of the steel, are normally very slow. However, the deicing salts induced scaling may accelerate them significantly [71]. Although the freeze-thaw resistance has received significant attention in northern countries, there are no efficient ways to prevent the deicing attack. Generally, the osmotic pressure model) [310], the thermal shock [236], the more porous structure of surface layer of cement-based materials [294], and the discrepancy between the thermal dilation coefficients of ice and solid skeleton (the so called "Glue spalling" model) [72, 405] can be responsible for the surface scaling (detailed review on the relevant content can be found in chapter 3 or other comprehensive review [101, 407, 408]).

The other important phenomena of freeze-thaw damage is the internal cracking [295, 296]. This alternative damage pattern, contrary to scaling, leads to the strength (or elastic modulus) loss with increasing freeze-thaw cycles. It is believed that this internal damage is associated with the micro cracks when ice forms in pores. The frozen damaged cement-based materials, like the weathered rock, can completely loss their serviceability (see for instance, (B) and (C) in Figure 1.2). The outstanding work on this issue was the studies performed during the 1940s and 50s in USA (cf. Powers [305], Powers and Helmuth [310]). With help of the entrained air voids which provide spaces to accommodate the excess water [305] and act as cyopump that attracts the water to the ice site nucleated on the interface of air voids [77, 342], the resistance to internal freeze-thaw damage has been improved significantly. This is still the most efficient way to protect the cement-based materials against freeze-thaw damage, although the understandings on the mechanisms of freeze-thaw damage having been deepened extensively (cf. the crystallization pressure model [342] and poromechanical analysis [77, 114, 451]).

1.2 Problem statement

The mechanisms of internal cracking induced by freeze-thaw attack are somehow complicated but generally clear through comprehensive researches during several decades: damage due to hydraulic pressure, crystallization pressure and/or discrepancy expansions between ice and solid skeleton. However, the mechanisms for the deteriorations induced by deicing are still enigma, although several hypotheses or models have been proposed for these specific issues, cf. the recent proposed "glue spalling" model by Valenza and Scherer [404–406]. Furthermore, very little attention has been payed to the crossed case: the freeze-thaw deteriorations of cement-based materials saturated with saline solution. In addition, very little literature concerned with the freeze-thaw performance of air voids entrained cement-based materials initially saturated with saline solution. Therefore, it is necessary to study this scope phenomenologically and to understand the hidden mechanisms, either being physical-chemical or mechanical or both.

The pore structure must be a factor intimately related to all durability problems of cement-based materials. With appropriate practice, the pore structure as well as the micro-structure of cement-based materials depend mainly on the compounds of raw materials, water to cement (w/c) ratios and curing conditions. The afore and on-going researches on these issues can provide us with the feature of pore structure/microstructure, although there are still many open questions. Knowledge of cement hydration allows us to predict the main hydration products quantitatively in engineering requirements. Through standard experiments, the pore structure of cement-based materials can be characterized. In addition, the mechanical and transport properties of cement-based materials can be evaluated in some extent by means of multi-scale modelling . These properties are quite important for durability of cement-based materials. But the relationship has not been clearly understood for freeze-thaw problem. For instance, most laboratory tests and field performance show that the cement-based materials with high strength and low porosity is better against frozen resistance [295]. However, some opposite observations (cf. [28, 115]) indicate that it is not a simple monotonous relationship between frost resistance and porosity or strength of cement-based materials.

With several, simultaneously acting mechanisms as above mentioned, the freeze-thaw damage can not be the consequence of any one of these mechanisms alone, and it seems not possible to identify the critical one(s) for a specific material design and environment. In addition, the severe lack of correlation between laboratory and field (on-site) performance should be noticed: the specific designed laboratory experiment, associated with some expected mechanisms, may not be adopted to on-site situation. Therefore, for both the laboratory tests and on-site observations, the controlled conditions, such as, humidity, temperature, salt concentrations, are crucial.

1.3 Research motivation

Following the aforementioned arguments, the present research work aims at:

❁ Establishing qualitative and, if possible, quantitative information on the ice nucleation temperature for well characterized cement pastes;

❁ Quantitatively assessing the characteristics of ice formation in pores of cement-based materials saturated with solution at different salinity;

❁ Extending the poromechanical modelling to describe freezing behavior of cement-based porous materials initially saturated with NaCl solution;

❁ Calibrating the hydration process of the cement pastes, assessing content of hydration products and characterizing the pore structure of paste I (w/c=0.5) and paste II (w/c=0.3);

❁ Evaluating/assessing the mechanical and transport properties of well identified cement pastes based on multi-scale modelling;

❁ Quantitatively explaining the observed strain variation of cement-based materials under different material and boundary conditions;

❁ Quantitatively explaining the observed instantaneous deformation of cement-based materials by bulk supercooling of pore water;

❁ Experimentally identifying the deformation of cement pastes saturated with saline solution subjected to freeze-thaw loadings;

❁ Experimentally identifying the deformation of air entrained cement pastes saturated with saline solution subject to freeze-thaw loadings.

1.4 Layout of this thesis

The present work is organized as follow:

Part I: Thermodynamic and mechanical analyses of freezing in porous materials. In chapter 2, we first review the principles of ice formation and the physico-chemical properties of ice in small pore size. In addition, the ubiquitous but often underestimated phenomena, viz. the freeze-thaw hysteresis, bulk supercooling and unfrozen layer (liquid like layer) between the surface of ice and solid matrix, are qualitatively and (in some extent) quantitatively analyzed and/or discussed. In chapter 3, we recapitulate the freeze-thaw deterioration phenomenologically and the corresponding mechanisms. Then, we use the thermalporoelasticity to describe the partially frozen porous materials saturated with saline solution (chapter 4) based on the comprehensive study by Olivier Coussy [76, 77, 79, 82]. In chapter 5, the deformation of cement-based materials saturated with pure water is analyzed by the established model and compared

with the results in literature as a case study. The strains resulting from the ice formation and thermal shock at the end of bulk supercooling of pore water are analyzed as another case study.

Part II: Freezing/thawing with salt: experiments, material properties and poromechanical analyses. In chapter 6, we start from the hydration processes of our cement pastes. Based on the afore and on-going work of cement chemistry, the main hydration products are evaluated and are compared with experimental results. The pore structure is comprehensively assessed by the MIP and NAD measurements. In chapter 7, we use the effective medium theory of composites with Eshelbian type morphology inclusions and multi-scale technique to estimate the effective mechanical and transport properties of cement pastes. In chapter 8, the physical properties of water, ice and NaCl solution in functions of temperature, pressure and salt concentration are evaluated by Archer's model. The water/ice saturation degree in terms to temperature is estimated based on the capillary invasion of ice during freezing. In chapter 9, we introduce the experimental procedures of freeze-thaw deformation measurement, and discuss the effects of pore structure and NaCl concentration on the freeze-thaw deformation by poromechanical analyses. In chapter 10, the effect of air voids on the deformation of both dried and saturated samples are analyzed.

We end this work with general conclusion and some unclear problems that need further research.

Part I

Thermodynamic and mechanical analyses of freezing in porous materials

Abstract of Part I

The aims of Part I are to: ❶, understand the freezing processes water confined in porous materials, the freeze-thaw hysteresis, capillary and bulk supercooling phenomena, which are basis for the problem at hand; ❷, understand the frost deterioration of cement-based materials comprehensively; ❸, establish a poromechanical model based on the variables of temperature, pressure and salt concentration for partially frozen cement-based materials; and ❹, verify the established model by data in literature and confirm the robustness of this model.

The basic principles of ice formation in porous materials were recapitulated in chapter 2. The necessary but not sufficient condition for ice formation is that the chemical potential of ice is equal to or lower than that of liquid water. The penetration of ice into porous materials is governed by capillary forces. Using the Young-Laplace equation and assuming that pores are cylindrical, the relation between pore size and melting temperature depression can be obtained, which is the principle of cryoporosimetry. The activity of ions is a combination of the individual ionic long-range interaction and short-range solvation effect. Ionic parameters based empirical models are adopted to estimate the ionic activity, osmotic coefficient and water activity. When water confined in pores of very small size, rather than the ordinary hexagonal ice (I_h), water prefers to form the cubic ice (I_c) during freezing. The ice growing rate and the structure of ice crystals vary with temperature as well. Like any other invasion/retreat processes of non-wetting phases in porous materials, hysteresis can be observed after one freeze-thaw cycle. This can be due to the contact angle difference between freezing and melting, pore curvature-induced metastability of the solid phase and the connectivity and/or "ink-bottle" structure of pores. The Gibbs free energy based principles were recalled to describe the widely observed bulk supercooling phenomenon for porous materials during freezing. The mean ice nucleation temperature varies from -8℃ to -17℃ and the contact angle varies from 25° to 20° when salt concentration increases from zero to 15 wt%. For cement pastes with pore size around 10 nm, the general bulk supercooling temperature is estimated to be 3.4∼11 K lower than the bulk melting temperature.

In chapter 3, both the phenomenology and proposed mechanisms of freeze-thaw deterioration of cement-based materials were reviewed. Basically, the internal cracking and surface scaling are the main deterioration patterns observed in both laboratory tests and on-site practice. From the work by Powers and co-workers, the internal cracking can be attributed to the hydraulic pressure induced by the viscous flow of water when ice forms. Later, as a supplementary model to account for the effect of deicing salts, the osmotic pressure hypothesis, was proposed by Helmuth and Powers. The local thermodynamic and mechanical equilibria of ice crystals and water lead to additional pore pressure, the so-called crystallization pressure. In addition, the local thermodynamic inequilibium governs the transport behaviors of water and

vapor, which is the principle of the so-called micro-ice-lens theory. In practice, a critical saturation degree in the range of about 0.7-0.9 for porous materials, rather than the 0.91 required by hydraulic pressure, was observed. The water uptake during freeze-thaw cycles as well as a low-cycle fatigue mechanism can be responsible for this phenomenon according to Fargelund. For salt scaling, the glue-spalling theory that is based on the discrepancy between thermal expansion coefficient of the ice and that of solid cement-based materials, was proposed by Valenza and Scherer. With the help of the comprehensive poromechanical work by Oliver Coussy and co-workers, the strains and the pore pressure of cement-based materials subjected to freezing can be clearly described mathematically. The entrained air voids provide with the negative liquid pressure in capillary pores acting as a cryosuction that drive the water to ice at the interface of air voids, which leads to additional contraction as observed in experiments.

Following the thermoporoelasticity, in chapter 4, we develop a poromechanical model to describe the partially frozen cement-based porous materials. We define the scope, phases and representative volume element adapted for the poromechanical descriptions in the present study firstly. By using the hypothesis of infinitesimal transformations and displacements, small variation of density of each phase, and recapitulating the state equations of unsaturated porous materials, we obtained the constitutive equations for describing the deformations of solid and pores. In addition, the mass conservation and heat transport equations are established to complete the model.

Then, in chapter 5, analysis on cement-based materials saturated with water has been performed and compared with experimental results in literature. Good agreement between the predicted curves and the measured curves confirms the robustness of the present poromechanical model. The negative liquid pressure accounts for the continual shrinkage after ice nucleation for air-entrained cement paste, and the pore pressure relaxation accounts for the slight shrinkage when temperature is kept constant. For the cement paste without air entrainment, the pore pressure can be built up rapidly when water crystallizes. In addition, the instantaneous deformation when ice suddenly nucleates at certain bulk supercooling, has been studied and compared to the data in literature. To follow the required thermodynamic equilibrium and to take account of the supercooling effect, the temperature is set to be constant at first, and then rapidly cooled down to the prescribed supercooled temperature. The predicted results indicated that the instantaneous deformation at the end of supercooling can be due to the immediate ice formation and the temperature shift (thermal shock) by heat release when ice forms.

Chapter 2

Ice formation in porous materials

Contents

2.1 Thermodynamic equilibrium between ice and water

Let us first consider the state of ice and aqueous solution in porous materials. Here we do not consider the possible dissolution/precipitation of solute from/to the solid matrix of cement hydrates, and any other possible related chemical processes. Let μ_w and μ_c denote the chemical potential of liquid water (solvent of the liquid solution) and the ice crystals. They can be expressed as [24],

$$\mu_w(T, P_l, a_w) = \mu_w^{\ominus}(T, P_l) + RT \ln a_w, \tag{2.1a}$$

$$\mu_c(T, P_c, a_c) = \mu_c^{\ominus}(T, P_c) + RT \ln a_c \tag{2.1b}$$

where $\mu_w^{\ominus}(T, P_l)$ and $\mu_c^{\ominus}(T, P_c)$ are the chemical potential of pure water and ice crystals, respectively. T is the current temperature; P_l and P_c are the pressure of liquid solution and ice; a_w is the activity of the water in the electrolyte solution that is related to the temperature, pressure and the solute concentrations c; a_c is the activity of the solid solvent, since the formed ice is in bulk phase, $a_c = 1$. Adopting the atmospheric pressure ($P_0 = 0.1$MPa) and the corresponding freezing point $T_0 = 273.15$K as the common reference states, $\mu_w^{\ominus}(T, P_l)$ and $\mu_c^{\ominus}(T, P_c)$ can be expressed as,

$$\mu_w^{\ominus} = \mu_w^{\ominus}(T_0, P_0) - \int_{T_0}^{T} \mathsf{S}_w \mathrm{d}T + \int_{P_0}^{P_l} \mathsf{V}_w \mathrm{d}P, \tag{2.2a}$$

$$\mu_c^{\ominus} = \mu_c^{\ominus}(T_0, P_0) - \int_{T_0}^{T} \mathsf{S}_c \mathrm{d}T + \int_{P_0}^{P_c} \mathsf{V}_c \mathrm{d}P \tag{2.2b}$$

where $\mu_w^{\ominus}(T_0, P_0)$ and $\mu_c^{\ominus}(T_0, P_0)$ are the chemical potential of pure water and ice in the reference equilibrium state; S_w and S_c are molar entropy of liquid water and ice crystals (in $\mathrm{J \cdot mol^{-1} \cdot K^{-1}}$), and V_w and V_c are molar volume of liquid water and ice crystals (in $\mathrm{m^3 \cdot mol^{-1}}$). It should be noted that the used molar volume and molar entropy of water are not the partial molar quantities but the apparent molar quantities used in Archer's model [15, 16], see also the definitions in section 4.1.5. Generally, the molar entropy and molar volume of ice (water in solution), depend on the temperature and pressure (and salt concentration for water, see Appendix D for detail). The necessary but not sufficient condition for ice formation is that the chemical potential of ice crystals is equal to or lower than that of liquid water. Although the metastable condition of water, i.e., bulk supercooled water, can be observed ubiquitously either naturally or artificially [372, 427], we here only consider the thermodynamic equilibrium case, which requires,

$$\mu_w(T, P_l, a_w) = \mu_c(T, P_c), \quad \text{and} \quad \mu_w^{\ominus}(T_0, P_0) = \mu_c^{\ominus}(T_0, P_0) \tag{2.3}$$

Combining the equations above mentioned and considering further that the molar volume of water and ice are constant, one thus obtains the relation:

$$RT \ln a_w = -\Delta G_{fus}\big|_{T_0}^{T} - \mathsf{V}_w(P_l - P_0) + \mathsf{V}_c(P_c - P_0) \quad \text{with} \quad \Delta G_{fus}\big|_{T_0}^{T} = -\int_{T_0}^{T} (\mathsf{S}_w - \mathsf{S}_c)\mathrm{d}T \tag{2.4}$$

where ΔG_{fus} is the Gibbs energy of fusion at reference pressure P_0 . According to the Gibbs-Helmholtz equation [134], the Gibbs fusion energy can be expressed as:

$$\frac{\partial}{\partial T}\left(\frac{\Delta G_{fus}}{T}\right) = -\frac{\Delta H_{fus}}{T^2} \rightarrow \Delta G_{fus}\big|_{T_0}^{T} = -T\int_{T_0}^{T} \frac{\Delta H_{fus}}{T^2}\mathrm{d}T \quad \text{at} \quad P = P_0 \tag{2.5}$$

where ΔH_{fus} denotes the enthalpy change of fusion at current lowered freezing temperature T, and it is related to the heat capacity change of fusion:

$$\Delta H_{fus} = \Delta H^{\circ}_{fus} + \int_{T_0}^{T} \mathsf{C}_f \mathrm{d}T, \quad \text{with} \quad \Delta H^{\circ}_{fus} = \mathsf{S}_f T_0 = (\mathsf{S}^{\circ}_w - \mathsf{S}^{\circ}_c) T_0 \tag{2.6}$$

where ΔH°_{fus} is the enthalpy change of fusion of ice at bulk melting temperature T_0; C_f is the difference of heat capacity between the liquid and solid phases at lowered temperature T, i.e, $\mathsf{C}_f = \mathsf{C}_{P,w} - \mathsf{C}_{P,c}$; S_f is defined as molar fusion entropy (in $\mathrm{J \cdot K^{-1} \cdot mol^{-1}}$). Taking here $\mathsf{C}_{P,\alpha}$ as constant (see section 8.1 for its dependence on the variables of temperature, pressure and salt concentration), the molar entropy of water and ice, $\mathsf{S}_{w,c}$, can be expressed to be function of temperature [114]:

$$\mathsf{S}_w = \mathsf{S}^{\circ}_w + \mathsf{C}_{P,w} \ln\left(\frac{T}{T_0}\right); \quad \text{and} \quad \mathsf{S}_c = \mathsf{S}^{\circ}_c + \mathsf{C}_{P,c} \ln\left(\frac{T}{T_0}\right) \tag{2.7}$$

In case of freezing of pure water, the term at the left side of eq(2.4) denoting the effect of water activity is

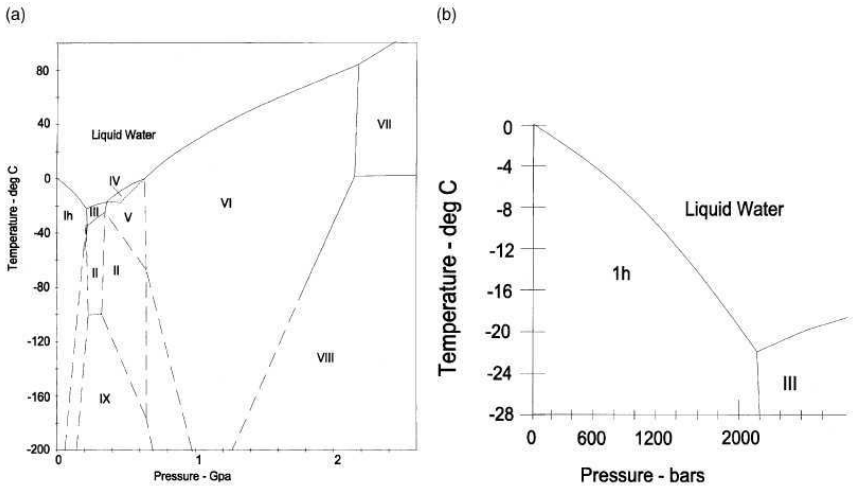

Figure 2.1: The phase diagram of ice and water (a) and local magnification under normal loading conditions (b). After Akyurt et al. (2002) [9].

zero. With further assuming that $P_c = P_l = P$ for water, then eq(2.4) reduces to a Clapeyron-like relation between temperature and pressure:

$$T \int_{T_0}^{T} \frac{\Delta H_{fus}}{T^2} \mathrm{d}T = -\Delta \mathsf{V}_{wc}(P - P_0) \tag{2.8}$$

where $\Delta \mathsf{V}_{wc}$ is the molar volume difference between ice and water, i.e., $\Delta \mathsf{V}_{wc} = \mathsf{V}_c - \mathsf{V}_w = \mathsf{M}_w \cdot (1/\rho_c - 1/\rho_w)$. This allows for plotting the boundaries of water-ice phase diagram. Figure 2.1(a) shows the phase diagram of water and ice in different crystal structures. The magnified phase diagram of water and ice (Ih and III)

is illustrated in Figure 2.1(b). Contrary to other usual liquids, the density of ice is lower than that of liquid water, viz. $\rho_c = 917(\mathrm{kg}\cdot\mathrm{m}^{-3}) < \rho_w = 997(\mathrm{kg}\cdot\mathrm{m}^{-3})$, thus the increment of pressure causes the depression of freezing/melting temperature, as shown in Figure 2.1(b).

2.1.1 Ice penetration

In this section, we follow the explanation in Ref. [341] of ice propagation in pores on the premise that water and ice are always in equilibrium. Recalling the equilibrium function, i.e, eq. (2.4),

$$-\Delta G_{fus}\big|_{T_0}^{T} + \mathsf{V}_c P_{cap} + \Delta \mathsf{V}_{wc}(P_l - P_0) - RT\ln a_w = 0 \tag{2.9}$$

where $P_{cap} = P_c - P_l$ denotes the capillary pressure. Substitution of the eq(2.6) in to eq(2.5), the Gibbs fusion energy is then given by:

$$\begin{aligned} -\Delta G_{fus}\big|_{T_0}^{T} &= T\int_{T_0}^{T}\frac{\Delta H_{fus}}{T^2}\mathrm{d}T = T\int_{T_0}^{T}\frac{1}{T^2}\left[\mathsf{S}_f T_0 + \mathsf{C}_f(T-T_0)\right]\mathrm{d}T \\ &= \mathsf{S}_f\left(T-T_0\right) + \mathsf{C}_f\left((T_0 - T) + T\ln\left(\frac{T}{T_0}\right)\right) \end{aligned} \tag{2.10}$$

In above equation, the term ΔG_{fus} has the same fusion energy form to that in Fabbri (eq(3.22) in [114]). Substitution of eq(2.10) into eq(2.9), one obtains:

$$P_{cap} = \left(\frac{\rho_c}{\rho_w} - 1\right)(P_l - P_0) + \frac{1}{\mathsf{V}_c}\left[RT\ln a_w + \mathsf{S}_f\left(T_0 - T\right) + \mathsf{C}_f\left((T - T_0) + T\ln\left(\frac{T_0}{T}\right)\right)\right] \tag{2.11}$$

If the equations are expressed on the unit of mass (see [76, 77, 82, 114]), rather than on the unit of mole, the capillary pressure can be expressed in the equivalent form:

$$P_{cap} = \left(\frac{\rho_c}{\rho_w} - 1\right)(P_l - P_0) + \rho_c\left[\frac{1}{\mathsf{M}_w}RT\ln a_w + \mathcal{S}_f\left(T_0 - T\right) + C_f\left((T - T_0) + T\ln\left(\frac{T_0}{T}\right)\right)\right] \tag{2.12}$$

with $\mathsf{S}_f = \mathcal{S}_f\cdot\mathsf{M}_w$ and $\mathsf{C}_f = C_f\cdot\mathsf{M}_w$. $\mathcal{S}_f$ (in $\mathrm{J}\cdot\mathrm{K}^{-1}\cdot\mathrm{kg}^{-1}$) and C_f (in $\mathrm{J}\cdot\mathrm{K}^{-1}\cdot\mathrm{kg}^{-1}$) are the fusion entropy and fusion heat capacity when one unit mass of ice transfers to water.

The capillary pressure P_{cap}, as a result of local mechanical equilibrium, is given by Young-Laplace equation:

$$P_{cap} = \frac{2\gamma_{cl}\cos\theta}{r - \delta} \tag{2.13}$$

where γ_{cl} is the surface tension between crystals and liquid (in $\mathrm{N}\cdot\mathrm{m}^{-1}$), θ is the contact angle, r is the pore radius, δ is the thickness of unfrozen layer, see section 2.5 for detail.

Substitution of Young-Laplace equation into eq(2.9), with the rough assumptions that $P_l = P_0$, the size

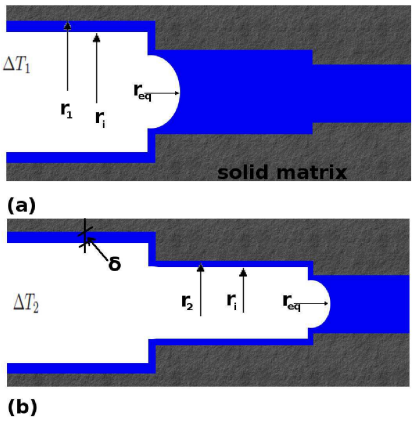

Figure 2.2: Schematic illustration of ice penetration along cylindrical pores. (a), Ice forms first in big pores, i.e., in pores with radius $r = r_1$; (b), as temperature decreases ice penetrates to smaller pores $r = r_2$. r_{eq} is the radius of ice tips that are equilibrium with water in small pore in vicinity. The interface layer (liquid like layer) thickness between solid matrix and ice δ relates to depressed freezing temperature ΔT.

of ice r_{eq} then can be expressed as:

$$r_{eq} = r - \delta = \frac{2\gamma_{cl}\cos\theta \mathsf{V}_c}{RT\ln a_w + \Delta G_{fus}} \tag{2.14}$$

In case that pore liquid is pure water, viz. $\ln a_w = 0$, and with assumption that, $-\Delta G_{fus} \approx \mathsf{S}_f(T - T_0) = \mathcal{S}_f(T - T_0)\cdot \mathsf{M}_w$, the eq(2.14) reduces to the classic Gibbs-Thomson equation:

$$\Delta T = T_0 - T = -\frac{2\gamma_{cl}\cos\theta \mathsf{V}_c}{\mathsf{S}_f r_{eq}} = -\frac{2\gamma_{cl}\cos\theta}{\rho_c \mathcal{S}_f r_{eq}} \tag{2.15}$$

To represent the ice formation processes in pores, we follow the classic Gibbs-Thomson equation given in eq(2.15) as adopted in [77, 257, 342, 381]. At the beginning of freezing, ice forms in big pores at temperature T_0. With decrease of temperature, ice penetrates into smaller pores as illustrated in Figure 2.2 schematically. In big pore r_1, the required depression temperature should be ΔT_1. As the depression temperature increases, the radius of ice tip r_{eq} decreases and ice penetrates into thinner pores until it matches the size of thinner pores, accordingly, the depression temperature should be ΔT_2 as illustrated in Figure 2.2. More detailed discussions on the ice penetration can be found elsewhere, cf. [226, 380, 451]. It also illustrates the liquid like layer between the ice crystals and the wall of solid in Figure 2.2, which is discussed in detail in section 2.5, and the related contents can be found in Refs. [89, 102].

2.1.2 Crystal structure of ice in pores

The water confined in porous materials is generally classified in two sorts: the free water (freezable water) in middle of pores and bound water (unfrozen water) adjacent to pore wall. Both the freezing and melting points of free pore water are lower than those of bulk water, which in known as the capillary supercooling. The structure of water and/or ice confined in pores is still unclear. Numerous researches indicate that the freezing of free water in small pores gives rise to the metastable cubic ice (I_c) instead of

Table 2.1: Basic physical parameters for the hexagonal ice I_h (a) and the cubic ice I_c. After Fletcher (1971) [125].

polymorph	density	Crystal system	Space group	Molecules per cell	cell dimensions($\AA$)
I_h	0.92	Hexagonal	$P6_3/mmc$	4	$a = 4.48$, $c = 7.31$
I_c	0.92	Cubic	Fd3m	8	$a = 6.35$

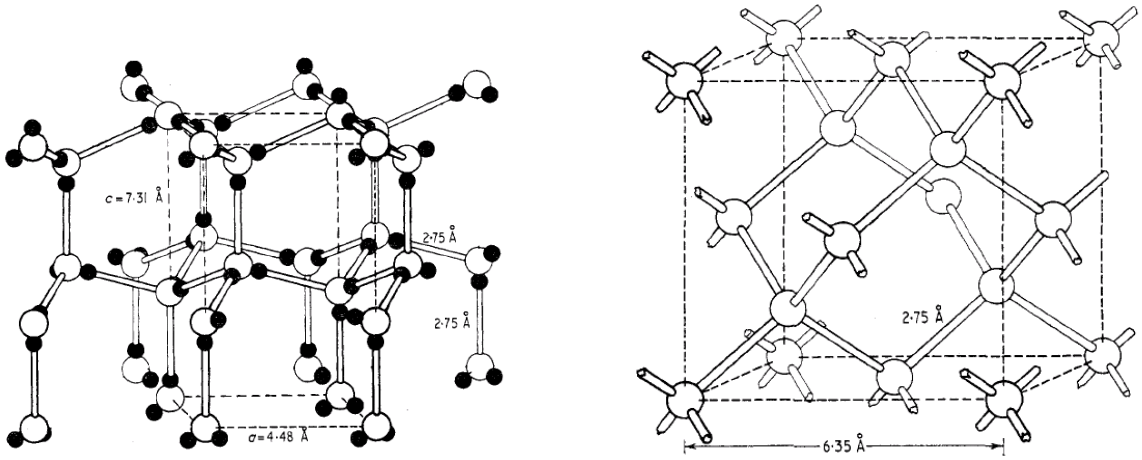

(a) (b)

Figure 2.3: The crystal structure and unit cell for the hexagonal ice I_h (a) and the cubic ice I_c (b). After Fletcher (1971) [125].

the ordinary hexagonal ice (I_h) [38, 106, 259, 374, 375, 384]. As observed by Dunn et al. [106], for porous silica, both I_c and I_h coexist at the beginning of freezing, and the amount of I_h increases significantly as temperature decreases. It is believed that the interactions between the surface of silica and water, mainly induced by van der Waals force, can be the main reason for I_c formation instead of I_h [38] in small pores. Furthermore, some researches indicated that it is much more stable for ice to nucleate in cubic structure than in hexagonal structure in fine pore space [20, 123, 375]. I_c has similar structure and properties as I_h, see Figure 2.3 and Table 2.1 [125]. The lattice energy difference between I_h and I_c approximates 5%, and it remains unclear why the hexagonal form should be more stable than the cubic form for bulk ice [375]. The rate of transferring from I_c to I_h is very slow. However, it has been reported that this transferring becomes easier at vicinity of melting point, which may be due to the factor that the molecular distances increase mear melting point [38, 383]. Johari [181] found that $\approx$ 15nm radius for droplet and $\approx$ 10nm thickness of flat film might be the critical size. When smaller than the critical size, water forms cubic ice rather than hexagonal ice during freezing.

For water confined in cement-based material, it freezes in the hexagonal structure generally [121, 349]. This may be due to the reason that the rough surface of solid skeleton acts as the nucleation agent and the temperature in conventional atmospheric environments for cold regions can be rarely down to 230 K. Note that even for the ordinary hexagonal ice, the macro crystals appear in different structures at different temperature, see Table 2.2 [333].

Table 2.2: Variation of crystal structures of ice with temperature [333].

Temperature range	Form of ice crystal
$0 \sim -3$℃	Thin hexagonal plates
$-3 \sim -5$℃	Needles
$-5 \sim -8$℃	Hollow prisms
$-8 \sim -12$℃	Hexagonal plates
$-12 \sim -16$℃	Dentritic crystals
$-16 \sim -25$℃	Plates
$-25 \sim -50$℃	Hollow prisms

2.2 Effect of salt

The activity coefficient determines the deviation from the ideality of a solution [24]. This deviation may become more or less dependent on the magnitude of interactions between ions. The chemical activity of the solution is related to two types of interactions: ion-ion interactions and ion-solvent interactions, cf. Pitzer [301], and Robinson and Stokes [326]. The sources for these interactions can be:

❶, Electrostatic interactions which depend on the distance that separates two molecules; Electrostatic interactions are the main cause of non-ideality of solutions;
❷, Relaxation which is due to the ionic atmosphere deformation in presence of a difference in local potential;
❸, Ion-solvent interactions (electrophoresis) which can be due to the disruption of the forces of friction caused by clusters of solvent molecules attached to the ion cloud;
❹, Solvation interactions which can be due to the energy decrease of ions when salts are introduced into the water;
❺, Association of ions in solution, which can be due to the ionic escape from the hydrated pairs or triplets.

The overall effect of these interactions is constated as an activity coefficient. It is very difficult to propose a mathematical model to quantify these phenomena. The chemists have often worked in an empirical way: setting up hypotheses, and establishing equations and then comparing the results obtained with the experimental results. The activity coefficients steming from the preceding phenomena are very complex. Several semi-empirical models have been developed to predict the chemical activity of a species ion in solution, among which the Pitzer's model and relevant models [301, 302] are most widely used.

2.2.1 Activity of ions

The first comprehensive semi-empirical model on describing the ion activity solutions that has been extensively quoted and developed was proposed by Debye and Hückel [94]. The principle of their theory starts from the assumption that departure from non-ideality is due to electrostatic interactions between ions, associated Coulomb's law and the relatively small electrical potential fluctuations. This model can calculate the activity of single electrolytes. It is very relevant, but its applications are limited because it applies only to solutions of very low ionic concentration. In fact, during the establishment of Debye-Hückel law, integration of energy by electrostatic forces requires the same approach distance for all ions, which

does not correspond to reality. It is thus an empirical correction that allows the Debye-Hückel law to extend to concentrated solutions.

When the solutions are concentrated, short-range interactions become more significant and the law of Debye- Hückel and the extended models can not take into account all the actions, which means these models are not adapted to the case of brines. Pitzer [302] has, meanwhile, proposed an empirical equation that best describes the behavior of electrolytes. This model takes the additional terms to account for short-range forces given by the actions between two or three ions and allows to calculate not only the activity coefficient of a solute simple but also much of the solutes complex. Based on the Pitzers model, Lin and Lee [217] proposed a semi-empirical model to calculate activity using two adjustable parameters with relative simple expressions and good accuracy. At the same period, Khoshkbarchi and Vera proposed a semi-empirical model with three adjustable parameters [193, 194]. The predicted values of activity for individual ions are well consistent with experimental results to high ionic strength as well. Also, there exist numerous semi-empirical models derived from Debye-Hückel law with consideration of the the short range effect, cf. model proposed by Zhao et al. [445], Papaiconomou et al. [279] and Pazuki and Rohani [281].

Table 2.3: The semi-empirical expressions of long range and short range effects for ionic activity calculation.

Long range effect	Short range effect	Authors	References
$-A_\phi z_i^2 \left[\frac{I^{1/2}}{1+B_i I^{1/2}} + \frac{2}{B_i}\ln(1+B_i I^{1/2})\right]$	$\frac{C_i z_i^2 I^a}{T}$	Lin and Li[a]	[216, 217]
$\frac{-A_x z_i^2 I_x^{1/2}}{1+\rho I_x^{1/2}} + \frac{B_i I_x^{3/2}}{1+\rho I_x^{1/2}}$	$C_i \ln\left(1+\rho I_x^{2/3}\right)$	Khoshkbarchi and Vera[b]	[193, 194]
$\frac{-A_\phi z_i^2 I^{1/2}}{1+B_i I^{1/2}}$	$C_i I$	Pitzer and coworkers	[300–302]
$\frac{-A_\phi z_i^2 I^{1/2}}{1+B_i I^{1/2}}$	$\frac{C_i z_i^2 I^a}{T}$	Pazuki and Rohani	[281]

[a] A_ϕ and I are the Debye-Hückel constant and the ionic strength on concentration base respectively, B_i and C_i are the adjustable parameters, $\rho = 9$ and $a = 1.29$;
[b] A_x and I_x are the Debye-Hückel constant and the ionic strength on molar fraction base respectively.

Table 2.4: Parameters required by the selected semi-empirical models for the activity coefficient of individual ion for single electrolyte solution at 25℃.

Electrolyte	Ion	Lin & Lee		Pitzer		Khoshkbarchi & Vera		Pazuki & Rohani		Reference
		B_i	C_i	B_i	C_i	B_i	C_i	B_i	C_i	
NaCl	Na^+	4.352	26.448	95.891	0.557	95.891	0.577	3.627	28.265	[193]
	Cl^-	1.827	19.245	60.973	-0.409	60.973	-0.409	0.676	12.958	[193]
KCl	K^+	1.243	13.296	45.877	-0.293	45.877	-0.29	0.807	9.883	[193]
	Cl^-	3.235	11.158	16.791	0.221	16.791	0.221	1.737	6.692	[193]
NaOH	Na^+	0.971	59.306	299.712	0.671	299.712	0.671	3.963	95.763	[327]
	OH^-	6.052	15.685	-120.072	-0.481	-120.072	-0.481	0.506	30.460	[327]
KOH	K^+	0.002	36.479	90.248	-0.054	90.248	-0.054	1.148	25.206	[327]
	OH^-	22.347	159.038	257.028	0.241	257.028	0.241	1.903	75.406	[327]

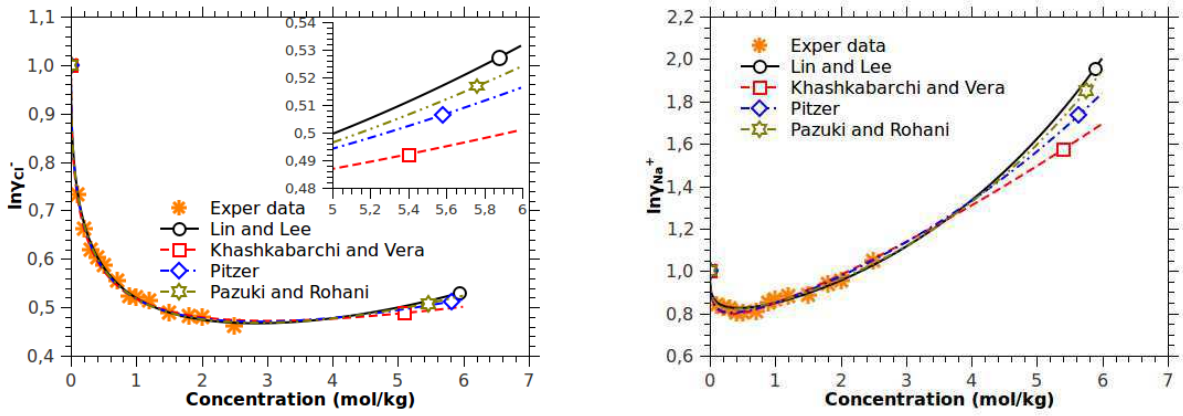

(a) (b)

Figure 2.4: Individual activity coefficients of chloride (a) and sodium (b) ions in aqueous NaCl solution predicted by models of Lin and Lee [216, 217], Khoshkbarch and Vera [193, 194], Pitzer [301, 302], and Pozuki and Rohani [281]. Experimental data is adopted from Khoshkbarchi and Vera [194].

These proposed semi-empirical models can be schematically expressed in the form:

$$\ln \gamma_i = \text{long range effect} + \text{short range effect} \tag{2.16}$$

Table 2.3 shows the selected semi-empirical expressions for long range and short range effects of ionic activities [193, 194, 216, 217, 281, 300–302]. The adjustable parameters (B_i and C_i) for common solution (NaCl, KCl, NaOH and KOH) are presented in Table 2.4. The calculated individual activity coefficients of chloride and sodium ions are shown in Figure 2.4. Compared to the experimental data, all the selected models can predict the individual ionic activity coefficients very well., see Appendix A.1 for detailed derivations.

2.2.2 Water activity and osmotic coefficient

The osmotic coefficient is defined as a quantity which characterizes the deviation of a solvent from ideal behavior. Based on the Gibbs-Duhem equation for an aqueous solution, the osmotic coefficient can be obtained as [216, 217]:

$$\Pi = 1 + \sum_i x_i \ln \gamma_i - \sum_i x_i \frac{1}{I} \int_0^I \ln \gamma_i dI \tag{2.17}$$

where x_i is the molar fraction defined as $x_i = m_i/m_T$, with m_i the molar concentration of species i (in $\text{mol} \cdot \text{kg}^{-1}$) and $m_T = \sum m_i$. By substitution of the expressions of the ionic activity coefficient $\ln \gamma_i$ (see Table 2.3) into eq(2.17), the osmotic coefficient derived from the selected semi-empirical models then can

be presented as (see Appendix A.2 for derivation details):

$$\Pi = 1 - A_\phi \sum_i x_i z_i^2 \frac{I^{1/2}}{1 + B_i I^{1/2}} + \frac{a I^a}{(1+a)T} \sum_i x_i z_i^2 C_i, \quad \text{Lin\&Lee} \tag{2.18a}$$

$$\begin{aligned}\Pi = 1 &+ \frac{I^{1/2}}{1+\rho I^{1/2}} \left(-A \sum_i x_i z_i^2 + I \sum_i x_i B_i \right) + \ln(1+\rho I^{1/2}) \sum_i x_i C_i + \frac{A}{I\rho^3} \left(\rho^2 I + 2\ln(1+\rho I^{1/2}) - 2\rho I^{1/2} \right) \sum_i x_i z_i^2 \\ &- \frac{1}{\rho^5 I} \left[2\ln(1+\rho I^{1/2}) - 2\rho I^{1/2} + \rho^2 I - \frac{2}{3}\rho^3 I^{3/2} + \frac{\rho^4}{2} I^2 \right] \sum_i x_i B_i \\ &- \left[\ln\left(1+\rho I^{2/3}\right) - \frac{2\tan^{-1}(\rho^{1/2} I^{1/3})}{I\rho^{3/2}} + \frac{2}{\rho I^{2/3}} - \frac{2}{3} \right] \sum_i x_i C_i, \quad \text{Khoshkbarchi \& Vera}\end{aligned} \tag{2.18b}$$

$$\Pi = 1 - A I^{1/2} \sum_i \left(\frac{x_i z_i^2}{1 + B_i I^{1/2}} \right) + \sum_i C_i x_i I - \frac{I}{2} \sum_i x_i C_i + A \sum_i \left[\frac{x_i z_i^2}{B_i} \left(1 - \frac{2}{B_i I^{1/2}} + \frac{2\ln(1 + B_i I^{1/2})}{B_i^2 I} \right) \right], \quad \text{Pitzer} \tag{2.18c}$$

$$\begin{aligned}\Pi = 1 &- A I^{1/2} \sum_i \left(\frac{x_i z_i^2}{1 + B_i I^{1/2}} \right) + \frac{I^a}{T} \sum_i x_i C_i z_i^2 \\ &+ A \sum_i \left[\frac{x_i z_i^2}{B_i} \left(1 - \frac{2}{B_i I^{1/2}} + \frac{2}{B_i^2 I} \ln(1 + B_i I^{1/2}) \right) \right] - \frac{I^a}{(1+a)T} \sum_i x_i C_i, \quad \text{Pazuki\&Rohani}\end{aligned} \tag{2.18d}$$

The water activity is related to the osmotic coefficient by the formula [216, 217]:

$$\ln a_w = -\frac{m_t \mathsf{M}_w}{1000} \Pi \tag{2.19}$$

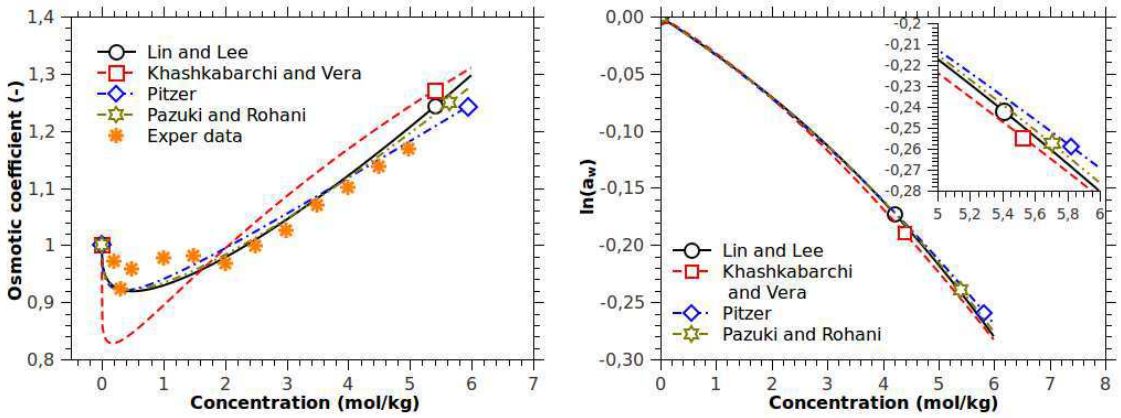

(a) (b)

Figure 2.5: Calculated osmotic coefficient Π (a) and logarithm value of water activity $\ln a_w$ (b) in terms of the NaCl concentrations by models of Lin and Lee [216, 217], Khoshkbarch and Vera [193, 194], Pitzer [301, 302], and Pozuki and Rohani [281]. Experimental data is adopted from Guendouzi et al. [147].

Figure 2.5(a) shows the variation of calculated osmotic coefficient Π of NaCl solution with the NaCl concentration. It can be found that those values are well consistent with the experimental results when the models of Lin and Lee [216, 217], Pitzer [300–302] and Pozuki and Rohani [281] are used. Whereas the values calculated by model of Khoshkbarchi and Vera [193, 194] show more differences than the other

models. However, the logarithm values of water activity, calculated by all models, show no significant differences, see Figure 2.5(b). In the present work, we choose the Lin and Lee's model, because it has relative simple expressions for both the individual ionic activity and the water activity.

2.3 Freeze-thaw hysteresis

2.3.1 Introduction to freeze-thaw hysteresis

The freeze-thaw hysteresis has been widely observed for porous materials [188, 308, 310, 380]. Analogous to the other observed hysteresis, cf. wetting-drying, gas adsorption-desorption and mercury intrusion-extrusion in porous materials, there are several mechanisms responsible for these behaviors. It is believed that the contact angle between ice crystals and pore wall contributes, not mainly but to some extent, to the freeze-thaw hysteresis [145]. This mechanism lies on that the contact angle during freezing is larger than that during thawing, so that the depressed freezing temperature is lower than the depressed melting temperature. The energy barrier between ice crystals and liquid water might be another source for the phenomena of supercooling and superheating [369]. This concept is, physically, similar to the earlier approach for gas adsorption-desorption hysteresis by Broekhoff and de Boer [52]. The energy barrier between small liquid droplets and the unfrozen surface layer has been verified in Ref. [413]. For liquid confined in very thin pore, i.e., the micro-pores [1], the energy barrier is not significant, therefore, the freeze-thaw hysteresis is not significant either. This has been verified from the experimental observations by Morishige and Kawano [259] and Schreiber et al. [346]. Morishige and Kawano [259] performed X-ray diffraction measurements of water confined inside the cylindrical pores of silica with different pore radii (1.2-2.9) nm and the interconnected pores of Vycor glass as a function of temperature. The results indicated that the hysteresis depends markedly on the size of the cylindrical pores: the hysteresis is negligibly small in smaller pores and becomes remarkable in larger pores. This phenomenon also has been verified by replacing water with methanol as pore liquid [260]. According to the Gibbs energy based theory, water does not crystallize spontaneously due to the energy barrier of creating stable ice embryos [53, 402]. However, once temperature depresses to -40℃ (233K), the thermal agitation energy of water equals to the required energy barrier, the freeze-thaw hysteresis disappears [259]. Under commonly encountered conditions, Petrov and Furo [288] stated that the freeze-thaw hysteresis can be readily explained by different paths along which solid-liquid interface propagates during freezing and thawing. Within the approach by Petrov and Furo [288] that was developed from the model proposed by Denoyel and Pellenq [97], the hysteresis is caused

1. According to IUPAC [439] notation, micropores have width of less than 2 nm, mesopores have width between 2 nm and 50 nm and macropes have width of greater than 50 nm. This classification of pore size is used in this study except specific notation.

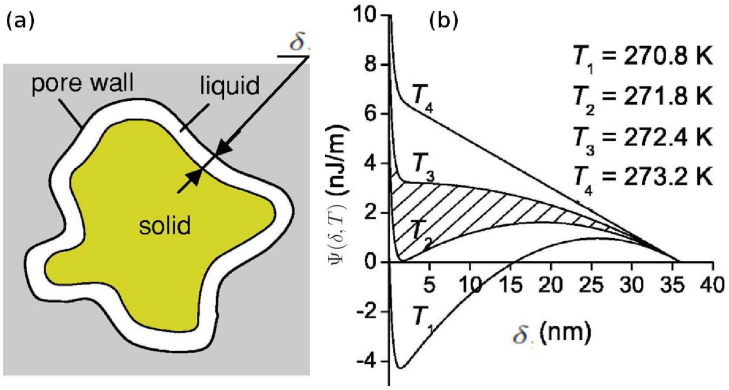

Figure 2.6: (a), Cross-sectional view of a pore filled by a solid core and a liquid layer of uniform width δ; (b) The free energy of water for a unit length of a cylindrical pore of 36 nm radius as function of thickness δ and temperature T, as provided by eq (2.20) with $\gamma_{lc} = 30$ mJ/ m^2 and $\xi = 0.4$ nm (roughly two molecules thick). The metastable region providing the freezing-melting hysteresis is hatched. After Petrov and Furo (2006) [288].

by pore curvature-induced metastability of the solid phase and, thereby, is an intrinsic property of the system defined by the pore morphology and the interfacial interactions. Those coincide with the concepts or approaches by other researchers [97, 259, 383]. In addition to the physical chemistry characteristics of processes of water-ice transferring, the characteristics of pore structure contribute largely to the freeze-thaw hysteresis as well, which will be introduced in section 2.3.3. This concept was also applied to explain the behaviors of capillary condensation/evaporation in cylindrical mesopores [282].

2.3.2 Effect of pore curvature

The Helmholtz free energy of a partial frozen porous system (cf. Figure 2.6(a)) can be expressed as a function of the thickness of unfrozen layer or the distance away from the pore wall, δ, as follows [288]:

$$\Psi(\delta, T) = \frac{\Delta H_{fus}}{\mathsf{V}_c} \frac{T - T_0}{T_0} V_c + \gamma_{lc} A_c + \Delta\gamma A \exp(-2\delta/\xi) \tag{2.20}$$

where T_0 is the bulk freezing/melting temperature at $P = P_0$, ΔH_{fus} is the latent heat (enthalpy) of fusion, V_c is the molar volume of ice , V_c is the volume of ice in this system, A_c is the surface area of ice crystals, A is the surface area of pore wall, γ_{lc} is the interface energy between liquid water and ice crystals. $\Delta\gamma$ is defined as a excess free energy when a ice-wall interface is separated by a liquid phase that covers the solid wall and ice crystal (cf. Figure 2.6a), $\Delta\gamma = \gamma_{sc} - (\gamma_{lc} + \gamma_{ls})$. γ_{sc} is the interface energy between solid wall and ice crystals and γ_{ls} is the interface energy between liquid water and solid wall. The exponential term "$\exp(-2\delta/\xi)$" accounts for the short range ($\sim \xi$) surface-induced perturbation in the liquid [219].

The variation of Helmholtz free energy in form of eq(2.20) with thickness of liquid layer δ and tempera-

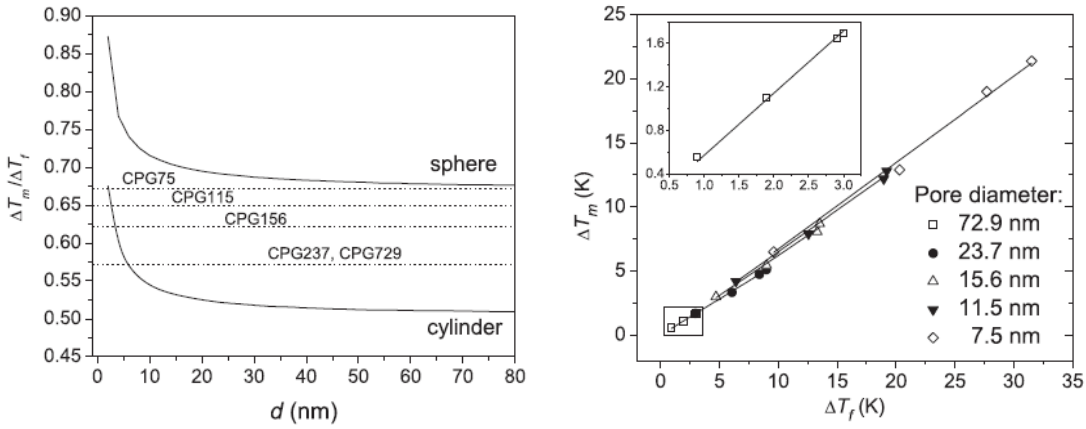

(a) (b)

Figure 2.7: (a), Theoretical ratio $\Delta T_m/\Delta T_f$ depends on the pore diameter for spherical and cylindrical geometry. The dashed lines indicate experimental ratios for different sized controlled pore glass (CPGs), the solid lines indicate the calculated ratios for cylindrical and spherical pores by eq(2.21) with $\xi = 0.4$nm; (b), Correlation between average values of ΔT_m and ΔT_f in different-sized CPGs. The straight lines with zero intercept have the slopes 0.67, 0.65, 0.62, 0.57 and 0.57 for CPG75, CPG115, CPG156, CPG237 and CPG729, respectively. The insert enlarges the data points for CPG729. The four points of $\Delta T_m/\Delta T_f$ for each CPG are determined with the pore liquid of water, benzene, cyclohexane and cyclooctane, which have the bulk melting temperature of 273.2K, 278.8K, 279.9K and 287K respectively at $P = 0.1$MPa. After Petrov and Furo (2010) [290].

ture T is illustrated in Figure 2.6(b). As shown in Figure 2.6(b), there are two minima at low temperature: one minimum at $\delta(\xi, T)$ near zero corresponds to a pore filled by ice crystals with a nonfreezing film induced by the short-range surface effect [97, 259, 282, 288, 383, 413], while the minimum $\delta = r$ to a pore filled by liquid, with r the pore radius. The liquid like film is a criterion for freeze-thaw hysteresis in Petrov and Furo's model [288]. In Figure 2.6(b), as the temperature increases from (T_1), Helmholtz free energy at first minimum increases. As temperature increases further to the solid-liquid equilibrium point T_2, the two corresponding minima of Helmholtz free energy are equally deep. A expected phenomenon that melting begins at $T = T_2$, would not be observed, because growing the liquid phase from the nonfreezing film at the pore wall requires to surmount the additional free energy. Accordingly, until the temperature approximates T_3, where thermal fluctuations are sufficient to surmount the energetic barrier, it will not start to melt. During cooling process, the temperature decreases from T_4, and the pore is filled by liquid initially. The freezing temperature depends on the two typical freezing patterns: (a) the solidification takes place in the presence of preexisting crystallites adjacent to the pore and (b) it nucleates at certain supercooling. The effect of supercooling and nucleation will be briefly reviewed in section 2.4. If there is no nucleation barrier, the material freezes at the equilibrium point $T_f = T_2$, where T_f stands for the freezing temperature of pore liquid. If there is nucleation barrier, it needs further cooling to overcome the nucleation barrier, thus $T_f < T_2$. Obviously, $T_2 < T_3 = T_m$ and $T_f < T_m$, where T_m stands for the melting temperature of pore

liquid at $P = P_0$. The freezing and melting depressed temperature, ΔT_f and ΔT_m respectively, can be given by [290]:

$$\Delta T_f = -\frac{\mathsf{V}_c \gamma_{lc} T_0}{\Delta H_{fus}} \frac{A_c + \xi A_c'}{V_c + \xi V_c'} \quad \text{and} \quad \Delta T_m = -\frac{\mathsf{V}_c \gamma_{lc} T_0}{\Delta H_{fus}} \frac{A_c' + \xi A_c''}{V_c' + \xi V_c''} \tag{2.21}$$

On condition that pore size is much larger than the thickness of unfrozen film, $r \gg \delta$, Petrov and Furo [288, 291] derived the expressions to estimate the depressed freezing and thawing temperature as:

$$\Delta T_f \approx -\frac{\mathsf{V}_c \gamma_{lc} T_0}{\Delta H_{fus}} \frac{A_c}{V_c} \quad \text{and} \quad \Delta T_m \approx -\frac{\mathsf{V}_c \gamma_{lc} T_0}{\Delta H_{fus}} \frac{\partial A_c}{\partial V_c} \tag{2.22}$$

Note that the eq(2.22) can be applicable to any particular pore geometry. For pores in convex geometry, the volume $V_c(\delta)$ enclosed by surface $A_c(\delta)$ can be expressed as a third order polynomial equation of thickness δ, which is known as the Steiner's formula [215]:

$$V_c(\delta) = V + A\delta + \kappa A\delta^2 + \frac{4}{3}\pi\delta^3 \quad \text{and} \quad A_c(\delta) = A + 2\kappa A\delta + 4\pi\delta^2 \tag{2.23}$$

where κ is the mean curvature, defined as: $\kappa = (1/2A)\int(1/r_1 + 1/r_2)dA$ with the principle radii of curvature r_1 and r_2. In large pore area, $r \gg \delta$, one can get the approximation, $V_c(\delta)/A_c(\delta) \approx V/A$ and $\partial A_c/\partial V_c \approx 2\kappa$. From eq(2.22) one obtains the relation between depressed freezing temperature ΔT_f and depressed melting temperature ΔT_m [288]:

$$\Delta T_m = \Delta T_f \frac{2\kappa V}{A} \tag{2.24}$$

For spherical pores, $V/A = 2r/3$ and $2\kappa V/A = 2/3$, while for cylindrical pores $V/A = r/2$ and $2\kappa V/A = 1/2$. Those values are different from the values by Brun et al. [53], who obtained the value of $\Delta T_m/\Delta T_f$ equal to 1/2 and 1 for cylindrical and spherical pores respectively. The ratios of depressed thawing temperature to depressed freezing temperature for spherical pores and cylindrical pores calculated by eq(2.21) are plotted in Figure 2.7(a), where the pore size of controlled pore glass (CPGs) determined by NMR cryoporometry are also presented [290]. The detailed correlation between average values of ΔT_m and ΔT_f in different-sized CPGs are illustrated in Figure 2.7(b). It can be found that the values of $2\kappa V/A$ for CPGs lie between the value 1/2 and 2/3. In addition, the smaller the pore size of CPGs, the closer the value of $\Delta T_m/\Delta T_f$ to 2/3. According to the Gibbs-based model or phenomenological model [97], the difference between the depressed freezing temperature and depressed melting temperature vanishes as pore size decreases further. The critical pore radius is estimated to be 1.2 nm. When the pore size lower than the critical value, $\Delta T_m/\Delta T_f$ reduces to 1 (see Figure for example 2.8). For droplets in size of about 5 μm, the average values of $\Delta T_m/\Delta T_f$ are in the range $0.5 \sim 0.588$, see Ref. [195] for detail. For mortar, the values of $\Delta T_m/\Delta T_f$ are systematically much lower than those for silica porous materials as studied by Sun and Scherer [381].

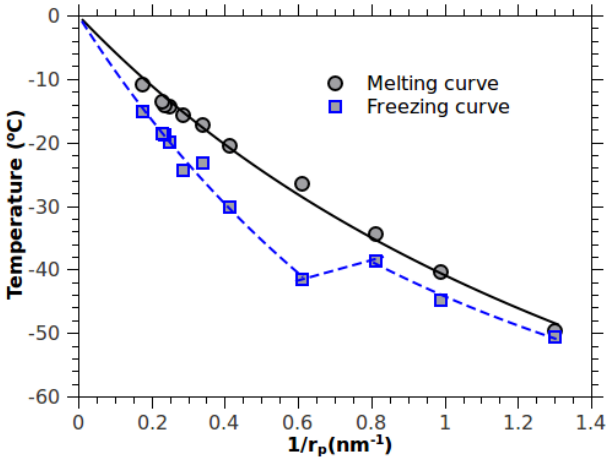

Figure 2.8: Determined freezing/melting temperature in terms of the inverse of pore size. The MCM-41 and SBA-15 porous materials, which have different pore sizes, are used. The freezing/melting temperature is determined by the differential scanning calorimetry (DSC). After Schreiber et al. (2001) [346].

In addition to the hemispherical interface penetration during freezing and cylindrical interface withdraw during melting, the reason of causing the values of $\Delta T_m/\Delta T_f$ to be under 1/2 in mortar samples is more likely to be pore blocking effects, according to Riikonen et al. [323, 324], see the followed section 2.3.3.

2.3.3 Effect of pore connectivity

The pore connectivity effect is also an important factor for freeze-thaw hysteresis. As illustrated in Figure 2.9, this factor that is described by Sun and Scherer [381] in a simplified model, shows a mechanism of hysteresis as well as an interpretation on the measurement of pore shape by means of differential scanning calorimetry (DSC) method. Assuming a pore model as shown in left side of Figure 2.9, where B and D have the same pore radius connected by thinner pore C. At first cooling, ice penetrates into pore A at the corresponding depressed temperature $-\Delta T_F^A$, the ice volume in pore A is represented by the length of vertical blue line at right side of Figure 2.9. When cooling to $-\Delta T_F^B$, the ice fullfills pore B, but does not penetrate to the smaller pore C. According to the Gibbs-Thomson equation, ice shall fill pore D at $-\Delta T_F^B$ under equilibrium. However, this can not happen unless the temperature is cooled enough to allow ice to enter pore C. At $-\Delta T_F^C$, the ice volume is the sum of ice volumes in both pore C and pore D, as represented as "C+D" in Figure 2.9. When the temperature is raised, the ice in pore C will melt first, at an subzero temperature of $-\Delta T_M^C = -\Delta T_F^C/2$ as first presented by Brun et al. [53] [2]. The melted ice volume is C in stead of $C + D$ during freezing. When the temperature rises to $-\Delta T_M^B = -\Delta T_M^D = -\Delta T_F^B/2$, ice in pores B and D will melt. The melted ice volume is sum of the space of pore B and D, represented by the length of red line at right side of Figure 2.9. As temperature increases further, the ice in pore A melts. Note that two different melting paths exist during melting, 1, the melting begins at ice side, 2, the melting begins at ice front. When the temperature is such that $\Delta T_M^B \geq \Delta T_F^A$ or $-\Delta T_M^B \leq -\Delta T_F^A$, ice melts

2. The ratios of $\Delta T_M/\Delta T_F^C = 0.5$ is used also by Sun and Scherer. Note that other constants can be used for this ratio for more accurate modification, an it will not change the mechanism of freeze-thaw hysteresis presented by Sun and Scherer [381].

from the side of cylinder pore A, otherwise, ice melts from the front between ice and water. The melting process from pore B to pore A is thus not shown in Figure 2.9 correctly. To sum up, the characteristics of pore connectivity lead to the freeze-thaw hysteresis in addition to the aforementioned contact angle effect and pore curvature-induced metastability of the solid phase. This feature also provides a method to determine the pore shapes or structures by performing DSC measurement in small temperature range for every freeze-thaw cycle. This method has been executed and extended for characterizing nano-porous materials and meso-porous materials [200, 290].

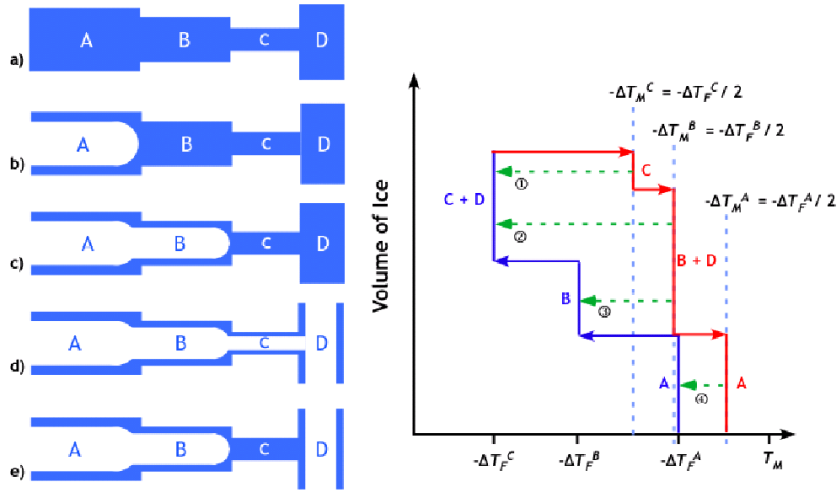

Figure 2.9: A simplified model for ice formation along cylindrical pores during freezing and withdrawal during thawing (left); The corresponding ice content at each equilibrium temperature (right). After Sun and Scherer [380].

2.4 Bulk supercooling and ice nucleation

2.4.1 Experimental evidence

As aforementioned, freezing of water confined in small pores, as stated by Petrov and Furo [288], depends on two different ways: ❶ ice homogeneously nucleates everywhere and grows spontaneously, and ❷ heterogeneously nucleates somewhere then penetrates into smaller pores until the required equilibrium between ice crystals and liquid water is achieved, see Figure 2.10. The different ice formation patterns, governed by different physic principles, can lead to different consequences. The homogeneous nucleation of ice is often companied with large supercooling due to the large surface energy barriers [341], which is widely observed during cooling of porous media. For instance, in Figure 2.11(a), the nucleation temperature of cement pastes saturated with NaCl solution is about 3.4-11 K lower than the freezing point of bulk solution. This has been observed elsewhere, see Figure 2.11(b). Figure 2.12 shows the temperature shift when ice

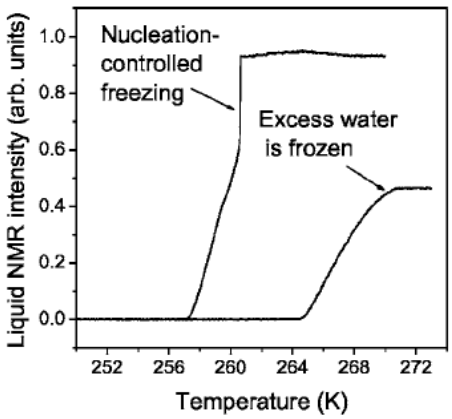

Figure 2.10: Illustration of changes in the liquid signal intensity in sized controlled pore glass in size of 23.7 nm (CPG237) filled with water with 100% excess to the pore volume, as recorded on cooling at a constant rate of 0.04 K/s. Upper curve: both confined and excess water are initially in the liquid state and freezing is nucleation controlled with corresponding supercooling. Lower curve: excess water is frozen, and therefore, no nucleation is required for the pore water to freeze. After Petrov and Furo (2006) [288].

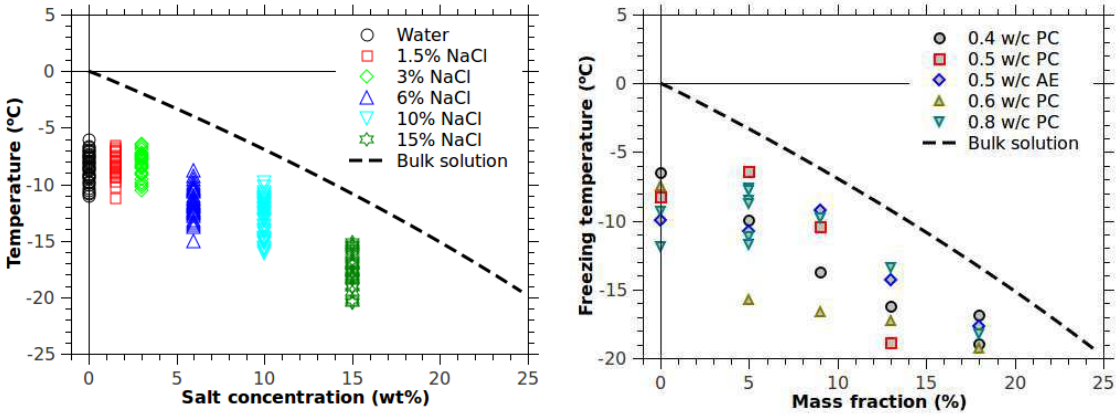

(a) (b)

Figure 2.11: (a), Measured ice nucleation temperature of cement paste saturated with NaCl solution at different concentration in the present study, the cooling rate is 0.33 K/min. (b), Incipient freezing point as a function of salt concentration, the cooling rate is 0.33 K/min. The PC denotes the plain cement paste and the AE denotes the air-entrained cement paste. After Litvan (1975) [223].

nucleates in cement-based materials that have been initially saturated with NaCl solution at different concentration. However, the large supercooling would be a catastrophe for cryoporosimetry, because the pores can not be detected when the bulk supercooled temperature is lower than the equilibrium temperature (capillary supercooled temperature) given by the Gibbs-Thomson equation. Furthermore, supercooling can lead to rapid ice formation and large heat releasing, which may cause significant higher stresses on pore wall than those under equilibrium case. This has been verified by experimental results of saturated cement-based materials under freezing, cf. Grübl and Soktin [146].

Another interesting phenomenon of ice nucleation and growth is the process in tubes or capsule upon cooling. The typical experimental observations on freezing processes of water confined in cylindrical capsule are presented in Figure 2.13 [149]. As showed in Figure 2.13, five different stages can be observed, of which some or all appear upon cooling depending on the materials of capsule and cooling rate [149]. The stage (a) represents the liquid sensible heat release to the density inversion temperature ($T_{di} = 4$°C). The stage (b) is

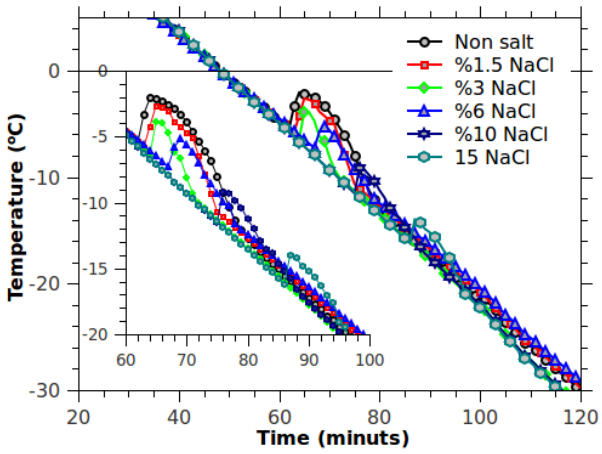

Figure 2.12: Temperature shift when ice nucleates in cement pastes initially saturated with NaCl solution at concentration of 0%, 1.5%, 3%, 6%, 10% and 15%. The temperature is measured by thermocouple in accuracy of 0.1 K. The cooling rate is controlled to be 0.33 K/min.

Nucleation temperature measurement:
The used materials are cement pastes with w/c=0.5 and 0.3. The preparation procedures and the physical properties of the used cement pastes can be found in chapter 6. The temperature and deformation measurements were performed simultaneously as shown in chapter 9. The temperature was measured by thermocouple in accuracy of ±0.1°C. NaCl at concentrations of 0% t0 15% are used. For each salt concentration, 54 times of cooling were performed and the corresponding temperatures were recorded. Thus total $54 \times 6 = 324$ times freezing were performed. The ice formation or nucleation temperature can be inspected once the temperature shift is observed as shown in Figure 2.12.

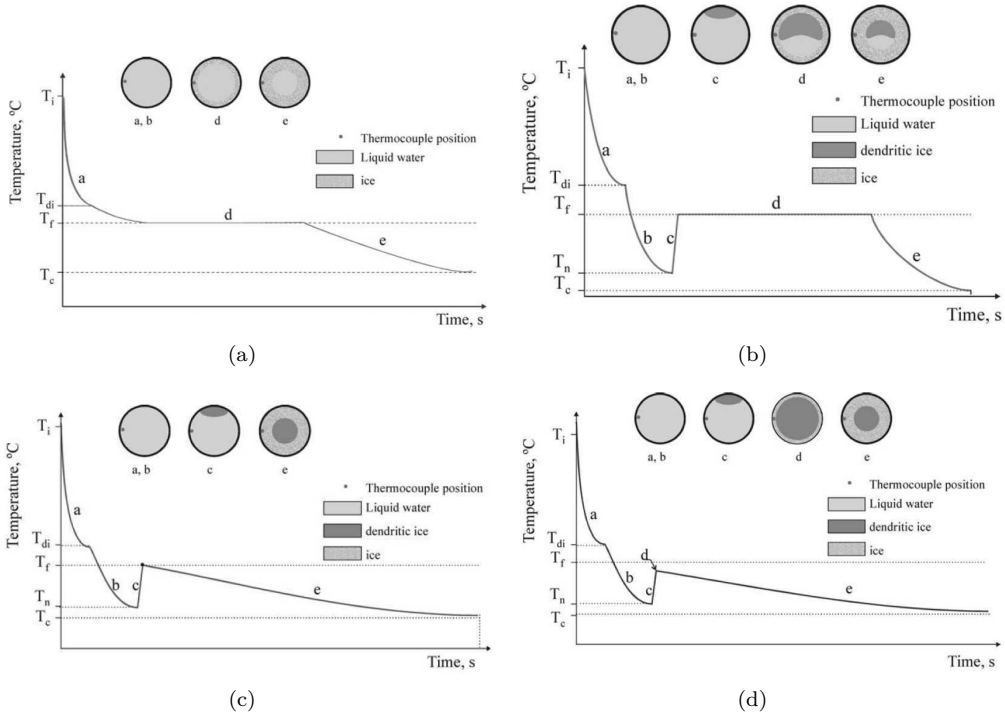

Figure 2.13: Freezing processes of water confined in cylindrical capsule: (a) Freezing process without supercooling; (b), Freezing process with supercooling and large heat releasing; (c), Freezing process with supercooling and instantaneous freezing; (d), Freezing process with hypercooling and instantaneous freezing. The different freezing stages of *a*, *b*, *c*, *d* and *e* are figured out specifically in text. Afterm Guzman and Braga (2005) [149]

the region where water is in metastable liquid state, and the temperature decreases monotonously until the ice nucleation temperature T_n. The stage (b), although frequently observed, is not sufficient condition for ice formation. In stage (c), thin-plaque-like crystals of dendritic ice grows on the interface of supercooled water and capsule. At the end of this dendritic growth process, the water temperature usually returns to its bulk freezing/melting point (T_f) and isothermal phase change starts in stage (d). The length of this stage depends on the heat release rate or the ice formation rate. Once the heat release of ice formation is not enough to compensate the heat loss by cooling, the stage (e) starts. The length of each stage depends on the cooling rate, nature of substrate materials as well as the size of capsule as specifically presented in Figure 2.13 [149].

It is not possible to review all the water supercooling related phenomena and models, but the mechanisms of supercooling lie on the free energy of water and ice either in steady state or in metastable state, which can be described principally by Gibbs-based approaches. More general and generalized thermodynamic models based on Gibbs-based approach can be found in Refs. [195, 343–345].

2.4.2 Homogeneous nucleation or heterogeneous nucleation

The primary reason of supercooling which can be observed for freezing of porous materials till homogeneous nucleation or heterogeneous nucleation, is due to the energy barrier [125]. When a very small ice embryo forms, either surrounded by water (Figure 2.14a) or in contact with substrates (Figure 2.14b), it must surmount large surface energy, otherwise the ice embryo will not grow into bulk phase or large crystal. Keeping in mind that the pressure on ice embryo is determined by the surface tension and the curvature, the larger the embryo size, the lower the ice pressure. A critical embryo size is thus expected. The embryos which are smaller than the critical size will melt and transfer back to bulk water due to the high pressure induced by the interfacial energy. In contrary, once the embryos are larger than the critical size, they will grow spontaneously and rapidly because the free energy of ice is lower than that of supercooled water [125, 341]. The homogeneous nucleation temperature of bulk water is known to be about −39°C [427]. It was also reported that the nucleation temperature depends on the size of water droplets [154]. However, as stated by Wilson et al. [427], the ice formation temperature is higher than the homogeneous nucleation temperature whether the measured water is in state of small droplets, placed on substrate or confined in pores/tubes. This indicates that in water or aqueous solution occurs the heterogeneous nucleation rather than the homogeneous nucleation. Except adding the extremely efficient nucleation agent, such as silver iodide and cholesterol [187], the heterogeneous nucleation temperature were found in range of −30°C∼ −5°C depending on the size of droplets [104, 154, 163, 164, 207] and the nature of substrate [171, 444]. As stated by Dash et al. [89], the surface roughness, polycrystallinity, dislocations and impurity

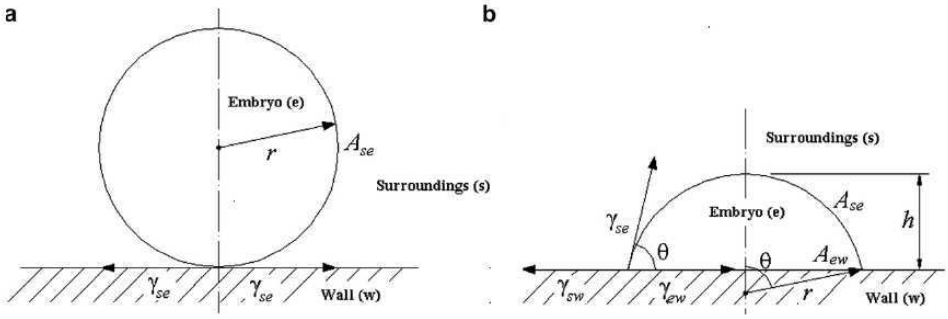

Figure 2.14: Schematic representation of a homogeneous (a) and a heterogeneous (b) nucleation. After Fletcher (1971) [125].

can cause heterogeneous nucleation. If water solution is used, the heterogeneous nucleation temperature is also related intimately to the salt concentration, see Figures 2.11(a) and 2.11(b).

Actually, the homogeneous nucleation is a special case of heterogeneous nucleation where no nucleation agent works. For planar substrate that acts as an agent, a widely applied model that has been proposed to describe this process, is considering the effect of contact angle as illustrated in Figure 2.14 [125, 402]. The temperature dependent nucleation rate J is given by [125, 402]:

$$J = J_0 \exp\left(-\frac{\Delta G^*_{hom} f(\theta)}{k_b T}\right) \tag{2.25}$$

where J_0 is the prefactor depending on the temperature, nature of substrate and contact surface or number of nucleation sites [312, 352, 380], k_b is Boltzmann constant (1.38066×10^{-23} J/K), T is absolute temperature (in K), ΔG^*_{hom} is the free energy excess of an ice embryo with critical size in homogeneous case, which is expressed as:

$$\Delta G^*_{hom} = \frac{16\pi\gamma^3_{cl}\mathrm{V}^2_c T^2_0}{3\Delta H^2_{fus}(T_0 - T)^2} \tag{2.26}$$

where ΔH_{fus} is the enthalpy change of ice formation. As a matter of factor, eq(2.26) can be derived directly by looking for the minimum of the free-energy difference ΔG_{hom} that is composed of volumetric term and interfacial term, i.e, $\Delta G_{hom} = 4/3\pi r^3 \Delta H_{fus} + 4\pi r^2 \gamma_{lc}$. The term $f(\theta)$ is the contact angle factor that accounts for the feature of substrate [125]:

$$f(\theta) = \frac{(1-\cos\theta)^2(2+\cos\theta)}{4} \tag{2.27}$$

To quantify the influence of depressed supercooling temperature on the nucleation rate J, it is preferred

to rewrite the eq(2.25) in the form:

$$\log J = \log J_0 - \frac{\Gamma}{2.303T(T_0 - T)^2} \quad \text{with} \quad \Gamma = \frac{16\pi\gamma_{cl}^3 \mathsf{V}_c^2 T_0^2 f(\theta)}{3\Delta H_{fus}^2 k_b} \tag{2.28}$$

The eq(2.28) was applied to best fit the measured data to compare the parameters $\ln(J_0)$ (or $\log(J_0)$) and Γ of specific treated liquid droplets with controlled liquid, cf. Seeley and Seilder [352]. Following the process of binning temperature distribution into numbers of temperature bins with widths ΔT_i, centered on temperatures T_i and containing n_i freezing events as presented by Seeley and Seilder [352], one can thus rewrite the ice nucleation rate formula as:

$$J(T_i) = \frac{\mathcal{R} n_i}{V \Delta T_i \left(n_i/2 + \sum_{j>i} n_j \right)} \tag{2.29}$$

where $\mathcal{R}$ is the cooling rate (K/s), V is the volume of liquid water (ml or m^3). Actually, eq(2.29) can be derived from the concept of inhomogeneous Poisson process when the observed freezing events are assumed to be random and uncorrelated for a given nucleation rate, cf. Shaw and Lamb [366], Shaw et al. [364, 365]. The detailed derivation processes of eq(2.29) are given in Appendix A.3.

Now let us consider the effect of solutes on heterogeneous nucleation, the energy barrier to formation of a spherical nucleus of the critical size is found to be [195]:

$$\Delta G_{hom,salt}^{*} = \frac{16\pi}{3} \frac{\gamma_{cl}^3 \mathsf{V}_c^2 T_0^2}{\left[\Delta H_{fus}(T_0 - T) + RTT_0 \ln(S_w)\right]^2} \tag{2.30}$$

where S_w is defined as the water saturation ratio [3]. In case that solution is confined in small pores, the water saturation ratio is related to the pore curvature and water activity, which is known as the Köhler equation [195]:

$$\ln(S_w) = \ln(a_w) + \frac{\mathsf{V}_w \gamma_{ls}}{RT} \frac{2}{r_p} \tag{2.31}$$

where V_w is the molar volume of water ($18 \times 10^{-6} m^3/mol$), r_p is the pore radius (nm or m). Substitution of the eqs(2.31) and (2.30) into eq(2.25), one obtains:

$$J = J_0 \exp\left\{ -\frac{16\pi}{3} \frac{\gamma_{cl}^3 \mathsf{V}_c^2 T_0^2 f(\theta)}{\left[\Delta H_{fus}(T_0 - T) + RTT_0 \ln(S_w)\right]^2 k_b T} \right\} \tag{2.32}$$

3. S_w is an environmental variable used in some cloud models [195]. It stands for the deviation extent from the state of pure water. In absence of curvature effect, $\ln S_w = \ln a_w$, and for pure bulk water $\ln S_w = 0$. This is quite different with the saturation degree S_l defined in chapter 4.

We further rewrite the eq(2.32) in form of eq(2.28):

$$\ln J = \ln J_0 - \frac{\Gamma}{T\left(T_0 - (1 - A_S)T\right)^2}, \quad \Gamma = \frac{16\pi\gamma_{cl}^3 \mathsf{V}_c^2 T_0^2 f(\theta)}{3\Delta H_{fus}^2 k_b}, \quad A_S = \frac{RT_0 \ln(S_w)}{\Delta H_{fus}} \tag{2.33}$$

To estimate the relation of depressed temperature to the salt concentration, liquid size and nucleation rate, we rewrite the eq(2.32) as:

$$\Delta T = T - T_0 = A_s T - \left(\frac{\Gamma}{T\ln(J_0/J)}\right)^{1/2} = \frac{RTT_0 \ln(S_w)}{\Delta H_{fus}} - \left[\frac{16\pi}{3}\frac{\gamma_{cl}^3 \mathsf{V}_c^2 T_0^2 f(\theta)}{\Delta H_{fus}^2 k_b T \ln(J_0/J)}\right]^{1/2} \tag{2.34}$$

Actually, eq(2.34) is a specific case of depressed temperature upon freezing, more general discussion on this issues can be found elsewhere, cf. Khvorostyanov and Curry (2004) [195].

2.4.3 Results and discussions

Figure 2.15 illustrates the normalized frequency of ice nucleation in terms of depressed supercooling temperature for NaCl solutions at different salinity confined in porous cement pastes. The temperature curves of samples during freezing were determined by thermocouple, of which the procedures are briefly shown in the sidebar of Figure 2.12. The normalized frequency is calculated as: $f = \sum_{i=1}^{j} n_i / \sum_{i=1}^{N} n_i$ for $T < T_j$, where N is the number of temperature bins shown in Table 2.5 and $\sum_{i=1}^{N} n_i = 54$, T_j is the center temperature of jth temperature bin. The binning temperature width and the temperature range are presented in Table 2.5. The frequency of nucleation temperature distribution ($f = n_j / \sum_{i=1}^{N} n_i$ at T_j) and the corresponding Gauss fitting can be found in Figure 2.15(b). To represent the heterogeneous nucleation temperature for samples saturated with salt concentration, the mean heterogeneous nucleation temperature T_f^*, defined as the temperature where the normalized frequency is equal to 0.5, is evaluated. It decreases from about -8℃ to -17℃ as salt concentration increases from zero to 15 wt%. It also can be found in Figure 2.15 that the supercooling temperature distribution shows no significant difference when NaCl concentration is lower than 6%. As salt concentration increases, the ice formation temperature decreases progressively, which can be due to the lowering of water activity when mixed with salts (see Figure 2.5(b)). For cement-based materials, the pore radius can range from nano-size to millimeter-size, which depends on the initial compounds, water to cement ratio, curing condition and so on [247]. Based on the Mercury intrusion porosimetry and gas sorption porosimetry, the mean pore size of hardened cement pastes, both with high w/c (0.5) and with low w/c (0.3), defined as $r_p = d/2 = 2V/A$, are about 10 nm [443]. The value of the second term in right hand side of eq(2.31) is estimated as 0.036 for water confined in cylindrical pores, with $\gamma_{ls} = 45\text{mJ/m}^2$ [44]. This value approximates the logarithmic value of water activity when NaCl concentration is about 1.1 mol/kg (calculated by Lin and Lee's model [216]), viz. $\ln(a_w) = -\frac{\mathsf{V}_w \gamma_{ls}}{RT}\frac{2}{r_p}$

Table 2.5: Parameters for the normalized frequency (see Figure 2.15) and the mean depressed supercooling temperature T_f^*.

Samples	Non salt	%1.5 NaCl	%3 NaCl	% 6 NaCl	%10 NaCl	%15 NaCl
Temperature range ($T_{min} \sim T_{max}$)	$-11 \sim -6$	$-12 \sim -6$	$-11 \sim -6$	$-15 \sim -8$	$-17 \sim -8$	$-21 \sim -13$
Temperature widths ΔT_i	0.2	0.2	0.2	0.2	0.2	0.2
Number of temperature bins	25	30	25	35	45	40
Temperature T_f^* at $f = 0.5$	-8.2	-8.4	-7.7	-11.5	-12.9	-17

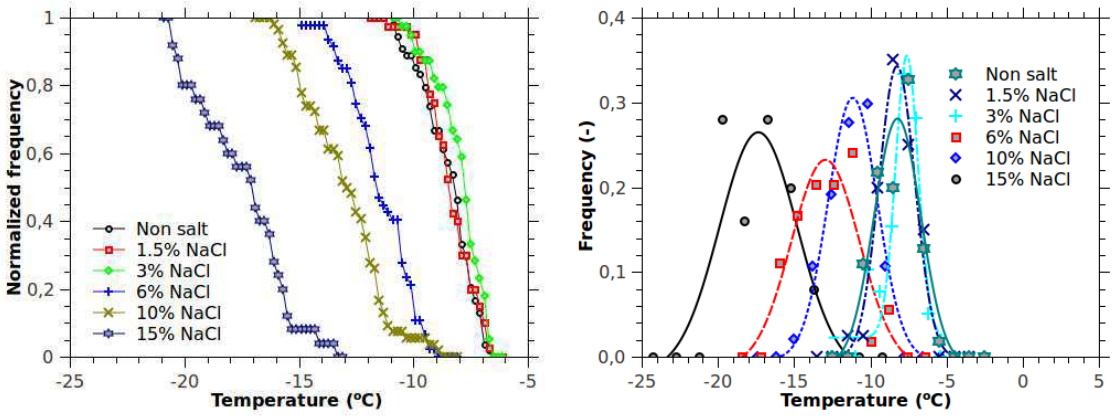

(a) (b)

Figure 2.15: The normalized frequency of ice nucleation for solution confined in cement paste with NaCl at concentration of 0%, 1.5%, 3%, 6%, 10% and 15%. The nucleation temperature values are from Figure 2.11(a).

with $m_{NaCl} = 1.1$mol/kg and $r_p = d/2 = 10$nm. This may be the reason why there are no significant differences in the depressed supercooling temperature when the salt concentration is not larger than %6 (≈ 1.03mol/kg).

The ice nucleation rate J can be evaluated by eq(2.29) using the measured freezing events and the corresponding nucleation temperature presented in Figure 2.12. The obtained nucleation rates for materials saturated with salt solution at different concentration are presented in Figure 2.16. Best-fitting the obtained nucleation rate – temperature data through the heterogeneous nucleation equation, cf. eq(2.33), one can obtain the parameters: prefactor ($\log J_0$), Γ and contact angle function $f(\theta)$. The best-fitting curves are shown in Figure 2.16 as well. Two conditions are considered in fitting equation (eq(2.33)): 1, only the salt concentration is encountered, viz. $\ln(S_w) = \ln(a_w)$ in eq(2.31); 2, both the salt concentration and the pore size effect are encountered, viz. $\ln(S_w) = \ln(a_w) + \frac{V_w \gamma_{ls}}{RT} \frac{2}{r_p}$. The parameters for both best fitting conditions are presented in Table 2.6. It can be seen that the logarithm values of prefactor ($\log J_0$) decreases slightly with salt concentration for both conditions 1 and 2, see also Figure 2.17(a). And the values for fitting condition 1 are lower than those with condition 2, which indicates easier nucleation for condition 1 because of the excess energy by curvature effect in condition 2. The parameters Γ and $f(\theta)$ decrease with salt concentration, indicating that easier ice nucleation for more saline solution under the

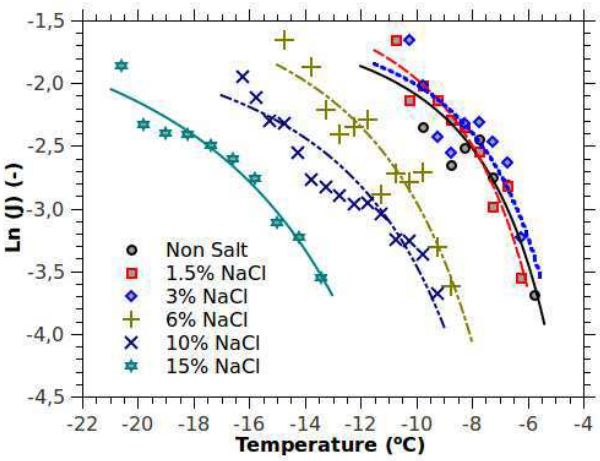

Figure 2.16: The logarithm value of nucleation rate ($\ln J$) in terms of temperature for cement samples saturated with NaCl solution at concentration of 0% (non salt), 1.5%, 3%, 6%, 10% and 15%. The points are calculated through eq(2.28) and the lines are fitted by eq(2.33), the cooling rate is 0.00556K/s. The obtained parameters, such as the prefactor J_0, the factors Γ and A_s in eq(2.33) are presented in Table 2.6 for condition 2.

Table 2.6: Nucleation parameters extracted from the best-fit curves evaluated by eq(2.28) for the cement pastes saturated with NaCl solution at concentration of 0% (non salt), 1.5%, 3%, 6%, 10% and 15%. Two conditions are considered, see text for detail.

Samples	Non salt	%1.5 NaCl	%3 NaCl	% 6 NaCl	%10 NaCl	%15 NaCl	Homogeneous[352]
Condition 1: only salt concentration is considered							
$\ln J_0$	-1.359	-1.173	-1.572	-1.493	-2.267	-2.075	35
Γ	4.79×10^4	4.06×10^4	1.85×10^4	3.69×10^4	1.11×10^4	1.42×10^4	2.4×10^7
R^2	0.866	0.925	0.818	0.867	0.866	0.843	-
$f(\theta)$	0.002	0.00169	0.00077	0.00154	0.000463	0.000592	1.0
θ	18.58	17.80	14.58	17.38	12.83	13.65	180
A_s	0	-0.00324	-0.00645	-0.013	-0.02236	-0.037	0
Condition 2: both salt concentration and pore size are considered							
$\ln J_0$	-0.686	-0.479	-1.049	-1.154	-1.812	-1.600	35
Γ	15.41×10^4	14.06×10^4	8.02×10^4	12.72×10^4	5.76×10^4	7.38×10^4	2.4×10^7
R^2	0.862	0.921	0.815	0.861	0.869	0.939	-
$f(\theta)$	0.00642	0.00586	0.00334	0.0053	0.0024	0.00303	1.0
θ	25.04	24.46	21.63	23.83	19.46	20.65	180
A_s	0.0136	0.0104	0.00715	0.000604	-0.00876	-0.02145	0

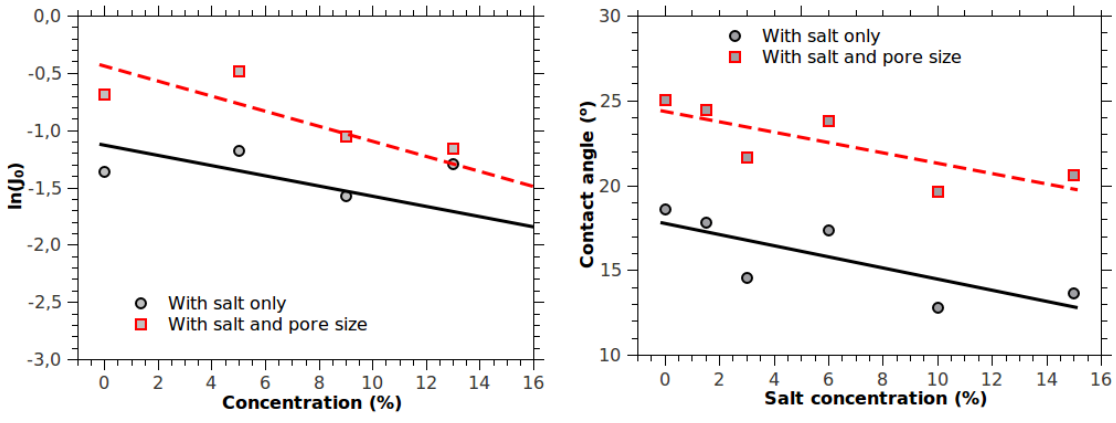

(a) (b)

Figure 2.17: (a), The logarithm values of prefactor ($\ln J_0$) in terms of the salt concentration. (b), The contact angle θ in terms of concentration. Both the prefactor ($\ln J_0$) and contact angle θ are evaluated from best fitting of eq(2.33) on the nucleation rates evaluated by eq(2.29). With salt only: fitting under condition that $\ln(S_w) = \ln(a_w)$ in eq(2.31); With salt and pore size: fitting under condition that $\ln(S_w) = \ln(a_w) + \frac{V_w \gamma_{ls}}{RT} \frac{2}{r_p}$.

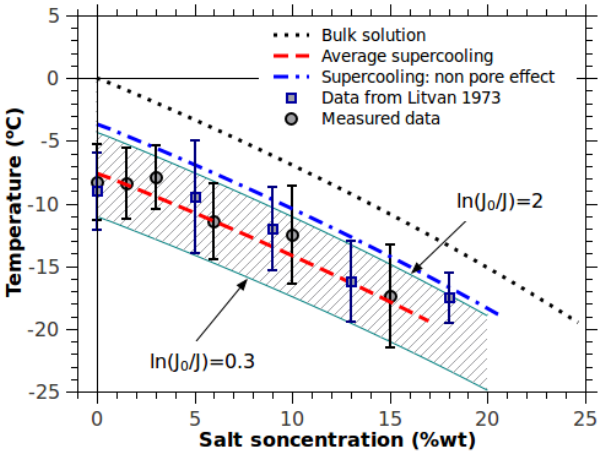

Figure 2.18: The measured freezing point as function of salt concentration that is confined in porous cement paste, and the calculated supercooling temperature. The cooling rate is 0.33 K/min. Grey filled circle: measured depressed supercooling temperature, data from Figure 2.11(a); Grey filled square: measured depressed supercooling temperature, data from Litvan (1973) [221]; Dot line: equilibrium freezing temperature of bulk solution; Dash line: Supercooling calculated by eq(2.34); Dash dot line: Supercooling calculated by eq(2.34) without consideration of pore size effect.

same supercooling temperature (see Figure 2.17(b)). The contact angle decreases from about 18° to 13° and from 25° to 20° as salt concentration increases from zero to 15wt% when conditions 1 and 2 are considered respectively. However, because the water activity decreases significantly as salt concentration increases (see Figure 2.5(b)), the overall heterogeneous nucleation energy, $|\Delta G^*_{hom,salt} f(\theta)|$ in eq(2.32) where $\Delta G^*_{hom,salt}$ is expressed as eq(2.30) and f_θ is expressed as eq(2.27), increases with salt concentration. Therefore, the observed depressed nucleation temperature decreases with increasing of salt concentration.

If the ice nucleates on a planar surface, the depressed temperature would be smaller than the one when ice nucleates in pores due to the excess energy induced by the pore curvature. In this study, the temperature shift required by ice formation in pores in size of 10 nm is calculated to be about -3.4℃ by Gibbs-Thomson equation. Therefore, the values corresponding to "supercooling: non pore effect" in Figure 2.18 are equal to the depressed temperature calculated by eq(2.34) minus the temperature shift required by pore size effect. Interestingly, the obtained values of "supercooling: non pore effect" appears as an upper bound of measured supercooling temperature interval, see Figure 2.18. However, it is more likely a coincidence, because there is no specific physical meaning for this estimation. In addition, the eq(2.34) also allows us to estimate the supercooling temperature range by changing the logarithm value of ratio of prefactor to ice nucleation rate, $\ln(J_0/J)$. This ratio actually indicates the potential of ice nucleation. The higher the ratio, the lower the probability of ice nucleation. The region of supercooling temperature corresponding to the $0.3 \leq \ln(J_0/J) \leq 2$ is plotted in Figure 2.18.

2.5 Thickness of liquid-like layer

The liquid like layer (unfrozen layer) on the surface of ice has been observed more than 150 years. There are three proposed mechanisms for the formation of this layer: pressure melting, frictional heating, and intrinsic premelting [213]. The thickness of this layer, which is reported to be ranging from one to three

molecular layers [97, 289], depends preliminary on the temperature [89, 102]. To derive the relationship between the thickness of liquid-like layer (unfrozen layer) and the temperature, we recall the Helmholtz free energy of a convex pore filled with ice and a layer of unfrozen water as presented by Petrov and Furo [288, 291] and Dash [89]. The requirement of minimal Helmholtz free energy (or Gibbs free energy instead when the work by pressure is negligible) in equilibrium, leads to an equation for the equilibrium thickness of the liquid-like layer δ by substituting the Steiner's equation (eq(2.23)) in eq(2.20):

$$\frac{\partial \Psi(\delta,T)}{\partial \delta} = 0 = A\left[\frac{\Delta H_{fus}}{\mathsf{V}_c}\frac{T-T_0}{T_0}(1+2\kappa\delta) + 2\kappa\gamma_{lc} + \Delta\gamma\frac{\partial F}{\partial \delta}\right] \tag{2.35}$$

Where F is the specific interfacial potential [89]. T_0 is the equilibrium bulk freezing/melting temperature at $P = P_0$. Note during the processes of deducing eq(2.35), the approaches $\frac{\partial V(\delta)}{\partial \delta} \approx A(1+2\kappa\delta)$ and $\frac{\partial A(\delta)}{\partial \delta} \approx 2\kappa A$ are adopted [4]. In case that $1 \gg 2\kappa\delta$ and temperature is not in the close vicinity of the bulk melting point within the pore, the term $2\kappa\tau$ at the right side of eq(2.35) can be neglected. Also the relation, $2\kappa\gamma_{lc} = \Delta H_{fus}(T_0 - T_m)/\mathsf{V}_c/T_0$, is adopted according to the Gibbs-Thomson equation, where T_m is the melting temperature of ice in the pore with only the effect of curvature at κ. Thus the equation for evaluating the thickness of liquid-like layer in form of eq(2.35) is reduced to the classic approach as presented in [89], with the formula:

$$\frac{\Delta H_{fus}(T_m - T)}{T_0 \mathsf{V}_c} = \frac{\Delta\gamma \partial F}{\partial \delta} \tag{2.36}$$

Once the term $\partial F/\partial\delta$ is determined, the relationship between the thickness of liquid like layer and the temperature can be evaluated specifically. In addition, the choice of $F(\delta)$ depends on the surface force acting between the solid-liquid and the liquid-ice interfaces for ice growing in fine pores and on those between the solid-liquid and the liquid-vapor interfaces for ice exposed to air [102]. For an exponentially distributing force between the two interfaces, $F = \exp(-2\delta/\xi)$, cf. [288, 291], the thickness of unfrozen layer can be expressed as:

$$\delta = -\frac{\xi}{2}\ln\left[-\frac{\xi\Delta H_{fus}(T_m - T)}{2T_0\mathsf{V}_c\Delta\gamma}\right] \tag{2.37}$$

The parameter ξ in eq(2.37) can be determined by experiments. Often, for convenience, the thickness of liquid like layer on ice surface is expressed as a simpler equation [102]:

$$\delta = A - B\ln(T_m - T) \tag{2.38}$$

4. In Refs. [215, 288], the eq(2.23) is used, while in Ref. [291], the expressions, $A(\delta) = A(1-2\kappa\delta)$ and $V(\delta) = V - A(\delta - \kappa\delta^2)$ are used. In the present study, we use the formulas in Refs. [215, 288].

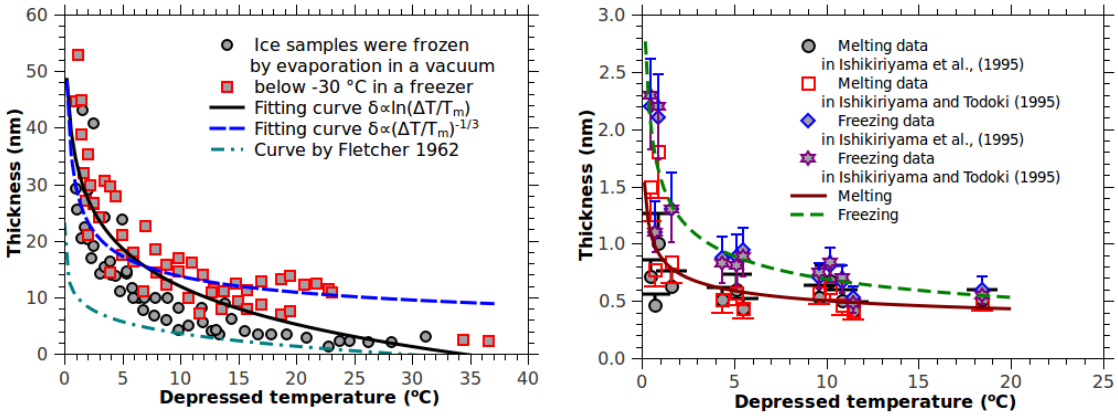

(a) (b)

Figure 2.19: (a), Atomic force microscopy (AFM) measured thickness of liquid like layer on ice surface, data from Döppenschmidt and Butt (2000) [102], and the expression: $\delta = 2.8\ln(40/\Delta T - 0.4)$nm, by Fletcher (1968) [124]. (b), The calculated thickness of liquid like layer between ice and silica-gel, the lines were fitted by the relation $\delta \propto \Delta T^{-1/3}$, data from Ishikiriyama et al. (1995) [174] and Ishikiriyama and Todoki, (1995) [173].

The parameters A and B depend on the nature of substrate that is in contact with the liquid like layer. Thus, those parameters were applied to evaluate the hydrophilic or the hydrophobic degree of a material whose surface properties are unknown. When ice exposed to air, $A = 140(\pm 10)$ nm and $B = 41(\pm 4)$nm according to Goertz et al. [143].

If van der Waals forces were considered, where the repulsive dispersion force between two microscopic bodies is in a limiting separation σ, $F = \delta^2/(\delta^2 + \sigma^2)$ was substituted into eq(2.36) and $\delta \gg \sigma$ was adopted in general case, the thickness of liquid like layer is then given by:

$$\delta = \left[\frac{-\Delta H_{fus}}{2\Delta\gamma\sigma^2 T_0 \mathsf{V}_c}(T_m - T)\right]^{-1/3} \tag{2.39}$$

The eq(2.39) is actually a special case of $\delta = [-\Delta H_{fus} \cdot (T_m - T)/(2\Delta\gamma\sigma^2 T_0 \mathsf{V}_c)]^{\alpha}$, with $F = \delta^n/(\delta^n + \sigma^n)$ and $\alpha = -1/(1+n)$ [102, 425]. If the curvature effect is neglected, $T_m = T_0$, eq(2.39) reduces to the well used formula: $\delta \propto (\Delta T)^{-1/3}$ [89]. Figure 2.19(a) illustrates the Atomic force microscopy (AFM) measured thickness of liquid like layer in terms of the supercooling temperature, and the fitted curves by eqs(2.38) and (2.39) respectively. It appears that eq(2.38) can describe the thickness of liquid like layer better than eq(2.39) when ice exposed to air (see Figure 2.19a). This conclusion was also verified when ice is in contact with silica [143]. But Dash et al. [89] argued that the eq(2.39) is better than the eq(2.38) to describe the thickness of liquid like layer when ice is in contact with rough solid surface. In addition, the eq(2.39) was adopted widely in engineering application [116, 450, 451], see Figure 2.19(b).

Again, the effects of salt on the thickness of liquid like layer will be derived through the classic Gibbs

approaches as shown in Schmelzer et al. (2006) [344], Khvorostyanov and Curry (2004) [195]. By rewriting the terms in left side of eq(2.36), one obtains a novel formula that includes the effect of water activity as follow:

$$\frac{1}{\mathsf{V}_c\Delta\gamma}\left[\frac{\Delta H_{fus}(T_0-T)}{T_0}+RT\ln(a_w)\right]=\frac{RT\sum c_i\ln\gamma_i}{\Delta\gamma}+\frac{2\kappa\gamma_{lc}}{\Delta\gamma}+\frac{\partial F}{\partial\delta} \tag{2.40}$$

The Derjaguin-Landau-Verwey-Overbeek (DLVO) theory is retained to evaluate the specific interfacial energy induced by van der Waals forces and Coulombic interactions within solution films, cf. in Wettlaufer [424] [5]:

$$F=\gamma_d-\Delta\gamma\left[1-\frac{\sigma^2}{2\delta^2}-\frac{1}{2}\exp\left(-A_k\delta^{-1/2}(\delta-\sigma)\right)\right] \tag{2.41}$$

where γ_d is the dry interfacial energy and A_k is a parameter associated with N_i, which represents moles per unit area of a single species of monovalent nonvolatile impurities deposited in the film ($A_k \propto N_i^{1/2}$) [424]. Substituting of eq(2.41) into the eq(2.40) and considering again $2\kappa\gamma_{lc}=\Delta H_{fus}(T_0-T_m)/\mathsf{V}_c/T_0$, one obtains:

$$T_m-T=\frac{T_0\mathsf{V}_c}{\Delta H_{fus}}\left[RT\sum c_i\ln\gamma_i+\frac{\Delta\gamma\sigma^2}{\delta^3}+\frac{\Delta\gamma}{2}A_k\delta^{-1/2}\left(1+\frac{\sigma}{\delta}\right)\exp\left(-A_k\delta^{-1/2}(\delta-\sigma)\right)\right] \tag{2.42}$$

The detail derivation of eq(2.42) is given in Appendix A.4. In case that surface melting occurs for planar ice with an ideal dilute solution assumption, $\ln\gamma_i\approx 1$, eq(2.42) reduces to the eq(7) in [424].

In addition, based on the X-ray reflectivity techniques, Engemann et al. (2004) [110] observed that the liquid like layer (quasiliquid layer defined in [110]) between ice and SiO_2 has a large density to be $\rho=1.17$ g/ml. This value is very close to the density of water strongly adsorbed on C-S-H, $\rho\approx 1.16$ g/ml, according to Allen et al. [12] and Thomas et al. [397].

5. The second term in the right hand side of eq(2.41) has the opposite signal of that initially shown in [424], because the term $\Delta\gamma=\gamma_{ls}+\gamma_{lc}-\gamma_{sc}$ is defined in [424]. Here we use the definition of $\Delta\gamma=\gamma_{sc}-(\gamma_{lc}+\gamma_{ls})$ in [290].

Chapter 3

Deterioration of cement-based materials by freeze-thaw loading

Contents

In chapter 2, the thermodynamics and mechanisms of ice formation in porous materials were discussed comprehensively, which did not concern specifically with the macro properties and/or problems of porous materials. Yet how and in what extent freeze-thaw influences the mechanical behaviors and durability of porous materials were not addressed. For cement-based porous materials, these are especially important. In this chapter, we will introduce the deterioration of cement-based materials subjected to freeze-thaw loading phenomenologically and the corresponding models/hypotheses developed in the last decades. These deterioration phenomena and models/hypotheses can help us to understand the hidden mechanisms qualitatively and (in some extent) quantitatively.

3.1 Phenomenology of freeze-thaw deterioration

3.1.1 Internal damage

It is well known that the inner cracking and surface scaling are the two main deterioration patterns for cement-based materials subjected to freeze-thaw loading [294]. Both in laboratory tests and on-situ practice, the inner cracking and/or surface scaling have been observed frequently [235, 236, 294, 305, 348, 379, 406, 407, 415]. The internal deterioration of cement-based materials subjected to freeze-thaw loadings is a progressive damage due to the nucleation, growth and percolation of cracks in the materials [296]. This damage thus exhibits as strength or (dynamic) elastic modulus loss of solid materials progressively [127, 287, 296, 420], see for instance Figure 3.1. The (dynamic) elastic modulus loss is often measured by ultrasonic methods [7, 434, 435]. Due to the very importance of (dynamic) elastic modulus of cement-based materials, it has been adopted as an important frost resistance factor, cf. ASTM C 666 [21] and RILEM recommended freeze-thaw test method, CDF [360]. The practice in cold regions indicated that the internal cracking highly depends on the intrinsic properties of cement-based materials, such as compressive strength, pore structure and permeability. Materials with lower porosity (denser material), thinner pore size distributions have better frost resistance [294, 296]. Phenomenologically, significant dilation can be observed after ice nucleation for the initially saturated cement-based materials, especially when significant bulk supercooling occurs [35, 36, 107, 188]. In addition, after one whole freeze-thaw cycle, the displacements usually can not go back to the original points, which indicates that the permanent residual deformation is created, and this kind of permanent deformation is, obviously, an evidence of internal cracking [187]. In some extent, the porosity and pore size distribution modifications were observed for internal freeze-thaw deteriorations usually [239, 261, 420]. Comprehensive researches indicated that the total porosity increases with the increment of freeze-thaw cycles, and more pores distribute in larger size, which is probably due to the formation of percolated internal cracks [239, 261]. Understandably, the permeability must increase, since the percolated cracks provide additional paths for gas or water transport [287, 420]. Moreover, increase of water content or water saturation degree with freeze-thaw cycles can be observed frequently, when samples are measured in open condition where it permits free water movement [261]. It has been reported that the content of water uptake does not depend significantly on the salt concentration [59]. On contrary, Fagerlund [120] proposed that the water uptake is more severe when material surface is covered with more concentrated solution. The increased water content aggravates the internal frost deteriorations. Furthermore, for sealed tests, a critical saturation degree can be observed for all sorts of porous materials and it ranges between 0.7-0.9 for cement-based porous materials [117–120]. After numbers of freeze-thaw cycles, some visible macro cracks can be observed directly [417, 420]. Eventually, the strength or (dynamic)

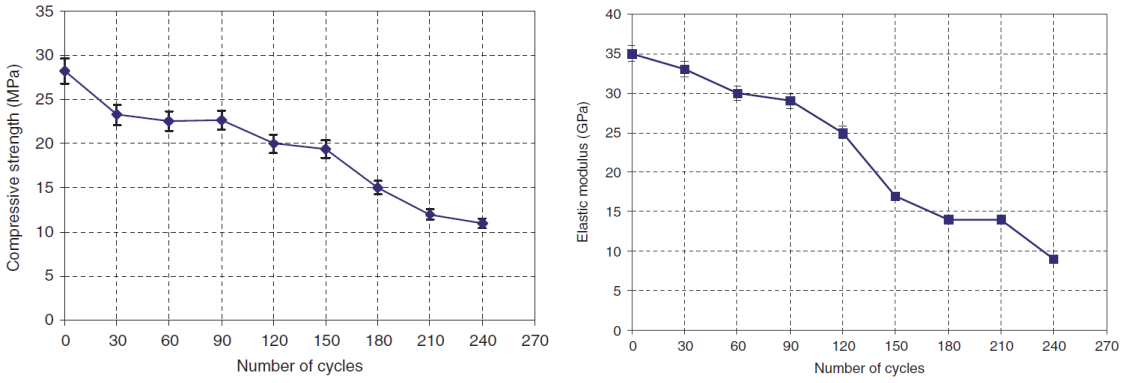

(a) (b)

Figure 3.1: Compressive strength (a) and dynamic elastic modulus (b) loss of typical ordinary Portland cement (OPC) concrete (w/c=0.457). After Wardeh et al. [420].

elastic modulus of materials loses significantly, and the cohesion of the cement pastes becomes very weak, which means the cement-based materials have been damaged completely. When cement-based materials are entrained with air voids appropriately, the frost resistance can be improved significantly. In addition, contrary to the significant dilation after ice nucleation for normal cement-based materials, it contracts after ice nucleation for air-entrained materials [310], see section 5.1 for detailed discussions. To sum up, the phenomenological characteristics of internal frost deterioration of cement-based materials are:

❶ The internal cracking highly depends on the pore structure of materials, materials with lower porosity (denser material), thinner pore size distributions have better frost resistance [294, 296];
❷ The water content or saturation degree increases progressively with the freeze-thaw cycles in open condition [59, 120];
❸ The higher the saturation degree, the higher the risk of frost deterioration, and it exists a critical saturation degree in range of 0.7-0.9 [119, 120];
❹ Significant dilation after ice nucleation and residual dilation after a whole freeze-thaw cycle can be observed, these dilations depend highly on the saturation degree [35, 36, 107, 188];
❺ The mechanical properties, such as elastic modulus, compressive strength, split and tension strength decrease significantly once internal cracking happens [127, 420];
❻ The total porosity increases progressively with the freeze-thaw cycles, and the pore size distribution is altered by micro cracks [239, 261];
❼ The permeability of materials increases progressively with the freeze-thaw cycles [420];
❽ There are visible cracks after numbers of freeze-thaw cycles [417, 420].
❾ Properly entrained air voids can significantly improve the frost resistance [296, 305, 310];
❿ Continual shrinkage occurs when freezing is suddenly stopped for air-entrained materials, whereas continually expansion occurs for non-air-entrained materials [310, 380].

3.2 Surface scaling

As to salt scaling, significant different phenomenological characteristics have been observed. The most crucial one must be that the salt scaling is a progressive superficial damage of cementitious surface [296, 406]. It is known that the salt scaling consists of the removal of small chips or flakes of binder and even of some

small aggregates after numbers of freeze-thaw cycles [295, 406]. Therefore, the amount of mass removal per unit surface area is an important frost resistance factor for cement-based materials with deicing salts, see for instance RILEM recommended freeze-thaw test method, CDF [360] and CIF [358, 361]. In addition, a significant anomalous phenomenon is the occurrence of a maximum amount of damage with a "pessimum" of solution concentration around 3 wt% [225, 235, 236, 296, 406, 407, 415], see Figure 3.2 for instance. Thus the proposed experimental procedures or codes, cf. CDF/CIF [360, 361] and ASTM C672 [22] (see Appendix A.5 for detial), recommended that one surface of samples shall be exposed to 3 wt% NaCl solution with depth of several millimeters. In addition, this kind of surface damage and the pessimum value of solution concentration are reported to be independent of the sorts of solutes [87, 101, 175, 176, 405, 415]. Interestingly, no significant strength or (dynamic) elastic modulus loss occurs when only surface scaling occurs [236, 296]. Some studies indicated that the layer of salt solution is a necessary but not a sufficient condition for surface scaling [354, 415], which is to say the scaling will not occur in the absence of the layer of salt solution. Furthermore, it has been reported that when the thickness of the salt solution is larger, the scaling is more severe [71, 72]. However, Fabbri et al. [115] reported that scaling can occur even without the superficial salt solution. Another relevant issue that is full of argument, is if the pure water can cause scaling. As reported by Klieger [197] and Klieger and Perenchio [198], water can cause scaling as well. However, Valenza and Scherer [406] stated that this kind of observations are misleading, because the number of freeze-thaw cycles required by pure water tests for scaling is almost twice that required by salt solution, and the authors attributed the scaling caused by pure water to the weak surface or low quality of samples. When samples are not sealed and in contact with superficial salt solution, the water uptake and/or solution uptake occurs as the number of freeze-thaw cycle increases [119, 387]. This phenomenon has been partially addressed by the micro-ice-lens theory by Setzer [356, 357], and will be shortly recapitulated in the following sections. The minimum temperature and the duration of samples at subzero temperature have been reported to have significant influences on the surface scaling. The lower the minimum temperature and/or the longer the duration of subzero temperature, the more severe the surface scaling [153, 354, 406]. Because there are numerous characteristics of surface scaling that are different from those of internal deterioration, it is stated that the susceptibility to salt scaling is not correlated with susceptibility to internal frost action [405–407]. However, the practice of cement-based material against frost actions indicated that improving the strength and appropriate air voids entrainment can improve the frost resistance against surface scaling significantly. These are exactly the same ways to fight against the internal cracking as introduced in previous paragraphs. Briefly, the characteristics of surface scaling of cement-based materials can be presented as (see also the comprehensive reviews by Valenza and Scherer [406, 407]):

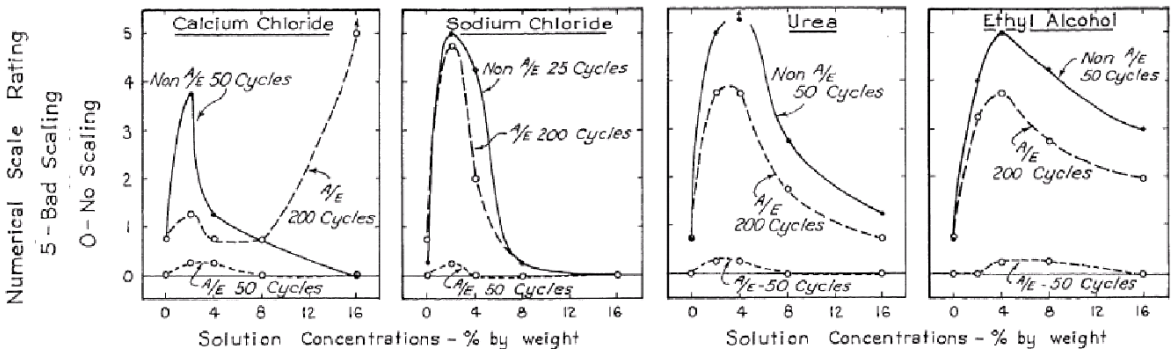

Figure 3.2: Effect of deicing salt concentration and sorts of deicing salt on the surface scaling. After Verbeck and Klinger (1957) [415].

❶ The progressive removal of small flakes of binder on surface of cement-based materials appears along with freeze-thaw cycles [176, 177, 294];
❷ The most severe scaling occurs at a solute concentration of ≈3%, independent of the type of solute used [221, 225, 415];
❸ There is no significant strength or (dynamic) elastic modulus loss if only surface scaling occurs [236, 296];
❹ SSuperficial salt solution is a necessary but not a sufficient condition for surface scaling [354, 415];
❺ Saturation degree increases with freeze-thaw cycles, which is the same as that observed for internal freezing [119, 387];
❻ The lower the minimum temperature and/or the longer the duration of subzero temperature, the more severe the surface scaling [153, 354, 406]
❼ Both strength increment and air void entrainment can improve the frost resistance against salt scaling [296, 380, 406].

Air voids are known for their protection of cement-based materials against both the internal cracking and surface scaling when they are entrained in cement-based materials properly [101]. The spacing factor that is deduced from Powers hydraulic pressure theory [305] has been widely used in engineering practice. However, only recently, the mechanisms of contraction for air void entrained cement-based materials after ice nucleation, have been addressed [77, 82, 381]. The mechanisms of air voids protecting against the surface scaling have been comprehensively studied by Sun and Scherer [379, 380]. Some details will be discussed in section 3.4.

3.2.1 Relevant issues

Although most observations are consistent with the phenomena summarized above, there are still many conflicting experimental observations. For example, Litvan showed that the maximum dilation occurred for cement-based materials saturated with 3% NaCl solution [224], which is consistent with the pessimum concentration observed for surface scaling. However, some results indicated that the dilation decreases with increase of salt concentration [59] or that there is no statistical tendency of the maximum deformation for

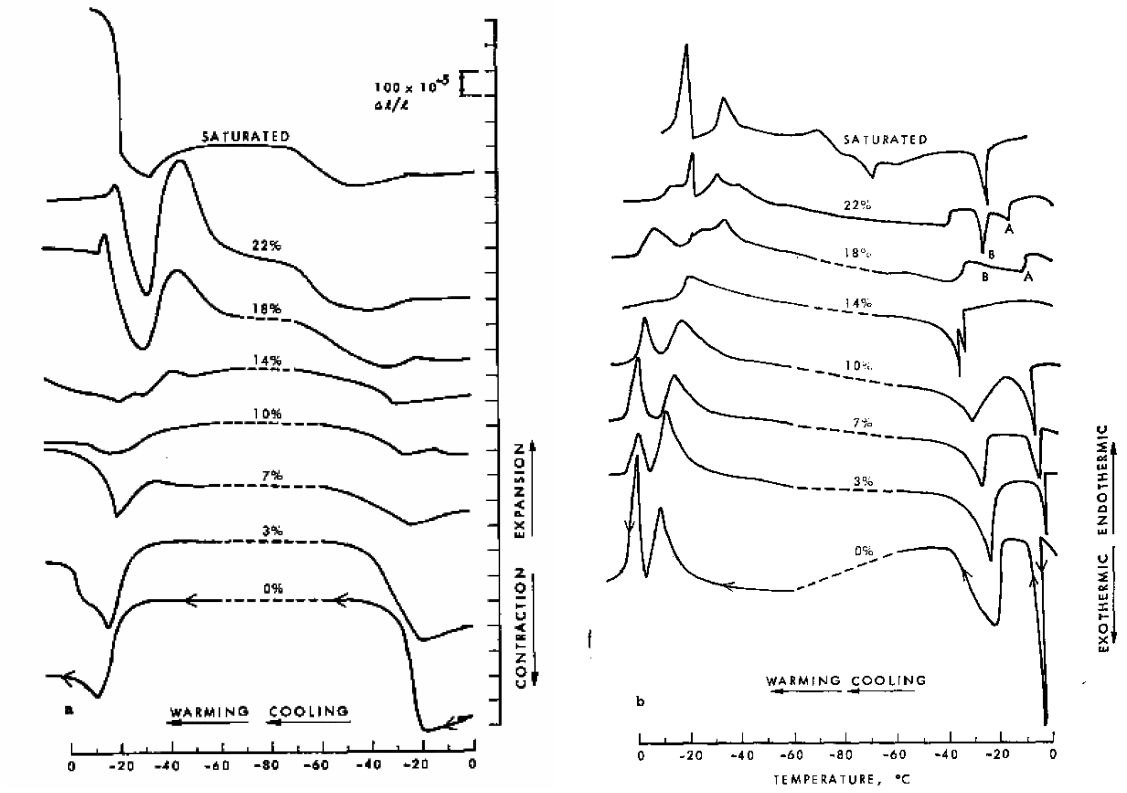

(a) (b)

Figure 3.3: The dimensional change (a) and differential thermogravimetry (DTG) (b) of porous glass saturated with NaCl solution at different concentrations. After Litvan, (1973) [222].

freeze-thaw tests with 3 wt% NaCl superficial solution [354]. Even the results measured by Litvan himself did not support the "pessimum" of 3 wt% NaCl, see Figure 3.3. Litvan measured the dimensional change and the differential thermogravimetry of porous glass saturated with NaCl solution at different concentrations. As shown in Figure 3.3(a), the dilation after ice nucleation decreases as the salt concentration increases, and the maximum residual deformation ($\Delta l/l \approx 700 \times 10^{-5}$) was observed for samples with saturated saline solution (about 36% at 25°C). The ice content, as shown in Figure 3.3(b), decreases as salt concentration increases.

In addition, contrary to the conclusion obtained in Ref. [406] that the scaling is independent of the type of salts used, different types of salts lead to different damage extents. For instance, Wang et al. [418] found that calcium chloride ($CaCl_2$) solutions cause the most damage, but potassium acetate (CH_3CO_2K) solutions cause minor scaling. McDonald and Perenchio [243] obtained the opposite results, they found that salts containing potassium can cause more scaling damage. Recent investigations by Shi et al. [368] indicated that the calcium magnesium acetate (CMA) ($CaMg(CH_3COO)_2$) deicing solids and the magnesium chloride (MgCl) deicing solutions are harmless to the concrete durability, the K-formate and the Na-acetate/Na-formate blend deicing agent has moderate scaling damage to concrete, and the NaCl-based

deicing salt (including NaCl) and the K-acetate-based deicing salt lead to the most serious damage to the concrete. A report by Darwin et al. [87] indicated that at low concentrations, magnesium chloride ($MgCl_2$) and CMA cause measurable damage to concrete, while at high concentrations, $CaCl_2$, $MgCl_2$, and CMA cause significant changes in concrete: loss of material and reduction in stiffness and strength. Those observation are consistent with the results in [243]. In addition, it has been reported that some deicing salts, such as $MgCl_2$ and CMA, can react with hardened cement paste, which may lead to additional deteriorations [367, 368]. However, the chemical reaction between the deicing salts and hardened cement pastes is beyond our scope, thus this will not be discussed in this study.

3.3 Models and/or mechanisms for freeze-thaw deterioration

The mechanisms behind deteriorations arising upon freeze-thaw cycles can be based on scientific and/or engineering knowledge. However, it has been not possible to have a mechanism accounting for all the deterioration phenomena presented in section 3.1. Indeed numerous models were developed by many researchers. Of course, it is required to know these mechanisms/models briefly to extend the research work. Therefore, in this section, the deterioration mechanisms of cement-based porous materials arising upon freeze-thaw are reviewed briefly.

3.3.1 Hydraulic model

The hydraulic pressure theory developed by Powers is based on the viscous water flow expelled from the partial frozen pore volume if the porous space can not accommodate the almost 9% volume increase associated with ice crystallization [305], see Figure 3.4. This pressure, as shown in eq(3.1), is a function of the saturation degree S_l, ice formation rate $\mathrm{d}w_f/\mathrm{d}T$ and the pore structures. It is shown [305]:

$$P_{max} = \frac{1}{3}\left(1.09 - \frac{1}{S_l}\right)\frac{\eta_l}{\kappa}\frac{\mathrm{d}w_f}{\mathrm{d}T}\frac{\mathrm{d}T}{\mathrm{d}t}\varphi_l; \quad \text{with} \quad \varphi_l = \frac{(\bar{L}+r_0)^3}{r_0} + \frac{(r_0)^2}{2} - \frac{(\bar{L}+r_0)^2}{l} - \frac{l^2}{2}. \tag{3.1}$$

where η_l is the viscosity of liquid pore water (in $\mathrm{Pa}\cdot\mathrm{s}$), κ the water permeability of hardened cement pastes (in m^2), $\mathrm{d}T/\mathrm{d}t$ the freezing rate (in K/s), r_0 average radius of air voids, l the distance to air void, $\bar{L}$ the spacing factor. φ_l is the pressure distribution function, where φ_r has maximum as $l = \bar{L} + r_0$, and φ_l has minimum as $l = r_0$.

As suggested by Powers and co-workers [305, 308, 310], the average half distance between adjacent voids should be limited to avoid the deterioration by the hydraulic pressure that arises upon freezing. The suggested values based on the hydraulic pressure for concrete are within the interval of $250 - 300\mu$m, which

has been verified by many researchers later [82, 101, 294, 298].

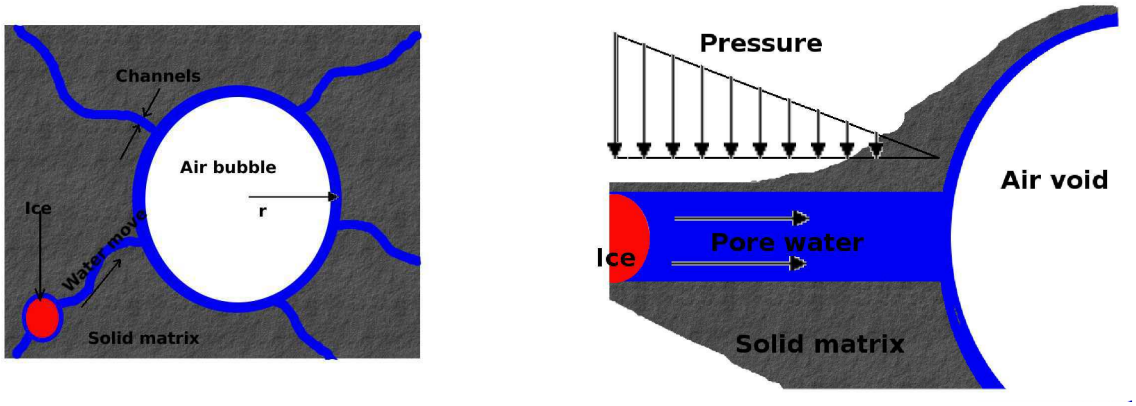

(a) (b)

Figure 3.4: (a), Illustration of ice formation in capillary pores in vicinity of air bubble; (b), Schematic presentation of hydraulic pressure model by Powers.

It has been observed that the volume change is reversed as the air void spacing is reduced, dilation of a non-air-entrained sample does not relax away, and it contracts continually for air-entrained sample when temperature is held constant [310]. The hydraulic pressure theory can not account for either of these observations. Powers suggested that this contraction after ice nucleation can be due to ice melting in the capillary pores and the diffusion of gel water to ice nucleated in the big capillary pores [310]. However, the thermodynamic equilibrium of ice-water in capillary pores does not confirm the hypothesis proposed by Powers, and the so-called thermodynamic framework will be discussed in detail in section 3.3.3. Furthermore, when material is saturated with benzene instead of water, the dilation can be detected although the molar volume of benzene contracts [1] when liquid benzene solidifies [36, 169]. The dilation should also increase with increasing freezing rates since the hydraulic pressure is proportional to the freezing rate according to hydraulic theory, but the opposite results were observed in [441].

3.3.2 Osmotic model

As previous mentioned, the shrinkage upon freezing after first dilation was observed for air entrained cement-based materials [310, 380]. Powers and Helmuth proposed a hypothesis that water moved towards the capillary pores where ice has formed, which was then developed as the osmotic hypothesis to explain the deterioration of cement-based materials upon freezing with/without deicing salts [310]. The liquid phase in pores of cement-based materials contains alkali with rather high concentrations, i.e., the pH in range of $\geq$ 12.5 [247, 253] and the total ionic strength can be as high as 0.5-1 mol/l [227, 232, 329]. Once ice forms and grows in big capillary pores, the pore solution is concentrated. Therefore, the pore solution in thinner pores where no ice forms due to surface tension, evolves at lower concentration than the unfrozen pore solution in capillary pores. The induced chemical potential difference causes a osmotic pressure built

1. The density of liquid benzene at 298K: 0.8765 g/cm^3 [214], the density of crystallized benzene at 258K: 1.031g/cm^3 [218].

up from water migrating from lower concentration areas (thinner capillary pores and/or gel pores) to the higher concentration areas (larger capillary pores). The water migration/diffusion was put forward to explain the continual shrinkage after first expansion for samples with air-entrainment [310].

Furthermore, the osmotic model coupled with hydraulic model has been applied to account for the pessimum salt concentration on surface scaling [118]. The hydraulic pressure arises upon freezing as soon as ice forms, and it highly depends on the amount of ice formed and ice formation rates. According to thermodynamic laws, for a given cement-based material and a given subzero temperature, the ice volume decreases with increasing salt concentration. The osmotic pressure, on the contrary, increases with increasing salt concentration. Therefore it is expected that introducing the sum of hydraulic pressure and osmotic pressure should account for the pessimum salt concentration as illustrated in Figure 3.5. However, Valenza and Scherer indicated that the osmotic pressure could not be built up because the pressure relaxation is rather fast [405]. In addition, the osmotic model only provided a conceptual description rather than a quantitative assessment of the freeze-thaw deterioration.

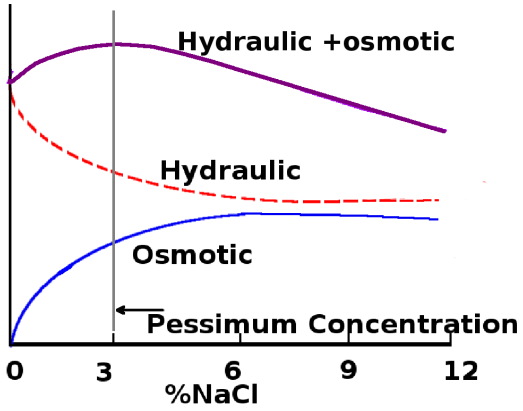

Figure 3.5: The schematic illustration of the pessimum effect of '3 wt%' salt solution by osmotic model.

3.3.3 Thermodynamic models

3.3.3.1 Everett's model

Based on the thermodynamic equilibrium between water and ice crystals formed in porous materials, Everett [113] pointed out that the pressure difference between water and ice accounts for the deterioration of porous materials. Two different ice growth models have been pointed out by Everett [113], as shown in Figure 3.6. When the applied pressure on ice surface P_c remains constant and is not large enough to prevent the movement of the top piston, water in reservoir A would transport to the reservoir B and the top piston will move upward. However, if the applied pressure on ice P_c is large enough

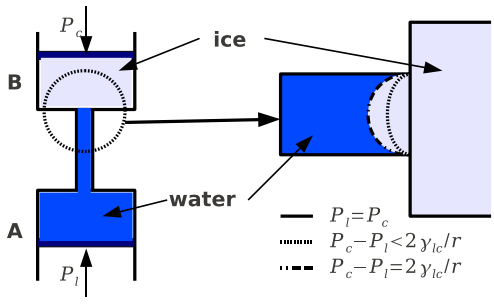

Figure 3.6: The thermodynamic model for ice growing in small pores. After Everett, (1961) [113].

to prevent the movement of piston, it is more likely that ice penetrates along the small capillary. Again, the Gibbs-Thomson equation is recalled to describe ice-water equilibrium with small hemispherical cap. Once the surface tension induced pressure difference exceeds the strength of porous materials, frost damage occurs.

3.3.3.2 Micro-ice-lens theory

The micro-ice-lens model is based on the stability criteria for triple-phase condition of water liquid, water vapor and ice in pores at temperature below bulk water freezing point [355–357]. Briefly, micro-ice-lens act as water pump to achieve an artificial supersaturation condition due to the shift of triple-phase conditions with temperature as well as a non-infinitely rigid solid matrix. The micro-ice-lens theory focuses on the heat and mass transfer of water, moisture and ice, but not on the possible induced pressure which causes deterioration of porous materials.

The micro-ice-lens theory can be graphically recapitulated in Figure 3.7. During freezing, as required by thermodynamic equilibrium, high negative liquid pressure is created, so that the solid skeleton contracts more in addition to the thermal contraction. The water in reducing volume by solid skeleton shrinkage, therefore must flow to the adjacent ice. Analogous to dry-shrinkage, water in gel pores goes into big capillary pores in vicinity progressively, see top half of Figure 3.7. During heating, water transfers from big capillary pores filled by ice to gel pores in inverse process of freezing. Two transportation routines: evaporation-condensation and melting directly at the interface between ice and water, may take place during thawing. If extra water source exists, it will be sucked into the gel efficiently by viscous flow, see bottom half of Figure 3.7. This may be, in some extent, the reason for water uptake during freeze-thaw cycles. The saturation increment during freeze-thaw cycles must be an important factor for the frozen deterioration of porous materials, since it has been found that a critical

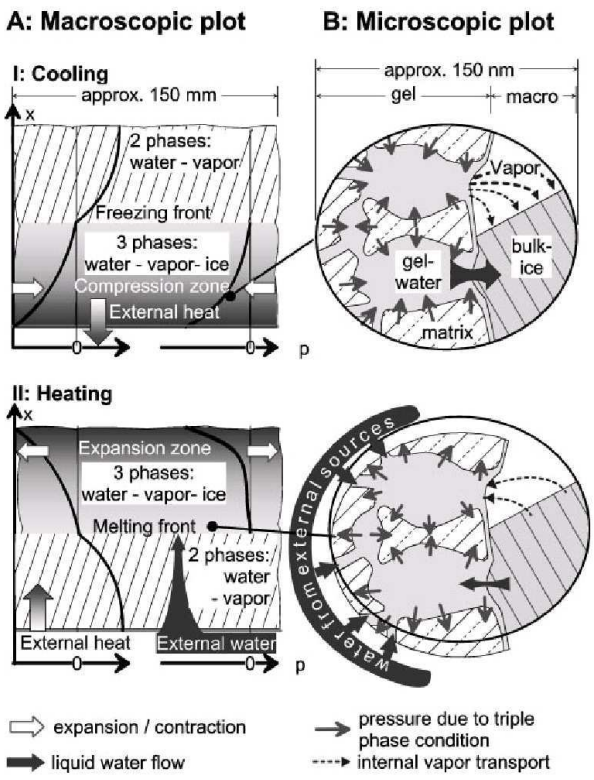

Figure 3.7: Schematically illustration of Micro-ice-lens model. Part I shows the cooling (Top) and Part II shows the heating (Bottom) phase of freeze-thaw cycle. Adopted from Setzer, (2001) [356].

saturation degree that is not unique for porous materials, exists [117, 118]. The related content will be presented in section 3.3.4.

3.3.3.3 Crystallization pressure

When ice crystallizes in capillary pore and/or grows from external surface, see Figure 3.8, the hemispherical ice front as well as the sides of cylindrical ice should observe mechanical equilibrium. However, the curvature difference between the cylindrical side and hemispherical front of ice requires an additional pressure exerted by pore wall, otherwise, the pressure inside the ice crystals would not be uniform, and ice would melt from the region of higher pressure and crystallize elsewhere to make sure the equilibrium of the whole ice crystals. The pressure between the crystal and the pore wall is so large that the pressure necessary to force them into contact is greater than the tensile strength of cement paste [342]. In order to equilibrate the forces, the crystal attempts to grow towards the wall, pushing the wall away. This is exactly the same as the mechanism of frost heave. More comprehensive and extensive discussion on the crystallization pressure can be found in [342, 407].

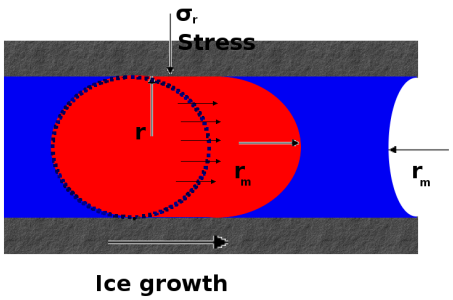

Figure 3.8: The schematic illustration for crystallization pressure generated on ice.

3.3.4 Critical saturation degree and fatigue

The critical saturation degree S_{cr} exists for all porous materials subjected to freeze-thaw loading. Based on series of experimental observations, Fagerlund [117, 118] suggested that low-cycle fatigue as well as gradual water adsorption (water uptake) should account for the frost damage. Two sorts of freeze-thaw experiments were performed by Fagerlund [120]: the open freeze-thaw test and the closed (sealed) freeze-thaw test. The former experimental condition allows mass and heat transport freely. This is quite practical, because most of concrete structures in civil engineering are exposed freely. It has been observed that, for cement-based materials, the water content increases step by step for each freeze-thaw cycle [117, 118, 120, 387]. Yet the mechanisms for water uptake during freeze-thaw cycles have not been clarified. Kaufmann [188] suggested that the thermal contraction of ice can contribute to both the water uptake and the frost damage. As presented in Figure 3.9, ice contacts much more than cement-based solid when temperature decreases (see Figure 3.9(1)); therefore, it provides the residual volume to accommodate more water migrated from thinner capillary pores in vicinity or water source outside (see Figure.3.9(2)); when temperature rises again, it would create damage due to ice expansion since there is no room to accommodate

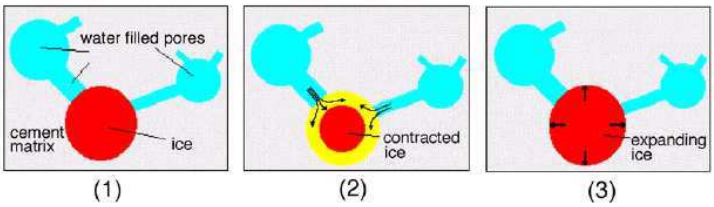

Figure 3.9: Thermal contraction of ice when temperature decreases (1) and resaturation with pore solution which then freezes (2). Ice expands as temperatures rises, which induces tension in the cement matrix (3). After Kaufmann (2004) [188].

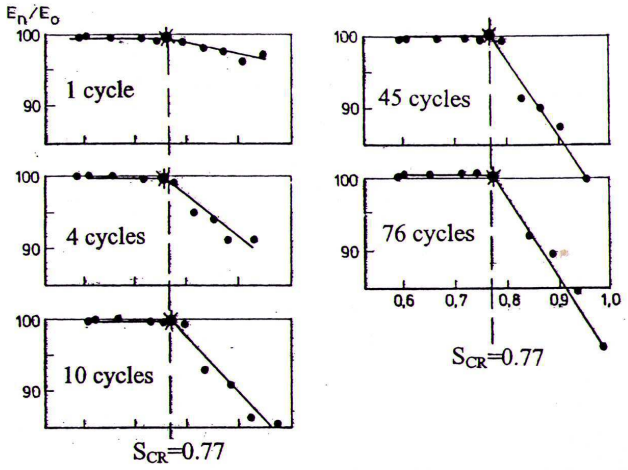

Figure 3.10: Effect of the water saturation degree and the number of freeze-thaw cycles on the relative elastic modulus (E_n/E_0) of a cement mortar measured by closed (sealed) freeze-thaw test. After Fagerlund (2002) [120].

the additional volume because ice engulfed the pores completely. This could be also a reason for freeze-thaw hysteresis [188]. Another mechanism for water uptake is the so-called 'Micro-ice-lens' model [356], which was introduced in previous section.

Table 3.1: The critical saturation degree for different porous materials.

Material	S_{cr}	references
Mortar	0.77	Figure 3 in Fagerlund (2002) [120]
Concrete	0.845	Figure 4 in Fagerlund (2002) [120]
Concrete Type I	0.90	Figure 5 in Fagerlund (2002) [120]
Concrete Type II	0.80	Figure 5 in Fagerlund (2002) [120]
Sand lime brick	0.80	Figure 6 in Fagerlund (2002) [120]
Concrete	≈0.830	Figure 7 in Fagerlund (2002) [120]
Concrete with steel fibers	0.86	Figure 1 in Fagerlund (1975b) [117]
Concrete without fibers	0.86	Figure 1 in Fagerlund (1975b) [117]
Cellular concerete, Type I	0.62	Table 1 in Fagerlund (1975b) [117]
Cellular concerete, Type III	0.48	Table 1 in Fagerlund (1975b) [117]
Underburnt clay brick	0.85	Figure 12 in Fagerlund (1975b) [117]
Wellburnt clay brick	0.76	Figure 12 in Fagerlund (1975b) [117]
10 rocks in France	0.60-0.93	Table 1 in Prick (1997) [311]

Under condition of closed freeze-thaw, the material is sealed to avoid water uptake and/or loss. A critical saturation degree S_{cr} is found independent of freeze-thaw cycles, when the relative elastic modulus versus saturation degree are plotted at different freeze-thaw cycles, see Figure 3.10. Table 3.1 shows the critical saturation degree for different porous materials from numerous experimental measurements. It can be found that there is no unique value for all the porous materials. Besides, the critical saturation degree is lower than the values estimated by Powers hydraulic pressure theory: around 0.91. A possibility of application of critical saturation degree for surface scaling by deicing salts was also discussed by Fagerlund [117]. The saturation degree would increase if deicing salts exist at surface of material due to osmotic

theory on one hand, on the other hand, the amount of freezable water would be decreased due to the high salt concentrations contained in pore solution. Therefore, a pessimum salt concentration that creates most severe damage to cement-based materials is expected.

3.3.5 Glue spalling model

The glue spalling model was inspired by an industrial technique to decorate glass surface [148]. The mechanism of glue spalling is schematically illustrated in Figure 3.11. The rough glass surface is coated with a layer of epoxy at first, then the temperature drops. Because of the mismatch of thermal dilation between glass and epoxy, high tensile stresses are created in the glass surface at the boundary of the islands as the epoxy shrinks relative to the substrate. These stresses make cracks propagate in the glass surface, culminating in the removal of the island and a thin piece of glass [405].

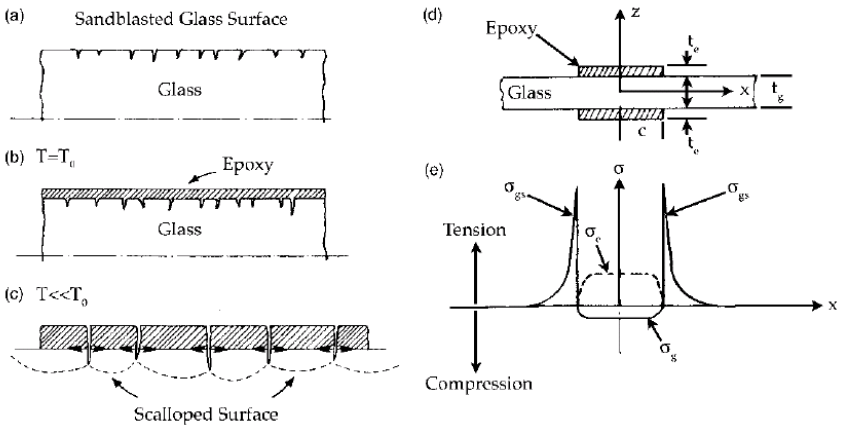

Figure 3.11: (a-c) Schematic representation of the glue-spalling mechanism: (a) sandblasted glass surface with rough surface, (b) covered with epoxy surface layer at initial temperature, T_0, and (c) scaling of glass when $T \ll T_0$. (d,e) Schematic representation of an epoxy/glass/epoxy sandwich seal and the stress that arises in the composite: (d) sandwich seal, dimensions and orientation; (e) schematic of stress that arises in the glass surface under the epoxy, σ_g, in the epoxy, σ_e, and the glue-spalling stress around the boundary of the epoxy, σ_{gs}. After Valenza and Scherer (2006) [405]. These figures were initially presented by Gulati et al. 1982 [148].

The glue spalling stress in the glass surface can be approximated, by elastic analysis, as a function of the difference between the stress from the thermal expansion mismatch and the tensile stress in the epoxy. This stress as well as the stress in the epoxy and glass are given by [405]:

$$\sigma_{gs} = \frac{E_g}{1-v_g}\left[\Delta\alpha - \sigma_e \frac{1-v_e}{E_e}\right]; \quad \sigma_e = \frac{0.5 t_g \left[E_g/(1-v_g)\right]\Delta\alpha\Delta T}{0.5(E_g/E_e)[(1-v_g)/(1-v_e)] + t_e}; \quad \sigma_g = -2\sigma_e \frac{t_g}{t_e} \tag{3.2}$$

where σ is stress as introduced in Figure 3.11, E is the elastic modulus, v is the poisson ratio, t is the thickness, $\Delta\alpha$ is the thermal expansion mismatch $\Delta\alpha = \alpha_e - \alpha_g$ and the subscript e, g and gs denote the

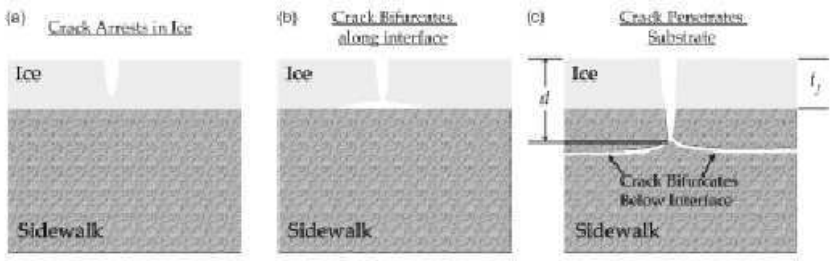

Figure 3.12: Illustration of the three situations that may occur when the ice layer cracks from the mismatch stress. The crack may (a) arrest in the ice, (b) bifurcate along the ice/cement interface, or (c) penetrate the cement surface. After Valenza and Scherer (2006) [405].

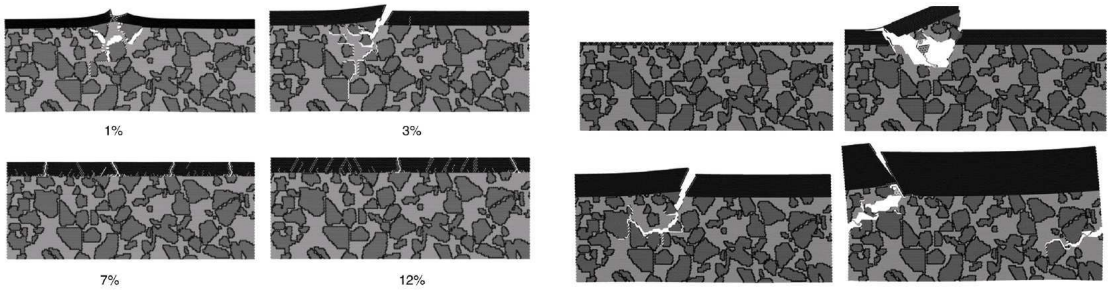

Figure 3.13: (a), Numerical modeling of the pessimum salt concentration effect on the frost scaling damage; (b) Effect of ice-layer thickness (1, 3, 5 and 10 mm) on the frost surface scaling damage magnitude. After Copuroglu and Schlangen (2008) [72].

epoxy, glass and glue-spalling stress around the boundary of the epoxy.

Valenza and Scherer introduced this model to explain the surface scaling of cement-based materials with deicing salts upon freezing [404–408]. The mismatch of thermal expansion coefficients of ice and cement-based substrate mainly contributes to the surface scaling (the thermal (volumetric) expansion coefficient of ice is about $159 \times 10^{-6}\mathrm{K}^{-1}$ [263], while that of the cement paste is about $30 \times 10^{-6}\mathrm{K}^{-1}$ [310]). The layer of pool solution acts as the epoxy as illustrated in Figure 3.11. As analyzed by the authors [405], for a cement-based material covered with a layer of ice, the glue spalling stress is estimated as ≈ 2.6MPa when the temperature change is $\Delta T = 20$℃, which is capable of damaging the surface of cement-based materials. To explain the pessimum concentration for material deterioration, the authors [405] stated that the brine pockets that impact the mechanical properties of brine ice were the main reason for pessimum concentration. Ice crystallizing from pure water is too strong to crack, while the brine ice crystallizing from high concentrated solution is too weak to damage the surface of materials [405]. As presented by Valenza and Scherer [405], three different situations for ice cracking may occur, see Figure 3.12: it arrests at the interface (Figure 3.12(a)), bifurcates along the interface (Figure 3.12(b)), or penetrates the substrate (Figure 3.12(c)). The third situation is likely to occur due to the weak surface layer of cement-based materials and the weak interface transition zone (ITZ).

The numerical simulation results by Copuroglu and Schlangen [72] were consistent with those by Valenza

and Scherer [404–407], see Figure 3.13(a). Furthermore, the experimental results obtained by the authors [72] indicated that the larger the thickness of superficial pool solution, the more severe the surface scaling. The results by numerical modeling confirmed their conclusions [72], see Figure 3.13(b). Recent study by Sun and Scherer [380] indicated that the mismatch stress on substrate decreases when air voids are entrained into cement-based materials due to the cryo-suction of ice, which forms first in capillary pores in vicinity of air voids or at the interface between air voids and solid skeleton. Therefore, the frost resistance of cement-based materials against surface scaling can be improved by air entrainment.

3.3.6 Poromechanical model

The Poromechanics has been widely applied in fields of rock engineering, soil engineering, petrol engineering and bio-engineering [76, 92, 105]. For a porous material, the constitutive equation for mechanical equilibrium is [76, 79]:

$$\boldsymbol{\sigma} = \mathbb{C} : \boldsymbol{\epsilon} - \boldsymbol{b}P^* - \mathbb{C} : \boldsymbol{\alpha}_{th}\Delta T \tag{3.3}$$

where $\boldsymbol{\sigma}$ is the macro stress tensor, $\boldsymbol{b}$ is the tensor of Biot's coefficient, P^* is the effective pressure, $\mathbb{C}$ is the fourth order tensor of material stiffness, $\boldsymbol{\alpha}_{th}$ is the thermal (volumetric) expansion coefficient of solid skeleton.

According to Coussy [77], the sources for stresses arising upon freezing could be: ①, the pressure induced by the volume or density change of ice formation; ②, the pressure induced by interfacial energy; ③, the pressure created by ice crystallization (crystallization pressure); ④, the discrepancy between thermal expansion coefficients of solid matrix, pore liquid and ice crystals; ⑤, the pressure induced by the fusion heat, which is the reason of immediate expansion of crystallization of Benzene in cement pastes and porous glass observed in [36, 169].

Table 3.2 presents the equations for effective or mean pore pressure of poromechanical models applied for describing the freezing behaviors of cement-based materials. For a stress-free loaded cement-based material, the strain arises upon freezing due to the density change, the entropy change during freezing/melting, thermal dilation mismatch between solid matrix and pore phases, and the surface energy change as ice penetrating into thin pores [77]. It thus requires,

$$\boldsymbol{\epsilon} = \boldsymbol{\epsilon}_{\Delta\rho} + \boldsymbol{\epsilon}_{\mathcal{S}_f} + \boldsymbol{\epsilon}_T + \boldsymbol{\epsilon}_U \tag{3.4}$$

In case that a cement-based material is initially saturated with water, the deformation comes mostly from hydraulic pressure associated with phase change. However, if cement-based material is entrained with air

Table 3.2: The effective/mean pore pressure of poromechanical models used in literature.

The effective/mean pore pressure	Authors	References
$P^* = \frac{1}{\phi}\left(\int_{r_{eq}}^{0} P_l \frac{d\varphi}{dr} + \int_{\infty}^{r_{eq}} \sigma_r \frac{d\varphi}{dr}\right)$[a]	Zuber and Marchand (2000,2004) Wardeh and Perrin (2008a,2008b)	[449–451] [421, 422]
$P^* = \frac{1}{\phi}\left(\phi_c P_A + \phi_l P_l\right)$[b]	Sun and Scherer (2010)	[380]
$P^* = S_l P_l + S_c P_c - \frac{2}{3}U$[c]	Coussy (2005), Coussy and Monterio (2008)	[77, 82]
$P^* = \chi(t)P_\infty + (\dot{\phi}t - \chi(t))\rho_c \mathcal{S}_f (T - T_m)$[d] $0 < t \leq 1/\dot{\phi} = \theta$ $P^* = \rho_c^0 \Delta\mu^* + (P_\theta - \rho_c^0 \Delta\mu^*)\exp(-\mu/\tau)$ $\mu = t - \theta \geq 0$ $P^* = \rho_c^0 \Delta\mu^* + [-\mathcal{S}_f \dot{T} t + (\mathcal{S}_f \dot{T} t + P_\theta - \rho_c^0 \Delta\mu^*)\exp(-\mu/\tau)]$ $\mu = t - \theta \geq 0$	Coussy and Teddy Fen-Chong (2005)	[80]

[a] P_l is the liquid pore pressure, σ_r is the stress on pore wall, r_{eq} is the radius of ice at equilibrium with water, $\frac{d\varphi}{dr}$ is the pore size distribution, ϕ is porosity of material.

[b] $\phi_{j=l,c}$ is volume fraction of ice and water respectively, P_A is the stress on pore wall. $P_l = \Delta\mathcal{S}_f \Delta T$, $< P_A \phi_c >= \phi_c \int_T^{T_{mr}} \mathcal{S}_f dT - \int_T^{T_m} \left(\lambda(T') \int_{T'}^{T_{mr}} \mathcal{S}_f dT"\right) \phi_c(T) dT$, T_{mr} is the melting temperature of water confined in pores with radius r.

[c] S is the volume fraction of ice (with subscript c) and water (with subscript l), U is the surface energy.

[d] $\rho_c^0 \Delta\mu^* = P_c - P_l = -\Delta\mathcal{S}_f \Delta T$, ρ_c^0 is the ice mass density at atmospheric pressure, $P_\infty = \frac{4G_s K_c}{4G_s + 3K_c}\left(\frac{\rho_l^0}{\rho_c^0} - 1\right)$ representing the pore pressure arising upon an instantaneous freezing of the whole pore liquid, $\chi(t) = \frac{\dot{\phi}\tau}{1-\alpha\dot{\phi}\tau}\left[1 - \left(\frac{1+\alpha-\alpha\dot{\phi}}{1+\alpha}\right)^{\frac{1}{\alpha\dot{\phi}\tau}-1}\right]$. $P_\theta = \chi_\theta P_\infty + (1 - \chi_\theta \rho_c^0 \Delta\mu^*)$, $\chi_\theta = \frac{\dot{\phi}\tau}{1-\alpha\dot{\phi}\tau}\left[1 - (1+\alpha)^{1-\frac{1}{\alpha\dot{\phi}\tau}}\right]$ the pressure at $\theta = \frac{1}{\dot{\phi}}$, $\tau = \eta\left(\frac{3}{4G_s} + \frac{1}{K_c}\right)$.

voids properly, the second term in eq(3.4) would contribute mostly on the stain arising upon freezing [82]. The effects of air-entrainment on the frost resistance of cement-based materials will be discussed in section 3.4 in detail. Interestingly, the pore pressure can be deduced when the strains upon freezing are obtained, cf. Wardeh and Perrin [421] and Wardeh et al. [420].

3.3.7 Summary

As introduced in previous sections, the models/theories are based on either the principles of thermodynamic laws or the concept of Darcean flow or them both. Figure 3.14 illustrates the models with time arrow. Any model/theory can not catch all the deterioration phenomena exhibited on the field practice and/or laboratory experiments. In Table 3.3, the scope and advantages/disadvantages are summarized. As shown in Table 3.3, even the most widely used model, the hydraulic pressure model can not explain the continual expansion of non-air-entrained samples and the continual shrinkage of air-entrained samples when temperature is held constant after ice nucleation [310]. The later developed osmotic hypothesis by Powers and Helmuth may provide a reasonable concept for both internal cracking and surface scaling. However, there is no mathematical expression to quantify the osmotic pressure [235, 236]. In addition, the time required to build up the osmotic pressure is significantly longer than that required to relax [405]. Based on the experimental observations, the critical humidity and fatigue model are very practical for concrete engineering [120]. Furthermore, the phenomenon of water uptake during freeze-thaw cycles has been ver-

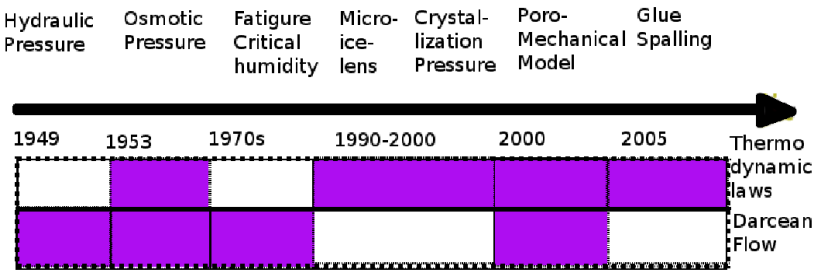

Figure 3.14: A schematic illustration of the models of frost deteriorations of cement-based materials with time arrow.

ified by experiments extensively [120, 387]. The micro-ice-lens model developed by Setzer [356] based on the triple phase thermodynamic equilibrium provided a mechanism for water uptake during freeze-thaw, but in the absence of mechanical consideration. Based on the point view of thermodynamics, the micro-ice-lens model and crystallization model are quite similar, the former focuses on the stability criteria for triple-phase condition of water liquid, water vapor and ice in pores materials [356], while the later focuses on the stress exerted on pore wall during freezing [342]. The crystallization pressure and the hydraulic pressure may contribute most to the stress on solid skeleton during freezing. Therefore, by combining both pressure sources, the strains can be predicted by means of poromechanical approach [450, 451], and it has been further developed by Coussy and co-workers comprehensively and extensively [77, 82].

For surface scaling, numerous experiments have been carried out to identify the mechanisms of salt scaling. However, it seems that none of them can explain most of the observations. Recently, a model inspired by a industrial technique, the glass decoration, has been proposed by Valenza and Scherer [404, 405]. As shown in section 3.3.5, this model is stated to be capable catching all the characteristics of salt scaling. However, some arguments about the phenomena of surface scaling may be of interest. For instance, the authors suggest that the surface scaling with pool of pure water is misleading, while this scaling has been verified by many experiments [115, 223, 354]. Furthermore, Sellevold and Farstad [354] reported that for a given concentration of outer solution, scaling is more severe for water saturated samples than for those which have been impregnated with the salt solution prior to test. In addition, it is well recognized that chloride-related deicing chemicals often brought about leaching of calcium hydroxide, as well as chemical alterations in concrete [37, 119, 266, 418], while magnesium chloride, in particular, results in the conversion of calcium silicate hydrate to non-cement-based magnesium silicate hydrate [87, 382, 391]. Therefore, the mechanisms for salt scaling may be not as simple as any single model provided before.

Of course, numerous studies on the relevant issues of freeze-thaw deterioration of cement-based materials are not presented in this work, cf. the contribution from Litvan [221–224] and Penttala and coworkers [284–286]. Litvan suggested that water migrates from thin pores to the air void or cracks due to the difference between the vapor pressure over supercooled water and that over ice, which is very similar to the micro-ice-lens theory developed by Setzer [356]. In addition, Litvan indicated that the pessimum can be attributed

Table 3.3: Recapitulation of models/theories for cement-based material subjected to freeze-thaw loadings.

Model	Internal cracking	Surface scaling	Advantages	Disadvantages	Representative references
Hydraulic pressure	√		Comprehensive model for the internal frost cracking and effect of air voids.	Can not explain the continual expansion of non-air-entrained samples and the continual shrinkage of air-entrained samples when temperature is held constant after ice nucleation	[305]
Osmotic pressure	√	√	Concept to explain the continual shrinkage after ice nucleation for air entrained samples and the effect of deicing salts.	It has no quantitative expression, and the time required to build up the osmotic pressure is significantly longer than that to relax.	[310]
Crystallization pressure	√		Help to understand the local equilibrium in pores.	Not at the scale of macroscopic condition.	[342]
Critical saturation degree and fatigue	√	√	A practical model with an important factor, the critical saturation degree.	No description of microscopic mechanisms, and the results depends much on the experimental conditions.	[120]
Micro-ice-lens	√		Help to understand the microscopic equilibrium in pores and water uptake.	No mechanical theory	[356]
Glue-spalling		√	Specially for surface scaling, help to understand the mechanisms of scaling		[404, 405]
Poromechanics	√	√	Comprehensive model for understanding the couplings between physical, thermodynamic and mechanical phenomena and for predicting macroscopic volume change.	Relatively complicated and it needs numerical calculations.	[77, 82]

to the increase of the saturation degree and lowering of the temperature of ice formation [221], which is similar to the opinion of Fagerlund [120]. Penttala and coworkers used the classical mechanical theory to predict the volumetric behavior of cement-based materials during freeze-thaw cycles. The internal pressure was deduced from the triple-phase equilibrium among pore water, ice and vapor. Rather rough consistent results were obtained for Penttala's model. The similar model was established by Zhou and Mihashi [447] and Mihashi et al. [250]. Some other important but not vital factors, such as the thermal shock [203, 231, 261, 283], and the variation of the microstructure and pore structure of porous solid along the distance beneath the surface [294], are not considered in the present work.

3.4 Effect of air-entrainment

The air-entrainment technique was developed to improve the frost resistance of cement-based materials in 1930s. When air entrainment agents were mixed with fresh concrete, it would form a series of air bubbles with diameters in range of 10μm$\sim$500μm because the air entrainment agents are hydrophobic generally. The fresh concrete contains $\approx$ 1.5% air content, even when no air entrainment agents are applied. However, these air voids would not improve the frost resistance of concrete because the air voids are in relatively large size, i.e., $d \geq 100\mu$m, and they do not have appropriate spatial distribution in cement pastes. Numerous research indicated that it would improve the frost resistance of concrete both for internal

cracking and surface scaling significantly, when 5%~6% properly distributed air voids are entrained into concrete [96, 305, 310, 380, 407, 408]. As shown in Figure 3.15(a), the number of freeze-thaw cycles required to reduce the relative elastic modulus to 50% increases significantly as the air content increases. Under the same freeze-thaw cycles, cement-based materials with more air voids can have larger relative elastic modulus, see Figure 3.15(b). Note that the air void content is only a factor necessary but not sufficient for improving frost resistance. Studies indicated that improperly air void entrainment, eg inadequate amounts of entrained air, or a 'coarse' air void system, show a worse internal and surface scaling resistance against freezing [101, 175, 176]. ACI Committee 201 and 318 suggest that a good air void system is made up of a system of uniformly distributed, numerous, very fine, spherical and nearly spherical entrained voids that are situated close to each other so that the specific surface and the void spacing factor of air voids fulfill the respective industry requirements of at least 600 in^2/in^3 (23.4 mm^2/mm^3) and at most 0.008 in.(0.2 mm) [101]. Note that the void spacing factor, first introduced by Powers [305], is a factor representing the maximum half distance between adjacent voids. The void spacing factor, compared to the air void content, is a more efficient factor to judge the frost resistance of an air entrained cement-based material.

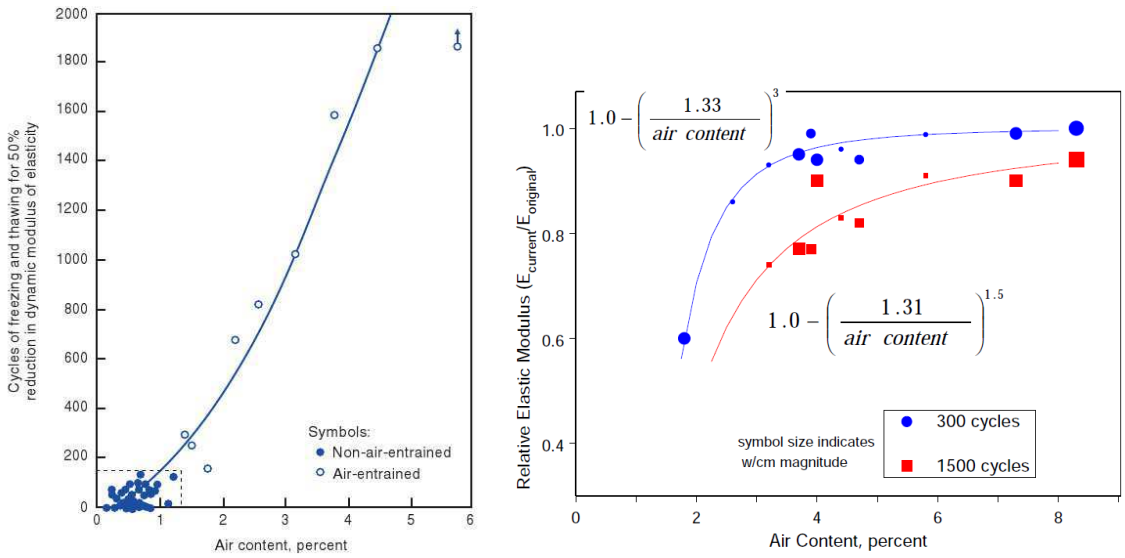

Figure 3.15: Effect of entrained air voids on the resistance of concrete against freeze-thaw in laboratory tests. (a) The required freeze-thaw cycles for 50% reduction on relative dynamic elastic modulus in terms of air void content. The used concrete samples were made with cements of different fineness and composition and with various cement contents and water-cement ratios. After [2]. (b) Variation of relative elastic modulus with air void content under 300 and 1500 freeze-thaw cycles. The used concrete samples were blended with fly ash in different dosages, 1.33 and 1.31 are constants depending on mix characteristics durability level. After Cramer and Walls [83].

The mechanisms of frost resistance improvement by air entrainment were studied since this technique has been used in concrete engineering. Powers, who may be one of the earliest researchers to study the air

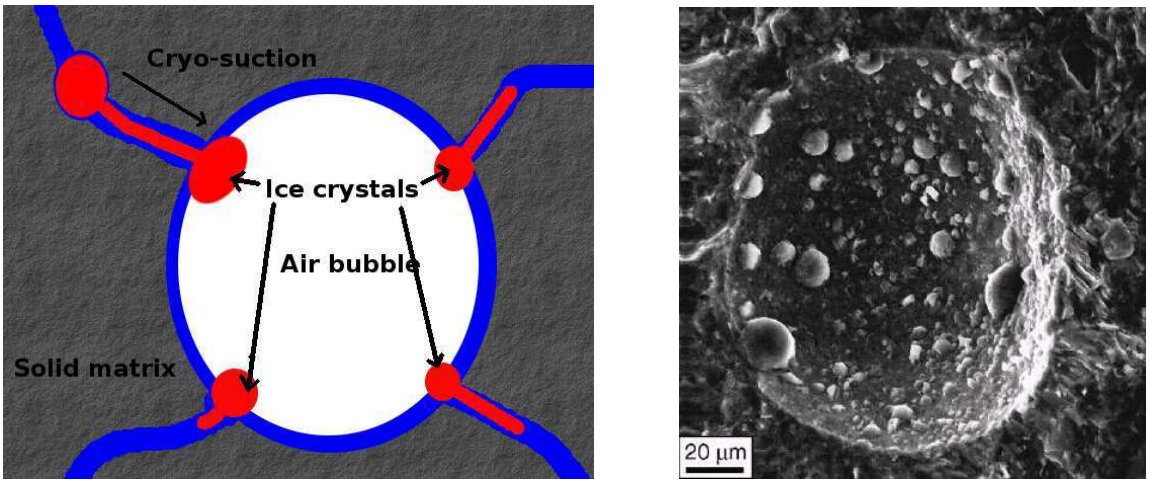

(a) (b)

Figure 3.16: (a), Schematic illustration of cryosuction effects of air bubbles. (b), The ice crystals observed by environmental scanning electric microscopy (ESEM). After Corr et al. (2004) [73].

void effects quantitatively, proposed the famous hydraulic pressure theory as previous described, correlating the pore pressure to the spacing factor [305], see section 3.3.1 for detail. It is the air void that provides the space accommodating the water expelled from the capillary pores due to the 9% volume increase when water transfers to ice during cooling. By means of the hydraulic pressure theory, the safety void spacing factor is estimated to be 200∼250 μm, which has been verified by many researches and engineers later, cf. [82, 114, 296, 297]. According to Pigeon et al. [297], the spacing factors required for protecting concrete decrease with the freezing rates. Lower freezing rate provides larger safety spacing factors.

In addition, according to the investigation of the freezing process of air void entrained concrete by means of environmental scanning electron microscopy (ESEM) by Corr et al. [73, 74], the interface between air void and solid skeleton acts as ice nucleation agents, especially for the area connected with the capillary pores. This mechanism is illustrated in Figure 3.16(a). As observed in Figure 3.16(b), the ice forming on the surface of air void is found to be in hemisphere and the contact angle between ice and solid skeleton is about 91° [74].

The mechanism of cryosuction can account for the continual shrinkage of air entrained cement-based materials after a first peak of ice formation as observed by Powers and Helmuth [310]. Because air voids are generally much larger than capillary pores where ice gem penetrates, the effect of size on the ice crystals on the air void interface can be neglected. The ice pressure thus can be assumed to be equal to atmospheric pressure or to be be zero [406]. Therefore, the liquid pressure is negative and proportional to the depression temperature, viz. $P_l = \Delta\mathcal{S}_f(T - T_m), \quad P_c = 0.1\text{MPa}$. At -20℃, the liquid pressure would be $-20 \times 1.22275 = -24.455$MPa, which is capable of creating large contraction in addition to the thermal shrinkage. Detailed quantitative analysis can be found in Ref. [77, 82, 114] and in section 5.1.

Chapter 4

Poromechanical framework

Contents

4.1 Basic notations and definitions of the present work

This part of the present work focuses on the thermoporomechanical description on behaviors of initial solution saturated cement-based materials subjected to freeze-thaw loading. It starts from the well-established thermoporoelasticity theory, cf. [76, 79]. The fracture behaviors of cement-based materials are thus beyond this scope although the elastic and fracture deformations are symbiotic when cement-based materials suffer

severe mechanical and/or environment loadings. A symmetrical geometry of sample is considered in this study (see Figure 4.1). The surface of sample is covered with a layer of epoxy resin in thickness of about 1 mm and a layer of latex membrane, see section 9.1.1 for detailed procedures. It causes hydraulic isolation corresponding to undrained condition as defined in classical poromechanics [77, 79, 135, 137–139]. On the surface of samples, heat exchanges freely. During the freeze-thaw processes, no additional surface stresses are exerted on samples.

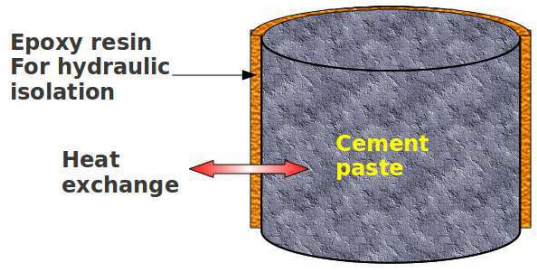

Figure 4.1: Schematic representation of the geometry structure of samples in the present study.

The used material in this work, is hardened cement paste, which is widely used as a main and the most important compound of concrete in civil engineering [247, 391], support and sealing materials in petrol engineering [138], and materials for CO_2 storage [57, 183]. As a typical porous material, the specific characteristics of cement pastes will not be addressed in this chapter (see chapters 6 and 7 for the detailed physico-chemical properties of cement pastes used in this study) but the general characteristics of porous materials are recalled for poromechanical description.

4.1.1 Basic phases definition

In this subsection, we recall the basic definitions of partially frozen porous materials. A **porous medium** is defined as a continuous medium formed from the superimposition of continuous skeleton and continuous porous spaces. The latter has been solution infiltrated initially and frozen partially with temperature decreasing [76]. In this study, one classifies the phases of porous medium as follows (see for instance [76, 77, 79, 98, 114], see also the definition illustrated in Figure 4.2):

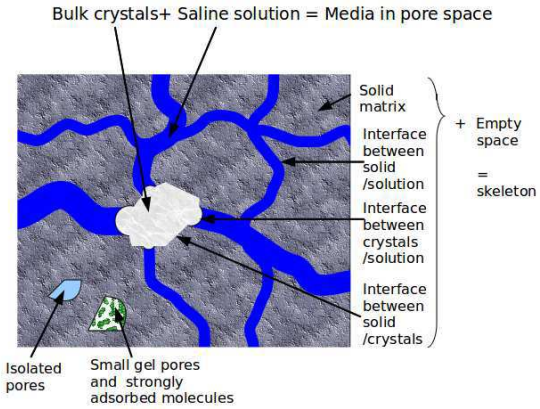

Figure 4.2: Presentation of relation of the porous medium, matrix and skeleton.

❁ The **pore space** is the space of connected pores and it could be filled by saline solution, ice crystals and/or both of them. We mark ϕ for porosity in Lagrangian description, and ϕ_l and ϕ_c for the relative pore volume (partial porosity) occupied by liquid and crystals respectively.

❁ The **solid matrix** is the phase excluding the connected pore space described above. For the cement-based materials, the solid matrix can be composed of the cement-based binders (hardened cement pastes), aggregates (if exist), the isolated pores, water molecules and/or ions strongly adsorbed on the solid surface, as well as the small gel pores in scale of Angstrom meter. This phase is somehow scale dependent, which has been validated by some relevant multiscaling techniques, cf. [67, 68, 403].
❁ The **skeleton** is a continuous medium composed of the matrix, empty pore space and the interfaces of liquid/solids, liquid/crystals, and crystals/solids [76, 79].

4.1.2 Description of representative volume element

Strictly speaking, cement-based materials are heterogeneous at any scale (cf. Figure 4.3). For instance, concrete and mortar are heterogeneous materials at both macro- and meso-scale; cement paste is heterogeneous at meso- and micro-scale [66, 67, 136, 403]. It is thus important to define representative volume element (RVE) appropriately. For hardened cement pastes, the unreacted clinkers as well as the large crystals, such as Portlandite, ettringite, can be as large as 10 μm [391], therefore the characteristic length of heterogeneity is estimated in the same scale $l_h \approx 10\mu$m. To obtain homogeneous properties of cement pastes, it is thus required that:

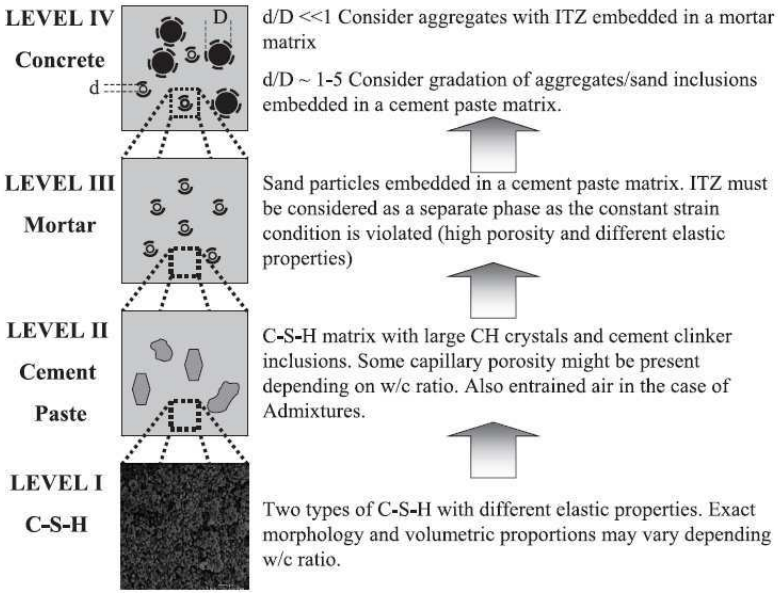

Figure 4.3: Multi-scale heterogeneous microstructure of cement-based composite materials. After Constantinides and Ulm (2004) [67], see also [66, 403].

$$l_{d\Omega} \gg l_h \tag{4.1}$$

where $l_{d\Omega}$ is the characteristic length of RVE, and its value is chosen in the range:

$$l_{d\Omega} \in (100, 1000)\mu\text{m} \tag{4.2}$$

The retained value is somewhat larger than the RVE scale, to say $l_{d\Omega} \in (1, 100)\mu$m, adopted by Fabbri [114], but agrees well with the value of 100 μm retained for comprehensive simulation on the properties of cement pastes by Garboczi, Bentz and coworkers [42, 43, 131].

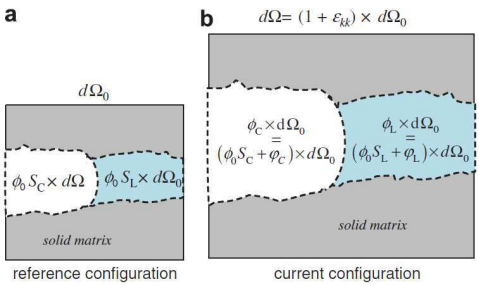

Figure 4.4: Schematic definition of: (a) Lagrangian saturation S_α capturing the invading process (drainage process); (b) Lagrangian change φ_α in partial porosity ϕ_α capturing the deformation process. After Coussy and Monterio (2007) [81].

4.1.3 Hypotheses of small deformation and small displacement

We adopt the frame of small perturbation hypothesis (cf. [76, 79, 114]). Thus we assume the classical hypotheses of infinitesimal transformations and displacements.We also adopt the hypotheses of small variation of porosity and temperature during freeze-thaw:

$$\left|1 - \frac{\phi}{\phi_0}\right| \ll 1; \quad \text{and} \quad \left|1 - \frac{T}{T_0}\right| \ll 1 \tag{4.3}$$

For cement-based materials, under linear elasticity consideration, these hypotheses are particularly true for very limited pore volume deformation due to high bulk modulus and shear modulus of solid matrix. Again, the additional pore volume deformation by any fracture crack in cement-based materials [79] is out of the scope of this study.

At last, we assume the small variation of density of solid phase:

$$\frac{\rho_\alpha - \rho_\alpha^0}{\rho_\alpha^0} \ll 1 \tag{4.4}$$

where ρ_α^0 is the initial phase density. This hypothesis allows us to replace the ρ_α by the ρ_α^0 whenever required. But only solid phases obey this hypothesis. For liquid solution in this study, its density can be influenced significantly by the concentration of salts, which will be specifically considered in Appendix D.

4.1.4 Partial porosities and degree of saturation

During the freeze-thaw processes, the pore space of cement-based materials is partially filled by saline solution $\alpha = l$ and/or ice crystals $\alpha = c$, thus the total porosity ϕ is sum of partial porosity ϕ_α:

$$\phi = \phi_l + \phi_c \tag{4.5}$$

The partial porosity ϕ_α results from the porosity change by an invading process (drainage process) and that by deformation [81], it thus has:

$$\phi_\alpha = \phi_0 S_\alpha + \varphi_\alpha; \quad \sum_\alpha S_\alpha = 1 \tag{4.6}$$

where S_α is the saturation degree. The definition of partial porosity and saturation degree are schematically illustrated in Figure 4.4. According to this definition, the term $\phi_0 S_\alpha$ and φ_α represent the drainage/imbibition process and skeleton deformation of phase α, respectively.

4.1.5 Partial molar quantities and apparent molar quantities

For saline solution, the quantities of volume, heat capacity and compressibility (or bulk modulus) of a mixture can not be obtained by the simple weighted average method. In addition, there is limited data on the partial molar quantities of saline solution, particularly when it is subjected to the variation of pressure, temperature and salt concentrations. For simplification, the apparent molar quantities are introduced. For NaCl solution, the apparent molar volume is defined as the volume change of solution when one mole NaCl is added to a large volume of the mixture, while the water molar volume is retained to be bulk molar volume [17]. It thus requires:

$$\mathsf{V}_{\text{total}} = n_{\text{NaCl}}\mathsf{V}_{\phi} + n_w\mathsf{V}_w \tag{4.7}$$

where $\mathsf{V}_{\text{total}}$ is the total volume (m^3), n_{NaCl} and n_w are the mole number of NaCl and water respectively (mole), V_w is the bulk molar volume of water ($\text{m}^3 \cdot \text{mol}^{-1}$), and V_{ϕ} is the apparent molar volume of NaCl ($\text{m}^3 \cdot \text{mol}^{-1}$). Note that the apparent molar volume is equal to the partial molar volume in case of infinite dilution. Figure 4.5 shows the variation of apparent molar volume of Na^+, Cl^- and NaCl with temperature, where the pressure is kept constant at 0.1 MPa. It can be seen that as the temperature decreases, the apparent molar volume of NaCl decreases to be negative, which means more NaCl is added, less total volume is obtained. The derivations of apparent molar volume, heat capacity and compressibility in terms of pressure, temperature and salt concentration for NaCl solution by Archer's model, cf. [15–17], are presented in Appendix D.

In addition, the compatibility of volume of solution requires:

$$c_w\mathsf{V}_w + \sum_i c_i\mathsf{V}_i = 1 \tag{4.8}$$

where c_w is concentration of water ($\text{mol} \cdot \text{m}^{-3}$), c_i is concentration of species i ($\text{mol} \cdot \text{m}^{-3}$) and $\mathsf{V}_{\phi,i}$ is the apparent molar volume of species i ($\text{m}^3 \cdot \text{mol}^{-1}$). The overall density of solution is defined as:

$$\rho_l \equiv \rho_w + \sum_i^N \rho_i \tag{4.9}$$

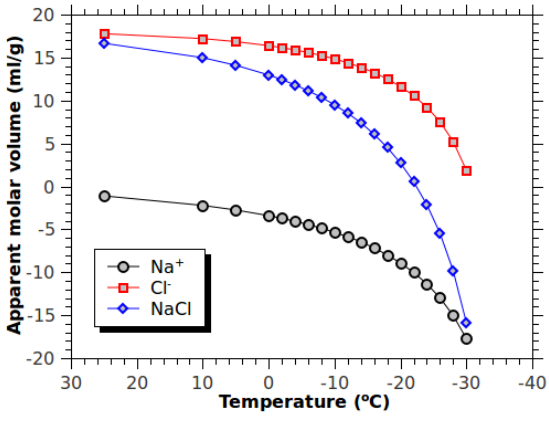

Figure 4.5: Apparent molar volume of Na^+, Cl^- and NaCl in terms of temperature. Data from Tanger and Hegelson [388].

where ρ_l is the total density liquid phase ($\text{kg} \cdot \text{m}^{-3}$), ρ_w the partial mass density of water ($\text{kg} \cdot \text{m}^{-3}$) and ρ_i the partial mass density of species i ($\text{kg} \cdot \text{m}^{-3}$), with relation $\rho_w = \mathsf{M}_w c_w$, $\rho_i = \mathsf{M}_i c_i$, and M_w the molar mass of water ($\text{kg} \cdot \text{mol}^{-1}$) and M_i the molar mass of species i ($\text{kg} \cdot \text{mol}^{-1}$). By substituting of eq(4.8) into

eq(4.9), the overall density then can be rewritten as:

$$\rho_l = \mathsf{M}_w \left(\frac{1 - \sum_i c_i \mathsf{V}_{\phi,i}}{\mathsf{V}_w} \right) + \sum_i^N \mathsf{M}_i c_i = \frac{\mathsf{M}_w}{\mathsf{V}_w} + \sum_i^N \left(\mathsf{M}_i - \mathsf{V}_{\phi,i} \frac{\mathsf{M}_w}{\mathsf{V}_w} \right) c_i \tag{4.10}$$

4.2 Mass conservation of pore fluid

4.2.1 Mass conservation of liquid phase and ice crystals

Let m_α denotes the mass of phase α in a RVE:

$$m_\alpha = \rho_\alpha \phi_\alpha = \rho_\alpha (\phi_0 S_\alpha + \varphi_\alpha) \tag{4.11}$$

According to the conservation law, the mass variation rate is the sum of the Darcean flux $\boldsymbol{\omega}$ and solidification rate (during freezing) $\mathring{m}_{w\to c}$, one can write the conservation expression for liquid saline solution and ice crystals as:

$$\frac{\partial m_l}{\partial t} + \nabla \cdot \boldsymbol{\omega}_l + \mathring{m}_{w\to c} = 0 \quad \text{and} \quad \frac{\partial m_c}{\partial t} - \mathring{m}_{w\to c} = 0 \tag{4.12}$$

Consider a saline solution confined in pore space composed of liquid water (with subscript w) and N ionic species (with subscript i). The flux of saline solution is the sum of the flux of each species [317]:

$$\rho_l \boldsymbol{v}_l \equiv \rho_w \boldsymbol{v}_w + \sum_i^N \rho_i \boldsymbol{v}_i \tag{4.13}$$

where $\boldsymbol{v}_l$ is the velocity of the barycentric center of mass (see for instance, [267, 317]), $\boldsymbol{v}_w$ the velocity of water, $\boldsymbol{v}_i$ the velocity of species i. The mass flux of diffusion of water and species i are then respectively, given by:

$$\boldsymbol{J}_w = \rho_w \phi_l (\boldsymbol{v}_w - \boldsymbol{v}_l) = \mathsf{M}_w c_w (\phi_0 S_l + \varphi_l)(\boldsymbol{v}_w - \boldsymbol{v}_l) \tag{4.14a}$$

$$\boldsymbol{J}_i = \rho_i \phi_l (\boldsymbol{v}_i - \boldsymbol{v}_l) = \mathsf{M}_i c_i (\phi_0 S_l + \varphi_l)(\boldsymbol{v}_i - \boldsymbol{v}_l) \tag{4.14b}$$

From the definition of partial flux of diffusion $\boldsymbol{J}_{J=w,i}$ in eq(4.14) and the barycentric velocity defined in eq(4.13), the sum of all the diffusion fluxes is equal to zero:

$$\boldsymbol{J}_w + \sum_i^N \boldsymbol{J}_i = \boldsymbol{0} \tag{4.15}$$

Let $\boldsymbol{\omega}_l$ denote the flux of liquid regarding the skeleton as reference frame, which can be expressed as:

$$\boldsymbol{\omega}_l = \rho_l \phi_l \boldsymbol{v}_l \tag{4.16}$$

Then the flux of water and solute i are given by:

$$\boldsymbol{\omega}_w = \mathsf{M}_w c_w (\phi_0 S_l + \varphi_l) \boldsymbol{v}_l + \boldsymbol{J}_w \quad \text{and} \quad \boldsymbol{\omega}_i = \mathsf{M}_i c_i (\phi_0 S_l + \varphi_l) \boldsymbol{v}_l + \boldsymbol{J}_i \tag{4.17}$$

Obviously, $\boldsymbol{\omega}_l = \boldsymbol{\omega}_w + \sum_i^N \boldsymbol{\omega}_i$.

4.2.1.1 Darcean transport

A viscous Newtonian liquid transport in a porous medium can be described by the Darcy's law:

$$\boldsymbol{\omega}_l = -\rho_l \frac{\kappa}{\eta_l} \nabla(P_l) \tag{4.18}$$

where κ is the permeability of material to the pore fluid, η_l is the viscosity of pore fluid, P_l is the liquid pressure.

The permeability is one of the most important properties of cement-based materials, and it is related intimately to their durability [122, 247]. Physically, permeability is determined by the square of the critical pore diameter [77, 79, 184, 185]. In concrete engineering, the lower the permeability, the more durable the material is expected [247]. Generally, the permeability can be expressed as function of relative permeability and intrinsic permeability:

$$\kappa = \kappa_r(\phi, S_l)\kappa_0 \tag{4.19}$$

where κ_0 is the intrinsic permeability of a material, it varies from 10^{-16} to 10^{-21} (in m^2) for cement-based materials [76, 271], see also section 7.3 in the present work. Although, physically, the intrinsic permeability depends only on the geometry of the porous network [76, 79], it takes different value for different fluids. For instance, the permeability of gas is systematically higher than that of water [316, 399]. The term $\kappa_r(\phi, S_l)$ denotes the relative permeability related to the porosity and saturation degree. The influence of porosity and saturation degree on the permeability of cement-based materials is specifically addressed and discussed in section 7.3.

4.2.1.2 Fickian transport

As mentioned above, $\boldsymbol{J}_i$ is the diffusion mass flow ($\mathrm{kg} \cdot \mathrm{m}^{-2} \cdot \mathrm{s}^{-1}$) which is related to the gradient of ionic concentration, electric potential and temperature. This physical phenomenon can be described by the extended Nernst-Planck model (cf. [267, 269, 335–337]):

$$\boldsymbol{J}_i = -\frac{\phi_l \mathsf{M}_i D_i c_i}{RT} \nabla\mu = -\phi_l \mathsf{M}_i c_i D_i \left[\frac{1}{c_i} \nabla c_i + \nabla \ln \gamma_i + \frac{\ln(\gamma_i c_i)}{T} \nabla T + \frac{z_i F}{RT} \nabla \Psi_E \right] \tag{4.20}$$

where μ is the electrochemical potential, ϕ_l is the porosity occupied by liquid phase (-), M_i is the molar mass of species i ($\mathrm{kg} \cdot \mathrm{mol}^{-1}$), D_i is diffusion coefficient of species i ($\mathrm{m}^2 \cdot \mathrm{s}^{-1}$), γ_i the activity coefficient of species i (-), Ψ_E the electric potential (V), R is the ideal gas constant $R = 8.314472$ ($\mathrm{J} \cdot \mathrm{mol}^{-1} \cdot \mathrm{K}^{-1}$), z_i is the valence of species i (-), F is the Faraday constant $F = 96485.309$ ($\mathrm{C} \cdot \mathrm{mol}^{-1}$). Note again that the used flow is the mass content per square meter per second, rather than the molar flow of species $\boldsymbol{J}_i$ ($\mathrm{mol} \cdot \mathrm{m}^{-2} \cdot \mathrm{s}^{-1}$) used in [267, 336, 337].

The diffusion coefficient is an important property characterizing the diffusivity of solutes in porous

media, it is often expressed as:

$$D_i = \tau(\phi) D_i^0 \mathcal{G}(\phi, S_l) \tag{4.21}$$

where D_i^0 is the intrinsic diffusion coefficient of species i ($\mathrm{m}^2 \cdot \mathrm{s}^{-1}$), τ is the tortuosity, $\mathcal{G}(\phi, S_l)$ is the function of porosity ϕ and saturation degree S_l (-), see section 7.3 for detail. In many studies, the latter two terms are merged together in one term named relative diffusion coefficient $D_r = D_i^0 \mathcal{G}(\phi, S_l)$.

The intrinsic diffusion coefficient D_i^0 is defined as the diffusion coefficient of ionic species i at the infinite dilution case. It is directly proportional to the mobility of solution and can be given by the Nernst-Einstein approach [47]:

$$D_i^0 = \frac{\kappa_b T \beta_i}{e|z_i|} \tag{4.22}$$

where κ_b is the Boltzmann constant ($1.381 \times 10^{23} \mathrm{J} \cdot \mathrm{K}^{-1}$), β_i is the mobility of species i in free electrolyte (in $\mathrm{m}^2 \cdot \mathrm{s}^{-1} \cdot \mathrm{V}^{-1}$), e is the charge of electron (-1.602×10^{-19} C), z_i is the valence of i (-).

4.2.2 Electroneutrality and Poisson equation

4.2.2.1 Electroneutrality

Let q_i denotes the charge per unit mass of component i ($\mathrm{C} \cdot \mathrm{kg}^{-1}$). For water, it is neutral, thus $q_w = 0$. Then the total current density $\boldsymbol{\omega}_q$ (in $\mathrm{A} \cdot \mathrm{m}^{-2}$) is defined as the net amount of charge flowing per unit surface area and per unit time:

$$\boldsymbol{\omega}_q = \sum_i^N \rho_i q_i \phi_l \boldsymbol{\upsilon}_i \tag{4.23}$$

The total charge per unit mass of the system q is defined by

$$q = \frac{1}{\rho_l} \sum_i^N \rho_i q_i \tag{4.24}$$

Using the eq(4.15), one thus obtains the total current density as:

$$\boldsymbol{\omega}_q = \boldsymbol{J}_c + \rho_l q \phi_l \boldsymbol{\upsilon}_l \quad \text{with} \quad \boldsymbol{J}_c = \sum_i^N q_i \boldsymbol{J}_i \tag{4.25}$$

where $\boldsymbol{J}_c$ is the conduction current (in $\mathrm{A} \cdot \mathrm{m}^{-2}$). Therefore the total current density is equal to the conduction current density plus a convective term $\rho_l q \phi_l \boldsymbol{\upsilon}_l$. The porous medium or the colloidal suspension is also characterized by a global electroneutrality condition: the net charge of the grains is exactly counterbalanced by the net charge of the pore water. Consequently q = 0 and therefore the convective term is equal to zero in the Lagrangian framework attached to the barycentric center of mass [317, 318].

Since it is global electroneutrality in the system ($q = 0$), the continuity equation for the electrical charge,

i.e, $\partial q/\partial t + \nabla \cdot \boldsymbol{J}_c = 0$, then reduces to:

$$\nabla \cdot \boldsymbol{J}_c = 0 \tag{4.26}$$

4.2.2.2 Poisson equation

The electric field built by the net charge q per unit mass ($\mathrm{C \cdot kg^{-1}}$) is given by the Gauss theorem [210]:

$$\nabla \cdot \boldsymbol{E} = \frac{\rho_l q}{\xi_r \xi_0} \tag{4.27}$$

where $\boldsymbol{E}$ is the electric field (in $\mathrm{V \cdot m^{-1}}$), ξ_r the relative permittivity of the medium ($\xi_r = 80$ at 293K for water, the variation of relative permittivity of water with temperature and pressure can be found in [15, 196], and briefly presented in Appendix D.2), ξ_0 the permittivity of free space ($\xi_0 = 8.854 \times 10^{-12}$ $\mathrm{C^2 \cdot J^{-1} \cdot m^{-1}}$). q is excess of charge, which is the sum of charges for all species:

$$q\rho_l = F \sum_i^N z_i c_i \tag{4.28}$$

where z_i (-) and c_i ($\mathrm{mol \cdot kg^{-1}}$) are the valence and the concentration of species i, F is the Faraday constant ($F = 9.6486 \times 10^4$ $\mathrm{C \cdot mol^{-1}}$). The electric field $\boldsymbol{E}$ being the gradient of electric potential Ψ_E:

$$\boldsymbol{E} = -\nabla \Psi_E \tag{4.29}$$

Substitution of eqs(4.27) and (4.28) into eq(4.29), one obtains the Poisson equation:

$$\nabla^2 \Psi_E = -\frac{q\rho_l}{\xi_r \xi_0} = -\frac{F \sum_i z_i c_i}{\xi_r \xi_0} \tag{4.30}$$

The previous two sections (sections 4.2.2.1 and 4.2.2.2) provide two approaches to complete the extended Nernst-Planck equation (cf. eq(4.20)). Both approaches are extensively used in modeling the transport of ions in porous media [317, 336, 337]. Nguyen et al. [268] compared the ions transport depth in concrete through numerical model, see left half of Figure 4.6, and concluded that both electroneutrality and Poisson approaches lead to the same results. Also, it does not exist obvious difference for electrical charge and potential, see right half of Figure 4.6.

4.2.3 Final expression

The transport model is based on the observation that the transport of ions only occurs in the liquid phase. The conservation equations for water w and an ionic species i in the liquid phase at pore scale are

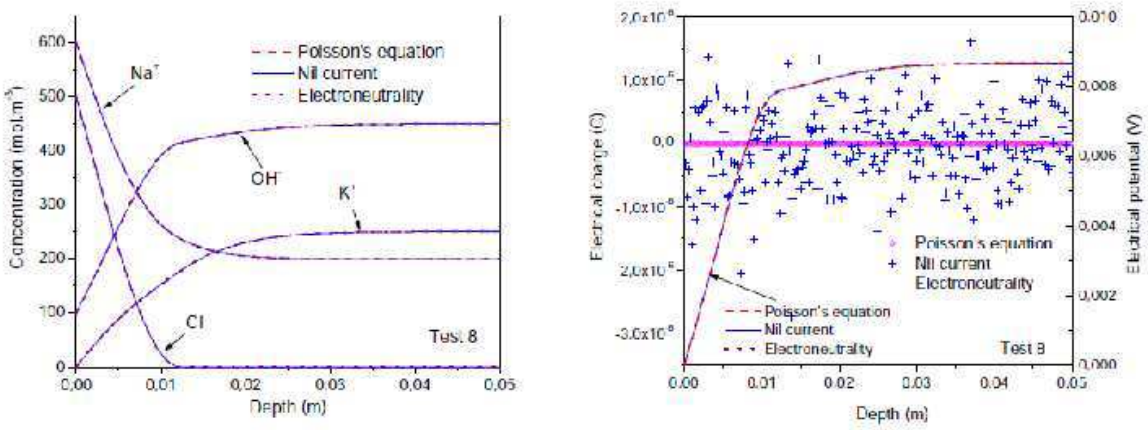

Figure 4.6: Effects of different methods on prediction the concentration profiles (left) and evaluating the electric potential (right). After Nguyen et al. [267, 268].

given as follows [33]:

$$\frac{\partial m_i}{\partial t} + \nabla \cdot \boldsymbol{\omega}_i = 0 \tag{4.31a}$$

$$\frac{\partial m_w}{\partial t} + \nabla \cdot \boldsymbol{\omega}_w + \mathring{m}_{w\to c} = 0 \tag{4.31b}$$

Substitution of eqs(4.16), (4.17b) and (4.20) into eq(4.31a), one obtains:

$$\frac{\partial m_i}{\partial t} - \mathsf{M}_i c_i \phi_l \frac{\kappa}{\eta_l} \nabla^2(P_l) - \nabla \cdot \left\{ \mathsf{M}_i c_i \phi_l D_i \left[\frac{1}{c_i} \nabla c_i + \nabla \ln \gamma_i + \frac{\ln(\gamma_i c_i)}{T} \nabla T + \frac{z_i F}{RT} \nabla \Psi_E \right] \right\} = 0 \tag{4.32}$$

For water, one can derive the conservation equations by the same procedure (substitution of eqs(4.15), (4.17a) and (4.20) into eq(4.31b)) as follows:

$$\frac{\partial m_w}{\partial t} - \mathsf{M}_w c_w \phi_l \frac{\kappa}{\eta_l} \nabla^2(P_l) + \sum_i^N \nabla \cdot \left\{ \mathsf{M}_i c_i \phi_l D_i \left[\frac{1}{c_i} \nabla c_i + \nabla \ln \gamma_i + \frac{\ln(\gamma_i c_i)}{T} \nabla (T) + \frac{z_i F}{RT} \nabla \Psi_E \right] \right\} + \mathring{m}_{w\to c} = 0 \tag{4.33}$$

4.2.4 Heat transfer

The law of heat conduction, known as Fourier's law, states that the rate of heat transfer through a material is proportional to the gradient of temperature [172]:

$$\mathbf{q} = -\boldsymbol{\lambda} \cdot \nabla T \tag{4.34}$$

where $\boldsymbol{\lambda}$ is the tensor of coefficient of heat conductivity. Let $\boldsymbol{\lambda}_\alpha$ stand for the tensor of heat conductivity coefficient of phase α. For isotropic or statistical isotropic materials, $\boldsymbol{\lambda}_\alpha = \mathbf{I}\lambda_\alpha$, where $\mathbf{I}$ is the unit second

order tensor, with $\mathbf{I}_{ij} = \mathbf{I}_{ji}$. For composites, the overall heat conductivity coefficient $\boldsymbol{\lambda}$ depends on the specific heat conductivity coefficient λ_α and the microstructure modes. More details can be found in section refsec:heat-conduct.

4.3 State equations of solid matrix

4.3.1 Dissipation contribution

Considering a deformable porous material, the dissipation can be expressed by the well known Clausius-Duhem inequality [76, 114], and is given by (see Appendix B.1 for detailed derivation):

$$\mathcal{D} = T\frac{\partial \mathcal{S}}{\partial t} - \mathring{r} + T\nabla \cdot s_l \boldsymbol{\omega}_l + \nabla \cdot \mathbf{q} - \frac{\mathbf{q} \cdot \nabla T}{T} \geq 0 \tag{4.35}$$

where $\mathcal{S}$ is the overall entropy density of the considered RVE, $\mathring{r}$ is source of heat, $\boldsymbol{q}$ is the current of outgoing heat, s_l is the specific entropy density of liquid phase, $\boldsymbol{\omega}_l$ is the flow of liquid phase. The overall Helmholtz free energy rate can be written as (see Appendix B.1.1, see also [77, 114]):

$$\frac{\partial \Psi}{\partial t} = \boldsymbol{\sigma} : \frac{\partial \boldsymbol{\varepsilon}}{\partial t} - \nabla \cdot \left[\left(\frac{P_l}{\rho_l} + \psi_l \right) \boldsymbol{\omega}_l + \mathbf{q} \right] + \mathring{r} - \mathcal{S}\frac{\partial T}{\partial t} - \left(\frac{\partial \mathcal{S}}{\partial t} + \nabla \cdot (s_l \boldsymbol{\omega}_l) \right) T \tag{4.36}$$

where Ψ is the overall Helmholtz free energy density, $\boldsymbol{\sigma}$ is the stress tensor, $\boldsymbol{\varepsilon}$ is the strain tensor, ψ_l is the Helmholtz free energy density of liquid phase. Substitution of eq(4.36) into eq(4.35) and separating the global dissipation into three uncoupled terms (cf. [76]): $\mathcal{D}_{sk}$ the skeleton dissipation, $\mathcal{D}_f$ the fluid dissipation and $\mathcal{D}_{th}$ the thermal dissipation, which have the forms:

$$\mathcal{D}_{sk} = \boldsymbol{\sigma} : \frac{\partial \boldsymbol{\varepsilon}}{\partial t} - g_l \nabla \cdot \boldsymbol{\omega}_l - \mathcal{S}\frac{\partial T}{\partial t} - \frac{\partial \Psi}{\partial t}; \quad \mathcal{D}_f = -\boldsymbol{\omega}_l \cdot \nabla g_l; \quad \mathcal{D}_{th} = -\frac{\mathbf{q} \cdot \nabla T}{T} \tag{4.37}$$

where g_l is the Gibbs free energy density of liquid phase, it can be written alternatively in:

$$g_l = \psi_l + \frac{P_l}{\rho_l} = e_l - T s_l + \frac{P_l}{\rho_l} \quad \text{and} \quad \mathrm{d}g_l = -s_l \mathrm{d}T + \frac{1}{\rho_l}\mathrm{d}P \tag{4.38}$$

where e_l is the internal energy density of liquid phase.

4.3.2 Energy balance of skeleton

Let us consider the skeleton dissipation $\mathcal{D}_{sk}$. Substitution of eq(4.12) into eq(4.37a), one obtains:

$$\mathcal{D}_{sk} = \boldsymbol{\sigma} : \frac{\partial \boldsymbol{\varepsilon}}{\partial t} + g_l \frac{\partial m_l}{\partial t} + g_c \frac{\partial m_c}{\partial t} - \mathcal{S}\frac{\partial T}{\partial t} - \frac{\partial \Psi}{\partial t} + \mathring{m}_{w\to c}(g_l - g_c) \tag{4.39}$$

where $\mathring{m}_{w\to c}$ is the ice formation rate and $(g_l - g_c)$ the Gibbs free energy change of ice crystallization. In equilibrium case, $(g_l - g_c) = 0$. The skeleton Helmholtz free energy density Ψ_{sk} and the skeleton entropy density $\mathcal{S}_{sk}$ can be given by:

$$\Psi_{sk} = \Psi - \rho_l \phi_l \psi_l - \rho_c \phi_c \psi_c; \quad \text{and} \quad \mathcal{S}_{sk} = \mathcal{S} - \rho_l \phi_l s_l - \rho_c \phi_c s_c \tag{4.40}$$

where Ψ and $\mathcal{S}$ are, respectively, the total Helmholtz free energy density and total entropy density. Considering further the relations: $m_\alpha = \phi_\alpha \rho_\alpha$ and $d\psi_\alpha = -P_\alpha d(1/\rho_\alpha) - s_\alpha dT$ with $\alpha = l, c$, one can rewrite eq(4.39) as:

$$\mathcal{D}_{sk} = \boldsymbol{\sigma} : \frac{\partial \boldsymbol{\varepsilon}}{\partial t} + \sum_{\alpha=l,c} P_\alpha \frac{\partial \phi_\alpha}{\partial t} - \mathcal{S}_{sk} \frac{\partial T}{\partial t} - \frac{\partial \Psi_{sk}}{\partial t} \tag{4.41}$$

In thermoporoelasticity this dissipation is zero ($\mathcal{D}_{sk} = 0$), we rewrite the eq(4.41) as:

$$\boldsymbol{\sigma} : \frac{\partial \boldsymbol{\varepsilon}}{\partial t} + \sum_{\alpha=l,c} P_\alpha \frac{\partial \phi_\alpha}{\partial t} - \mathcal{S}_{sk} \frac{\partial T}{\partial t} - \frac{\partial \Psi_{sk}}{\partial t} = 0 \tag{4.42}$$

4.3.3 Surface energy and effective pressure

As stated in section 4.1.1, the skeleton is composed of solid matrix and the interface between different components. Considering that the interface between different components possesses their own proper interfacial energy and entropy, and using the additive character of energy, one obtains (cf. [76]):

$$\Psi_{sk} = \Psi_m + \phi U \tag{4.43}$$

where Ψ_m is the Helmholtz free energy density of solid matrix, ϕU is the total interface energy density. Then the state equation of Helmholtz free energy of solid matrix is given by:

$$\boldsymbol{\sigma} : \frac{\partial \boldsymbol{\varepsilon}}{\partial t} + \sum_{\alpha=l,c} P^*_\alpha \frac{\partial \phi_\alpha}{\partial t} - \mathcal{S}_m \frac{\partial T}{\partial t} - \frac{\partial \Psi_m}{\partial t} = 0 \tag{4.44}$$

with the additional equations:

$$\mathcal{S}_m = \mathcal{S}_{sk} + \frac{\partial(\phi U)}{\partial T} \quad \text{and} \quad P^*_\alpha = P_\alpha - \frac{\partial(\phi U)}{\partial \phi} \tag{4.45}$$

where $\mathcal{S}_m$ is identified as the entropy density of solid matrix, and P^*_α the apparent pore pressure of phase α. In an unsaturated porous medium, the macroscopic interfacial energy is a function of the saturation degree and capillary pressure P_{cap} according to [76, 77]:

$$U = \int_{S_l}^{1} P_{cap}(S) \mathrm{d}S_l \quad \text{and} \quad \frac{\partial(\phi U)}{\partial \phi} = \frac{2}{3} U \tag{4.46}$$

In the case of drying of porous medium, the relation between capillary pressure and saturation degree can be obtained by experiment.

Figure 4.7(a) shows the interfacial energy U in terms of saturation degree S_l from eq(4.46), where the used data are adopted from Fabbri (2006) [114]. It indicates that the interfacial energy is not significant

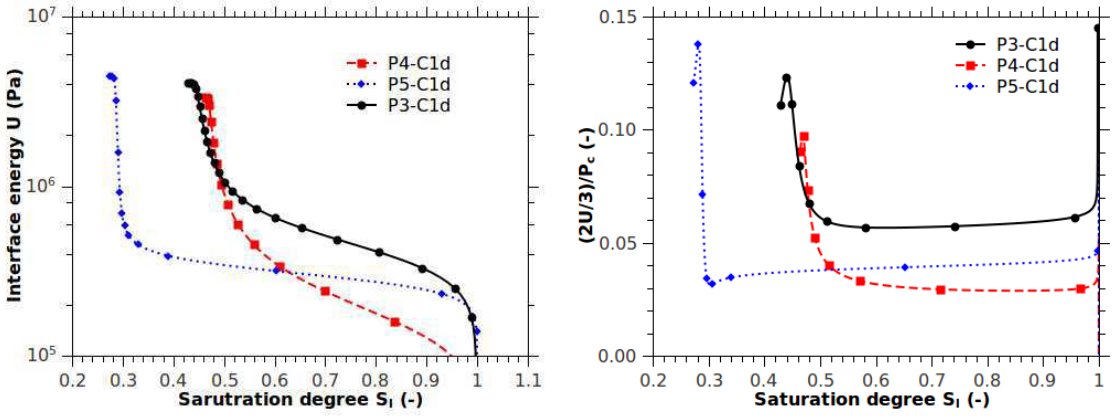

(a) (b)

Figure 4.7: (a), The calculated interfacial energy U in terms of saturation degree S_l from eq(4.46); (b), The ratio of pressure created by interfacial energy $2U/3$ to capillary pressure P_{cap} in terms of saturation degree S_l. The label "P(X)-C(x)d" represents the paste with w/c=(X/10) and curing age of (x) day(s). Data from Fabbri (2006) [114].

until the saturation degree S_l is lowered down to a certain value, which depends on the pore size distribution of porous materials. Figure 4.7(b) shows the ratio of pressure created by interfacial energy $2U/3$ to capillary pressure P_{cap} in terms of saturation degree S_l. The results indicate the influence of interfacial energy on the pore pressure is not significant. Generally, this term can be neglected [114, 115]. In addition, the influence of interfacial energy on the entropy (see eq(4.45)a) is reported to be rather small [114].

4.3.4 State equations of solid matrix

Let G_m denote the free energy density of solid matrix defined by:

$$G_m = \Psi_m - P_l^* \phi_l - P_c^* \phi_c \tag{4.47}$$

Substitution of eq(4.47) in eq(4.44), one thus obtains:

$$\boldsymbol{\sigma} : \frac{\partial \boldsymbol{\varepsilon}}{\partial t} - \sum_{\alpha=l,c} \phi_\alpha \frac{\partial P_\alpha^*}{\partial t} - \mathcal{S}_m \frac{\partial T}{\partial t} - \frac{\partial G_m}{\partial t} = 0 \tag{4.48}$$

Finally, we can derive the state equation of unsaturated thermoporoelasticity in the form:

$$G_m = G_m(\varepsilon, P_i^*, P_l^*, T) : \quad \boldsymbol{\sigma} = \frac{\partial G_m}{\partial \boldsymbol{\varepsilon}}, \quad \phi_\alpha = -\frac{\partial G_m}{\partial P_\alpha^*}, \quad \mathcal{S}_m = -\frac{\partial G_m}{\partial T} \tag{4.49}$$

4.3.5 Constitutive equations

Considering the Maxwell symmetric relation of Gibbs free energy density of matrix G_m, i.e., $\partial^2 G_m/\partial\alpha\partial\beta = \partial^2 G_m/\partial\beta\partial\alpha$, one can finally obtain [76, 77, 79]:

$$\mathrm{d}\boldsymbol{\sigma} = \mathbb{C} : \mathrm{d}\boldsymbol{\varepsilon} - \mathbf{b}_l \mathrm{d}P_l^* - \mathbf{b}_c \mathrm{d}P_c^* - \mathbb{C} : \boldsymbol{\alpha}_{th}\mathrm{d}T \tag{4.50a}$$

$$\mathrm{d}\phi_l = \mathbf{b}_l : \mathrm{d}\boldsymbol{\varepsilon} + \mathbf{N}_{ll}^{-1} : \mathbf{I}\mathrm{d}P_l^* + \mathbf{N}_{lc}^{-1} : \mathbf{I}\mathrm{d}P_c^* - \boldsymbol{\alpha}_{\phi l} : \mathbf{I}\mathrm{d}T \tag{4.50b}$$

$$\mathrm{d}\phi_c = \mathbf{b}_c : \mathrm{d}\boldsymbol{\varepsilon} + \mathbf{N}_{lc}^{-1} : \mathbf{I}\mathrm{d}P_l^* + \mathbf{N}_{cc}^{-1} : \mathbf{I}\mathrm{d}P_c^* - \boldsymbol{\alpha}_{\phi c} : \mathbf{I}\mathrm{d}T \tag{4.50c}$$

$$\mathrm{d}\mathcal{S}_m = \mathbb{C} : \boldsymbol{\alpha}_{th} : \mathrm{d}\boldsymbol{\varepsilon} - \boldsymbol{\alpha}_{\phi l} : \mathbf{I}\mathrm{d}P_l^* - \boldsymbol{\alpha}_{\phi c} : \mathbf{I}\mathrm{d}P_c^* + C_s\frac{\mathrm{d}T}{T} \tag{4.50d}$$

where $\mathbb{C}, \mathbf{b}_\alpha, \boldsymbol{\alpha}_\beta, \mathbf{N}_{lc}^{-1}$ and C_s are the thermoporoelastic tangent properties. They have properties as follows:

- $\mathbb{C} = \partial G_m/\partial\varepsilon_{ij}\partial\varepsilon kl$ stands for the 4th order tensor of solid matrix tangent elastic stiffness moduli. For an isotropic material, the linear stiffness moduli provides (cf. [129, 419]):

$$\mathbb{C} : \boldsymbol{\varepsilon} = \left(K - \frac{2}{3}G\right)\boldsymbol{\epsilon} + 2G\boldsymbol{\varepsilon} \tag{4.51}$$

where K and G are the bulk moduli and shear moduli of solid matrix respectively. $\boldsymbol{\epsilon}$ is the volumetric dilation of strain tensor.
- $b_{\alpha ij} = \partial G_m/\partial\varepsilon_{ij}\partial P_\alpha$ is the ij^{th} component of Biot's tangent tensor with symmetry $b_{\alpha ij} = b_{\alpha ji}$, so that $b_{\alpha ij}$ can be replaced by $b_\alpha\mathbf{I}$ in case of isotropy. When the temperature is hold constant, the Biot's tangent coefficient is the ratio of porosity changes to drained strain changes. In the case of partial frozen porous materials, it has:

$$\mathbf{b}_\alpha = b_\alpha\mathbf{I}; \quad b = b_l + b_c = 1 - \frac{K}{K_s} \tag{4.52}$$

with hypothesis that the liquid phase and ice crystals have similar morphology:

$$b_l = bS_l; \quad b_c = b(1 - S_l) \tag{4.53}$$

This hypothesis has been applied to describe the contribution of water and ice when cement-based materials are subject to freezing [81, 82].
- $\boldsymbol{\alpha}_{th}$ is the tangent thermal (volumetric) expansion coefficient tensor of solid matrix, with symmetry $\alpha_{th}|_{ij} = \alpha_{th}|_{ji}$. Again, for an isotropic material or statistical isotropic material, it has $\boldsymbol{\alpha}_{th} = \alpha_{th}\mathbf{I}$ and $\mathbb{C} : \boldsymbol{\alpha}_{th}T = K\alpha_{th}\mathbf{I}T$. The term $\mathbb{C} : \boldsymbol{\alpha}_{th} = -\partial^2 G_m/\partial T\partial\boldsymbol{\varepsilon}$ represents the solid matrix tangent strain latent heat, i.e., the heat per unit of strain that the skeleton exchange with outside when pressure and temperature are held constant according to eq(4.50d).
- $\mathbf{N}_{\alpha\beta}^{-1}$ with $\alpha, \beta \in \{l, c\}$ is the inverse of Biot's tangent modulus related to the pore pressure variation with porosity as strain and temperature are held constant.
- $\boldsymbol{\alpha}_{\phi\alpha} : \mathbf{I} = \partial^2 G_m/\partial T\partial P_\alpha^*$ represents a thermal (volumetric) expansion coefficient related to partial porosity.
- $C_s = -T\partial^2 G_m/\partial T\partial T$ stands for the tangent heat capacity of solid matrix.

In macromechanical viewpoint, both the cement-based material and the phases in pore space, are often adopted to be isotropic and elastic (cf.[76, 82, 114, 247]). This allows us to rewrite the eq(4.50) in the form

[76, 77, 82]:

$$\boldsymbol{\sigma} = \left(K - \frac{2}{3}G\right)\epsilon\mathbf{I} + 2G\boldsymbol{\varepsilon} - b_l P_l^*\mathbf{I} - b_c P_c^*\mathbf{I} - K\alpha_{th}(T - T_0)\mathbf{I} \tag{4.54a}$$

$$\varphi_l = b_l\epsilon + \frac{1}{N_{ll}}P_l^* + \frac{1}{N_{lc}}P_c^* - \alpha_{\phi l}(T - T_0) \tag{4.54b}$$

$$\varphi_c = b_c\epsilon + \frac{1}{N_{lc}}P_l^* + \frac{1}{N_{cc}}P_c^* - \alpha_{\phi c}(T - T_0) \tag{4.54c}$$

$$\mathcal{S}_m = K\epsilon\alpha_{th} - \alpha_{\phi l}P_l^* - \alpha_{\phi c}P_c^* + C_s\ln(T/T_0) \tag{4.54d}$$

4.4 Macroscopic description

Partially frozen porous material is investigated by means of thermoporoelastic approach. Like the established unsaturated poroelastic model concerning with drying-wetting or crystallization, several basic hypotheses allow us to approximate the mechanical equations in linear form. From the mass conservation law applied to pore phases (liquid and ice in this study), the state equations of solid matrix derived from thermodynamics of porous media, the constitutive equations of liquid phase and ice crystals as well as the chemical equilibrium between liquid and ice, one obtains the relations describing the mechanical behavior of frozen porous media, as recapitulated in Table 4.1. The basic variables in this study are the liquid pore pressure P_l, temperature T and salt concentrations c_i of species i (Na^+ and Cl^-). Through the equations presented in Table 4.1, the capillary pressure P_{cap}, stress $\boldsymbol{\sigma}$, strain $\boldsymbol{\epsilon}$, state quantities of liquid, ice and solid matrix, which are related directly to the basic variables, can be evaluated.

Note that one of the basic variables, the concentration of solute c_i, does not explicitly contribute to the constitutive equations of solid matrix (cf. eq(4.54)) directly. Actually, the liquid saline solution can be replaced by any other isotropic mobile phase and the state equations can be applied on other unsaturated cases in poromechanics, such as freezing behaviors of cement pastes saturated with pure liquid water initially (cf. [81, 82, 114]), drying of cement-based materials [78]. However, the capillary pressure is related to concentrations of solutes intimately. As discussed in chapter 2 and Appendix D, the thermodynamic properties of saline solution are quite different with those of pure water. For instance, the liquid density ρ_l, liquid heat capacity $C_{P,l}$, and liquid thermal dilation coefficient α_l are function of pressure, temperature and solute concentrations. Furthermore, the saturation degree in terms of temperature is significantly different from the case of freezing of porous material saturated with pure water initially (see section 8.3 for detail). Due to the lower free energy with adding salts, the ice formation temperature will decrease with the augmentation of salt concentration. It is the saturation degree that connects the physico-chemical changes in pores to the macroscopic deformation. This model is completed with help of the saturation degree curves presented in section 8.3.

Table 4.1: Recapitulation of parameters and equations for themoporoelasticial description of partial frozen porous media

Nature	Description	Number of unknowns	Number of Eqs
Mass continuity		$11+4N$	$4+N$
$\frac{\partial m_s}{\partial t}=0$	Solid matrix continuity	m_s	
$\frac{\partial m_c}{\partial t}-\mathring{m}_{w\to c}=0$	Ice crystal continuity	$m_c, \mathring{m}_{w\to c}$	
$\frac{\partial m_w}{\partial t}+\nabla\cdot\boldsymbol{\omega}_w+\mathring{m}_{w\to c}=0$	Water continuity	$m_w, \boldsymbol{\omega}_w$	
$\frac{\partial m_i}{\partial t}+\nabla\cdot\boldsymbol{\omega}_i=0$	Solutes continuity	$m_i, \boldsymbol{\omega}_i$	
$\frac{\partial m_l}{\partial t}+\nabla\cdot\boldsymbol{\omega}_l+\mathring{m}_{w\to c}=0$	Liquid continuity	$m_l, \boldsymbol{\omega}_l$	
Compatibility		$13+5N$	$15+N$
$\rho_l=\mathsf{M}_w c_w+\sum_i \mathsf{M}_i c_i$	Total density	ρ_l, ρ_w, ρ_i	
$c_w V_w+\sum_i^N c_i V_i=1$	Volume compatibility	c_w, c_i	
$\mathbf{J}_w+\sum_i^N \mathbf{J}_i=0$		$\mathbf{J}_w, \mathbf{J}_i$	
$m_\alpha=\rho_\alpha\phi_\alpha$		ϕ_l, ϕ_c	
$S_l+S_c=1$		S_l, S_c	
$\varphi_l=\phi_l-\phi_0 S_l, \quad \varphi_c=\phi_c-\phi_0 S_c$		φ_l, φ_c	
$\phi_l+\phi_c=\phi$		ϕ	
Darcean transport		1	$6+3N$
$\boldsymbol{\omega}_l=-\rho_l\frac{\kappa}{\eta_l}\nabla(P_l)$	Liquid phase	P_l	
$\boldsymbol{\omega}_w=-\rho_w\frac{\kappa}{\eta_l}\nabla(P_l)$	Water		
$\boldsymbol{\omega}_i=-\rho_i\frac{\kappa}{\eta_l}\nabla(P_l)$	Ions		
Fickian transport		2+N	$3N$
$\mathbf{J}_i=-\phi_l\mathsf{M}_i c_i D_i\left[1/c_i\nabla(c_i)+\nabla(\ln(\gamma_i))\right]$		γ_i	
$-\phi_l\mathsf{M}_i c_i D_i\left[\ln(\gamma_i c_i)/T\nabla(T)+z_i F/(RT)\nabla(\Psi_E)\right]$		T, Ψ_E	
Poisson equation		1	2
$\nabla^2\Psi=-\frac{q}{\varepsilon\varepsilon_0}$		q	
$q=\sum_i z_i c_i F$			
Momentum balance		9	6
$\nabla\cdot\boldsymbol{\sigma}=\mathbf{0}$			
$\boldsymbol{\sigma}^T=\boldsymbol{\sigma}$			
Constitutive equation of solid matrix		12	9
$\boldsymbol{\sigma}=\left(K-\frac{2}{3}G\right)\epsilon\mathbf{I}+2G\boldsymbol{\varepsilon}$			
$-b_l P_l^*\mathbf{I}-b_c P_c^*\mathbf{I}-K\alpha_{th}(T-T_0)\mathbf{I}$	Total stress of solid matrix	$\boldsymbol{\varepsilon}, P_l^*, P_c^*$	
$\varphi_l=b_l\epsilon+\frac{1}{N_{ll}}P_l^*+\frac{1}{N_{lc}}P_c^*-\alpha_{\phi l}(T-T_0)$	Pore deformation of liquid phase		
$\varphi_c=b_c\epsilon+\frac{1}{N_{lc}}P_l^*+\frac{1}{N_{cc}}P_c^*-\alpha_{\phi c}(T-T_0)$	Pore deformation of crystals		
$\mathcal{S}_m=K\epsilon\alpha_{th}-\alpha_{\phi l}P_l^*-\alpha_{\phi c}P_c^*+C_s\ln(T/T_0)$	Entropy of solid matrix	$\mathcal{S}_m$	
Effect of surface energy		2	3
$P_l^*=P_l-2/3U$	Liquid pressure	U	
$P_c^*=P_c-2/3U$	Ice pressure	P_c	
$U=\int_1^{S_l} P_{cap}dS_l,\ P_{cap}=P_c-P_l$	Interfacial energy		
Constitutive equation of phase in pore space		8+N	4
$\mathrm{d}\rho_l=\mathrm{d}\rho_w+\sum_i\left(\mathsf{M}_i-\mathsf{M}_w\frac{\mathsf{V}_{\phi,i}}{\mathsf{V}_w}\right)\mathrm{d}c_i-\sum_i c_i\mathsf{M}_w\mathrm{d}\left(\frac{\mathsf{V}_{\phi,i}}{\mathsf{V}_w}\right)$	constitutive equation	$\mathsf{V}_{\phi,i}$	
$ds_l=C_{p,l}dT/T-\alpha_l/\rho_l dP_l$	of liquid phase	s_l,$C_{p,l}$,K_l,α_l	
$d\rho_c=\rho_c\left(1/K_c dP_c-\alpha_c dT\right)$	constitutive equation	K_c,α_c	
$ds_c=C_{p,c}dT/T-\alpha_c/\rho_c dP_c$	of ice crystals	s_c,$C_{p,c}$	
Chemical equilibrium between ice and liquid		3	3
$d\mu_w=-s_l dT+dP_l/\rho_w-RT/\mathsf{M}_w d(\ln(a_w))$	Chemical potential of water	μ_w, a_w	
$d\mu_c=-s_c dT+dP_c/\rho_c$	Chemical potential of ice	μ_c	
$d\mu_w=d\mu_c$	Equilibrium		
Mechanical equilibrium of capillary interface		1	1
$P_c-P_l=-\frac{2\gamma_{lc}}{r}$	interfacial force	r	
Entropy balance		3	1
$T\frac{\partial\mathcal{S}}{\partial t}\geq\mathring{r}-T\nabla\cdot s_l\boldsymbol{\omega}_l$			
$-\nabla\cdot\mathbf{q}+\frac{\mathbf{q}\cdot\nabla T}{T}$		$\mathbf{q}$	
Heat conductivity		9	3
$\mathbf{q}=-\boldsymbol{\lambda}\nabla T$		$\boldsymbol{\lambda}$	
parameters		0	$19+2N$
γ_i	ionic activity coefficient		
a_w	Water activity		
S_l	Saturation degree		
$\mathsf{V}_{\phi,i}$	Apparent molar volume		
$\boldsymbol{\lambda}$	Thermal conductivity		
$C_{P,l}$, $C_{P,c}$	Heat capacity		
α_l, α_c	Thermal expansion coefficient		
K_l, K_c	Bulk modulus		
Total		$77+10N$	$77+10N$

Chapter 5

Case studies: the robustness of poromechanics

Contents

5.1 Freezing strains of saturated cement pastes

The established model is applied to calculate the freezing strains of saturated cement pastes published in [310] and compare the model prediction with the experimental data [440]. Since the pore structure of samples were not available in [310], the pore structure data with a similar mixing (w/c=0.62) from the same author is retained in our analysis [308]. Using the Gibbs-Thompson equation, the relation between pore liquid saturation and temperature is calculated and presented in Figure 5.1(b). The used parameters are presented in Table 5.1. More details can be found in [440].

Freezing strains are calculated for samples with and without entrained air for one dimensional case. The initial conditions and boundary conditions for both cases are listed in Table 5.2. For both cases, cooling is prescribed on one edge of sample, viz. $T(t, x = 0) = f(t)$, and according to the curve shown in top half of Fig. 5.1(a) given in [310]. For air entrained sample, the ice pressure at one edge is set to be constant and equal to 0.1 MPa ($P_c(t, x = 0) = 0.1$ MPa), while the liquid pressure is taken the same value for non air entrained sample ($P_l(t, x = 0) = 0.1$ MPa). The length retained for air-entrained sample is the half distance of two adjacent air voids measured by the authors, i.e., $L = 0.016\text{in} \approx 0.4\text{mm}$ while for the sample without air entrainment the length is taken as the half of sample length, i.e. $L = 0.125\text{in} \approx 3.2\text{mm}$. The

Table 5.1: Thermoporoelastic properties required in numerical analysis.

Parameter	Value	Unit	Significance	References
ϕ	0.45	-	Porosity	[310]
ρ_l^0	999	kg/m^3	Water Density	[372]
ρ_c^0	917	kg/m^3	Ice Density	[372]
K_l	1.75	GPa	Water Compressibility	[373]
K_c	8.65	GPa	Ice Compressibility	[263]
λ_l	0.56	w/(mK)	Heat conductivity of water	[214]
λ_c	2.14	w/(mK)	Heat conductivity of ice	[214]
λ_s	0.53	w/(mK)	Heat conductivity of skeleton	[433]
$C_{P,l}^0$	4218	J/(kgK)	Heat capacity of water	[214]
$C_{P,c}^0$	2110	J/(kgK)	Heat capacity of ice	[214]
C_s^0	1.47×10^6	J/(m^{3}K)	Heat capacity of solid skeleton	[433]
α_l	-298×10^{-6}	K^{-1}	Water dilation coefficient	[372]
α_c	154×10^{-6}	K^{-1}	Ice dilation coefficient	[263]
α_s	30×10^{-6}	K^{-1}	Skeleton dilation coefficient	[308]
κ_l	2×10^{-19}	m^2	Water permeability	[310]
K_s	31.8	GPa	Bulk modulus of skeleton	[403]
G_s	19.1	GPa	Shear modulus of skeleton	[403]

observed and predicted freezing strains are presented in Figure 5.1(a).

It can be seen that the numerical results reproduce reasonably well the experimental observations in [310]. As the cooling process starts from about 4℃, material begins to shrink for both samples due to thermal contraction, followed by an expansion peak at t=12min (~ -1℃) due to relatively important quantity of ice formation. To simulate this expansion peak, the nucleation point is delayed to ℃ in Figure 5.1(b), hence the numerical simulation also gives the expansion peak at this moment. This reflects in fact the energy barrier to overcome for liquid water in pores to nucleate. After this point, the pore pressure is simultaneously controlled by viscous pressure by liquid flow and crystallization pressure by ice formation (see Figure 5.2), of which the relative importance depends on the ice formation rate and pore structure.

For air-entrained case, this expansion behavior in Figure 5.1(a) ends at t=15min. One can assume that both effects are present during this period. As cooling suddenly stops at t =30min, the contraction of material does not stop simultaneously but presents a transitional contraction. That is an obvious evidence for pore pressure relaxation by viscous flow. The pore pressure relaxation time lasts about 7 minutes, which can be estimated by viscous flow: $\tau = \eta_l \cdot L^2/(4\kappa_l \cdot \Delta P_l) \approx 420$s with $\eta_l \approx 1.633 \times 10^{-3}Pa\cdot$s, $L^2 = 16 \times 10^{-8}$m^2, $\kappa_l \approx 3.11 \times 10^{-20}$m^2, $\Delta P_l \approx 5 \times 10^6$Pa. As cooling restarts from t=52min, the numerical prediction gives firstly a small expansion followed by a contraction. In Figure 5.1(c) are illustrated separately the thermal shrinkage and pore pressure-induced strain, showing that the thermal contraction is relatively small compared to the contribution of pore pressure. For air-entrained sample, see Figure 5.2, the pore pressure is the main contraction source, and this negative pore pressure arises from the capillary equilibrium of liquid water and ice crystals as entrained air voids provide an atmospheric pressure to ice.

For non-air-entrained case, the sample undergoes significant expansion from t=12min to t=30min, due to viscous flow pressure as well as pore crystallization pressure. As the cooling stopped at t =30min and the temperature was kept constant for 22 minutes, the sample was observed to expands slightly, probably

Table 5.2: Initial and boundary conditions in applied case

	Initial condition	Boundary condition
Cement paste with entrained air		
Temperature	$T(t=0,x)=277\,(\mathrm{K})$	$T(t,x=0)$ according to Fig.5.1(a)
Heat flow	-	$\boldsymbol{Q}\cdot\boldsymbol{n}(t,x=L)=0$
Liquid pressure	$P_l(t=0,x)=0.1\,(\mathrm{MPa})$	$P_c(t,x=0)=0.1\mathrm{MPa}$
Water flow	-	$\boldsymbol{w}_l\cdot\boldsymbol{n}(t,x=L)=0$
Cement paste without entrained air		
Temperature	$T(t=0,x)=277\,(\mathrm{K})$	$T(t,x=0)$ according to Fig.5.1(a)
Heat flow	-	$\boldsymbol{Q}\cdot\boldsymbol{n}(t,x=L)=0$
Liquid pressure	$P_l(t=0,x)=0.1\,(\mathrm{MPa})$	$P_l(t,x=0)=0.1\,(\mathrm{MPa})$
Water flow	-	$\boldsymbol{w}_l\cdot\boldsymbol{n}(t,x=L)=0$

due to the diffusion process of gel water to ice nucleation site according to Powers [310]. Our model predicts a continuous expansion from t=10min to t=30min, a slight contraction during the cooling platform and an expansion afterwards, see Figure 5.1(a). According to our modeling, the continuing ice formation between t=12min to t=30min supports the expansion, during the cooling platform the pore pressure relaxes very slowly due to much longer distance between (natural) air voids and lower permeability of partially ice filled pores ($\approx 10^{-23}\mathrm{m}^2$). As the cooling resumes from t=52min, the ice formation compensates both the contraction by pressure relaxation and the thermal shrinkage.

Form the above case study, it is showed that the freezing strain is largely controlled by the pore pressure accumulated during the freezing, which is intimately related to one intrinsic property of porous medium: pore structure. Pore structure or pore size distribution, intrinsic property of porous material, is a basis for ice or water content determination under freezing. According to the Gibbs-Thomson equation, the equilibrium temperature or depressed temperature is reciprocal of throat size. Therefore, if the pore structure contains more large pores, most of freezable pore water can be frozen under small depressed temperature, the freezing expansion peak, consequently, is significant even for cement pastes with air entrainment. If, on the contrary, the pore distribution is more centered on small pores, the freezing expansion peak is to be delayed to larger supercooling degrees, the freezing peak will even not appear since the thermal contraction can dominate the pore pressure effect. Pore structure determines another fundamental property of porous medium: permeability. Pore structure with high percolation degree gives large permeability. The pore pressure relaxation directly depends on the permeability of porous medium to liquid water. Larger permeability gives shorter relaxation time, thus more freezable water can be transported to nucleation sites, giving more important ice formation and usually more detrimental to material durability.

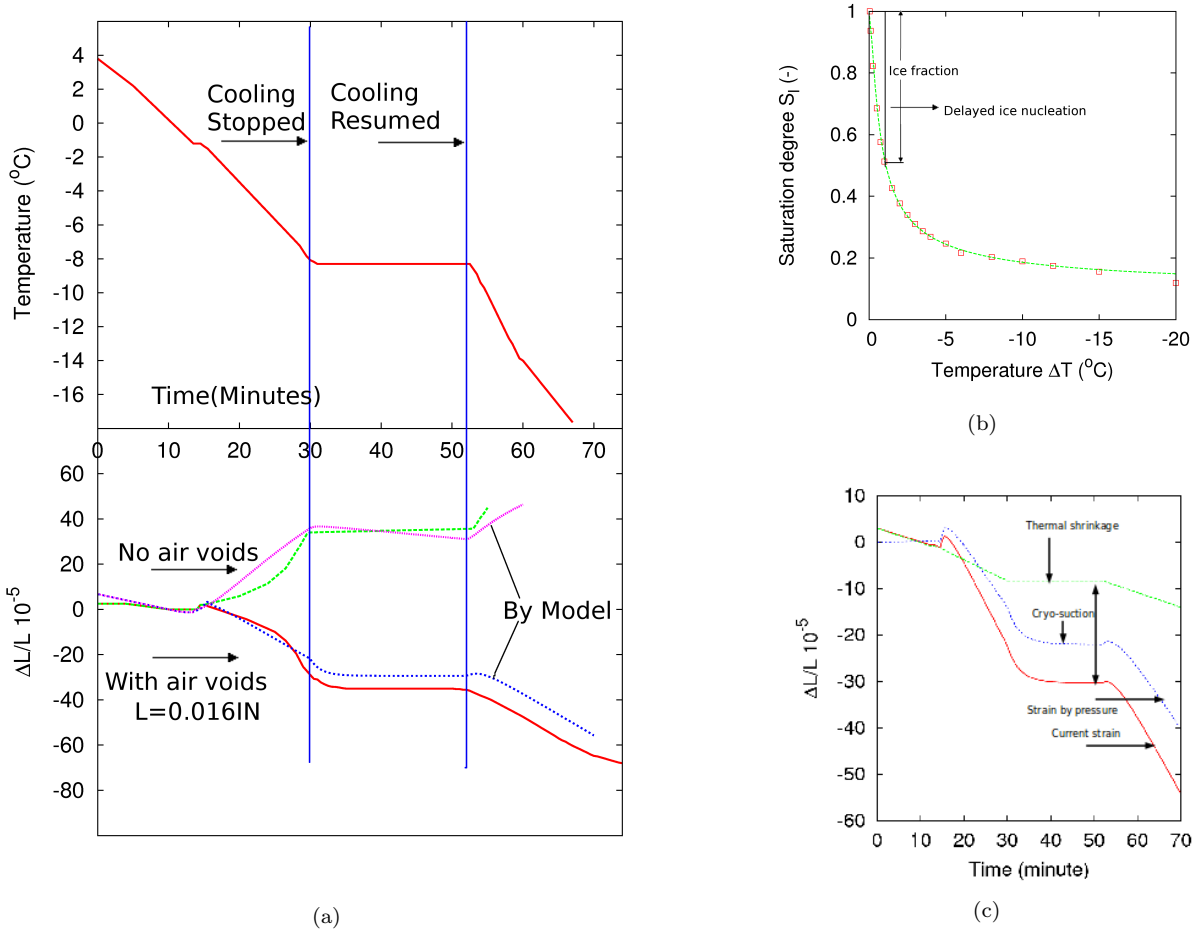

(a) (b) (c)

Figure 5.1: (a), Modeling and experimental results for freezing expansion of saturated cement paste: $L = 400\mu m$ retained for numerical simulation and experimental curves regenerated from Fig.2, pp286 in [310]; (b), Liquid saturation degree during freezing vs temperature. The void square is profiled with data from [308], pp: 955-956, Table 8.6-8.7. w/c = 0.62, 28day aged; the dash line is fit by modified van Genuchten equation, see [440] for detail; (c), The strain contributions of temperature and pore pressure with air void; the thermal dilation/contraction is relatively small, while the shrinkage by cryo-suction is much larger than that by thermal effect.

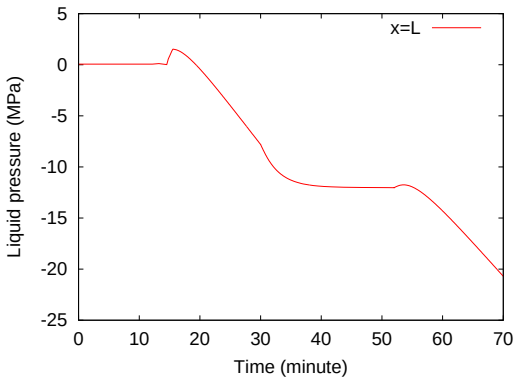

Figure 5.2: The calculated liquid pressure at $x = L$ of cement paste with air void. The peak at around 15 minutes is due to the hydraulic pressure with rapid ice formation, and the negative pressure after this peak is required by the thermodynamic equilibrium between ice and water, $P_l \approx -1.2227 \times \Delta T$ MPa.

5.2 Instantaneous thermal dilation at the end of supercooling

As aforementioned in chapter 2, the bulk supercooling of liquid is very common for porous materials during freezing [427]. The high degree of metastability of supercooled water leads to high potential for water transferring to ice. Once the metastable water begins to transfer to ice, the rapid ice formation may lead to significant hydraulic pressure and instantaneous dilation. Rather than retarded ice formation by capillary (capillary supercooling), the rapid ice formation at the end of bulk supercooling can lead to much more severe damage to porous materials. To quantify the relation between the supercooled temperature and the instantaneous dilation, two sorts of pore size distribution and four different supercooling degrees are retained in the present study for cases study. Figure 5.3 illustrates the saturation-temperature curves, where the 'Curve 1' represents a material with more small pores, while the 'Curve 2' represents a material with more large pores. Obviously, more ice forms for pore structure of 'Curve 2' than that of 'Curve 1' at the same cooling temperature. Typically, for cement-based materials, pore structure with 'Curve 1' can be the materials with lower w/c ratio than that with 'Curve 2'. These are consistent with the freezable water for cement pastes with different w/c ratios obtained by Powers [308] and Bager and Sellevold [25–27].

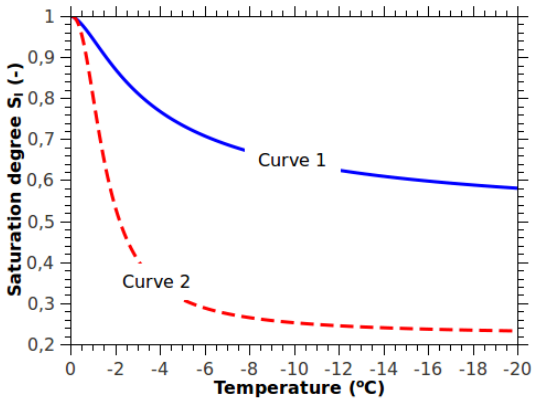

Figure 5.3: Liquid saturation degree of typical pore structure of 'Curve 1' and 'Curve 2'.

The typical temperature curves of supercooling in porous materials is the temperature decreases firstly to a certain subzero degree, then it rapidly rises to or near to the triple point (0.1°C) due to the large amount of heat releasing as ice forms. Then temperature drops again monotonously with the decrease of prescribed temperature. Figure 5.4(a) illustrates the temperature curves with different supercooling degrees, and this kind of temperature curves has been observed experimentally [146]. However, the established model is only adapted for the equilibrium case, which is to say, the metastable (supercooled) water can not exist except capillary supercooling condition. This inequilibrium case has not been considered in the models by other authors either, cf. Coussy [77, 82], Fabbri et al. [115] and Zuber and Marchand [450, 451]. Assuming that there are no obvious changes on the physical properties of supercooled water if the supercooling degree is not significant, the bulk supercooled water can be replaced by the water at triple phase point. We thus design the routines of cooling as shown in Figure 5.4(b) to avoid the water metastability with supercooling and to predict the equivalent supercooling effect on the instantaneous dilation. Temperature is held constant at triple phase point at first, where no ice forms. Then it drops rapidly to subzero, where the water and ice are still in equilibrium. Then it follows

the prescribed temperature at a rate of 0.18 ℃/min. The duration of rapid cooling is set to be 30 seconds, thus for the required supercooling of $\Delta T = 0.5, 1.0, 2.0$ and 3.0 K, the corresponding cooling rates are 1, 2, 4 and 6 ℃/min. These values are somewhat in the range of the cooling rates of DSC measurement [206], but are still far larger than the cooling rates in nature [272].

However, these designed temperature-time curves do not include the immediate temperature augmentation due to heat releasing when ice forms, as illustrated in Figure 5.5. To complement this thermal effect, additional strain due to the immediate temperature increment (thermal shock) should be considered. Therefore, the total strains $\varepsilon_{\text{Total}}$ at the end of supercooling peaks can be given by:

$$\varepsilon_{\text{Total}} = \varepsilon_{\text{IF}} + \varepsilon_{\text{Tem}} \tag{5.1}$$

where ε_{IF} denotes the strains due to the liquid pressure by immediate ice formation and ε_{Tem} represents the strains due to the immediate temperature augmentation, and it can be directly expressed as: $\varepsilon_{\text{Tem}} = \alpha_s \cdot \Delta T$, with α_s the thermal expansion coefficient of solid skeleton. The thermal expansion coefficient of OPC is usually about 10 $\times 10^{-6} \cdot \text{K}^{-1}$ [249], so that the instantaneous thermal dilation can be estimated as $\varepsilon_{\text{Tem}} \approx 10 \cdot \Delta T \times 10^{-6}$. Even the supercooled temperature is as large as 10 K, the total thermal strains is about 100 $\times 10^{-6}$, which is only 1/4 of the total instantaneous dilation according the experimental results by Grübl and Stokin [146]. As an example, the determination of the instantaneous dilation by supercooling effect ε_{IF} and that by therm effect ε_{Tem} are illustrated in Figure 5.6.

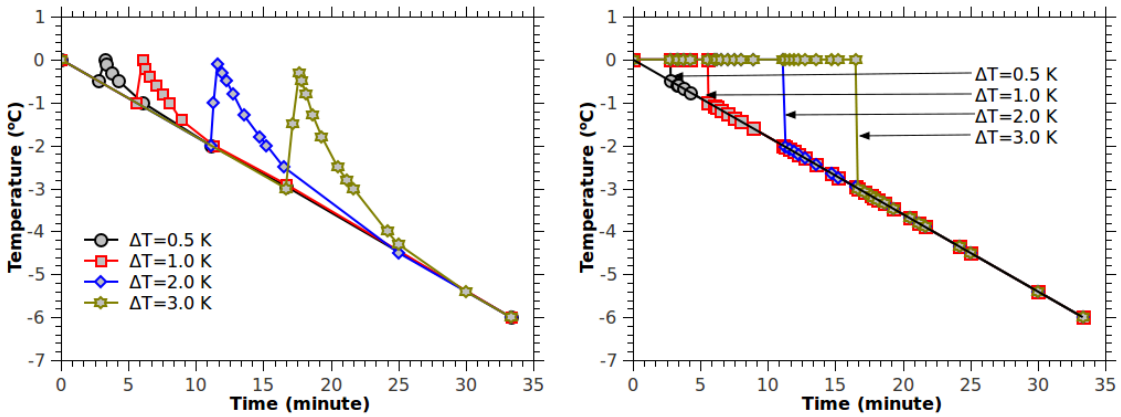

Figure 5.4: Illustration of (a) the temperature curves of porous materials in different supercooling degree and (b) the temperature curves designed for calculation of the instantaneous thermal dilation by supercooling. The prescribed cooling rate of environment is set to be 0.18 ℃/min.

The initial and boundary conditions presented in Table 5.3 are retained for predicting the effect of supercooling on the instantaneous dilation. Figures 5.7(a) and 5.7(b) show the variations of strains with temperature for materials with pore structure of 'Curve 1' and 'Curve 2' respectively. Material with pore

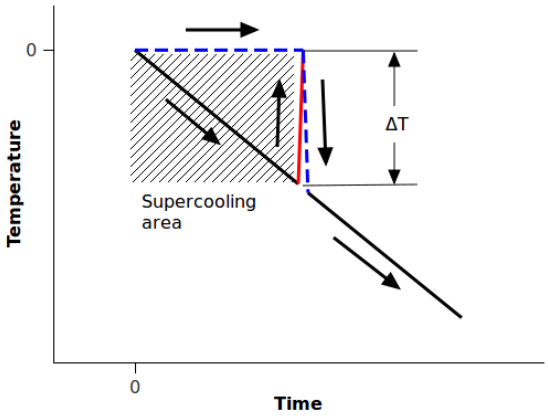

Figure 5.5: Schematic illustration of the designed temperature-time curve. The temperature is held constant at zero firstly, then drops rapidly in 30 seconds to the equilibrium temperature (dash lines). The metastability of water (in the shadow area) under the real cooling curves (bold lines) is thus avoid.

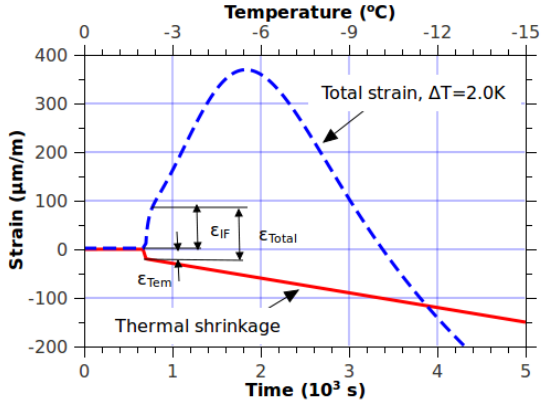

Figure 5.6: Determination of the instantaneous dilation at the end of supercooling, see eq(5.1), ε_{IF} is the strain by rapid ice formation and ε_{Tem} is the strain by thermal effect. Dash line: the calculated total strain for material with pore structure of "Curve 2"; solid line: the thermal shrinkage following the prescribed temperature curve shown in Figure 5.5.

Table 5.3: Initial and boundary conditions in applied case for predicting the instantaneous dilation by the effect of supercooling.

	Initial condition	Boundary condition
Temperature	$T(t=0,x)=273\,(\mathrm{K})$	$T(t,x=0)$ according to Figure 5.4(b)
Heat flow	-	$\boldsymbol{Q}\cdot\boldsymbol{n}(t,x=L)=0$
Liquid pressure	$P_l(t=0,x)=0.1\,(\mathrm{MPa})$	$P_c(t,x=0)=0.1\mathrm{MPa}$
Water flow	-	$\boldsymbol{w}_l\cdot\boldsymbol{n}(t,x=L)=0$

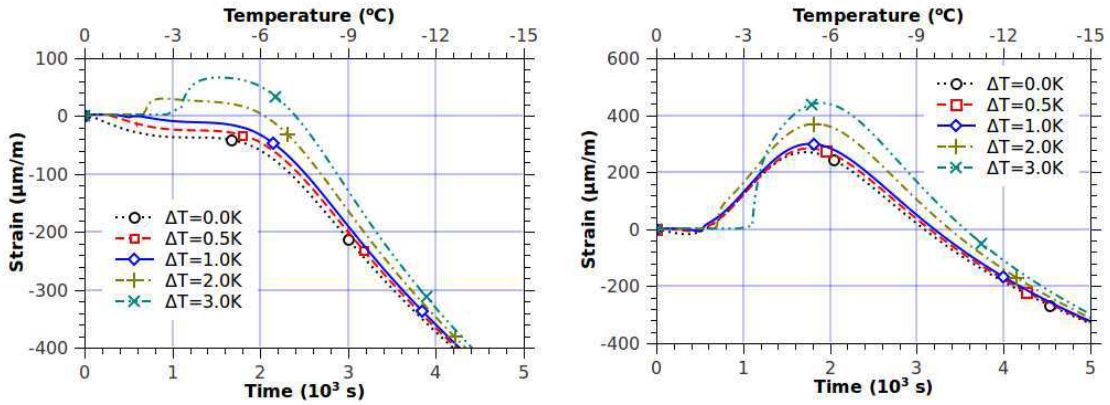

(a) (b)

Figure 5.7: Variation of strains for materials with pore structure of 'Curve 1' (a) and 'Curve 2' (b) with different supercooling degree.

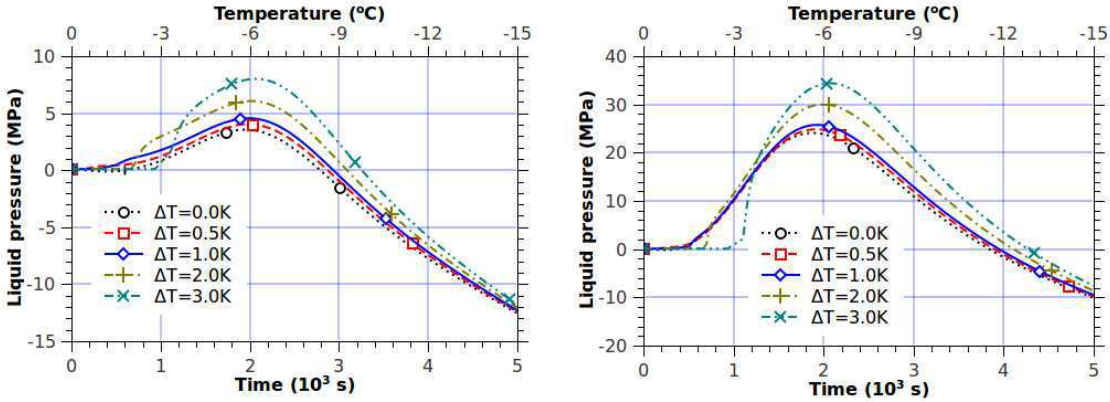

Figure 5.8: Variation of effective liquid pressure for materials with pore structure of 'Curve 1' (a) and 'Curve 2' (b) with different supercooling degree.

structure of 'Curve 1' shrinks with the prescribed temperature for the cases $\Delta T \leq 1$K, and expanses slightly after ice nucleation for the cases $\Delta T = 2$K and $\Delta T = 3$K. Whereas material with pore structure of 'Curve 2' expands for all supercooling decreases, and continual expanses as the temperature drops to around -5℃, which can be due to that factor that most of ice forms at this temperature, see Figure 5.3. Obviously, as the supercooling degree increases, the instantaneous dilation increases significantly. This is due to the large hydraulic pressure by rapid ice formation. Figure 5.8 shows the variation of liquid pore pressure with cooling. It can be found that, at the end of the supercooling $\Delta T = 3$K, the instantaneous average liquid pressure can be as high as about 2.5 MPa and 15 MPa for materials with pore structure of Curves 1 and 2 respectively. After the continual expansion to about -5℃, rapid shrinkages can be observed in Figures 5.7(a) for all materials, which can be due to the pore pressure relaxation. Obviously, the pore pressure relaxes much faster for material of 'Curve 1' than that of 'Curve 2'. As discussed in section 5.1, the relaxation time for viscous flow can be estimated as: $\tau = \eta_l \cdot L^2/(4\kappa_l \cdot \Delta P_l)$. Taking the length $L = 0.01$m for the materials with 'Curve 1' and 'Curve 2', and considering the relation for estimating the permeability, $\kappa_l \propto \phi^{3.6}$ [305] (for partially frozen, $\kappa_l \propto (\phi S_l)^{3.6}$ [450, 451]), the ratio of characteristic pressure relaxation time is then estimated as: $\tau_1/\tau_2 \approx (\Delta P_{l,2}\kappa_{l,2})/(\Delta P_{l,1}\kappa_{l,1}) \approx (\Delta P_{l,2}/\Delta P_{l,1})(S_{l,2}/S_{l,1})^{3.6}$. Take the supercooling of $\Delta T = 3$K for example, the $S_{l,1} \approx 0.9$, $S_{l,2} \approx 0.5$, and $\Delta P_{l,1} \approx 7.5$MPa, $\Delta P_{l,2} \approx 35$MPa, thus $\tau_1/\tau_2 \approx (0.5/0.9)^{3.6} \cdot 35/7.5 \approx 0.56$. This estimation is consistent with the observations presented in Figure 5.8. The required time for relaxation from maximum pressure to the zero are about 1000s and 2000s for materials with pore structure of "Curve 1" and "Curve 2" respectively.

The predicted instantaneous dilations for materials with pore structure of 'Curve 1' and 'Curve 2' are shown in Figure 5.9, where the measured data by Grübl and Stokin [146] have been illustrated as well (denoted by small cycles). It can be seen that almost all the measured data are located in the region of the

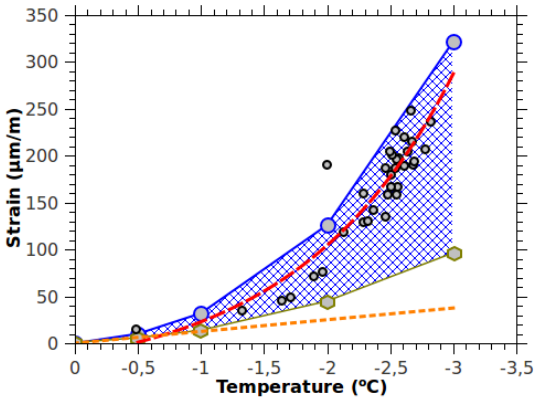

Figure 5.9: The instantaneous thermal dilation of cement-based materials subject to freezing. (Line + hexagon): The instantaneous thermal dilation of porous materials with pore structure of "Curve 1" at the supercooling extent of 0K, 0.5K, 1K and 2K and 3K; (Line + circ): The instantaneous thermal dilation of porous materials with pore structure of in "Curve 2" at the same supercooling extent; (Small circ): The experiment data from Grübl and Stokin, (1980) [146]; (Dash line): the fitting curve; (Dot line): the dilation of pure thermal effect.

predicted curves (the crossed area in Figure 5.9). This indicates that the established model can predict the instantaneous dilation by the effect of supercooling appropriately. In addition, it can be deduced that the pore size distribution of the porous materials used by Grübl and Stokin [146] must be between the 'Curve 1' and 'Curve 2' as shown in Figure 5.3.

Part II

Freezing/thawing with salt: experiments, material properties and poromechanical analyses

Abstract of Part II

The aims of Part II are to: ❶, assess the microstructure and pore structure of cement pastes qualitatively and quantitatively; ❷, evaluate the mechanical and transport properties of the used cement pastes based on multi-scale modelling; ❸, evaluate the physico-chemical properties of NaCl solution with temperature, pressure and salt concentration; ❹, evaluate the saturation degree versus temperature curves for cement pastes initially saturated with solution at different salinity; ❺, characterize the strain variation of cement pastes subjected to freeze-thaw loading experimentally; ❻, identify the mechanisms of freezing behaviors of cement pastes and the influence of salt; ❼, characterize the freezing behaviors of air entrained cement pastes by experiments and modelling at undrained and drained conditions.

The hydration of ordinary Portland cement can be quantitatively described by the Avrami's equation in chapter 6. Combining with the microstructure model of C-S-H proposed by Jennings and coworkers, the contents of hydration products are evaluated. Comprehensive experiments were proposed to access the pore structure of our hardened cement pastes. The specific surface area, pore volume, porosity, characteristic pore size and pore size distribution of pore surface were studied by means of nitrogen adsorption/desorption (NAD) and mercury intrusion porosimetry (MIP). The obtained results provide us with comprehensive information of pore structure of our hardened cement pastes.

Following the well established multiscale composite theory, the concentration, representation and homogenization steps of multi-scale modelling were addressed firstly in chapter 7. By using the multi-scaling method and the properties of compounds of our cement pastes, the macro-thermal-poroelastic properties were evaluated. Within the same approaches, but different specific homogenization equations, the transport properties, such as hydraulic permeability, conductivity and diffusivity, were estimated.

The significance of the physico-chemical properties of saline solution comes from the effect of salt. By using the Archer's empirical equations developed from the Pitzer's model, we obtained the physico-chemical properties of NaCl solution, such as, density, heat capacity, thermal expansion coefficient and bulk modulus in chapter 8. The apparent molar quantities instead of the partial molar quantities are used to represent the effect of NaCl, because the bulk molar quantities of water are well known, and the apparent molar quantities are easier to be measured than the partial molar quantities. The correlation between the water or ice saturation degree and the pore structure can be described by the capillary-saturation relations, which is alike the imbibition-drying problems. Based on the pore structure obtained by means of MIP measurements, the pore size distribution curves of our cement pastes were evaluated by using the multi-Gauss fitting. Then, the curves of ice content versus cooling temperature for paste I and paste II saturated with NaCl solution at different salinities were evaluated.

Freezing strains for cement pastes initially dried and/or saturated with NaCl solution at different

salinities were studied by experiments and poromechanical modelling in chapter 9. Paste II has larger thermal expansion coefficient (TEC) than paste I, because paste II contains more C-S-H and Calcium Hydroxide. Samples of paste I showed significant expansion after ice nucleation, whereas samples of paste II showed no dilation. The primary reason for this observation is their intrinsic pore structures. We classified six sorts of deformation based on the shapes of strain-temperature curves. Samples with significant expansion at low temperature also presented large residual deformation after one complete freeze-thaw cycle, which indicated that the fracture deterioration occurs during freezing. The poromechanical calculations were performed to analyze the freezing strains and compared to the experimental results. Acceptable agreement between the experimental curves and the predicted curves were obtained.

The effects of air voids on the strains of our samples have been specifically discussed in chapter 10. The TEC of pastes and mortars with four different dosages of air voids were measured. Analyses indicated that the TEC can be expressed in terms of total porosity (including the capillary porosity and air void content) or entrained air void content through a power law, $\alpha_d = \alpha_0(1-\phi)^C$. The exponents C for pastes (mortars) are respectively 2.66 (2.38) when ϕ is defined as total porosity, and 3.74 (2.69) when ϕ is defined as air void content. The decreased TEC with air-entrainment can probably be attributed to the existence of dense shell structures around the air voids.

Comprehensive experimental studies have been performed on the deformations of air entrained cement pastes saturated with NaCl solution at different salinity subjected to freeze-thaw loading. Contrary to the 3% pessimum concentration for surface scaling, the maximum ultimate deformation at -35°C for samples with rather high salt concentrations (cf. 10% and 15% NaCl) were observed. In addition, the samples entrained with more air voids exhibit larger deformations. Yet there is no proposed mechanism accounting for these observations to the author's knowledge. The classifications on the deformation curves indicated that the initial saturation degree may govern these deformation curves. The air entrained pastes with boundary conditions of undrained freezing and these of drained freezing were analyzed by the established poromechanical model. Some of the measured curves lie between the predicted curves under undrained and drained freezing conditions, while the other measured curves are beyond the predicted areas. This confirms partially the relevance of our self-contained approach developed in the present work, but also requires further deepened investigation.

Chapter 6

Hydration and pore structure of cement paste

Contents

6.1 Materials and experiments

6.1.1 Materials

A type I ordinary Portland cement (OPC) was used in the present study. The chemical composition and physical properties of cement as well as their mineral contents are given in Table 6.1. The mineral contents of cement were analyzed through Bogue's procedure [48].

Table 6.1: Chemical composition and physical properties and mineralogical composition of cement.

Chemical composition/ physical properties	Formula or abbreviation	Content (%)	Minerals (Bogue)	Formula	Content (%)
Silica	SiO_2 (S)	22.93	Tricalcium silicate	C_2S	21.38
Alumina	Al_2O_3 (A)	4.29	Dicalcium silicate	C_3S	58.88
Iron oxide	Fe_2O_3 (F)	2.89	Tricalcium aluminate	C_3A	6.49
Calcium oxide	CaO (C)	66.23	Tetracalcium aluminoferrite	C_4AF	8.77
Magnesium oxide	MgO (-)	1.92	Gypsum	$C\bar{S}H_2$	0.75
Sulfur trioxide	SO_3 ($\bar{S}$)	0.35		Other	3.73
Sodium oxide	Na_2O(eq)(-)	0.70			
Free calcium oxide	CaO(f) (C)	0.64			
Chloride	Cl (-)	0.05			
Loss on ignition	-(LOI)	1.70			
Density (g/ml)		3.12			
Specific area (m^2/kg)		343			

6.1.2 Sample preparation

Cement paste samples were prepared with two water to cement (w/c) ratios (0.5, 0.3), named as paste I and paste II respectively. The mixing procedure observes the ACI Committee 211 [64], see also Figure 6.1. After mixing, cement pastes of different mixtures were casted into cylinder tubes of 10mm in diameter and the hardened specimens were demoulded from the tubes at the age of 3 days (D) (see Figure 6.2), then immersed into water. At the ages of 7D, 28D, 90D and 180D, specimens were taken out of water and crushed to particle samples of size in 1mm∼2mm for later experiments. The MIP and NAD experiments on the samples were to characterize the porosity, pore size distribution, specific surface area and the skeleton density. The porosity was also evaluated directly with the help of gravimetry method. The helium pycnometry method was employed to measure the skeleton density. The thermogravimetric analysis (TGA) was used to quantify the non-evaporable water (Wn) and the $Ca(OH)_2$ (CH) content.

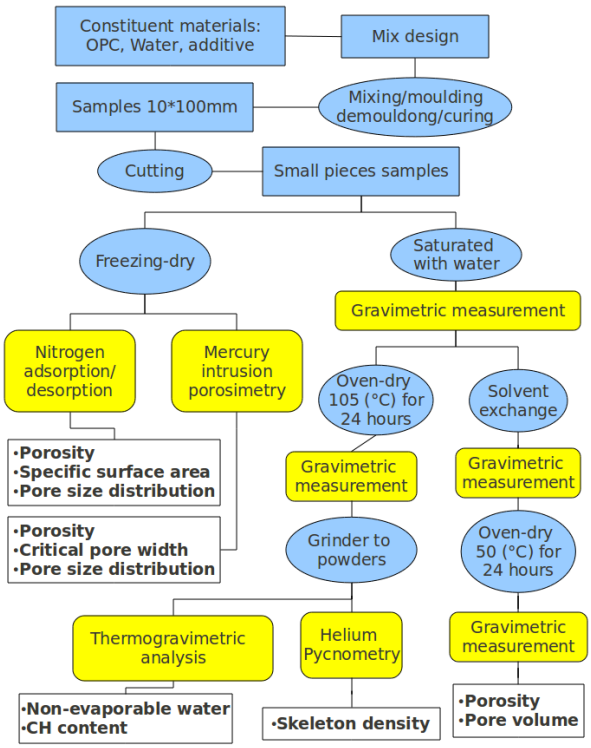

Figure 6.1: Sequences of sample preparation and experimental procedures.

The procedure of sample preparation was adapted for different experiments, of which the sequences are presented in Figure 6.1. For MIP and NAD tests, the samples were subjected to drying procedure by freezing (F-drying). The samples, together with the container, were firstly immersed into liquid nitrogen (N_2, −196℃) for about 5min, then transferred to the freeze-dryer system and vacuumed for 24 hours (h)

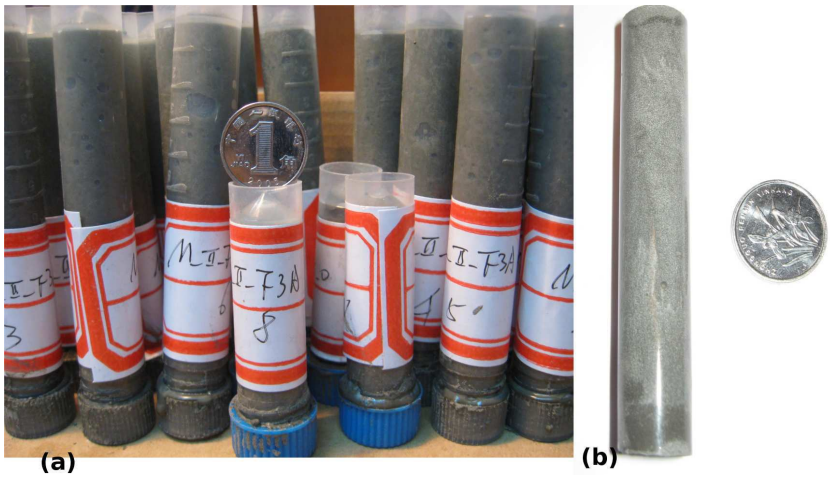

Figure 6.2: Samples casted in cylindrical tubes (a) and a demoulded cylindrical sample (b).

Table 6.2: Experiments, sample preparation methods and measurements.

Experiment	Sample treatment	Measurement
MIP, NAD	Freezing-dry in liquid nitrogen (-196℃) and vacuumed for 24h	Porosity, pore size distribution, critical pore size, specific surface, skeleton density (only MIP)
Gravimetry	Water saturated, solvent exchange in methanol and acetone for 7D, oven-dry at 50℃ for 24h	Porosity
Helium Pycnometry	Water saturated, oven-dry at 105℃ for 24h, ground to powder $d_{95\%} = 80\mu$m	Skeleton density
TGA	Water saturated, oven-dry at 105℃ for 24h, ground to powder $d_{95\%} = 80\mu$m	Non-evaporable water, $Ca(OH)_2$ content

before MIP or NAD experiments. For porosity evaluation by gravimetry method, the samples, each 1-1.5g, were firstly vacuum-saturated by liquid water and then immersed both in methanol and acetone of 100ml. The solvent (methanol or acetone) was renewed every hour during the first 24h, and every 24h afterwards for 7D. The samples were then oven-dried at 50 ℃ for 24h. Before and after oven-dry procedure the weight of samples was measured to the accuracy to 0.001g.

For helium pycnometry, selective dissolution and TGA experiments, the samples were firstly vacuum-saturated by liquid water and then oven-dried at 105±1℃ for 24h. The dried samples were ground to powder, having the 80μm-sieve passing ratio of 95%. The experiments and their respective sample treatment procedures are summarized in Table 6.2.

6.1.3 Determination of pore structure

6.1.3.1 Gravimetry

The principle of evaluating porosity by gravimetry is that the pore space occupied by a liquid can be determined via pore liquid evaporation or pore liquid replacement by another liquid. The sample saturated with a known liquid is weighted as m_s, after the oven-drying (105±℃ for 24 hrs) and solvent exchange

Table 6.3: Skeleton density of porous cement pastes at different ages (g/cm^3).

Sample	Helium pycometry				MIP			
	7D	28D	90D	180D	7D	28D	90D	180D
PI	2.355	2.251	2.110	2.056	3.092	2.025	2.110	2.380
PII	2.383	2.410	2.347	2.384	2.647	2.254	2.191	2.414

procedures the sample is weighted as m_0 and m_d respectively. The porosity, therefore, can be calculated as,

$$\phi = \frac{(m_s - m_d)/(\rho_o - \rho_r)}{(m_s - m_d)/(\rho_o - \rho_r) + m_0/\rho_s} \tag{6.1}$$

where ρ_s is the density of solid skeleton, ρ_o is the density of the initial pore liquid phase and ρ_r is the density of phase occupying the pore spaces after drying or liquid exchange. For samples after oven-drying, ρ_r is the density of air, $\rho_r = 1.2041 \times 10^{-3}$ g/ml at 20℃, which is negligible compared to liquid water density, ρ_o=0.997g/ml at 20℃ with $m_d = m_0$. For samples after solvent exchange, ρ_r are the densities of methanol and acetone, 0.7918 g/ml and 0.7925 g/ml at 20℃ respectively. The skeleton density ρ_s was determined by helium pycnometry and MIP, given in Table 6.3.

6.1.3.2 Mercury intrusion porosimetry

Mercury intrusion porosimetry is based on the principle that the intrusion volume of mercury into a porous medium depends on the applied pressure. If the pore geometry is assumed to be cylindrical, the pore diameter(size) d can be related to the applied pressure P using Washburn equation [423],

$$d = -\frac{4\gamma \cos\theta}{P} \tag{6.2}$$

where γ is the surface tension of mercury (0.485 N/m), θ is the contact angle between mercury and pore wall and θ =130° is commonly adopted for cement-based materials [186]. A volume-weighted pore size distribution can be obtained by associating the intruded mercury volume at a given pressure with the pore size evaluated from eq(6.2). It is noted that the above assumption of straight cylindrical pores can lead to inaccurate interpretation for pore structure if "ink-bottle" pores exist. The mercury intrusion porosimetry used in this study is of type Autopore IV 9510 with maximum and minimum applied pressures as 414 MPa and 1.4 kPa, corresponding to a minimum pore size of 3 nm and maximum pore size of 800 μm.

6.1.3.3 Nitrogen adsorption/desorption

As a dried porous medium is put into a gas (nitrogen) environment, the internal surface of pores can adsorb a certain quantity of gas (nitrogen) molecules. The nitrogen adsorption/desorption (NAD) experiment records the nitrogen gas pressure and the adsorbed nitrogen quantity, providing an adsorption isotherm. These data need further interpretation to deduce the pore structure of the porous medium. As the gas pressure is relatively low, it can be assumed that surface adsorption dominates. The Langmuir and

BET approaches are most used to deduce the internal specific surface area of pores, based on monomolecular adsorption and multimoleculars adsorption assumptions respectively. As the gas pressure goes on, condensation of nitrogen happens in mesopores. The Barrett-Joyner-Halenda (BJH) interpretation uses pore condensation principle to evaluate the pore size distribution from the adsorption isotherm [29]. The relation between capillary condensation pressure and the interface radius r_k can be described by Kelvin equation,

$$2r_k = \frac{-19.18}{\ln(P/P_0)} \times 10^{-10} \quad \text{m} \tag{6.3}$$

where P, P_0 stand for the present and saturated vapor pressure. To obtain the real pore size r, the thickness of adsorption layer t should be considered: $r = r_k + t$. More details of the thickness can be found in [90, 91, 220] and Appendix A.6. Note that this estimation holds just for the mesopores and small capillary pores, since the pore condensation cannot happen for larger pores [10, 322]. Also from BJH interpretation of adsorption isotherm the pore specific area is evaluated through pore condensation volume and the average pore size with cylindrical pore geometry assumption. The NAD on powder samples was carried out by a NAD device of type ASAP2010 with the nitrogen pressure range up to 126.66 kPa.

6.2 Hydration of ordinary Portland cement

6.2.1 Stoichiometry analysis

In this section, the simple stoichiometric reactions for the hydration of the several dominant compounds in ordinary Portland cement, i.e., C_3S, C_2S, C_3A, C_4AF and $3C\bar{S}H_2$ are adopted to represent the whole hydration, and this assumption has been widely applied in many quantitative and qualitative models [391, 392]. The formulas for complete hydration for these compounds are given by [391]:

$$C_3S + 5.3H \rightarrow C_{1.7}SH_4 + 1.3CH \tag{6.4a}$$

$$C_2S + 4.3H \rightarrow C_{1.7}SH_4 + 0.6CH \tag{6.4b}$$

$$C_3A + 3C\bar{S}H_2 + 26H \rightarrow C_6A\bar{S}_3H_{32} \tag{6.4c}$$

$$2C_3A + C_6A\bar{S}_3H_{32} + 4H \rightarrow 3C_4A\bar{S}H_{12} \tag{6.4d}$$

$$C_3A + CH + 12H \rightarrow C_4AH_{13} \tag{6.4e}$$

$$C_4AF + 2CH + 10H \rightarrow 2C_3AFH_6 \tag{6.4f}$$

Note that the first two formulas, by which the average stoichiometry of the C-S-H is determined, are the most important. The bound water or water/silica ratio of C-S-H depends on the drying condition, the high C-S-H water content (H/S = 4) used in eqs (6.4a) and (6.4b) corresponds to the bulk phase including water trapped in the gel pore spaces between the nanoparticles [397]. The eq(6.4c) is used for

the initial reactions of C_3A in the presence of sulfate to form ettringite ($C_6A\bar{S}_3H_{32}$). If the initial supply of sulfate is depleted, the additional reaction of C_3A with formed ettringite forms monosulfoaluminates ($3C_4A\bar{S}H_{12}$) as shown in eq(6.4d). If all Gypsum is consumed, C_3A further reacts with calcium hydroxide (CH) and water (H) producing the hexagonal tetracalcium aluminate hydrate (C_4AH_{13}) as presented by eq(6.4e). In eq(6.4f), the product of the ferrite reaction is a hydrogarnet (C_3AFH_6). Generally, the sulfate in OPC is in relative low content, the ultimated hydration products with the sulfate element would be monosulfoaluminates ($3C_4A\bar{S}H_{12}$). The basic physical and chemical properties of OPC and their hydration products are presented in Table 6.4.

Let f_α^m and f_α^v denote the mass and volume fraction of compound α respectively. The amount of each product can be estimated by the aforementioned stoichiometry analysis once the hydration degree of each compound is determined. Let α_α denotes the hydration degree of the main compounds of OPC, the mass contents of hydration products per mass unit of unhydrated cement powder are then given by:

$$\text{C-S-H} = 0.9956 f^m_{(C_3S)}\alpha_{(C_3S)} + 1.3198 f^m_{(C_2S)}\alpha_{(C_2S)} \tag{6.5a}$$

$$C_6A\bar{S}_3H_{32} = 2.4322 f^m_{(C\bar{S}H_2)}\alpha_{(C\bar{S}H_2)} - m_{(C_6A\bar{S}_3H_{32})} \quad \text{(intermediate)} \tag{6.5b}$$

$$C_4A\bar{S}H_{12} = 0.4964 m_{(C_6A\bar{S}_3H_{32})} \tag{6.5c}$$

$$C_4AH_{13} = 2.0741 f^m_{(C_3A)}\alpha_{(C_3A)} - 1.9111 f^m_{(C\bar{S}H_2)}\alpha_{(C\bar{S}H_2)} - 2.3241 m_{(C_6A\bar{S}_3H_{32})} \tag{6.5d}$$

$$C_3AFH_6 = 1.6749 f^m_{(C_4AF)}\alpha_{(C_4AF)} \tag{6.5e}$$

$$\begin{aligned} CH = {} & 0.4219 f^m_{(C_3S)}\alpha_{(C_3S)} + 0.2581 f^m_{(C_2S)}\alpha_{(C_2S)} - 0.2741 f^m_{(C_3A)}\alpha_{(C_3A)} + 0.2525 f^m_{(C\bar{S}H_2)}\alpha_{(C\bar{S}H_2)} \\ & + 0.3071 m_{(C_6A\bar{S}_3H_{32})} - 0.3045 f^m_{(C_4AF)}\alpha_{(C_4AF)} \end{aligned} \tag{6.5f}$$

where $m_{(C_6A\bar{S}_3H_{32})}$ denotes the mass of AFt that is an intermediate product and reacts with C_3A further. If the AFt is consumed, the formulas of eqs(6.4c) and (6.4d) then reduce to:

$$C_3A + C\bar{S}H_2 + 10H \rightarrow C_4A\bar{S}H_{12} \tag{6.6}$$

The amount of monosulfate (AFm), calcium aluminate hydrate, hydrogarnel and calcium hydroxide thus can be expressed ultimately as:

$$\begin{aligned} C_4A\bar{S}H_{12} &= 3.661 f^m_{(C\bar{S}H_2)}\alpha_{(C\bar{S}H_2)}; \quad C_3AFH_6 = 1.6749 f^m_{(C_4AF)}\alpha_{(C_4AF)} \\ C_4AH_{13} &= 2.0741 f^m_{(C_3A)}\alpha_{(C_3A)} - 1.5699 f^m_{(C\bar{S}H_2)}\alpha_{(C\bar{S}H_2)} \\ CH &= 0.4219 f^m_{(C_3S)}\alpha_{(C_3S)} + 0.2581 f^m_{(C_2S)}\alpha_{(C_2S)} - 0.2741 f^m_{(C_3A)}\alpha_{(C_3A)} \\ &\quad + 0.4302 f^m_{(C\bar{S}H_2)}\alpha_{(C\bar{S}H_2)} - 0.3045 f^m_{(C_4AF)}\alpha_{(C_4AF)} \end{aligned} \tag{6.7}$$

Table 6.4: Physical properties of reactants and products of ordinary Portland cement.

Compound name	Symbol	State	Density Mg/m^3	Molar volume ml/mol	Molar mass g/mol	Heat of formation kJ/mol	References
Tricalcium silicate	C_3S	Bulk	3.15	72.4	228	-2927.82	[392]
Dicalcium silicate	C_2S	Bulk	3.28	52	172	-2311.6	[40, 392]
Tricalcium aluminate	C_3A	Bulk	3.03	89.1	270	-3587.8	[40, 392]
Tetracalcium aluminoferrite	C_4AF	Bulk	3.73	120.3	486	-5090.3	[392]
Gypsum	$C\bar{S}H_2$	Bulk	2.32	74.2	172	-2022.6	[40, 392]
Calcium silicate hydrate	$C_{1.7}SH_4$	Saturated	2.03	111.8	227	-3283	[40, 178, 392]
Calcium silicate hydrate (LD)	$C_{1.7}SH_4$	Pore empty	1.44	157.6	227	-	[178, 396]
Calcium silicate hydrate (HD)	$C_{1.7}SH_4$	Pore empty	1.75	129.7	227	-	[178, 396]
Calcium silicate hydrate (LD)	$C_{1.7}SH_4$	Pore full	1.93	117.6	227	-	[178, 396]
Calcium silicate hydrate (HD)	$C_{1.7}SH_4$	Pore full	2.13	106.5	227	-	[178, 396]
Calcium silicate hydrate	$C_{1.7}SH_{2.1}$	11% Hr	2.47	78	193	-	[178, 396]
Calcium silicate hydrate	$C_{1.7}SH_{1.8}$	dries	2.60	72.2	187.6	-	[12, 397]
Calcium silicate hydrate	$C_{1.7}SH_{1.2\text{-}1.4}$	D-dried	2.86	62.4	178.6	-	[178, 397]
Calcium hydroxide	CH	Bulk	2.24	33.1	74	-986.1	[40, 392]
Ettringite (AFT)	$C_6A\bar{S}_3H_{32}$	Bulk (saturated)	1.75	717	1255	-17539	[40, 392]
Ettringite (AFT)	$C_6A\bar{S}_3H_7$	Bulk (dried)	2.38	338	805	-	[392]
Monosulfate	$C_4A\bar{S}H_{12}$	Bulk (saturated)	1.99	346	623	-8778	[40, 392]
Monosulfate	$C_4A\bar{S}H_8$	Bulk (dried)	2.40	229	551	-	[392]
Calcium aluminate hydrate (AFm)	C_4AH_{13}	Bulk	2.05	273.2	560	-5548	[392]
Hydrogarnel	C_3AFH_6	Bulk	2.67	152.4	407	-	[392]
Water	H	Bulk	0.997	18.0	18.0	-285.83	[40]
		Confined in gel	1.163	15.48	18.0	-	[308]
		Chemical bound	1.1	16.28	18.0	-	[397]

The amount of non-evaporable water Wn (g/g cement) is then expressed as:

$$\begin{aligned} \mathrm{Wn} &= 0.1310\mathrm{C_{1.7}SH_{1.3}} + 0.2432\mathrm{CH} + 0.2613\mathrm{C_4A\bar{S}H_8} + 0.2654\mathrm{C_3AFH_6} \\ &= 0.2053 f^m_{(\mathrm{C_3S})}\alpha_{(\mathrm{C_3S})} + 0.1988 f^m_{(\mathrm{C_2S})}\alpha_{(\mathrm{C_2S})} + 0.3704 f^m_{(\mathrm{C_4AF})}\alpha_{(\mathrm{C_4AF})} \\ &+ 0.8000 f^m_{(\mathrm{C_3A})}\alpha_{(\mathrm{C_3A})} + 0.6207 f^m_{(\mathrm{C\bar{S}H_2})}\alpha_{(\mathrm{C\bar{S}H_2})} \end{aligned} \tag{6.8}$$

For a type I OPC that has a composition of $C_3S = 58.88\%, C_2S = 21.38\%, C_3A = 6.49\%, C_4AF = 8.77\%$ (see Table 6.1), the amount of non-evaporable water Wn for complete hydration is estimated to be 0.257 ($= W_{n\infty}$), which is close to the value obtained by Powers [308] and Garcia [111]. Note that the ultimate Wn is intimately related to the state of hydration products. For instance, if the water in small gel pores and/or layers and the mono-layer adsorbed water are adopted in calculating the Wn: H/S = 2.1 [178, 397], the ultimate Wn is estimated to be 0.302, which is much higher than the value measured by TGA for OPC. This overestimation of non-evaporable water has been extensively studied by Hobbs [168].

The porosity of cement paste, varying with the hydration processes, is related to the initial water volume fraction V_w and the volume fraction change by chemical reaction V_c. The capillary porosity V_{cp} is defined as:

$$V_{cp} = V_w - V_c = V_w - \sum_i (V_{p,i} - V_{r,i}) \tag{6.9}$$

where $V_{p,i}$ and $V_{r,i}$ represent the volume percentage of hydration products and that of reactants i respectively. Again, the water in small gel pores and the mono-layer adsorbed water should be included for

calculating the volume percentage of hydration products, because the space occupied by the gel water and the adsorbed water do not belong to capillary pores [178, 308]. Therefore, the products in state of saturated condition, presented in Table 6.4 are employed in the calculations.

Two types of C-S-H have been observed for decades, and they were presented either as inner products and outer products [320, 321] or high density (HD) C-S-H and low density (LD) C-S-H [178, 392, 396]. We here follow the second definition, and hereafter all the approaches on the microstructures and the correlated issues are according to this second definition. According to Tennis and Jennings [392], only the LD C-S-H is accessible by Nitrogen, thus the surface area measured by NAD represents the surface area of the LD C-S-H. Based on a series of experimental results, the authors [392] obtained an equation that correlate the fraction of LD C-S-H to the w/c ratio and total hydration degree α_t:

$$f_{LD} = 3.017(\text{w/c})\alpha_t - 1.347\alpha_t + 0.538 \tag{6.10}$$

where f_{LD} is the mass ratio of LD C-S-H to total C-S-H. Note that eq(6.10) was fitted from data of the materials with the w/c ratios in range of 0.25-0.5. Use of this equation when w/c ratios are beyond this interval is thus debatable. The volume of LD C-S-H and HD C-S-H can be given by [392]:

$$V_{LD} = \frac{f_{LD} M(\text{C-S-H})}{\rho_{LD}}, \quad \text{and} \quad V_{HD} = \frac{(1 - f_{LD}) M(\text{C-S-H})}{\rho_{HD}} \tag{6.11}$$

where ρ_{LD} and ρ_{HD} are density of LD C-S-H and HD C-S-H respectively, M(C-S-H) represents the total mass of C-S-H. The gel pore volume in LD C-S-H is then calculated by [392]:

$$V_{gel} = V_{LD} \left(1 - \frac{\rho_{LD}}{\rho_{HD}}\right) \tag{6.12}$$

6.2.2 Hydration degree and content of products

The aforementioned stoichiometry analyses allow us to estimate the main hydration products quantitatively. However, the reaction rates of the compounds usually have not the same values. For instance, the C_3A and C_3S react much faster than other compounds. In addition, the reaction rates are influenced much by the additives, among which the Gypsum and the $CaCl_2$ are known as retarding and accelerating additives respectively. The aim of this section is to evaluate the hydration processes and to estimate the contents of hydration products. The effects of additives are thus out of the scope. The Avrami equation is employed to estimate the hydration degree of each compound, which has the form [392]:

$$\alpha_i = 1 - \exp\left[-a_i \left(t - b_i\right)^{c_i}\right] \tag{6.13}$$

where α_i is the hydration degree of compound i at time t (in days), a_i, b_i and c_i are adjustable constants determined empirically and given in Table 6.5. The Avrami equation provides a simple kinetic method that fits the hydration of OPC approximately well, although it was argued that the hydration of OPC and

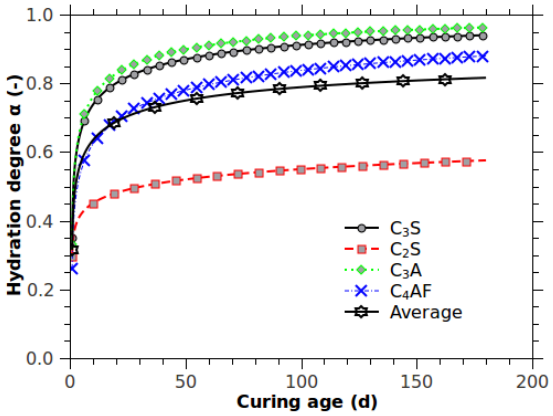

Figure 6.3: Hydration degree of compounds with time. Each of the principal compounds is assumed to hydrate independently as shown. The curve labeled "average" represents the weighted average hydration degree (eq(6.14)) of cement that has a composition of C_3S = 58.88%, C_2S = 21.38%, C_3A = 6.49%, C_4AF = 8.77%.

blended cement paste are far beyond the capability of this simple model [392]. More precise models can refer to Lothenbach et al. [227, 228], and a comprehensive review on hydration models can be found in Thomas et al. [394].

Table 6.5: The adjustable constants used in Avrami equation (see eq(6.13)) [390, 392].

Compounds i	Formula	a	b	c
Tricalcium silicate	C_3S	0.90	0.70	0.25
Dicalcium silicate	C_2S	0	0.12	0.46
Tricalcium aluminate	C_3A	0.90	0.77	0.28
Tetracalcium aluminoferrite	C_4AF	0.90	0.55	0.26

The average hydration degree is defined as a weighted averaged value of hydration degrees of all compounds:

$$\alpha_t = \sum_i \alpha_i f_i^m \tag{6.14}$$

where f_i^m is the mass fraction of compound i. The hydration degrees of typical Type I OPC (see Table 6.1) evaluated by Avrami equation are presented in Figure 6.3. It can be seen that C_3A hydrates faster than other compounds, C_2S has the lowest hydration rate, and the average hydration degree is slightly lower than that of C_4AF.

The amount of non-evaporable water Wn is often employed to estimate the mean hydration degree of OPC that is determined as the ratio of measured value to the ultimate value for complete hydration, i.e, $\alpha_t = Wn/Wn_\infty$. Figure 6.4 illustrates the amount of non-evaporable water Wn that is evaluated by the weighted average for all compounds and by the linear estimation, i.e, Wn = $0.257\alpha_t$. The good agreement between the two estimation methods indicates that the Wn is a reliable factor to assess the hydration degree of OPC.

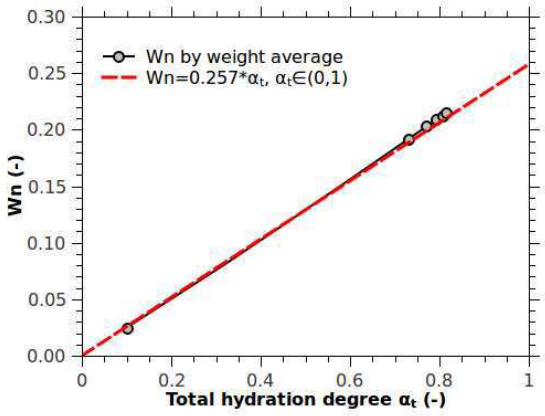

Figure 6.4: Calculated value by eq (6.8) and by linear equation $y = a * \alpha_t$ for non-evaporable water content Wn with hydration degree. The applied cement has the same compounds as shown in Figure 6.3.

Let us now consider the volumetric variation of all components with time or with hydration degree. We will process this evaluation referring to a mass unit of unhydrated OPC. Given a w/c, the total volume at initial mixture state is:

$$V_{in} = V_w^{in} + \sum_i f_i^m/\rho_i \tag{6.15}$$

with $i = \mathrm{C_3S}, \mathrm{C_2S}, \mathrm{C_3A}, \mathrm{C_4AF}, \mathrm{C\bar{S}H_2}$ and innert (nonactive compounds), of which the density are presented in Table 6.4, $V_w^{in} = (\mathrm{w/c})/\rho_w$ is the initial volume of water before mixing with cement clinkers. As reaction proceeds, water is consumed and new hydration products appear, the total volume is then composed of the unhydrated components and new created components:

$$V_t = V_{in} = V_{cp} + \sum_i f_{i,unhydr}^m/\rho_i + V_{\text{C-S-H}} + V_{\mathrm{CH}} + V_{\mathrm{C_3AFH_{16}}} + V_{\mathrm{C_4AH_{13}}} + V_{\mathrm{C_4A\bar{S}H_{12}}} \tag{6.16}$$

where V_{cp} is the volume of capillary pores, $f_{i,unhydr}^m$ is the mass fraction of unhydrated compound i per unit mass of initial unhydrated OPC, V_{CSH} is the volume of the C-S-H that is composed of the HD C-S-H, LD C-S-H and the accessible pores in LD C-S-H. The quantitative relations among them have been given by eqs(6.10), (6.11) and (6.12). The terms V_i is volume of product i, with $i = \mathrm{CH}, \mathrm{C_3AFH_{16}}, \mathrm{C_4AH_{13}}$ and $\mathrm{C_4A\bar{S}H_{12}}$, and given by:

$$V_{\mathrm{CH}} = \frac{\mathrm{CH}}{\rho_{\mathrm{CH}}}; \quad V_{\mathrm{C_3AFH_{16}}} = \frac{\mathrm{C_3AFH_{16}}}{\rho_{\mathrm{C_3AFH_{16}}}}; \quad V_{\mathrm{C_4AH_{13}}} = \frac{\mathrm{C_4AH_{13}}}{\rho_{\mathrm{C_4AH_{13}}}}; \quad V_{\mathrm{C_4A\bar{S}H_{12}}} = \frac{\mathrm{C_4A\bar{S}H_{12}}}{\rho_{\mathrm{C_4A\bar{S}H_{12}}}} \tag{6.17}$$

where the mass $\mathrm{CH}, \mathrm{C_3AFH_{16}}, \mathrm{C_4AH_{13}}$ and $\mathrm{C_4A\bar{S}H_{12}}$ are given by eq(6.5) and eq(6.7).

Substitution of eqs(6.5), (6.7), (6.10), (6.11), (6.12) and (6.17) into the eq(6.16), and considering the parameters given in Table 6.4, one obtains the volumes of unhydrated phases for a material with a composition shown in Table 6.1:

$$\begin{aligned} V_{\text{unhydr}} = {} & 0.3205 - 0.1869\alpha_{\mathrm{C_3S}} - 6.5183\times10^{-2}\alpha_{\mathrm{C_2S}} - 2.1419\times10^{-2}\alpha_{\mathrm{C_3A}} \\ & - 2.3512\times10^{-2}\alpha_{\mathrm{C_4AF}} - 2.2328\times10^{-3}\alpha_{\mathrm{C\bar{S}H_2}} \end{aligned} \tag{6.18}$$

The volume of monosulfate (AFm), calcium aluminate hydrate, hydrogarnel and calcium hydroxide thus can be expressed ultimately as:

$$V_{\mathrm{C_4A\bar{S}H_{12}}} = 0.013799\alpha_{(\mathrm{C\bar{S}H_2})}; \quad V_{\mathrm{C_3AFH_6}} = 0.05502\alpha_{(\mathrm{C_4AF})} \tag{6.19a}$$

$$V_{\mathrm{C_4AH_{13}}} = 0.06566\alpha_{(\mathrm{C_3A})} - 0.0057415\alpha_{(\mathrm{C\bar{S}H_2})}; \tag{6.19b}$$

$$V_{\mathrm{CH}} = 0.11089\alpha_{(\mathrm{C_3S})} + 0.024634\alpha_{(\mathrm{C_2S})} - 0.007942\alpha_{(\mathrm{C_3A})} + 0.00133\alpha_{(\mathrm{C\bar{S}H_2})} - 0.0119\alpha_{(\mathrm{C_4AF})} \tag{6.19c}$$

The volume of LD C-S-H is given by:

$$\begin{aligned} V_{\text{LD-CSH}} = {} & 0.1634\alpha_{\mathrm{C_3S}} + 0.07879\alpha_{\mathrm{C_2S}} - 0.2377\alpha_{\mathrm{C_3S}}^2 - 0.04210\alpha_{\mathrm{C_2S}}^2 - 0.2034\alpha_{\mathrm{C_3S}}\alpha_{\mathrm{C_2S}} \\ & + \left(0.5395\alpha_{\mathrm{C_3S}}^2 + 0.09431\alpha_{\mathrm{C_2S}}^2 + 0.4556\alpha_{\mathrm{C_3S}}\alpha_{\mathrm{C_2S}}\right)(\mathrm{w/c}) \end{aligned} \tag{6.20}$$

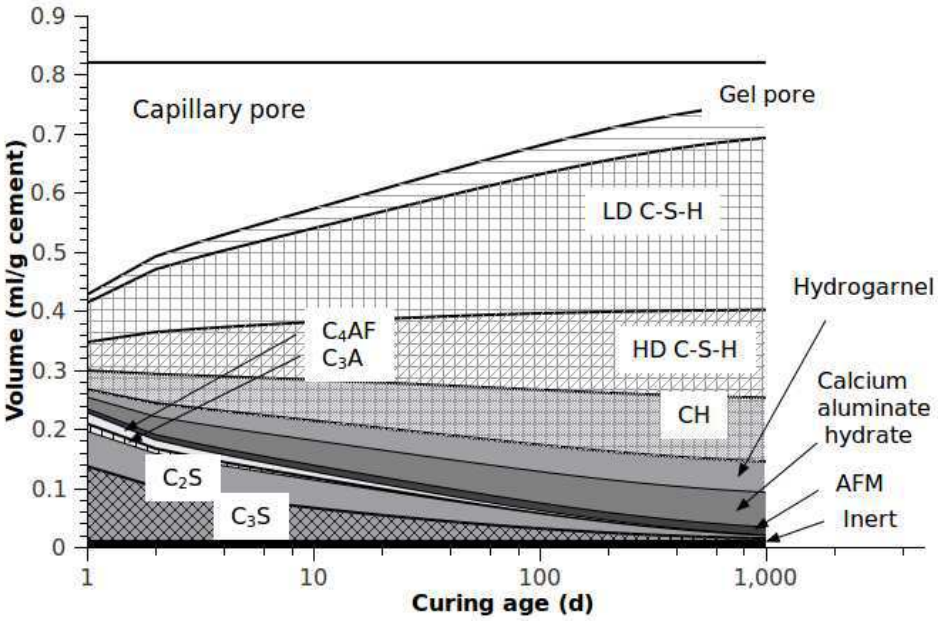

Figure 6.5: Variation of volume (ml/g cement) of components with curing age for paste I (w/c=0.5).

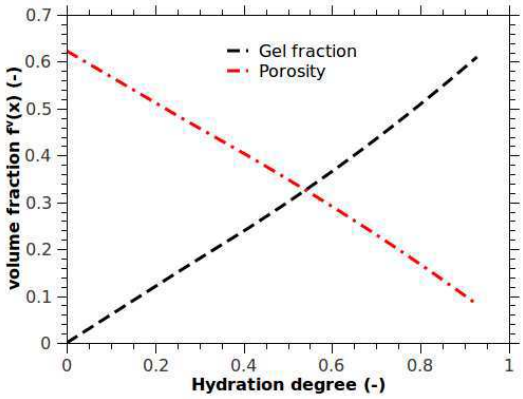

Figure 6.6: Variation of capillary porosity (dash dot line) and C-S-H gel volume fraction (dash line) with hydration degree. The capillary porosity is calculated by eq(6.9) The gel volume is the sum of the volume of LD and HD C-S-H, calculated by eqs(6.20) and (6.21) respectively. w/c=0.5 and the used OPC has a composition of $C_3S = 58.88\%, C_2S = 21.38\%, C_3A = 6.49\%, C_4AF = 8.77\%$ as shown in Table 6.1.

and the volume of HD C-S-H is given by:

$$\begin{aligned} V_{\text{HD-CSH}} = {} & 0.1481\alpha_{C_3S} + 0.07139\alpha_{C_2S} + 0.2183\alpha_{C_3S}^2 + 0.03815\alpha_{C_2S}^2 + 0.1843\alpha_{C_3S}\alpha_{C_2S} \\ & - \left(0.4888\alpha_{C_3S}^2 + 0.08545\alpha_{C_2S}^2 + 0.4128\alpha_{C_3S}\alpha_{C_2S}\right)(\text{w/c}) \end{aligned} \tag{6.21}$$

The initial volume of mixture with a given OPC and w/c can be calculated as [1] :

$$V_{in} = \text{w/c} + 0.3205 \tag{6.22}$$

Figure 6.5 shows the variation of volume of components with curing age. Note that, during the hydration, the intermediate product AFt (ettringite) has not been considered, because the AFt transfers to AFm ultimately and the amount of Gypsum in the raw OPC is very low (0.75%). In addition, the kinetics of AFt formation is relatively complex. It can be seen that the volume of C-S-H increases significantly as hydration goes on and the amount of LD C-S-H is larger than that of HD C-S-H obviously. The volume of

1. The value 0.3205 is calculated as : (1 gram OPC)/ρ_{OPC}, with $\rho_{\text{OPC}} = 3.12$ as shown in Table 6.1.

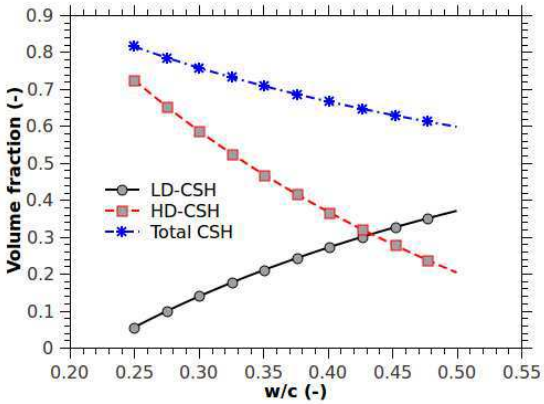

Figure 6.7: Variation of volume fraction (-) of LD C-S-H (open circles), HD C-S-H (open rectangle) and the total C-S-H (stars) with water cement ratios (w/c). The values are calculated by eqs(6.20) and (6.21) with hypothesis that $\alpha_i = 1$ for compound i. The OPC has a composition of $C_3S = 58.88\%, C_2S = 21.38\%, C_3A = 6.49\%, C_4AF = 8.77\%$ as shown in Table 6.1.

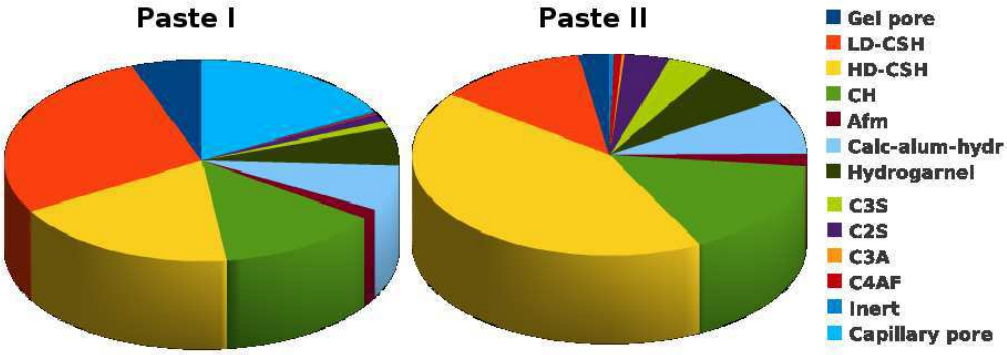

Figure 6.8: The volume fraction of all compounds of paste I (a) and paste II (b) evaluated by Avrami's empirical equation at curing age of 360D.

Monosulfate (AFm), Calcium aluminate hydrate and Hydrogarnel increase with curing age progressively, and the amount of those products are much lower than those of C-S-H and CH due to the low content of alumina and ferrite in raw material. The porosity and the main reactants, i.e, C_3S, C_2S, C_3A, C_4AF decrease with curing age, and the later four components will vanish ultimately.

Figure 6.6 shows the variation of volume fraction of capillary pores and C-S-H gels with hydration degree. The volume fraction of C-S-H gels increases to about 60%, and that of capillary pore decreases to about 10% when the hydration degree arrives 90%. Figure 6.7 shows the variation of volume fractions of LD C-S-H, HD C-S-H and total C-S-H with w/c. The amount of LD C-S-H increases progressively with w/c, whereas the amount of HD C-S-H decreases significantly with w/c. The volume fraction of total C-S-H thus decreases as w/c increases, because of the increase of initial total volume, see eq(6.22).

6.2.3 Summary

By use of semi-empirical equations, the main hydration products of our cement pastes can be estimated. Those values are the basic data for evaluating the mechanical and transport properties of cement pastes in chapter 7. Figure 6.8 shows the volume fraction of the main compounds for past I and paste II at 360D

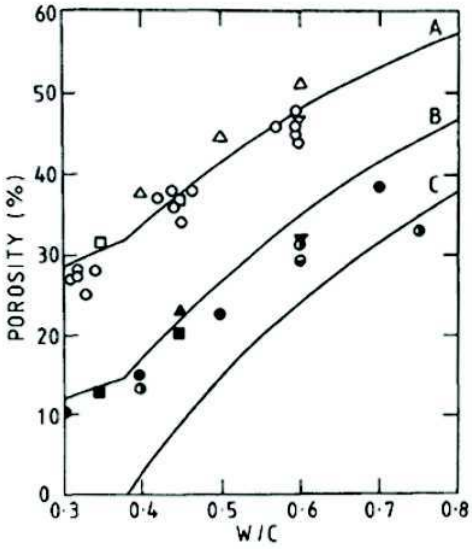

Figure 6.9: Variation of porosity with water to cement ratio (w/c). The solid lines are calculated from the model by Powers and Brownyard [308]. Line A: Porosity with total water; line B: porosity with free water; and line C: porosity with capillary water. The empty symbols (circle, square and triangle) represent the experimental data by complete drying. The filled and partially filled symbols (filled triangle and square and partially filled circle) represent the experimental data by MIP. After Taylor, 1997 [391].

respectively. It can be found that the volume of C-S-H that is composed of LD C-S-H, HD C-S-H and gel pore, occupies more than half of the total volume for both paste I and II. The capillary porosity is about 16% for paste I, while that for paste II is negligible. These results are consistent with the value obtained by Powers [308], see Figure 6.9. Those values are somehow different from the experimental results in the next section, where the 26% and 13% porosity for paste I and II are obtained by MIP measurement (see Figures 6.16 and 6.17 and the drying technique is freezing-dry). Figure 6.9 also shows that the MIP porosity is systematically larger than the capillary porosity. Several reasons account for the differences between the values by model and those by experiments. Firstly, the measured porosity includes not only the capillary pores but also part of gel pores. According to Jennings, the size of large gel pores can be as large as about 12 nm [178]. The pore volume in the size interval $d \in (3-12)$nm takes 30% and 70% of total pore volume for paste I and paste II respectively (see Figures 6.18(a) and 6.18(b)). The capillary porosity for paste I and paste II thus are: $\phi_{cap}(\text{Paste I}) = 26\% \times (1-30\%) = 18.2\%$ and $\phi_{cap}(\text{Paste II}) = 13\% \times (1-70\%) = 3.9\%$. These values are comparable with the predicted ones. Secondly, it is well known that the high pressure during MIP measurement may induce the additional deformation which can be either elastic solid deformation or cracks [99], therefore, the MIP measurement may overestimate the total pore volume. Thirdly, the capillary pores do not include the water adsorbed on pore walls, but drying procedures may remove some adsorbed water so that more pore volume is obtained.

6.3 Pore structure of ordinary Portland cement

As typical porous media, cement pastes adopt a pore structure with broad pore size distribution from nanometer to micrometer scales [170, 247] (see Figure 6.10). Moreover, the connectivity of the pores of different sizes seem to be complicated and “ink-bottle” geometry exists extensively in the pore network

[99]. Nowadays, no experimental method allows to measure the pore structure of cement pastes completely. So far, numerous experimental methods have been developed to measure or assess the pore structure, and the most widely used methods include the mercury intrusion porosimetry (MIP) and nitrogen adsorption/desorption (NAD) methods. The MIP measurement still remains the preferred method for pore structure evaluation due to its large range of pore size measurement and easy operation [211], although the measurement may lose its accuracy for the "ink-bottle" pores and fractures can be possibly induced in samples by the high intrusion pressure [99, 140].

The gas adsorption method has also been used for identifying the pore structure of cement-based materials for decades [29, 133, 251, 308]. On the basis of the adsorbed gas quantity, the internal surface area of pores can be evaluated from the Langmuir monomolecular layer theory, the BET multilayer adsorption theory and the t-plot method. Furthermore, the pore size distribution can be obtained using Barret-Joyner-Halenda (BJH) interpretation based on capillary condensation [29]. Note that the desorption phase of NAD is similar to the intrusion phase of MIP from the point of view of non wetting phase propagation in pores [278]. Thus the pore size distributions obtained from NAD and MIP measurements can be compared for the mutual range of pore size. Actually, the combination of MIP and NAD for pore structure characterization has been widely used in such fields as industry catalyst [278], soil engineering [108] and artificial materials [158]. Recent works by Kaufmann et al. [186] and Kaufmann [190] showed the application of NAD, MIP and other methods combined together to evaluate the pore structure of cement-based materials.

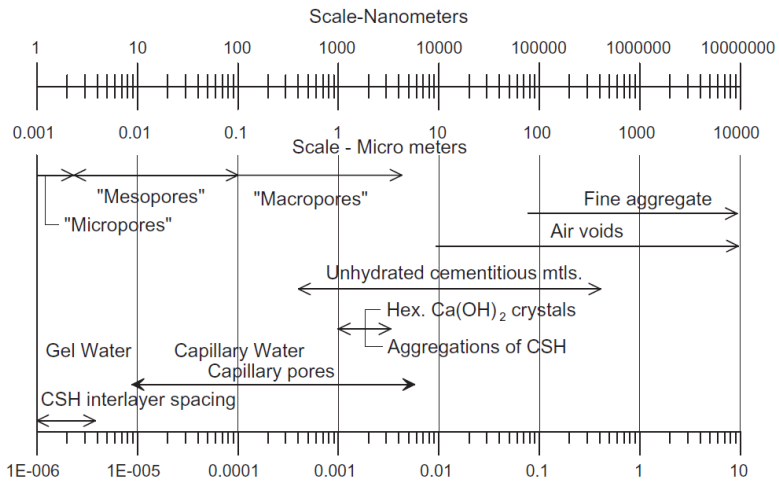

Figure 6.10: Approximate ranges of pores and other microscopic features in hardened cement paste. After Hover (2011) [170].

6.3.1 Specific surface area

Figures 6.11(a) and 6.11(b) show the isotherm NAD curves at −196℃ on paste I and paste II respectively. For paste I, it can be seen that the adsorbed volume increases with curing age in all relative pressure interval (see Figure 6.11(a)). A significant augmentation of isotherm adsorption/desorption curves is observed when curing age increases from 7D to 28D. For instance, the maximum adsorbed volume at

saturation case ($P/P_0 = 1$) increases from 37.5 ml/g at 7D to 63.6 ml/g at 28D. After 28D, only slight increment of isotherm adsorption/desorption curves is observed as curing age goes on. There are no significant differences among the normalized isotherm adsorption/desorption curves for paste I at all curing ages, see Figure 6.12(a). For paste II, the isotherm adsorption/desorption curve for sample at 7D is different from those at longer curing ages in the whole relative pressure interval $P/P_0 \in (0, 1)$, see Figure 6.11(b). The adsorbed volume keeps almost constant in the relative pressure interval $P/P_0 \in (0, 0.8)$ for paste II at 7D, compared to the samples at longer curing age, of which the adsorbed volume increases with relative pressure monotonously. This can be also verified by the normalized isotherm adsorption curves as shown in Figure 6.12(b). After significant increase of adsorbed volume as the curing age increases from 7D to 28D, the adsorbed volume keeps almost constant when curing age goes on. Those observations may be governed by the hydration processes of cement pastes. According to Jennings and coworkers [178, 392], the nitrogen adsorption technique can only access the LD C-S-H, which has the specific surface area about 250 m^2/g. The observation that the isotherm sorption/desorption curves for Paste I increase with curing age monotonously, is thus reasonable due to the monotonously increase of the amount of LD C-S-H with curing age (see Figure 6.5). However, for paste II (w/c=0.3), the hydration rate is much lower than that of Paste I, and more unaccessible HD C-S-H is created, thus the measured isotherm adsorption/desorption curves are not sensitive to curing age when curing age is longer than 28D.

Table 6.6 summarizes the specific surface area evaluated by Langmuir, BET, t-plot and BJH approaches by means of NAD data and that by MIP data. Obviously, the specific surface area of Paste II is much lower than that of Paste I, independent of the evaluation methods. Again, the model by Tennis and Jennings [392] is adopted to explain the obtained data. Recalling Figure 6.7, for Paste II, it only has about 15% of the accessible LD C-S-H, one third of those for Paste I, which coincides roughly with the data presented in Table 6.6.

Table 6.6: The specific surface area of paste I (II) by different measurement.

Curing age (days)	BET (m^2/g)	t-plot Micropore area[a](m^2/g)	t-plot External area[b](m^2/g)	Langmuir m^2/g
7D	26.689(9.000)	8.440(8.792)	18.287(0.210)	36.455(12.201)
28D	36.622(17.922)	8.078(1.856)	28.548(16.066)	50.380(24.880)
90D	40.415(16.682)	3.352(1.200)	37.110(15.482)	56.107(23.214)
180D	44.656(16.961)	2.984(1.042)	41.672(15.919)	61.853(23.634)
Curing age (days)	BJH (sorp) (m^2/g)	BJH (desorp) (m^2/g)	MIP (m^2/g)	
7D	21.166(5.071)	32.030(13.071)	35.525(17.788)	
28D	33.610(18.552)	56.437(26.538)	64.432(23.267)	
90D	42.980(17.715)	58.510(25.256)	58.824(22.307)	
180D	48.444(17.632)	61.943(22.553)	55.322(23.990)	

[a] The micropore defined here is different with that defined by IUPAC [439], the details of determination of micropore is presented in Figure 6.15.
[b] The external area is defined as the slope of the t-plot, whose range lies between monolayer and capillary condensation.

The Langmuir specific surface area is systematically larger than BET one. This is due to the intrinsic mechanism differences between BET and Langmuir approaches (see Appendix A.6). It can be further found

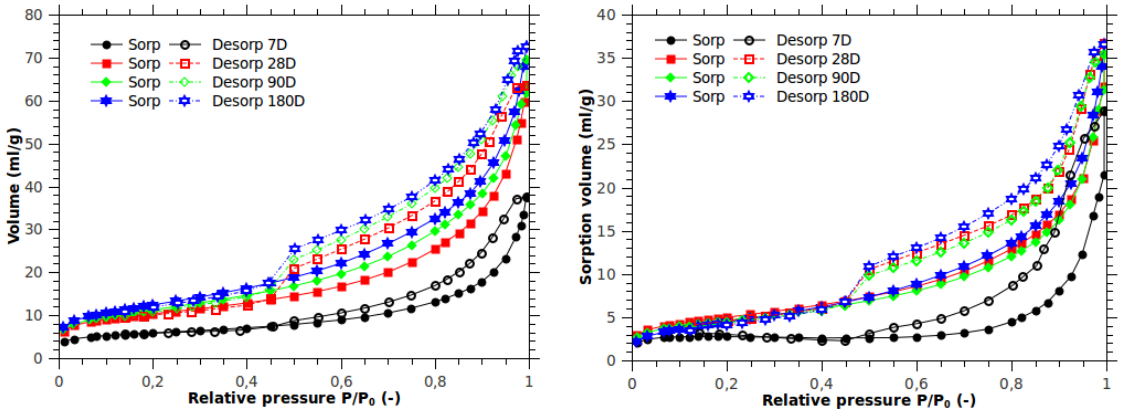

(a) (b)

Figure 6.11: Isotherm curves of nitrogen sorption and desorption near the boiling point of nitrogen on paste I (a) and paste II (b).

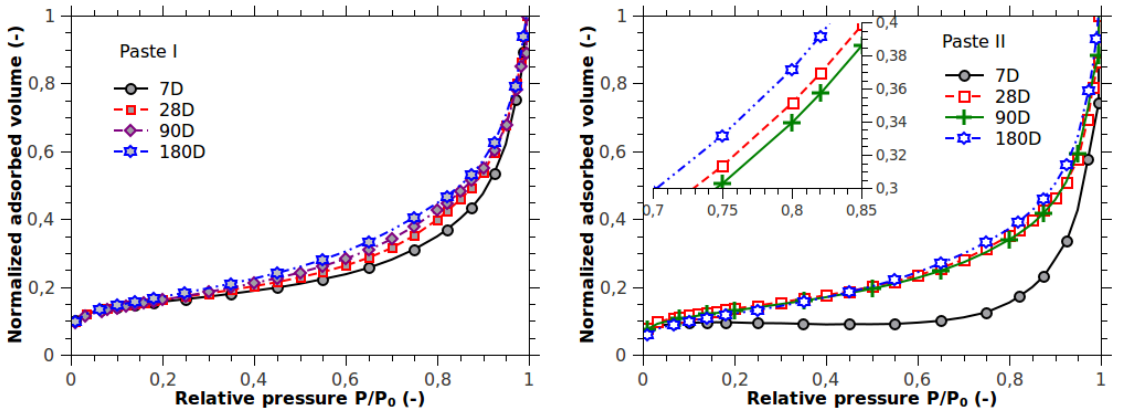

(a) (b)

Figure 6.12: The normalized isotherm sorption curves for paste I (a) and II (b). The normalized value $= V/V(P/P_0 = 1)$.

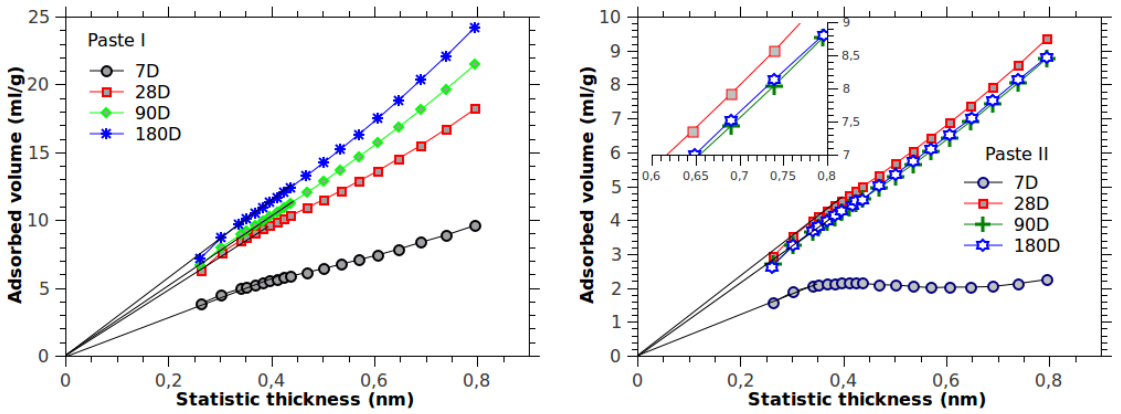

(a) (b)

Figure 6.13: The t-plot curves for paste I (a) and paste II (b) at different curing age.

that the BET specific surface area is very close to the total t-plot specific surface area (t-plot micropore area + t-plot external area, and the determination of the micropore is given in following section 6.3.2). This has been verified by the NAD results on the pastes blended with silica fume by Khalil [191]. The t-plot curves for Paste I and II are illustrated in Figure 6.13(a) and 6.13(b) respectively. It can be seen that, except the curves of pastes at 7D, all the curves show almost linear relations. According to de Boer et al. [90, 91] and Mikhail et al. [251], the filling of some narrowest pores by multilayer adsorption firstly may lead to the phenomenon that the t-plot curve begins to drop below the straight line as the thickness increases. The authors [90, 91] also pointed out that if the capillary condensation starts in certain pores in addition to multilayer adsorption, the points of the t-plot should begin to deviate upward [90, 91, 251]. This is not observed in our results. Note that, different t-curves (adsorption thickness) may cause the different t-plot curves. In the t-plot by Mikhail et al. [251], the Cranston and Inkley t-curve [84] was applied. In this study, the Hakins and Jura t-curve (see eq(A.41)) is employed for t-plot evaluation. Table 6.6 also presents the sorption and desorption BJH specific surface area.

The cumulative specific surface area distribution in terms of pore size are illustrated in Figure 6.14(a) for Paste I and in Figure 6.14(b) for Paste II. Obviously, a significant augmentation of specific surface area at pore size (diameter) around 3.5 nm is observed for almost all samples, which may be due to the fact that the average size (diameter) of gel pores in C-S-H [178, 308] is 3.5 nm. Interestingly, the BJH(sorp) specific surface area is close to the BET specific surface area, while the BJH (desorp) specific surface area is close to the Langmuir specific surface area. This must be coincidence because the region of BET approach ($P/P_0 \in (0.05, 0.35)$) is different with that of BJH approach ($P/P_0 \in (0.45, 0.967)$), and there is no physical basis for this observation. However, the observation that the desorption BJH specific surface area is larger than the adsorption one, can be due to the "ink-bottle" effect and the connectivity of percolated pores with different sizes. In addition, the BET approach was originally developed for estimating the specific surface of flat solid rather than that of porous materials, and the BJH approach requires the cylindric pore geometry which was criticized for its oversimplification.

Table 6.6 shows the specific surface areas evaluated by means of MIP data as well. Similar to the values obtained by means of NAD data, the MIP specific surface area for paste I is higher than that of paste II because paste I has more capillary pores and more large gel pores accessible by MIP measurement (minimum accessible pore size for MIP measurement used in this study is 3 nm). However, a maximum value of specific surface area for Paste I at 28D is obtained. This can be attributed to, firstly, a large amount of gels and crystals with high specific surface area that are formed by elimination of capillary pores as hydration goes on, and this hydration finishes about 70% during the first 28 days [247, 253]; secondly, at later curing age (cf. curing age is longer than 28D) denser C-S-H that can not be penetrated by mercury

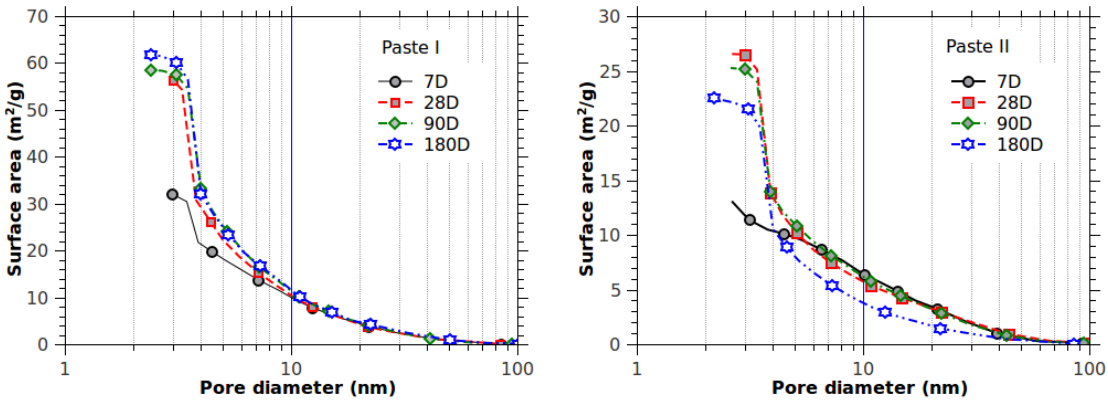

(a) (b)

Figure 6.14: The BJH cumulative surface area in terms of pore size for paste I (a) and paste II (b) at different curing ages.

even under high pressure, forms.

Table 6.7: The pore volume of paste I (II) by different measurements.

Curing age (days)	Total Pore Volume (NAD)[a](μl/g)	Micro pore volume (NAD)[b](μl/g)	BJH (sorp)[c](μl/g)
7D	56.521(25.868)	3.774(4.141)	73.426(31.075)
28D	78.751(39.336)	3.492(0.684)	98.294(49.622)
90D	84.077(39.959)	1.159(0.380)	97.065(48.892)
180D	88.915(31.534)	0.960(0.291)	114.548(39.482)

Curing age (days)	BJH (desorp) [d](μl/g)	MIP (μl/g)	MIP (3-70 nm) (μl/g)
7D	75.800(44.788)	208.119(90.300)	104.300(74.200)
28D	99.317(57.127)	177.801(87.642)	113.869(77.562)
90D	108.550(55.220)	164.776(75.202)	139.800(69.107)
180D	113.567(38.958)	160.794(62.540)	140.354(55.515)

[a] Single point adsorption total pore volume of pores less than 70.7 nm at $P/P_0 = 0.972$;
[b] Pore size rang 0.7-1.8 nm, and the determination method refers to Figure 6.15;
[c] Nominal BJH adsorption cumulative pore volume of pores between 1.7 and 300.0 nm Diameter;
[d] Nominal BJH desorption cumulative pore volume of pores between 1.7 and 300.0 nm Diameter.

6.3.2 Pore volume, porosity and characteristic pore size

Table 6.7 presents the pore volume evaluated by t-plot, BJH approaches from NAD data and by Washburn equation from MIP data. It can be found that the total pore volume (NAD) increases with curing age due to the continual formation of porous LD C-S-H. For paste II, the total pore volume is much lower due to less porous LD C-S-H formed compared to Paste I. In addition, the maximum total pore volume (NAD) appears for paste II at 90D, then it decreases slightly as curing age increases, which can be due to the microstructure changing of C-S-H: LD C-S-H transferring to HD C-S-H

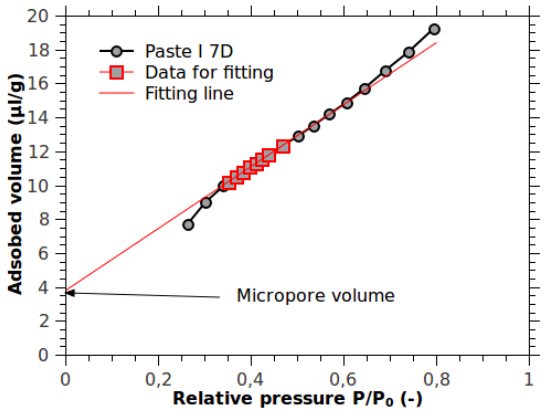

Figure 6.15: Determination of micropore volume of paste I at 7D.

progressively [178].

The micropore volume, as shown in second column in Table 6.7, is determined by the method proposed by de Boer et al. [90, 91] and Lippens and de Boer [220]. As shown in typical t-plot (see Figure 6.15), a downward deviation from linearity at low relative pressures is observed, i.e., after the third point at relative pressure of 0.39 in Figure 6.15. This downward deviation indicates that micropores become filled by multilayer adsorption at low relative pressure, thus the surface available for continual adsorption reduces [10]. Through the extrapolation of the second straight line to zero relative pressure, one yields a measure of the volume of the adsorbate in the previously blocked micropores. This extrapolation process is illustrated in Figure 6.15. Korpa and Trettin [202] suggested that supermicropores and very narrow mesopores in size of 0.7-1.8 nm, which are presented in slit-shaped, sheet-like nanostructures that are typical microstructures of cement-based materials, can be filled in the range ($P/P_0 \in (0.01, 0.4)$). Contrary to the total pore volume, the micropore volume decreases with curing age monotonously for both Paste I and II, see the second column in Table 6.7. This may be due to the drying technique applied in this study. Since the freezing dry with vacuum for 24 hours at outgass of 8-13 Pa is a mild drying method, some of the micropores are still filled with water (this kind of water can be structural water or strongly adsorbed water). In addition, as curing age increases, the gel structure becomes denser so that some of the micropores are blocked by gel solid, which is similar to the hindered pore identified by Jennings [178]. The reduction of micropores is particularly severe for Paste II. As shown in Table 6.7, the volume of micropores reduces from 4.141 to 0.219 (μl/g) when curing age of samples increases from 7D to 180D.

Similar to the variation of total pore volume with curing age, the pore volumes for paste I both from BJH sorption and desorption branches increase with curing age. For paste II, the BJH pore volume (sorption and desorption) increases as curing age increases from 7D to 28D, then it decreases when curing age goes on. The reasons are the same with those for the BJH surface area variation with curing age: accessible porous gels increase firstly, then become inaccessible denser structure.

The MIP total volume decreases with curing age monotonously for both paste I and paste II, which can be attributed to the continual pore volume elimination by hydration. However, once the pore region reduces to 3-70 nm, the variation of pore volume obtained by MIP data is similar to that by BJH: it increases with curing age monotonously for paste I, while it increases first then decreases when curing age is longer than 28D for paste II. Note that this pore size interval $d \in 3 - 70$ nm for MIP is close to that of BJH ($d \in 1.7 - 100$nm) as shown in Figures 6.14(a) and 6.14(b).

The total porosity can be evaluated once the pore volume and the solid volume are determined. Since the pore volume determined by the NAD is limited in magnitude of hundred nanometers in average [10], it thus will not be used to evaluate the total porosity. Instead, the pore volume determined by gravimetry

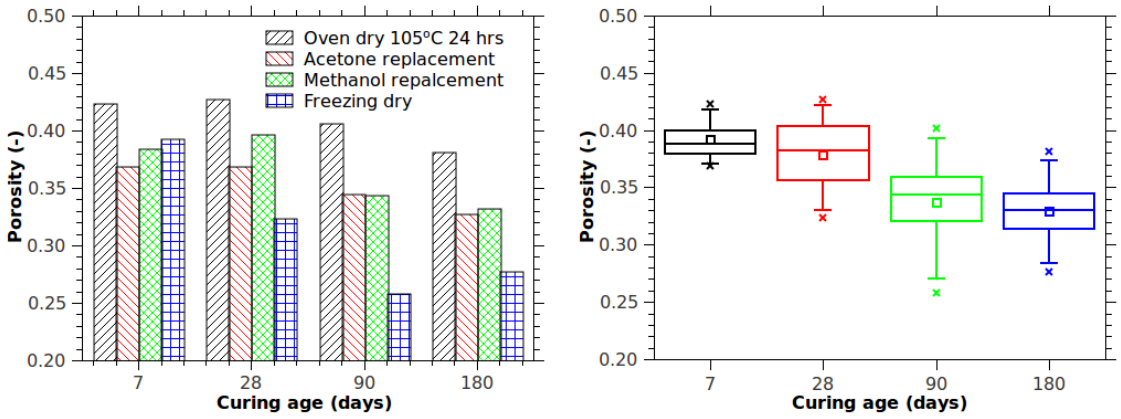

(a) (b)

Figure 6.16: (a), Porosity of paste I measured by different drying technology in terms of curing age. (b), The statistical results of the porosity in terms of curing age.

and MIP methods are employed to evaluate the total porosity. The drying methods for MIP and gravity methods are summerized in Table 6.2. The samples for MIP measurement were dried by method of freezing dry, while the samples for gravity measurement are dried by methods of solvent exchange and of oven dry (105℃ for 24 hours). The drying techniques have significant influence on pore structure measurement [202]. The porosity pretreated by different drying techniques is shown in Figure 6.16(a). It can be seen that oven dried samples exhibit the largest porosity, while the freezing dried samples have almost lowest porosity except for paste I at 7D. This can be due to the fact that the oven dry in 105℃ removes water in capillary pore and part of water in gel pores [10], while freezing dry is much mild and slow. The porosity of samples dried by methanol exchange is slightly larger than those by acetone exchange because the molecule size of methanol is smaller than that of acetone, and the affinity of hydrogen of acetone with pore wall make it easier to penetrate into pores but harder to remove from pores. Figure 6.16(b) illustrates the statistical results of the porosity measured by different drying techniques for paste I. The average porosity decreases from 0.39 to 0.33 consistently as curing age increases. Figures 6.17(a) and 6.17(b) show the similar observations for paste II, but the porosity for paste II is much lower than that of paste I: the average porosity decreases from 0.24 to 0.21 as curing age increases from 7D to 180D.

To characterize the pore structure of blended cement pastes comprehensively and extensively, three different characteristics of pore size are addressed by means of NAD and MIP data. The critical radius is the inflection point on the volume intrusion versus radius curve (the maximum value of the dV/dP curve), which corresponds to the smallest pore size of the subset of the largest pores creating a connected path through the sample as suggested by Katz and Thompson [184]. It is also reported the strong correlation between the critical pore size and water permeability or ions diffusion coefficients [151]. The threshold pore size (diameter) is defined as the diameter where mercury begins to enter and percolate the pore system in

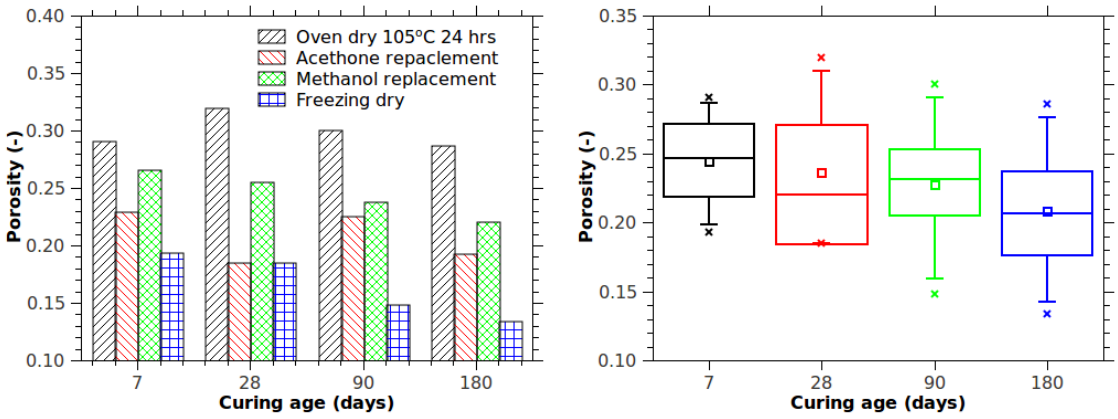

(a) (b)

Figure 6.17: (a), Porosity of paste II measured by different drying technology in terms of curing age. (b), The statistical results of the porosity in terms of curing age.

Table 6.8: The characteristic pore size of paste I (II) by different measurements.

Curing age (days)	Critical pore size (nm)	threshold pore size (nm)	4V/S MIP (nm)
7D	75.0(13.2)	544.6(95.6)	23.448(20.306)
28D	38.5(13.2)	225.2(83.3)	11.038(15.063)
90D	21.1(8.6)	77.4(40.3)	11.206(13.489)
180D	17.2(3.6)	95.6(15.4)	11.631(10.421)
Curing age (days)	4V/S BJH (adsorp) (nm)	4V/S BJH (desorp) (nm)	4V/S BET (nm)
7D	138.764(114.964)	94.662(254.108)	84.711(137.058)
28D	11.698(10.699)	7.039(8.611)	8.602(8.779)
90D	9.034(11.040)	7.421(8.746)	8.321(9.581)
180D	9.458(8.957)	7.334(6.910)	7.964(7.437)

appreciable quantity [428]. The average pore size or mean pore size is determined by the ratio of total pore volume to surface area, $d = 4 \times$ volume/surface area. The average pore size is also addressed through BJH (adsorption and desorption branches) and BET approach by means of NAD data.

As presented in Table 6.8, the critical pore radii decreases as curing time increases, so do the other characteristics of pore size. The critical pore radius for paste I are larger than those for paste II obviously due to the larger w/c ratio for paste I. The decrease of characteristic pore sizes with curing age is undoubtedly due to the hydration processes that form new C-S-H gel and other crystals filling the capillary pores.

A noticeable observation is that some of the average pore size determined by all the four data branches (MIP, BJH sorption and desorption, and BET), for paste II are slightly larger than those for paste I. This anomalous observation may be due to the microstructure change of C-S-H with curing age. On one hand, for paste I, the formed porous LD C-S-H augments the specific surface area as observed in Table 6.6; on the other hand, paste II that has denser compaction and forms more HD C-S-H, eliminates the capillary pores and leads to a small amount of pore volume accessed by NAD. The coupling of the above mentioned effects may lead to the anomalous observation of average pore size for paste I and II as shown in Table 6.8.

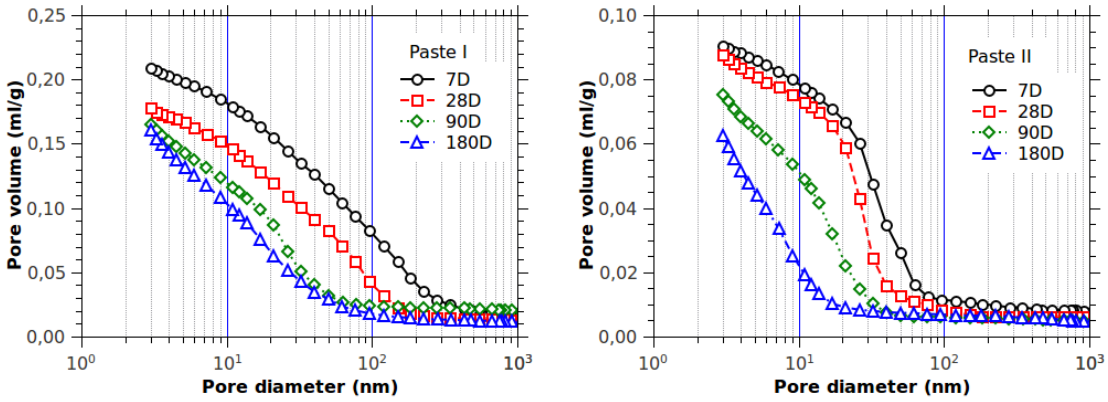

(a) (b)

Figure 6.18: Cumulative pore size distribution measured by MIP for paste I (w/c=0.5) (a) and paste II (w/c=0.3) (b) at different curing age.

6.3.3 Pore size distribution

The MIP measurement can present both cumulative pore size distribution (CPSD) and differential pore size distribution (DPSD). As shown in Figures 6.18, the CPSD profiles of paste I and paste II with curing age have similar curves but are full of different pore feature information. As presented in Figures 6.18(a) and 6.18(b), the intruded pore volume shown in CPSD profiles of paste I is larger than that of paste II, which indicates the amount of capillary pores of paste I is larger than that of paste II systematically. It also clearly shows that the pore width decreases as curing time increases for paste I and II. Figures 6.19(a) and 6.19(b) show the variation of intruded pore volume fraction of paste I and II with curing age. The intruded pore volume fraction is obtained by a normalization that divides the current intruded pore volume by the total intruded pore volume. The narrowing of pore size with hydration time can be found for paste I and II as obviously shown in Figure 6.19(a) and 6.19(b).

Figures 6.20(a) and 6.20(b) illustrate the DPSD profiles of paste I and II respectively. Two pore size regions are used to analyze the PSDs. The region I that is defined in scale of $d \in (3 \sim 20)$ nm, determines the variation of gel pores and part of small capillary pores. In this region, the ink-bottle effect is not significant, so that the variation of pores in this scale may be captured well by DPSD. The region II is defined in scale of $d \in (20 \sim 1000)$ nm. In this region, the critical pore size that actually is the throat pore size of ink bottle as extensively analyzed by Diamond [99], can be clearly figured out. It can be seen, in Figures 6.20(a) and 6.20(b), that the DPSD in region I increases with curing age for both paste I and II due to the formation of porous C-S-H gel. In region II, the peak point that is the critical pore size, and the peak area that is the cumulative pore size distribution, decrease with the augmentation of curing age for both paste I and II.

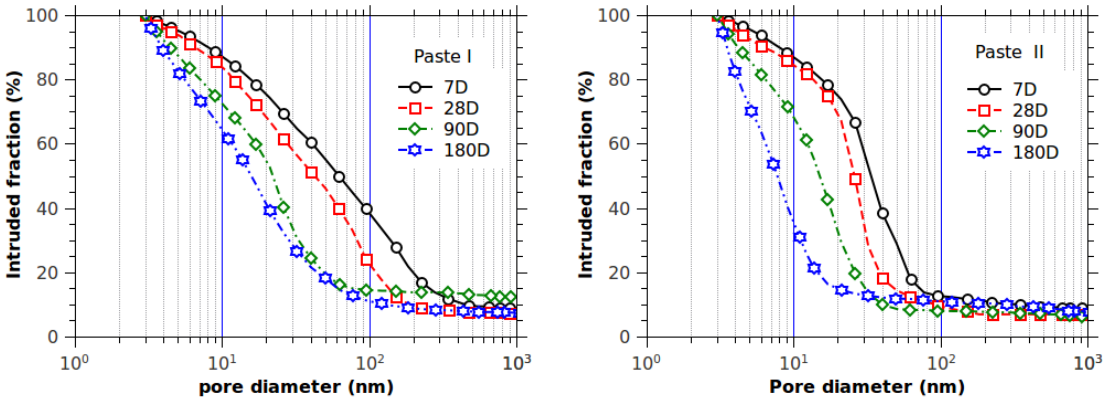

(a) (b)

Figure 6.19: Normalized CPSD or intruded pore fraction measured by MIP for paste I (w/c=0.5) (a) and paste II (w/c=0.3) (b) at different curing ages.

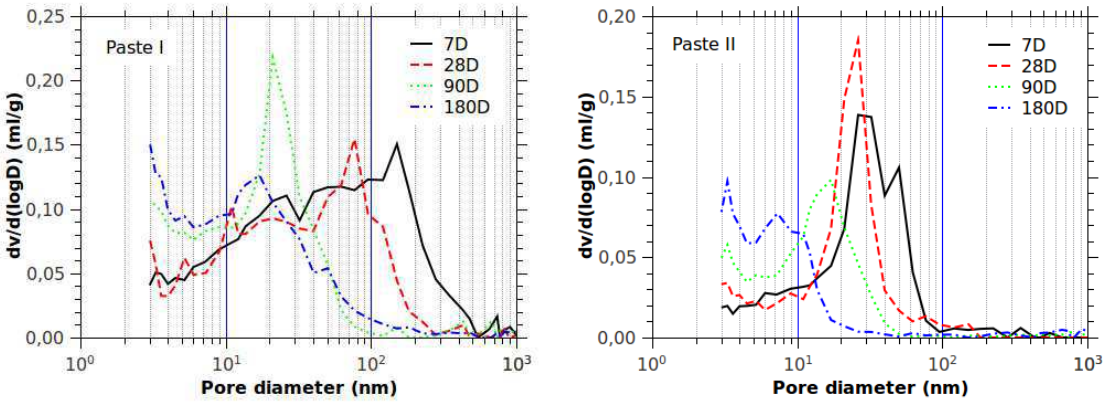

(a) (b)

Figure 6.20: Differential pore size distribution measured by MIP for paste I (w/c=0.5) (a) and paste II (w/c=0.3) (b) at different curing ages.

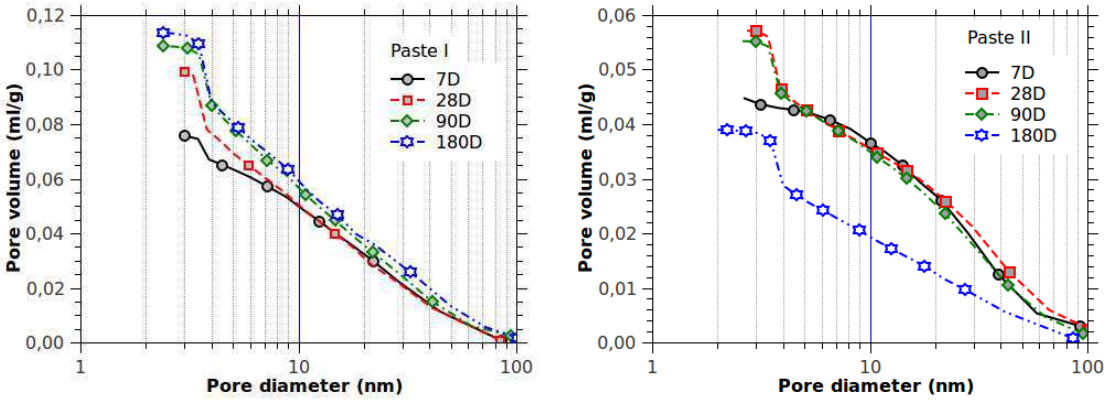

(a) (b)

Figure 6.21: The cumulative pore size distributions for paste I (a) and paste II (b) with different curing ages by means of BJH desorption data.

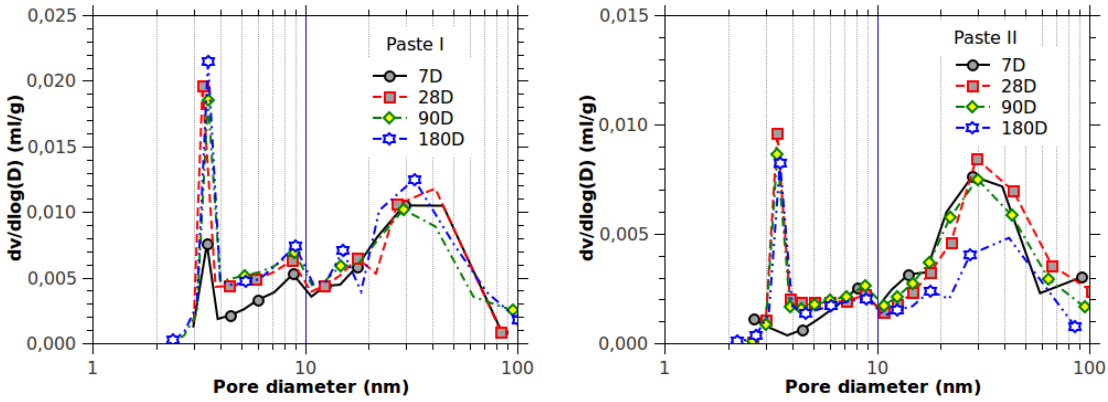

(a) (b)

Figure 6.22: The differential pore size distributions for paste I (a) and paste II (b) with different curing age by means of BJH desorption data.

The CPSD and DPSD of all paste samples evaluated by BJH desorption data are presented in Figures 6.21 and 6.22 respectively. The average pore size region for BJH desorption analysis is limited in about (2∼100) nm. Furthermore, the effective region of pore size for BJH approach is argued to be less than 60 nm since the upper boundary of relative pressure is 0.967 [10]. For all samples, an almost linear increase of CPSD with logarithm value of pore diameter can be seen down to 3.5 nm. At this size, a significant increment of pore volume is observed, see Figure 6.21 and 6.22. The corresponding pore size agrees well with the interlayer pore size of hydration product C-S-H, and this peak is due to the gel (interlayer) pore condensation of nitrogen. The same conclusion is also reached by other authors [12, 306].

In summary, for pore size distribution measurement, MIP provides a reliable distribution on a large pore size range while for micropore and meso-pore ranges, the NAD measurement affords more detailed information on gel pores of C-S-H hydrates. The combined MIP and NAD methods have been extensively studied to evaluate the pore structure of cement-based materials by Kaufmann and Kaufmann et al. [186, 189, 190]. Due to the large scale availability of MIP measurement, and the same physic meaning of ice penetration and mercury intrusion, the pore structure measured by MIP is selected for evaluating the curves of ice or liquid saturation degree in terms of temperature (see section 8.3 for detail).

Chapter 7

Evaluation of the mechanical and transport properties of hardened cement pastes

Contents

In this chapter the classical homogenization procedure for multi-level or multi-scale composites, used for example by Ulm et al. [403], is applied to evaluate the macroscopic poro-elastic properties of hardened cement pastes, which will be useful in the description of cement-based materials submitted to freeze-thaw loading in next chapter. In the present work, we start the homogenization procedures from the microstructure of hardened cement paste since the components and pore structure have been evaluated in

chapter 6. Also through the classical homogenization procedure, the transport properties of cement-based materials are to be evaluated and validated by experimental results in literature.

7.1 Principle of multi-scale modelling

The global behavior of composites depends not only on the materials of compounds, but also the their microstructural morphology and their interactions. The classical homogenization technique is actually a method to estimate the global behavior through replacing an actual heterogeneous complex body by a fictitious homogeneous one which behaves globally in the same way. Cement-based materials are typical composites which are heterogeneous at micro-scale or meso-scale, and homogeneous at macro-scale. It is thus not surprising that numerous multi-scale models have been used to assess the global behaviors of cement-based materials, cf. [137, 179, 338, 403, 411]. The first but significant important procedure is to define a RVE, see also chapter 4. Over the RVE, the average behaviors of locally heterogeneous materials can be represented by a fictitious homogeneous material. Generally, the homogenization method includes three steps [438]: description/representation, concentration/localization and homogenization/upscaling. In the step of description, the different phases of the microstructure in the RVE of the considered heterogeneous material must be identified clearly. This step is very important not only for multiscale modelling, but also for the properties of materials themselves. That is why many researches pay much attention on the nano-structure of C-S-H in cement-based materials, cf. [66, 68, 179, 411, 412]. The concentration step is concerned with the principles of mechanical and transport behaviors of each phase as well their interactions. The homogenization step is actually a method that estimates the macroscopic properties by means of the local constitutive equations and the concentration relations. Based on different hypotheses, there are many different homogenization/upscaling methods. More details can be found in relevant comprehensive reviews [159, 438, 446]. In this work, we follow the widely used Mori-Tanaka and self-consistent methods. The detailed homogenization procedures for mechanical and transport properties can be found in Appendix C.

7.2 Mechanical properties of cement paste

7.2.1 Multiscale nature of cement paste

In this subsection, we recapitulate the nature of microstructure of hardened cement paste as extensively discussed in chapter 6. The two types of C-S-H that were originally observed by Taplin [389] have been extensively studied by researchers afterwards. Based on the data by means of nitrogen sorption, Jennings and coworkers proposed the widely employed cement model, named CM, in which the LD C-S-H and HD C-S-H are structurally distinct but compositionally similar. The CM model was then after verified and calibrated by nanoidentation measurement by Ulm et al. [403] and Constantinides and Ulm [65–67, 69] and

by the small-angle neutron scattering (SANS) measurement and small-angle X-radian scattering (SAXS) measurement by Allen, Thomas and Jennings et al. [11, 12, 179, 393, 395, 397]. Based on the flourishing contribution aforementioned, it is thus not difficult to represent the complex microstructure as an ideal multiscale composite system as illustrated in Figure 7.1.

In order to address the micromechanical modelling and homogenization of poroelastic properties, the microstructure of the hardened cement paste is divided into the following three scale levels:

- Level-I, ($10^{-9} \sim 10^{-8}$m, the LD and HD C-S-H solid): the LD and HD C-S-H are composed of the basic globules and the gel pores.
- Level-II, ($10^{-8} \sim 10^{-6}$m, the C-S-H solid matrix): the C-S-H solid matrix is composed of LD and HD C-S-H.
- Level-III, ($10^{-6} \sim 10^{-4}$m, the cement paste): the cement paste is composed of C-S-H matrix, CH, Al and Fe minerals, unhydrated cement clinkers and capillary pores.

More details on microstructure modelling of cement paste can be found in Ulm et al. [403], Constantinides and Ulm [67], Dormieux et al. [103], Bernard et al. [46] and Pichler and Hellmich [292].

7.2.2 Homogenization equations

The nature of multi-scale microstructure of the cement paste (cf. three different levels presented in Figure 7.1) allows us to write the homogenization equations of the macroscopic parameters in three steps, first for HD and LD C-S-H (from nano-structure of C-S-H globules to level-I), then for the C-S-H colloid (from Level I to Level II), and last for the cement paste (from level-II to level-III). The description on the micromechanics representation of the RVEs of C-S-H and cement paste has been extensively discussed in Refs. [46, 136, 137, 292].

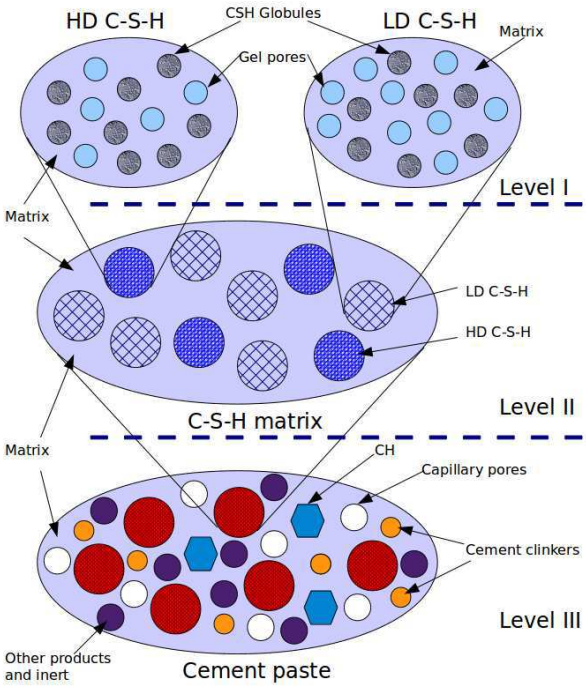

Figure 7.1: Micromechanical representation of the cement paste through a three-step homogenization scheme.

7.2.2.1 Level-I: LD and HD C-S-H

According to the CM model by Jennings and coworkers [178, 392, 396], the LD and HD C-S-H are constituted by the same solid matrix, named the globules in size of 3nm. The globules are considered to be identical in LD and HD C-S-H. The different packing density or patterns of globules lead to the different porosity between these two types of C-S-H, i.e., the gel porosity is about 0.24 for HD C-S-H and 0.37 for

LD C-S-H [392]. The pores then can be regarded as a kind of inclusion in the continual C-S-H matrix, the poroelastic properties of C-S-H matrix can therefore be evaluated by means of homogenization presented in Appendix C. For this purpose, the porosities, ϕ_{LD} and ϕ_{HD}, the elastic modulus k_s and g_s and the thermal expansion of the C-S-H solid α_s are needed. Considering one solid phase and one porous phase, the homogenized drained bulk modulus and the shear modulus can be given by [137]:

$$K_X^{hom} = (1-\phi_X)k_s A_{s,X}^v, \quad G_X^{hom} = (1-\phi_X)g_s A_{s,X}^d \tag{7.1a}$$

$$b_x^{hom} = 1 - \frac{K_X^{hom}}{k_s}, \quad \frac{1}{N_X^{hom}} = \frac{(1-\phi_x)\left(1-A_{s,X}^v\right)}{k_s} \tag{7.1b}$$

where the subscript X represents LD or HD. $A_{s,X}^v$ and $A_{s,X}^d$ are the strain localization tensor parameters of phase LD C-S-H or HD C-S-H. If an Eshelbian type morphology inclusion that is proved to be a suitable assumption for elastic properties homogenization of cement based materials [103, 376], is considered, and the self consistent scheme, i.e, $k_0 = K_X^{hom}$ and $g_0 = G_X^{hom}$, is applied, the parameters α_0 and β_0 in concentration equation are given by:

$$\alpha_0 = \frac{3K_X^{hom}}{3K_X^{hom}+4G_X^{hom}}; \quad \beta_0 = \frac{6\left(K_X^{hom}+2G_X^{hom}\right)}{5\left(3K_X^{hom}+4G_X^{hom}\right)} \tag{7.2}$$

By using the eq(C.33) and (C.37) in Appendix C, and the relation $\boldsymbol{\alpha}_d^{hom} = (\mathbb{C})^{-1} : \boldsymbol{\kappa}^{hom}$, the homogenized thermal parameters can be evaluated in:

$$\kappa_X^{hom} = (1-\phi_X)k_s\alpha_s A_{s,X}^v, \quad \alpha_{d,X}^{hom} = \alpha_s, \quad Q_X^{hom} = \alpha_s(1-\phi_x)\left(1-A_{s,X}^v\right) \tag{7.3}$$

We follow the assumption that the porosity in HD C-S-H is not active [1] as is done by Ghabezloo [136, 137, 139]. The water in HD C-S-H, strongly adsorbed by the van der Waals forces, can not be removed except in severe drying condition, cf. O-dry with 105℃ and D-dry, and can sustain the mechanical loading partially [178]. Thus the undrained condition should be specifically considered in homogenization procedure. The undrained homogenized bulk modulus and thermal dilation coefficient are then given by [137]:

$$K_{u,HD}^{hom} = K_{HD}^{hom} + \frac{(b_{HD}^{hom})^2}{\frac{1}{N_{HD}^{hom}} + \frac{\phi_{HD}}{K_f}} \tag{7.4a}$$

$$\alpha_{u,HD}^{hom} = \alpha_{d,HD}^{hom} + \frac{Q^{hom} + \phi_{HD}\alpha_{f,HD} - b_{HD}^{hom}\alpha_{d,HD}^{hom}}{\frac{K_{HD}^{hom}}{b_{HD}^{hom}}\left(\frac{1}{N_{HD}^{hom}} + \frac{\phi_{HD}}{K_f}\right) + b_{HD}^{hom}} \tag{7.4b}$$

where $\alpha_{f,HD}$ is the thermal dilation coefficient for pore fluid in HD C-S-H, which is much larger than that for solid phases in cement-based materials [136, 248, 249, 370].

The homogenized elastic properties of LD C-S-H and HD C-S-H are presented in Table 7.1. It can be

1. According to [136], the active pore is defined as : the pore fluid can exchange with the fluid filling the pore volume situated in its neighbourhood under the effect of a pressure gradient. Otherwise, the pore is not active

found that the evaluated results are lower than those homogenized by Mori-Tanaka scheme in Refs. [67, 403] and experimental results in Ref [6, 448], but are comparable to the values homogenized by self-consistent scheme in Refs. [136].

Table 7.1: The evaluated poromechanical parameters in Level-I.

Level-I	Young's modulus	Bulk modulus	Shear Modulus	Bulk modulus	References
	E_X^{hom} (GPa)	K_X^{hom} (GPa) (Drained case)	G_X^{hom} (GPa)	Ku_X^{hom} (GPa) (Undrained case)	
LD C-S-H	13.63	9.03	5.21	11.88	This study[a,b]
	21.7 ± 2.2(M-T)[b,c]	14.47	8.75	-	[67, 403]
	12.46[d]	7.99	4.93	8.59	[136]
	23.4 ± 3.4	-	-	-	[448]
	21 ± 2	-	-	-	[6]
HD C-S-H	26.33	16.81	10.22	18.74	This study[b]
	29.4 ± 2.4(M-T)	18.84	11.85	-	[67, 403]
	21.95[d]	14.07	9.75	14.36	[136]
	31.4 ± 2.1	-	-	-	[448]
	30 ± 4	-	-	-	[6]

Level-I	Poisson ratio	Biot coefficient	Biot moduli	Thermal dilation coefficient		References
	v (-)	b_X^{hom}(-)	N_X^{hom} (GPa)	$\alpha_{d,X}^{hom}$ (μm/m) (Drained case)	$\alpha_{u,X}^{hom}$ (μm/m) (Undrained case)	
LD C-S-H	0.25	0.72	92.72	42	96.62	This study
	0.25	0.71	93.1	-	-	[67, 403]
	0.25	0.68	81.0	42	100.23[d]	[137]
HD C-S-H	0.25	0.47	135.72	42	64.68	This study
	0.25	0.61	85.9	-	-	[67, 403]
	0.25	0.44	124.91	42	66.93	[137]

[a] The poisson ratio is assumed to be 0.25 [67, 403];
[b] The used LD C-S-H and HD C-S-H porosity are 0.37 and 0.24 respectively [392];
[c] M-T represents the Mori-Tanaka homogenization scheme;
[d] Calculated from the data in Ref. [136], $E = 44.3, v = 0.204, k_s = 25, g_s = 18.4$ and $\phi_{\text{LD}} = 0.37$, $\phi_{\text{HD}} = 0.24$.

7.2.2.2 Level-II: C-S-H matrix

The homogenized poromechanical properties of C-S-H that is composed of LD and HD C-S-H, can then be evaluated as:

$$K_{CSH}^{hom} = f_{LD} K_{LD}^{hom} A_{LD,CSH}^{v} + f_{HD} K_{u,HD}^{hom} A_{HD,CSH}^{v} \tag{7.5a}$$

$$G_{CSH}^{hom} = f_{LD} G_{LD}^{hom} A_{HD,CSH}^{d} + f_{HD} GHD^{hom} A_{HD,CSH}^{d} \tag{7.5b}$$

$$b_{CSH}^{hom} = 1 - f_{LD} A_{LD,CSH}^{v} \left(1 - b_{LD}^{hom}\right) - f_{HD} A_{HD,CSH}^{v} \tag{7.5c}$$

$$\frac{1}{N_{CSH}^{hom}} = f_{LD} \left(\frac{\left(1 - b_{LD}^{hom}\right)\left(1 - A_{LD,CSH}^{v}\right)}{k_s} + \frac{1}{N_{LD}^{hom}} \right) + f_{HD} \frac{1 - A_{HD,CSH}^{v}}{K_{u,HD}^{hom}} \tag{7.5d}$$

Again, the Eshelbian type solutions of strain localization tensor parameters, $A_{X,CSH}^{v}$ and $A_{X,CSH}^{d}$, can be evaluated (see eq(C.9)). Under the self consistent scheme: $k_0 = K_{CSH}^{hom}$ and $g_0 = G_{CSH}^{hom}$, the parameters α_0 and β_0 are given by:

$$\alpha_0 = \frac{3K_{CSH}^{hom}}{3K_{CSH}^{hom} + 4G_{CSH}^{hom}}; \quad \beta_0 = \frac{6\left(K_{CSH}^{hom} + 2G_{CSH}^{hom}\right)}{5\left(3K_{CSH}^{hom} + 4G_{CSH}^{hom}\right)} \tag{7.6}$$

Recalling again the eqs(C.33) and (C.37), and the relation $\boldsymbol{\alpha}_d^{hom} = (\mathbb{C})^{-1} : \boldsymbol{\kappa}^{hom}$, the homogenized thermal parameters can be evaluated in:

$$\alpha_d^{hom} = f_{LD} K_{LD}^{hom} \alpha_{d,LD}^{hom} A_{LD,CSH}^{c} + f_{HD} K_{HD}^{hom} \alpha_{u,HD}^{hom} A_{HD,CSH}^{c} \tag{7.7a}$$

$$Q_{CSH}^{hom} = \alpha_{u,HD}^{hom} f_{HD} \left(1 - A_{HD,CSH}^{v}\right) + f_{LD} \left(\alpha_{d,LD}^{hom}(1 - A_{LD,CSH}^{v})(1 - b_{LD}^{hom}) + Q_{LD}^{hom}\right) \tag{7.7b}$$

The term $\alpha_{d,X}^{hom} = \alpha_s$, is retained for any elastic porous medium [192].

For the C-S-H phase, the active porosity is only contributed by the pores in LD C-S-H with a form $\phi_{CSH}^{act} = f_{LD}\phi_{LD}$. One thus can evaluate the undrained bulk modulus $K_{u,CSH}^{hom}$ and thermal dilation expansion coefficient $\alpha_{u,CSH}^{hom}$ as follows:

$$K_{u,CSH}^{hom} = f_{HD} K_{u,HD}^{hom} A_{HD,CSH}^{v} + f_{LD} K_{d,LD}^{hom} A_{LD,CSH}^{v} + \frac{(b_{CSH}^{hom})^2}{\frac{1}{N_{CSH}^{hom}} + \frac{\phi_{CSH}^{act}}{K_f}} \tag{7.8a}$$

$$\begin{aligned} \alpha_{u,CSH}^{hom} = {} & \alpha_{u,HD}^{hom} f_{HD} A_{HD,CSH}^{v} + \alpha_{d,LD}^{hom} f_{LD} A_{LD,CSH}^{v} \\ & + \frac{Q_{CSH}^{hom} + \phi_{CSH}^{act}\alpha_{f,CSH} - b_{CSH}^{hom}\left(\alpha_{u,HD}^{hom} f_{HD} A_{HD,CSH}^{v} + \alpha_{d,LD}^{hom} f_{LD} A_{LD,CSH}^{v}\right)}{\frac{K_{CSH}^{hom}}{b_{CSH}^{hom}}\left(\frac{1}{N_{CSH}^{hom}} + \frac{\phi_{CSH}^{act}}{K_f}\right) + b_{CSH}^{hom}} \end{aligned} \tag{7.8b}$$

The homogenized properties are related intimately to the volume fraction of all compounds. Table 7.2 presents the volume fraction of LD C-S-H and HD C-S-H of paste I and paste II estimated by Avrami equations as is used by Tennis and Jennings [392]. Those values are also compared to those in Refs [67, 403, 448]. It can be seen that roughly, the ratio of LD C-S-H to HD C-S-H is 7:3 for w/c=0.5.

Table 7.2: The volume fraction (absolute volume (ml/g cement)) of LD, HD C-S-H and active porosity in Level-II.

Level-II	HD C-S-H $f_{HD,CSH}$ (V_{HD})	LD C-S-H $f_{LD,CSH}(V_{LD})$	Active porosity $\phi_{CSH}^{act}(V_{act})$	References
Paste I	0.358 (0.155)	0.642 (0.273)	0.238 (0.101) [a]	This study
	0.3[b](-)	0.7 (-)	-(-)	[67, 403]
	0.241[c](-)	0.759 (-)	-(-)	[448]
Paste II	0.744 (0.267)	0.256 (0.092)	0.095 (0.034)[a]	This study

[a] Calculated as $\phi_{CSH}^{act} = f_{LD,CSH} \times 0.37$;
[b] w/c=0.5;
[c] w/c=0.35.

The homogenized elastic properties of C-S-H that is composed of LD C-S-H and HD C-S-H are presented in Table 7.3. Obviously, the elastic properties of C-S-H for paste I is significantly lower than those for paste II due to more HD C-S-H in paste II.

Table 7.3: The evaluated poromechanical parameters in Level-II.

Level-I: C-S-H	Young's modulus	Bulk modulus	Shear Modulus	Bulk modulus		References
	E^{hom}_{CSH} (GPa)	K^{hom}_{CSH} (GPa) (Drained case)	G^{hom}_{CSH} (GPa)	$Ku^{hom}_{CSH}(GPa)$ (Undrained case)		
Paste I	13.53 23.94(M-T)[a]	11.62 15	5.25 9.7	13.94 -		This study [67, 403]
Paste II	23.25	15.51	9.60	16.61		This study
Level-II: C-S-H	**Poisson ratio**	**Biot coefficient**	**Biot moduli**	**Thermal dilation coefficient**		**References**
	v	b_{CSH}	N^{hom}_{CSH} (GPa)	$\alpha^{hom}_{d,CSH}$ (μm/m) (Drained case)	$\alpha^{hom}_{u,CSH}$ (μm/m) (Undrained case)	
Paste I	0.30[b] 0.23[b]	0.53 0.69	91.22 90.8	42 -	80.58 -	This study [67, 403]
Paste II	0.25[b]	0.24	162.85	42	68.87	This study

[a] M-T represent the Mori-Tanaka homogenization scheme.
[b] Calculated from the bulk modulus and shear modulus, $v = (3K - 2G)/(2(3K + G))$.

7.2.2.3 Level-III: Cement paste

In this homogenization step, the cement paste is considered. The microstructure of cement paste is constituted by several phases, of which the C-S-H, Portlandite, AFm, Hydrogernol, anhydrous clinkers and the macro-pores occupy most of the volume. The volume fraction of these phases and their elastic constants are presented in Table 7.4. Among these phases, Portlandite crystals, AFm, Hydrogernol and anhydrous clinkers can be considered as non-porous solids, while C-S-H are porous solids which have been homogenized in previous subsection. Again, the homogenization of multiphase porous materials are applied in this system, and the formulas are presented as:

$$K^{hom}_{CP} = \sum_{X}^{m} f_{X,CP} K^{hom}_{X,CP} A^{v}_{X,CP} \tag{7.9a}$$

$$G^{hom}_{CP} = \sum_{X}^{m} f_{X,CP} G^{hom}_{X,CP} A^{d}_{X,CP} \tag{7.9b}$$

$$b^{hom}_{CP} = 1 - f_{CSH} A^{v}_{CSH,CP} \left(1 - b^{hom}_{CSH}\right) - \left(\sum_{X}^{m-1} f_{X,CP} A^{d}_{X,CP}\right) \tag{7.9c}$$

$$\frac{1}{N^{hom}_{CP}} = f_{CSH,CP} \left(\frac{\left(1 - b^{hom}_{CSH,CP}\right)\left(1 - A^{v}_{CSH,CP}\right)}{K^{hom}_{CSH}} + \frac{1}{N^{hom}_{CSH}} \right) + \sum_{X}^{m-1} f_{X,CP} \frac{1 - A^{v}_{X,CP}}{K^{hom}_{X,CP}} \tag{7.9d}$$

Again, the solutions of Eshelbian type inclusions of the strain localization tensor parameters, $A^{v}_{X,CSH}$ and $A^{d}_{X,CSH}$ in the level of cement pastes, can be evaluated by eq(C.9). With help of the self consistent scheme: $k_0 = K^{hom}_{CP}$ and $g_0 = G^{hom}_{CP}$, the parameters α_0 and β_0 are expressed as:

$$\alpha_0 = \frac{3K^{hom}_{CP}}{3K^{hom}_{CP} + 4G^{hom}_{CP}}; \quad \beta_0 = \frac{6\left(K^{hom}_{CP} + 2G^{hom}_{CP}\right)}{5\left(3K^{hom}_{CP} + 4G^{hom}_{CP}\right)} \tag{7.10}$$

Table 7.4: The volume fraction and elastic properties of paste I (paste II).

Compounds	Volume fraction	Elastic Modulus	Possion ratio	References
	$f_{X,CP}$	E_X (GPa)	v(-)	
CSH	0.5196(0.5745)	13.53 (23.25)	0.3 (0.25)	This study
	-	23.9	0.234	[67, 403]
C_3S	0.0108(0.0398)			This study
		135 ± 7	0.28	[6, 234]
		147 ± 5	0.3	[414]
C_2S	0.0131(0.0370)			This study
		130 ± 20	0.3 (βC_2S)	[234, 414]
		140 ± 10	0.3	[6]
C_3A	0.0005(0.0023)			This study
		145 ± 10		[414]
		160 ± 10		[6]
C_4AF	0.0023(0.0066)			This study
		125 ± 25		[414]
AFm	0.0882(0.1097)			This study
		42.3	0.324	
Hydrogarnel	0.0614(0.0718)			This study
		22.4	0.25	[150]
CH	0.1325(0.1551)			This study
		35.24		[34]
		48		[429]
		39.77-44.22	3.05-3.25	[258]
		36 ± 3		[6]
		38 ± 5		[65, 67, 69]
		35.2	0.31	[234]
Inert	0.0024(0.0029)			This study
		the same as C-S-H		
Capillary Pores	0.1689(≈ 0)			

Table 7.5: The evaluated poromechanical parameters in Level-III.

Level-III: Cement paste	Young's modulus E^{hom}_{CP} (GPa)	Bulk modulus K^{hom}_{CP} (GPa) (Drained case)	Shear Modulus G^{hom}_{CP} (GPa)	Bulk modulus Ku^{hom}_{CP} (GPa) (Undrained case)	References
Paste I	17.53	14.61	6.41	17.39	This study
	22.3(M-T)[a]	14.1	8.7	16.6	[67, 403]
Paste II	24.2	20.18	10.02	23.48	This study

Level-III: Cement paste	Poisson ratio v	Biot coefficient b_{CP}	Biot moduli N^{hom}_{CP} (GPa)	Thermal dilation coefficient $\alpha^{hom}_{d,CP}$ (μm/m) (Drained case)	Thermal dilation coefficient $\alpha^{hom}_{u,CP}$ (μm/m) (Undrained case)	References
Paste I	0.30[b]	0.49	122.2	-	68.08	This study
	0.25	0.69	90.8	-	-	[67, 403]
Paste II	0.3	0.33	179.7	42	55.4	This study

[a] M-T represent the Mori-Tanaka homogenization scheme.
[b] Calculated from the bulk modulus and shear modulus, $v = (3K - 2G)/(2(3K + G))$.

The homogenized thermal parameters can be evaluated as:

$$\kappa^{hom}_{CP} = \sum_{X,CP}^{m} f_{X,CP} K^{hom}_{X,CP} \alpha^{hom}_{X,CP} A^{c}_{X,CP} \tag{7.11a}$$

$$Q^{hom}_{CP} = \sum_{X,CP}^{m-1} \alpha^{hom}_{X,CP} f_{X,CP} \left(1 - A^{v}_{X,CP}\right) + \alpha^{hom}_{CSH,CP} \left[f_{CSH,CP} \left(1 - A^{v}_{HD,CSH}\right) \left(1 - b^{hom}_{CSH,CP}\right) + Q^{hom}_{CSH}\right] \tag{7.11b}$$

For the cement paste, the active porosity is contributed by the capillary pores and the gel pores in LD

C-S-H. The active porosity is expressed as $\phi_{CP}^{act} = \phi_{CP} + f_{CSH,CP} f_{LD,CSH} \phi_{LD}$. One thus can evaluate the undrained bulk modulus $K_{u,CP}^{hom}$ and thermal dilation expansion coefficient $\alpha_{u,CP}^{hom}$ of cement paste as follow:

$$K_{u,CP}^{hom} = \sum_{X}^{m} f_{X,CP} K_{d,X}^{hom} A_{X,CSH}^{v} + \frac{(b_{CP}^{hom})^2}{\frac{1}{N_{CP}^{hom}} + \frac{\phi_{CP}^{act}}{K_f}} \tag{7.12a}$$

$$\alpha_{u,CP}^{hom} = \alpha_{t,CP} + \frac{Q_{CP}^{hom} + \phi_{CP}^{act} \alpha_{f,CP} - b_{CP}^{hom} \alpha_{t,CP}}{\frac{K_{CP}^{hom}}{b_{CP}^{hom}} \left(\frac{1}{N_{CP}^{hom}} + \frac{\phi_{CP}^{act}}{K_f} \right) + b_{CP}^{hom}} \tag{7.12b}$$

with

$$\alpha_{t,CP} = f_{CSH} \left(\alpha_{u,HD}^{hom} f_{HD} A_{HD,CSH}^{v} + \alpha_{d,LD}^{hom} f_{LD} A_{LD,CSH}^{v} \right) + \sum_{X}^{m-1} \alpha_{d,X}^{hom} f_{X,CP} A_{X,CP}^{v} \tag{7.13}$$

where $\alpha_{t,CP}$ represents the total thermal expansion coefficient of the material in which the active pore water (gel pore water in LD C-S-H and capillary pore water) is removed.

As shown in Table 7.4, the C-S-H occupies more than half of the total volume. For all the hydration products, their volume for paste II are slightly higher than those for paste I due to the lower initial volume of paste II: $V_{in} = 0.8205$ for Paste I and $V_{in} = 0.6205$ for paste II referring to 1 gram of unhydrated cement powder. Table 7.4 also presents the elastic properties of main compounds of cement paste adopted in literature. The unhydrated cement clinkers have much higher elastic modulus, i.e, 125-160 GPa, compared to those values of C-S-H and CH, which occupies around 70% total volume of cement paste.

The homogenized elastic properties of cement pastes are presented in Tables 7.5. It can be found that the evaluated results are comparable to those homogenized by Mori-Tanaka scheme in Ref [67, 403]. The elastic modulus and shear modulus for paste I is lower than those values in Ref [67, 403] due to the different Poisson ratios, see Table 7.5. Paste II has higher elastic constants due to the fact that it has more minerals that have higher elastic constants. It can be also found that the undrained bulk modulus of cement paste is higher than that in drained case due to pressure sustainability of the liquid phase. The undrained thermal expansion coefficient for paste II is lower than that of paste I because paste II has lower porosity.

7.3 Transport properties of hardened cement paste

7.3.1 Introduction to the transport properties of hardened cement paste

As a typical porous material, the properties of electrical conductivity, permeability and diffusivity of cement-based materials are of significant interest for engineering application. In addition, sustainability issues require more durable cement-based materials with low water permeability and diffusivity because

the permeability is related intimately to the normal deterioration phenomena of cement-based materials, such as, freeze-thaw deformation, carbonation, chloride ingression and corrosion of steel reinforcement [247]. However, direct measurement of transport properties of cement-based materials usually requires specialized equipment and costs long time [271], and the obtained data are scattered due to the microstructure heterogeneity of cement-based materials. A noticeable effect of microstructure change on the transport properties of cement-based materials is the interfacial transition zone (ITZ) for concrete and mortars [100, 276], which increases the ability of mass transport in porous cement-based materials due to the more porous structure of ITZ. Nevertheless, many additives, such as, silica fume [41, 42], fly ash [13, 280], ground granulated blast furnace slag (GGBS) [241, 242], lime stone powder [161], polymer [130, 204] and other nano particles [160, 180], used in cement-based materials for both sustainability and durability consideration, have significant influences on their transport properties. For instance, by adding nano-particles into Portland cement mortars, the chloride diffusivity is lowered due to both physical and chemical effects, such as, space filling, nucleus agent for cement hydration, formation of the denser C-S-H, and possible pozzolanic reactions [160]. In addition, the obtained diffusivity of cement-based materials is rather influenced by the measurement methods. As shown in Buenfield and Newman [55], the three typical chloride diffusion methods for cement-based materials: the concentration-profile technique, the diffusion-cell technique and the electrical conductivity technique, have significant shortages for ionic diffusivity. Both the concentration-profile technique and the electrical conductivity technique are rather approximate and the former method requires very long test time. The diffusion-cell technique is said to be the most appropriate laboratory method for determining the ions diffusivity, but the technique is unable to monitor changes in diffusion rate during long-term exposure to a source of the ion in question [55]. The conflict between accuracy, convenience and/or low cost requirements of experiments on the transport properties of cement-based materials contributes to the models development. Based on the percolation theory, many works on the conductivity of porous medium have been published for either theoretical discussion or applications on soil, petrol and cement-based science/engineering [41, 184, 351, 426]. In this section, we thus try to estimate the transport properties of cement-based materials by the effective methods presented before.

7.3.1.1 Conductivity and diffusivity

For a porous material, the relative diffusivity and relative electrical conductivity are defined as the ratio of diffusivity D (conductivity σ) to the bulk diffusivity D_0 (bulk conductivity σ_0) of pore-filled liquid:

$$\frac{D}{D_0} = \frac{\sigma}{\sigma_0} = \frac{1}{F} = \frac{\phi}{\tau} \tag{7.14}$$

where F is the formation factor, ϕ is connected porosity, τ is the tortuosity. Note that in eq(7.14) the tortuosity is somewhat different from the definition in [409]. The relationship $\sigma/\sigma_0 = (\phi\delta_c)/\tau^2$ was retained

by Brakel and Heertjes [409], with δ_c the constrictivity. Obviously $\tau = \delta_c/\tau^2|_{BH}$. Except some applications, cf. [264, 378], the tortuosity in eq(7.14) rather than that in Brakel-Heerthes form, was used. An empirical equation that relates the conductivity to the porosity is the Archie's law [19]:

$$\sigma = C_A \phi^{m_A} \tag{7.15}$$

where C_A and m_A are adjustable constants. When the percolation of the entire pore network are taken into account, a more appropriate formula with a critical porosity ϕ_c than the Archie's law [246] can be obtained:

$$\frac{\sigma}{\sigma_0} = \left(\frac{\phi - \phi_c}{1 - \phi_c}\right)^{m_p} \tag{7.16}$$

where m_p is defined as a percolation exponent. Also, on percolation consideration, the porosity ϕ in Archie's law (eq (7.15)) can be replaced by a effective porosity $\phi - \phi_c$. For $\phi_c \ll 1$, eq(7.16) reduces to the percolation modified Archie's equation, $\sigma = C_A(\phi - \phi_c)^{m_A}$.

Table 7.6: Parameters of conductivity in empirical equations with or without percolation consideration.

Materials	Constant C	Constant m	Percolation porosityϕ_c	Equation	Methods	References
Model porous media		2-4	0.125	Eq(7.16)	ballistic deposition model	[88]
Cement-based materials	0.036-210	1.34-4.73		Eq(7.15)	30 Volt/15 min	[271]
Model porous media		2-2.4	0.27-0.3	Eq(7.16)	Lattice Boltzmann method	[238]
Model porous media		2.8	0.33	Eq(7.16)	Lattice simulation	[201]

Table 7.7: Summary of some mixing models for conductivity of porous materials.

Name	Scope	Formula σ_{eff} =	Note	References
Parallel model	1-many phases	$\sum_i^N \phi_i \sigma_i$	Parallel axially layered structure of phase i with σ_i	[230]
Perpendicular model	1-many phases	$\frac{1}{\sigma_{eff}} = \sum_i^N \frac{\phi_i}{\sigma_i}$	Parallel normally layered structure of phase i with σ_i	[142, 230]
Modified parallel model	2 phases	$\sigma_1\phi_2\beta_1 + \sigma_2\phi_2\beta_2$	β_i connectivity factor	[265]
Random model	1-many	$\prod_i^N \sigma_i^{\phi_i}$	Arbitrary oriented phase i with σ_i	[142]
Archie-based model	2 phases	$\sigma_1(1-\phi_2)^{[\log(1-\phi_2^m)/\log(1-\phi_2)]} + \sigma_2\phi_2^m$	with boundary constriction	[142]
Archie-based model	2 phases	$\sigma_1\phi^m + \sigma_2\phi_2^n$		[56, 265]
Bruggeman-Hanay approach	2 phases	$\sigma_1\phi_1^m\,[(1-\sigma_2/\sigma_1)/(1-\sigma_2/\sigma_{eff})]^m$ with $\sigma_1 < \sigma_2$	Composite theory	[56]
Waff model	2 phases	$[\sigma_2 + (\sigma_1 - \sigma_2)(1 - 2\phi_2/3)]/[1 + (\phi_2/3)(\sigma_1/\sigma_2 - 1)]$	Composite theory	[416]

Table 7.6 presents the parameters of conductivity in Archie's law for common porous materials from literature. Note that, for cement-based materials, both the C_A and m_a have large deviation compared to other porous materials. Therefore, for complex composites, such as cement-base materials, the Archie's

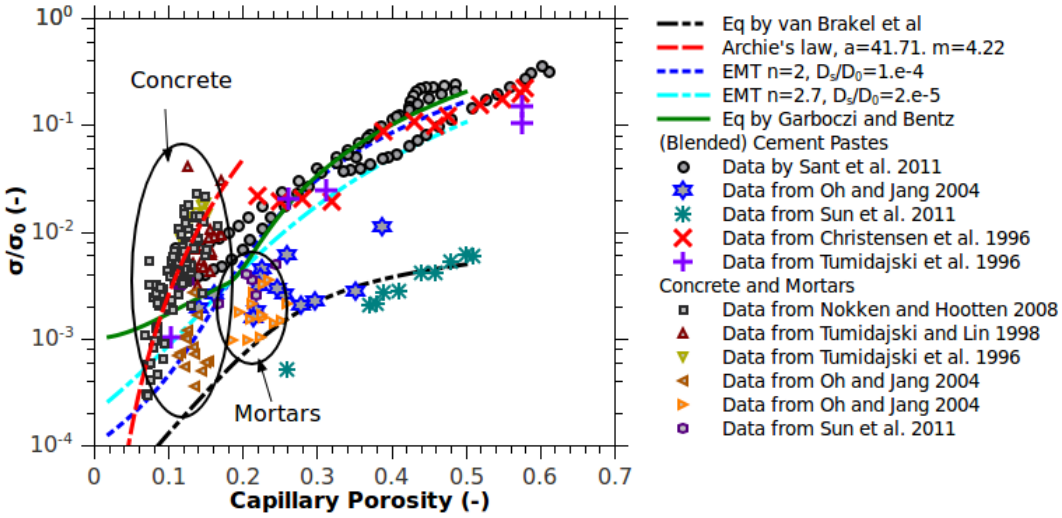

Figure 7.2: The reciprocal of formation factor $1/F = \sigma/\sigma_0$ for cement-based materials in terms of porosity. Data from [61, 271, 275, 339, 378, 400, 401, 409].

Table 7.8: The expressions for curves presented in Figure 7.2.

Name	Formula	References
Brakel-Heerthes equation	$\frac{\sigma}{\sigma_0} = \frac{\phi\delta_c}{\tau_{BH}^2}$ $\delta_c = 0.395\tanh[4(\log r_p + 6.2)] + 0.405$ $\tau_{BH} = -1.5\tanh[8(\phi - 0.25)] + 2.5$	[264, 378, 409]
Effective medium theory	$\frac{\sigma}{\sigma_0} = \frac{D}{D_0} = \left[m_\phi + \sqrt{m_\phi^2 + \frac{\phi_c}{1-\phi_c}(D_s/D_0)^{1/n}}\right]^n$ $m_\phi = \frac{1}{2}\left[(D_s/D_0)^{1/n} + \frac{\phi_c}{1-\phi_c}\left(1 - (D_s/D_0)^{1/n}\right) - \frac{\phi_c}{1-\phi_c}\right]^n$	[275]
Garboczi-Bentz equation	$\frac{\sigma}{\sigma_0} = 0.001 + 0.07\phi^2 + H(\phi - \phi_c)\cdot 1.8(\phi - \phi_c)^2$	[40]

law in simple power formula may be not suitable for describing their conductivities. Instead of the simple Archie's law, many mixing models for conductivity of porous materials have been developed, cf. Table 7.7. Figure 7.2 shows the curves predicted by selected models (see Table 7.8) and measured data by different authors for cement-based materials. It can be found that no uniform formula can capture all the experiment data for cement-based materials and there exist two distinct data areas for blended cement pastes and mortars and/or concrete respectively. For the blended cement pastes, a large variation of regions of porosity in about 0.1∼0.6 can be observed and numerous data of the distribution of relative conductivity in terms of porosity are close to the values predicted by Ghaboczi-Bentz equation [40] and the EMT by Oh et al. [275]. For concrete and mortars, the porosity is much lower than that of cement pastes, but the conductivity does not decrease due to the percolated pores in interface transition zone (ITZ).

7.3.1.2 Permeability of porous materials

A well known empirical equation describing the permeability of porous materials is the Kozeny-Carman equation:

$$\kappa = C_{KC}\frac{\phi^3}{S^2} \quad \text{or} \quad = \frac{\phi(V/S)^2}{C_{KC}^*} \tag{7.17}$$

Table 7.9: Constant and factor of permeability in Katz-Thompson formula fro cement-based materials.

Materials	Measurement method	Constant C_H	Formation factor F	Acuurancy	References
Mortars	Pressure permeability cell	180	E-D equation	normal	[151].
Cement pastes	References [4,5] there in	226	Impedance spectroscopy	normal	[61]
Mortars	Pressure permeability cell	180-2000			[109, 237]

where C_{KC} and C^*_{KC} are adjustable constants, V is the pore volume, S is the specific surface area. Actually V/S is a geometric length, and generally, $2V/S$ is defined as a mean pore radius r_m. Alternatively, Johnson et al. [182] introduced another geometric parameter Λ instead of the $2V/S$ used in eq(7.17). This parameter is a measure of dynamic connected pore size that is related directly to transport in porous medium. Generally, $2V/S \neq \Lambda$. Based on electrical conductivity measurement, Katz-Thompson addressed an elegant formula as follows [184]:

$$\kappa = \frac{r_c^2}{C_H F} \tag{7.18}$$

where r_c is the critical pore radius, C_H is a adjustable constant and F is the formation factor defined in eq(7.14). Again, $r_c \neq 2V/S \neq \Lambda$ generally. However, From the Kozeny-Carman and Katz-Thompson equations, for porous media the permeability is proportional to the hydraulic characteristic length l_H^2 ($l_H = V/S$ for Kozeny-Carman equation and $l_H = r_c$ for Katz-Thompson equation). This was also verified by Friedman and Seaton [126], who applied the critical path analysis to both the electric and hydraulic conductivities, and derived by dimensional analysis by Coussy [76].

Compared to the direct measurement of the permeability, which is long time cost especially for low permeable cement-based materials, measurement of the electrical conductivity of porous materials is much easier. Note that the deduction of the permeability through measurements of the electrical conductivity may be a problem of some experimental interest. For cement-based materials which have pore size distributions from nano-meter to millimeter (air-voids), the mass transport mechanisms in capillary pores and in gel pores can be quite different. For instance, with the percolated ITZ that has large capillary pores in size of 10-40 μm [237], the permeability deviates much from the predicted values by Katz-Thompson relation [271]. Therefore, Martys concluded that estimation of permeability of cement-based materials from r_c determined by MIP would be too simple, unless it has a clear explanation for the anomalously large Katz-Thompson constant C_H in terms of the pore structure [237]. Table 7.9 presents the constant and factor of permeability in Katz-Thompson formula for cement-based materials. It can be seen that the constant C_H has no unique value for cement-based materials. However, with comprehensive study several models on calculating the permeability, Bernabe and Bruderer [45] concluded that the Katz-Thompson model provides the best description of trends of the permeability with width of the pore distribution.

Besides the Katz-Thompson equation, a widely used expression is a power law equation like Archie's law, fitted from experimental data:

$$\kappa = C_r r_c^m \quad \text{or} \quad = C_\phi \phi^m \tag{7.19}$$

Nyame and Illston [273] (cited from [151]) obtained the exponent value $m = 3.28$ for cement pastes with w/c in 0.25∼1.0. For mortars, with w/c=0.4 and 0.5 and the sand volume fraction 0, 0.35, 0.45 and 0.55, Halamickova et al. [151] obtained a close exponent value $m = 3.35$. This relation is very similar to the formula obtained by Powers [305], in which the variable is porosity ϕ rather than the critical pore size r_c, and a close exponent value $m = 3.6$ is found for mortars. Breysse and Gerard [51] found the exponent values $m = 5.9$ for cement pastes and $m = 3.1$ for concrete, and the correlation between permeability and porosity is very poor for concrete. The constants in above mentioned equations were obtained from fitting with numerous experimental data, and it seems not suitable for predicting the permeability of cement-based materials in general case, because each experimental conditions are different. Therefore, it is very necessary to develop a reliable model for evaluating the transport properties of cement-based materials.

7.3.2 Multi-scale modelling on the transport properties of cement pastes

Compared to the mechanical problem in cement-based materials aforementioned, in the transport problem the capillary pores have to be specially considered, because the percolated capillary pores has significant influence on the transport properties of porous materials. In addition, it is not meaningful to start the transport properties of cement-based materials from the size of C-S-H globules, since the transport properties at such scale are still enigma and of unknown importance. Therefore, three steps are proposed to address the multi-scale system:

- Step 1, Estimating the conductivity of LD C-S-H and HD C-S-H specifically. Microstructure differences between LD and HD C-S-H may lead to significant transport properties differences, although they have the same basic globules. Thus specific considerations on LD and HD C-S-H are necessary.
- Step 2, Estimating the conductivity of solid phases of cement paste which is composed of LD/HD C-S-H, CH, unhydrated cement clinkers. The same homogeneous method as explored in previous sections can be applied to estimate the overall conductivity of solid phase.
- Step 3, Specific consideration of the effect of capillary pores. The influence of the percolated capillary pores on the conductivity of cement-based materials maybe beyond the classic homogenization approach. Although numerous works on the overall transport properties of cement-based materials have been published, the used parameters have been significantly modified to fit the experimental results, cf. [275, 378], which does not follow the physical principle.

7.3.2.1 Transport properties of LD and HD C-S-H

Experimentally, one can not obtain the transport properties of LD/HD C-S-H directly and there are very limited knowledge on them. We here adopt the conductivity in literature and with help of homogenization as demonstrated in Appendix C, we access the transport properties of C-S-H with different LD/HD C-S-H ratios. The relative conductivity of LD C-S-H and HD C-S-H are reported respectively to be 1.7×10^{-3} and 0.415×10^{-3} [31]. Those values were adopted as the relative conductivity of outer layer and inner layer C-S-H by Bary and Béjaoui [31]. Imagine that the HD C-S-H is embedded in the percolated LD C-S-H, which is similar to the observed microstructure of C-S-H gel: the inner layer appears to be denser structure,

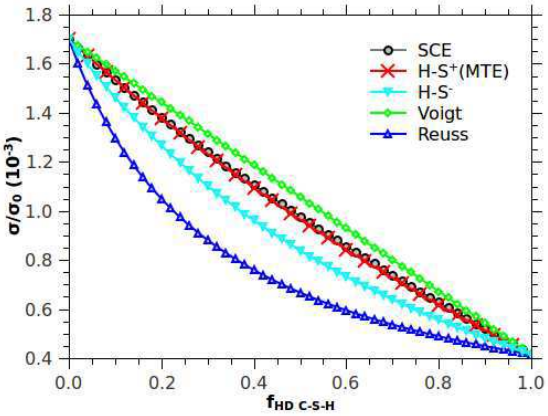

Figure 7.3: Variation of relative conductivity with volume fraction of HD C-S-H in a binary composites which is composed of only LD and HD C-S-H. $\sigma/\sigma_0 = 1.7 \times 10^{-3}$ for LD C-S-H and $\sigma/\sigma_0 = 0.415 \times 10^{-3}$ for HD C-S-H are adopted [31]. SCE: Self-consistent estimation, HS^+: Hashin-Stricktman upper bound (=MTE:Mori-Tanaka estimation), HS^-: Hashin-Striktman lower bound, Voigt: Voigt estimation and Reuss: Reuss estimation.

the outer layer appears to be more porous structure, the solution of Eshelbian inclusions thus can be used to access the effective relative conductivity. Figure 7.3 shows the effective relative conductivities evaluated by different homogenization methods as the volume fraction of HD C-S-H increases from 0 to 1. Very closed value between the self-consistent scheme (SCE) and Mori-Tanaka scheme can be observed.

To quantity the permeability of LD/HD C-S-H system, the Katz-Thompson equation is recalled, cf. eq(7.18). As discussed in foregoing section, the factor $C_H = 226$ (see Table 7.9) which has been verified by experiment [61], is adopted. The difficulty in evaluating the permeability of LD/HD C-S-H is that it is hard to determine the critical geometric length or critical pore size that percolates the matrix. We here use the term $r_c = 2V/S$ with V the specific pore volume and S the specific surface area. For LD C-S-H, $V = \phi_{LD}/\rho_{LD} = 0.37/1.44 \times 10^6 = 0.26 \times 10^{-6}\text{m}^3/\text{g}$ and $S = 250\text{m}^2/\text{g}$ [396], one thus obtains $r_c(\text{LD}) = 2.06\text{nm}$. For HD C-S-H, there is no values for the specific surface areas in the CM model by Jennings and coworkers [178, 392] who assume only the LD C-S-H are accessible. However, according to the CM model, the basic globules for both LD and HD C-S-H are the same but with different packing patterns, and the microstructure in size of 3-30 nm is fractal with a relation $1-\phi \propto r^{D-3}$, with $D = 2.67$ the fractal dimension [178] [2]. Apparently, the specific surface area of HD C-S-H can be larger than that of LD C-S-H, but lower than that of globules. By using the fractal relation for both LD and HD C-S-H, $1-\phi \propto r^{D-3}$, the critical radius of HD C-S-H is estimated as: $\frac{1-\phi_{LD}}{1-\phi_{HD}} = \left(\frac{r_c(\text{LD})}{r_c(\text{HD})}\right)^{D-3} \rightarrow r_c(\text{HD}) = r_c(\text{LD}) \cdot \left(\frac{1-\phi_{LD}}{1-\phi_{HD}}\right)^{-1/(D-3)}$. Using the values, $\phi_{LD} = 0.37, \phi_{HD} = 0.24, \rho_{LD} = 1.44 \times 10^6\text{g/m}^{-3}, \rho_{\text{HD}} = 1.75 \times 10^6\text{g/m}^{-3}, \text{D} = 2.67$, [178, 396], the critical pore size is estimated as $r_c(\text{HD}) = 1.17\text{nm}$. This value is very close to the 1.1 nm small gel pores (SGP) as presented in [178]. By using the Katz-Thompson equation, the permeability of LD C-S-H is estimated as $3.35 \times 10^{-23}\text{m}^2$, which is comparable with the value by Powers ($\approx 7 \times 10^{-23}\text{m}^2$) [306], whereas the permeability of HD C-S-H is estimated as $0.25 \times 10^{-23}\text{m}^2$. Again, using the effective medium theory, the permeability of a system in which HD C-S-H is embedded in LD C-S-H with different volume fractions, can be evaluated as:

2. The original equation used in Ref. [178] is $1-\phi = r^D$. This relation must be incorrect, see Ref. [30, 95, 233].

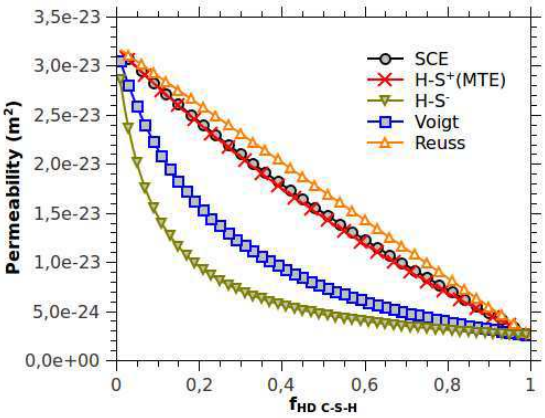

Figure 7.4: Variation of permeability with volume fraction of HD C-S-H in a binary composites which is composed of only LD and HD C-S-H. SCE: Self-consistent estimation, HS^+: Hashin-Stricktman upper bound (=MTE:Mori-Tanaka estimation), HS^-: Hashin-Striktman lower bound, Voigt: Voigt estimation and Reuss: Reuss estimation.

$$\sigma_{CSH}^{hom} = f_{LD}\sigma_{LD}^{hom}A_{LD,CSH}^{v} + f_{HD}\sigma_{HD}^{hom}A_{HD,CSH}^{v} \tag{7.20a}$$

$$\kappa_{CSH}^{hom} = f_{LD}\kappa_{LD}^{hom}A_{LD,CSH}^{v} + f_{HD}\kappa_{HD}^{hom}A_{HD,CSH}^{v} \tag{7.20b}$$

As shown in Figure 7.4, the effective permeability evaluated by Hashin-Striktman lower bound and Reuss bound appear to be lower than the values estimated by other scheme as HD C-S-H concentration varies from 0 to 1. The volume fraction of LD C-S-H to total C-S-H gels for paste I and II are 0.627 and 0.237 respectively. The relative conductivity and permeability calculated by self consistent scheme and Mori-Tanaka scheme are shown in Table 7.10.

Table 7.10: Relative conductivity (permeability) of C-S-H gels for paste I and II estimated by self-consistent and Mori-Tanaka scheme. The permeability is calculated by Katz-Thompson equation (eq(7.18)) with $C_H = 226$.

materials	LD C-S-H content	Self-consistent estimation	Mori-Tanaka estimation
Paste I	0.627	$1.141 \times 10^{-3}(1.872 \times 10^{-23}\mathrm{m}^2)$	$1.131 \times 10^{-3}(1.833 \times 10^{-23}\mathrm{m}^2)$
Paste II	0.237	$0.668 \times 10^{-3}(0.809 \times 10^{-23}\mathrm{m}^2)$	$0.657 \times 10^{-3}(0.772 \times 10^{-23}\mathrm{m}^2)$

7.3.2.2 Effective transport properties of solid phase

In this subsection, we consider further the effective transport properties of solid phase in which the impermeable minerals, such as the unhydrated cement clinkers, Portlandite, Hydrogarnel, AFm, are embedded. As demonstrated in Figure 7.5, the HS^-, Reuss estimations of the ratio of effective conductivity to that of high permeable phase may lead to the underestimated values when σ_{LP}/σ_{HP} is large. Therefore, in the following sections, the HS^- and Reuss approaches will not be considered.

Table 7.11 shows the volume content of unhydrated compounds and hydration products for paste I and paste II, which are calculated from the Avrami's equation, see chapter 6. It can be seen that the impermeable solids occupy more than one third of total solid volume. This may lead to significant decrease of overall conductivity and permeability. For this solid system, where the capillary pores are not considered, assuming that the impermeable solids are embedded in the homogeneously percolated permeable C-S-H, the

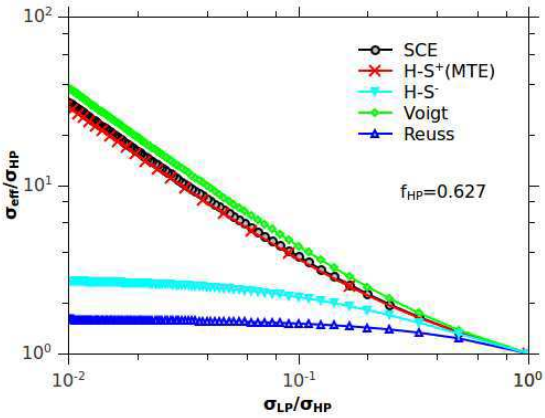

Figure 7.5: Variation of σ_{eff}/σ_{HP} (ratio of effective conductivity to the conductivity of high permeable phase) with σ_{LP}/σ_{HP} (ratio of conductivity of low permeable phase to that of high permeable phase). The volume fraction of high permeable phase is set to be $f_{HP} = 0.627$. SCE: Self-consistent estimation, HS^+: Hashin-Stricktman upper bound (=MTE:Mori-Tanaka estimation), HS^-: Hashin-Striktman lower bound , Voigt: Voigt estimation and Reuss: Reuss estimation.

solution for Eshelbian inclusion can be used again to estimate the overall transport properties. Although the concentration of different solids in cement pastes may be heterogeneously distributed, for instance, the AFm and Portlandite are observed to accumulate around the air voids [212], an arithmetic average relation was adopted in many works [31, 403]. The effective relative conductivity σ_S^{hom} and permeability κ_S^{hom} can be expressed as:

$$\sigma_S^{hom} = f_{CSH}\sigma_{CSH}^{hom}A_{CSH,SOLID}^{v} + f_{IM}\sigma_{IM}A_{IM,SOLID}^{v} \tag{7.21a}$$

$$\kappa_S^{hom} = f_{CSH}\kappa_{CSH}^{hom}A_{CSH,SOLID}^{v} + f_{IM}\kappa_{IM}A_{IM,SOLID}^{v} \tag{7.21b}$$

where the subscripts IM represents the impermeable solids shown in Table 7.11. Table 7.12 presents the effective relative conductivities and permeabilities evaluated by eq(7.21). These values are significantly lower than the usual measured values for cement pastes in literature [275, 339, 378] because the very permeable capillary pores are not considered. In addition, the estimated relative conductivity of solid phases, for both paste I and II, is consistent with the values used for effective theory fitted by Oh et al. [275], who obtained the $5 \times 10^{-5} \leq \sigma_s/\sigma_0 \leq 10^{-3}$.

Table 7.11: The volume fraction and permeability of paste I and II at 360D.

Compounds	Volume fraction		Permeability
	w/c=0.5	w/c=0.3	
LD C-S-H	0.3330	0.1363	Low permeable
HD C-S-H	0.1866	0.4385	Very low permeable
Total permeable porous phase	0.5196	0.5748	Permeable
C_3S	0.0108	0.0398	Impermeable
C_2S	0.0131	0.0370	Impermeable
C_3A	0.0005	0.0023	Impermeable
C_4AF	0.0023	0.0066	Impermeable
AFm	0.0882	0.1097	Impermeable
Hydrogarnel	0.0614	0.0718	Impermeable
CH	0.1325	0.1551	Impermeable
Inert	0.0024	0.0029	Impermeable
Total impermeable solid	0.3115	0.4222	
Capillary Pores	0.1689	≈ 0	

Table 7.12: Relative conductivity (permeability) of solid phases for paste I and II estimated by self-consistent and Mori-Tanaka scheme.

materials	Permeable C-S-H content	Self-consistent estimation	Mori-Tanaka estimation
Paste I	0.625	$0.619 \times 10^{-3}(1.015 \times 10^{-23}\mathrm{m}^2)$	$0.601 \times 10^{-3}(0.994 \times 10^{-23}\mathrm{m}^2)$
Paste II	0.538	$0.328 \times 10^{-3}(0.398 \times 10^{-23}\mathrm{m}^2)$	$0.323 \times 10^{-3}(0.379 \times 10^{-23}\mathrm{m}^2)$

7.3.3 Effect of capillary pores

The transport properties of porous materials are related intimately to the properties of capillary pores, especially the connectivity or percolation of pores. Therefore, using the classical solution of Eshelbian inclusion to estimate the effective conductivity for a porous materials with percolating pores may lead to incorrect results. For example, Figure 7.6 shows significant differences of the relative conductivities for a system that is composed of percolating high permeable pores and homogeneous embedded solids, as evaluated by Mori-Tanaka estimation and effective medium theory estimation. The values by M-T method are much lower than those by EMT method. For the EMT method, it has been widely developed to estimate the effective conductivity and/or permeability of porous materials, cf. McLachlan [244, 245], Youngs[437], Cui and Cahyadi [85], Sant et al. [339], Sun et al. [378] and Oh et al. [275]. We here follow the modified effective medium theory by Oh et al. [275], who expressed the effective relative conductivity in an explicit expression:

$$\frac{\sigma}{\sigma_0} = \frac{D}{D_0} = \left[m_\phi + \sqrt{m_\phi^2 + \frac{\phi_c}{1-\phi_c}\left(D_s/D_0\right)^{1/n}} \right]^n \tag{7.22}$$

with

$$m_\phi = \frac{1}{2}\left[\left(D_s/D_0\right)^{1/n} + \frac{\phi_{cap}}{1-\phi_c}\left(1 - \left(D_s/D_0\right)^{1/n}\right) - \frac{\phi_c}{1-\phi_c} \right] \tag{7.23}$$

where ϕ_{cap} is the capillary pores, $D_s/D_0 = \sigma_s/\sigma_0$ is the normalized diffusivity or conductivity of the solid phase. By fitting the data in literature, the authors obtained that the normalized diffusivity or conductivity of the solid phase is in rang of $2 \times 10^{-6} \sim 1 \times 10^{-3}$ depending on type of cement used and curing conditions [275], while Bentz et al. [41] obtained the values in similar range $1 \times 10^{-5} \sim 4 \times 10^{-4}$ varying with the silica fume content. These values are comparable with the relative conductivity presented in Table 7.12. The term n in eq(7.22) is the percolation exponent. Comparing with the range of 1.65 to 2.0 conventionally, it was found that for cement-based materials, it has higher value. For instance, Oh et al. obtained n in range of $2.7 \sim 4.5$ [275]. ϕ_c is the critical porosity at which the pore network percolates. Bentz and Garboczi [40–42, 132] obtained a critical porosity $\phi_c = 0.17$. Powers et al. [309] reported that the porosity required for percolation is about 0.2, while Ye found that for OPC in w/c=0.3, with 68% hydration degree, capillary depercolation is only 5% [436]. Therefore, the capillary porosity for Paste II near zero as presented in Table 7.11 is acceptable.

Substituting the value of σ_s/σ_0 obtained by multi-scale modelling of Eshelbian enclusion for solid phases for paste I and II into eq(7.22), one obtains the curves of effective conductivity in terms of porosity. Very good agreement between the estimated values by EMT methods and the measured values is obtained, see

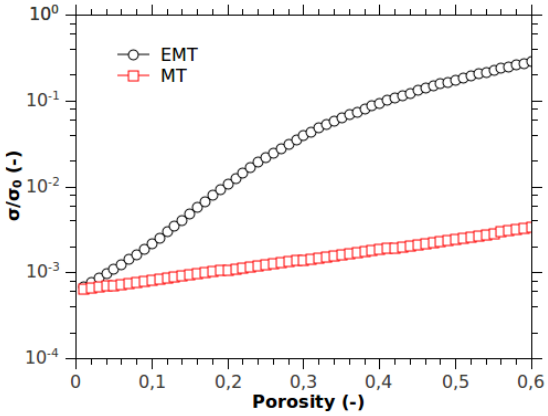

Figure 7.6: The estimation of effective conductivity of cement pastes by Mori-Tanaka estimation and effective medium theory (EMT) estimation. The ratio of conductivity of capillary pores to that of solid phase, $\sigma_s/\sigma_0 = 0.000619$ [275], is retained for the estimations.

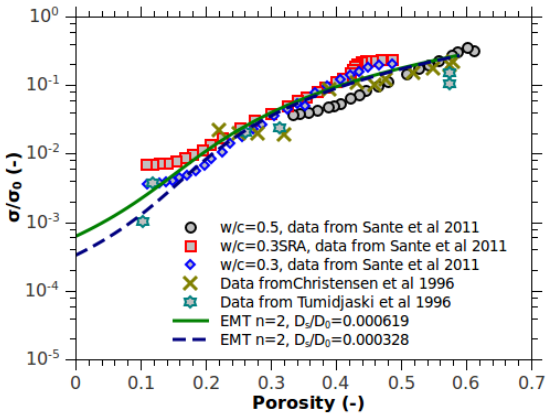

Figure 7.7: The estimation of effective conductivity of cement pastes by effective medium theory (EMT). Note the 'SRA' in data by Sant et al. [339] represents the shrinkage-reducing admixture. Other data adopted from [61, 401].

Figure 7.7 where a critical porosity $\phi_c = 0.17$ is adopted in the calculations. The good agreement between the predicted values and the measured values indicates that the multi-scale modelling can predict the effective transport properties successfully. Again, by using the Katz-Thompson equation, the permeability can be obtained. However, here we can not present the variation of permeability with porosity as that of relative conductivity illustrated in Figure 7.2, because of the lack of the critical pore width values.

7.3.4 Effect of saturation degree

As discussed in the previous section, the capillary pores play important roles in the transport properties of cement-based porous materials. However, the presented data in previous section is in the saturated condition. The complete saturation does not occur in practice for cement-based porous materials generally, except structures under water. Thus the influence of the saturation must be considered, and it, actually, has significant impact on the transport properties of porous materials [238, 410].

The relative permeability in terms of saturation degree is often expressed by the van Genuchten equation [410], which is based on the curves of capillary-saturation relation:

$$\kappa_r(S_l) = \sqrt{S_l}\left[1 - \left(1 - S_l^{1/m}\right)^m\right]^2 \tag{7.24}$$

where S_l is the saturation degree, m is a constant depending on the material. Figure 7.8(a) presents the curves of relative permeability versus saturation degree with m varying from 0.4 to 0.9. Through capillary

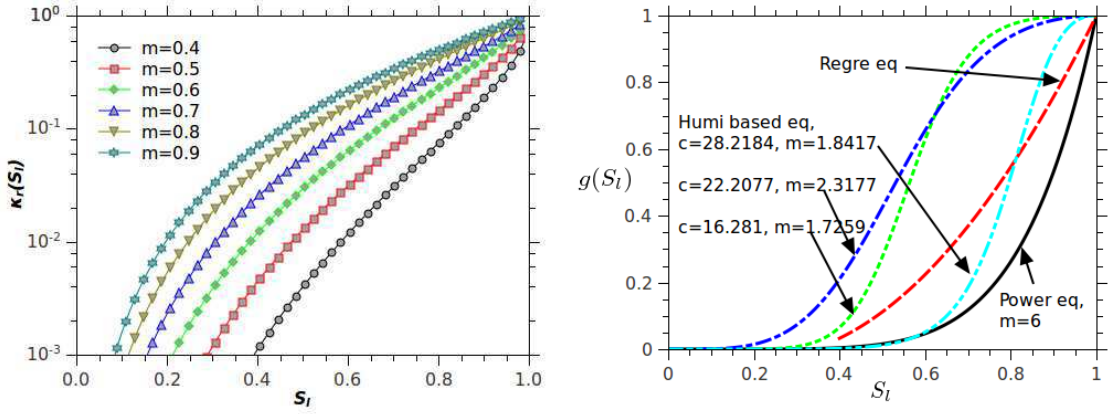

(a) (b)

Figure 7.8: (a), The variation of relative permeability in terms of the saturation degree. (b) The relative diffusion quantity $\mathcal{G}_r(S_l)$ in terms of S_l, the values of constant c and m are adopted from [267]. Regre eq: the regressed equation present in second row of Table 7.13 [63, 93]; Humi based eq: Humidify based formula presented in the third row of Table 7.13 [3, 270, 332].

Table 7.13: Relationship between the relative diffusion quantity $\mathcal{G}_r(S_l)$ (see eq(4.21)) and S_l for cement-based materials.

Power law
$\mathcal{G}_r(S_l) = S_l^m$, $m = 6$ [267], $m = 7/3$ [336] for concrete
Regressed formula
$\mathcal{G}_r(S_l) = S_l^m = 0.04514 - 0.6889S_l + 1.6438S_l^2$ [63, 93]
Humidity based formula
$\mathcal{G}_r(S_l) = \left[1 + \left(\left(1 - \exp(b(S_l^{m/(1-m)} - 1)^{1/m})\right)/(1 - H_0)\right)^4\right]^{-1}$
$b = cv_l/RT = 7.389c$, $H_0 = 0.75$, m the constant [3, 270, 332].

curves, Nguyen obtained that m varies from 0.42 to 0.57 for different concrete samples [267, 269].

For the relative diffusion quantity, $\mathcal{G}_r(S_l)$ (see eq(4.21)), numerous semi-empirical relations have been proposed. Table 7.13 and Figure 7.8(b) present the frequently used expressions of $\mathcal{G}_r(S_l)$ for cement-based materials. It can be found that there are significant differences among these formulas for $\mathcal{G}_r(S_l)$, which can be due to the different pore structure. Therefore, to evaluate the relative permeability of porous materials, sufficient information on the pore structure/microstructure of material is necessary.

7.4 Heat conductivity of composites

The effective medium approaches for estimating thermal conductivity, are first applied for solution-ice system (see Figure 7.9). It is then considered as a homogeneous component of composites. This kind of method has been widely used on estimating the effective properties of multi-phase composites [66, 67, 136, 137, 165]. In this section, semi-empirical formulas on thermal conductivity and the self-consistent homogenization [165], which have been proved to be practicable for many composites (cf. [39, 430], more

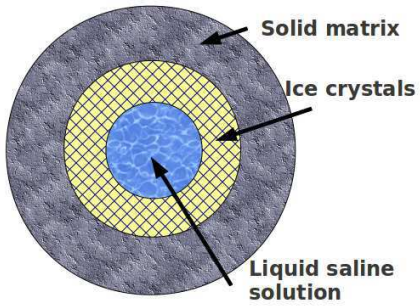

Figure 7.9: Schematic illustration of a partially frozen porous materials. It is assumed that liquid solution is embedded into ice crystals (this assumption actually can be observed in the freezing process of cylindrical capsule, see Figure 2.13 by Guzman and Braga (2005) [149]), then the solution-ice system is embedded into the solid matrix.

details can be found in previous sections in this chapter), are considered for estimating the effective heat conductivity coefficient.

Based on the Maxwell's work on two-phase mixture, Brailsford and Major [50] derived a semi-empirical equation in estimating the effective thermal conductivity of composites composed of three phases:

$$\lambda = \frac{\lambda_s(1-\phi) + \lambda_l \phi S_l 3\lambda_s/(2\lambda_s+\lambda_l) + \lambda_c \phi(1-S_l)3\lambda_s/(2\lambda_s+\lambda_l)}{(1-\phi) + \phi S_l 3\lambda_s/(2\lambda_s+\lambda_l) + \phi(1-S_l)3\lambda_s/(2\lambda_s+\lambda_l)} \tag{7.25}$$

where the subscript s, l and c denote the solid skeleton, liquid phase and ice crystals, ϕ is porosity and S is saturation degree.

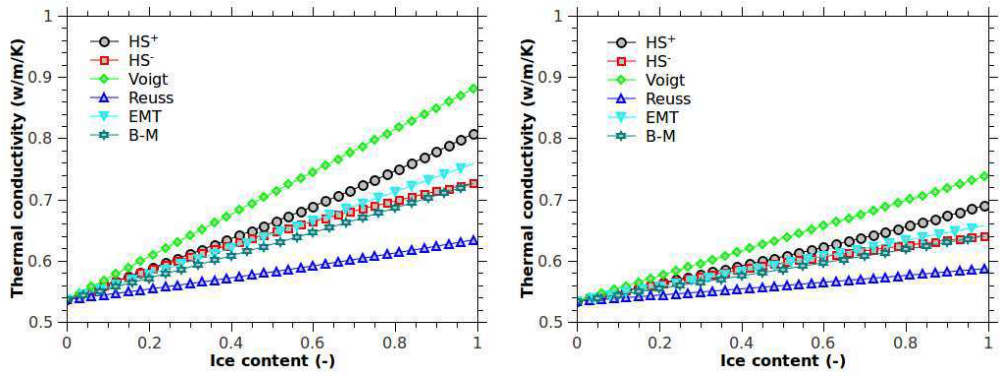

(a) (b)

Figure 7.10: Variation of effective thermal conductivity estimated by different methods with ice content for paste I (a) and paste II (b). HS^+: Hashin-Stricktman upper bound, HS^-: Hashin-Striktman lower bound, Voigt: Voigt estimation, Reuss: Reuss estimation, EMT: Effective medium theory, B-D: the Brailsford-Major estimation method.

Figure 7.10 shows the effective thermal conductivity of a partial frozen cement-based materials in terms of ice content. The porosity of used material is 0.26 for paste I and 0.13 for paste II (180D MIP measurement presented in chapter 6), the thermal conductivity of solid skeleton, ice and water, respectively are, 0.53 (W/m·K), 2.14 (W/m·K) and 0.56 (W/m·K) [214, 433]. Except the simple estimation models, cf. the Reuss estimation ($\frac{1}{\mathcal{L}} = \sum f_i/\mathcal{L}_i$, with f_i the volume fraction of phase i) and the Voigt estimation ($\mathcal{L} = \sum f_i \mathcal{L}_i$), the values estimated by other models do not show significant differences. We thus choose the self consistent homogenization model in this work, since it has been used for partially frozen cement-based materials

elsewhere [114, 115].

Chapter 8

Properties of NaCl solution and saturation-temperature curves

Contents

8.1 Physical properties of pure water and ice Ih

Physical properties of water and ice are of importance for calculating the capillary pressure and the accuracy of apparent molar quantities of NaCl solution. The heat capacity, thermal expansion coefficient, heat conductivity and bulk modulus of supercooled water and ice are presented in Table 8.1. Note that only a linear variation with temperature has been adopted in this study, which can be found in [114] as well.

Table 8.1: Physical properties of water and ice [114].

Parameter	Symbol	Liquid water (supercooling)	Ice (Ih)	Unit
Thermal (volumetric) expansion coefficient	α_w	$-68.7 + 24.732(T - T_0)$	$158.15 + 0.67(T - T_0)$	$10^{-6}\mathrm{K}^{-1}$
Heat capacity	$C_{P,w}$	$4.2 - 0.0023(T - T_0)$	$2.1 + 0.00712(T - T_0)$	$\mathrm{J \cdot g^{-1} \cdot K^{-1}}$
Heat conductivity	λ_w	$0.5622 + 0.0017(T - T_0)$	$2.15 - 0.0123(T - T_0)$	$\mathrm{W \cdot m^{-1} \cdot K^{-1}}$
Bulk modulus	K_w	$1970 + 19.7(T - T_0)$	$4305 - 8.18(T - T_0)$	MPa

8.2 Physical properties of NaCl solution

The physical properties of NaCl solution are function of current temperature, liquid pressure as well as the salt concentration. However, few data on the coupled physical properties of aqueous solution can be found in literature. This may be due to the difficulties in measurements. From the limited reference data, we choose the model developed by Archer [15, 16], which is based on the Pitzer's theory on aqueous solution, see for instance [299, 303, 304]. The details of derivation of the formulas are given in Appendix D. In the present section, we just recapitulate some important formulas and parameters. More information can be found in [8, 15–18] and references there in. For NaCl solution with molality m $(\mathrm{mol}\cdot\mathrm{kg}^{-1})$ [1], the overall property $\mathcal{P}$ per mass unit of solution can be given by:

$$\mathcal{P} = \frac{\mathcal{P}_s \cdot m + \mathcal{P}_w \cdot 1000/\mathsf{M}_w}{m \cdot \mathsf{M}_s + 1000} \tag{8.1}$$

where $\mathcal{P}_w$ represents the quantity $\mathcal{P}$ per unit mole of water. Note $\mathcal{P}_s$ is the apparent molar quantity $\mathcal{P}$ of salt. In Pitzer's model, the excess Gibbs free energy is related to m by the following equation [15, 16, 18]:

$$G^E = n_w RT\left[-4A_\phi \ln(1+b\sqrt{I}) + 2(m^2B + m^3C)\right] \tag{8.2}$$

where n_w is the molarity of water, A_ϕ is the Debye-Hückel coefficient for osmotic coefficient, B and C are parameters related to ionic strength I, temperature and pressure, see eqs(D.3a) and (D.3b). The apparent molar volume V_ϕ and apparent heat capacity $C_{P,\phi}$, thus can be given by [16, 17]:

$$\mathsf{V}_\phi = \mathsf{V}^0_m + \mathsf{V}_E, \quad \text{with} \quad \mathsf{V}_E = \left.\frac{\partial G^E}{\partial P}\right|_T \tag{8.3a}$$

$$C_{P,\phi} = C^0_{P,m} + C_{P,E}, \quad \text{with} \quad C_{P,E} = -T\left.\frac{\partial^2 G^E}{\partial T^2}\right|_P \tag{8.3b}$$

with V^0_m and $C^0_{P,m}$ are, respectively the apparent molar volume and the apparent molar heat capacity of the electrolyte at infinite dilution. The detailed expressions with 56 adjustable constants, which are obtained from least squares fitting, are presented in Appendix D.

8.3 Evaluation of saturation degree curves

Physically, the principles of ice penetration, mercury intrusion and drying are the same: the non-wetting phase invades the pore space progressively, and the wetting phase retreats correspondingly. The interface between wetting phase and non-wetting phase moves from surface of porous materials into the inner part or from big pores to the connected small pores. The driving force of ice penetration, mercury intrusion and drying respectively are the chemical potential difference between ice and liquid water at the

1. The molality m is defined as mole number of salt per kilogram of pure water $m = c \cdot \rho_l$, with c the mole number of salt per volume unit of solution $(\mathrm{mol}\cdot\mathrm{m}^{-3})$.

same environmental temperature, applied pressure on liquid mercury and the chemical potential difference between liquid water and water vapor (or humidity) at the same environmental temperature. The force balancing them is the surface tension. It is thus possible to estimate the amount of non-wetting phase according to the local mechanical equilibrium, which is described by the Young-Laplace equation:

$$\begin{aligned} P_{cap} &= P_{n-w} - P_w \\ &= -\frac{2\gamma_{cl}\cos\theta_F}{r_F - \delta_F(T)}(\text{Freezing}) = -\frac{2\gamma_{mg}\cos\theta_{\text{MIP}}}{r_{\text{MIP}}}(\text{Mercury intrusion}) = \frac{2\gamma_{lg}\cos\theta_D}{r_D - \delta_D(\text{HR})}(\text{Drying}) \end{aligned} \tag{8.4}$$

where P_{cap} is the capillary pressure (Pa), P_{n-w} is the pressure of non-wetting phase (Pa) and P_w is the pressure of wetting phase (Pa). For freezing process, $P_{n-w} = P_c$ and $P_w = P_l$, with P_c the pressure of ice, P_l the pressure of liquid water, γ_{cl} is the surface tension between ice crystals and liquid water, θ_F is the contact angle between ice and solid wall, usually θ_F is taken equal to 180°, r_F is the pore radius, and δ_F is the thickness of unfrozen layer that is a function of temperature. $r_F - \delta_F$ is the radius of cylinderical size near ice tip at equilibrium with surrounding liquid water. For mercury intrusion process, $P_{n-w} = P_{ex}$ and $P_w = P_m$, with P_{ex} the exerted pressure on mercury, P_m the atmospheric pressure, γ_{mg} is the surface tension between liquid mercury and air, θ_{MIP} is the contact angle between mercury and solid wall, and its values is often retained as $\theta_{\text{MIP}} = 130°$ [186], r_{MIP} is the pore radius. For drying process, $P_{n-w} = P_g$ and $P_w = P_l$, with P_g the gas pressure, P_l the liquid pressure, γ_{lg} is the surface tension between liquid water and gas, θ_D is the contact angle between water and solid wall, usually θ_D is taken equal to 180°, r_D is the pore radius at equilibrium, and $\delta_D(\text{HR})$ is the thickness of adsorbed layer which is a function of humidity HR.

8.3.1 Non-wetting phase volume

Using the mercury intrusion porosimetry (MIP), the pore size distribution can be obtained directly by the Washburn equation [423] by assuming that the pores have cylindrical shape. Based on the relation presented in eq(8.4), it is expected that the ice volume can be estimated with the help of the pore size distribution and the curvature of ice interface. In equilibrium case, the volume of ice V_c with tip at size of r_{eq} and its fraction S_c can be estimated as [450]:

$$V_c = \int_{r_{eq}}^{\infty} \frac{\mathrm{d}V}{\mathrm{d}r_{eq}}\mathrm{d}r \tag{8.5a}$$

$$S_c = \frac{V_c}{V_T}, \quad \text{with} \quad V_T = \int_{r_{min}}^{\infty} \frac{\mathrm{d}V}{\mathrm{d}r}\mathrm{d}r \tag{8.5b}$$

where r_{eq} is the radius of ice tip at equilibrium, r_{min} is the minimum pore radius of cement-based materials. In the present study, $r_{min} = 3$nm is retained since the maximum pressure of MIP is around 400 MPa. $\frac{\mathrm{d}V}{\mathrm{d}r_{eq}}$ is the pore size distribution occupied by ice, $\frac{\mathrm{d}V}{\mathrm{d}r}$ is the real pore size distribution. V_T is the total pore

volume, V_c is the ice volume. In addition to the pore space of small size where ice can not penetrate, there is the volume occupied by the liquid-like layer with thickness of δ, which has been extensively discussed in chapter 2. The estimation of the volume fraction of the liquid-like layer here follows nearly Zuber and Marchand's procedure [450, 451]:

$$\phi_\delta(T) = \frac{\text{liquid like layer volume}}{\text{ice volume + liquid like layer volume}} = \frac{\int_r^\infty \frac{\mathrm{d}V}{\mathrm{d}r} g(r,\delta)\mathrm{d}r}{\int_r^\infty \frac{\mathrm{d}V}{\mathrm{d}r}\mathrm{d}r} \tag{8.6}$$

where $g(r,\delta)$ is the pore shape function, which can be expressed as:

$$g(r,\delta) = 1 - \left(1 - \frac{\delta}{r}\right)^2 \quad \text{for cylindrical pores} \tag{8.7a}$$

$$g(r,\delta) = 1 - \left(1 - \frac{\delta}{r}\right)^3 \quad \text{for spherical pores} \tag{8.7b}$$

The relation between the ice volume to the total volume is then retained as:

$$\frac{\mathrm{d}V}{\mathrm{d}r_{eq}} = \frac{\mathrm{d}V}{\mathrm{d}r}(1-\phi_\delta) \tag{8.8}$$

Note again, r is the pore radius and r_{eq} the radius of ice tips at equilibrium with surrounding liquid water. The ice volume and its fraction are then obtained as:

$$V_c = \int_{r_{eq}}^\infty \frac{\mathrm{d}V}{\mathrm{d}r}(1-\phi_\delta)\mathrm{d}r \tag{8.9a}$$

$$S_c = \frac{1}{V_T}\int_{r_{eq}}^\infty \frac{\mathrm{d}V}{\mathrm{d}r}(1-\phi_\delta)\mathrm{d}r = \int_{r_{eq}}^\infty \frac{\mathrm{d}\phi}{\mathrm{d}r}(1-\phi_\delta)\mathrm{d}r \tag{8.9b}$$

Since $r_{eq} = r - \delta = -2\gamma_{lc}\cos\theta_F / P_{cap}$, by assuming that $\gamma_{lc}\cos\theta_F$ is constant, it can be found:

$$\mathrm{d}r_{eq} = -\frac{r_{eq}}{P_{cap}}\mathrm{d}P_{cap} \quad \text{and} \quad \mathrm{d}P_{cap} = -\frac{P_{cap}}{r_{eq}}\mathrm{d}r_{eq} \tag{8.10}$$

Taking the differential form of eq(8.9b), and combining the eq(8.10), one obtains:

$$\mathrm{d}S_c = -\mathrm{d}S_l = \frac{\mathrm{d}\phi}{\mathrm{d}r}(1-\phi_\delta)\mathrm{d}r_{eq} = -\frac{\mathrm{d}\phi}{\mathrm{d}r}(1-\phi_\delta)\frac{r_{eq}}{P_{cap}}\mathrm{d}P_{cap} \tag{8.11}$$

where S_l is the liquid saturation degree, $S_l = 1 - S_c$. The differential form of capillary pressure is given by (cf. eq(2.12)):

$$\mathrm{d}P_{cap} = \left(\frac{\rho_c}{\rho_w} - 1\right)\mathrm{d}P_l - \rho_c\left(\mathcal{S}_f + C_f \ln\left(\frac{T}{T_0}\right)\right)\mathrm{d}T + \sum_i \frac{\rho_c RT}{\mathsf{M}_w}\frac{\mathrm{d}\ln a_w}{\mathrm{d}c_i}\mathrm{d}c_i \tag{8.12}$$

If we further assume that the porous material is sealed so that the salinity of pore solution must increase as ice forms and obeys:

$$c_i S_l = c_i^0 \quad \text{and} \quad \mathrm{d}c_i = -\frac{c_i}{S_l}\mathrm{d}S_l \tag{8.13}$$

where c_i^0 is the initial concentration of species i. The eq(8.13) describes exactly the salinity balance of frozen solution in impermeable container or in undrained freezing condition.

Substitution of eqs(8.12) and (8.13) into eq(8.11), and eliminating the term $\mathrm{d}P_{cap}$, one can deduce an equation correlating the saturation degree with the liquid pressure P_l, the current temperature T and the initial salt concentration c_i, which is given by:

$$\mathrm{d}S_l = \frac{\frac{\mathrm{d}\phi}{\mathrm{d}r}\frac{r_{eq}}{P_{cap}}(1-\phi_\delta)}{1+\frac{\mathrm{d}\phi}{\mathrm{d}r}\frac{r_{eq}}{P_{cap}}(1-\phi_\delta)\frac{\rho_c RT}{\mathsf{M}_w}\sum_i \frac{\mathrm{d}\ln a_w}{\mathrm{d}c_i}\frac{c_i}{S_l}}\left\{\left(\frac{\rho_c}{\rho_w}-1\right)\mathrm{d}P_l - \rho_c\left(\mathcal{S}_f + C_f\ln\left(\frac{T}{T_0}\right)\right)\mathrm{d}T\right\} \tag{8.14}$$

In above equation, $\frac{\mathrm{d}\phi}{\mathrm{d}r}$ represents the pore structure of porous materials, which can be determined by MIP or other porosimetry techniques. The term $(\mathcal{S}_f + C_f\ln(T/T_0))$ only depends on the temperature and the term $\frac{\mathrm{d}\ln a_w}{\mathrm{d}c_i}$ can be derived by solution thermodynamic models, such as Lin and Lee's model [216, 217], of which the detail can be found in chapter 2.

If the effect of liquid pressure is not significant, cf. in drained freezing condition where the liquid pressure is equal to the atmospheric pressure constantly, the first term in the brace of the right hand side of eq(8.14) can be neglected. Thus the saturation degree is only related to the temperature and the pore structure. In the undrained freezing condition, the liquid pressure can be significant as ice forms, and is function of initial salt concentration, ice formation rate and entropy change during freezing, see Appendix B.3.1 for detail. However, eq(8.14) is still an implicit form for calculating the saturation degree, it must be evaluated by iterative method.

8.3.2 Pore size distribution by multi-Gauss fitting

In order to obtain the curves of the pore size distribution (PSD), the multi-peak Gauss formula is employed to fit the differential pore size distribution (DPSD) curves by means of MIP. It has the form [157, 325, 347]:

$$\frac{\mathrm{d}V}{\mathrm{d}\log(d)} = f_0 + \sum_i^N\left[\frac{\sqrt{2}A_i}{w_i\sqrt{\pi}}\exp\left(-2(\log d - \log d_i)^2/w_i^2\right)\right] \tag{8.15}$$

where d is the pore diameter, f_0, A_i, w_i and d_i are the adjustable constants. Considering now the paste I and Paste II which have been extensively studied in chapter 6, and using the eq(8.15) one can obtain well fitted curves for both samples, cf. Figure 8.1.

The integration of standard Gauss equation leads to the error equation, which can be expressed as: $\int \exp\left(-2(\log(d/d_i))^2/w_i^2\right)\cdot\sqrt{2}/(w_i\sqrt{\pi})\,\mathrm{d}\log(d) = 1/2\cdot erf((\sqrt{2}(\log d/d_i)^2)/w_i)$. If the CPSD curves plot

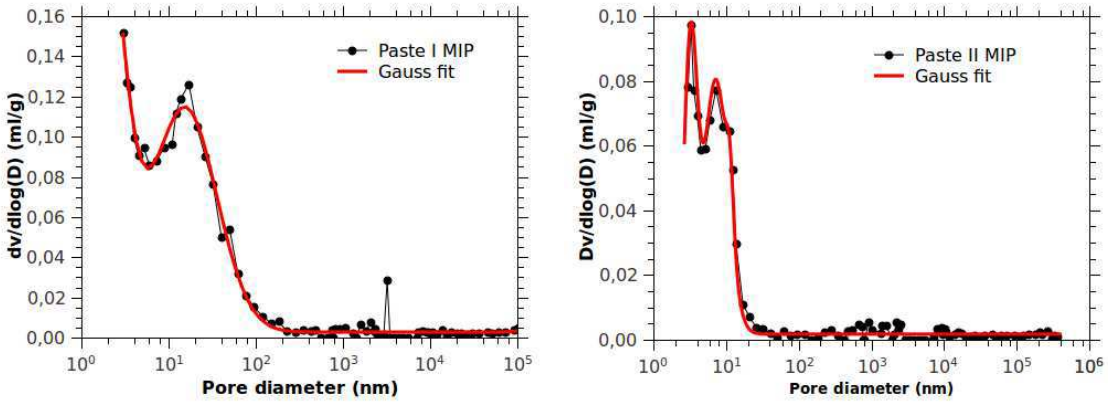

(a) (b)

Figure 8.1: Multi-gauss fitting of MIP DPSD of paste I(w/c=0.5) (a) and paste II (w/c=0.3) (b).

from large pores to fine pores, one obtains the formula:

$$\begin{aligned}&\int_{\log d_{max}}^{\log d}\left[\frac{\sqrt{2}A_i}{w_i\sqrt{\pi}}\exp\left(-2(\log d-\log d_i)^2/w_i^2\right)\right]\mathrm{d}\log(d)\\&=A_i\left[1-\frac{1}{2}\left(1+erf\left(\frac{\sqrt{2}(\log d-\log d_i)^2}{w_i}\right)\right)\right]_{\log d}^{\log d_{max}}\end{aligned}\tag{8.16}$$

Through integration procedure of eq(8.15), the CPSD curve is then given by:

$$\begin{aligned}V(d)&=\int_{\log d_{max}}^{\log d}\left[f_0+\sum_i^N\left[\frac{\sqrt{2}A_i}{w_i\sqrt{\pi}}\exp\left(-2(\log d-\log d_i)^2/w_i^2\right)\right]\right]d\log(d)\\&=f_0(|\log d-\log d_{max}|)+\sum_i^N A_i\left[1-\frac{1}{2}\left(1+erf\left(\frac{\sqrt{2}(\log d-\log d_i)^2}{w_i}\right)\right)\right]_{\log d}^{\log d_{max}}\end{aligned}\tag{8.17}$$

Table 8.2 presents the parameters required for multi-peak Gauss fitting. It can be found that the characteristic pore size for each peak of Paste II is systematically smaller than that of Paste I, of which the mechanisms are comprehensively presented in chapter 6.

Table 8.2: Parameters of multi-peak Gauss fitting for paste I and paste II.

Samples	Peaks	f_0	A_i	w_i	$\log d_i(d_i)$ (nm)	Coefficient R^2
Paste I	1	0.00271	0.00621	0.432	5.515 (327340)	0.999
	2		0.102	0.727	1.190 (15.488)	
	3		0.301	0.647	0.0145 (1.0304)	
Paste II	1	0.00176	0.00250	0.0996	1.055 (11.350)	0.999
	2		0.0324	0.329	0.858 (6.9984)	
	3		0.0199	0.181	0.511 (3.2434)	

The Gauss-fitting and/or multi-Gauss-fitting procedure in characterizing the pore size distribution have been applied for over a century, and they were employed to characterize many different porous materials through different experimental methods, cf. [157, 325, 347]. Figures 8.1 and 8.2 show the PSD measured by MIP and the multi-Gauss fitting (eqs(8.15) and (8.17)), which present good agreement. Note again, the pore size distribution obtained by MIP measurement may be not the real pore size distribution due to the

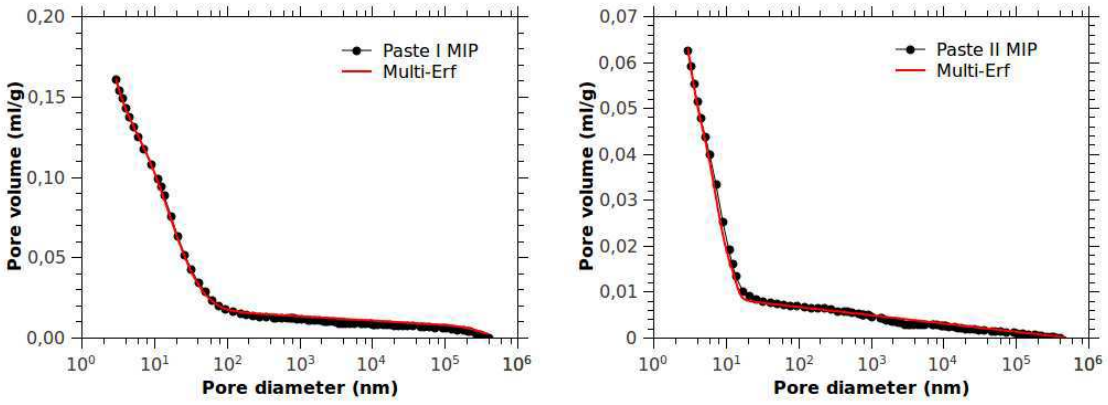

(a) (b)

Figure 8.2: Multi-Erf fitting of CPSD of paste I (w/c=0.5) (a) and paste II (w/c=0.3) (b).

ink-bottle like pores and the connectivity of pores with different sizes. But the similar physical processes between ice penetration and mercury invasion allows us to neglect the effect of ink-bottle like pores.

8.3.3 Saturation degree of cement pastes with freezing

As explicitly shown in eq(8.14), the ice volume or saturation degree with decreasing temperature, can be calculated numerically, once the pore size distribution, $\mathrm{d}\phi/\mathrm{d}r$, is determined. In section 8.3.2, the multi-Gauss fitting is used to describe the PSD of cement pastes measured by MIP. One most but not the least advantage of using multi-Gauss fitting to describe the PSD of porous materials, is that it is more flexible in numerical calculation to turn data into PSD continuous curve. Note that, for convenience, the pore size distribution in form of $\mathrm{d}\phi/\mathrm{d}\log r$ or $\mathrm{d}\phi/\mathrm{d}\log d$, rather than $\mathrm{d}\phi/\mathrm{d}r$, is retained for presenting the pore information. The eq(8.15) and the data in Table 8.2 for two sorts of cement pastes with different w/c ratios, are retained to estimate the curves of saturation degree with temperature.

The ice volume – temperature curves of paste I and II are illustrated in Figure 8.3(a), where only pure water in pore space is considered. It can be found that ice forms progressively in the pore space of paste I because of large pores, whereas almost no ice forms in paste II until -15℃. The first visible peak for ice volume –temperature curve of paste I is about -5℃ due to the ice formation in pores with diameter of about 15 nm. However, when ice forms in pores in diameter of 327340 nm and in 1 nm as presented in Table 8.2, there are not visible peaks shown in Figure 8.3(a), because the macropore volume is very small and the ice formation temperature is only about -0.027℃ according to the Gibbs-Thomson equation [342], while ice can not form in 1 nm pore due to the large van der Waals forces induced by pore wall that makes the water in highly stressed state [195]. Even when this stress is not considered, the temperature of ice formation in 1 nm can be as low as -89℃ estimated by Gibbs-Thomson equation.

The volume of unfrozen layer is considered in this study. Figure 8.3(b) shows the ratio of liquid like

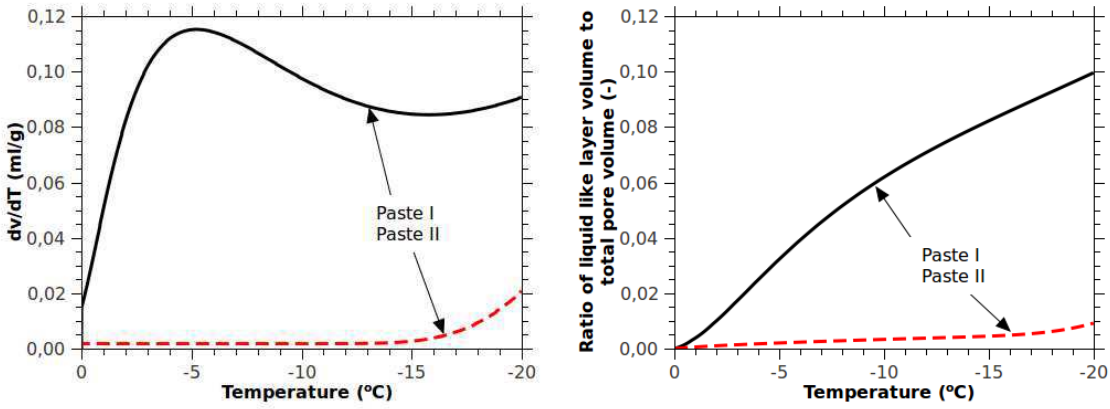

(a) (b)

Figure 8.3: (a), Ice volume – temperature curves of paste I (in solid line) and II (in dash line); (b), Ratio of liquid like layer volume to total pore volume as temperature decreases for paste I (in solid line) and II (in dash line).

layer volume to total pore volume as temperature decreases. For paste I, the volume ratio of unfrozen layer increases monotonously to about 0.1 when temperature decreases to -20℃, while for paste II, it only increases to about 0.01. Figures 8.4(a) and 8.4(b) show the saturation degree of paste I and II respectively, in terms of temperature with and without unfrozen layer. Obviously, the volume of unfrozen layer has significant influence on the saturation degree of pastes used in this study. Take paste I for example, as temperature decreases to -20℃, the saturation degree, if the volume of unfrozen layer is not considered, is about 0.33, which indicates about 67% total volume has been frozen. It decreases to 57% when the volume of unfrozen layer is considered. A critical case should be noticed, when the unfrozen layer equals the pore radius, then it could not form ice any more because of the previously mentioned stress by van der Waals forces induced by pore wall [195]. In this case, the saturation degree could be constant as temperature decreases further. The volume fraction of unfrozen layer, eventually can be estimated as: $\phi_\delta = \delta \times S/V$, with δ the thickness of unfrozen layer (estimated as 0.8 nm [381]), S the specific surface area of porous materials, V the pore volume. Taking account of the data, ($S = 55$ $(\mathrm{m}^2 \cdot \mathrm{g}^{-1})$, $V = 0.1608$ $(\mathrm{ml} \cdot \mathrm{g}^{-1})$ for paste I and $S = 24$ $(\mathrm{m}^2 \cdot \mathrm{g}^{-1})$, $V = 0.0625$ $(\mathrm{ml} \cdot \mathrm{g}^{-1})$ for paste II, see chapter 6 for detail), one obtains the eventual volume fraction of unfrozen layer, $\phi_\delta = 0.274$ for paste I and $\phi_\delta = 0.307$ for paste II. Those values are comparable to values predicted in this section, $\phi_\delta = 0.195$ for paste I and $\phi_\delta = 0.252$ for paste II.

When the pore space is occupied by saline solution, the ice formation temperature decreases due to the decrease of chemical potential of liquid phase. This is exactly the principle of using salts for melting ice on roads or pavements in winter. For bulk saline solution, the ice formation follows the classical phase diagram, in which the depression temperature is only due to the adding of salts. For pore solution, again, the local mechanical equilibrium, viz, the Young-Laplace equation, allows us to associate the pore size to capillary pressure as explicitly shown in eq(8.4). So the phase diagram of saline solution in porous materials depends

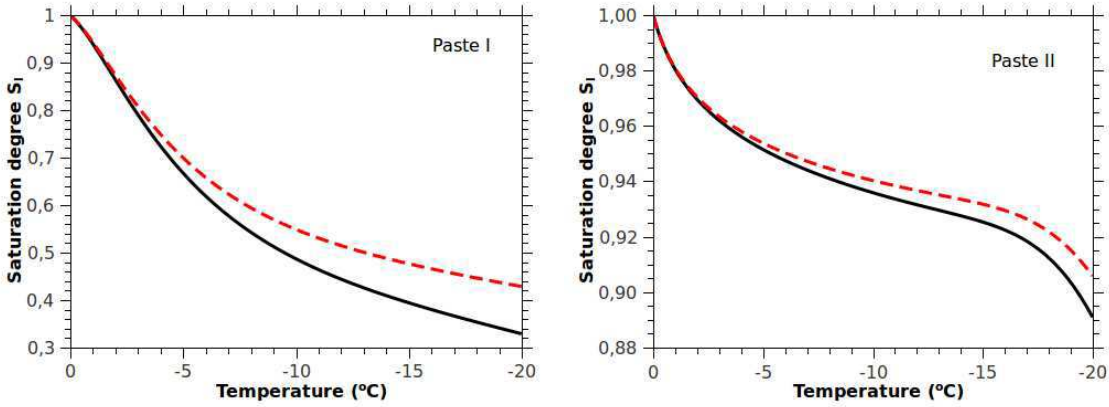

(a) (b)

Figure 8.4: Liquid saturation degree of Paste I (a) and II (b) in function of temperature with (in dash line) and without (in solid line) liquid like layer.

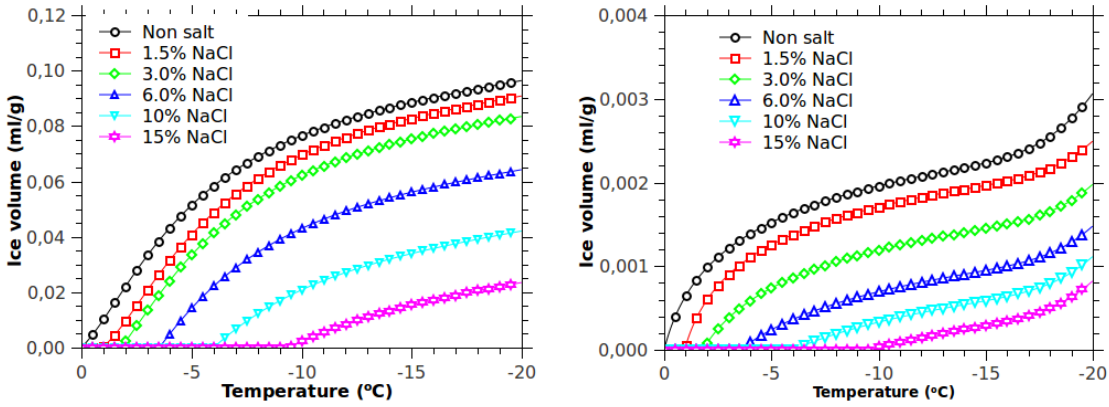

(a) (b)

Figure 8.5: Ice volume of Paste I (a) and II (b) initially saturated with 0% (non salt), 1.5%, 3%, 6%, 10% and 15% NaCl, in function of temperature.

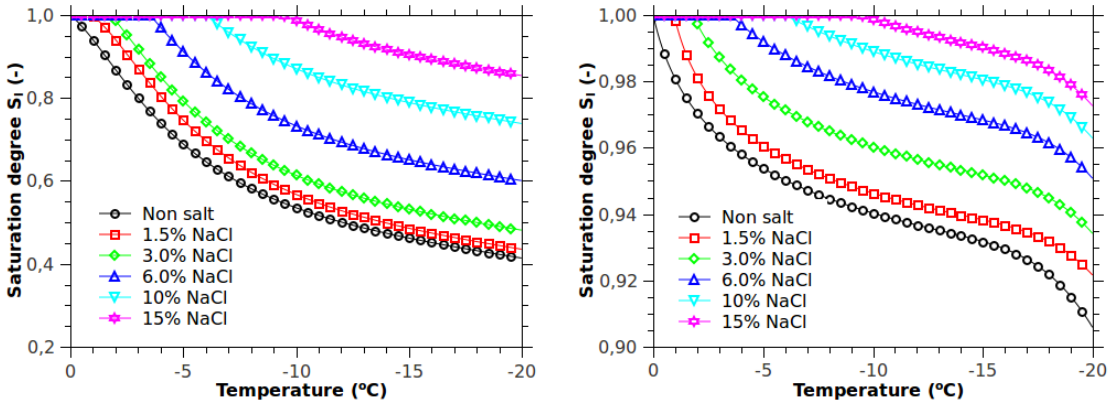

(a) (b)

Figure 8.6: Liquid saturation degree of Paste I (a) and II (b) initially saturated with 0% (non salt), 1.5%, 3%, 6%, 10% and 15% NaCl, in function of temperature.

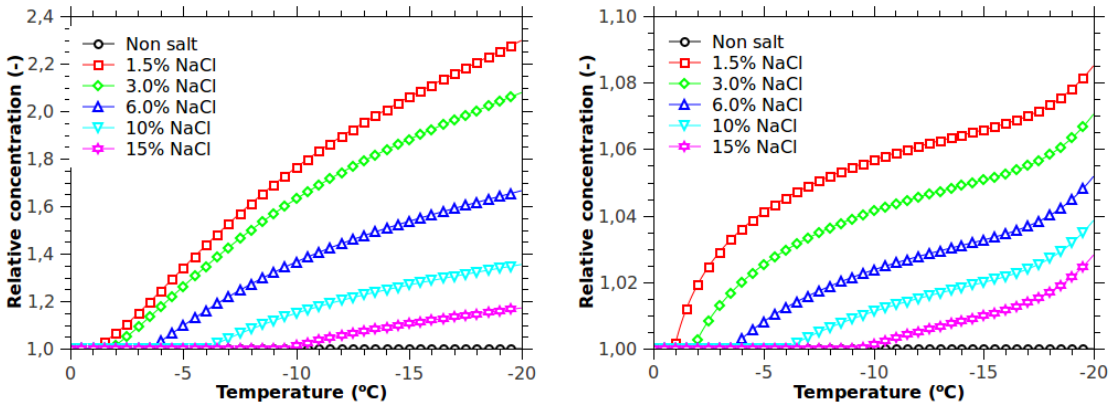

Figure 8.7: Relative salt concentration ($c/c^0 = 1/S_l$) of Paste I (a) and II (b) initially saturated with 0% (non salt), 1.5%, 3%, 6%, 10% and 15% NaCl, in function of temperature.

on both the salinity of solution and the pore size distribution. Figures 8.5(a) and 8.5(b) show the volume of ice formation with temperature for paste I and II respectively. It can be found that more ice formed in paste I than that in paste II because the former has larger pores. Also, due to aforementioned effect of salinity, the ice formation temperature decreases as initial salinity increases. As the concentration of NaCl increases to 15% wt, the ice formation temperature decreases to about −10°C. Note that here we assume that ice forms instantaneously, without any barrier against ice nucleation, once the chemical potentials of water and ice are equal. Figures 8.6(a) and 8.6(b) illustrate the variation of liquid saturation degree of paste I and paste II that initially saturated with 0% to 15% NaCl solution when temperature drops to −20°C. For paste I, it can be found that only about 10% of pore volume is occupied by ice when the material is initially saturated with 15% NaCl solution as temperature decreases to −20°C. When paste I is initially saturated with pure water, the temperature required for ice volume fraction approaching this value is only −1.5°C. For paste II, a very small amount of ice forms due to, as previously mentioned, the thinner pore size distribution. The ice content is only 8% to 2% as initial salt concentration increases from 0% to 15% when temperature drops to −20°C. Obviously, as ice progressively forms in pores, the solution in vicinity becomes more concentrated. Figures 8.7(a) and 8.7(b) show the relative salt concentration ($c/c^0 = 1/S_l$, see eq(8.13)) with temperature. Again, due to the larger pore size distribution of paste I, it has larger relative salt concentration in terms of temperature. In addition, the lower the initial salt concentration, the higher the ultimate relative salt concentration because more ice forms when initial salt concentration is lower. When the materials are saturated with pure water, the effect of salt concentration is null: $c/c^0 = 1$.

Chapter 9

Strains of cement pastes saturated with NaCl solution

Contents

9.1 Experimental procedures

9.1.1 Sample preparation

The chemical and physical properties of raw cement clinkers and the mixing, moulding/demoudling procedures have been introduced in chapter 6. The cylindrical samples in age of 360D were selected for experiments in next step. Figure 9.1 shows the sequences of deformation measurements of cement pastes briefly. For more comprehensive study on the deformation of cement paste subjected to freeze-thaw loading, two sorts of samples were planned. One sort of cement pastes were oven dried at 50℃ for 7 days to avoid freezable water in capillary pores in the range of the freeze-thaw temperature, 20℃ ~ -35℃. The other sort of samples were saturated with NaCl solution at concentrations of 0%, 1.5%, 3%, 6%, 10% and 15% by vacuum saturation for 24 hours. The solution-saturated cylinders were placed in a box with NaCl solution

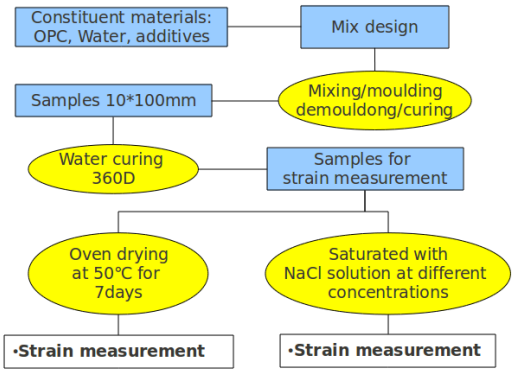

Figure 9.1: Sequences of experimental procedures on the deformation measurement.

Figure 9.2: Preparation procedures of saturated cylindrical samples to obtain an undrained condition during freeze-thaw tests.

Table 9.1: Nomenclature of pretreated samples.

Samples	Non salt (Oven dried)	1.5% NaCl	3% NaCl	6% NaCl	10% NaCl	15% NaCl
Paste I						
No air entrainment	PI-S0 (PI-S0-D)	PI-S1	PI-S2	PI-S3	PI-S4	PI-S5
1.5%	PIA1-S0 (PIA1-S0-D)	PIA1-S1	PIA1-S2	PIA1-S3	PIA1-S4	PIA1-S5
3.0%	PIA2-S0 (PIA2-S0-D)	PIA2-S1	PIA2-S2	PIA2-S3	PIA2-S4	PIA2-S5
4.5%	PIA3-S0 (PIA3-S0-D)	PIA3-S1	PIA3-S2	PIA3-S3	PIA3-S4	PIA3-S5
6.0%	PIA4-S0 (PIA4-S0-D)	PIA4-S1	PIA4-S2	PIA4-S3	PIA4-S4	PIA4-S5
Paste II						
No air entrainment	PII-S0 (PII-S0-D)	PII-S1	PII-S2	PII-S3	PII-S4	PII-S5

at the same concentration for at least 7 days. After that period, the samples were removed from NaCl solution and allowed to achieve a surface dried condition. The samples were then covered by a thin layer of resin epoxy, and enclosed in a latex membrane to avoid the moisture exchange, the details of this procedure can be seen in Figure 9.2. In addition, samples of paste I entrained with air voids in dosages of 1.5%, 3%, 4.5% and 6% were considered as shown in Table 9.1. More details on the air entrained samples can be found in chapter 10.

9.1.2 Deformation measurement

After the cylindrical samples were sealed by resin epoxy and latex membrane, the length of sample i was measured and marked as L_i^0. The samples were then placed in the LVDT-stand. Figure 9.3 shows the well placed samples, LVDTs and the data logger. The temperature were controlled by an environmental chamber of Type Espec PL-2k, of which the temperature range is $-40 \sim 150$°C, the humidity range is 20% $\sim$ 100%. The dilation of samples were measured by spring loaded LVDTs (Type Macrosensor 750) and the data was accorded by data logger. The strains of samples then can be calculated as:

$$\varepsilon = \frac{\Delta L_i}{L_i^0} = \frac{L_i - L_i^0 - L_{LVDT,i}}{L_i^0} \tag{9.1}$$

where L_i is the current measured displacement of samples i, $L_{LVDT,i}$ is the displacement by LVDT i it self, and it can be calculated as:

$$L_{LVDT,i} = \beta_i \times (T - T_0) \tag{9.2}$$

with $T_0 = 20$℃ is the initial temperature. The linear displacement-temperature slope β_i of used LVDTs are validated respectively to be 0.5770, 0.5875, 0.5541, 0.5622, 0.5969 and 0.5637 μm/℃, instead of the nominal 0.56 μm/℃. The details of validations on the linear displacement-temperature slope of used LVDTs can be found in Appendix E.1.

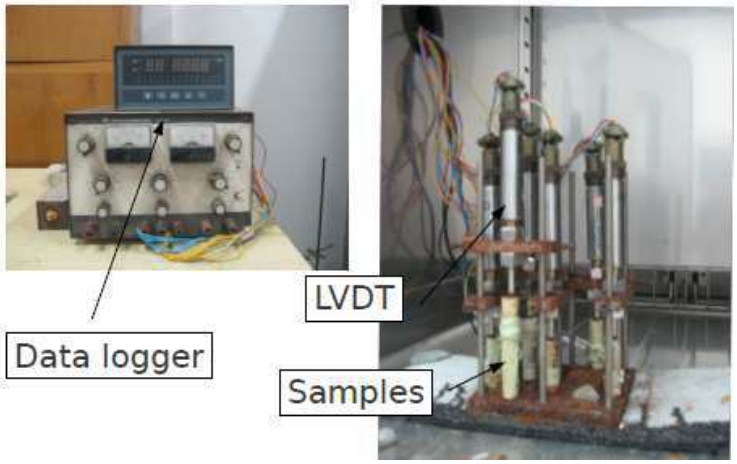

Figure 9.3: The experimental setup for deformation measurement.

9.2 Experimental results

9.2.1 Deformation of cement pastes subjected freeze-thaw loading

9.2.1.1 Pre-dried samples

The drying of cement pastes was inspected by gravimetric measurement. Figure 9.4 shows the normalized samples weight loss for paste I and paste II during oven-drying period at temperature 50 ± 1℃. Very quick weight loss in first 48 hours was observed for past I, while that for paste II was relatively slow due to its denser microstructure and less percolated pores as presented in chapter 6.

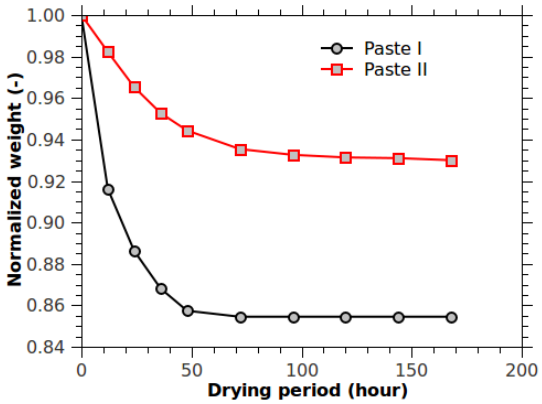

Figure 9.4: Normalized sample weight loss for oven-dried paste I and paste II at temperature 50 ± 1℃.

The deformation of dried samples were measured by LVDTs and calculated by eq(9.1). Figure 9.5 illustrates the typical strain-temperature curves for paste I and paste II respectively. The thermal expansion coefficient (TEC) is then obtained as: $\alpha = \varepsilon/\Delta T$. Four independent measurements on the dilations of dried pastes were performed, and the minimum strain and the calculated TEC are shown in Table 9.2. It can be found that the TEC of paste II is systematically larger than that of paste I. This may be due to the differences of mineral content for paste I and II. For paste II with w/c=0.3, it contains more C-S-H gel and Portlandite, cf. $f_{\text{C-S-H=0.5745}}$ for w/c=0.3 and $f_{\text{C-S-H=0.5196}}$ for w/c=0.5 according to the Avrami's model [392]. The TEC of C-S-H solid $\alpha_{\text{C-S-H}} = 14 \times 10^{-6}\text{°C}^{-1}$, estimated by multiscale model in [137] and that of Portlandite $\alpha_{\text{CH}} = 23.3 \times 10^{-6}\text{°C}^{-1}$, evaluated by using neutron diffraction method [383]. Consequently a reduction of the C-S-H and Portlandite fraction results in a decrease of the TEC of dried paste. These observations are consistent with the results obtained by Ghabezloo [137] who used a multiscale model to analyze the thermal expansion behaviors of hardened cement pastes.

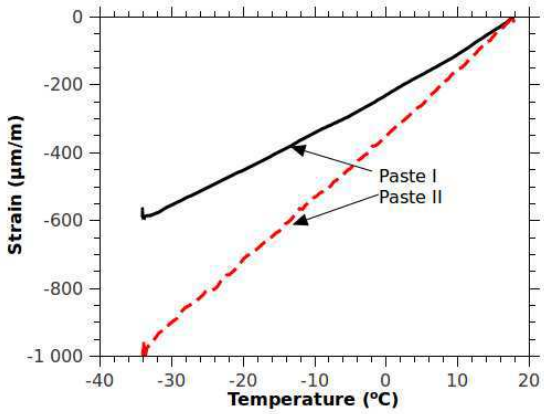

Figure 9.5: Strain-temperature curves for pre-dried paste I and paste II.

Table 9.2: Measured strains and TEC for paste I (paste II).

Measurements	Temperature range	Minimum strain[a]	TEC
	(°C)	(μm · m^{-1} at −35°C)	(μm · m^{-1} · °C^{-1})
1st	18 ∼ −35	-586 (-936)	11.052 (17.67)
2^{ed}	20 ∼ −35	-657 (-964)	11.941 (17.54)
3rd	20 ∼ −35	-629 (-971)	11.442 (17.66)
4th	20 ∼ −35	-634 (-991)	11.532 (18.01)
average		-626 (-975)	11.388 (17.72)

[a] The reference state is at 20°C.

9.2.1.2 Samples saturated with NaCl solution

For hardened cement pastes saturated with NaCl solution at different salinityies: non-salt (0%), 1.5%, 3%, 6%, 10% and 15% in weight fraction, significant different deformation curves can be observed, compared to those of dried samples. Figures 9.6 and 9.7 show, respectively, the deformation curves in terms of freeze-thaw time and temperature for paste I initially saturated with NaCl solution at different salinities. Except the samples of PI-S1 and PI-S5 (samples saturated with 1.5% and 15% NaCl solution), all the other samples show significant expansion as temperature is lower than the nucleation point. For PI-S1, a slight contraction when the temperature is lower than the ice nucleation point, is observed. This might be due to the incomplete saturation. Some occluded voids are empty, and they act as cryo-pump similar to the

effect of air voids [77, 342], which attract water confined in capillary pores in the vicinity. The preference of ice nucleation on the interface of air voids has been observed by the environmental scanning electron microscopy (ESEM) by Corr et al, [73]. This kind of contraction after ice nucleation can also be observed for sample of PI-S2 (sample saturated with 3% NaCl solution) at the third and the fourth freeze-thaw cycles, but accompanied with much more severe expansion as temperature is cooled down to −35°C, see Figure 9.7. For PI-S5, neither the significant expansion, nor the obvious residual strains can be observed. This may be because only the small amount of ice forms during freezing. Another important observation on the strain-time or strain-temperature curves is the evolution of maximum strains for solution saturated samples: the maximum strains increase for the first 3 cycles, then keep constant, even decrease (see PI-S3 for example). In addition, except the PI-S5, all samples have residual deformation, which might be due to the cracks induced by freeze-thaw damage. Quantitative analyses on the strains are given in section 9.2.2.

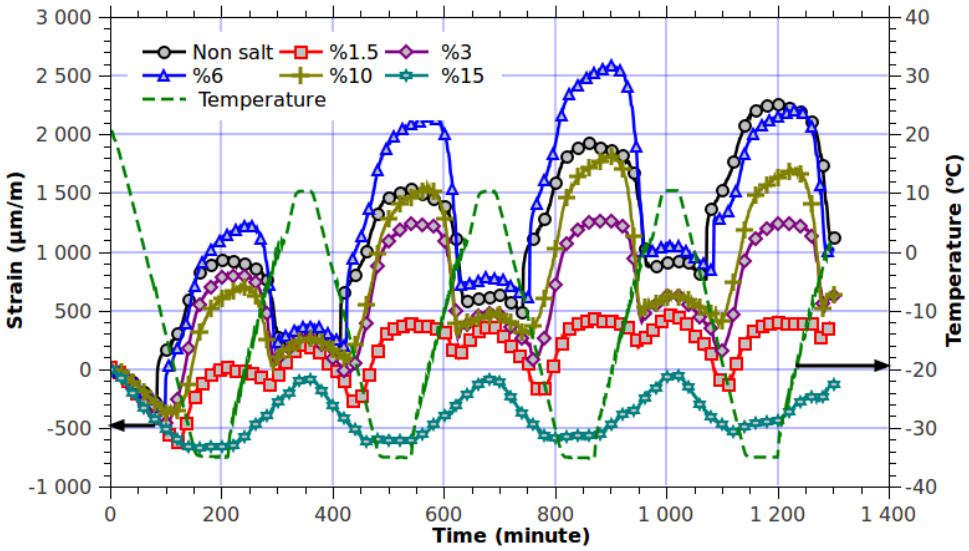

Figure 9.6: Deformation of paste I saturated with NaCl solution in terms of freeze-thaw time.

For paste II, with the same pretreatment conditions as those of paste I, completely different strain-time or strain-temperature curves can be observed. As shown in Figures 9.8 and 9.9, except for PII-S0 (water saturated sample), all other samples do not exhibit expansion at low temperature (cf. −35°C). These observations may be due to the dense microstructure and very limited percolated pores for paste II. Therefore, during freezing, only small amount of ice forms in this pore system, see section 8.3.3 for detail. In addition, the ice nucleation points can not be detected for all samples of paste II based on strain-temperature curves.

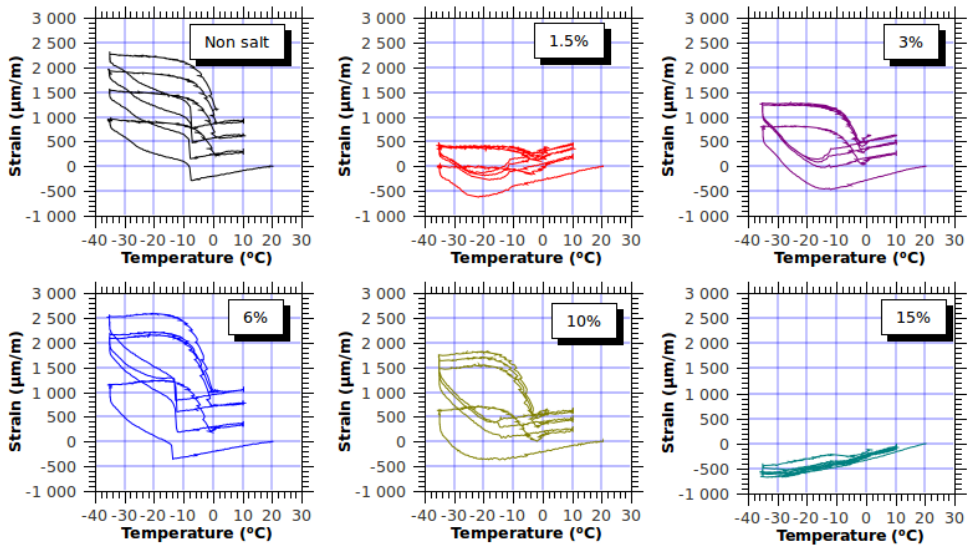

Figure 9.7: Deformation of paste I saturated with NaCl solution in terms of temperature.

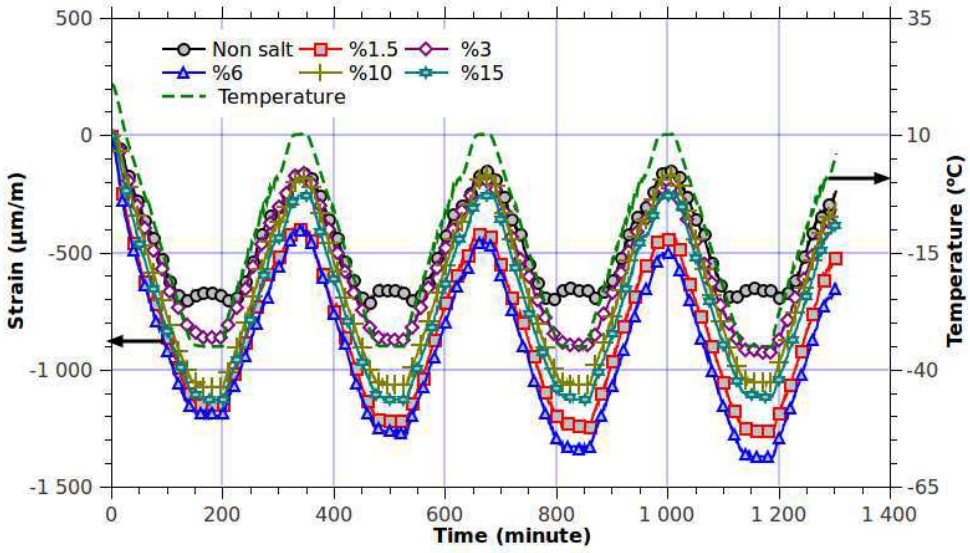

Figure 9.8: Deformation of paste II saturated with NaCl solution in terms of freeze-thaw time.

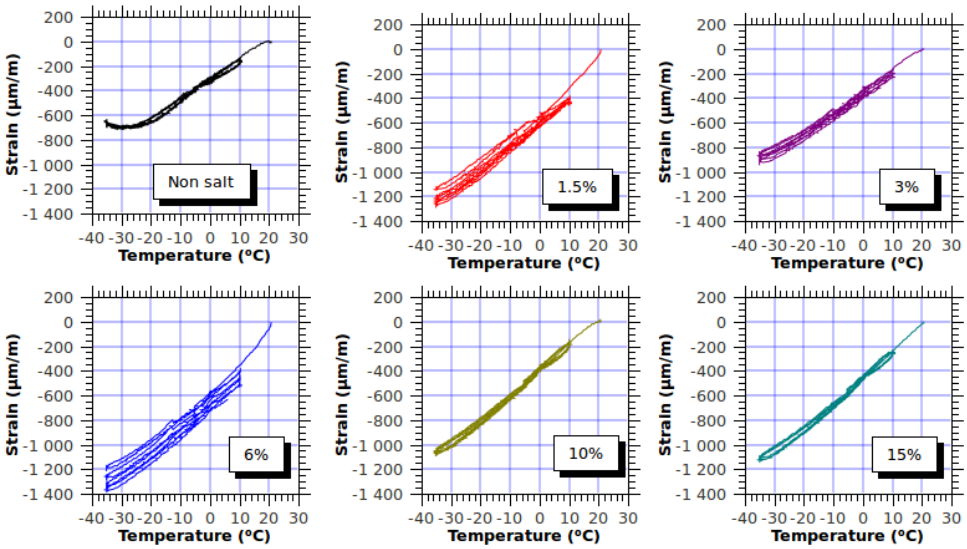

Figure 9.9: Deformation of paste II saturated with NaCl solution in terms of temperature.

9.2.2 Quantitative analysis of strain evolution with freeze-thaw cycles

Figures 9.10(a) and 9.10(b) show the strain-time and strain-temperature curves for PI-S0. From the observations, several deformations can be identified. The deformation at −35℃ due to pure thermal contraction of a porous materials composed of skeleton and confined solution in the pore space, is defined as $\varepsilon_{\mathrm{th}}$. Note that the defined $\varepsilon_{\mathrm{th}}$ is different from the measured deformation of pre-dried samples as presented in section 9.2.1.1, because the hydrothermal effect of confined pore solutions has influence on the deformation of saturated porous materials for undrained heating-cooling test. More quantitative analysis on this issue can be found in [137, 431, 432], see also section 10.1.1 for more comprehensive review. The instantaneous deformation at the vicinity of ice nucleation point is defined as $\varepsilon_{\mathrm{nu}}$. This value depends on the water content, solution concentration, depressed solidification temperature (nucleation temperature) and freezing rates. The maximum deformation at −35℃ referring to the initial state of a freeze-thaw cycle is named $\varepsilon_{\mathrm{ex}}$, and the difference between maximum deformation at −35℃ ant the deformation $\varepsilon_{\mathrm{th}}$ due to pure thermal contraction is the deformation by pore pressure, viz. $\varepsilon_{\mathrm{pr}} = \varepsilon_{\mathrm{ex}} - \varepsilon_{\mathrm{th}}$. When a freeze-thaw cycle finishes, it generally can not go back to the initial state, the corresponding deformation is the residual deformation, viz. $\varepsilon_{\mathrm{re}}$. Note that the start temperature is 20℃, whereas the end temperature is 10℃ for the first freeze-thaw cycle. The difference of the maximum deformation of $(i+1)$th cycle to that of the (i)th cycle is defined as $\varepsilon_{\mathrm{if}}$. All the definitions of deformations are recapitulated in Table 9.3 and illustrated in Figure 9.10.

The defined deformations for paste I and II subjected freeze-thaw cycles are presented in Table 9.4. It can be seen that the (absolute) values of $\varepsilon_{\mathrm{th}}$ of paste II are systematically larger than those of paste I. Two

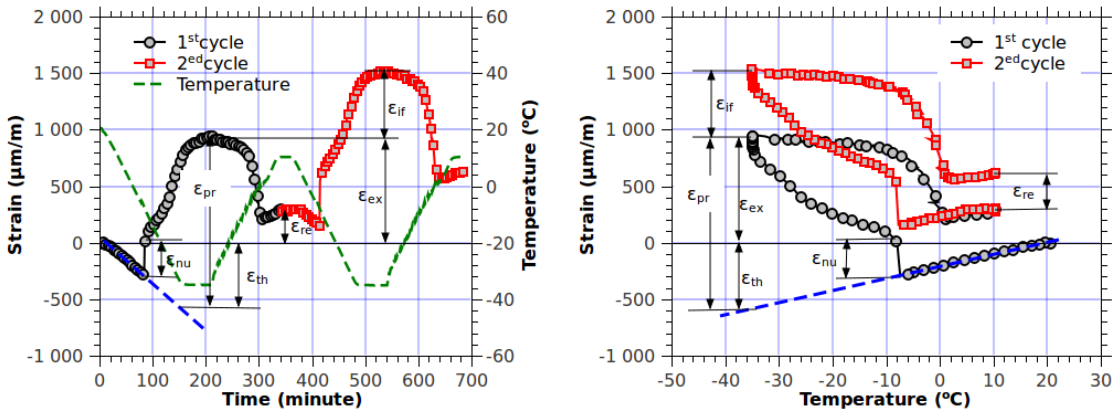

(a) (b)

Figure 9.10: Specific deformations for samples subject to freeze-thaw cycles loading (a) in terms of loading time, (b) in terms of loading temperature. The selected curves are the first and second freeze-thaw circles of Paste I saturated with water (PI-S0, see nomenclature in Table 9.1).

Table 9.3: Definition of the deformations based on strain-temperature/strain-time curves.

Deformation	Definition
$\varepsilon_{\mathrm{th}}$	Pure thermal dilation of saturated porous medium;
$\varepsilon_{\mathrm{nu}}$	Deformation for ice nucleation;
$\varepsilon_{\mathrm{ex}}$	Maximum deformation at -35°C based on the zero point in a cycle;
$\varepsilon_{\mathrm{pr}}$	Deformation by pore pressure, $\varepsilon_{\mathrm{ex}} - \varepsilon_{\mathrm{th}}$;
$\varepsilon_{\mathrm{re}}$	Residual deformation
$\varepsilon_{\mathrm{if}}$	Difference of the maximum deformation of $(i+1)$th cycle to that of the (i)th cycle;

reasons are responsible for the differences, one is the larger TEC of samples of paste II, as shown in section 9.2.1.1, the other is the hydrothermal pressure induced by pore fluid. Samples of paste II are less permeable, thus have higher hydrothermal pressure: more negative/positive deformation during cooling/heating. The significant nucleation strain $\varepsilon_{\mathrm{nu}}$ can be found for PI-S0 and PI-S3, and the values increase with freeze-thaw cycles. The strains by pore pressure $\varepsilon_{\mathrm{pr}}$ at -35°C for all samples are positive, due to the phase change in pore space, which can be either the ice formation in pores and/or the formation of eutectic mixture of NaCl solution and ice at about -23°C. This eutectic mixture does not lead to an abrupt deformation as the ice nucleation. As shown in Figure 9.7, for paste I, except for PI-S5, the residual deformations $\varepsilon_{\mathrm{re}}$ and the differential deformation $\varepsilon_{\mathrm{if}}$ are significant, which indicate that in addition to the elastic deformation, the permanent fracture deformation after one freeze-thaw cycle occurs,.

Table 9.4: Deformations for paste I and II saturated with NaCl solution at different concentration subject to freeze-thaw loading.

Sorts	1st cycle ($\times 10^{-6}$)		2ed cycle ($\times 10^{-6}$)		3rd cycle ($\times 10^{-6}$)		4th cycle ($\times 10^{-6}$)	
	PI	PII	PI	PII	PI	PII	PI	PII
Samples saturated with water								
ε_{th}	−577	−878	−509	−715	−560	−710	−547	−703
ε_{nu}	306	0	414	0	425	0	468	0
ε_{ex}	944	−672	1231	−507	1305	−497	1337	−497
ε_{pr}	1521	206	1740	208	1865	213	1884	206
ε_{re}	305	−154	313	−10	300	10	−[a]	–
ε_{if}	592	11	336	0	332	10	–	–
Samples saturated with %1.5 NaCl solution								
ε_{th}	−746	−1322	−675	−930	−704	−915	−706	−893
ε_{nu}	0	0	0	0	0	0	0	0
ε_{ex}	0	−1157	183	−819	72	−809	−55	−820
ε_{pr}	746	165	858	111	776	106	651	73
ε_{re}	205	−401	155	−31	104	−10	–	–
ε_{if}	388	−63	44	−21	−23	−21	–	–
Samples saturated with %3 NaCl solution								
ε_{th}	−829	−897	−622	−804	−574	−785	−639	−764
ε_{nu}	0	0	0	0	0	0	0	0
ε_{ex}	802	−863	982	−708	787	−698	614	−699
ε_{pr}	1631	34	1604	−96	1461	87	1253	65
ε_{re}	257	−165	230	−32	138	−20	–	–
ε_{if}	437	−10	35	−22	−35	−21	–	–
Samples saturated with %6 NaCl solution								
ε_{th}	−589	−1285	−390	−937	−371	−929	−437	−923
ε_{nu}	306	0	467	0	575	0	445	0
ε_{ex}	1051	−1197	1749	−854	1782	−865	1153	−867
ε_{pr}	1640	88	2139	83	2133	64	1590	56
ε_{re}	359	−408	419	−54	269	−43	–	–
ε_{if}	1049	−65	460	−65	−360	−45	–	–
Samples saturated with %10 NaCl solution								
ε_{th}	−617	−1135	−348	−955	−336	−968	−338	−966
ε_{nu}	0	0	25	0	98	0	49	0
ε_{ex}	700	−1074	1284	−882	1356	−888	1037	−883
ε_{pr}	1317	61	1632	73	1692	80	1375	83
ε_{re}	257	−182	199	10	209	1	–	–
ε_{if}	841	10	269	0	−110	10	–	–
Samples saturated with %15 NaCl solution								
ε_{th}	−892	−1189	−715	−997	−786	−931	−766	−947
ε_{nu}	0	0	0	0	0	0	0	0
ε_{ex}	−665	−1128	−513	−869	−490	−871	−405	−860
ε_{pr}	217	61	202	128	296	60	361	87
ε_{re}	−91	−259	1	2	35	0	–	–
ε_{if}	61	0	24	0	120	11	–	–

[a] − stands for the undetectable data.

9.3 Discussion

From the experimental curves depicted in Figures 9.6 to 9.8, the significant different deformations between paste I and paste II can be observed. In this section, we try to explain the reasons being responsible for the observed deformations. Figure 9.11 and 9.12 show, respectively, the comparisons of the measured and simulated strains for paste I and paste II saturated with saline solution at different concentrations. For simulation, the initial and boundary conditions are presented in Table 9.5. The freezing rate is 20℃/h, about 0.0056 ℃/s. The cooling begins from the lateral surface $x = 0$ to the center $x = L$ of sample (see the schematic representation in Figure 4.1). Due to the symmetric geometry of the sample, the heat flow at $x = L$ is $\boldsymbol{Q} \cdot \boldsymbol{n}(t, x = L) = 0$. Under the undrained condition, both water and salt flow are zero at

$x = 0$ and $x = L$, see Table 9.5. The section at the middle of the sample is selected for simulation since the material properties were characterized at this location, and for better approaching the one dimensional modelling [1] since the length of sample is much larger than its radius.

For the samples of paste I, as shown in Figures 9.11, acceptable agreement between the measured and predicted deformation curves can be obtained, except the PI-S1 as depicted in Figure 9.11(b). This may be due to the incomplete initial saturation of the sample as discussed in previous section. The significant dilation of paste I after a certain cooling can be due to the ice formation of pore solution. For the paste II samples, as shown in Figure 9.12, rather good agreement between the measured and predicted deformation can be observed. All the observations indicate again, that the poromechanical approach can describe the freezing deformation of cement-based materials saturated with saline solution.

As is clearly presented in section 9.1.1, the experiments are performed under the undrained freezing, where the moisture and/or salt exchanging with environment are prohibited. This undrained freezing for porous materials saturated with pure water has been studied by Coussy [77] comprehensively, and later for cement-based materials by Coussy and Monteiro [82]. The linear deformation of porous samples in case of free loading ($\sigma = 0$) is hydrostatics and can be written as:

$$\varepsilon = \frac{1}{3}\frac{b(P_l - \frac{2}{3}U) + b_c P_{cap}}{K} + \alpha_s (T - T_0) \tag{9.3}$$

For the undrained freezing, the conservation law for total mass allows us to derive a relation correlating the liquid pore pressure with the temperature, salinity and saturation degree (see Appendix B.3.1 for detailed derivation):

$$\begin{aligned} P_l = &\left(\frac{b^2}{K} + \frac{1}{M}\right)^{-1}\left(\frac{b^2}{K} + \frac{1}{M}\right)\frac{2}{3}U - \left(\frac{b^2}{K} + \frac{1}{M}\right)^{-1}\left(\frac{bb_c}{K} + \frac{1}{M_c}\right)\frac{\rho_c^0 RT \ln a_w}{\mathsf{M}_w} + \left(\frac{b^2}{K} + \frac{1}{M}\right)^{-1} 3\alpha_\phi (T - T_0) \\ &+ \left(\frac{b^2}{K} + \frac{1}{M}\right)^{-1}\left(\frac{bb_c}{K} + \frac{1}{M_c}\right)\left[\mathcal{S}_f (T - T_0) - \mathcal{C}_f \left((T - T_0) + T \ln \frac{T_0}{T}\right)\right] \\ &- \left(\frac{b^2}{K} + \frac{1}{M}\right)^{-1}\left[\left(\frac{\rho_c^0}{\rho_l^0} - 1\right) - \frac{1}{\rho_l^0}\sum\left(\mathsf{M}_i - \rho_w^0 V_{\phi,s}\right) c_i^0\right]\phi_0 (1 - S_l) \end{aligned} \tag{9.4}$$

The parameters $1/M, 1/M_c, \alpha_\phi$ can be found in Appendix B.3.1 as well. The first term in the right hand side of eq(9.4) denotes the contribution of interfacial energy U to the liquid pressure; the second term represents the effect of salts, if pore liquid is pure water, this term is reduced to zero; the third term is the contribution of hydrothermal effect of liquid solution confined in pores; the fourth term accounts for the fusion entropy; and the last term is the effect of density difference when ice forms, in which the effect of salt is associated by the apparent molar volume $V_{\phi,s}$.

The total deformation of porous materials under undrained freezing and under free stress loading as

1. The modelling is performed with help of the code "BIL" developed by Patrick Dangla [86].

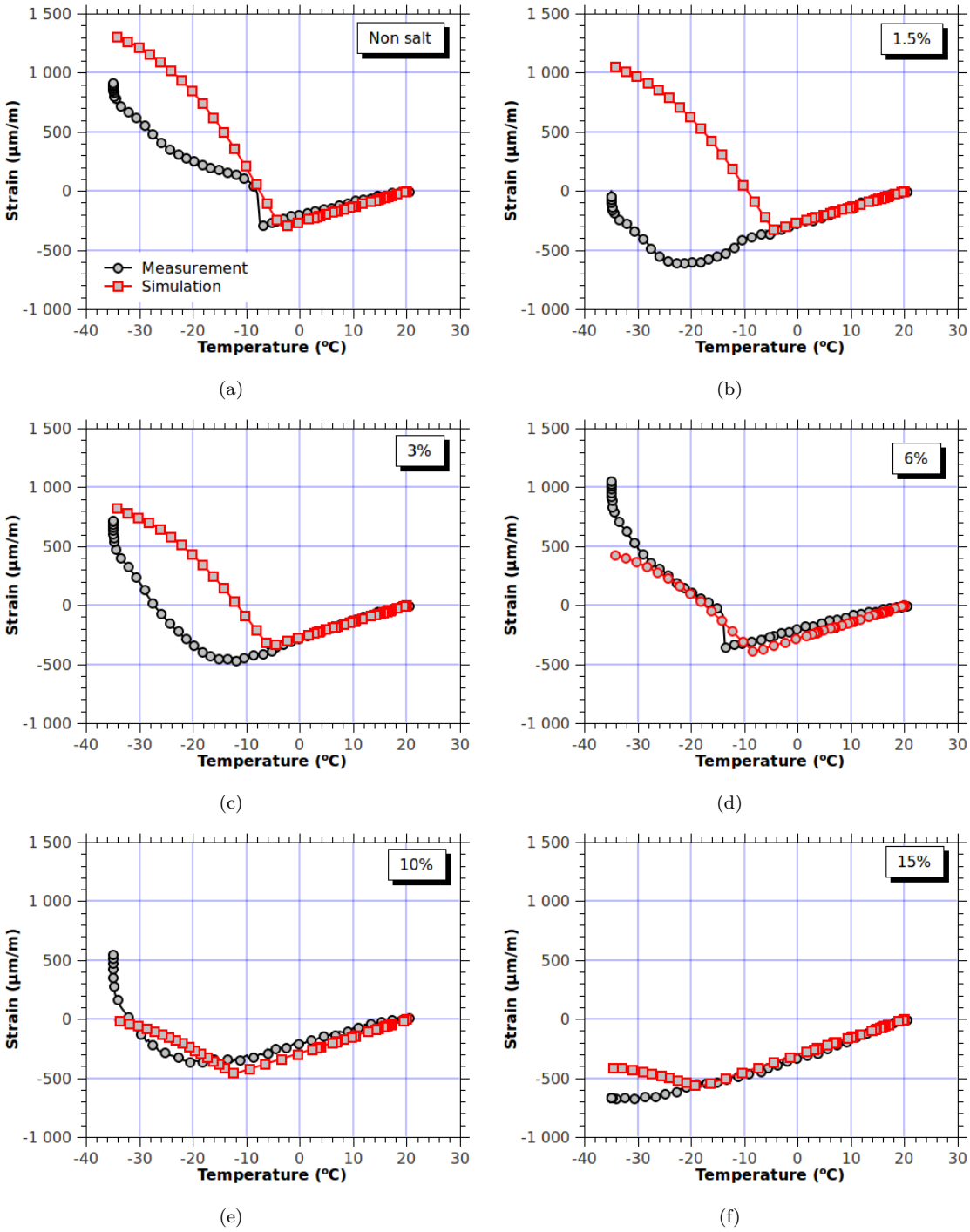

Figure 9.11: Comparison of the measured and simulated strains for samples of paste I, saturated with (a) water (non-salt), (b) 1.5%, (c) 3%, (d) 6%, (e) 10% and (f) 15% NaCl solution.

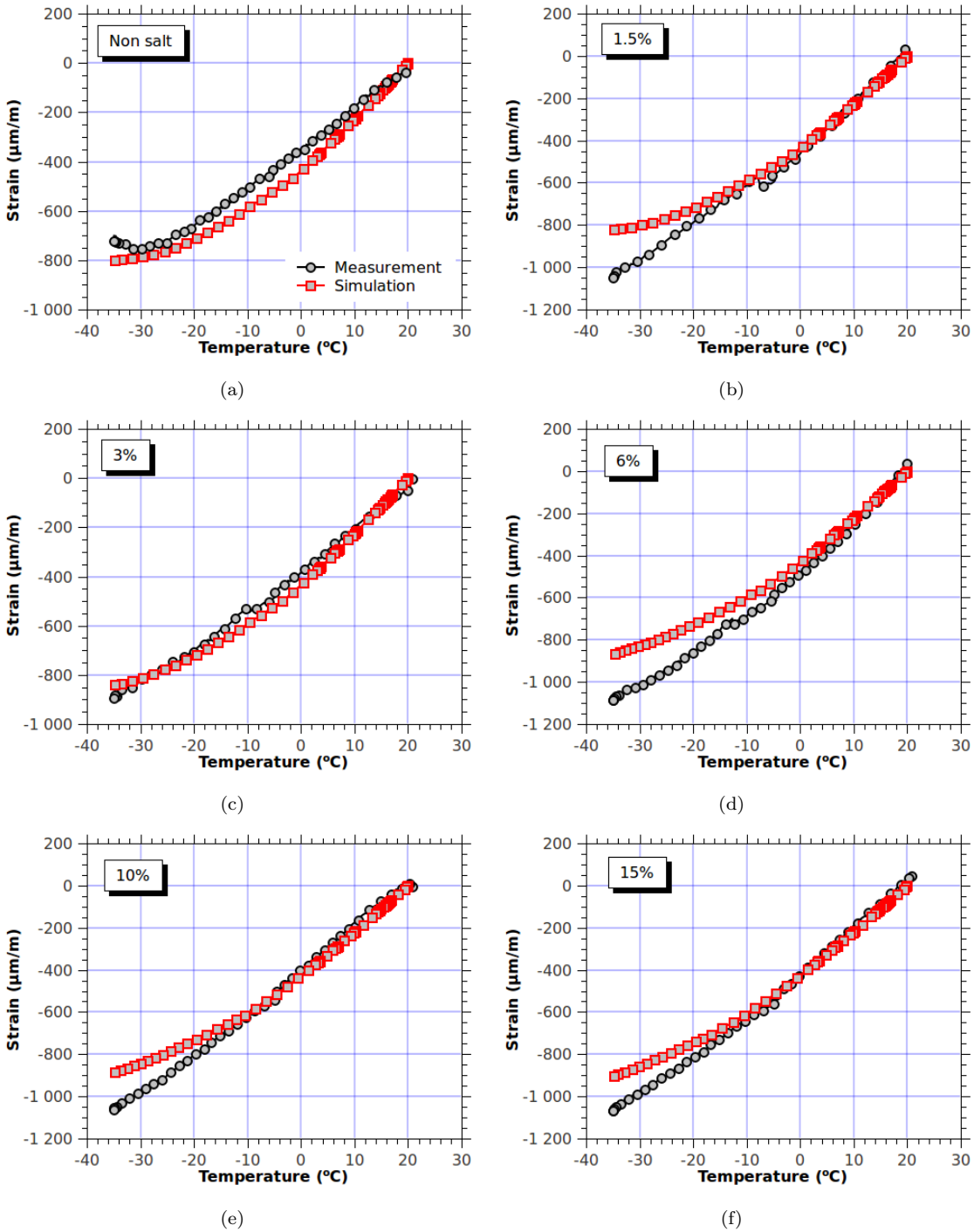

Figure 9.12: Comparison of the measured and simulated strains for samples of paste II, saturated with (a) water (non-salt), (b) 1.5%, (c) 3%, (d) 6%, (e) 10% and (f) 15% NaCl solution.

Table 9.5: Initial and boundary conditions for calculating the deformation of samples saturated with NaCl solution at different salinities. L represents the radius of sample.

	Initial condition	Boundary condition
Temperature	$T(t=0,x)=293\,(\mathrm{K})$	$T(t,x=0)=293-0.00556\times t$
Heat flow	-	$\boldsymbol{Q}\cdot\boldsymbol{n}(t,x=L)=0$
Liquid pressure	$P_l(t=0,x)=0.1\,(\mathrm{MPa})$	-
Water flow	-	$\boldsymbol{w}_w\cdot\boldsymbol{n}(t,x=0,x=L)=0$
Salt concentration	$c_i(t=0,x)=0\%,1.5\%,3\%,6\%,10\%$ and 15%	-
Salt flow	-	$\boldsymbol{w}_i\cdot\boldsymbol{n}(t,x=0,x=L)=0$

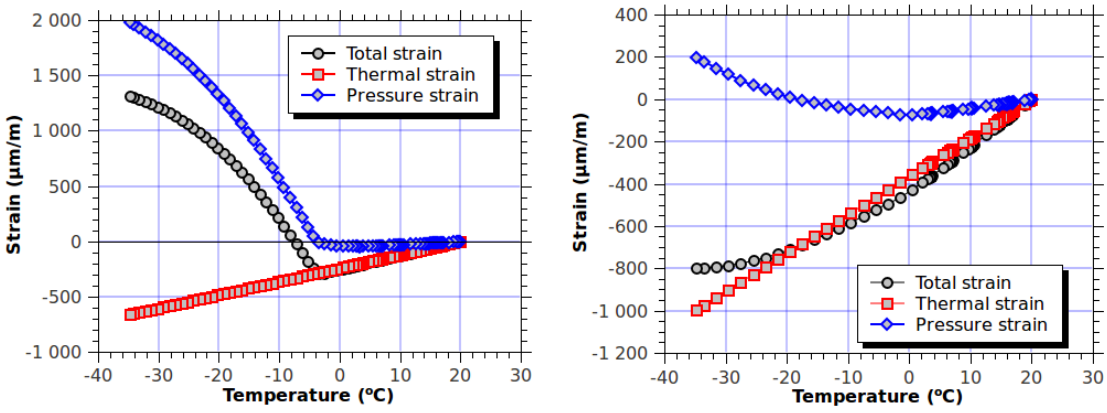

(a) (b)

Figure 9.13: Detail of deformation in (a) Figure 9.11(a) (paste I) and (b) Figure 9.12(a) (paste II). Thermal strain: the strain by pure thermal effect; Pressure strain: the strain by pore pressure induced by ice formation and hydrothermal effect of pore solution.

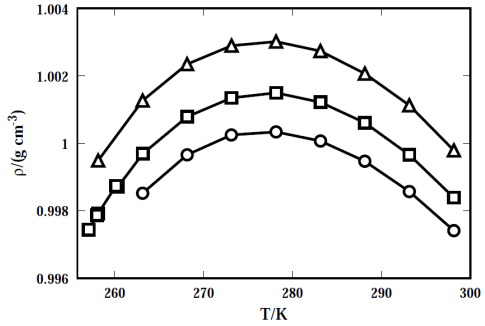

Figure 9.14: Density of NaCl solution at different salinity as function of temperature. ◯:0.00858 mol/kg, □:0.0343 mol/kg, △:0.09707 mol/kg. After Mironenko et la. (2001) [255].

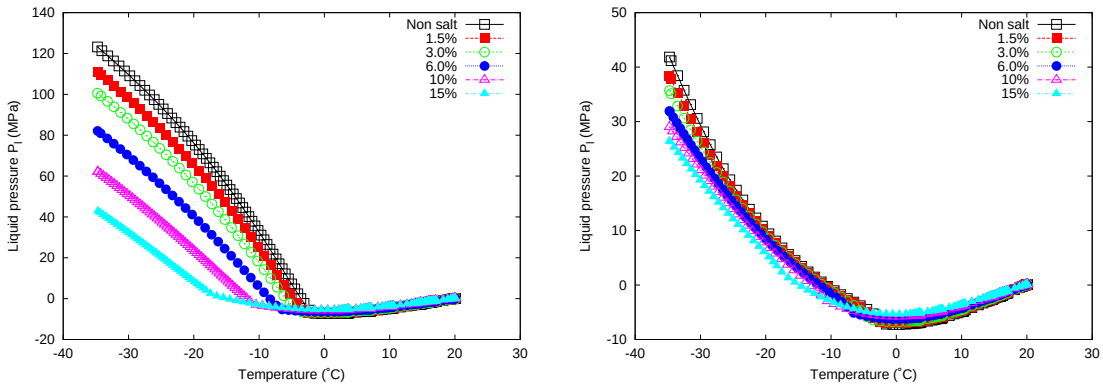

Figure 9.15: Variation of liquid pressure with temperature for (a) paste I and (b) paste II initially saturated with salt solution at different salinities.

depicted by eq(9.3) is composed of the deformation by pure thermal contraction of solid skeleton and that induced by internal pressure. Note the second term in the right hand side of eq(9.3) present the pure thermal deformation of solid skeleton without the hydrothermal effect of pore solution. Figures 9.13(a) and 9.13(b) show the thermal contraction and deformation by pore pressure for water saturated paste I and paste II respectively. Obviously, the thermal shrinkage increases monotonously as temperature decreases, while the deformation induced by pore pressure decreases slightly at first, then expands significantly. The first contraction can be due to the temperature dependent density of liquid solution, viz. the highest density of saline solution appears at about 4℃ (cf. Figure 9.14). Therefore, the contraction of liquid phase with decrement of temperature leads to the negative liquid pressure, see Figures 9.15(a) and 9.15(b). The lowest negative pressure can be about 7 MPa for samples saturated with pure water, when temperature decreases from 20℃ to 4℃. The pressurization coefficient thus is estimated to be 0.5 MPa/℃, which is very close to the value of well paste (0.6 MPa/℃) obtained by Ghabezloo [137]. As cooling goes on, the liquid pressure increases significantly due to the formation of ice, and the more ice forms, the higher the liquid pressure is obtained. As the salt concentration increases from zero to 15%, the maximum liquid pressure at -35℃ decreases from 125 MPa to 42 MPa for paste I, and from 42 MPa to 27 MPa for paste II. The huge difference of liquid pressure between the paste I and II is due to their pore structure. Recalling the saturation degree-temperature curves, cf. Figures 8.6(a) and 8.6(b), very limited amount of ice forms in pores of paste II because it has thinner pore size distribtuion, while more ice forms in paste I at the same subzero temperature.

Chapter 10

The effect of air voids

Contents

10.1 Effect of air voids on freezing strain of dried samples

10.1.1 Problems with the TEC of cement-based materials

The thermal expansion coefficient (TEC) is one of the most important thermo-mechanical properties for cement-based materials. It relates the thermal strain and the induced thermal stress at fixed displacement boundary condition. Thus, the common practice of concrete technology is to keep the material TEC as low as possible. Furthermore, the TEC of cement paste is of particular interest since it is a fundamental parameter to determine the internal stress among the different phases in cement-based materials and

to correctly predict the possible damage induced by the mismatch of thermal dilatation among phases [128, 383].

Available experimental results show that the typical values for TEC of hardened cement paste are about 15-20 $\mu\text{m} \cdot \text{m}^{-1} \cdot ℃^{-1}$ [248, 249]. These values are larger than TEC of aggregates, varying from 5 to 12 $\mu\text{m}^{-1} \cdot ℃^{-1}$ depending on the mineral composition [205]. Cement pastes are typical porous materials with total porosity of 20%-40% [247], and the pore water has been proved to have a significant influence on the material TEC due to the facts that liquid water has a larger TEC than the solid skeleton and that the pore water can accumulate stress during thermal process [137, 170]. The thermal dilation behavior of liquids confined in small pores has been investigated recently [431, 432]. Meanwhile, numerous experimental results indicate that, under drained condition, the TEC of saturated samples of cement pastes have almost the same TEC as dried samples [144, 353], and the TEC shows a maximum value at humidity of 65% [162]. Adopting the microstructure model of hydrates by Powers [307], Bazant[32] developed a hydrothermal model for cement paste TEC, decomposing the total thermal dilation into pure thermal dilation of skeleton, thermal shrinkage (swelling) of pore liquid and hydrothermic dilation of paste. This model was further extended by other authors for different moisture conditions [144, 331, 353].

Compared to the detailed research on the role of pore water, little attention has been paid to the influence of material porosity on TEC. For most ceramics, it is reported that the TEC is independent of porosity [319]. However, the porosity of ceramics is controlled, in industry, to fabricate the low TEC materials. For instance, the cordierite ceramics were sintered with porosity about 40% to obtain a TEC as low as 0.4 $\mu\text{m} \cdot \text{m}^{-1} \cdot ℃^{-1}$ [167]. For cement-based materials, Shui et al. [370] showed that the TEC decreased with the increase of material porosity and explained that this decrease was due to the pores accommodating a part of the internal thermal expansion of solid skeleton. This argument was further supported by other experimental observations [313]. However, based on the poromechanics analysis, Ghabezloo obtained the opposite conclusion [136]. Thus, more research is needed to understand the mechanism of porosity's impact on TEC. To this aim, the TEC of cement pastes and mortars with different porosities are investigated in this section (see also [442]). The temperature range of TEC measurement is $-35 \sim 20℃$, a usual range for atmospheric exposure of engineering cement-based materials. The thermogravimetric analysis (TGA) was performed to characterize the hydration products respectively. On the basis of the measurements, the role of porosity on TEC is discussed in depth.

10.1.2 Theoretical basis

Several available models for TEC for porous media are recalled in this section to provide a theoretical basis for data interpretation of the experimental data in the present study. For sintered porous metals, the TEC relates intimately to the porosity [14] through a power law,

$$\alpha_d = \alpha_s \rho^{1/3} = \alpha_s (1-\phi)^{1/3} \tag{10.1}$$

where α_{d} is the global TEC of the porous material in drained condition, α_s is the TEC of the solid matrix, ρ is the compactness of the porous materials. From this relation, the increase of porosity leads to the decrease of material TEC. Ghabezloo [136] gave a poroelastic description of thermal deformation of porous material and derived the differential of TEC with respect to porosity as,

$$\frac{\partial \alpha_d}{\partial \phi} = -\frac{1}{K_d^2}\left[\frac{1-\phi}{K_d} - \frac{1}{K_s}\right]^{-1} \frac{\partial K_d}{\partial T} \tag{10.2}$$

where K_d is the drained bulk modulus of porous material, and K_s the unjacked bulk modulus or the bulk modulus of solid matrix. The detailed derivation of these equations is given in Appendix A.7, see also [76]. The experimental results by Odelson et al. [274] show that the drained bulk modulus decreases with temperature, i.e. $\partial K_d/\partial T < 0$. The term $-1/K_d^2[(1-\phi)/K_d - 1/K_s]^{-1}$ is negative too since the inequality $1-\phi > K_d/K_s$ holds for most cement-based materials, e.g. Ghabezloo measured $K_d/K_s = 0.414$ and $1-\phi = 0.74$ for oil-well cement pastes [139]. Accordingly, it is stated that the TEC of cement-based materials, in drained condition, increases with porosity [136]. Note that if the drained bulk modulus K_d is regarded as independent on temperature, i.e. $\partial K_d/\partial T = 0$, then eq(10.2) depicts a simple fact that,

$$\frac{\partial \alpha_d}{\partial \phi} = 0: \quad \alpha_d = \alpha_d(\phi = 0) = \alpha_s \tag{10.3}$$

In fact, Khalili et al. [192] provide the proof of this relation from a boundary value problem in classical poroelasticity with the bulk modulus independent of temperature.

10.1.3 Experimental procedures

10.1.3.1 Sample preparation

Cement pastes and mortars were prepared with w/c=0.5. For mortars, the sand-cement ratio was retained as 2.25 and the modulus of fineness [1] of sands is 2.5. Air entrainment agent (AEA) was added, in four dosages, into the cement paste and mortar mixtures to create different porosities in hardened samples. Note P(M)-i the paste (mortar) sample with $i = 0, 1, 2, 3, 4$ standing for the dosage, that is to say AEA mass over cement mass: $0, 30, 60, 90$ and 120μg/g respectively. After mixing, cement pastes and mortars were cast into cylinder tubes of 10mm diameter and the hardened specimens were demoulded from the tubes at 3 days, then immersed into saturated water.

The samples with curing age of 300D were taken out from water and weighted as M_0. The samples were then oven-dried at 50℃ to constant weight M_d. This temperature is regarded as capable to avoid the

1. The modulus of fineness is defined as: an empirical factor obtained by adding the total percentages of a sample of the aggregate retained on each of a specified series of sieves, and dividing the sum by 100 [5].

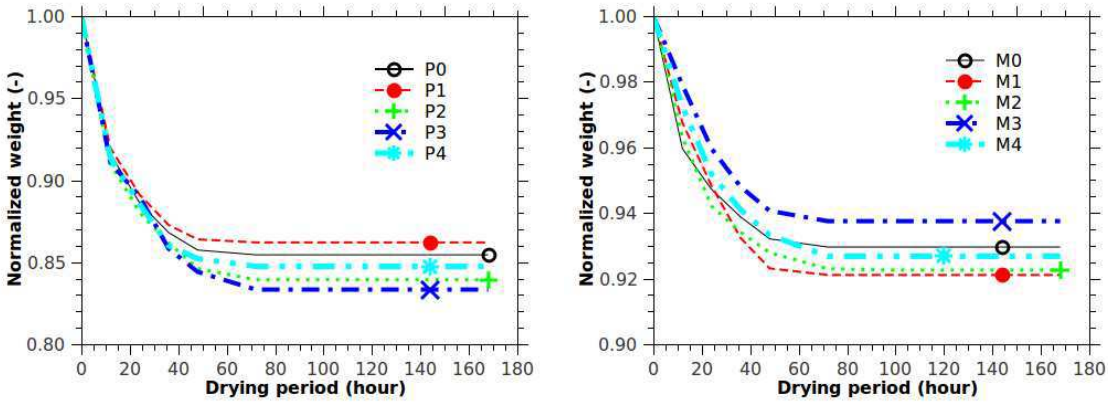

(a) (b)

Figure 10.1: Normalized sample weight loss for pastes (a) and mortars (b) during oven-drying period at temperature 50℃.

possible drying damage in samples [10]. The normalized weight loss ((absolute mass loss)/(total mass)) in drying process of pastes and mortars are presented in Figure 10.1. The weight of all samples became nearly constant after drying of 60h. For each material, the dried samples were divided into three groups. The first group was kept in desiccator for the thermal dilation measurement, the second group was vacuum-saturated with water and/or NaCl solution. The outgass pressure was controlled to under 0.1atm, and the vacuum-saturation last 48h to guarantee the saturation of the air voids as well. The vacuum-saturated samples were weighted as M_s. The last group of dried samples were then ground into small particles to perform helium pycnometry (HP), mercury intrusion porosimetry (MIP) and thermogravimetric analysis (TGA).

Table 10.1: Physical and chemical properties of cement pastes (mortars).

AEA dosage	P0(M0) 0	P1(M1) 1	P2(M2) 2	P3(M3) 3	P4(M4) 4
Bulk density (MIP) (g/ml)	1.85(2.06)	1.78(2.01)	1.65(1.76)	1.58(1.70)	1.52(1.67)
Bulk density (Gravimetry) (g/ml) [a]	1.52(1.99)	1.57(1.87)	1.39(1.81)	1.39(2.00)	1.33(1.76)
Skeleton density (HP) (g/ml)	2.06(2.35)	2.12(2.23)	1.98(2.24)	2.01(2.18)	1.97(2.20)
Skeleton density (MIP) (g/ml)	2.38(2.48)	2.36(2.40)	2.30(2.47)	2.24(2.47)	2.30(2.48)
Air void (Nominal) (%)	0(0)	1.5 (1.5)	3.0(3.0)	4.5(4.5)	6.0(6.0)
Air void (Gravimetry) (%) [b]	0(0)	1.8(1.7)	3.2(3.1)	4.5(5.5)	6.3(6.1)
Porosity (Gravimetry) (-) [c]	0.26(0.15)	0.26(0.16)	0.27 (0.15)	0.27(0.13)	0.26(0.15)
Porosity (MIP) (-)	0.22(0.13)	0.25(0.16)	0.28 (0.18)	0.29(0.19)	0.32(0.22)
Wn content (TGA) (-)	0.24(0.23)	0.24(0.23)	0.26 (0.23)	0.26(0.24)	0.25(0.24)
CH content (TGA) (-)	0.18(0.16)	0.18(0.16)	0.19 (0.16)	0.18(0.14)	0.18(0.19)
Hydration degree (-)	0.90(0.90)	0.90(0.89)	0.99(0.90)	0.99(0.92)	0.95(0.92)

[a] The bulk density by gravimetry is calculated as: $\rho = \rho_s \cdot \phi$ with ρ_s the skeleton density by helium pycnometry, ϕ the porosity by gravimetry determined by eq(10.4a);
[b] The air void content is calculated by eq(10.4b), where ρ_s is determined by helium pycnometry;
[c] The porosity is calculated by eq(10.4a), where ρ_s is determined by helium pycnometry.

10.1.3.2 Porosity and air void content

By the gravimetry method mentioned above, the porosity ϕ_m and the air-void content ϕ_{av}, for each material, are obtained through weight measurement:

$$\phi_m = \frac{(M_0 - M_d)/\rho_w}{M_d/\rho_s + (M_0 - M_d)/\rho_w} \quad \text{and} \quad \phi_{\text{av}} = \frac{(M_s - M_d)/\rho_w - (M_0 - M_d)/\rho_w}{M_d/\rho_s + (M_s - M_0)/\rho_w} \tag{10.4}$$

where ρ_w is the density of pore liquid ($\rho_w = 0.997\text{kg/m}^3$ for water) and ρ_s is the skeleton density which can be measured by helium pycnometry (HP) or mercury intrusion porosimetry (MIP). The analysis results are given in Table 10.1.

10.1.3.3 Thermogravimetric analysis

Grounded powder of samples, about 20g, was analyzed by thermogravimetric analysis (TGA) method to determine the non-evaporable water (Wn) and the calcium hydroxide (CH) content. It is known that 1g of ignited Portland cement, completely hydrated, contains 23-27% of non-evaporable water, i.e. $\text{Wn}_c(\infty)$=0.23-0.27 [391]. The stoichiometry analysis from cement hydration reactions gives $\text{Wn}_c(\infty) = 0.26$, see chapter 6 for detail. Note that the ignition loss of sand is relatively small $R_s = 0.003$ [2], the non-evaporable water Wn_m for cement in mortar samples is then calculated as,

$$\text{Wn}_m = m_n^m \cdot \frac{3.25 - R_c - 2.25R_s}{m_m \cdot (1 - R_c)} \tag{10.5}$$

where m_n^m stands for the measured non-evaporable water from mortar samples by TGA, m_m represents the ignited weight of mortar and R_c the ignition loss of cement (0.7%). The term $\frac{m_m \cdot (1-R_c)}{3.25-R_c-2.25R_s}$ represents the ignited weight of cement. For both cement pastes and mortars, the hydration degree of samples is calculated by

$$\alpha_{c,m} = \frac{\text{Wn}_{c,m}}{\text{Wn}_c(\infty)} = \frac{\text{Wn}_{c,m}}{0.26} \tag{10.6}$$

The calculated hydration degrees of cement pastes and mortars are presented in Table 10.1.

10.1.3.4 Thermal expansion coefficient measurement

The thermal expansion coefficient of samples was measured with LVDT of Type Macrosensor 750. Both the samples and LVDTs were placed in an environmental chamber of Type Espec PL-2k. The temperature range was set as -35℃ $\sim$ 20 ℃. Compared to the conventional range for TEC measurement, e.g. 20 ℃ $\sim$ 85 ℃ [370], this temperature range is more centered on low(negative) temperature and the measurements intend to give TEC for cement-based pastes in conventional atmospheric environments for cold regions. The cooling rate is 0.33 ℃/min. Since the geometry of samples is relatively small, the temperature distribution in samples can be assumed uniform under this rate. In addition, the humidity of the environmental chamber during TEC measurement was controlled as 25%. The recordings of temperature and the deformation of samples were synchronized by digital data logger. The TEC is calculated from the linear regression of recorded deformation with respect to temperature T,

$$\alpha_d = \frac{1}{L_0}\frac{\partial L}{\partial T} = \frac{\partial \varepsilon}{\partial T} \tag{10.7}$$

2. Sample was ignited at 1000℃ in a furnace for 1 hour.

where α_d is the TEC of samples in drained condition, L, L_0 are respectively the lengths of samples at test temperature T and reference temperature 20℃, ε is the linear strain of samples $\varepsilon = (L - L_0)/L_0$.

10.1.4 Experimental results

10.1.4.1 Thermal expansion coefficient

The measured thermal strains are presented in Figure 10.2(a) and 10.2(b) for dried cement pastes and mortars. It can be seen in Figure 10.2 that as the air void content decreases from 6.0% (AEA dosage 4) to zero the strains at −35℃ of cement pastes decrease from -450μm/m to -600μm/m and strains of mortars decrease from -360μm/m to -520μm/m. Note that for cement pastes and mortars, the largest thermal contractions happen for samples with AEA dosage of 1.5%, i.e. -680μm/m and -520μm/m for pastes and mortars respectively.

The TEC for each sample was obtained by means of linear regression $\varepsilon - T$. For each total porosity (material pores ϕ_m plus entrained air content ϕ_{av}), 4 samples were measured and the TEC is plotted in terms of total porosity in Figure 10.3, giving both average and dispersion of TEC values for cement pastes and mortars. Obviously, the TEC decreases with the augmentation of total porosity for both cement pastes and mortars. In Figure 10.3, eq(10.1) is used to fit the TEC value in terms of total porosity as well. It can be seen that eq(10.1) can not capture the TEC in terms of porosity for cement pastes and mortars. A better fitting relation for samples in this study is proposed as,

$$\alpha_d = \begin{cases} \alpha_0(1-\phi)^{2.66}, & \alpha_0 = 26.98(\mu m \cdot m^{-1} \cdot ℃^{-1}) \quad \text{for cement pastes} \\ \alpha_0(1-\phi)^{2.38}, & \alpha_0 = 14.71(\mu m \cdot m^{-1} \cdot ℃^{-1}) \quad \text{for mortars} \end{cases} \tag{10.8}$$

where α_0 is the fitted TEC value for $\phi = 0$. For cement pastes, the value of α_0 is similar to the TEC of Portlandite, i.e. 23.3 $\mu m \cdot m^{-1} \cdot ℃^{-1}$. For mortars, the value of α_c is much smaller than that of pastes, due to the large volumetric content of quartz sands of which the TEC is about 12 $\mu m \cdot m^{-1} \cdot ℃^{-1}$. The TEC values are also fitted with respect to entrained air content ϕ_{av} as,

$$\alpha_d = \begin{cases} \alpha_0(1-\phi_{\text{av}})^{3.74}, & \alpha_0 = 12.05(\mu m \cdot m^{-1} \cdot ℃^{-1}) \quad \text{for cement pastes} \\ \alpha_0(1-\phi_{\text{av}})^{2.69}, & \alpha_0 = 9.99(\mu m \cdot m^{-1} \cdot ℃^{-1}) \quad \text{for mortars} \end{cases} \tag{10.9}$$

In Figure 10.4(a) and 10.4(b) are shown the measured and fitted TEC for samples in terms of air void content. From these figures, it is confirmed that TEC is related to porosity, or entrained air content, through a power law, with different exponents for pastes and mortars.

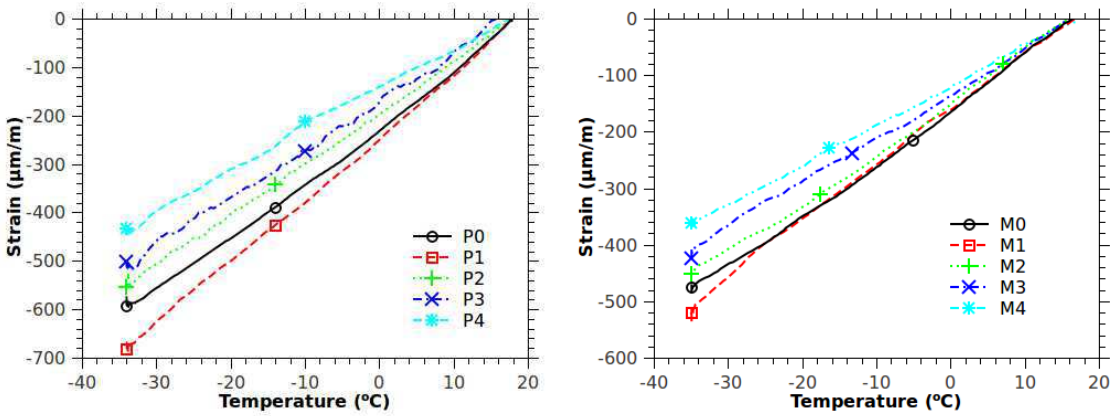

(a) (b)

Figure 10.2: Measured thermal deformations of dried air-entrained cement pastes (a) and mortars (b).

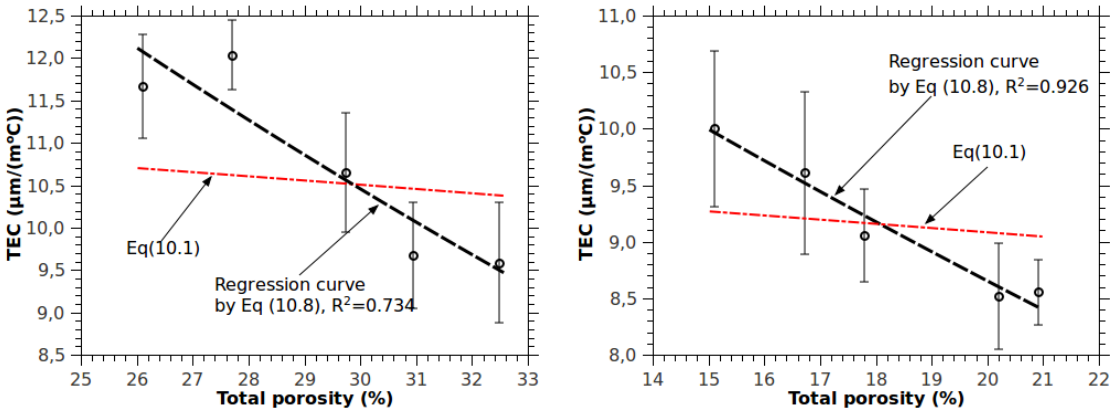

(a) (b)

Figure 10.3: Measured and fitted TEC values for dried air-entrained cement pastes (a) and mortars (b) in terms of total porosity ($= \phi_m + \phi_{\text{av}}$).

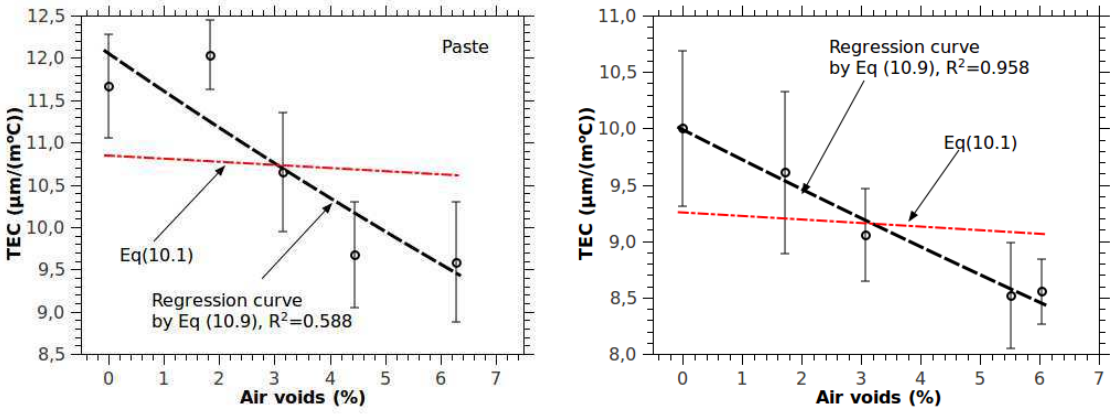

(a) (b)

Figure 10.4: Measured and fitted TEC values for air-entrained cement pastes (a) and mortars (b) in terms of air voids content.

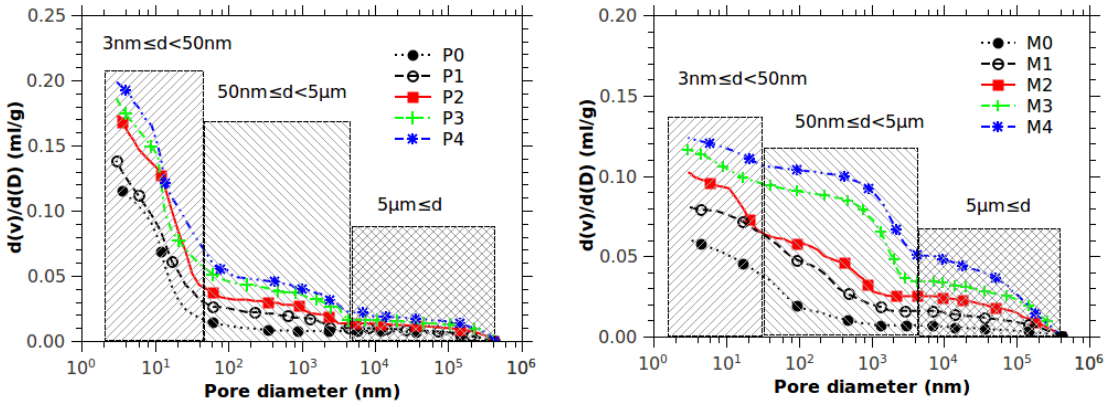

(a) (b)

Figure 10.5: Pore size distribution measured by MIP for pastes (a) and mortars (b) with different air void contents.

10.1.4.2 Pore structure

The capillary porosity and air void content measured by gravimetry for all samples are presented in Table 6.3. The capillary porosity is measured by the gravimetry during the drying procedure described in Section 3.3 and calculated through eq(10.4a). It can be shown that the capillary porosity of pastes is rather constant, around 26%, and that of mortars varies within 13-16%. These values are rather independent of the air voids content and this observation indicates that the air void system introduced by AEA does not interfere with the capillary pore system.

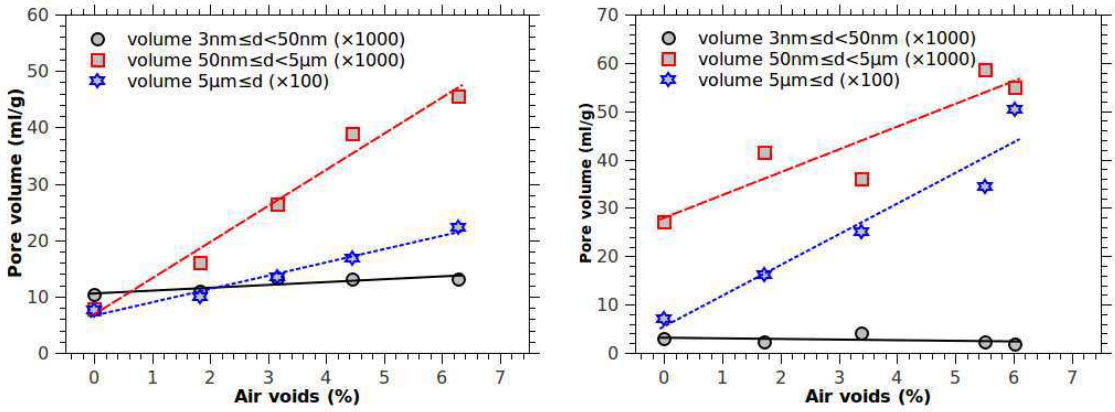

(a) (b)

Figure 10.6: The intruded pore volume at different pore size ranges for paste (a) and mortar (b).

The pore size distribution (PSD) of pastes and mortars, measured by MIP, is illustrated in Figure 10.5(a) and Figure 10.5(b). Significant difference can be observed between the PSD of air-entrained samples and that of the non air-entrained samples. The total intruded pore volume increases with the AEA content, from 0.12 ml/g to 0.20 ml/g for pastes and from 0.061 ml/g to 0.128 ml/g for mortars. Evidently, the

air voids introduced by AEA do have influence on the mercury intrusion process. Three characteristic pore ranges are identified and intrusion volume for each range is illustrated in Figure 10.6. The detailed influence of air voids on the MIP measurement for each pore range is described as follows.

Range of $d \geq 5\mu$m. Compared to non air-entrained samples, the intruded volume increases slightly for pastes but substantially for mortars, cf. Figure 10.6. For pastes, this slight increase can be attributed to the mechanical damage of surface air voids of samples by mercury pressure. For mortars, the important increase of intrusion volume is due to the percolation of mercury into air voids through two neighbouring interfacial transition zones (ITZ) between aggregates and cement paste, noting that ITZ contains more and larger capillary pores [350]. The mechanism is shown in Figure 10.7a.

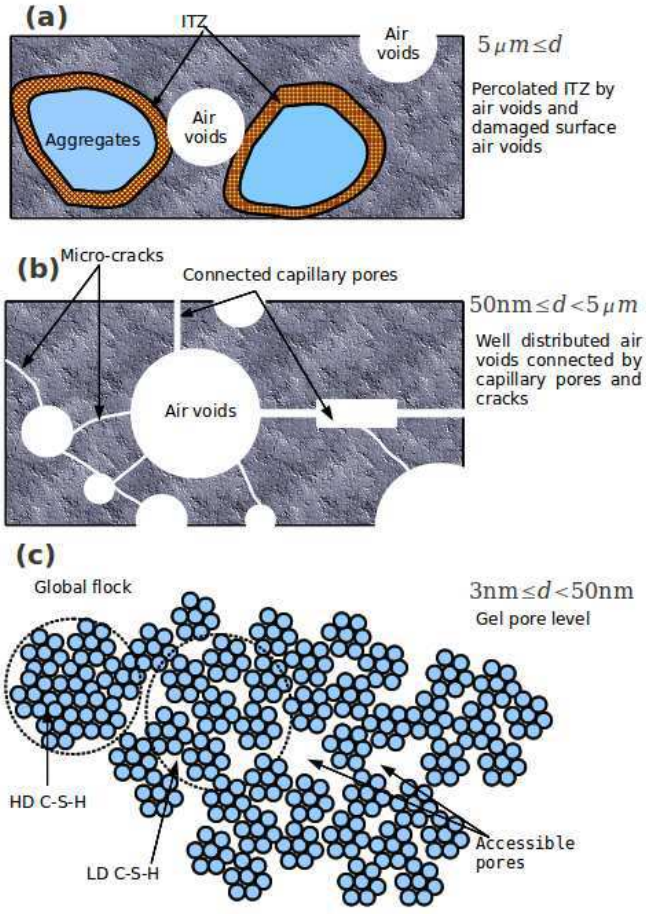

Figure 10.7: Influence of entrained air voids on three characteristic pore size ranges.

Range of 50nm$\leq d < 5\mu$m. It is observed from Figure 10.6 that in this range both paste and mortar samples have important increase of intrusion volume. This observation can be explained by the mercury percolation into air voids through the capillary pores (or microcracks) in hardened cement pastes, cf. Figure 10.7b. Note that SEM image analysis of "ink-bottle" shape pores in cement pastes shows that the "neck" size is about 2 magnitudes smaller than the "bottle" size [99]. Therefore, the "bottle" rather than the "neck" accommodates the important increase of intrusion volume in this pore size range.

Range of 3nm$\leq d <$ 50nm. In this range no significant different intrusion volumes are observed for samples with different entrained air void contents. According to the C-S-H model proposed by Jennings and coworkers [392], at this scale we are approaching the inter-granular space (∼10nm) between C-S-H bundles and the internal space (∼3nm) in a C-S-H bundle. In fact, this observation indicates the entrained air voids interfere very little with the pore structure at the scale near C-S-H structures, cf. Figure 10.7c.

10.1.4.3 Thermogravimetric analysis

The TGA results for pastes and mortars are presented in Figure 10.8. It can be seen that these thermogravimetric curves are quite similar. The measured Wn and CH are evaluated from these TGA results and presented in Table 10.1. The Wn values for hydrated cement in pastes and mortars are about 23-25% and the CH values for hydrated cement in pastes and mortars are 14%-19%. The hydration extent of cement, calculated by eq(10.6), attains about 90% for all samples at age of 300D and no significant difference of hydration extents is observed between pastes and mortars. This confirms that AEA dosage, with entrained air voids, has no influence on the cement hydration kinetics.

10.1.5 Discussion

According to classical thermo-elasticity [262], the TEC of a dried porous medium with homogeneous matrix is independent of its porosity and equal to the TEC of the matrix. Ghabezloo [139] derived the TEC of cement-based porous materials under drained and undrained conditions, and predicted a material TEC keeping constant for drained condition and increasing with porosity for undrained condition. However, our TEC measurements on both pastes and mortars specimens in this study do not support these statements. Several causes can be responsible for this discrepancy. Firstly, different porosity in this study is created by entrained air contents and the matrix of pastes and mortars is not homogeneous between the air void surface and bulk paste. Relevant investigations show that, once air voids is entrained by AEA in cement paste, a surface shell of about 1 μm thickness is formed with very dense microstructure [23, 212, 314, 315]. Through EDXA examination, it was also revealed that the C/S ratio in this shell was equal to 1.1, compared to C/S=1.5 in bulk

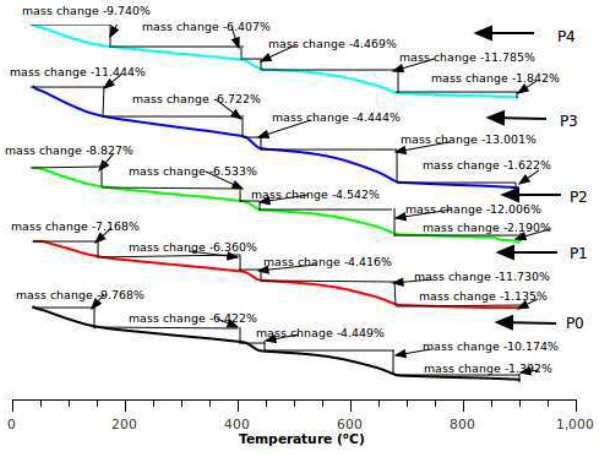

(a)

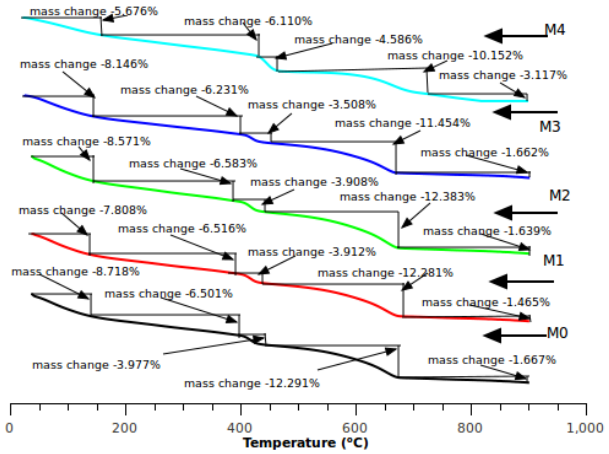

(b)

Figure 10.8: Thermogravimetric results for pastes (a) and mortars (b) with different air void contents.

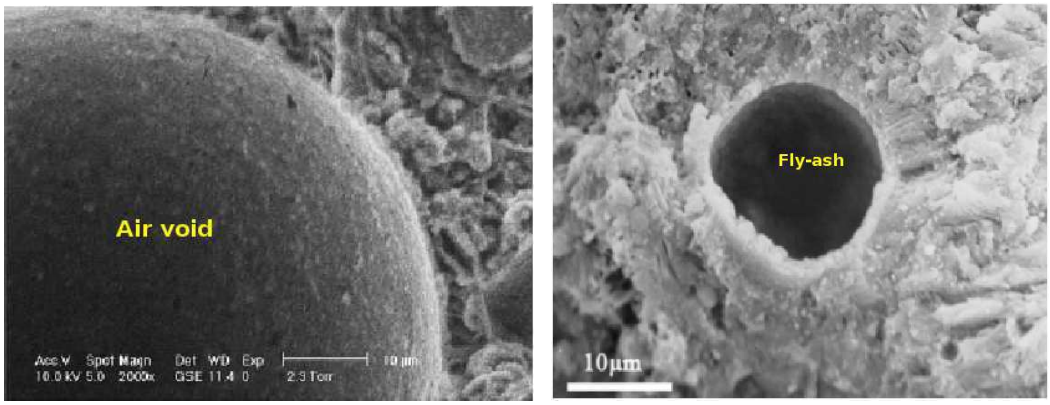

(a) (b)

Figure 10.9: SEM observations on microstructure of air void shell (a) (After Atahan et al., 2008 [23]) and fly ash (b) (After Luke and Lachowski, 2008 [229]).

paste [212]. Although no direct evidence is available to quantify the thermal deformation behavior of this shell, it is believed that this shell, together with the discontinuity created between this shell and the bulk paste, would have a direct impact on the TEC of entrained pastes and mortars. It is interesting to note that, in the works of Shui et al. [370], smaller TEC was measured for fly-ash pastes, and at the surface of fly-ash particles (void shell) similar C-S-H product with low C/S ratio was also observed [229, 293]. They also have morphology similarity, cf. Figure 10.9.

Secondly, the samples in this study were dried under temperature fixed at 50℃ but it is not sure that all pores are totally dried. In our TGA results, the mass loss during 50℃ and 150℃ was recorded as 7.2∼11.4% for pastes, and 5.6∼8.7% for mortars, cf. Figure 10.8. This mass loss is mainly the evaporated water. The existence of this quantity of water in pastes and mortars can have an additional effect on the TEC measurement by the possible water flow in pore structure [307]. At last, the thermal strain of solid skeleton of pastes and mortars can more or less deviate from the ideal thermo-elasticity due to the cracks and defects in skeleton especially with the presence of entrained air voids [70].

10.2 Strains of saturated air-entrained cement pastes subjected to freeze-thaw loading

10.2.1 Experimental observations

Comprehensive experimental studies have been performed on the deformation variation of air-entrained cement pastes saturated with NaCl solution at different concentrations subject to freeze-thaw loading. Figures 10.10 to 10.17 show the deformation variation with testing time and temperature for paste I entrained with dosage of 1.5%, 3%, 4.5% and 6% air void respectively. The porosity and air void content

are given in Table 10.1 in previous section. Contrary to the expectation that the samples saturated with pure water exhibit much larger deformation after ice nucleation, very limited deformation for samples saturated with water, while a large amount of deformation for samples saturated with saline solutions, are observed. It can be seen that, all samples, except the PIA1-S5, PIA2-S0, PIA4-S0 (see the nomenclature in Table 9.1), present the obvious freeze-thaw hysteresis and the residual deformation. This indicates that samples have been damaged under freeze-thaw loading. The values of deformation defined in section 9.2.2 (see Table 9.3), are recalled to characterize the deformations shown in Figures 10.10 to 10.17, see Table 10.2. It can be found that the maximum nucleation deformation $\varepsilon_{\text{nu}} = 1156 \times 10^{-6}$ for PIA3-S5 appears at second cycle, and this value is even larger than the free deformation when ice immediately forms in porous materials with 4.5% air voids saturated with 15% NaCl solution, viz. $\varepsilon_{\text{vnu}} = 0.045 \times 0.34 \times 0.09/3 = 459 \times 10^{-6}$. The value 0.34 is the ultimate ice volume formed in 15% NaCl solution [3]. The value 0.09 is the excess volume as ice forms. The maximum total deformation $\varepsilon_{\text{total}} = 4726 \times 10^{-6}$ is observed for PIA4-S5 at third cycle. Again, this value is larger than the free deformation when ice forms in porous materials with total 28% porosity saturated with 15% NaCl solution, viz. $\varepsilon_{\text{vto}} = 0.28 \times 0.34 \times 0.09/3 = 2856 \times 10^{-6}$. These observations indicate, at least that the volume increment associated with water solidification can be an important, but not the only reason for anomalous deformations of air entrained cement-pastes saturated with saline solution subjected to freeze-thaw loading.

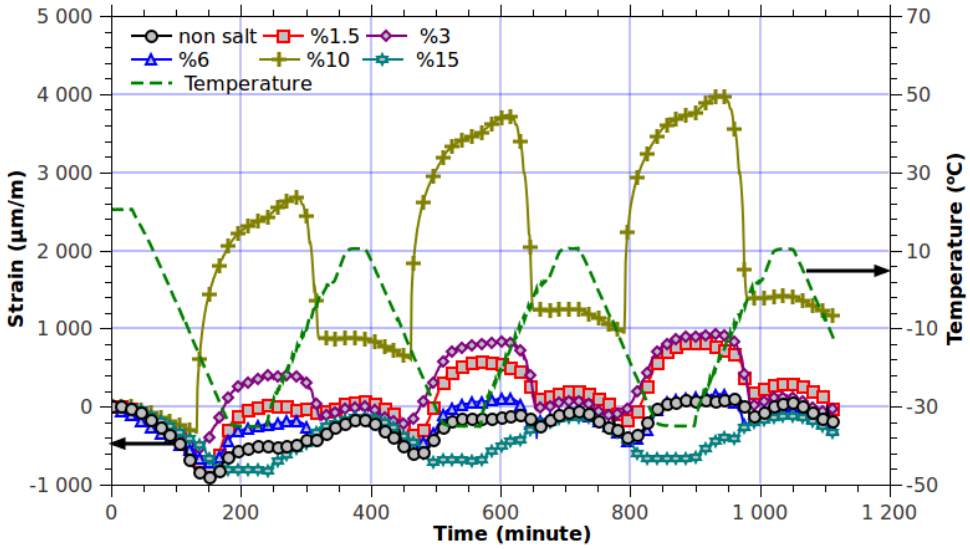

Figure 10.10: Deformation of saturated samples entrained with nominal 1.5% air voids (PIA1-S0→5) in terms of freeze-thaw time.

3. The volume fraction of water that is capable to solidify, is estimated by: $f_{ice} = (m^* - m)/m^* \times (\rho - m_b)$, where $m^* = 0.2331$g/g is the eutectic concentration, $m = 0.15$g/g is the current concentration, $\rho \approx 1.108$ml/g is the density of solution with mass concentration $m_b \approx 0.166$g/ml.

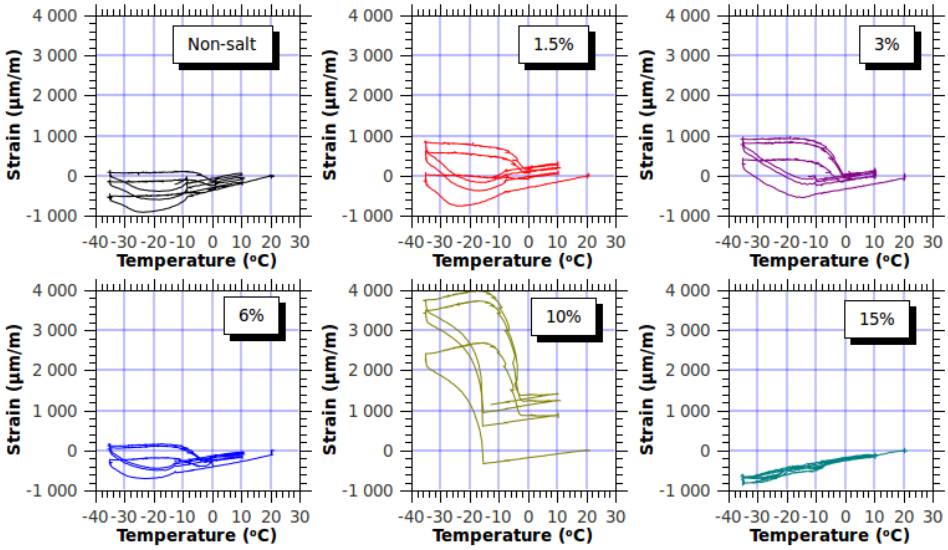

Figure 10.11: Deformation of saturated samples entrained with nominal 1.5% air voids (PIA1-S0→5) in terms of temperature.

Table 10.2: Deformations for air entrained pastes saturated with NaCl solution subject to freeze-thaw loading.

Sorts	1st cycle ($\times 10^{-6}$)				2ed cycle ($\times 10^{-6}$)				3rd cycle ($\times 10^{-6}$)			
	%1.5	%3	%4.5	%6	%1.5	%3	%4.5	%6	%1.5	%3	%4.5	%6
Samples saturated with water												
ε_{th}	−1004	−875	−659	−1250	−654	−637	−498	−868	−651	−644	−449	−993
ε_{nu}	0	0	0	46	0	0	36	78	0	0	0	110
ε_{ex}	−509	−649	55	−1119	17	−438	206	−685	146	−439	139	−502
ε_{pr}	495	226	1014	131	671	199	704	183	797	205	588	491
ε_{re}	−178	−252	150	−229	109	−20	156	32	121	−1	111	54
ε_{if}	348	−41	301	205	84	−21	89	215	−[a]	–	–	–
Samples saturated with %1.5 NaCl solution												
ε_{th}	−806	−1063	−619	−808	−509	−788	−419	−696	−474	−744	−420	−743
ε_{nu}	0	20	0	513	0	0	75	602	0	0	98	624
ε_{ex}	0	−556	0	1260	530	−273	452	1434	624	−252	428	1449
ε_{pr}	806	507	619	2068	1039	515	871	2120	1098	492	848	2192
ε_{re}	54	−36	30	126	143	129	121	152	95	96	72	111
ε_{if}	584	247	482	300	237	150	97	167	–	–	–	–
Samples saturated with %3 NaCl solution												
ε_{th}	−721	−663	−648	−736	−524	−433	−469	−529	−537	−417	−482	−495
ε_{nu}	0	61	315	135	0	71	178	334	0	141	152	500
ε_{ex}	390	10	954	40	814	569	868	765	838	724	751	1063
ε_{pr}	1111	673	1602	776	1338	1002	1337	1394	1375	1141	1233	1558
ε_{re}	−4	65	−51	65	77	155	36	272	45	133	21	220
ε_{if}	420	624	−135	790	101	310	−81	570	–	–	–	–
Samples saturated with %6 NaCl solution												
ε_{th}	−735	−774	−602	−396	−514	−455	−471	−341	−536	−371	−473	−356
ε_{nu}	0	35	332	616	0	187	631	772	0	327	434	817
ε_{ex}	−231	−286	1406	2240	205	583	1654	2439	194	1150	1666	2386
ε_{pr}	504	488	2008	2636	719	1028	2125	2780	730	1521	2139	2742
ε_{re}	−148	−15	336	551	66	222	336	223	35	299	120	133
ε_{if}	288	854	584	750	55	789	584	170	–	–	–	–
Samples saturated with %10 NaCl solution												
ε_{th}	−515	−705	*[b]	−526	−474	−557	*	−477	−548	−620	*	−485
ε_{nu}	703	445	271	572	994	681	861	838	898	759	827	849
ε_{ex}	2680	2165	2170	2150	2851	2543	3892	2367	2737	2491	5123	2357
ε_{pr}	3195	2870	*	2676	3325	3100	*	2844	3285	3111	*	2842
ε_{re}	877	587	583	373	366	452	834	200	162	247	622	134
ε_{if}	1032	965	2305	590	252	400	2065	190	–	–	–	–
Samples saturated with %15 NaCl solution												
ε_{th}	−720	−948	*	−695	−561	−775	*	−593	−552	−774	*	−635
ε_{nu}	0	91	448	560	0	103	1156	571	0	103	1023	793
ε_{ex}	−813	−630	2930	2900	−538	−372	3253	4015	−528	−406	3176	4091
ε_{pr}	−97	318	*	3595	23	403	*	4608	24	368	*	4726
ε_{re}	−145	−81	632	485	11	34	442	511	12	33	247	356
ε_{if}	130	177	845	1600	21	1	365	587	–	–	–	–

[a] − stands for the undetectable data;
[b] * is the anomalous value obtained from the measured data, so that it is not adopted in the table.

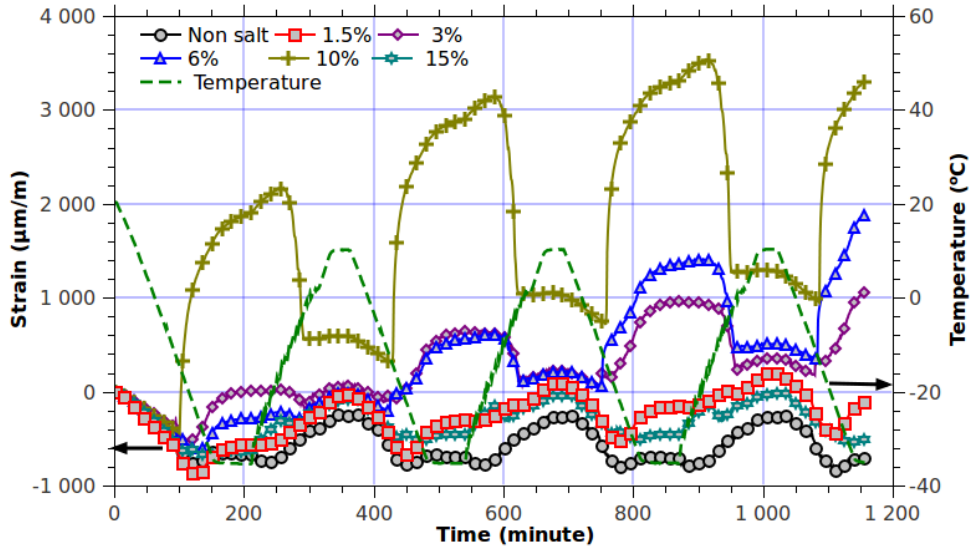

Figure 10.12: Deformation of saturated samples entrained with nominal 3% air voids (PIA2-S0→5) in terms of freeze-thaw time.

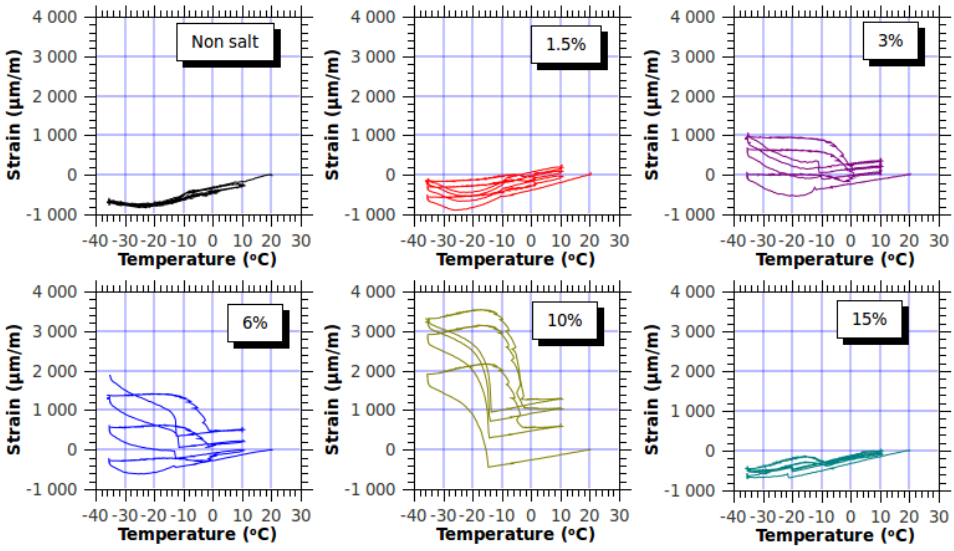

Figure 10.13: Deformation of saturated samples entrained with nominal 3% air voids (PIA2-S0→5) in terms of temperature.

10.2.2 Is it the effect of saturation degree of air voids?

Apparently, the higher the concentration with which the cement pastes have been initially saturated, the higher the maximum deformation, the residual deformation and the area of freeze-thaw deformation hysteresis (especially for samples saturated with NaCl at concentration of 6% (PIAX-S3) and 10% (PIAX-S4)). These observations have also been verified by the results obtained from comprehensive tests on the materials with the same compounds, see Appendix E.2. As to the author's knowledge, these phenomena have not been observed elsewhere, yet there have no proposed mechanisms accounting for these observations.

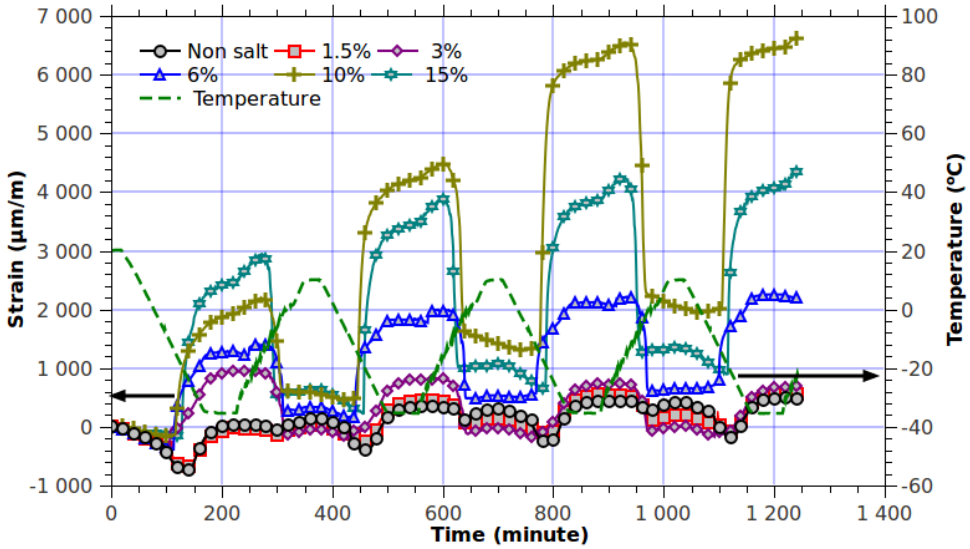

Figure 10.14: Deformation of saturated samples entrained with nominal 4.5% air voids (PIA3-S0→5) in terms of freeze-thaw time.

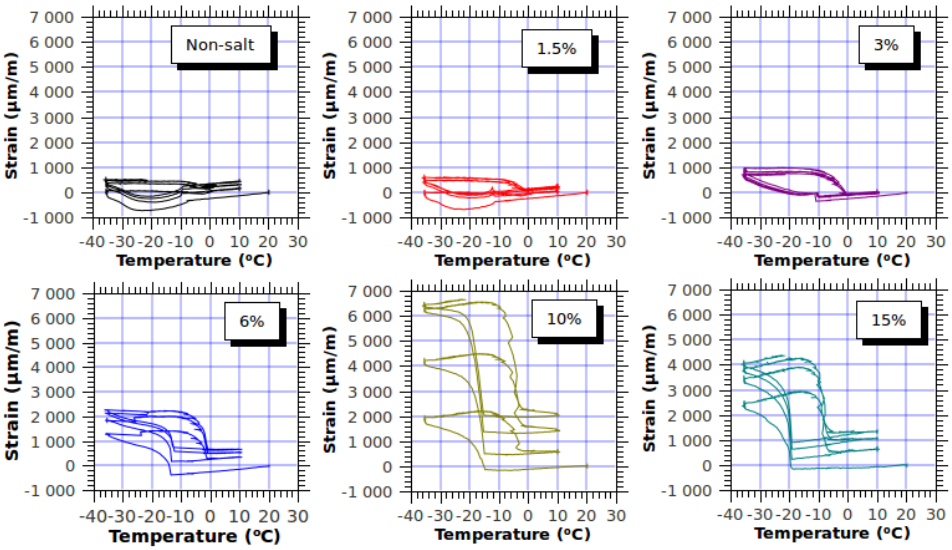

Figure 10.15: Deformation of saturated samples entrained with nominal 4.5% air voids (PIA3-S0→5) in terms of temperature.

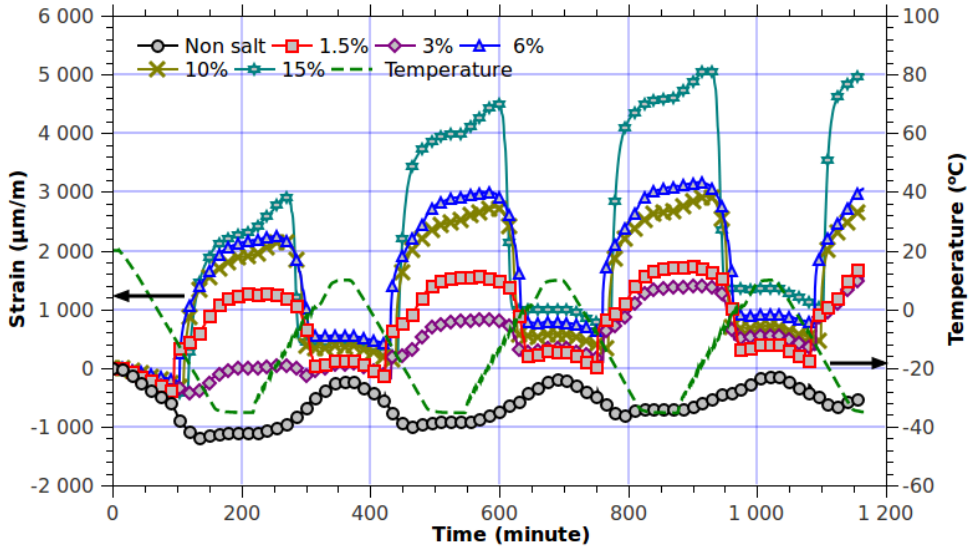

Figure 10.16: Deformation of saturated samples entrained with nominal 6% air voids (PIA4-S0→5) in terms of freeze-thaw time.

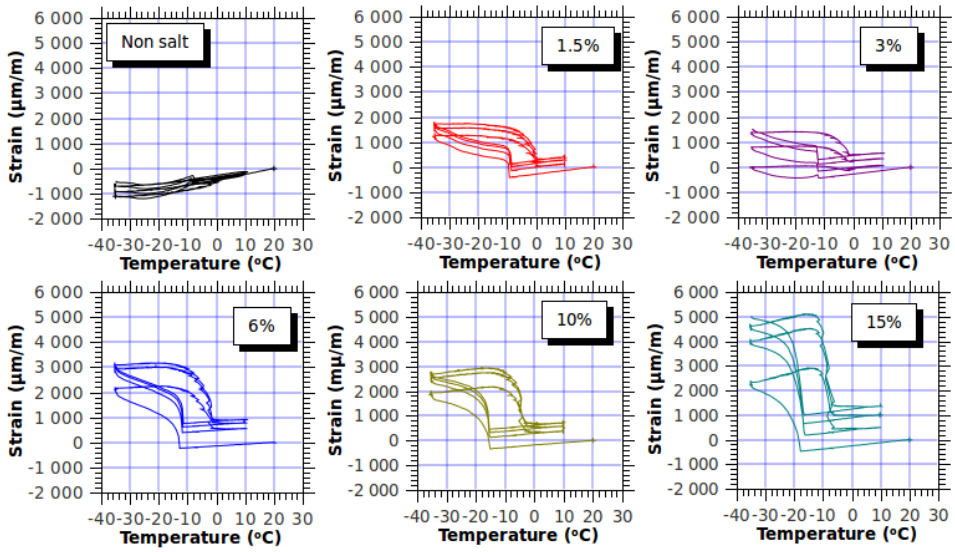

Figure 10.17: Deformation of saturated samples entrained with nominal 6% air voids (PIA4-S0→5) in terms of temperature.

Morphologically, the deformation of air-entrained cement pastes subjected to freeze-thaw loadings can be classified as three different sorts based on the characteristics of deformation curves, see Table 10.3 and top half of Figure 10.18.

For class I, no or slight nucleation deformation is followed by continual contraction and/or slight expansion when temperature is cooled down to -35℃, and no significant residual deformation occurs. The slight nucleation deformation can be due to the energy change of ice formation, which is exactly the same reason for the dilation of porous materials when the benzene is used as saturating liquid as observed in [36, 169]. The following contraction is due to the negative water pressure when the ice-water equilibrium is required at ice tip in pores [342]. The negative pressure is roughly proportional to depressed temperature as $P_l \approx -1.2227\Delta T$ MPa [356]. As freezing goes on, some capillary pores are then partially occupied by ice, and the water in 'ink-bottle' like pores is blocked. Once the blocked water crystallizes, the formed hydraulic pressure can cause damage eventually due to relatively slow pore pressure relaxation. In addition, as illustrated in Figure 10.18(a), the saturation degree of air void would increase continually with freeze-thaw cycles because the ice gem nucleated on the void-solid interface sucks the water in the adjacent capillary pore according to the cryosuction process.

For class II, the initial saturation of air void is larger. For instance, $S_l \approx 90\%$ but not arrives at full saturation, the formed ice will fill the unsaturated space due to cryosuction process mentioned above [77], which creates slight contraction after nucleation as observed in Figure 10.18(b). For further freezing, it has no room to accommodate the sucked water, the contraction stops, and it begins to expanse as ice penetrates into smaller pores.

For class III, the sample is initially saturated completely, as shown in Figure 10.18(c), once ice gem nucleates on the interface of air voids, the porous material begins to expanse. Since the samples were enclosed with resin epoxy and latex membrane, freezing occurs under undrained condition, therefore any further formation of ice will create significant hydraulic pressure and cause significant expansion as shown in Figure 10.18(c).

Definitely, the high hydraulic pressure can damage the solid skeleton of cement paste, thus significant residual deformation can be observed. It has been reported that, for the samples initially saturated with water, the surface scaling increases as the air void content increases [328]. In addition, all the three classes of saturation degree may occur in one sample: some air voids are empty, some are partially saturated and/or some are completely saturated. As in heating, the discrepancy of thermal expansion coefficients of ice and cement matrix can cause additional damage to the porous material, and the expansion of ice with temperature is probably the reason why samples continually expanse as temperature increases from -35℃ to about -15℃. Then samples contract significantly as temperature further increases to melting point

due to ice melting. The similar observations of deformation versus temperature can be found for cement based materials [107, 239, 284, 286, 340] and rock samples [330], but these experiments did not include the salt solution. Figure 10.19 shows the images of sample PIA2-S4 before and after 16 freeze-thaw cycles. It can be seen that significant damages have been caused by freeze-thaw, the strength of cement paste has been lost completely, similar to some pulverization of the normal cement-based materials after hundreds of freeze-thaw cycles under drained condition, cf. [296].

Table 10.3: The classification of deformation of air-entrained cement pastes subject to freeze-thaw loadings.

Deformation class	Description	Materials
Class I	❁ Contraction after ice nucleation; ❁ No or slight nucleation deformation $\varepsilon_{\mathrm{nu}}$; ❁ Very small deformation $\varepsilon_{\mathrm{pr}}$ by pore pressure.	PIA1-S5, PIA2-S0, PIA4-S0
Class II	❁ Slight contraction after ice nucleation; ❁ Middle nucleation deformation $\varepsilon_{\mathrm{nu}}$; ❁ Large deformation $\varepsilon_{\mathrm{pr}}$ by pore pressure, tiny extra deformation $\varepsilon_{\mathrm{ex}}$.	PIA1-S0, PIA1-S3, PIA2-S1, PIA4-S1, PIA4-S2, PIA4-S3
Class III	❁ No contraction after ice nucleation; ❁ Significant nucleation deformation $\varepsilon_{\mathrm{nu}}$; ❁ Significant deformation for both $\varepsilon_{\mathrm{pr}}$ and $\varepsilon_{\mathrm{ex}}$.	PIA1-S1, PIA1-S2, PIA1-S4, PIA2-S2, PIA2-S3, PIA2-S4, PIA3-S3, PIA3-S4, PIA3-S5, PIA4-S1, PIA4-S2, PIA4-S3, PIA4-S4, PIA4-S5.

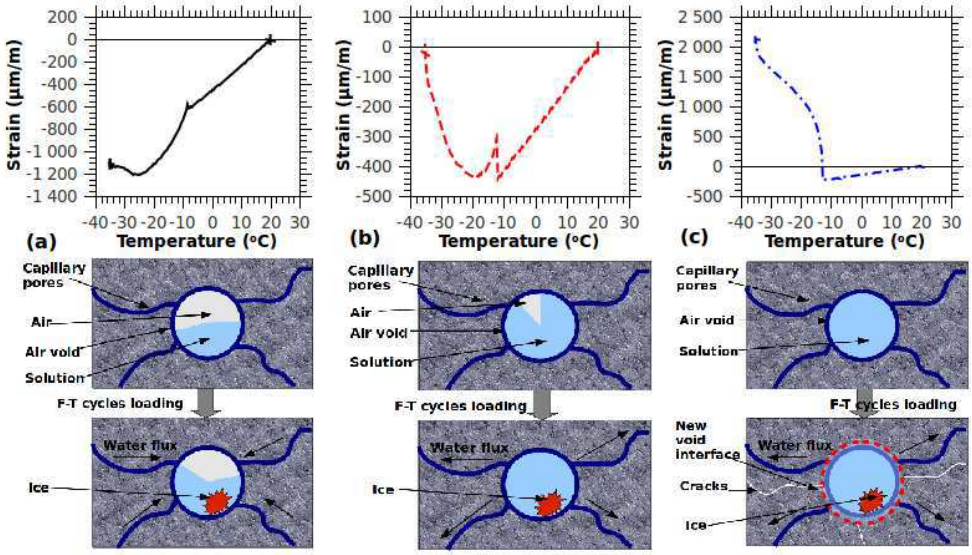

Figure 10.18: Three different sorts of deformation in terms of temperature after ice nucleation point (Top) and the proposed possible mechanisms for different deformation styles (Bottom). (a), Contraction as water flows to air voids due to negative liquid pressure; (b) Slight contraction after ice nucleation point then expansion to certain extent; (c), Significant expansion after ice nucleation.

However, the proposed mechanisms presented in Figure 10.18 can not explain the weak tendency that the samples with more NaCl salt concentration show larger deformation as presented in Table 10.3. This may be related to the saturation processes. Since the solution with higher NaCl concentration has larger surface tension, $\gamma_{lv} = 73.6 + 1.62 \times m$ mN/m at 25℃, with m the molar concentration mol/kg [240], the bigger capillary pressure can be achieved for a given pore size r by Young-Laplace law, $P_c = 2\gamma_{lv}/r$. Thus more solutions flow into air voids and achieve higher saturation degree. This hypothesis, however needs

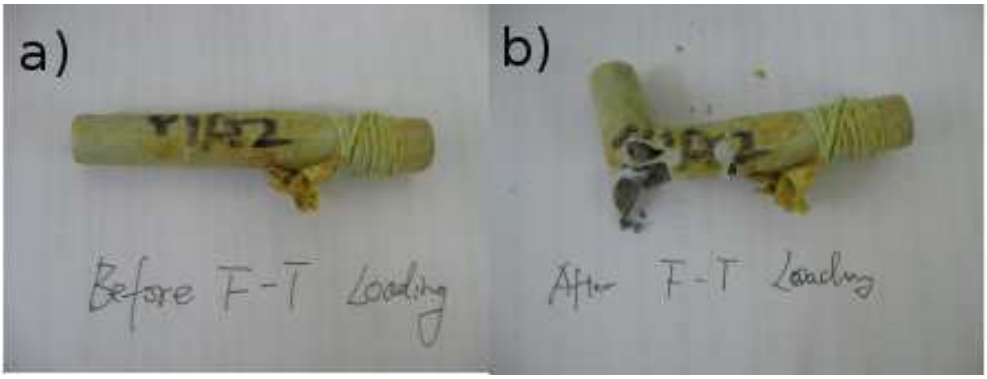

Figure 10.19: Image of an air-entrained sample before (a) and after (b) 16 freeze-thaw cycles.

further verification by experiments systematically.

10.2.3 Poromechanical analysis and discussion

The anomalous experimental observations in the previous sections may present some conflicting conclusions in the effects of air voids entrainment on deformations of cement-based materials subjected to freeze-thaw loading. The concepts of mechanisms illustrated in Figure 10.18 present us the effects of saturation degree on air voids entrained cement-based materials qualitatively. In this section, we try to address the effect of saturation degree of air voids on the strains of cement-based materials appropriately.

The average spacing factor $\bar{L}$ can be estimated by Powers theory [305],

$$\bar{L} = \frac{3}{S_a}\left[1.4\left(\frac{\phi_{\text{paste}}}{\phi_{\text{av}}}+1\right)^{1/3}-1\right] \quad \text{when} \quad \frac{\phi_{\text{paste}}}{\phi_{\text{av}}} \geq 4.342 \tag{10.10}$$

where S_a denotes the average specific surface area of spheres, $S_a = (4\pi r^2)/(\frac{4\pi}{3}r^3) = 3/r$. ϕ_{paste} represents the volume fraction of paste, ϕ_{av} represents air void content (see Table 10.1), and $\phi_{\text{paste}} + \phi_{\text{av}} = 1$. The calculated spacing factors are shown in Table 10.4, where the average size of air voids is assumed as 100μm.

Table 10.4: Powers spacing factor estimated by eq(10.10).

Materials	PA1	PA2	PA3	PA4
Air void content (%)	1.8	3.2	4.5	6.3
Spacing factor (μm)	434	341	294	252

Analogous to the calculation performed in section 5.1, different boundary conditions are used for the saturated and unsaturated cases (see Table 10.5). For the air void saturated condition, which is equivalent to undrained condition, the initial and boundary conditions are the same as those presented in Table 9.5. For the air void unsaturated condition, the element of an air void with the surrounding cement paste with thickness of $\bar{L}$ is studied. The initial and boundary conditions are similar to those presented in Table 5.2 in section 5.1, where the negative liquid pressure (when ice forms) is imposed at the surface of air void $x = 0$, and there are no water and salt flows at $x = \bar{L}$. The deformation of the cement paste embedding the air void can represent the whole deformation of material if the air voids are homogeneously distributed.

Table 10.5: Initial and boundary conditions for calculating the deformation of samples in air void saturated and unsaturated condition. The size L is the radius of sample for saturated (undrained) condition and the spacing factor $\bar{L}$ for unsaturated (drained) condition.

	Initial condition	Boundary condition
Saturated case		
Temperature	$T(t=0,x)=293(\mathrm{K})$	$T(t,x=0)=293-0.00556\times t$
Heat flow	-	$\boldsymbol{Q}\cdot\boldsymbol{n}(t,x=L)=0$
Liquid pressure	$P_l(t=0,x)=0.1(\mathrm{MPa})$	-
Water flow	-	$\boldsymbol{w}_l\cdot\boldsymbol{n}(t,x=0 \quad \text{and} \quad L)=0$
Salt concentration	$c_i(t=0,x)=0\%,1.5\%,3\%,6\%,10\%$ and 15%	-
Salt flow	-	$\boldsymbol{w}_i\cdot\boldsymbol{n}(t,x=0,x=L)=0$
Unsaturated case		
Temperature	$T(t=0,x)=293(\mathrm{K})$	$T(t)=293-0.00556\times t$
Heat flow	-	$\boldsymbol{Q}\cdot\boldsymbol{n}(t,x=\bar{L})=0$
Liquid pressure	$P_l(t=0,x)=0.1(\mathrm{MPa})$	$P_l=-P_{cap},(\mathrm{MPa})$
Water flow	-	$\boldsymbol{w}_w\cdot\boldsymbol{n}(t,x=\bar{L})=0$
Salt concentration	$c_i(t=0,x)=0\%,1.5\%,3\%,6\%,10\%$ and 15%	-
Salt flow	-	$\boldsymbol{w}_i\cdot\boldsymbol{n}(t,x=\bar{L})=0$

Because of the small size of the air void element, we assume the homogeneous temperature distribution in the surrounding cement paste. The calculation of the linear strain for air entrained cement is given in Appendix B.3.2.

Figures 10.20 to 10.23 show the deformation curves for materials under both conditions. The experimental curves are also presented in the figures for comparison. It can be found that some of the measured curves lie between the predicted curves under undrained and drained conditions, which confirms the mechanisms proposed in section 10.2.2 in some extent. From the figures, it can be found that at the cooling stage before ice nucleation, the experimental curves are above the predicted curves for both saturated and unsaturated cases. This indicates that the experimental curves show less contraction than the predicted ones at this cooling stage: the thermal expansion coefficient is lower than the used value ($11\times10^{-6}\mathrm{m}\cdot\mathrm{m}^{-1}\cdot{}^{\circ}\mathrm{C}^{-1}$). This may be due to the effect of moisture in the microstructure of cement pastes as shown in [32, 144, 353], see the literature study in section 10.1.1. For the unsaturated cases, the results show more contraction than those in saturated cases in this cooling stage. The negative pressure induced by the contraction of liquid phases under cooling can be the reason for this observation (the same observation in section 9.3 and Figure 9.15). As the cooling continues, ice nucleates at the interface of air voids and propagates into pores. For drained freezing (air void is unsaturated), the negative pressure of liquid phase required by the thermodynamic equilibrium of water-ice leads to the additional contraction of the whole material. The negative pressure of liquid phase around the ice tips also attracts the water in the smaller adjacent pores so that more contraction occurs as observed by Powers and Helmuth [310]. However, for the undrained freezing (air void is saturated), as studied in section 9.3, the negative pressure of liquid phase thus can not be valid any more. Therefore, it can be expected that, for the undrained freezing, the more the air void

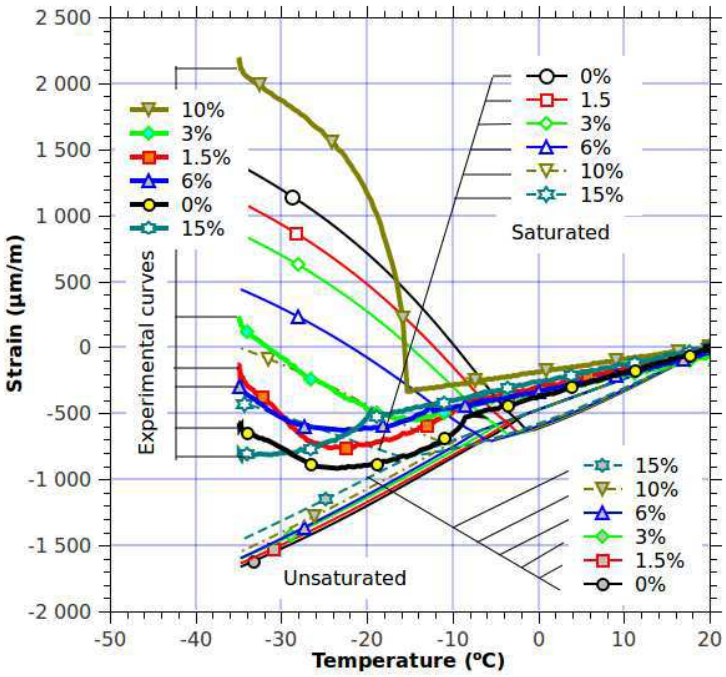

Figure 10.20: Comparison of the measured and predicted freezing deformation for samples with 1.5% air content for saturated (undrained) case and unsaturated (drained) case.

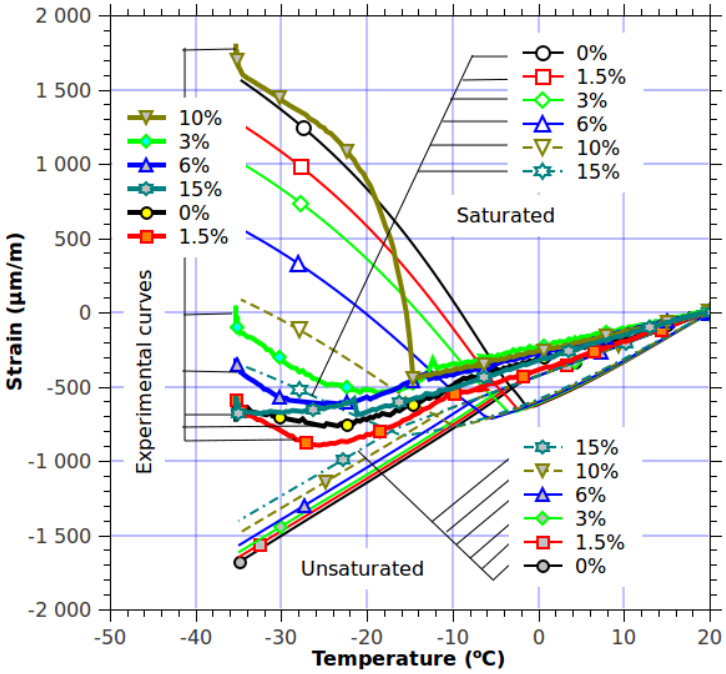

Figure 10.21: Comparison of the measured and predicted freezing deformation for samples with 3% air content for saturated (undrained) case and unsaturated (drained) case.

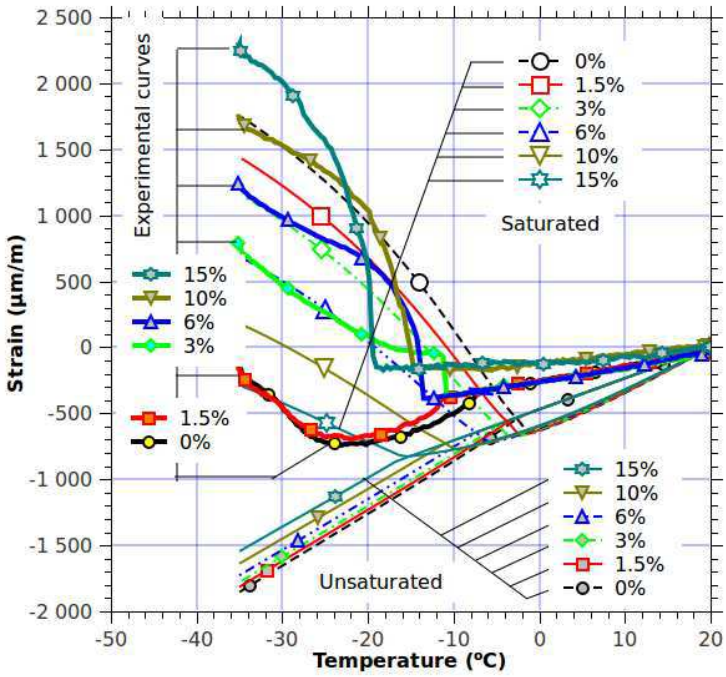

Figure 10.22: Comparison of the measured and predicted freezing deformation for samples with 4.5% air content for saturated (undrained) case and unsaturated (drained) case.

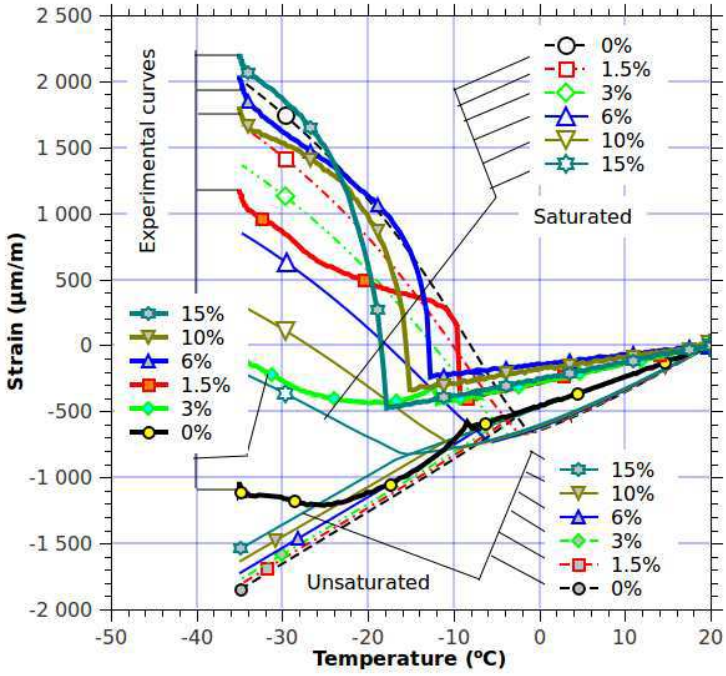

Figure 10.23: Comparison of the measured and predicted freezing deformation for samples with 6% air content for saturated (undrained) case and unsaturated (drained) case.

content, the higher the liquid pressure and the larger the ultimate expansion. As shown in Figures 10.20 to 10.23, the maximum expansion for samples initially saturated with pure water show 1400 μm/m to 2000 μm/m as air content increases from 1.5% to 6%.

Unfortunately, we can not figure out the saturation degree required by the experimental curves for all specimens quantitatively. Nevertheless, the continual expansion when temperature is held constant at -35℃ shown in Figures 10.10 to 10.17, can not be explained by the present model. This kind of expansion has been recognized for more than half century by Powers and Helmuth [310]. In addition, some samples saturated with saline solution show larger expansion than those with pure water, see the deformation curves for samples saturated with, for instance, 10% NaCl in Figures 10.20 and 10.21, and samples saturated with brine in Figures 10.22 and 10.23, which are rather anomalous. All the above mentioned questions need further researches systematically.

Conclusion

Ice formation in porous materials

The basic principle of ice formation in porous materials relies on the thermodynamic equilibrium. This allows us to find a equation to relate the capillary pressure to the liquid pressure, water activity and entropy change of melting. As a non-wetting invasion process, the penetration of ice with the depression temperature provides us a method to measure the pore size distribution, named cryo-porosimetry. The activity of ions can be a combination of the individual ionic long-rang interaction and short-range solvation effect. The ionic parameter approaches are used to evaluate the ionic activity, the osmotic coefficient and water activity.

Literature study indicated that water is more likely to transfer to the cubic ice (I_c) rather than the hexagonal ice (I_h) when confined in pores of nano-size. The ice growth rate and ice crystal structure are associated with temperature. The freeze-thaw hysteresis can be due to the contact angle difference between freezing and melting, the pore curvature-induced metastability of the solid phase and the 'ink-bottle' like pore structure. Experimental measurements indicated that the depressed supercooling temperature is 3.4∼11 K lower than the bulk melting temperature. By using the probability analysis and the Gibbs energy based theory, the contact angle between ice and pore wall is evaluated and it decreases from 25° to 20° when the NaCl concentration increases from zero to 15 wt%.

Hydration and pore structure of cement pastes

With help of the Avrami equation and the CM model proposed by Jennings and coworkers, the content of hydration products and porosity are evaluated explicitly. The pore structure of our cement pastes is studied comprehensively by nitrogen adsorption/desorption (NAD) and mercury intrusion porosimetry (MIP). The pore structure is the result of the related hydration processes of cement. Both chemical reaction kinetics and physical packing of hydrates account for the pore structure. For specific surface area measurements, the Langmuir, BET, BJH and t-plot approaches give comprehensive information. The specific surface area

of paste I is systematically larger than that of paste II because paste I contains more accessible LD C-S-H. The maximum pore volume and specific surface area for paste II at 28 D are observed due to the coupled hydration and miscrostructure change of C-S-H with time. The average porosity of paste I and paste II decrease from 0.39 and 0.24 to 0.33 and 0.21 respectively as curing age increases from 7D to 180D. The critical pore size, threshold pore size and mean pore size decrease with curing age monotonously due to the elimination of percolated capillary pores. For pore size distribution measurement, MIP provides a reliable distribution on a large pore size range, while the NAD measurement affords more detailed information on ton micropore and meso-pore ranges.

Mechanical and transport properties of cement pastes

By means of a multi-scale homogenization model, we are capable of predicting the poroelastic parameters of a hardened cement paste by knowing the volume fractions and the elastic properties of the constituents of its microstructure. Appropriate models are presented for evaluation of the volume fractions by knowing the chemical composition and density of the cement clinkers and w/c ratio. The evaluated bulk modulus, shear modulus and undrained bulk modulus for paste I(II), respectively, are 14.6(20.2) GPa, 6.4(10.0) GPa and 17.4(23.5) GPa, which are close to the data in literature.

The transport properties of cement pastes are also evaluated by the multi-scale modeling. The Eshelbian form solution is recalled for approaching the effective conductivity/permeability by assuming permeable and/or impermeable phases embedded in the homogenized medium. The Katz-Thompson equation is recalled to correlate the conductivity to the permeability. At the level of cement pastes, the capillary pores are specially considered, and the effective medium theory is adopted to calculate the overall conductivity. A good agreement between the predicted results and the experimental results from literature confirms the capability of this kind of model.

Freezing strains of cement pastes: poromechanical analysis and experimental observation

A thermoporomechanical model is established to describe the behaviors of cement-based materials subjected to freeze-thaw loading, following the comprehensive studies by Olivier Coussy and coworkers. This model takes the basic variables: temperature, liquid pressure and salt concentrations. To achieve more accuracy results, the physico-chemical properties of NaCl solution are estimated by the Archer's empirical equations. The saturation degree curve, which is a governable parameter correlating the pore structure to the macromechanical properties by poromechanics, is evaluated by means of the capillary

relations. The multi-Gauss fitting is retained to characterize the pore size distribution by means of the MIP data. Because paste I contains more large capillary pores, more ice forms in paste I than in paste II at a certain subzero temperature. The more salt it contains, the less ice forms.

Analysis on the cement-based materials saturated with water in literature has been performed as a case study. Good agreement between the predicted curves and the measured curves confirms the robustness of the poromechanical model. The negative liquid pressure required by the thermodynamic equilibrium between ice and water accounts for the continual shrinkage after ice nucleation for air-entrained cement paste, and the pore pressure relaxation accounts for the slight shrinkage when temperature is kept constant. For the cement paste without air entrainment, the pore pressure can be built up rapidly when water crystallizes. The effect of supercooling on the instantaneous dilation is analyzed and compared to the experimental data obtained by Glüble and Stokin as another case study. To avoid the metastability of water under supercooling before ice nucleation, a temperature routine is designed specially. The temperature is first kept at zero, then rapidly cooled to the depressed supercooling temperature. The thermal shock by heat releasing when ice forms is considered as well. The predicted results indicated that the instantaneous deformation at the end of supercooling can be due to the immediate ice formation and the thermal shock.

Deformations for cement pastes initially dried and saturated with NaCl solution at different concentrations are measured. Carefully sample preparation and apparatus calibration are performed to avoid undesirable errors. Samples are covered with a layer of thin epoxy and condom to prevent the mass exchange. For dried samples, paste II has larger TEC than paste I, because paste II contains more CH and C-S-H. For samples saturated with saline solutions, almost all the samples of paste I show significant expansion after ice nucleation, whereas samples of paste II show no expansion. The primary reason for the observation is the pore structure: paste II has thinner pore size distribution thus contains less ice during freezing. Six sorts of deformations are classified based on the shape of the strain-temperature or strain-time curves. The residual deformation after one complete freeze-thaw cycle indicates the permanent deterioration induced by the fracture damage. The poromechanical analyses on the freezing behaviors of initially saturated samples indicate that the ice formation can be one of the most important deformation sources. The thermal contraction at the cooling stage before ice nucleation can be due to the pure thermal deformation of paste solids and the negative pressure induced by the temperature dependent mass density of liquid solution.

Effect of air voids and saturation degree

The effect of air voids on the freezing behaviors of cement pastes has been specifically considered in the present work. Following the arguments on the effect of the porosity on TEC, we measured the TEC

of pastes and mortars entrained with four different dosages of air voids. The results show that the TEC decreases with porosity and/or air void content through a power law, $\alpha_d = \alpha_0(1-\phi)^C$. The exponents C of pastes and mortars are respectively 2.66 and 2.38 for ϕ = total porosity and 3.74 and 2.69 for ϕ = air void content. From the available chemistry and microstructure analyses of air voids entrained in cement pastes, is confirmed the existence of a dense shell around air void and rich in low C/S ratio C-S-H. This shell structure, associated with the entrained air voids, may be responsible for the TEC decrease.

Deformation measurements have been performed when air entrained cement pastes saturated with NaCl solution at different concentrations are subjected to freeze-thaw loading. Very anomalous deformation-time and/or deformation-temperature curves can be observed: the significant ultimate deformation at -35℃ appears for samples with high salt concentrations (cf. PIAX-S4 with 10% NaCl and PIAX-S5 with 15% NaCl). Three different sorts of freezing deformation curves can be classified according to their shapes. The crucial factor for the deformations may be the initial saturation degree in air voids. Poromechanical analyses under the undrained and drained condition have been performed. Some of the measured curves lie between the predicted curves of undrained and drained conditions, which confirms the relevance of our self-contained approach developed in the present work. However, some deformation curves lie beyond the predicted area and samples show continual expansion when temperature is held constant at -35℃, which can not be explained by this model. Those need further relevant researches.

Bibliography

[1] http://www.cement.org/tech/cct_dur_freeze-thaw.asp.

[2] http://www.ctu.edu.vn/colleges/tech/bomon/ktxd/baigiang/CONCRETE-/Chap.8./Chap8.pdf, 2009.

[3] A. Ababneh, F. Benboudjema, and Y. Xi. Chloride penetration in nonsaturated concrete. *J. Mater. Civil Eng. -ASCE*, 15(2):183–191, 2003.

[4] I. M. Abdulagatov and U. B. Magomedov. Thermal conductivity of aqueous solutions of NaCl and KCl at high pressures. *Int. J. Thermophys.*, 15(3):401–413, 1994.

[5] D. Abrams. *Design of concrete mixtures*, volume 1. Structural Materials Research Laboratory, Lewis Institute, 1919.

[6] P. Acker. Micromechanical analysis of creep and shrinkage mechanisms. In *Creep, Shrinkage and Durability Mechanics of Concrete and other quasi-brittle Materials: Proc. Int. Conf. CONCREEP*, pages 15–25, Cambridge, MA, UAS, August 2001.

[7] N. M. Akhras. Detecting freezing and thawing damage in concrete using signal energy. *Cem. Concr. Res.*, 28(9):1275–1280, 1998.

[8] N. N. Akinfiev, M. V. Mironenko, and S. A. Grant. Thermodynamic properties of NaCl solutions at subzero temperatures. *J. Solut. Chem.*, 30(12):1065–1080, 2001.

[9] M. Akyurt, G. Zaki, and B. Habeebullah. Freezing phenomena in ice-water systems. *Energy Convers. Manage.*, 43(14):1773–1789, 2002.

[10] K. K. Aligizaki. *Pore structure of cement-based materials: testing, interpretation and requirements*. Spon Press, 2006.

[11] A. J. Allen and J. J. Thomas. Analysis of csh gel and cement paste by small-angle neutron scattering. *Cem. Concr. Res.*, 37(3):319–324, 2007.

[12] A. J. Allen, J. J. Thomas, and H. M. Jennings. Composition and density of nanoscale calcium–silicate–hydrate in cement. *Nat. Mater.*, 6(4):311–316, 2007.

[13] K. O. Ampadu, K. Torii, and M. Kawamura. Beneficial effect of fly ash on chloride diffusivity of hardened cement paste. *Cem. Concr. Res.*, 29(4):585–590, 1999.

[14] A. Antonyraj, S. J. Park, and R. German. Thermal expansion and viscoelastic properties of sintered porous compact. In *Proceedings of the 2007 International Conference On Powder Metallurgy & Particulate Materials: Part I, Design & Modeling of PM Materials, Components & Processes*, Denver, Colorado, USA, May 2007.

[15] D. G. Archer. Thermodynamic properties of the NaCl+ H2O system. i. thermodynamic properties of nacl (cr). *J. Phys. Chem. Ref. Data*, 21(1):1–21, 1992.

[16] D. G. Archer. Thermodynamic properties of the NaCl+ H2O system. ii. thermodynamic properties of nacl (aq), nacl·2h2o, and phase equilibria. *J. Phys. Chem. Ref. Data*, 21(4):793–829, 1992.

[17] D. G. Archer and R. W. Carter. Thermodynamic properties of the NaCl+ H2O system. 4. heat capacities of h2o and nacl (aq) in cold-stable and supercooled states. *J. Phys. Chem. B*, 104(35):8563–8584, 2000.

[18] D. G. Archer and P. Wang. The dielectric constant of water and Debye-Hückel limiting law slopes. *J. Phys. Chem. Ref. Data*, 19(2):371–411, 1990.

[19] G. E. Archie. The electrical resistivity log as an aid in determining some reservoir characteristics. *Am. Inst. Min. Metal. Trans.*, 146:54–62, 1942.

[20] G. P. Arnold, E. D. Finch, S. W. Rabideau, and R. G. Wenzel. Neutron-diffraction study of ice polymorphs. iii. ice ih. *J. Chem. Phys.*, 49:4365–4369, 1968.

[21] C. ASTM. 666. *Standard Test Method for Resistance of Concrete to Rapid Freezing and Thawing," American Society for Testing Materials, West Conshohocken, PA*, 2003.

[22] C. ASTM. 672. *Standard Test Method for Scaling Resistance of Concrete Surfaces Exposed to Deicing Chemicals", Annual Book of ASTM Standards*, 4, 2003.

[23] H. N. Atahan, C. Carlos Jr, S. Chae, P. J. M. Monteiro, and J. Bastacky. The morphology of entrained air voids in hardened cement paste generated with different anionic surfactants. *Cem. Concr. Compos.*, 30(7):566–575, 2008.

[24] P. Atkins and J. de Paula. *Physical chemistry*. Oxford, 8th, edition, 2006.

[25] D. H. Bager and E. J. Sellevold. Ice formation in hardened cement paste, part i–room temperature cured pastes with variable moisture contents. *Cem. Concr. Res.*, 16(5):709–720, 1986.

[26] D. H. Bager and E. J. Sellevold. Ice formation in hardened cement paste, part ii–drying and resaturation on room temperature cured pastes. *Cem. Concr. Res.*, 16(6):835–844, 1986.

[27] D. H. Bager and E. J. Sellevold. Ice formation in hardened cement paste, part iii–slow resaturation of room temperature cured pastes. *Cem. Concr. Res.*, 17(1):1–11, 1987.

[28] V. Baroghel-Bouny, S. Arnaud, D. Henry, M. Carcasses, and D. Quenard. Vieillissement des bt́ons en milieu naturel : une expérimentation pour le XXIe siècle. iii-propriétés de durabilité des bétons mesurées sur éprouvettes conservées en laboratoir. *Bulletin des laboratoires des ponts et chaussées*, 241:13–59, 2002.

[29] E. P. Barrett, L. G. Joyner, and P. P. Halenda. The determination of pore volume and area distributions in porous substances. i. computations from nitrogen isotherms. *J. Am. Chem. Soc.*, 73(1):373–380, 1951.

[30] F. Bartoli, N. Bird, V. Gomendy, H. Vivier, and S. Niquet. The relation between silty soil structures and their mercury porosimetry curve counterparts: fractals and percolation. *Euro. J. soil Sci.*, 50(1):9–22, 1999.

[31] B. Bary and S. Béjaoui. Assessment of diffusive and mechanical properties of hardened cement pastes using a multi-coated sphere assemblage model. *Cem. Concr. Res.*, 36(2):245–258, 2006.

[32] Z. P. Bazant. Delayed thermal dilatations of cement paste and concrete due to mass transport. *Nucl. Eng. Des.*, 14(2):308–318, 1970.

[33] J. Bear and Y. Bachmat. *Introduction to modeling of transport phenomena in porous media*. Kluwer Academic Publishers, The Netherlands, 1991.

[34] J. J. Beaudoin. Comparison of mechanical properties of compacted calcium hydroxide and portland cement paste systems. *Cem. Concr. Res.*, 13(3):319–324, 1983.

[35] J. J. Beaudoin and C. MacInnis. The effect of admixtures on length change anomalies due to slow cooling and warming of hardened cement paste. *Cem. Concr. Res.*, 4(3):347–356, 1974.

[36] J. J. Beaudoin and C. MacInnis. The mechanism of frost damage in hardened cement paste. *Cem. Concr. Res.*, 4(2):139–147, 1974.

[37] R. E. Beddoe and M. J. Setzer. A low-temperature DSC investigation of hardened cement paste subjected to chloride action. *Cem. Concr. Res.*, 18(2):249–256, 1988.

[38] M. C. Bellissent-Funel, J. Lal, and L. Bosio. Structural study of water confined in porous glass by neutron scattering. *J. Chem. Phys.*, 98:4246–4248, 1993.

[39] A. Benazzouk, O. Douzane, K. Mezreb, B. Laidoudi, and M. Quéneudec. Thermal conductivity of cement composites containing rubber waste particles: Experimental study and modelling. *Constr. Build. Mater.*, 22(4):573–579, 2008.

[40] D. P. Bentz. Three-dimensional computer simulation of portland cement hydration and microstructure development. *J. Am. Ceram. Soc.*, 80(1):3–21, 1997.

[41] D. P. Bentz. Influence of silica fume on diffusivity in cement-based materials:: II. multi-scale modeling of concrete diffusivity. *Cem. Concr. Res.*, 30(7):1121–1129, 2000.

[42] D. P. Bentz, O. M. Jensen, A. M. Coats, and F. P. Glasser. Influence of silica fume on diffusivity in cement-based materials:: I. experimental and computer modeling studies on cement pastes. *Cem. Concr. Res.*, 30(6):953–962, 2000.

[43] D. P. Bentz, O. M. Jensen, K. K. Hansen, J. F. Olesen, H. Stang, and C. J. Haecker. Influence of cement particle-size distribution on early age autogenous strains and stresses in cement-based materials. *J. Am. Ceram. Soc.*, 84(1):129–135, 2001.

[44] K. Benzarti, C. Perruchot, and M. M. Chehimi. Surface energetics of cementitious materials and their wettability by an epoxy adhesive. *Colloids Surf., A*, 286(1-3):78–91, 2006.

[45] Y. Bernabé and C. Bruderer. Effect of the variance of pore size distribution on the transport properties of heterogeneous networks. *J. Geophys. Res.*, 103:513–525, 1998.

[46] O. Bernard, F. J. Ulm, and E. Lemarchand. A multiscale micromechanics-hydration model for the early-age elastic properties of cement-based materials. *Cem. Concr. Res.*, 33(9):1293–1309, 2003.

[47] J. O. M. Bockris and A. K. N. Reddy. *Modern electrochemistry*. Springer Us, 2nd, eds. edition, 2001.

[48] R. H. Bogue. Calculation of the compounds in portland cement. *Ind. Eng. Chem. Anal.*, 1(4):192–197, 1929.

[49] N. Boukpeti. One-dimensional analysis of a poroelastic medium during freezing. *Int. J. Num. Anal. Met. Geom.*, 32(13):1661–1691, 2008.

[50] A. D. Brailsford and K. G. Major. The thermal conductivity of aggregates of several phases, including porous materials. *Br. J. Appl. Phys.*, 15:313, 1964.

[51] D. Breysse and B. Gerard. Modelling of permeability in cement-based materials: Part 1, uncracked medium. *Cem. Concr. Res.*, 27(5):761–775, 1997.

[52] J. C. P. Broekhof and J. H. de Boer. Studies on pore systems in catalysts : Ix. calculation of pore distributions from the adsorption branch of nitrogen sorption isotherms in the case of open cylindrical pores a. fundamental equations. *J. Cata.*, 9:8–14, 1967.

[53] M. Brun, A. J. Lallement, F. Quinson, and C. Eyraudand. A new mehtod for the simultaneous determination of the size and the shape of pores:the thermoporometry. *Thermochimica Acta*, 21:59–88, 1977.

[54] S. Brunauer, P. H. Emmett, and E. Teller. Adsorption of gases in multimolecular layers. *J. Am. Chem. Soc.*, 60(2):309–319, 1938.

[55] N. R. Buenfeld and J. B. Newman. Examination of three methods for studying ion diffusion in cement pastes, mortars and concrete. *Mater. Struct.*, 20(1):3–10, 1987.

[56] A. E. Bussian. Electrical conductance in a porous medium. *Geophys.*, 48(9):1258–1268, 1983.

[57] M. A. Celia, S. Bachu, J. M. Nordbotten, S. E. Gasda, and H. K. Dahle. Quantitative estimation of CO2 leakage from geological storage: Analytical models, numerical models and data needs. In *Proceedings of 7th International Conference on Greenhouse Gas Control Technologies.(GHGT-7)*, pages 5–9, September 2004.

[58] cembureau. World cement production 2010, by region and main countries. http://www.cembureau.be/about-cement/key-facts-figures, 2010.

[59] S. Chandra and A. Xu. Influence of presaturation and freeze-thaw test conditions on length changes of portland cement mortar. *Cem. concr. res.*, 22(4):515–524, 1992.

[60] T. Cho. Prediction of cyclic freeze-thaw damage in concrete structures based on response surface method. *Constr. Build. Mater.*, 21(12):2031–2040, 2007.

[61] B. J. Christensen, T. O. Mason, and H. M. Jennings. Comparison of measured and calculated permeabilities for hardened cement pastes. *Cem. Concr. Res.*, 26(9):1325–1334, 1996.

[62] CIMBÉTON. Collection technique cimb'eton g12: Les ouvrages en béton: durabilité, dimensionnementet esthétique. http://www.scribd.com/doc/54192613/10/Recommandations-pour-la-durabilite-des-betons.

[63] M. A. Climent, G. de Vera, J. F. López, E. Viqueira, and C. Andrade. A test method for measuring chloride diffusion coefficients through nonsaturated concrete. Part I: The instantaneous plane source diffusion case. *Cem. Concr. Res.*, 32(7):1113–1123, 2002.

[64] A. Commitee. 211.1-91. standard practice for selecting proportions for normal, heavyweight, and mass concrete. *ACI manual of concrete practice, Part*, 1:1–38, 1991.

[65] G. Constantinides. The elastic properties of calcium-leached cement pastes and mortars:a multi-scale investigation. Master's thesis, Massachusetts Institute of Technology, Cambridge, MA, USA, 2002.

[66] G. Constantinides. *Invariant Mechanical Properties of Calcium-Silicate-Hydrates (C-S-H) in Cement-Based Materials: Instrumented Nanoindentation and Microporomechanical Modeling.* PhD thesis, Massachusetts Institute of Technology, USA, 2006.

[67] G. Constantinides and F. J. Ulm. The effect of two types of csh on the elasticity of cement-based materials: Results from nanoindentation and micromechanical modeling. *Cem. Concr. Res.*, 34(1):67–80, 2004.

[68] G. Constantinides and F. J. Ulm. The nanogranular nature of CSH. *J. Mech. Phys. Solid.*, 55(1):64–90, 2007.

[69] G. Constantinides, F. J. Ulm, and K. Van Vliet. On the use of nanoindentation for cementitious materials. *Mater. Struct.*, 36(3):191–196, 2003.

[70] H. W. Cooper and G. Simmons. The effect of cracks on the thermal expansion of rocks. *Earth Planet. Sci. Lett.*, 36(3):404–412, 1977.

[71] O. Copuroglu. *The characterization, improvement and modelling aspects of Frost Salt Scaling of Cement-Based Materials with a High Slag Content.* PhD thesis, Technische Universiteit Delft, The Netherlander, 2006.

[72] O. Copuroglu and E. Schlangen. Modeling of frost salt scaling. *Cem. Concr. Res.*, 38(1):27–39, 2008.

[73] D. J. Corr, M. C. G. Juenger, P. J. M. Monteiro, and J. Bastacky. Investigating entrained air voids and portland cement hydration with low-temperature scanning electron microscopy. *Cem. Concr. Comp.*, 26(8):1007–1012, 2004.

[74] D. J. Corr, P. J. M. Monterio, and J. Baskacky. Microscopic characterization of ice morphology in entrained air voids. *ACI Material Journa*, 99(2):190–195, 2002.

[75] E. R. Cortez and R. A. Eaton. Freeze-thaw tests of full-scale roller-compacted concrete test sections. Technical report, U.S. Army Engineer Research and Development Center, July 1990.

[76] O. Coussy. *Poromechanics.* John Wiley&Sons, The Atrium, Southern Gate, Chichester, West Sussex, second edition, 2004.

[77] O. Coussy. Poromechanics of freezing materials. *J. Mech. Phys. Solids*, 53(8):1689–1718, 2005.

[78] O. Coussy. Deformation and stress from in-pore drying-induced crystallization of salt. *J. Mech. Phys. Solids*, 54(8):1517–1547, 2006.

[79] O. Coussy. *Mechanics and physics of porous solids*. John Wiley&Sons, The Atrium, Southern Gate, Chichester, West Sussex, 2010.

[80] O. Coussy and T. Fen-Chong. Crystallization, pore relaxation and micro-cryosuction in cohesive porous materials. *C. R. Mécanique.*, 333(6):507–512, 2005.

[81] O. Coussy and P. J. M. Monteiro. Unsaturated poroelasticity for crystallization in pores. *Comput. Geotech.*, 34(4):279–290, 2007.

[82] O. Coussy and P. J. M. Monteiro. Poroelastic model for concrete exposed to freezing temperature. *Cem. Concr. Res.*, 38(1):40–48, 2008.

[83] S. M. Cramer and J. R. A. Walls. Strategies for enhancing the freeze-thaw durability of portland cement concrete pavements. Technical report, University of Wisconsin - Madison Department of Civil and Environmental Engineering, Report Number: WI/SPR-06-01, July 2001.

[84] R. W. Cranston and F. A. Inkley. The determination of pore structures from nitrogen adsorption isotherms. In *Proc. Inter. Congr. Cata.*, pages 143–154. Academic Press, 1957.

[85] L. Cui and J. H. Cahyadi. Permeability and pore structure of OPC paste. *Cem. Concr. Res.*, 31(2):277–282, 2001.

[86] P. Dangla. Bil: a finite volume and/or element code. http://perso.lcpc.fr/dangla.patrick/bil/, 2009.

[87] D. Darwin, J. A. Browning, L. Gong, and S. R. Hughes. Effects of deicers on concrete deterioration. *ACI Mater. J.*, 105(6):622–627, 2008.

[88] R. Dasgupta, S. Roy, and S. Tarafdar. Correlation between porosity, conductivity and permeability of sedimentary rocks–a ballistic deposition model. *Physica A*, 275(1-2):22–32, 2000.

[89] J. G. Dash, H. Fu, and J. S. Wettlaufer. The premelting of ice and its environmental consequences. *Rep. Progr. Phys.*, 58:115–167, 1995.

[90] J. H. De Boer, B. G. Linsen, and T. J. Osinga. Studies on pore systems in catalysts:: Vi. the universal t curve. *J. Cata.*, 4(6):643–648, 1965.

[91] J. H. De Boer, B. C. Lippens, B. G. Linsen, J. C. P. Broekhoff, A. Van den Heuvel, and T. J. Osinga. Thet-curve of multimolecular n2-adsorption. *J. Colloid Interf. Sci.*, 21(4):405–414, 1966.

[92] R. de Boer and N. Katsube. Theory of porous media: Highlights in historical development and current state. *Appl. Mech. Rev.*, 55:B32, 2002.

[93] G. de Vera, M. A. Climent, E. Viqueira, C. Anton, and C. Andrade. A test method for measuring chloride diffusion coefficients through partially saturated concrete. Part II: The instantaneous plane source diffusion case with chloride binding consideration. *Cem. Concr. Res.*, 37(5):714–724, 2007.

[94] P. Debye and E. Hückel. The theory of electrolytes. I. lowering of freezing point and related phenomena. *Zeitschrift für Physik*, 24:304–324, 1923.

[95] M. R. Deinert, A. Dathe, J. Y. Parlange, and K. B. Cady. Capillary pressure in a porous medium with distinct pore surface and pore volume fractal dimensions. *Phys. Rev. E.*, 77(2):021203, 2008.

[96] J. Deja. Freezing and de-icing salt resistance of blast furnace slag concretes. *Cem. Concr. Compos.*, 25(3):357–361, 2003.

[97] R. Denoyel and R. J. M. Pellenq. Simple phenomenological models for phase transitions in a confined geometry. 1: Melting and solidification in a cylindrical pore. *Langmuir*, 18(7):2710–2716, 2002.

[98] E. Detournay and H. D. C. Alexander. *Fundamentals of Poroelasticity*, volume Vol. II, Analysis and Design Method, pages 113–171. Pergamon Press, 1993.

[99] S. Diamond. Mercury porosimetry:: An inappropriate method for the measurement of pore size distributions in cement-based materials. *Cem. Concr. Res.*, 30(10):1517–1525, 2000.

[100] S. Diamond. Percolation due to overlapping ITZs in laboratory mortars? a microstructural evaluation. *Cem. Concr. Res.*, 33(7):949–955, 2003.

[101] J. Dipayan. Concrete scaling - a critical review,. In *Proceedings of the twenty-ninth conference on cement microscopy*, Quebec city, PQ, Canada, May 2007.

[102] A. Döppenschmidt and H. J. Butt. Measuring the thickness of the liquid-like layer on ice surfaces with atomic force microscopy. *Langmuir*, 16(16):6709–6714, 2000.

[103] L. Dormieux, A. Molinari, and D. Kondo. Micromechanical approach to the behavior of poroelastic materials. *J. Mech. Phys. Solids*, 50(10):2203–2231, 2002.

[104] N. E. Dorsey. The freezing of supercooled water. *Trans. Am. Philos. Soc.*, 38(3):247–328, 1948.

[105] F. A. L. Dullien. *Porous Media: Fluid Transport and Pore Structure*. Academic Press, 1992.

[106] M. Dunn, J. C. Dore, , and P. Chieux. Structure study of ice formation in porous silics by neutron diffraction. *J. Cryst. Growth.*, 92:233–238, 1988.

[107] A. Durekovic, V. Calogovic, and K. Popovic. Frost resistance of OPC-CSF mortars investigated by means of repeated cycle-and one cycle-freezing test. *Cem. Concr. Res.*, 19(2):267–277, 1989.

[108] J. C. Echeverria, M. T. Morera, C. Mazkiarán, and J. J. Garrido. Characterization of the porous structure of soils: Adsorption of nitrogen (77 k) and carbon dioxide (273 k), and mercury porosimetry. *Eur. J. Soil Sci.*, 50(3):497–503, 1999.

[109] A. El-Dieb and R. Hooton. Water-permeability measurement of high performance concrete using a high-pressure triaxial cell. *Cem. Concr. Res.*, 25(6):1199–1208, 1995.

[110] S. Engemann, H. Reichert, H. Dosch, J. Bilgram, V. Honkimäki, and A. Snigirev. Interfacial melting of ice in contact with SiO2. *Phys. Rev. Lett.*, 92(20):205701–704, 2004.

[111] J. I. Escalante-Garcia. Nonevaporable water from neat opc and replacement materials in composite cements hydrated at different temperatures. *Cem. Concr. Res.*, 33(11):1883–1888, 2003.

[112] J. D. Eshelby. The determination of the elastic field of an ellipsoidal inclusion, and related problems. *Proc. Roy. Soc. A.*, 241(1226):376–392, 1957.

[113] D. H. Everett. The thermodynamics of frost damage to porous solids. *Trans. Faraday Soc.*, 57:1541–1551, 1961.

[114] A. Fabbri. *Physico-mécanique des matériaux cimentares soumis au gel-d'gel*. PhD thesis, Department of civil engineering, Unversité de Marne-La-Vallée, France, 2006.

[115] A. Fabbri, O. Coussy, T. Fen-Chong, and P. J. M. Monteiro. Are deicing salts necessary to promote scaling in concrete? *J. Eng. Mech.-ASCE*, 134:589–601, 2008.

[116] G. Fagerlund. Determination of pore size distribution by suction porosimetry. *Mater. Structr.*, 6(3):191–201, 1973.

[117] G. G. Fagerlund. The significance of critical degrees of saturation at freezing of porous and brittle materials. In *Durability of concrete. ACI Publication SP-47*, pages 13–66, Detroit, USA, 1975.

[118] G. G. Fagerlund. Studies of the destruction mechanism at freezing of porous materials. In *Proceedings of the 6th international congress on the problems raised by frost action*, Le Havre, France, April 1975.

[119] G. G. Fagerlund. Absorption and dilation of cement mortar specimens exposed to freezing and thawing in NaCl solution. In J. Marchand, M.Pigeon, and M. J. Setzer, editors, *Freezing Thaw Durability of Concrete: Proceedings of the International Workshop in the Resistance of Concrete to Scaling Due to Freezing in the Presence of De-icing Salts*, pages 51–66, Sainte-Foy, Québec, Canada, 1992.

[120] G. G. Fagerlund. Mechanical damage and fatigue effects associated with freeze-thaw of materials. In Setzer et al. [359], pages 117–132.

[121] M. P. Fang, P. E. Sokol, J. Y. Jehng, and W. P. Halperin. Neutron diffraction study of cement. *J. Porous Mater.*, 6:95–99, 1999.

[122] R. F. Feldman. Pore structure, permeability and diffusivity as related to durability. In *Proceedings of 8th International Congress on the Chemistry of Cement*, pages 1–21, Rio de Janeiro, Brazil, September 1986. National Research Council Canada, Institute for Research in Construction.

[123] E. D. Finch, S. W. Rabideau, R. G. Wenzel, and N. G. Nereson. Neutron-diffraction study of ice polymorphs. ii. ice ii. *J. Chem. Phys.*, 49:4361–4365, 1968.

[124] N. H. Fletcher. Surface structure of water and ice. *Philos. Mag.*, 18:1287–1300, 1968.

[125] N. H. Fletcher. Structural aspects of the ice-water system. *Rep. Prog. Phys.*, 34:913–994, 1971.

[126] S. P. Friedman and N. A. Seaton. Critical path analysis of the relationship between permeability and electrical conductivity of three-dimensional pore networks. *Water Resour. Res.*, 34(7):1703–1710, 1998.

[127] Y. Fu, L. Cai, and W. Yonggen. Freeze-thaw cycle test and damage mechanics models of alkali-activated slag concrete. doi:10.1016/j.conbuildmat.2010.12.006, 2011.

[128] Y. F. Fu, Y. L. Wong, C. S. Poon, and C. A. Tang. Numerical tests of thermal cracking induced by temperature gradient in cement-based composites under thermal loads. *Cem. Concr. Compos.*, 29(2):103–116, 2007.

[129] Y. C. Fung and P. Tong. *Classical and computational solid mechanics*. World Science Printers, Singapore, 2001.

[130] J. M. Gao, C. X. Qian, B. Wang, and K. Morino. Experimental study on properties of polymer-modified cement mortars with silica fume. *Cem. Concr. Res.*, 32(1):41–45, 2002.

[131] E. J. Garboczi. Computational materials science of cement-based materials. *Mater. Struct.*, 26(4):191–195, 1993.

[132] E. J. Garboczi and D. P. Bentz. Computer simulation of the diffusivity of cement-based materials. *J. Mater. Sci.*, 27(8):2083–2092, 1992.

[133] M. C. Garci Juenger and H. M. Jennings. The use of nitrogen adsorption to assess the microstructure of cement paste. *Cem. Concr. Res.*, 31(6):883–892, 2001.

[134] X. Ge and X. Wang. Estimation of freezing point depression, boiling point elevation, and vaporization enthalpies of electrolyte solutions. *Ind. Eng. Chem. Res.*, 48(4):2229–2235, 2009.

[135] S. Ghabezloo. *Comportement thermo-poro-mécanique d'un ciment pétrolier*. PhD thesis, Ecole Nationale des Ponts et Chaussées. Paris., France, 2008.

[136] S. Ghabezloo. Association of macroscopic laboratory testing and micromechanics modelling for the evaluation of the poroelastic parameters of a hardened cement paste. *Cem. Concr. Res.*, 40(8):1197–1210, 2010.

[137] S. Ghabezloo. Micromechanics analysis of thermal expansion and thermal pressurization of a hardened cement paste. doi:10.1016/j.cemconres.2011.01.023, 2011.

[138] S. Ghabezloo, J. Sulem, S. Guédon, F. Martineau, and J. Saint-Marc. Poromechanical behaviour of hardened cement paste under isotropic loading. *Cem. Concr. Res.*, 38(12):1424–1437, 2008.

[139] S. Ghabezloo, J. Sulem, and J. Saint-Marc. The effect of undrained heating on a fluid-saturated hardened cement paste. *Cem. Concr. Res.*, 39(1):54–64, 2009.

[140] H. Giesche. Mercury porosimetry: a general (practical) overview. *Part. Part. Syst. Charact.*, 23(1):9–19, 2006.

[141] M. A. Glinicki and M. Zielinski. Frost salt scaling resistance of concrete containing CFBC fly ash. *Mater. Struct.*, 42(7):993–1002, 2009.

[142] P. W. J. Glover, M. J. Hole, and J. Pous. A modified Archie's law for two conducting phases. *Earth Planet. Sci. Lett.*, 180(3-4):369–383, 2000.

[143] M. P. Goertz, X. Y. Zhu, and J. E. Houston. Exploring the liquid-like layer on the ice surface. *Langmuir*, 25(12):6905–6908, 2009.

[144] Z. C. Grasley and D. A. Lange. Thermal dilation and internal relative humidity of hardened cement paste. *Mater. Struct.*, 40(3):311–317, 2007.

[145] K. Grosse, L. Ratke, and B. Feuerbacher. Solidification and melting of succinonitrile within the porous network of an aerogel. *Phys. Rev. B.*, 55:2894–2902, 1997.

[146] P. Grübl and A. Sotkin. Rapid ice formation in hardened cement paste, mortar and concrete due to supercooling. *Cem. Concr. Res.*, 10(3):333–345, 1980.

[147] M. Guendouzi, A. Dinane, and A. Mounir. Water activities, osmotic and activity coefficients in aqueous chloride solutions att 298.15 k by the hygrometric method. *J. Chem. Thermodyn.*, 33(9):1059–1072, 2001.

[148] S. T. Gulati and H. E. Hagy. Analysis and measurement of glue-spall stresses in glass-epoxy bonds. *J. Am. Ceram. Soc.*, 65(1):1–5, 1982.

[149] J. J. M. Guzman and S. L. Braga. Supercooling water in cylindrical capsules. *Int. J. Thermophys.*, 26(6):1781–1802, 2005.

[150] C. J. Haecker, E. J. Garboczi, J. W. Bullard, R. B. Bohn, Z. Sun, S. P. Shah, and T. Voigt. Modeling the linear elastic properties of portland cement paste. *Cem. Concr. Res.*, 35(10):1948–1960, 2005.

[151] P. Halamickova, R. J. Detwiler, D. P. Bentz, and E. J. Garboczi. Water permeability and chloride ion diffusion in portland cement mortars: relationship to sand content and critical pore diameter. *Cem. Concr. Res.*, 25(4):790–802, 1995.

[152] G. Halsey. Physical adsorption on non-uniform surfaces. *J. Chem. Phys.*, 16:931–938, 1948.

[153] T. A. Hammer and E. J. Sellevold. Frost resistance of high strength concrete. *ACI special publication SP1521, ACI Detroit,*, pages 457–487, 1990.

[154] D. E. Hare and C. M. Sorensen. The density of supercooled water. ii. bulk samples cooled to the homogeneous nucleation limit. *J. Chem. Phys.*, 87:4840, 1987.

[155] W. D. Harkins and G. Jura. Surfaces of solids. XII. an absolute method for the determination of the area of a finely divided crystalline solid. *J. Am. Chem. Soc.*, 66(8):1362–1366, 1944.

[156] W. D. Harkins and G. Jura. Surfaces of solids. XIII. a vapor adsorption method for the determination of the area of a solid without the assumption of a molecular area, and the areas occupied by nitrogen and other molecules on the surface of a solid. *J. Am. Chem. Soc.*, 66(8):1366–1373, 1944.

[157] J. E. Harlan, D. Picot, P. J. Loll, and R. M. Garavito. Calibration of size-exclusion chromatography: use of a double gaussian distribution function to describe pore sizes. *Anal. Biochem.*, 224(2):557–563, 1995.

[158] M. Hartmann and A. Vinu. Mechanical stability and porosity analysis of large-pore SBA-15 mesoporous molecular sieves by mercury porosimetry and organics adsorption. *Langmuir*, 18(21):8010–8016, 2002.

[159] Z. Hashin. Analysis of composite materials. *J. Appl. Mech*, 50(2):481–505, 1983.

[160] X. He and X. Shi. Chloride permeability and microstructure of portland cement mortars incorporating nanomaterials. *Transport. Res. Record: J. Transport. Res. Board*, 2070(1):13–21, 2008.

[161] M. Heikal, H. El-Didamony, and M. S. Morsy. Limestone-filled pozzolanic cement. *Cem. Concr. Res.*, 30(11):1827–1834, 2000.

[162] R. A. Helmuth. Dimensional changes of hardened portland cement pastes caused by temperature changes. In *Highw. Res. Board Proc.*, volume 40, pages 315–336, 1961.

[163] A. F. Heneghan and A. D. J. Haymet. Liquid-to-crystal nucleation: A new generation lag-time apparatus. *J. Chem. Phys.*, 117:5319–5327, 2002.

[164] A. F. Heneghan, P. W. Wilson, G. Wang, and A. D. J. Haymet. Liquid-to-crystal nucleation: Automated lag-time apparatus to study supercooled liquids. *J. Chem. Phys.*, 115:7599–7608, 2001.

[165] E. Hervé. Thermal and thermoelastic behaviour of multiply coated inclusion-reinforced composites. *Int. J. Solids Struct.*, 39(4):1041–1058, 2002.

[166] R. Hill. Elastic properties of reinforced solids: some theoretical principles. *J. Mech. Phys. Solids*, 11(5):357–372, 1963.

[167] Y. Hirose, H. Doi, and O. Kamigaito. Thermal expansion of hot-pressed cordierite glass ceramics. *J. Mater. Sci. Lett.*, 3(2):153–155, 1984.

[168] S. V. Hobbs. *A study of non-evaporable water content in cement based mixtures with and without pozzolanic materials*. PhD thesis, Cornell University, USA, 2001.

[169] C. Hodgson and R. McIntosh. The freezing of water and benzene in porous vycor glass. *Canadian Journal of Chemistry*, 38(6):958–971, 1960.

[170] K. C. Hover. The influence of water on the performance of concrete. doi:10.1016/j.conbuildmat.2011.01.010, 2011.

[171] T. Inada, X. Zhang, A. Yabe, and Y. Kozawa. Active control of phase change from supercooled water to ice by ultrasonic vibration 1. control of freezing temperature. *Int. J. Heat Mass Transfer*, 44(23):4523–4531, 2001.

[172] F. P. Incropera and D. P. De Witt. *Fundamentals of heat and mass transfer*. John Wiley and Sons Inc., New York, NY, 3rd edition, 2006.

[173] K. Ishikiriyama, M. Todoki, and K. Motomura. Pore size distribution measurements of silica gels by means of differential scanning calorimetry ii:thermoporosimetry. *J. Colloid Interf. Sci.*, 171:103–111, 1995.

[174] K. Ishikiriyama, M. Todoki, and K. Motomura. Pore size distribution measurements of silica gels by means of differential scanning calorimetry i:optimization for determination of dsc. *J. Colloid Interf. Sci.*, 171:92–102, 1995.

[175] D. Jana. Concrete, construction, or salt-which causes scaling? Part II: Importance of finishing practices. *Concr. Int.*, 26(11):51–56, 2004.

[176] D. Jana. Concrete, construction, or salt – which causes scaling? part i: Importance of air-void system in concrete. *Concr. Inter.*, 26(11):31–38, 2004.

[177] D. J. Janssen. The influence of material parameters on freeze-thaw resistance with and without deicing salt. In *Frost Resistance of Concrete. Proceedings of the international RILEM Workshop on Resistance of Concrete to Freezing ans Thawing With and Without De-icing Chemicals*, pages 3–10, Essen, Germany, September 1997.

[178] H. M. Jennings. Refinements to colloid model of C-S-H in cement: CM-II. *Cem. Concr. Res.*, 38(3):275–289, 2008.

[179] H. M. Jennings, J. J. Thomas, J. S. Gevrenov, G. Constantinides, and F. J. Ulm. A multi-technique investigation of the nanoporosity of cement paste. *Cem. Concr. Res.*, 37(3):329–336, 2007.

[180] T. Ji. Preliminary study on the water permeability and microstructure of concrete incorporating nano-sio2. *Cem. Concr. Res.*, 35(10):1943–1947, 2005.

[181] G. P. Johari. Water's size-dependent freezing to cubic ice. *J. Chem. Phys.*, 122:194504–08, 2005.

[182] D. L. Johnson, J. Koplik, and L. M. Schwartz. New pore-size parameter characterizing transport in porous media. *Phys. Rev. Lett.*, 57(20):2564–2567, Nov 1986.

[183] R. Juanes, E. J. Spiteri, F. M. Orr Jr, and M. J. Blunt. Impact of relative permeability hysteresis on geological CO2 storage. *Water Resour. Res*, 42:W12418, 2006.

[184] A. J. Katz and A. H. Thompson. Quantitative prediction of permeability in porous rock. *Phys. Rev. B.*, 34(11):8179–8181, 1986.

[185] A. J. Katz and A. H. Thompson. Prediction of rock electrical conductivity from mercury injection measurements. *J. Geophys. Res.*, 92(B1):599–607, 1987.

[186] J. Kaufmann, R. Loser, and A. Leemann. Analysis of cement-bonded materials by multi-cycle mercury intrusion and nitrogen sorption. *J. Colloid Interf. Sci.*, 336(2):730–737, 2009.

[187] J. P. Kaufmann. *Experimental identification of damage mechanisms in cementitious porous materials on phase transition of pore solution under frost deicing salt attack*. PhD thesis, EPFL, Lausanne, 1999.

[188] J. P. Kaufmann. Experimental identification of ice formation in small concrete pores. *Cem. Concr. Res.*, 34(8):1421–1427, 2004.

[189] J. P. Kaufmann. Characterization of pore space of cement-based materials by combined mercury and wood's metal intrusion. *J. Am. Ceram. Soc.*, 92(1):209–216, 2009.

[190] J. P. Kaufmann. Pore space analysis of cement-based materials by combined nitrogen sorption-wood's metal impregnation and multi-cycle mercury intrusion. *Cem. Concr. Compos.*, 32(7):514–522, 2010.

[191] K. A. Khalil. Pore structure and surface area of hardened cement pastes containing silica fume. *Mater. Lett.*, 26(4-5):259–264, 1996.

[192] N. Khalili, A. Uchaipichat, and A. A. Javadi. Skeletal thermal expansion coefficient and thermo-hydro-mechanical constitutive relations for saturated homogeneous porous media. *Mech. Mater.*, 42(6):593–598, 2010.

[193] M. K. Khoshkbarchi and J. H. Vera. Measurement and correlation of ion activity coefficients in aqueous solutions of mixed electrolyte with a common ion. *Fluid phase equilibria*, 121(1-2):253–265, 1996.

[194] M. K. Khoshkbarchi and J. H. Vera. Measurement and correlation of ion activity in aqueous single electrolyte solutions. *AIChE J.*, 42(1):249–258, 1996.

[195] V. I. Khvorostyanov and J. A. Curry. Thermodynamic theory of freezing and melting of water and aqueous solutions. *J. Phys. Chem. A.*, 108(50):11073–11085, 2004.

[196] J. G. Kirkwood. The dielectric polarization of polar liquids. *J. Chem. Phys.*, 7:911–919, 1939.

[197] P. Klieger. Curing requirements for scale resistance of concrete. *Highw. Res. Board Bull.*, 50:18–31, 1956.

[198] P. Klieger and W. Perenchio. Silicone influence on concrete resistance to freeze-thaw and deicer damage. *Highw. Res. Rec.*, 18:33–47, 1963.

[199] D. K. Kondepudi and I. Prigogine. *Modern thermodynamics: from heat engines to dissipative structures*. Wiley New York, 2002.

[200] D. Kondrashova, C. Reichenbach, and R. Valiullin. Probing pore connectivity in random porous materials by scanning freezing and melting experiments. *Langmuir*, 26(9):6380–6385, 2010.

[201] A. Koponen, M. Kataja, and J. Timonen. Permeability and effective porosity of porous media. *Phys. Rev. E*, 56(3):3319, 1997.

[202] A. Korpa and R. Trettin. The influence of different drying methods on cement paste microstructures as reflected by gas adsorption: Comparison between freeze-drying (f-drying), d-drying, p-drying and oven-drying methods. *Cem. Concr. Res.*, 36(4):634–649, 2006.

[203] L. Kristensen and T. Hansen. Cracks in concrete core due to fire or thermal heating shock. *ACI Mater. J.*, 91(5), 1994.

[204] W. Y. Kuo, J. S. Huang, and C. H. Lin. Effects of organo-modified montmorillonite on strengths and permeability of cement mortars. *Cem. Concr. Res.*, 36(5):886–895, 2006.

[205] O. S. Kwame. Assessment of the coefficient of thermal expansion of alabama concrete. Master's thesis, Auburn University, USA, 2008.

[206] M. R. Landry. Thermoporometry by differential scanning calorimetry: experimental considerations and applications. *Thermochimica acta*, 433(1-2):27–50, 2005.

[207] E. J. Langham and B. J. Mason. The heterogeneous and homogeneous nucleation of supercooled water. *Proc. R. Soc. London, Ser. A: Math. Phys. Sci.*, 247(1251):493–504, 1958.

[208] I. Langmuir. The adsorption of gases on plane surfaces of glass, mica and platinum. *J. Am. Chem. Soc.*, 40(9):1361–1403, 1918.

[209] P. Laugesen, M. Geiker, E. J. Pederson, N. Thaulow, and F. Thogersen. Hetek, method for test of the frost resistance of high performance concrete. Technical report, 2006.

[210] L. L. Lee. *Molecular thermodynamics of electrolyte solutions*. World Scientific Pub Co Inc, 2008.

[211] C. A. Leony Leon. New perspectives in mercury porosimetry. *Adv. Colloid. Interf. Sci.*, 76:341–372, 1998.

[212] M. T. Ley, R. Chancey, M. C. G. Juenger, and K. J. Folliard. The physical and chemical characteristics of the shell of air-entrained bubbles in cement paste. *Cem. Concr. Res.*, 39(5):417–425, 2009.

[213] Y. Li and G. A. Somorjai. Surface premelting of ice. *J. Phys. Chem. C.*, 111(27):9631–9637, 2007.

[214] D. R. Lide. *Handbook of chemistry and physics*. CRC, 2002.

[215] C. N. Likos, K. R. Mecke, and H. Wagner. Statistical morphology of random interfaces in microemulsions. *J. Chem. Phys.*, 102(23):9350–9361, 1995.

[216] C. Lin and L. Lee. A two-ionic-parameter approach for ion activity coefficients of aqueous electrolyte solutions. *Fluid phase equilibria*, 205(1):69–88, 2003.

[217] H. Lin and L. Lee. Estimations of activity coefficients of constituent ions in aqueous electrolyte solutions with the two-ionic-parameter approach. *Fluid phase equilibria*, 237(1-2):1–8, 2005.

[218] P. Linse. Thermodynamic and structural aspects of liquid and solid benzene. Monte Carlo study. *J. Am. Chem. Soc.*, 106(19):5425–5430, 1984.

[219] R. Lipowsky. Upper critical dimension for wetting in systems with long-range forces. *Phys. Rev. Lett.*, 52:1429–1432, 1984.

[220] B. C. Lippens and J. H. De Boer. Studies on pore systems in catalysts:: V. the t method. *J. Cata.*, 4(3):319–323, 1965.

[221] G. G. Litvan. Frost action in cement paste. *Mater. Struct.*, 6(4):293–298, 1973.

[222] G. G. Litvan. Phase transitions of adsorbates: V, aqueous sodium chloride solutions adsorbed of porous silica glass. *J. Colloid Interf. Sci.*, 45(1):154–169, 1973.

[223] G. G. Litvan. Phase transitions of adsorbates: VI, effect of deicing agents on the freezing of cement paste. *J. Am. Ceram. Soc.*, 58(1-2):26–30, 1975.

[224] G. G. Litvan. Frost action in cement in the presence of de-icers. *Cem. Concr. Res.*, 6(3):351–356, 1976.

[225] G. G. Litvan. Freeze-thaw durability of porous building materials. *ASTM special technical publication*, 691:455–463, 1980.

[226] L. Liu, G. Ye, E. Schlangen, H. Chen, Z. Qian, W. Sun, and K. van Breugel. Modeling of the internal damage of saturated cement paste due to ice crystallization pressure during freezing. doi:10.1016/j.cemconcomp.2011.03.001, 2011.

[227] B. Lothenbach, G. Le Saout, E. Gallucci, and K. Scrivener. Influence of limestone on the hydration of portland cements. *Cem. Concr. Res.*, 38(6):848–860, 2008.

[228] B. Lothenbach, F. Winnefeld, C. Alder, E. Wieland, and P. Lunk. Effect of temperature on the pore solution, microstructure and hydration products of portland cement pastes. *Cem. Concr. Res.*, 37(4):483–491, 2007.

[229] K. Luke and E. Lachowski. Internal composition of 20-year-old fly ash and slag-blended ordinary portland cement pastes. *J. Am. Ceram. Soc.*, 91(12):4084–4092, 2008.

[230] M. Luo, J. R. Wood, and L. M. Cathles. Prediction of thermal conductivity in reservoir rocks using fabric theory. *J. Appl. Geophys.*, 32(4):321–334, 1994.

[231] X. Luo, W. Sun, and S. Y. N. Chan. Effect of heating and cooling regimes on residual strength and microstructure of normal strength and high-performance concrete. *Cem. Concr. Res.*, 30(3):379–383, 2000.

[232] Y. Maltais, E. Samson, and J. Marchand. Predicting the durability of portland cement systems in aggressive environments–laboratory validation. *Cem. Concr. Res.*, 34(9):1579–1589, 2004.

[233] B. B. Mandelbrot. *The fractal geometry of nature*. WH Freeman and Co., New York, 1983.

[234] H. Manzano, J. S. Dolado, and A. Ayuela. Elastic properties of the main species present in portland cement pastes. *Acta Mater.*, 57(5):1666–1674, 2009.

[235] J. Marchand, M. Pigeon, D. Bager, and C. Talbot. Influnece of chloride solution concentration on deicer salt scaling deterioration of concrete. *ACI Mater. J.*, 96(4):429–435, 1999.

[236] J. Marchand, E. J. Sellod, and M. Pigeon. The deicer salt scaling deterioration of conceret: An overview. In *Proceeding of 3rd CAMNET/ACI International Conference*, pages 1–46, Mice, France, 1994.

[237] N. S. Martys. Survey of concrete transport properties and their measurement. Technical report, National Institute of Standards and Technology, 1996.

[238] N. S. Martys. Diffusion in partially-saturated porous materials. *Mater. Struct.*, 32(8):555–562, 1999.

[239] S. Marusin. The effect of variation in pore structure on the frost resistance of porous materials. *Cem. Concr. Res.*, 11:115–124, 1981.

[240] N. Matubayasi, H. Matsuo, K. Yamamoto, S. Yamaguchi, and A. Matuzawa. Thermodynamic quantities of surface formation of aqueous electrolyte solutions: I. aqueous solutions of NaCl, $MgCl_2$, and $LaCl_3$. *J. Colloid Interf. Sci.*, 209(2):398–402, 1999.

[241] W. J. McCarter, T. M. Chrisp, G. Starrs, and J. Blewett. Characterization and monitoring of cement-based systems using intrinsic electrical property measurements. *Cem. Concr. Res.*, 33(2):197–206, 2003.

[242] W. J. McCarter, G. Starrs, and T. M. Chrisp. Electrical conductivity, diffusion, and permeability of portland cement-based mortars. *Cem. Concr. Res.*, 30(9):1395–1400, 2000.

[243] D. McDonald and W. Perenchio. Effects of salt type on concrete scaling. *Concrete International*, 19:23–26, 1997.

[244] D. S. McLachlan. Equations for the conductivity of macroscopic mixtures. *J. Phys. C*, 19:1339–1354, 1986.

[245] D. S. McLachlan. Measurement and analysis of a model dual-conductivity medium using a generalised effective-medium theory. *J. Phys. C*, 21:1521–1532, 1988.

[246] D. S. McLachlan, M. Blaszkiewicz, and R. E. Newnham. Electrical resistivity of composites. *J. Am. Ceram. Soc.*, 73(8):2187–2203, 1990.

[247] P. K. Mehta and P. J. M. Monteiro. *Concrete: microstructure, properties, and materials*. McGraw-Hill New York, 2006.

[248] S. L. Meyers. Thermal coefficient of expansion of portland cement long time tests. *Ind. Eng. Chem.*, 32(8):1107–1112, 1940.

[249] S. L. Meyers. Thermal expansion characteristics of hardened cement paste and of concrete. *Hig. Res. Board Proc.*, 30:193–200, 1950.

[250] H. Mihashi, Z. Zhou, and S. Tada. Micro mechanics model to describe freezing induced strain behavior of concrete. In *Proceedings of the International Workshop on Microstructure and Durability to Predict Service Life of Concrete Structures Sapporo, Japan*, 2004.

[251] R. S. Mikhail, E. Copeland, and S. Brunauer. Pore structure and surface areas of hardened portland cement pastes by nitrogen adsorption. *Can. J. Chem.*, 42:426–438, 1964.

[252] T. Miloh and Y. Benveniste. On the effective conductivity of composites with ellipsoidal inhomogeneities and highly conducting interfaces. *Proc. Royal Soc. A: Math. Phys. Eng. Sci.*, 455(1987):2687, 1999.

[253] S. Mindess, J. F. Young, and D. Darwin. *Concrete*. Prentice Hall, 2003.

[254] A. Mirmiran and Y. Wei. Damage assessment of frp-encased concrete using ultrasonic pulse velocity. *J. Eng. Mec.*, 127(2):126–135, 2001.

[255] M. Mironenko, G. Boitnott, S. Grant, and R. Sletten. Experimental determination of the volumetric properties of nacl solutions to 253 k. *J. Phys. Chem. B*, 105(41):9909–9912, 2001.

[256] M. V. Mironenko, S. A. Grant, and G. M. Marion. Calculation of densities of aqueous electrolyte solutions at subzero temperatures. *J. Solut. Chem.*, 26(5):433–460, 1997.

[257] J. Mitchell, J. B. W. Webber, and J. H. Strange. Nuclear magnetic resonance cryoporometry. *Phys. Rep.*, 461(1):1–36, 2008.

[258] P. J. M. Monterio and C. T. Chang. The elastic moduli of calcium hydroxide. *Cem. Concr. Res.*, 25(8):1605–1609, 1995.

[259] K. Morishige and K. Kawano. Freezing and melting of water in a single cylindrical pore: The pore-size dependence of freezing and melting behavior. *J. Chem. Phys.*, 110:4687–4872, 1999.

[260] K. Morishige and K. Kawano. Freezing and melting of water in a single cylindrical pore: Dynamical supercooling and vitrification of methanol. *J. Chem. Phys.*, 112:11023–11029, 2000.

[261] M. Moukwa. Deterioration of concrete in cold sea waters. *Cem. Concr. Res.*, 20(3):439–446, 1990.

[262] N. I. Muskhelishvili. *Some basic problems of the mathematical theory of elasticity.* Springer, The Netherlands, 1977.

[263] O. V. Nagornov and V. E. Chizhov. Thermodynamic properties of ice, water, and a mixture of the two at high pressures. *J. Appl. Mech. Tech. Phys.*, 31(3):378–385, 1990.

[264] K. Nakarai, T. Ishida, and K. Maekawa. Multi-scale physicochemical modeling of soil-cementitious material interaction. *Soils Foundat.*, 46(5):653–663, 2006.

[265] N. Neithalath, J. Weiss, and J. Olek. Characterizing enhanced porosity concrete using electrical impedance to predict acoustic and hydraulic performance. *Cem. Concr. Res.*, 36(11):2074–2085, 2006.

[266] A. V. Neville. Behavior of concrete in saturated solutions and weak solutions of magnesium sulfate or calcium chloride. *J. Mater.*, 4:781–816, 1969.

[267] T. Q. Nguyen. *Modélisations physico-chimiques de la pénétration des ions chlorures dans les matériaux cimentaires.* PhD thesis, Civil Engineering, Ecole des Ponts ParisTech, France, 2007.

[268] T. Q. Nguyen, V. Baroghel-Boney, and P. Dangla. Prediction of chloride ingress into saturated concrete on the basis of a multi-species model by numerical calculations. *Comput. Concr.*, 3(6):401–422, 2006.

[269] T. Q. Nguyen, J. Petkovic, P. Dangla, and V. Baroghel-Bouny. Modeling of coupled ion and moisture transport in porous building materials. *Constr. Build. Mater.*, 22(11):2185–2195, 2008.

[270] E. P. Nielsen and M. R. Geiker. Chloride diffusion in partially saturated cementitious material. *Cem. Concr. Res.*, 33(1):133–138, 2003.

[271] M. R. Nokken and R. D. Hooton. Using pore parameters to estimate permeability or conductivity of concrete. *Mater. Struct.*, 41(1):1–16, 2008.

[272] M. R. Nokken, R. D. Hooton, and C. R. Roger. Measured internal temperature in concrete exposed to outdoor cyclic freezing. *Cem. Concr. Aggr.*, 26(1):26–32, 2004.

[273] B. K. Nyame and J. M. Illston. Capillary pore structure and permeability of hardened cement paste. In *7th International Symposium on the Chemistry of Cement*, volume III, pages VI181–VI186, France, 1980.

[274] J. B. Odelson, E. A. Kerr, and W. Vichit-Vadakan. Young's modulus of cement paste at elevated temperatures. *Cem. Concr. Res.*, 37(2):258–263, 2007.

[275] B. H. Oh and S. Y. Jang. Prediction of diffusivity of concrete based on simple analytic equations. *Cem. Concr. Res.*, 34(3):463–480, 2004.

[276] J. P. Ollivier, J. C. Maso, and B. Bourdette. Interfacial transition zone in concrete. *Adv. Cem. Based Mater.*, 2(1):30–38, 1995.

[277] H. Ozbek and S. L. Phillips. Thermal conductivity of aqueous sodium chloride solutions from 20 to 330 °C. *J. Chem. Eng. Data*, 25(3):263–267, 1980.

[278] S. P. Rigby, R. S. Fletcher, and S. N. Riley. Characterisation of porous solids using integrated nitrogen sorption and mercury porosimetry. *Chem. Eng. Sci.*, 59(1):41–51, 2004.

[279] N. Papaiconomou, J. P. Simonin, O. Bernard, and W. Kunz. New approaches to the calculation of thermodynamic properties of electrolyte solutions. *J. Mol. Liq.*, 113(1-3):5–8, 2004.

[280] J. Paya, M. Borrachero, J. Monzo, E. Peris-Mora, and F. Amahjour. Enhanced conductivity measurement techniques for evaluation of fly ash pozzolanic activity. *Cem. Concr. Res.*, 31(1):41–49, 2001.

[281] G. R. Pazuki and A. A. Rohani. A new model for the activity coefficients of individual ions in aqueous electrolyte solutions. *Fluid phase equilibria*, 242(1):65–71, 2006.

[282] R. J. M. Pellenq, B. Coasne, R. O. Denoyel, and O. Coussy. Simple phenomenological model for phase transitions in confined geometry. 2. capillary condensation/evaporation in cylindrical mesopores. *Langmuir*, 25(3):1393–1402, 2009.

[283] G. F. Peng, S. H. Bian, Z. Q. Guo, J. Zhao, X. L. Peng, and Y. C. Jiang. Effect of thermal shock due to rapid cooling on residual mechanical properties of fiber concrete exposed to high temperatures. *Constr. Build. Mater.*, 22(5):948–955, 2008.

[284] V. Penttala. Freezing-induced strains and pressures in wet porous materials and especially in concrete mortars. *Adv. Cem. Res.*, 7:8–19, 1998.

[285] V. Penttala. Surface and internal deterioration of concrete due to saline and non-saline freeze-thaw loads. *Cem. Concr. Res.*, 36(5):921–928, 2006.

[286] V. Penttala and F. Al-Neshawy. Stress and strain state of concrete during freezing and thawing cycles. *Cem. Concr. Res.*, 32:1407–1420, 2002.

[287] B. Perrin, N. Vu, S. Multon, T. Voland, and C. Ducroquetz. Mechanical behaviour of fired clay materials subjected to freeze-thaw cycles. *Constr. Build. Mater.*, 25(2):1052–1064, 2011.

[288] O. V. Petrov and I. Furó. Curvature-dependent metastability of the solid phase and the freezing-melting hysteresis in pores. *Phys. Rev. E.*, 73:011608–619, 2006.

[289] O. V. Petrov and I. Furó. NMR cryoporometry: Principles, applications and potential. *Prog. Nucl. Magn. Reson. Spectrosc.*, 54(0):97–122, 2009.

[290] O. V. Petrov and I. Furó. A joint use of melting and freezing data in NMR cryoporometry. *Microporous Mesoporous Mater.*, 2010.

[291] O. V. Petrov, D. Vargas-Florencia, and I. Furó. Surface melting of octamethylcyclotetrasiloxane confined in controlled pore glasses: curvature effects observed by 1H NMR. *J. Phys. Chem. B.*, 111(7):1574–1581, 2007.

[292] B. Pichler and C. Hellmich. Upscaling quasi-brittle strength of cement paste and mortar: A multi-scale engineering mechanics model. *Cem. Concr. Res.*, 41(5):467–476, 2011.

[293] H. S. Pieterson. Application of tem to characterize fly ash- and slag cements. *HEeron*, 44:299–310, 1999.

[294] M. Pigeon, J. Marchand, and R. Pleau. Frost resistant concrete. *Cons. Build. Mater.*, 10:339–348, 1996.

[295] M. Pigeon, J. Marchand, and B. Zuber. Freeze/thaw resistance. In J. Newman and B. S. Choo, editors, *Advanced Concrete Technology: Concrete Properties*, pages 11/1–16. Elsivier, 2003.

[296] M. Pigeon and R. Pleau. *Durability of concrete in Cold Climates*. E&FN SPON, LONDON, 1995.

[297] M. Pigeon, J. Provest, and J. M. Simard. Freeze-thaw durability versus freezing rate. *ACI Mater. J.*, pages 684–492, Sept./Oct. 1985.

[298] M. Pigeon, C. Talbot, J. Marchand, and H. Hornan. Surface microstructure and scaling resistance of concrete. *Cem. Concr. Res.*, 26(10):1555–1566, 1996.

[299] K. S. Pitzer. Thermodynamics of electrolytes. I. theoretical basis and general equations. *J. Phys. Chem.y*, 77(2):268–277, 1973.

[300] K. S. Pitzer. Electrolytes. from dilute solutions to fused salts. *J. Am. Chem. Soc.*, 102(9):2902–2906, 1980.

[301] K. S. Pitzer. *Activity coefficients in electrolyte solutions*. CRC, 2ed, edition, 1991.

[302] K. S. Pitzer and J. J. Kim. Thermodynamics of electrolytes. IV. activity and osmotic coefficients for mixed electrolytes. *J. Am. Chem. Soc.*, 96(18):5701–5707, 1974.

[303] K. S. Pitzer and G. Mayorga. Thermodynamics of electrolytes. II. activity and osmotic coefficients for strong electrolytes with one or both ions univalent. *J. Phys. Chem.*, 77(19):2300–2308, 1973.

[304] K. S. Pitzer and J. M. Simonson. Thermodynamics of multicomponent, miscible, ionic systems: Theory and equations. *J. Phys. Chem.*, 90(13):3005–3009, 1986.

[305] T. C. Powers. The air requirement of frost resistant concrete. *Proc. Highw. Res. Board.*, 29:183–211, 1949.

[306] T. C. Powers. Structure and physical properties of hardened portland cement paste. *J. Am. Ceram. Soc.*, 41(1):1–6, 1958.

[307] T. C. Powers. The thermodynamics of volume change and creep. *Mater. Struct.*, 1(6):487–507, 1968.

[308] T. C. Powers and T. L. Bronyard. *Physical properties of cement-paste*. ACI: Res. Labs. Port. Cem. Ass. Bulletin, Chicago, 1947.

[309] T. C. Powers, L. E. Copeland, and H. M. Mann. Capillary continuity or discontinuity in cement pastes. *PCA Bull.*, 1(110):2–12, 1959.

[310] T. C. Powers and R. Helmuth. Theory of volume changes in hardened portland cement paste during freezing. *Proc. Highw. Res. Board*, 32:285–297, 1953.

[311] A. Prick. Critical degree of saturation as a threshold moisture level in frost weathering of limestones. *Permafrost and Periglacial Processes*, 8(1):91–99, 1997.

[312] H. R. Pruppacher. A new look at homogeneous ice nucleation in supercooled water drops. *J. Atmos. Sci.*, 52(11):1924–1933, 1995.

[313] C. X. Qian and C. F. Zhu. Influence of mineral admixture and air-entraining agent on thermal expansion property of cement based materials. (in chinese). *J Build Mater*, 12:310–315, 2009.

[314] A. I. Rashed and R. B. Williamson. Microstructure of entrained air voids in concrete, Part I. *J. Mater. Res.*, 6(11):404–412, 1991.

[315] A. I. Rashed and R. B. Williamson. Microstructure of entrained air voids in concrete, Part II. *J. Mater. Res.*, 6(11):2474–2483, 1991.

[316] H. W. Reinhardt and K. Gaber. From pore size distribution to an equivalent pore size of cement mortar. *Mater. Struct.*, 23(1):3–15, 1990.

[317] A. Revil. Thermodynamics of ions and water transport in porous media. *J. Colloid Interf. Sci.*, 307(1):254–264, 2007.

[318] A. Revil and D. Jougnot. Diffusion of ions in unsaturated porous materials. *J. Colloid Interf. Sci.*, 319(1):226–235, 2008.

[319] R. W. Rice. *Porosity of Ceramics*. Marcel Dekker Inc., New York, 1999.

[320] I. G. Richardson. The nature of CSH in hardened cements. *Cem. Concr. Res.*, 29(8):1131–1147, 1999.

[321] I. G. Richardson. The nature of the hydration products in hardened cement pastes. *Cem. Concr. Res.*, 22(2):97–113, 2000.

[322] S. P. Rigby, R. S. Fletcher, J. H. Raistrick, and S. N. Riley. Characterisation of porous solids using a synergistic combination of nitrogen sorption, mercury porosimetry, electron microscopy and micro-focus x-ray imaging techniques. *Phys. Chem. Chem. Phys.*, 4(14):3467–3481, 2002.

[323] J. Riikonen, J. Salonen, and V. P. Lehto. Utilising thermoporometry to obtain new insights into nanostructured materials, Part I. *J. Therm. Anal. Calorim.*, pages 1–11, 2010.

[324] J. Riikonen, J. Salonen, and V. P. Lehto. Utilising thermoporometry to obtain new insights into nanostructured materials, Part II. *J. Therm. Anal. Calorim.*, pages 12–19, 2010.

[325] H. L. Ritter and L. C. Erich. Pore size distribution in porous materials. *Anal. Chem.*, 20(7):665–670, 1948.

[326] R. A. Robinson and R. H. Stokes. *Electrolyte solutions*. Dover Pubns, 2002.

[327] E. Rodil, K. Persson, J. H. Vera, and G. Wilczek-Vera. Determination of the activity of H+ ions within and beyond the ph meter range. *AIChE J.*, 47(12):2807–2818, 2001.

[328] T. F. Ronnings. *Freeze-Thaw Resistance of Concrete Effect of : Curing Conditions, Moisture Exchange and Materials*. PhD thesis, The Norwegian Institute of Technology, Division of Structural Engineering, Concrete Section, Trondheim, Norwegian, 2001.

[329] D. Rothstein, J. J. Thomas, B. J. Christensen, and H. M. Jennings. Solubility behavior of Ca-, S-, Al-, and Si- bearing solid phases in portland cement pore solutions as a function of hydration time. *Cem. Concr. Res.*, 32(10):1663–1671, 2002.

[330] J. Ruedrich and S. Siegesmund. Salt and ice crystallization in porous sandstones. *Environ Geol*, 52:225–249, 2007.

[331] S. Sabri and J. M. Illston. Immediate and delayed thermal expansion of hardened cement paste. *Cem. Concr. Res.*, 12(2):199–208, 1982.

[332] A. V. Saetta, R. V. Scotta, and R. V. Vitaliani. Analysis of chloride diffusion into partially saturated concrete. *ACI Mater. J.*, 90(5):441–451, 1993.

[333] A. Z. Sahin. An analytical study of frost nucleation and growth during the crystal growth period. *Heat Mass Transfer*, 30(5):321–330, 1995.

[334] Salt-Institute. Deicing salt and corrosion. http://www.saltinstitute.org/th2020s.html., 2007.

[335] E. Samson and J. Marchand. Modeling the effect of temperature on ionic transport in cementitious materials. *Cem. Concr. Res.*, 37(3):455–468, 2007.

[336] E. Samson and J. Marchand. Modeling the transport of ions in unsaturated cement-based materials. *Comput. Struct.*, 85(23-24):1740–1756, 2007.

[337] E. Samson, J. Marchand, K. A. Snyder, and J. J. Beaudoin. Modeling ion and fluid transport in unsaturated cement systems for isothermal conditions. *Cem. Concr. Res.*, 35(1):141–153, 2005.

[338] J. Sanahuja, L. Dormieux, and G. Chanvillard. Modelling elasticity of a hydrating cement paste. *Cem. Concr. Res.*, 37(10):1427–1439, 2007.

[339] G. Sant, D. Bentz, and J. Weiss. Capillary porosity depercolation in cement-based materials: Measurement techniques and factors which influence their interpretation. doi:10.1016/j.cemconres.2011.04.006, 2011.

[340] T. Sato and J. J. Beaudoin. Coupled AC impedance and thermo-mechanical analysis of freezing phenomena in cement paste. *Mater. Struct.*, 44:405–414, 2011.

[341] G. W. Scherer. Freezing gels. *J. Non-Cryst. Soild.*, 155:1–25, 1993.

[342] G. W. Scherer. Crystallization in pores. *Cem. Concr. Res.*, 29(8):1347–1358, 1999.

[343] J. W. P. Schmelzer and V. G. Baidakov. On different possibilities of a thermodynamically consistent determination of the work of critical cluster formation in nucleation theory. *J. Chem. Phys.*, 119:10759, 2003.

[344] J. W. P. Schmelzer, G. S. Boltachev, and V. G. Baidakov. Classical and generalized Gibbs' approaches and the work of critical cluster formation in nucleation theory. *J. Chem. Phys.*, 124:194503, 2006.

[345] J. W. P. Schmelzer, J. Schmelzer Jr, and I. S. Gutzow. Reconciling Gibbs and van der Waals: A new approach to nucleation theory. *J. Chem. Phys.*, 112:3820, 2000.

[346] A. Schreiber, I. Ketelsen, and G. H. Findenegg. Melting and freezing of water in ordered mesoporous silica materials. *Phys. Chem. Chem. Phys.*, 3:1185–1196, 2001.

[347] C. G. Schull. The determination of pore size distribution from gas adsorption data. *J. Am. Chem. Soc.*, 70(4):1405–1410, 1948.

[348] E. J. Schulson. Ice damage to concrete. Technical report, U.S. Army Engineer Research and Development Center, Apirl 1998.

[349] E. M. Schulson, I. P. Swainson, T. M. Holden, and C. J. Korhonen. Hexagonal ice in hardened cement. *Cem. Concr. Res.*, 30:191–196, 2000.

[350] K. L. Scrivener. Backscattered electron imaging of cementitious microstructures: understanding and quantification. *Cem. Concr. Compos.*, 26(8):935–945, 2004.

[351] N. A. Seaton and E. D. Glandt. Conductivity from simulations of percolating systems of interacting particles. *J. Phys. A: Math. Gen.*, 20:3029–3034, 1987.

[352] L. H. Seeley and G. T. Seidler. Two-dimensional nucleation of ice from supercooled water. *Phys. Rev. Lett.*, 87(5):55702–55705, 2001.

[353] E. J. Sellevold and Ø. Bjøntegaard. Coefficient of thermal expansion of cement paste and concrete: Mechanisms of moisture interaction. *Mater. Struct.*, 39(9):809–815, 2006.

[354] E. J. Sellevold and T. Farstad. Frost/salt testing of concrete: Effect of the test parameters and concrete moisture history. *Nordic Concr. Res.*, 10:121–138, 1991.

[355] M. J. Setzer. Mechanical stability criterion, triple-phase condition, and pressure differences of matter condensed in a porous matrix. *J. Colloid Interf. Sci.*, 235(1):170–182, 2001.

[356] M. J. Setzer. Micro-ice-lens formation in porous solid. *J. Coll. Inter. Sci.*, 243(1):193–201, 2001.

[357] M. J. Setzer. Development of the micro-ice-lens model. In Setzer et al. [359], pages 133–142.

[358] M. J. Setzer, R. Auberg, S. Kasparek, S. Palecki, and P. Heine. CIF test - capillary suction, internal damage and freeze thaw test. *Materials and Structures*, 34(9):515–525, 2001.

[359] M. J. Setzer, R. Auberg, and H. J. Keck, editors. *Frost Resistance of Concrete-From Nano-Structure and Pore Solution to Macroscopic Behaviour and Testing*, Essen, Germany, 2002. RILEM Publications.

[360] M. J. Setzer, G. Fagerlund, and D. J. Janssen. CDF test - test method for the freeze-thaw resistance of concrete-tests with sodium chloride solution (CDF). *Mater. Struct.*, 29(9):523–528, 1996.

[361] M. J. Setzer, P. Heine, S. Kasparek, S. Palecki, R. Auberg, V. Feldrappe, and E. Siebel. Test methods of frost resistance of concrete: CIF-Test: Capillary suction, internal damage and freeze thaw test-reference method and alternative methods A and B. *Materials and structures*, 37(10):743–753, 2004.

[362] H. S. Shang and Y. P. Song. Experimental study of strength and deformation of plain concrete under biaxial compression after freezing and thawing cycles. *Cem. Concr. Res.*, 36(10):1857–1864, 2006.

[363] H. S. Shang, Y. P. Song, and L. K. Qin. Experimental study on strength and deformation of plain concrete under triaxial compression after freeze-thaw cycles. *Build. Envir.*, 43(7):1197–1204, 2008.

[364] R. A. Shaw, A. J. Durant, and Y. Mi. Heterogeneous surface crystallization observed in undercooled water. *J. Phys. Chem. B.*, 109(20):9865–9868, 2005.

[365] R. A. Shaw, A. B. Konitinski, and M. L. Larson. Towards quantifying droplet clustering in clouds. *Q. J. R. Meteorol. Soc.*, 128:1043–1057, 2002.

[366] R. A. Shaw and D. Lamb. Homogeneous freezing of evaporating cloud droplets. *Geophys. Res. Lett.*, 26(8):1181–1184, 1999.

[367] X. Shi, M. Akin, T. Pan, L. Fay, Y. Liu, and Z. Yang. Deicer impacts on pavement materials: Introduction and recent developments. *Open Civil Engineering Journal*, 3:16–27, 2009.

[368] X. Shi, L. Fay, M. Peterson, and Z. Yang. Freeze–thaw damage and chemical change of a portland cement concrete in the presence of diluted deicers. *Mater. Struct.*, pages 1–14, 2010.

[369] M. Shimoda, T. Mizusaki, M. Hirai, and K. Eguchi. NMR study of the solidification and melting of ^{3}He in porous glasses. *J. Low Temp. Phy.*, 64:285–307, 1986.

[370] Z. Shui, R. Zhang, W. Chen, and D. Xuan. Effects of mineral admixtures on the thermal expansion properties of hardened cement paste. *Constr. Build. Mater.*, 24(9):1761–1767, 2010.

[371] R. J. Speedy. Limiting forms of the thermodynamic divergences at the conjectured stability limits in superheated and supercooled water. *J. Phys. Chem.*, 86(15):3002–3005, 1982.

[372] R. J. Speedy. Thermodynamic properties of supercooled water at 1 atm. *J. Phys. Chem.*, 91(12):3354–3358, 1987.

[373] R. J. Speedy and C. A. Angell. Isothermal compressibility of supercooled water and evidence for a thermodynamic singularity at −45°C. *J. Chem. Phys.*, 65:851–858, 1976.

[374] D. C. Steytler and J. C. Dore. Neutron diffraction studies of water in porous silica. II. temperature variation in the super-cooled regime. *Mol. Phys.*, 56:1001–1015, 1985.

[375] D. C. Steytler, J. C. Dore, and C. J. Wright. Neutron diffraction study of cubic ice nucleation in a porous silica network. *J. Phys. Chem. B.*, 87:2458–2459, 1983.

[376] E. Stora, Q. C. He, and B. Bary. Influence of inclusion shapes on the effective linear elastic properties of hardened cement pastes. *Cem. Concr. Res.*, 36(7):1330–1344, 2006.

[377] D. Stroud. Generalized effective-medium approach to the conductivity of an inhomogeneous material. *Phys. Rev. B*, 12(8):3368, 1975.

[378] G. Sun, Y. Zhang, W. Sun, Z. Liu, and C. Wang. Multi-scale prediction of the effective chloride diffusion coefficient of concrete. doi:10.1016/j.conbuildmat.2011.03.041., 2011.

[379] Z. Sun. *Mechanism of frost damage to concrete*. PhD thesis, Department of civil and environmental engineering, Princeton University, Princeton, USA, 2010.

[380] Z. Sun and G. W. Scherer. Effect of air voids on salt scaling and internal freezing. *Cem. Concr. Res.*, 40(2):260–270, 2010.

[381] Z. Sun and G. W. Scherer. Pore size and shape in mortar by thermoporometry. *Cem. Concr. Res.*, 40(5):740–751, 2010.

[382] L. Sutter, K. Peterson, S. Touton, T. Van Dam, and D. Johnston. Petrographic evidence of calcium oxychloride formation in mortars exposed to magnesium chloride solution. *Cem. Concr. Res.*, 36(8):1533–1541, 2006.

[383] I. P. Swainsona and E. M. Schulson. A neutron diffraction study of ice and water within a hardened cement paste during freeze-thaw. *Cem. Concr. Res.*, 31:1821–1830, 2001.

[384] T. Takamuku, M. Yamagami, H. Wakita, Y. Masuda, and T. Yamaguchi. Thermal property, structure, and dynamics of supercooled water in porous siclica by calorimetry, neutron scattering, and NMR relaxation. *J. Phys. Chem. B.*, 101:5730–5739, 1997.

[385] L. Tang and P. Petersson. Slab test: Freeze/thaw resistance of concrete-internal deterioration. *Materials and Structures*, 34(9):526–531, 2001.

[386] L. Tang and P. Petersson. Slab test: Freeze/thaw resistance of concrete-internal deterioration. *Materials and structures*, 37(10):754–759, 2004.

[387] L. Tang and P. E. Petersson. Water uptake, dilation and internal deterioration of concrete due to freezing-and thawing. In Setzer et al. [359], pages 287–294.

[388] J. C. Tanger and H. C. Helgeson. Calculation of the thermodynamic and transport properties of aqueous species at high pressures and temperatures; revised equations of state for the standard partial molal properties of ions and electrolytes. *Am J Sci*, 288:19–98, 1988.

[389] J. H. Taplin. A method for following the hydration reaction in portland cement paste. *Australian J. Appl. Sci.*, 10:329–345, 1959.

[390] H. F. W. Taylor. Method for predicting alkali ion concentrations in cement pore solutions. *Adv. Cem. Res.*, 1(1):5–16, 1987.

[391] H. F. W. Taylor. *Cement chemistry*. Thomas Telford Services Ltd, 1997.

[392] P. D. Tennis and H. M. Jennings. A model for two types of calcium silicate hydrate in the microstructure of portland cement pastes. *Cem. Concr. Res.*, 30(6):855–863, 2000.

[393] J. J. Thomas, A. J. Allen, and H. M. Jennings. Structural changes to the calcium-silicate-hydrate gel phase of hydrated cement with age, drying, and resaturation. *J. Am. Ceram. Soc.*, 91(10):3362–3369, 2008.

[394] J. J. Thomas, J. J. Biernacki, J. W. Bullard, S. Bishnoi, J. S. Dolado, G. W. Scherer, and A. Luttge. Modeling and simulation of cement hydration kinetics and microstructure development. doi:10.1016/j.cemconres.2010.10.004, 2010.

[395] J. J. Thomas, J. J. Chen, A. J. Allen, and H. M. Jennings. Effects of decalcification on the microstructure and surface area of cement and tricalcium silicate pastes. *Cem. Concr. Res.*, 34(12):2297–2307, 2004.

[396] J. J. Thomas and H. M. Jennings. A colloidal interpretation of chemical aging of the CSH gel and its effects on the properties of cement paste. *Cem. Concr. Res.*, 36(1):30–38, 2006.

[397] J. J. Thomas, H. M. Jennings, and A. J. Allen. Relationships between composition and density of Tobermorite, Jennite, and nanoscale CaO- SiO2- H2O. *J. Phys. Chem. C.*, 114(17):7594–7601, 2010.

[398] TRIP. Key facts about america's road and bridge conditions and federal funding. http://www.nssga.org/government/2011_Trip_Files/usa.pdf, 2011.

[399] S. Tsivilis, J. Tsantilas, G. Kakali, E. Chaniotakis, and A. Sakellariou. The permeability of portland limestone cement concrete. *Cem. Concr. Res.*, 33(9):1465–1471, 2003.

[400] P. J. Tumidajski and B. Lin. On the validity of the Katz-Thompson equation for permeabilities in concrete. *Cem. Concr. Res.*, 28(5):643–647, 1998.

[401] P. J. Tumidajski, A. S. Schumacher, S. Perron, P. Gu, and J. J. Beaudoin. On the relationship between porosity and electrical resistivity in cementitious systems. *Cem. Concr. Res.*, 26(4):539–544, 1996.

[402] D. Turnbull and B. Vonnegut. Nucleation catalysis. *Ind. Eng. Chem.*, 44(6):1292–1298, 1952.

[403] F. J. Ulm, G. Constantinide, and F. H. Heukamp. Is concrete a poromechanics material? - a multiscale investigation of poroelastic properties. *Mater. Struct.*, 37(1):43–58, 2004.

[404] J. J. Valenza and G. W. Scherer. Mechanisms of salt scaling. *Mater, Struct.*, 38(4):479–488, 2005.

[405] J. J. Valenza and G. W. Scherer. Mechanism for salt scaling. *J. Am. Ceram. Soc.*, 89(4):1161–1179, 2006.

[406] J. J. Valenza and G. W. Scherer. Mechanism for salt scaling of a cementitious surface. *Mater. Struct.*, 40(3):259–268, 2007.

[407] J. J. Valenza and G. W. Scherer. A review of salt scaling: I. phenomenology. *Cem. Concr. Res.*, 37(7):1007–1021, 2007.

[408] J. J. Valenza and G. W. Scherer. A review of salt scaling: II. mechanisms. *Cem. Concr. Res.*, 37(7):1022–1034, 2007.

[409] J. Van Brakel and P. M. Heertjes. Analysis of diffusion in macroporous media in terms of a porosity, a tortuosity and a constrictivity factor. *Int. J. Heat Mass Transfer*, 17(9):1093–1103, 1974.

[410] M. T. van Genuchten. A closed-form equation for predicting the hydraulic conductivity of unsaturated soils. *Soil Sci. Soc. Am. J*, 44(5):892–898, 1980.

[411] M. Vandamme and F. J. Ulm. Nanogranular origin of concrete creep. *Proc. Nat. Acad. Sci.*, 106(26):10552, 2009.

[412] M. Vandamme, F. J. Ulm, and P. Fonollosa. Nanogranular packing of csh at substochiometric conditions. *Cem. Concr. Res.*, 40(1):14–26, 2010.

[413] R. R. Vanfleet and J. Mochel. Thermodynamics of melting and freezing in small particles. *Surf. Sci.*, 341:40–50, 1995.

[414] K. Velez, S. Maximilien, D. Damidot, G. Fantozzi, and F. Sorrentino. Determination by nanoindentation of elastic modulus and hardness of pure constituents of portland cement clinker. *Cem. Concr. Res.*, 31(4):555–561, 2001.

[415] G. J. Verbeck and P. Klieger. Studies of 'salt' scaling of concrete. *Highw. Res. Board Bull.*, 150:1–17, 1957.

[416] H. S. Waff. Theoretical considerations of electrical conductivity in a partially molten mantle and implications for geothermometry. *J. Geophys. Res.*, 79(26):4003–4010, 1974.

[417] K. Wakimoto, J. Blunt, C. Carlos, P. Monteiro, C. Ostertag, and R. Albert. Digital laminography assessment of the damage in concrete exposed to freezing temperatures. *Cem. Concr. Res.*, 38(10):1232–1245, 2008.

[418] K. Wang, D. E. Nelsen, and W. A. Nixon. Damaging effects of deicing chemicals on concrete materials. *Cem. Concr. Comp.*, 28(2):173–188, 2006.

[419] J. P. Ward. *Solid mechanics, an introduction.* Kluwer Academic Press, Netherlander, 1992.

[420] G. Wardeh, M. A. S. Mohamed, and E. Ghorbel. Analysis of concrete internal deterioration due to frost action. *J. Build. Phys.*, 35(1):54, 2011.

[421] G. Wardeh and B. Perrin. Freezing-thawing phenomena in fired clay materials and consequences on their durability. *Constr. Build. Mater.*, 22(5):820–828, 2008.

[422] G. Wardeh and B. Perrin. Numerical modelling of the behaviour of consolidated porous media exposed to frost action. *Constr. Build. Mater.*, 22(4):600–608, 2008.

[423] E. W. Washburn. Note on a method of determining the distribution of pore sizes in a porous material. *Proc. Natl. Acad. Sci. U.S.A.*, 7(4):115–116, 1921.

[424] J. S. Wettlaufer. Impurity effects in the premelting of ice. *Phys. Rev. Lett.*, 82(12):2516–2519, 1999.

[425] J. S. Wettlaufer, M. G. Worster, L. A. Wilen, and J. G. Dash. A theory of premelting dynamics for all power law forces. *Phys. Rev. Lett.*, 76(19):3602–3605, 1996.

[426] D. Wilkinson and J. F. Willemsen. Invasion percolation: a new form of percolation theory. *J. Phy. A: Math. Gen.*, 16:3365–3376, 1983.

[427] P. W. Wilson, A. F. Heneghan, and A. D. J. Haymet. Ice nucleation in nature: supercooling point (scp) measurements and the role of heterogeneous nucleation. *Cryobiology*, 46(1):88–98, 2003.

[428] D. N. Winslow and S. Diamond. A mercury porosimetry study of the evaluation of porosity in portland cement. *ASTM. J. Mater.*, 5:564–585, 1970.

[429] F. H. Wittmann. Estimation of the modulus of elasticity of calcium hydroxide. *Cem. Concr. Res.*, 16(6):971–972, 1986.

[430] C. P. Wong and R. S. Bollampally. Thermal conductivity, elastic modulus, and coefficient of thermal expansion of polymer composites filled with ceramic particles for electronic packaging. *J. Appl. Polym. Sci.*, 74(14):3396–3403, 1999.

[431] S. Xu, G. W. Scherer, T. S. Mahadevan, and S. H. Garofalini. Thermal expansion of confined water. *Langmuir*, 25(9):5076–5083, 2009.

[432] S. Xu, G. C. Simmons, and G. W. Scherer. Thermal expansion and viscosity of confined liquids. In *Mat. Res. Soc. Symp. Proc. vol. 790, Materials Res. Soc.*, pages P6.8.1–P6.8.7., Warrendale, Pennsylvania, USA., 2004.

[433] Y. Xu and D. D. L. Chung. Effect of sand addition on the specific heat and thermal conductivity of cement. *Cem. Concr. Res.*, 30(1):59–61, 2000.

[434] Z. Yang, W. Weiss, and J. Olek. Interaction between micro-cracking, cracking, and reduced durability of concrete: Developing methods for quantifying the influence of cumulative damage in life-cycle modeling. http://docs.lib.purdue.edu/jtrp/132, 2005.

[435] Z. Yang, W. Weiss, and J. Olek. Using acoustic emission for the detection of damage caused by tensile loading and its impact on the freeze-thaw resistance of concrete. In *International Conference on Construction Materials: ConMat'05*, 2005.

[436] G. Ye. Percolation of capillary pores in hardening cement pastes. *Cem. Concr. Res.*, 35(1):167–176, 2005.

[437] I. J. Youngs. Exploring the universal nature of electrical percolation exponents by genetic algorithm fitting with general effective medium theory. *J. Phys. D*, 35:3127–3137, 2002.

[438] A. Zaoui. Continuum micromechanics: survey. *J. Eng. Mech.*, 128:808–817, 2002.

[439] B. D. Zdravkov, J. J. Čermák, M. Šefara, and J. Janku. Pore classification in the characterization of porous materials: A perspective. *CEJC*, 5(2):385–395, 2007.

[440] Q. Zeng, T. Fen-Chong, P. Dangla, and K. Li. A study of freezing behaviour of cementitious materials by poromechanical approach. *Int. J. Solids Struct.*, 48:3267–3273, 2011.

[441] Q. Zeng and K. Li. Influence of freezing rate on the cryo-deformation and cryo-damage of cement-based materials during freeze-thaw cycles (in chinese). *J Tsinghua Univ (Sci&Tech)*, 48(9):1390–1394, 2008.

[442] Q. Zeng, K. Li, T. Fen-Chong, and P. Dangla. Effect of porosity on thermal expansion coefficient of cement pastes and mortars. doi:10.1016/j.conbuildmat.2011.09.010, 2011.

[443] Q. Zeng, K. Li, T. Fen-Chong, and P. Dangla. Pore structure characterization of cement pastes blended with high-volume fly-ash. doi:10.1016/j.cemconres.2011.09.012, 2011.

[444] X. Zhang, T. Inada, A. Yabe, S. Lu, and Y. Kozawa. Active control of phase change from supercooled water to ice by ultrasonic vibration 2. generation of ice slurries and effect of bubble nuclei. *Int. J. Heat Mass Transfer*, 44(23):4533–4539, 2001.

[445] E. Zhao, M. Yu, R. Sauvé, and M. K. Khoshkbarchi. Extension of the Wilson model to electrolyte solutions. *Fluid phase equilibria*, 173(2):161–175, 2000.

[446] Q. Zheng and D. Du. An explicit and universally applicable estimate for the effective properties of multiphase composites which accounts for inclusion distribution. *J. Mech. Phys. Solids*, 49(11):2765–2788, 2001.

[447] Z. Zhou and H. Mihashi. Micromechanics model to describe strain behavior of concrete in freezing process. *Journal of Materials in Civil Engineering*, 20:46, 2008.

[448] W. Zhu, J. J. Hughes, N. Bicanic, and C. J. Pearce. Nanoindentation mapping of mechanical properties of cement paste and natural rocks. *Mater. Charact.*, 58(11-12):1189–1198, 2007.

[449] B. Zuber. *Vers Une modélisation du comportement des matériaux cimentaires exposés au gel.* PhD thesis, Université Laval, Quebec, Canada, 2002.

[450] B. Zuber and J. Marchand. Modeling the deterioration of hydrated cement systems exposed to frost action part 1: Description of the mathematical model. *Cem. Concr. Res.*, 30(12):1929–1939, 2000.

[451] B. Zuber and J. Marchand. Predicting the volume instability of hydrated cement systems upon freezing using poro-mechanics and local phase equilibria. *Mater. Struct.*, 37(4):257–270, 2004.

Appendix A

Equation derivation and activities

A.1 Activity coefficient of electrolytes

A.1.1 Selected activity models

A.1.1.1 Lin and Lee's model

According to Lin and Lee [216, 217], the activity coefficient of an individual ion is assumed as a combination of the individual ionic long-range interaction and short-range solvation effect, which is given by:

$$\ln \gamma_i = -A_\phi z_i^2 \left[\frac{I^{1/2}}{1 + B_i I^{1/2}} + \frac{2}{B_i} \ln(1 + B_i I^{1/2}) \right] + \frac{C_i z_i^2 I^a}{T} \tag{A.1}$$

where A_ϕ is the Debye-Hückel constant with a formula:

$$A_\phi = \frac{(2\pi N_A \rho_w)^{1/2}}{3} \cdot \left(\frac{e^2}{4\pi \xi_0 \xi_r K T} \right)^{3/2} \tag{A.2}$$

where, N_A is the Avogadro number ($6.023 \times 10^{23} \mathrm{mol}^{-1}$), ρ_w density of water ($9.997 \times 10^3 \mathrm{kg \cdot m^{-3}}$), ξ_0 the permittivity of free space ($8.8528 \times 10^{-12} \mathrm{C^2 J^{-1} m^{-1}}$), ξ_r the relative permittivity of the solvent, e the unit charge ($1.6021 \times 10^{-19} \mathrm{C}$). The Debye-Hückel constant A_ϕ is 0.39 $\mathrm{kg}^{1/2} \cdot \mathrm{mol}^{-1/2}$ at $T = 298\mathrm{K}$. Another very important parameter in eq(A.2) is the ionic strength, which is defined as:

$$I = \frac{1}{2} \sum m_i z_i^2 \tag{A.3}$$

with m_i the molality (mol/kg). The mean activity coefficients of an electrolyte is defined as:

$$\ln \gamma_\pm = \frac{v_+ \ln \gamma_+ + v_- \ln \gamma_-}{v_+ + v_-} \tag{A.4}$$

where $v_{+,-}$ represent the stoichiometric number of cation and anion. Substitution of eq(A.1) into eq(A.4), one obtains the mean activity coefficients of ions [216, 217]:

$$\ln \gamma_\pm = \frac{\sum_{i=+,-} v_i \left\{ - A_\phi z_i^2 \left[\frac{I^{1/2}}{1+B_i I^{1/2}} + \frac{2}{B_i} \ln(1 + B_i I^{1/2}) \right] + \frac{C_i z_i^2 I^a}{T} \right\}}{v_+ + v_-} \tag{A.5}$$

A.1.1.2 Khoshkbarchi and Vera's model

Khoshkbarchi and Vera extended the Pitzer's model to calculate the ionic activity coefficients [194]:

$$\ln \gamma_i = \frac{-A_x z_i^2 I_x^{1/2}}{1+\rho I_x^{1/2}} + \frac{B_i I_x^{3/2}}{1+\rho I_x^{1/2}} + C_i \ln\left(1+\rho I_x^{3/2}\right) \tag{A.6}$$

where A_x is the Debye-Hückel constant mole fraction base, B_i and C_i are the adjustable parameters, $\rho = 9$. Note that the ionic strength used in eq(A.6) is defined as:

$$I_x = \frac{1}{2}\sum x_i z_i^2 \tag{A.7}$$

where x_i is the mole fraction of species i in the mixture (mol/mol). Combining eq (A.6) and eq (A.4), one obtains the mean ionic activity coefficients as:

$$\ln \gamma_\pm = \frac{-A_x |z_+ z_-| I_x^{1/2}}{1+\rho I_x^{1/2}} + \frac{B_\pm I_x^{3/2}}{1+\rho I_x^{1/2}} + C_\pm \ln\left(1+\rho I_x^{3/2}\right) \tag{A.8}$$

where

$$B_\pm = \frac{v_+ B_+ + v_- B_-}{v_+ + v_-}; \quad \text{and} \quad C_\pm = \frac{v_+ C_+ + v_- C_-}{v_+ + v_-} \tag{A.9}$$

A.1.1.3 Pitzer's model

Based on the Debye-Hückel theory, Pitzer [300–302] proposed a semi-empirical model for predicting the activity coefficient of individual ions:

$$\ln \gamma_i = \frac{-A_\phi z_i^2 I^{1/2}}{1+B_i I^{1/2}} + C_i I \tag{A.10}$$

where A_ϕ is the Debye-Hückel constant molarity base that has a value 1.176, instead of 8.766 at 298.15K in the Khoshkbarchi and Vera model. B_i and C_i are the adjustable parameters for each ions. The mean ionic activity coefficient can be obtained by substituting of eq (A.10) in to eq (A.4) as follows:

$$\ln \gamma_\pm = \frac{\sum_{i=+,-} v_i \left\{ -A_\phi z_i^2 \frac{I^{1/2}}{1+B_i I^{1/2}} + C_i I \right\}}{v_+ + v_-} \tag{A.11}$$

A.1.1.4 Pazuki and Rohani's model

Combining the Pitzer's model and Lin and Lee's model, Pazuki and Rohani [281] proposed a new model to calculate the individual ionic activity coefficients:

$$\ln \gamma_i = \frac{-A_\phi z_i^2 I^{1/2}}{1+B_i I^{1/2}} + \frac{C_i z_i^2 I^a}{T} \tag{A.12}$$

where $a = 1.29$, B_i and C_i are the adjustable parameters. Again, substitution of eq(A.12) into the constitutive equation, eq(A.4), one finally obtains the mean ionic activity coefficient:

$$\ln \gamma_{\pm} = \frac{\sum_{i=+,-} v_i \Big\{ - A_\phi z_i^2 \frac{I^{1/2}}{1+B_i I^{1/2}} + \frac{C_i z_i^2 I^a}{T} \Big\}}{v_+ + v_-} \tag{A.13}$$

A.2 Osmotic coefficient and activity of water

The Gibbs-Duhem equation for a multi-electrolyte aqueous solution at constant temperature and pressure is expressed as:

$$n_w d\mu_w + \sum_i n_i d\mu_i = 0 \tag{A.14}$$

The summation is carried out over all the constituent ions in the solution except water. The relation between chemical potential and activity of water and ions in solution are given by:

$$d\mu_w = RT d\ln a_w, \quad \text{and} \quad d\mu_i = RT d\ln a_i \tag{A.15}$$

Then the eq(A.14) can be rewritten as:

$$\frac{1000}{\mathsf{M}_w} d\ln a_w + \sum_i m_i d\ln a_i = 0 \quad \text{with} \quad m_i = \frac{1000 n_i}{n_w \mathsf{M}_w} \tag{A.16}$$

This equation is obviously applicable to both single and multi-electrolyte solutions in which the activity of water depends on the electrolytes dissolved in the aqueous solutions. Let m_t and x_i denote the overall molality and the molar fraction respectively:

$$m_t = \sum_i m_i; \quad \text{and} \quad x_i = \frac{m_i}{m_t} \tag{A.17}$$

Using the eq(A.17) and the relation $a_i = m_i \gamma_i$, one obtains the water activity as follows:

$$d\ln a_w = - \frac{m_t \mathsf{M}_w}{1000 \sum_i x_i \left(d\ln m_i + d\ln \gamma_i \right)} \tag{A.18}$$

Using the eq(A.17) and the definition of ionic strength, one can get the following equations:

$$\sum_i x_i d\ln m_i = \frac{dm_t}{m_t}; \quad \sum_i x_i d\ln \gamma_i = \sum_i x_i z_i^2 \frac{\sum_i x_i d\ln \gamma_i}{\sum_i x_i z_i^2} = \frac{2I}{m_t} \frac{\sum_i x_i d\ln \gamma_i}{\sum_i x_i z_i^2} \tag{A.19}$$

The eq(A.18) can be rewritten as:

$$d\ln a_w = - \frac{\mathsf{M}_w}{1000} dm_t - \frac{\mathsf{M}_w I}{500} \frac{\sum_i x_i d\ln \gamma_i}{\sum_i x_i z_i^2} \rightarrow \ln a_w = - \frac{\mathsf{M}_w m_t}{1000} - \frac{\mathsf{M}_w}{500 \sum_i x_i z_i^2} \sum_i x_i \int_{I=0}^{I=I} I d\ln \gamma_i \tag{A.20}$$

The osmotic coefficient of a solution, Π, is defined as:

$$\Pi = \frac{-1000}{m_t \mathsf{M}_w} \ln a_w \tag{A.21}$$

where $\ln a_w$ can be determined as:

$$\ln a_w = - \frac{\mathsf{M}_w m_t}{1000} - \frac{\mathsf{M}_w m_t}{1000} \sum_i x_i \ln \gamma_i + \frac{\mathsf{M}_w m_t}{1000 I} \sum_i x_i \int_{I=0}^{I=I} \ln \gamma_i dI \tag{A.22}$$

Substitution of the expression of $\ln\gamma_i$ into eq(A.22), one can obtain the water activity with ions. Using the selected models, the term, $\int_{I=0}^{I=I}\ln\gamma_i dI$ can be given by:

$$\int_{I=0}^{I=I}\ln\gamma_i dI = \frac{-2A_\phi z_i^2}{B_i} I\ln(1+B_i I^{1/2}) + \frac{C_i z_i^2}{(a+1)T} I^{(a+1)}, \quad \text{Lin\&Lee} \tag{A.23a}$$

$$\int_{I=0}^{I=I}\ln\gamma_i dI = -\frac{Az_i^2}{\rho^3}\left(\rho^2 I - 2\rho I^{1/2} + 2\ln(1+\rho I^{1/2})\right) + \frac{B_i}{\rho^5}\left[2\ln(1+\rho I^{1/2}) - 2\rho I^{1/2} + \rho^2 I - \frac{2}{3}\rho^3 I^{3/2} + \frac{1}{2}\rho^4 I^2\right] + \frac{C_i}{\rho^{3/2}}\left[-2\tan^{-1}(\rho^{1/2} I^{1/3}) + I\rho^{3/2}\ln(1+\rho I^{2/3}) + 2\rho^{1/2} I^{1/3} - \frac{2}{3}\rho^{3/2}\right], \quad \text{Khoshkbarchi \& Vera} \tag{A.23b}$$

$$\int_{I=0}^{I=I}\ln\gamma_i dI = -Az_i^2\left[\frac{I}{B_i} - \frac{2I^{1/2}}{B_i^2} + \frac{2}{B_i^3}\ln\left(1+B_i I^{1/2}\right)\right] + \frac{1}{2}C_i I^2, \quad \text{Pitzer} \tag{A.23c}$$

$$\int_{I=0}^{I=I}\ln\gamma_i dI = -Az_i^2\left[\frac{I}{B_i} - \frac{2I^{1/2}}{B_i^2} + \frac{2}{B_i^3}\ln\left(1+B_i I^{1/2}\right)\right] + \frac{C_i z_i^2}{(a+1)T} I^{(a+1)}, \quad \text{Pazuki\&Rohani} \tag{A.23d}$$

Using the eq(A.22), one can rewrite the osmotic equation A.21 as

$$\Pi = 1 + \sum_i x_i \ln\gamma_i - \sum_i x_i \frac{1}{I}\int_0^I \ln\gamma_i dI \tag{A.24}$$

Using the eqs (A.1), (A.6), (A.10), (A.12) and eq(A.23), one can obtain the osmotic coefficient of a solution as presented in eq(2.18) by the selected models.

A.3 Derivation of eq(2.29)

The eq(2.29) was originally presented in [352], but the authors did not precisely figure out the physical meanings and the derivation processes. Here we employ the statistically inhomogeneous Poisson process that has been used to quantify droplet clustering in clouds, cf. Shaw et al. [364, 365]. We follow the definitions in [364, 365]: the freezing events which are assumed to be perfectly random and independent of each other and the measured substrates, observe the Poisson probability process. The freezing probability is the given by [364–366]:

$$P(N) = \frac{\left(\int_0^t Jdt\right)^N \exp\left(-\int_0^t Jdt\right)}{N!} \tag{A.25}$$

where N is the number of freezing events. The ratio of freezing events can be also accounted for the probability of freezing, $P = N_f/N_t$, with N_f freezing events and N_t total events. One obtains:

$$P = 1 - \exp\left(-\int_0^t Jdt\right) \tag{A.26}$$

where J is the total nucleation rate for the system. Taking in to account the cooling rate $\mathcal{R}$, one can rewrite the eq(A.26) as:

$$P = 1 - \exp\left(-1/\mathcal{R}\int_{T_m}^T JdT\right) \tag{A.27}$$

Applying the differential procedure to the eq(A.27), one obtains:

$$\frac{J}{\mathcal{R}} = \frac{dP(T)}{(1-P(T))dT} \tag{A.28}$$

Note that the unit of nucleation rate J in eq(A.28) is times/K, which is different from the widely used nucleation rate in unit of times/(K · ml) (cf. [380]). The volume of liquid phase V is thus added to be

consistent with eq(2.29):

$$\frac{JV}{\mathcal{R}} = \frac{dP(T)}{(1-P(T))dT} \tag{A.29}$$

Since the probability of freezing is determined by the independent freezing events, the term in the right hand side of eq(A.28) or (A.29) can be rewritten as follows by discretization process:

$$\frac{dP(T)}{(1-P(T))dT} = \frac{\Delta P}{(1-P(T))\Delta T} = \frac{n_i}{n_i/2 + \sum_{j>i} n_i \Delta T_i} \tag{A.30}$$

where n_i is the number of freezing events at temperature scale ΔT. The probability of freezing when temperature is larger than the center temperature T_i is evaluated as: $P(T > T_i) = \sum_{J>i} \Delta P(T(j)) + 1/2 \cdot \Delta P(T(j)) = n_i/2 + \sum_{j>i} n_j$. By substituting of eq(A.30) into eq(A.28), the eq(2.29) in [352] is obtained.

A.4 Thickness of liquid like layer for aqueous solution

When a convex pore composed of aqueous solution and ice is freezing progressively, the total Gibbs free energy (Helmholtz free energy when it has no volumetric work) can be expressed in eq(A.31), which is similar to the system of freezing pure water as shown in eq(2.20),

$$\Psi = \frac{V - V_c}{\mathsf{V}_w}\mu_w + \frac{V_c}{\mathsf{V}_c}\mu_c + (V - V_c)RT\sum c_i \ln(\gamma_i) + A\gamma_{ls} + A_c\gamma_{lc} + A\Delta\gamma F \tag{A.31}$$

where V and A are volume of pore and the interfacial area between pore and solid wall respectively, V_c and A_c are volume of the ice crystal and the interfacial area between ice and liquid solution respectively, V_w is the molar volume of water, V_c is molar volume of ice, μ_w represents the chemical potential of water, c_i is the concentration of species i (mol/l), γ_i is the activity of species i. γ_{ls} is the surface tension of liquid phase and solid wall, γ_{lc} the surface tension of liquid phase and ice crystal, $\Delta\gamma = \gamma_{ls} + \gamma_{lc} - \gamma_{cs}$ is defined as the free energy excess of a single ice crystal-solid wall (cs) interface over a crystal-liquid-solid 'sandwich'[89, 291], F is the total effective interfacial free energy, and it depends on the approaches used, cf. [89, 102, 291]. Substitution of eqs(2.1a) and (2.23) into eq(A.31), one can obtain the expression:

$$\begin{aligned}\Psi = {} & \frac{\mu_w}{\mathsf{V}_w}V - \frac{A_h}{\mathsf{V}_c}A(\delta + \kappa\delta^2) + A(\delta + \kappa\delta^2)RT\sum c_i \ln(\gamma_i) \\ & + A\gamma_{ls} + A(1 + 2\kappa\delta)\gamma_{lc} + A\Delta\gamma F; \quad \text{with} \quad A_h = \Delta H_{fus}\frac{T_0 - T}{T_0} + RT\ln(a_w)\end{aligned} \tag{A.32}$$

In the procedure of deriving eq(A.32), the widely used approaches that $\mathsf{V}_c \approx \mathsf{V}_w$ and $\mu_c - \mu_w \approx \Delta H_{fus}(T - T_0)/T_0 + RT\ln(a_w)$ are adopted. If the liquid like layer is in stable state, it must have $\partial\Psi/\partial\delta = 0$. Through simple calculations, one obtains:

$$\frac{A_h}{\mathsf{V}_c}(1 + 2\kappa\delta) = (1 + 2\kappa\delta)RT\sum c_i \ln\gamma_i + 2\kappa\gamma_{lc} + \Delta\gamma\frac{\partial F}{\partial\delta} \tag{A.33}$$

In case that $1 \gg 2\kappa\delta$, once thus obtains:

$$T - T_0 = -\frac{\mathsf{V}_c T_0}{\Delta H_{fus}}\left[-\frac{RT\ln(a_w)}{\mathsf{V}_c} + RT\sum c_i \ln\gamma_i + 2\kappa\gamma_{lc} + \Delta\gamma\frac{\partial F}{\partial\delta}\right] \tag{A.34}$$

The eq(A.33) is actually composed of two parts, one is the contribution of solidification temperature depression by solute and pore size effect, which is expressed as:

$$T_m - T_0 = \frac{\mathsf{V}_c T_0}{\Delta H_{fus}} \left[\frac{RT \ln(a_w)}{\mathsf{V}_c} - 2\kappa\gamma_{lc} \right] \tag{A.35}$$

The other part of contribution is the effect of ions and effective interfacial energy F. Substituting of eq(2.41) into the eq(A.34) and considering the eq(A.35), one obtains:

$$\begin{aligned} T_m - T &= T_0 - T - (T_0 - T_m) \\ &= \frac{T_0 \mathsf{V}_c}{\Delta H_{fus}} \left[RT \sum c_i \ln \gamma_i + \frac{\Delta\gamma\sigma^2}{\delta^3} + \frac{\Delta\gamma}{2} A_k \delta^{-1/2} \left(1 + \frac{\sigma}{\delta}\right) \exp\left(-A_k \delta^{-1/2} (\delta - \sigma)\right) \right] \end{aligned} \tag{A.36}$$

In the case that surface melting occurs for planar ice with a ideal dilute solution assumption, $\ln \gamma_i \approx 1$, the eq(A.36) reduces to the eq(7) in [424]. By combining the eqs(A.35) and (A.36), the eq(2.42) can be derived.

A.5 Test methods

There are numerous test methods to access the frost resistance of cement-based materials. Almost every country has its own test standard, for instance the well known ASTM C 666 [21] and C 672 [22], the RILEM recommended test method CDF/CIF [358, 360, 361] and the Swedish Standard SS 13 72 44 [209], the so-called Borås. Note that the RILEM recommended test method CDF/CIF contains the content of both the internal deterioration and surface scaling [358, 360, 361]. These test methods as well as the Modified SNV 64046 and RILEM recommended cubic tests are summarized in Tables A.1 and A.2.

For the internal damage tests, cf. ASTM C666 and CDF/CIF (partially), the dynamic modulus were adopted as an important factor for accessing the frozen damage. Because the dynamic modulus of porous materials are proportional to the square of the relative transition time, the ultrasonic method thus is often used [7, 254, 434, 435]. The damage criterion of the relative dynamic modulus for ASTM C666 and CIF test methods are 0.6 and 0.8 respectively. Below the values, the materials can be regarded to be damaged. In addition, both methods recommend the length change as alternative factor for damage assessment [21, 361].

For salt scaling tests, significant differences with the internal damage test methods can be obtained. As shown in Tables A.1 and A.2, the ASTM C 672 requires that a concrete slab with thickness ≥75 mm should be covered with a pool of 3 wt% NaCl solution with a depth of 6 mm, see Figure A.1(a). The similar requirements can be found in CDF/CIF and Barås methods [358, 360, 361, 385, 386]. But the CDF method is an "upside down" version of ASTM C672. The test configuration consists of supporting the slab 3 mm above the bottom of a stainless steel container that holds enough NaCl solution to submerge only a few mm of the test surface. The top of the slab that is originally the bottom molded surface, is

covered with 20 mm of insulation, see Figure A.1(b). To assess the damage of materials, the ASTM C672 applies a rating between 0 (no scaling) and 5 (severe scaling) to quantify the degree of scaling after every 5 freeze-thaw cycles, thorough a subjective analysis of the appearance of the surface. At the same time, it should measure the mass of the specimen and the change in mass referring to the original mass. However, this method may not assess the damage of porous solid properly, because the water uptake occurs during freeze-thaw cycles [387]. Therefore, the CDF/CIF test measures the mass of scaled-off material per unit area of the surface exposed to NaCl solution and the mass change by water uptake. This measurement is normally performed at frequent intervals, for instance, ASTM C672: every 5 cycles, CDF and Boras: 7, 14, 28, 42 and 56 freeze-thaw cycles. The test container is dipped into the contact liquid of an ultrasonic bath and subjected to ultrasonic cleaning for 3 minutes, in order to remove loosely adhering scaled material from the test surface at every measurement interval. The removed material is then oven-dried 24 hrs at 110±5℃ and cooled for 1 hr (±5 min) at 20 ±2℃C and 60 ±10 relative humidity before it is weighed.

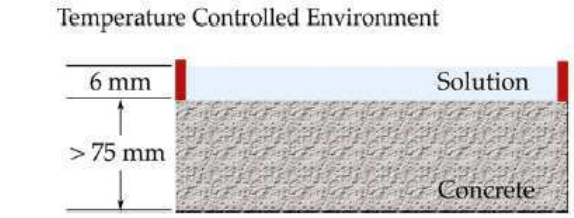

(a)

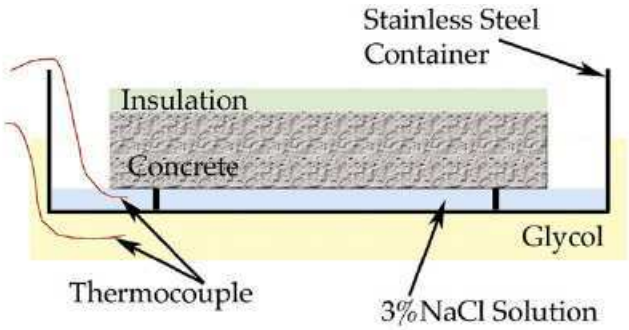

(b)

Figure A.1: Schematic illustration of ASTM standard C 672 and (b) CDF standard test methods. After Valenza and Scherer [406].

Table A.1: Comparison of the freeze-thaw test methods: ASTM C 666/672 and SNV 640461.

Parameters	ASTM C 666	Modified ASTM C 672	Modified SNV 640461
Temperature range	$-17.8 \sim +4.4$℃	$-17.8 \sim +23$℃	$-20 \sim +20$℃
Cooing(heating) rate	$9 \sim 22(9 \sim 22)$℃/h	$2.27 \sim 2.55(-)$℃/h	120(240)℃/h[a]
Max. temperature	4.4(±1.7)℃	23(±3)℃	20℃
Min. temperature	−17.8(±1.7)℃	−17.8(±2.8)℃	−20℃
Temperature measure-point	Center of dummy	Liquid bath	Liquid bath
Exposure	full test specimen	full test specimen	full test specimen
Exposure media	1-3 mm layer of tap water	cooling:6 mm layer of 3% NaCl solution heating: air	cooling:saturated CaCl solution, heating:running tap water
Freeze-thaw cycles	300	-	350
Duration of I cycle (hours)	2-5	24 ± 2	0.5
Measuring terms	per 36 cycles	per 5 cycles	per 50 cycles
Measuring parameters	E_{dyna} [b]and length	Surface appearance and length	length
Cleaning if surfaces	-	-	-
Sample curing before start of conditioning			
- mould:	1 day	1 day	1 day
- water curing:	13 days	-	$\geq$ 28days[c]
- air storage:	-	-	-
Test duration (days) after cutting			
- pre-drying[d]	0	0	0
- re-saturation	3	0	5[e]
- freeze-thaw	42	-	8
- total	45	-	13
Cost level	10000 per set of 6 cores	12000 per set of 12 specimens	5000 per set of 6 prisms

[a] Values for cooling/heating rates are approximated, because the test methods prescribe alternating immersion of test specimens into liquids of fixed temperatures
[b] E_{dyna} represents the dynamic elastic modulus
[c] The test method does not specify if the curing is in water or in air
[d] Condition: RH=65(±5)%. Evaporation from a free water surface =45(±15)g $\cdot$ m^{-2} $\cdot$ h^{-1}
[e] Re-saturation with tap water

Table A.2: Comparison of the freeze-thaw test methods: Borås, RILEM proposal CDF and Cube test.

Parameter	SS 137244 (Borås)	RILEM proposal: CDF	RILEM proposal 3: Cube test
Temperature range	$-18 \sim +20$℃	$-20 \sim +20$℃	$-20 \sim +20$℃
Cooing rate	5.3℃/h[+20 ∼ −4℃][a] and 1.9℃/h[−4 ∼ −28℃]	10℃/h	10℃/h[+20 ∼ 0℃] and 1.25℃/h[0 ∼ −15℃]
Heating rate	4.8℃/h	10℃/h	20℃/h
Max. temperature	20(±4)℃	20.0(±0.5)℃	20(±2)℃
Min. temperature	−18(±2)℃	−20.0(±0.5)℃	−15(±2)℃
Temperature measure-point	Center of exposure (test) liquid	Liquid bath	center of dummy
Exposure	one plane, from above	one plane, from above	full test specimen
Exposure media	3 mm layer of 3% NaCl in tap water	10mm layer of 3% NaCl in distilled water	10 mm layer of tap water or 3% NaCl in tap water
Freeze-thaw cycles	56	28	56
Duration of I cycle (hours)	24	12	24
Measuring terms	at 7, 14, 28, 42, 56 cycles	at (4, 6,)[b]	at 7, 14, 28, 42, 56 cycles
Measuring parameters	scaling	scaling	scaling
Cleaning if surfaces	squirt-bottle and brush	ultra sound bath	squirt-bottle and brush
Sample curing before start of conditioning			
- mould:	1 day	1 day	1 day
- water curing:	6 days	6	6 days
- air storage:	12 days[c]+ 2 days[d]	14[d]	-
Test duration (days) after cutting			
- pre-drying[e]	7	7	20
- re-saturation	3[g]	7[f]	1[fg]
- freeze-thaw	56	14	56
- total	66	28	77
Cost level	4500 per set of 5 samples	4500 per set of 4 samples	4000 per set of 4 samples

[a] Values in [] represent the temperature range
[b] Values in () represent the optional test
[c] Conditions: RH=60(±20)%. Evaporation from a free water surface =45(±15)g $\cdot$ m^{-2} $\cdot$ h^{-1}
[d] Condition: RH=65(±5)%. Evaporation from a free water surface =45(±15)g $\cdot$ m^{-2} $\cdot$ h^{-1}
[e] The test method does not specify if the curing is in water or in air
[f] Re-saturation with salt solution, 3% NaCl in tap water (Cuber test) or in distilled/demineralised water
[g] Re-saturation with tap water

In addition to the test and assessment methods in codes mentioned above, there are numerous test methods that were designed specially [75], and efficient assessment methods that were developed from other areas [60] or other factors to represent the frozen damage [141, 254, 362, 363]. We here will not adopt these methods, since they are beyond the scope of this short review.

To reduce the unacceptable variation of results obtained from laboratory tests, the carefully controlled experimental processes as required by ASTM C 666/672, CDF/CIF are very necessary. However, for cement-based construction on-situ, the temperature and the humidity can be rather different with these in laboratory. Thus, there may be a severe lack of correlation between laboratory and field performance. In addition, it is possible that too "liberal" tests and evaluation criteria may cause the use of inadequate materials and too conservative criteria may unjustly exclude excellent materials with adequate properties [328]. Therefore, an appropriate test method is required.

A.6 Methods for specific surface area

For a porous material, the specific surface area can be determined by deducing the amount of gas required to cover a monomolecular layer on the pore surface by means of isotherm sorption data. The formula for nitrogen sorption is then given by [10]:

$$S = \frac{V_{\text{mono}} N_A A_m}{\mathsf{V}_{N_2}} \times 10^{-20} = 4.35 V_{\text{mono}} \times 10^6 \quad (\text{m}^2/\text{g}) \tag{A.37}$$

where S is the specific surface area to be determined, V_{mono} the volume of gas adsorbed when the entire surface is covered by a monolayer, A_m is the average area of one molecule of adsorbate ($16.2\times10^{-20}\text{m}^2$/molecule for one molecule of nitrogen), V_{N_2} is the molar volume of nitrogen ($22.4 \times 10^{-3}\text{m}^3$/mol). The most widely used methods for evaluating the volume of gas V_{mono} required for the completion of monomolecular layer are the Langmuir approach and the BET approach.

Langmuir approach is based on that the adsorbate behaves as an ideal gas and monomolacular layer of gases that are independent of the nearby gases molecules, are adsorbed on solid surface. When the system is at equilibrium, the number of molecules evaporating from the solid surface is equal to those condensing on the solid surface, and the formula is given by [208]:

$$\frac{P}{V} = \frac{1}{K_L V_m} + \frac{P}{V_{mono}} \tag{A.38}$$

where P denotes the pressure (Pa), V the corresponding volume adsorbed on solid surface at pressure P, K_L the empirical constant. By plotting P/V in terms of P, the completion monomolecular adsorption V_m and the constant K_L can be evaluated by the slop and Y-intercept (see Figure A.2(a)).

BET approach was developed from Langmuir approach to a multilayer gas sorption. The BET theory assumed that the solid surface is energetically homogeneous and there is no interaction between adsorbate

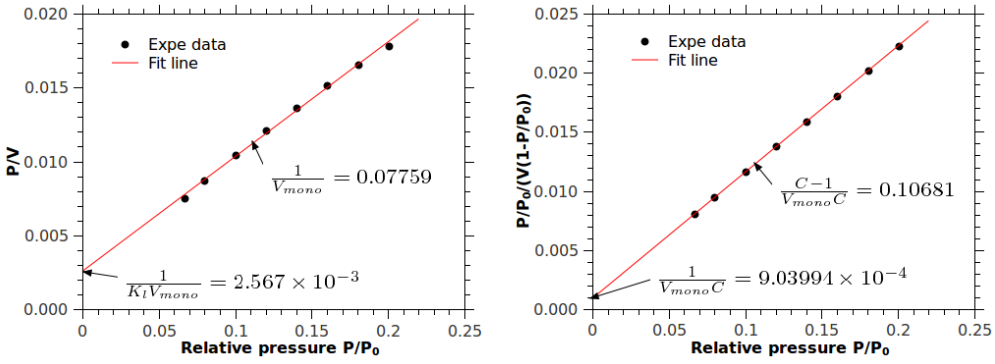

(a) (b)

Figure A.2: (a), Langmuir plot for calculating the mono-layer adsorbed volume V_{mono} from the slop; (b), BET plot for calculating the monolayer adsorbed volume V_{mono} and constant C from the Y intercept and slop.

and no variation in properties of adsorbed layers after the first layer. Again, at equilibrium, the number of molecules evaporating from a layer is equal to those condensing on the layer below surface. The equation for this concept is given by [54]:

$$\frac{P/P_0}{V(1-P/P_0)} = \frac{1}{V_{mono}C} + \frac{C-1}{V_{mono}C}\frac{P}{P_0} \tag{A.39}$$

where C is the BET constant related to the net heat of adsorption of the monomolecular layer. As illustrated in Figure A.2(b), the completion monomolecular adsorption V_m and the constant K_L by BET method can be evaluated through the the slop and Y-intercept.

In addition to the well known Langmuir and BET interpretations on NAD, the surface area can be evaluated thorough BJH method [29]. Once the adsorbed volume of nitrogen is measured, the specific surface can be estimated by:

$$S = \sum_i \left(\frac{\Delta V}{r_i}\right) \tag{A.40}$$

where ΔV is the volume increment stepwise, r_i the pore radius. Analogous to the mercury porosimetry, the cylindrical geometry of pore is adopted in BJH approach. The radius r_i is equal to the sum of Kelvin radius r_k and the thickness of adsorbed film t. There are many methods to determine the adsorbed thickness t [84, 90, 91, 152, 155, 156, 220], among which the most widely used method may be the Hakins and Jura's equation [155]:

$$t = \frac{1}{10}\left(\frac{13.99}{0.034 - \log(P/P_0)}\right)^{1/2} \quad \text{nm} \tag{A.41}$$

Then the specific surface can also be determined by (the named t-plot),:

$$S = 15.47 \times 10^{-4}\frac{V}{t} \tag{A.42}$$

where V is the adsorbed volume of Nitrogen.

A.7 Derivation of eq(10.2)

For a porous material, the thermoelasticity relates the total volume V and pore volume V_ϕ to the Terzaghi effective pressure σ_d, the pore pressure P and the temperature T through [76, 137, 139],

$$-\frac{dV}{V_0}=\frac{1}{K_d}d\sigma_d+\frac{1}{K_s}dP-3\alpha_d dT \quad \text{and} \quad -\frac{dV_\phi}{V_{\phi,0}}=\frac{1}{K_P}d\sigma_d+\frac{1}{K_\phi}dP-3\alpha_\phi dT \tag{A.43}$$

where dV/V_0 represents the total volumetric strain, $dV_\phi/V_{\phi,0}$ is the pore volumetric strain; K_d and K_s are the drained bulk and unjacked moduli; K_P and K_ϕ the moduli link pore volumetric strain with effective stress and pore pressure, and α_d is the linear drained TEC. Employing the Betti's reciprocal theorem, the moduli adopt the relation $\phi/K_p=1/K_d-1/K_s$. Under drained condition and $d\sigma_d=0, dP=0$, α_d can be given by:

$$\alpha_d=\frac{1}{3}\frac{1}{V_0}\left(\frac{\partial V}{\partial T}\right)_{P,\sigma_d} \tag{A.44}$$

Actually, eq(A.44) is the expression for TEC evaluation from drained tests. The variation of the drained TEC with porosity is then expressed as,

$$\frac{\partial\alpha_d}{\partial\phi}=\frac{\partial\alpha_d}{\partial\sigma_d}\cdot\frac{\partial\sigma_d}{\partial\phi} \tag{A.45}$$

Using eq(A.43b) and the relation $d\phi/\phi_0=(dV_\phi/V_{\phi,0})-(dV)/V_0)$, the variation of effective stress with the porosity is then given by,

$$\frac{\partial\sigma_d}{\partial\phi}=-\left[\phi\left(\frac{1}{K_P}-\frac{1}{K_d}\right)\right]^{-1}=-\left[\frac{1-\phi}{K_d}-\frac{1}{K_s}\right]^{-1} \tag{A.46}$$

Combining eqs(A.45) and (A.46), one obtains,

$$\frac{\partial\alpha_d}{\partial\phi}=-\left[\frac{1-\phi}{K_d}-\frac{1}{K_s}\right]^{-1}\frac{\partial\alpha_d}{\partial\sigma} \tag{A.47}$$

From eq(A.44), the variation of linear drained TEC with respect to effective pressure σ_d can be expressed as,

$$\frac{\partial\alpha_d}{\partial\sigma}=\frac{1}{3}\frac{1}{V_0}\left(\frac{\partial^2 V}{\partial T\partial\sigma_d}\right)=-\frac{1}{3}\frac{\partial 1/K_d}{\partial T}=\frac{1}{3K_d^2}\frac{\partial K_d}{\partial T} \tag{A.48}$$

Substituting eq(A.48) into qe(A.47), one gets,

$$\frac{\partial\alpha_d}{\partial\phi}=-\frac{1}{3K_d^2}\left[\frac{1-\phi}{K_d}-\frac{1}{K_s}\right]^{-1}\frac{\partial K_d}{\partial T} \tag{A.49}$$

Appendix B

Poromechanical description of unsaturated porous materials

B.1 Energy balance of porous materials

B.1.1 First principle of thermodynamic

In this section, the energy balance (first principle) of porous media is postulated, and more detail and deepen work on this theory can be found in [76, 79]. By neglecting the dynamic energy terms, the total internal energy rate of porous media $\dot{\mathcal{E}}$ is composed of the potential of deformation $\mathcal{P}_{def}$ and the heat exchange rate $\mathring{\mathcal{Q}}$:

$$\dot{\mathcal{E}} = \mathcal{P}_{def} + \mathring{\mathcal{Q}} \tag{B.1}$$

With hypothesis that the solid skeleton and ice crystals in pore space are immobile, the total internal energy rate of porous media $\dot{\mathcal{E}}$, the potential of deformation $\mathcal{P}_{def}$ and the heat exchange rate $\mathring{\mathcal{Q}}$ can be expressed as (cf.[76, 77, 79, 114]):

$$\dot{\mathcal{E}} = \int_{\Omega_0} \left[\frac{\partial E}{\partial t} + \nabla \cdot (e_l \boldsymbol{\omega}_l) \right] \mathrm{d}\Omega_0 \tag{B.2a}$$

$$\mathcal{P}_{def} = \int_{\Omega_0} \left[\boldsymbol{\sigma} : \frac{\partial \boldsymbol{\varepsilon}}{\partial t} - \nabla \cdot \left(\frac{P_l}{\rho_l} \boldsymbol{\omega}_l \right) \right] \mathrm{d}\Omega_0 \tag{B.2b}$$

$$\mathring{\mathcal{Q}} = \int_{\Omega_0} \mathring{r} \partial\Omega_0 - \int_{\partial\Omega} \mathbf{q} \cdot \mathbf{n} \mathrm{d}(\partial\Omega) \tag{B.2c}$$

where e_l is the internal energy of liquid phase, $\mathbf{q}$ is the current of heat outgoing and $\mathring{r}$ is the source of heat, E is the average local internal energy:

$$E = \rho_{sk}(1-\phi)e_{sk} + \rho_c \phi (1 - S_l) e_c + \rho_l \phi S_l e_l \tag{B.3}$$

where e_{sk} and e_c is the internal energy of solid skeleton and ice crystals.

Recalling the divergence theorem, $\int_{\partial\Omega} \boldsymbol{\mathcal{G}} \cdot \mathbf{n} \mathrm{d}(\partial\Omega) = \int_{\Omega_0} \nabla \cdot \boldsymbol{\mathcal{G}} \mathrm{d}\Omega_0$, and substitution of eq(B.2) into eq(B.1), one obtains the energy conservation state as:

$$\frac{\partial E}{\partial t} = \boldsymbol{\sigma} : \frac{\partial \boldsymbol{\varepsilon}}{\partial t} - \nabla \cdot \left[\left(\frac{P_l}{\rho_l} + e_l \right) \boldsymbol{\omega}_l + \mathbf{q} \right] + \mathring{r} \tag{B.4}$$

Let Ψ and ψ_α denote the overall Helmholtz free energy density and the specific Helmholtz free energy density of phase α; $\mathcal{S}$ and s_α stand for the overall entropy density and specific entropy density of phase α. The thermodynamic expression relating to Helmholtz free energy, internal energy and entropy is known as:

$$\Psi = E - T\mathcal{S} \quad \text{and} \quad \psi_\alpha = e_\alpha - T s_\alpha \tag{B.5}$$

Obviously, the overall property is composed of the specific property by volume average approach:

$$\Psi = \rho_{sk}(1-\phi)\psi_{sk} + \rho_c \phi (1 - S_l)\psi_c + \rho_l \phi S_l \psi_l \tag{B.6a}$$

$$\mathcal{S} = \rho_{sk}(1-\phi)s_{sk} + \rho_c \phi (1 - S_l) s_c + \rho_l \phi S_l s_l \tag{B.6b}$$

Substitution of eqs(B.5) and (B.6) into eq(B.4), one obtains:

$$\frac{\partial \Psi}{\mathrm{d}t} = \boldsymbol{\sigma} : \frac{\partial \boldsymbol{\varepsilon}}{\partial t} - \nabla \cdot \left[\left(\frac{P_l}{\rho_l} + \psi_l \right) \boldsymbol{\omega}_l + \mathbf{q} \right] + \mathring{r} - \mathcal{S} \frac{\partial T}{\partial t} - \left(\frac{\partial \mathcal{S}}{\partial t} + \nabla \cdot (s_l \boldsymbol{\omega}_l) \right) T \tag{B.7}$$

Eq(B.7) expresses the rate of overall Helmholtz free energy density.

B.1.2 Second principle of thermodynamics

According to Clausius statement of the second principle of thermodynamics [199], entropy is defined as a thermodynamic property that is a measure of the energy not available for useful work in a thermodynamic process, which has:

$$\mathring{\mathbb{S}} \geq \frac{\mathring{\mathcal{Q}}}{T} = \int_{\Omega_0} \frac{\mathring{r}}{T} \mathrm{d}\Omega_0 - \int_{\partial\Omega_0} \frac{\mathbf{q} \cdot \mathbf{n}}{T} \mathrm{d}(\partial\Omega_0) \tag{B.8}$$

where $\mathbb{S} = \int_\Omega \mathcal{S} d\Omega$ stands for the global entropy of porous media, which can be expressed as:

$$\begin{aligned} \mathring{\mathbb{S}} &= \frac{\partial}{\partial t} \int_{\Omega_0} \rho_{sk}(1-\phi) s_{sk} \mathrm{d}\Omega_0 + \frac{\mathrm{d}^l}{\mathrm{d}t} \int_{\Omega_0} \rho_l \phi S_l s_l \mathrm{d}\Omega_0 + \frac{\partial}{\partial t} \int_{\Omega_0} \rho_c \phi (1 - S_l) s_c \mathrm{d}\Omega_0 \\ &\simeq \int_{\Omega_0} \left[\frac{\partial}{\partial t} \left(\rho_{sk}(1-\phi)s_{sk} + \rho_c \phi (1 - S_l) s_c + \rho_l \phi S_l s_l \right) + \nabla \cdot (s_l \boldsymbol{\omega}_l) \right] \mathrm{d}\Omega_0 \end{aligned} \tag{B.9}$$

Combining eqs(B.6b), (B.9) and eq(B.8), one can obtains:

$$\int_{\Omega_0} \frac{\partial \mathcal{S}}{\partial t} \mathrm{d}\Omega_0 \geq \int_{\Omega_0} \frac{\mathring{r}}{T} \mathrm{d}\Omega_0 - \int_{\partial\Omega_0} \frac{\mathbf{q} \cdot \mathbf{n}}{T} \mathrm{d}(\partial\Omega_0) - \int_{\Omega_0} \nabla \cdot (s_l \boldsymbol{\omega}_l) \mathrm{d}\Omega_0 \tag{B.10}$$

Again, the divergence theorem is used for the second term at the right hand of eq(B.10), it thus has:

$$T \frac{\partial \mathcal{S}}{\partial t} \geq \mathring{r} - T \nabla \cdot s_l \boldsymbol{\omega}_l - \nabla \cdot \mathbf{q} + \frac{\mathbf{q} \cdot \nabla T}{T} \tag{B.11}$$

B.2 Principle equations

B.2.1 Momentum conservation

Considering a partial frozen porous medium, which is composed of skeleton, liquid saline solution and ice crystals. If neglecting field force (i.e. gravity force), and no surface force applied, according to solid mechanics [129, 419], the momentum balance in a RVE allows us to write:

$$\nabla \cdot \boldsymbol{\sigma} = \mathbf{0}, \quad \boldsymbol{\sigma}^T = \boldsymbol{\sigma} \tag{B.12}$$

Substitution of eq(4.54a) into eq(B.12), one obtains:

$$\nabla \cdot \left[\left(K - \frac{2}{3} G \right) \boldsymbol{\epsilon} + 2G\boldsymbol{\varepsilon} - b_l P_l^* \mathbf{I} - b_c P_c^* \mathbf{I} - K\alpha_{th}(T - T_0)\mathbf{I} \right] = \mathbf{0} \tag{B.13}$$

With linear elasticity hypothesis of solid matrix, one can rewrite the above equation as:

$$\left(K + \frac{4}{3} G \right) \nabla\epsilon - b_l \nabla P_l^* - b_c \nabla P_c^* - K\alpha_{TH} \nabla T - G\nabla \times (\nabla \times \boldsymbol{\varepsilon}) = \mathbf{0}. \tag{B.14}$$

Integration of the above equation, one obtains an one dimensional equation:

$$\left(K + \frac{4}{3} G \right) \epsilon - b_l P_l^* - b_c P_c^* - K\alpha_{TH}(T - T_0) = \mathcal{F}(t) \tag{B.15}$$

where $\mathcal{F}(t)$ is a function of time.

B.2.2 Partial and total pore deformation

Considering the eqs(4.54b) and (4.54c), the partial pore deformation of liquid phase φ_l is:

$$\begin{aligned} \varphi_l = & \left[\frac{b_l^2 + b_l b_c(\rho_c/\rho_l - 1)}{K + \frac{4}{3}G} + \frac{1}{N_{ll}} + \frac{1}{N_{lc}} \left(\frac{\rho_c}{\rho_w} - 1 \right) \right] P_l - \left[\frac{b b_l}{K + \frac{4}{3}G} + \frac{1}{N_{ll}} + \frac{1}{N_{lc}} \right] \frac{2}{3} U \\ & + \left[\frac{b_l K \alpha_{TH}}{K + \frac{4}{3}G} - \alpha_{\phi l} - \left(\frac{b_l b_c}{K + \frac{4}{3}G} + \frac{1}{N_{lc}} \right) \mathcal{S}_f \right] (T - T_0) - \left(\frac{b_l b_c}{K + \frac{4}{3}G} + \frac{1}{N_{lc}} \right) C_f \left[(T - T_0) + T \ln \left(\frac{T_0}{T} \right) \right] \\ & + \left(\frac{b_l b_c}{K + \frac{4}{3}G} + \frac{1}{N_{lc}} \right) \frac{\rho_c R T}{\mathsf{M}_w} \ln \left(\frac{a_w}{a_w^0} \right) + \frac{b_l}{K + \frac{4}{3}G} \mathcal{F}(t) \end{aligned} \tag{B.16}$$

and the differential term of partial pore deformation of liquid phase $\mathrm{d}\varphi_l$ can be expressed as:

$$\begin{aligned} \mathrm{d}\varphi_l = & \left[\frac{b_l^2 + b_l b_c(\rho_c/\rho_l - 1)}{K + \frac{4}{3}G} + \frac{1}{N_{ll}} + \frac{1}{N_{lc}} \left(\frac{\rho_c}{\rho_w} - 1 \right) \right] \mathrm{d}P_l + \left[\frac{b b_l}{K + \frac{4}{3}G} + \frac{1}{N_{ll}} + \frac{1}{N_{lc}} \right] \frac{2}{3} P_{cap} \mathrm{d}S_l \\ & + \left[\frac{b_l K \alpha_{TH}}{K + \frac{4}{3}G} - \alpha_{\phi l} - \left(\frac{b_l b_c}{K + \frac{4}{3}G} + \frac{1}{N_{lc}} \right) \left(\mathcal{S}_f + C_f \ln \left(\frac{T}{T_0} \right) \right) \right] \mathrm{d}T + \left(\frac{b_l b_c}{K + \frac{4}{3}G} + \frac{1}{N_{lc}} \right) \frac{\rho_c R T}{\mathsf{M}_w} \mathrm{d} \ln a_w + \frac{b_l}{K + \frac{4}{3}G} \mathrm{d}\mathcal{F}(t) \end{aligned} \tag{B.17}$$

With the same procedures, one can obtain the partial deformation of pore space by ice crystals φ_c as:

$$\begin{aligned}\varphi_c = &\left[\frac{b_l b_c + b_c^2(\rho_c/\rho_l - 1)}{K + \frac{4}{3}G} + \frac{1}{N_{lc}} + \frac{1}{N_{cc}}\left(\frac{\rho_c}{\rho_w} - 1\right)\right] P_l - \left[\frac{b_c^2 + b_l b_c}{K + \frac{4}{3}G} + \frac{1}{N_{cc}} + \frac{1}{N_{lc}}\right]\frac{2}{3}U \\ &+ \left[\frac{b_c K \alpha_{TH}}{K + \frac{4}{3}G} - \alpha_{\phi c} - \left(\frac{b_c^2}{K + \frac{4}{3}G} + \frac{1}{N_{cc}}\right)\mathcal{S}_f\right](T - T_0) - \left(\frac{b_c^2}{K + \frac{4}{3}G} + \frac{1}{N_{cc}}\right) C_f \left[(T - T_0) + T\ln\left(\frac{T_0}{T}\right)\right] \\ &+ \left(\frac{b_c^2}{K + \frac{4}{3}G} + \frac{1}{N_{cc}}\right)\frac{\rho_c RT}{\mathsf{M}_w}\ln\left(\frac{a_w}{a_w^0}\right) + \frac{b_c}{K + \frac{4}{3}G}\mathcal{F}(t)\end{aligned} \tag{B.18}$$

Again, the differential form of partial pore deformation of ice crystals $\mathrm{d}\varphi_c$ can be given by:

$$\begin{aligned}\mathrm{d}\varphi_c = &\left[\frac{b_l b_c + b_c^2(\rho_c/\rho_l - 1)}{K + \frac{4}{3}G} + \frac{1}{N_{lc}} + \frac{1}{N_{cc}}\left(\frac{\rho_c}{\rho_w} - 1\right)\right]\mathrm{d}P_l + \left[\frac{b_c^2 + b_l b_c}{K + \frac{4}{3}G} + \frac{1}{N_{cc}} + \frac{1}{N_{lc}}\right]\frac{2}{3}P_{cap}\mathrm{d}S_l \\ &+ \left[\frac{b_c K \alpha_{TH}}{K + \frac{4}{3}G} - \alpha_{\phi c} - \left(\frac{b_c^2}{K + \frac{4}{3}G} + \frac{1}{N_{cc}}\right)\left(\mathcal{S}_f + C_f\ln\left(\frac{T}{T_0}\right)\right)\right]\mathrm{d}T + \left(\frac{b_c^2}{K + \frac{4}{3}G} + \frac{1}{N_{cc}}\right)\frac{\rho_c RT}{\mathsf{M}_w}\mathrm{d}\ln a_w + \frac{b_c}{K + \frac{4}{3}G}\mathcal{F}(t)\end{aligned} \tag{B.19}$$

During the derivation processes of eqs(B.16) to (B.19), the capillary pressure and its differential form, viz. $P_{cap} = P_c - P_l$ and $\mathrm{d}P_{cap} = \mathrm{d}P_c - \mathrm{d}P_l$, are used:

$$P_{cap} = \left(\frac{\rho_c}{\rho_w} - 1\right)(P_l - P_0) + \mathcal{S}_f(T_0 - T) + C_f\left((T - T_0) + T\ln\left(\frac{T_0}{T}\right)\right) + \frac{\rho_c}{\mathsf{M}_w}RT\ln a_w \tag{B.20a}$$

$$\mathrm{d}P_{cap} = \left(\frac{\rho_c}{\rho_w} - 1\right)\mathrm{d}P_l - S_f\mathrm{d}T - \frac{C_f}{T^2}\mathrm{d}T + \frac{\rho_c}{\mathsf{M}_w}RT\mathrm{d}\ln a_w \tag{B.20b}$$

For the partial pore volume occupied by liquid phase, viz. $\phi_l = \phi_0 S_l + \varphi_l$, the saturation degree has significantly impact on the partial pore volume filled by liquid phase. Since the capillary pressure, required by local mechanical equilibrium between ice tips and liquid water, is only the function of surface tension and penetration pore size, the saturation degree thus can be expressed as a function of capillary pressure P_{cap}. The differential form of saturation degree to liquid pressure P_l, temperature T and salt concentration c_i is then given by:

$$\mathrm{d}S_l = \frac{\partial S_l}{\partial P_{cap}}\left[\frac{\partial P_{cap}}{\partial P_l}\mathrm{d}P_l + \frac{\partial P_{cap}}{\partial T}\mathrm{d}T + \sum_i \frac{\partial P_{cap}}{\partial c_i}\mathrm{d}c_i\right] \tag{B.21}$$

Combining eqs(B.20b), (B.21) and (B.17), the differential form of partial pore volume occupied by liquid phase, viz. $\mathrm{d}\phi_l = \phi_0\mathrm{d}S_l + \mathrm{d}\varphi_l$, is thus obtained as:

$$\mathrm{d}\phi_l = \frac{\partial \phi_l}{\partial P_l}\mathrm{d}P_l + \frac{\partial \phi_l}{\partial T}\mathrm{d}T + \frac{\partial \phi_l}{\partial c_i}\mathrm{d}c_i + \frac{b_l}{K + \frac{4}{3}G}\mathrm{d}\mathcal{F}(t) \tag{B.22}$$

where

$$\frac{\partial \phi_l}{\partial P_l} = \left[\phi_0 + \left[\frac{b b_l}{K + \frac{4}{3}G} + \frac{1}{N_{ll}} + \frac{1}{N_{lc}}\right]\frac{2}{3}P_{cap}\right]\left(\frac{\rho_c}{\rho_w} - 1\right)\frac{\partial S_l}{\partial P_{cap}} + \left[\frac{b_l^2 + b_l b_c(\rho_c/\rho_l - 1)}{K + \frac{4}{3}G} + \frac{1}{N_{ll}} + \frac{1}{N_{lc}}\left(\frac{\rho_c}{\rho_w} - 1\right)\right] \tag{B.23a}$$

$$\begin{aligned}\frac{\partial \phi_l}{\partial T} = &-\left[\phi_0 + \left[\frac{b b_l}{K + \frac{4}{3}G} + \frac{1}{N_{ll}} + \frac{1}{N_{lc}}\right]\frac{2}{3}P_{cap}\right]\left(S_f + C_f\ln\left(\frac{T}{T_0}\right)\right)\frac{\partial S_l}{\partial P_{cap}} \\ &+ \left[\frac{b_l K \alpha_{TH}}{K + \frac{4}{3}G} - \alpha_{\phi l} - \left(\frac{b_l b_c}{K + \frac{4}{3}G} + \frac{1}{N_{lc}}\right)\left(\mathcal{S}_f + C_f\ln\left(\frac{T}{T_0}\right)\right)\right]\end{aligned} \tag{B.23b}$$

$$\frac{\partial \phi_l}{\partial c_i} = \left[\phi_0 + \left[\frac{b b_l}{K + \frac{4}{3}G} + \frac{1}{N_{ll}} + \frac{1}{N_{lc}}\right]\frac{2}{3}P_{cap}\right]\frac{\partial S_l}{\partial P_{cap}}\frac{\rho_c RT}{\mathsf{M}_w}\frac{\partial \ln a_w}{\partial c_i} + \left(\frac{b_l b_c}{K + \frac{4}{3}G} + \frac{1}{N_{lc}}\right)\frac{\rho_c RT}{\mathsf{M}_w}\frac{\partial \ln a_w}{\partial c_i} \tag{B.23c}$$

The differential form of partial pore volume occupied by ice crystals, viz. $\mathrm{d}\phi_c = \phi_0\mathrm{d}S_c + \mathrm{d}\varphi_c = -\phi_0\mathrm{d}S_l + \mathrm{d}\varphi_c$, is then expressed explicitly as:

$$\mathrm{d}\phi_c = \frac{\partial \phi_c}{\partial P_l}\mathrm{d}P_l + \frac{\partial \phi_c}{\partial T}\mathrm{d}T + \frac{\partial \phi_c}{\partial c_i}\mathrm{d}c_i + \frac{b_l}{K+\frac{4}{3}G}\mathrm{d}\mathcal{F}(t) \tag{B.24}$$

where

$$\frac{\partial \phi_c}{\partial P_l} = \left[-\phi_0 + \left[\frac{bb_c}{K+\frac{4}{3}G} + \frac{1}{N_{cc}} + \frac{1}{N_{lc}}\right]\frac{2}{3}P_{cap}\right]\left(\frac{\rho_c}{\rho_w} - 1\right)\frac{\partial S_l}{\partial P_{cap}} + \left[\frac{b_l b_c + b_c^2(\rho_c/\rho_l - 1)}{K+\frac{4}{3}G} + \frac{1}{N_{lc}} + \frac{1}{N_{cc}}\left(\frac{\rho_c}{\rho_w} - 1\right)\right] \tag{B.25a}$$

$$\begin{aligned}\frac{\partial \phi_c}{\partial T} = &\left[\phi_0 - \left[\frac{bb_c}{K+\frac{4}{3}G} + \frac{1}{N_{cc}} + \frac{1}{N_{lc}}\right]\frac{2}{3}P_{cap}\right]\left(S_f + C_f \ln\left(\frac{T}{T_0}\right)\right)\frac{\partial S_l}{\partial P_{cap}} \\ &+ \left[\frac{b_c K \alpha_{TH}}{K+\frac{4}{3}G} - \alpha_{\phi c} - \left(\frac{b_c^2}{K+\frac{4}{3}G} + \frac{1}{N_{cc}}\right)\left(\mathcal{S}_f + C_f \ln\left(\frac{T}{T_0}\right)\right)\right]\end{aligned} \tag{B.25b}$$

$$\frac{\partial \phi_c}{\partial c_i} = \left[-\phi_0 + \left[\frac{bb_c}{K+\frac{4}{3}G} + \frac{1}{N_{cc}} + \frac{1}{N_{lc}}\right]\frac{2}{3}P_{cap}\right]\frac{\partial S_l}{\partial P_{cap}}\frac{\rho_c RT}{\mathsf{M}_w}\frac{\partial \ln a_w}{\partial c_i} + \left(\frac{b_c^2}{K+\frac{4}{3}G} + \frac{1}{N_{cc}}\right)\frac{\rho_c RT}{\mathsf{M}_w}\frac{\partial \ln a_w}{\partial c_i} \tag{B.25c}$$

B.2.3 Equations for ions

The total mass of species i in a porous material is given by:

$$m_i = \rho_i \phi_l = \mathsf{M}_i c_i(\phi_0 S_l + \varphi_l) \tag{B.26}$$

By using of the deformation of pore volume, eq(B.16), and its differential term, eq(B.17), the differential form of mass of species i then can be expressed as:

$$\begin{aligned}\mathrm{d}m_i &= \phi_l \mathsf{M}_i \mathrm{d}c_i + \mathsf{M}_i c_i\left(\phi_0 \mathrm{d}S_l + \mathrm{d}\varphi_l\right) \\ &= \phi_l \mathsf{M}_i \mathrm{d}c_i + \mathsf{M}_i c_i\left(\frac{\partial \phi_l}{\partial P_l}\mathrm{d}P_l + \frac{\partial \phi_l}{\partial T}\mathrm{d}T + \frac{\partial \phi_l}{\partial c_i}\mathrm{d}c_i + \frac{b_l}{K+\frac{4}{3}G}\mathrm{d}\mathcal{F}(t)\right)\end{aligned} \tag{B.27}$$

where the terms $\frac{\partial \phi_l}{\partial P_l}$, $\frac{\partial \phi_l}{\partial T}$ and $\frac{\partial \phi_l}{\partial c_i}$ can be found in eq(B.23). Substitution of eq(B.27) into eq(4.32), one gets the mass conservation equation for species i:

$$\begin{aligned}&\left(\phi_l + c_i\frac{\partial \phi_l}{\partial c_i}\right)\frac{\partial c_i}{\partial t} + c_i\frac{\partial \phi_l}{\partial P_l}\frac{\partial P_l}{\partial t} + c_i\frac{\partial \phi_l}{\partial T}\frac{\partial T}{\partial t} + c_i\frac{b_l}{K+\frac{4}{3}G}\frac{\partial \mathcal{F}(t)}{\partial t} \\ &= \nabla\cdot\left\{\frac{c_i\kappa}{\eta_l}\nabla P_l + c_i\phi S_l D_i\left[\frac{1}{c_i}\nabla c_i + \nabla\ln(\gamma_i) + \frac{\ln(\gamma_i c_i)}{T}\nabla T + \frac{z_i F}{RT}\nabla\Psi_E\right]\right\}\end{aligned} \tag{B.28}$$

B.2.4 Equations for water

The total mass of water in a porous material is given by:

$$m_w = \mathsf{M}_w c_w(\phi_0 S_l + \varphi_l) = \frac{\mathsf{M}_w}{\mathsf{V}_w}\left(1 - \sum_i c_i \mathsf{V}_{\phi,i}\right)(\phi_0 S_l + \varphi_l) \tag{B.29}$$

Again, using the differential terms of partial deformation of liquid phase $d\phi_l$, one obtains the differential form of water mass:

$$\begin{aligned}\mathrm{d}m_w = &\left(1 - \sum_i c_i \mathsf{V}_{\phi,i}\right)\phi_l \mathrm{d}\frac{\mathsf{M}_w}{\mathsf{V}_w} - \frac{\mathsf{M}_w}{\mathsf{V}_w}\phi_l\sum_i \mathsf{V}_{\phi,i}\mathrm{d}c_i - \frac{\mathsf{M}_w}{\mathsf{V}_w}\phi_l\sum_i c_i \mathrm{d}V_{\phi,i} \\ &+ \frac{\mathsf{M}_w}{\mathsf{V}_w}\left(1 - \sum_i c_i \mathsf{V}_{\phi,i}\right)\left[\frac{\partial \phi_l}{\partial P_l}\mathrm{d}P_l + \frac{\partial \phi_l}{\partial T}\mathrm{d}T + \frac{\partial \phi_l}{\partial c_i}\mathrm{d}c_i + \frac{b_l}{K+\frac{4}{3}G}\mathrm{d}\mathcal{F}(t)\right]\end{aligned} \tag{B.30}$$

where $\mathsf{V}_{\phi,i}$ is the apparent molar volume of species i. The expressions of $\partial\phi_l/\partial\alpha$ with $\alpha = P_l, T, c_i$ can be found in eq(B.23). Substitution of eq(B.30) into the liquid water conservation equation, eq(4.33), one can achieve:

$$\begin{aligned}
&\Big(1-\sum_i c_i\mathsf{V}_{\phi,i}\Big)\frac{\phi_l}{K_w}\frac{\mathsf{M}_w}{\mathsf{V}_w}\frac{\partial P_l}{\partial t} - \Big(1-\sum_i c_i\mathsf{V}_{\phi,i}\Big)\phi_l 3\alpha_w\rho_w\frac{\partial T}{\partial t}\\
&-\frac{\mathsf{M}_w}{\mathsf{V}_w}\phi_l\left[\sum_i\Big(\mathsf{V}_{\phi,i}+c_i\frac{\partial\mathsf{V}_{\phi,i}}{\partial c_i}\Big)\frac{\partial c_i}{\partial t}+\sum_i\frac{c_i}{K_{\phi,i}}\frac{1}{\mathsf{V}_{\phi,i}}\frac{\partial P_l}{\partial t}-\sum_i c_i\frac{1}{\mathsf{V}_{\phi,i}}3\alpha_{\phi,i}\frac{\partial T}{\partial t}\right]\\
&+\frac{\mathsf{M}_w}{\mathsf{V}_w}\Big(1-\sum_i c_i\mathsf{V}_{\phi,i}\Big)\left[\frac{\partial\phi_l}{\partial P_l}\frac{\partial P_l}{\partial t}+\frac{\partial\phi_l}{\partial T}\frac{\partial T}{\partial t}+\frac{\partial\phi_l}{\partial c_i}\frac{\partial c_i}{\partial t}+\frac{b_l}{K+\frac{4}{3}G}\frac{\partial\mathcal{F}(t)}{\partial t}\right]+\mathring{m}_{w\to c}\\
&=\nabla\cdot\left\{\frac{\mathsf{M}_w c_w\kappa}{\eta_l}\nabla P_l-\sum_i^N\mathsf{M}_i c_i(\phi_0 S_l+\varphi_l)D_i\left[\frac{1}{c_i}\nabla(c_i)+\nabla(\ln(\gamma_i))+\frac{\ln(\gamma_i c_i)}{T}\nabla(T)+\frac{z_i F}{RT}\nabla(\Psi_E)\right]\right\}
\end{aligned}\tag{B.31}$$

where $1/K_w$ is the compressibility of pure water (Pa^{-1}), $1/K_{\phi,i}$ is the apparent compressibility of species i (Pa^{-1}), α_w is the thermal expansion coefficient of pure water (K^{-1}) and $\alpha_{\phi,i}$ is the apparent thermal (volumetric) coefficient of species i (K^{-1}). These parameters for NaCl solution can be found in Appendix D. With hypothesis of an infinitesimal pore deformation, the ice formation rate $\mathring{m}_{w\to c}$ is then approached by:

$$\mathring{m}_{w\to c}=\frac{-\partial\rho_c\phi S_l}{\partial t}\approx-\rho_c\phi\frac{\partial S_l}{\partial P_{cap}}\left[\left(\frac{\rho_c}{\rho_w}-1\right)\frac{\partial P_l}{\partial t}-\left(\mathcal{S}_f+\frac{C_f}{T^2}\right)\frac{\partial T}{\partial t}+\frac{\rho_c}{\mathsf{M}_w}RT\frac{\partial\ln a_w}{\partial c_i}\frac{\partial c_i}{\partial t}\right]\tag{B.32}$$

Substitution of eq(B.32) into eq(B.31), one obtains:

$$\begin{aligned}
&\frac{\partial m_w}{\partial P_l}\cdot\frac{\partial P_l}{\partial t}+\frac{\partial m_w}{\partial T}\cdot\frac{\partial T}{\partial t}+\sum_i\frac{\partial m_w}{\partial c_i}\cdot\frac{\partial c_i}{\partial t}+\rho_w\Big(1-\sum_i c_i\mathsf{V}_{\phi,i}\Big)\frac{b_l}{K+\frac{4}{3}G}\frac{\partial\mathcal{F}(t)}{\partial t}\\
&=\nabla\cdot\left\{\frac{\mathsf{M}_w c_w\kappa}{\eta_l}\nabla P_l-\sum_i^N\mathsf{M}_i c_i\phi_l D_i\left[\frac{1}{c_i}\nabla(c_i)+\nabla(\ln(\gamma_i))+\frac{\ln(\gamma_i c_i)}{T}\nabla(T)+\frac{z_i F}{RT}\nabla(\Psi_E)\right]\right\}
\end{aligned}\tag{B.33}$$

With

$$\frac{\partial m_w}{\partial P_l}=\Big(1-\sum_i c_i\mathsf{V}_{\phi,i}\Big)\frac{\phi_l}{K_w}\frac{\mathsf{M}_w}{\mathsf{V}_w}-\frac{\mathsf{M}_w}{\mathsf{V}_w}\phi_l\sum_i c_i K_{\phi,i}\frac{1}{\mathsf{V}_{\phi,i}}+\frac{\mathsf{M}_w}{\mathsf{V}_w}\Big(1-\sum_i c_i V_{\phi,i}\Big)\frac{\partial\phi_l}{\partial P_l}-\rho_c\phi\frac{\partial S_l}{\partial P_{cap}}\left(\frac{\rho_c\mathsf{V}_w}{\mathsf{M}_w}-1\right)\tag{B.34a}$$

$$\frac{\partial m_w}{\partial T}=-\Big(1-\sum_i c_i\mathsf{V}_{\phi,i}\Big)\phi_l\alpha_w\frac{\mathsf{M}_w}{\mathsf{V}_w}+\frac{\mathsf{M}_w}{\mathsf{V}_w}\phi_l\sum_i c_i\frac{1}{\mathsf{V}_{\phi,i}}\alpha_{\phi,i}+\frac{\mathsf{M}_w}{\mathsf{V}_w}\Big(1-\sum_i c_i V_{\phi,i}\Big)\frac{\partial\phi_l}{\partial T}+\rho_c\phi\frac{\partial S_l}{\partial P_{cap}}\left(\mathcal{S}_f+\frac{C_f}{T^2}\right)\tag{B.34b}$$

$$\frac{\partial m_w}{\partial c_i}=-\frac{\mathsf{M}_w}{\mathsf{V}_w}\phi_l\sum_i\Big(\mathsf{V}_{\phi,i}+c_i\frac{\partial\mathsf{V}_{\phi,i}}{\partial c_i}\Big)+\frac{\mathsf{M}_w}{\mathsf{V}_w}\Big(1-\sum_i c_i\mathsf{V}_{\phi,i}\Big)\frac{\partial\phi_l}{\partial c_i}-\frac{\partial S_l}{\partial P_{cap}}\frac{\rho_c^2\phi}{\mathsf{M}_w}RT\frac{\partial\ln a_w}{\partial c_i}\tag{B.34c}$$

B.2.5 Equations for liquid phase

For porous medium saturated with saline solution initially, the total mass m in pore space currently contained in a RVE is given by:

$$m = m_l + m_c = \rho_l \phi_l + \rho_c \phi_c = \rho_l \phi_0 S_l + \rho_c \phi_0 S_c + \rho_l \varphi_l + \rho_c \varphi_c \tag{B.35}$$

and the differential form of total mass is given by:

$$\mathrm{d}m = \phi_l \mathrm{d}\rho_l + \rho_l d\phi_l + \phi_c \mathrm{d}\rho_c + \rho_c d\phi_c \tag{B.36}$$

Note ρ_l is the overall density of solution containing salts, and its normal expression and the differential expression are given by:

$$\rho_l = \mathsf{M}_w c_w + \sum_i \mathsf{M}_i c_i = \frac{\mathsf{M}_w}{\mathsf{V}_w} + \sum_i \left(\mathsf{M}_i - \mathsf{M}_w \frac{\mathsf{V}_{\phi,i}}{\mathsf{V}_w} \right) c_i \tag{B.37a}$$

$$\mathrm{d}\rho_l = \mathrm{d}\frac{\mathsf{M}_w}{\mathsf{V}_w} + \sum_i \left(\mathsf{M}_i - \mathsf{M}_w \frac{\mathsf{V}_{\phi,i}}{\mathsf{V}_w} \right) \mathrm{d}c_i - \sum_i c_i \mathsf{M}_w \mathrm{d}\left(\frac{\mathsf{V}_{\phi,i}}{\mathsf{V}_w} \right) \tag{B.37b}$$

where $\mathsf{V}_{\phi,i}$ is apparent molar volume of species i, of which the detail variations with pressure, temperature and salt concentrations can be found in Appendix D.

The compressibility of solution $1/K_l$ then can be expressed as:

$$\frac{1}{K_l} = \frac{1}{\rho_l} \frac{\partial \rho_l}{\partial P_l} = \frac{1}{\rho_l} \left[\frac{\mathsf{M}_w}{K_w \mathsf{V}_w} - \sum_i c_i \left(\frac{\mathsf{M}_w}{\mathsf{V}_w} \frac{\mathsf{V}_{\phi,i}}{K_w} + \frac{\mathsf{M}_w}{\mathsf{V}_w} \frac{\partial \mathsf{V}_{\phi,i}}{\partial P_l} \right) \right] = \frac{1}{K_w} + \sum_i c_i \frac{1}{K_{\phi,i}} \tag{B.38}$$

where $1/K_{\phi,i}$ is defined as the apparent compressibility of specie i:

$$\frac{1}{K_{\phi,i}} = -\frac{1}{\rho_l} \left(\frac{\mathsf{M}_i}{K_w} + \frac{\mathsf{M}_w}{\mathsf{V}_w} \frac{\partial \mathsf{V}_{\phi,i}}{\partial P_l} \right) \tag{B.39}$$

The thermal expansion coefficient of solution α_l then can be expressed as:

$$\alpha_l = -\frac{1}{3} \frac{1}{\rho_l} \frac{\partial \rho_l}{\partial T} = \frac{1}{3} \frac{1}{\rho_l} \left[\frac{\mathsf{M}_w}{\mathsf{V}_w} \alpha_w + \sum_i c_i \left(-\frac{\mathsf{M}_w}{\mathsf{V}_w} \alpha_w \mathsf{V}_{\phi,i} + \frac{\mathsf{M}_w}{\mathsf{V}_w} \frac{\partial \mathsf{V}_{\phi,i}}{\partial T} \right) \right] = \alpha_w + \sum_i c_i \alpha_{\phi,i} \tag{B.40}$$

where $\alpha_{\phi,i}$ is defined as the apparent thermal expansion coefficient of specie i:

$$\alpha_{\phi,i} = \frac{1}{3} \frac{1}{\rho_l} c_i \left(-\alpha_w \mathsf{M}_i + \frac{\mathsf{M}_w}{\mathsf{V}_w} \frac{\partial \mathsf{V}_{\phi,i}}{\partial T} \right) \tag{B.41}$$

For ice crystals, the constitutive equations can be given by:

$$\mathrm{d}\rho_c = \frac{\rho_c}{K_c}\mathrm{d}P_l - 3\rho_c\alpha_c\mathrm{d}T, \quad \text{with} \quad \frac{1}{K_c} = \frac{1}{\rho_c}\frac{\partial\rho_c}{\partial P_l}, \quad \text{and} \quad \alpha_c = -\frac{1}{3}\frac{1}{\rho_c}\frac{\partial\rho_c}{\partial T} \tag{B.42}$$

Substitution of eqs(B.20a) and (B.15) into eq(B.36), and combining the eq(4.12), on finally obtains:

$$\nabla\cdot\left(\frac{\rho_l\kappa}{\eta_l}\nabla P_l\right) = \mathcal{A}_{\Delta\rho}\frac{\partial S_l}{\partial t} + \mathcal{B}\frac{\partial T}{\partial t} + \mathcal{C}\frac{\partial P_l}{\partial t} + \mathcal{D}\frac{\partial U}{\partial t} + \sum_i^N \mathcal{H}_i\frac{\partial c_i}{\partial t} + \frac{b_l\rho_l + b_c\rho_c}{K+\frac{4}{3}G}\frac{\partial\mathcal{F}(t)}{\partial t} \tag{B.43}$$

with

$$\mathcal{A}_{\Delta\rho}(S_l) = \phi_0\left(\rho_l - \rho_c\right) \tag{B.44a}$$

$$\mathcal{B}(T) = \frac{(\rho_l b_l + \rho_c b_c)K3\alpha_s}{K+\frac{4}{3}G} - 3[\alpha_{\phi,l}\rho_l + \alpha_{\phi,c}\rho_c + (\rho_l\phi_l\alpha_l + \rho_c\phi_c\alpha_c)] - \left[\frac{b_c(\rho_l b_l + \rho_c b_c)}{K+\frac{4}{3}G} + \frac{\rho_l}{N_{ll}} + \frac{\rho_c}{N_{cc}}\right]\left(\mathcal{S}_f + C_f\ln\left(\frac{T}{T_0}\right)\right) \tag{B.44b}$$

$$\mathcal{C}(P_l) = \frac{b_l^2\rho_l + b_l b_c(2\rho_l - \rho_l) + b_c^2(\rho_c^2/\rho_l - \rho_c)}{K+\frac{4}{3}G} + \frac{\rho_l}{N_{ll}} + \frac{\rho_c(\rho_c - \rho_l)}{\rho_l N_{cc}} + \frac{2\rho_c - \rho_l}{N_{lc}} + \left(\frac{\rho_l\phi_l}{K_l} + \frac{\rho_c\phi_c}{K_c}\right) \tag{B.44c}$$

$$\mathcal{D}(U) = -\frac{2}{3}\left[\frac{b(\rho_l b_l + \rho_c b_c)}{K+\frac{4}{3}G} + \frac{\rho_l}{N_{ll}} + \frac{\rho_c}{N_{cc}} + \frac{\rho_c + \rho_l}{N_{lc}}\right] \tag{B.44d}$$

$$\mathcal{H}_i(c_i) = \left[\frac{b_c(\rho_l b_l + \rho_c b_c)}{K+\frac{4}{3}G} + \frac{\rho_l}{N_{ll}} + \frac{\rho_c}{N_{cc}}\right]\frac{\rho_c RT}{\mathsf{M}_w}\frac{\partial\ln a_w}{\partial c_i} + \phi_l M_i \tag{B.44e}$$

The $\mathcal{A}_{\Delta\rho}(S_l)$ denotes the mass change by the effect of density difference between ice and liquid phase. $\mathcal{B}(T)$ represents the mass change due to the temperature effects. $\mathcal{C}(P_l)$ is the mass change due to the liquid pressure P_l. $\mathcal{D}(U)$ accounts for the mass changing owing to the interfacial effect, and $\mathcal{H}_i(c_i)$ is the mass change by the water activity with salts.

B.2.6 Equations for heat transfer

We start to derive the equation of entropy from the dissipation equation (cf. eq(4.35)). Considering further the eq(B.11), one obtains:

$$T\frac{\partial\mathcal{S}}{\partial t} - \mathring{r} + T\nabla\cdot(s_l\omega_l) + \nabla\cdot\mathbf{q} = \mathcal{D}_{sk} + \mathcal{D}_l \tag{B.45}$$

Hypothesizing that no heat source exists in materials ($\mathring{r} = 0$), and the skeleton is elastic so that the skeleton dissipation can be neglected ($\mathcal{D}_{sk} = 0$). The eq(B.45) thus can be rewritten as:

$$T\left(\frac{\partial\mathcal{S}}{\partial t} + s_l\nabla\cdot\boldsymbol{\omega}_l\right) + T\boldsymbol{\omega}_l\cdot\nabla s_l + \boldsymbol{\omega}_l\cdot\nabla g_l + \nabla\cdot\mathbf{q} = 0 \tag{B.46}$$

Substitution of the relation, $\nabla g_l = -T\nabla s_l + \nabla P_l/\rho_l$, into eq(B.46), one obtains:

$$T\left(\frac{\partial\mathcal{S}}{\partial t} + s_l\nabla\cdot\boldsymbol{\omega}_l\right) + \boldsymbol{\omega}_l\cdot\frac{\nabla P_l}{\rho_l} + \nabla\cdot\mathbf{q} = 0 \tag{B.47}$$

Considering eq(4.12), one can rewrite the eq(B.46) as:

$$T\left(\frac{\partial\mathcal{S}}{\partial t} - s_l\frac{\partial m_l}{\partial t} - s_c\frac{\partial m_c}{\partial t}\right) = T\mathring{m}_{w\to c}(s_l - s_c) - \boldsymbol{\omega}_l\cdot\frac{\nabla P_l}{\rho_l} - \nabla\cdot\mathbf{q} \tag{B.48}$$

Owing to the additive character of total entropy density, viz. $\mathcal{S} = \mathcal{S}_{sk} + m_l s_l + m_c s_c$, and considering the limited contribution of surface energy, $\mathcal{S}_m \gg \frac{\partial\phi U}{\partial T}$ or $\mathcal{S}_m \approx \mathcal{S}_{sk}$, one can thus rewrite the eq(B.48) as:

$$T\left(\frac{\partial \mathcal{S}_m}{\partial t}+m_l\frac{\partial s_l}{\partial t}+m_c\frac{\partial s_c}{\partial t}\right)=T\mathring{m}_{w\to c}(s_l-s_c)-\boldsymbol{\omega}_l\cdot\frac{\nabla P_l}{\rho_l}-\nabla\cdot\mathbf{q} \tag{B.49}$$

The entropy density of solid matrix, liquid and ice crystals can be simplified as a function of temperature: $\partial s_\alpha/\partial t=\partial s_\alpha/\partial T\cdot(\partial T/\partial t)=C_{P,\alpha}/T(\partial T/\partial t)$. Combining these relations, eq(B.32) ($\mathring{m}_{w\to c}=\rho_c\phi_0\partial S_c/\partial t$) and Fourier's law presented in section 4.2.4, one obtains:

$$\begin{aligned}\nabla\cdot(\lambda\nabla T)+\boldsymbol{\omega}_l\cdot\frac{\nabla P_l}{\rho_l}=&-\left[T\rho_c\phi_0\left[\left(\mathcal{S}_f+C_f\ln\frac{T}{T_0}\right)\frac{\partial S_c}{\partial P_{cap}}\right]\left(\mathcal{S}_f+C_f\ln\left(\frac{T}{T_m}\right)\right)+(C_m+\rho_l\phi_0S_lC_{P,l}+\rho_c\phi_0S_cC_f)\right]\frac{\partial T}{\partial t}\\&+T\rho_c\phi_0\left[\left(\mathcal{S}_f+C_f\ln\frac{T}{T_0}\right)\frac{\partial S_c}{\partial P_{cap}}\right]\left(\frac{\rho_c}{\rho_w}-1\right)\frac{\partial P_l}{\partial t}+T\phi_0\left[\left(\mathcal{S}_f+C_f\ln\frac{T}{T_0}\right)\frac{\partial S_c}{\partial P_{cap}}\right]\frac{\rho_c^2RT}{\mathsf{M}_w}\frac{\partial\ln a_w}{\partial c_i}\frac{\partial c_i}{\partial t}\end{aligned} \tag{B.50}$$

where $C_{P,l}$ is the heat capacity per unit mass of liquid phase.

B.3 Undrained freezing and air voids

B.3.1 Undrained freezing of porous materials saturated with saline solution

Following the principles of undrained freezing of porous materials studied by Coussy [77] and Coussy and Monteirio [82], the total mass of phases occupied by liquid solution and ice crystals can be given by:

$$M_{\text{total}}=\rho_l(\phi_0S_l+\varphi_l)+\rho_c(\phi_0S_c+\varphi_c) \tag{B.51}$$

The current mass density of liquid water and ice crystals can be written as linear function of temperature and pressure, if the temperature and pressure shift are not so large,

$$\rho_w^*=\rho_w^0\left[1+\frac{P_w}{K_w}-3\alpha_w(T-T_0)\right]\quad\text{and}\quad\rho_c=\rho_c^0\left[1+\frac{P_c}{K_c}-3\alpha_c(T-T_0)\right] \tag{B.52}$$

where $\rho_w^*=\mathsf{M}_w/\mathsf{V}_w$, $K_{w,c}$ is the bulk modulus of liquid water (ice crystals), and $\alpha_{w,c}$ is the TEC of liquid water (ice crystals). In the case of undrained freezing, the ultimated concentration of solution is correlated with the saturation degree:

$$c_i=\frac{c_i^0}{S_l} \tag{B.53}$$

c_i and c_i^0 are the current and initial concentration of specie i. Substitution of eq(B.53) into eq(4.10) given in section 4.1.5, one thus gets the current density of liquid phase:

$$\begin{aligned}\rho_l=\rho_w^*+\sum(\mathsf{M}_i-\rho_w^*\mathsf{V}_{\phi,i})c_i&=\rho_w^0\left[1+\frac{P_l}{K_w}-3\alpha_w(T-T_0)\right]+\sum(\mathsf{M}_i-\rho_w^0V_{\phi,i})\frac{c_i^0}{S_l}\\&=\rho_l^0\left[1+\frac{P_l}{K_l}-3\alpha_l(T-T_0)\right]+\sum(\mathsf{M}_i-\rho_w^0\mathsf{V}_{\phi,i})\frac{c_i^0(1-S_l)}{S_l}\end{aligned} \tag{B.54}$$

where $\mathsf{V}_{\phi,i}$ is the apparent molar volume of specie i as introduced in section 4.1.5, K_l and α_l are bulk modulus and thermal expansion coefficient of liquid solution. Substitution of the eqs(B.52b), (B.54), (4.54b) and (4.54c) into eq(B.51), one obtains:

$$M_{\text{total}}=\rho_l^0\phi_0+\rho_l^0(v_{\Delta\rho}+v_\varphi+v_s) \tag{B.55}$$

where

$$v_{\Delta\rho} = \left(\frac{\rho_c^0}{\rho_l^0} - 1\right)\phi_0(1 - S_l) \tag{B.56a}$$

$$v_\varphi = b\epsilon + \frac{P_l}{M_l} + \frac{P_c}{M_c} - \frac{1}{N}\frac{2}{3}U - 3\left(\phi_0 S_l\alpha_l + \phi_0 S_c\alpha_c + \alpha_{\phi l} + \alpha_{\phi c}\right)(T - T_0) \tag{B.56b}$$

$$v_s = \frac{1}{\rho_l^0}\sum\left(\mathsf{M}_i - \rho_w^0 V_{\phi,s}\right)c_i^0(1 - S_l)\phi_0 \tag{B.56c}$$

with

$$\frac{1}{M_l} = \frac{1}{N_{ll}} + \frac{1}{N_{lc}} + \frac{\phi_0 S_l}{K_l} \tag{B.57a}$$

$$\frac{1}{M_c} = \frac{1}{N_{cc}} + \frac{1}{N_{lc}} + \frac{\phi_0 S_c}{K_c} \tag{B.57b}$$

$$\frac{1}{N} = \frac{1}{N_{ll}} + \frac{1}{N_{cc}} + \frac{2}{N_{lc}} \tag{B.57c}$$

If neglecting the term of interfacial energy U in eq(B.56b) and the term of salt in eq(B.56c), the equations reduce to these for porous materials with pure water, cf. eqs(17)-(21) in [82]. Since the total mass holds conservation all the time for undrained freezing, the second term at the right hand of eq(B.55) must be zero,

$$v_{\Delta\rho} + v_\varphi + v_s = 0 \tag{B.58}$$

Under the stress-free condition, the volumetric deformation ϵ can be expressed in the form [77, 82],

$$\epsilon = \frac{1}{K}\left[b\left(P_l - \frac{2}{3}U\right) + b_c P_{cap} + 3\alpha_s K(T - T_0)\right] \tag{B.59}$$

where $\alpha_s = 1/3\alpha_{th}$ is the TEC of solid skeleton. By substitution of the volumetric deformation under free stress in to eq(B.59) to eliminate the term ϵ and considering the formula of capillary pressure, eq(2.11), the liquid pressure is found to be depending on the temperature, initial salt concentration and saturation degree eventually for undrained freezing case,

$$P_l = \left(\frac{b^2}{K} + \frac{1}{M}\right)^{-1}\left[\left(\frac{b^2}{K} + \frac{1}{M}\right)\frac{2}{3}U - \left(\frac{bb_c}{K} + \frac{1}{M_c}\right)\frac{\rho_c^0 RT\ln a_w}{\mathsf{M}_w} + \left[3\alpha_\phi + \left(\frac{bb_c}{K} + \frac{1}{M_c}\right)\mathcal{S}_f\right](T - T_0)\right]$$
$$- \left(\frac{b^2}{K} + \frac{1}{M}\right)^{-1}\left[\left(\frac{\rho_c^0}{\rho_l^0} - 1\right) - \frac{1}{\rho_l^0}\sum\left(\mathsf{M}_i - \rho_w^0\mathsf{V}_{\phi,s}\right)c_i^0\right]\phi_0(1 - S_l)$$

with

$$\frac{1}{M} = \frac{1}{M_l} + \frac{1}{M_c} = \frac{1}{N} + \frac{\phi_0 S_l}{K_l} + \frac{\phi_0 S_c}{K_c} \tag{B.60a}$$

$$\alpha_\phi = \phi_0 S_l\alpha_l + \phi_0 S_c\alpha_c + \alpha_{\phi l} + \alpha_{\phi c} - \alpha_s \tag{B.60b}$$

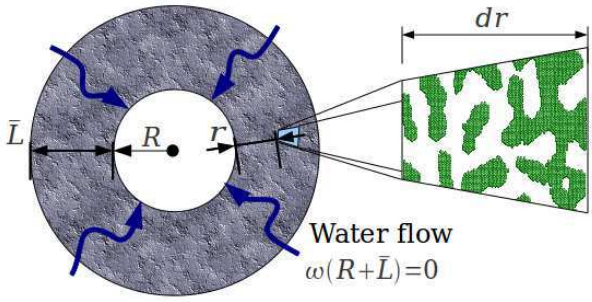

Figure B.1: Schematic illustration of a representative air-bubble and the surrounded paste.

B.3.2 Calculation of the strain of air void entrained paste

It has been well understood that the air voids act as a reservoir to accommodate the excess water due to about 9% volume increment as ice forms [305], and provide a boundary where liquid pressure is negative required by the thermodynamic equilibrium between ice and water [82]. Furthermore, the quantitative relationship between the content of air voids and frozen resistance has been obtained either by means of experimental observations [294, 296], or by means of theoretical calculation [82, 114, 305]. Figure B.1 shows a representative air-bubble and the surrounded paste schematically. It has more volume of paste when the distance away from air bubble is further. Thus the one dimensional calculation should be modified to adaptable for this condition. We assume that there are total N elements, and each has the same width Δx, thus the i^{th} element volume is given by:

$$V_i = 4\pi(R + i \cdot \Delta x)^2 \cdot \Delta x \tag{B.61}$$

where R is the radius of air bubble. The total volume of the paste V_T is: $V_T = \frac{4}{3}\pi\left[(R+\bar{L})^3 - R^3\right]$. The linear strain of i^{th} element is: $\varepsilon_i = \frac{1}{3}\epsilon_i = \frac{1}{3K+4G}(b_i P_i^* + K\Delta T)$. The overall linear strain is thus simplified as:

$$\varepsilon = \frac{\sum_i^N \varepsilon_i V_i}{V_T} = \frac{\sum_i^N \left[(R + i \cdot \Delta x)^2 \cdot \Delta x\right] \frac{3}{3K+4G}(b_i P_i^* + K\Delta T)}{(R+\bar{L})^3 - R^3} \tag{B.62}$$

Appendix C

Estimation method for multi-scale modelling

C.1 Representation

Let us consider a RVE of a heterogeneous material with volume V_0. The RVE is composed of n different phases with volumes V_i, $i = 1...n$, and volume fractions denoted by $f_i = V_i/V_0$. A phase is defined as a material domain that can be identified with on average constant material properties [137]. The phase defined here is related to the scale used. For example, at nano-scale, the LD C-S-H and HD C-S-H can be different phases, while at an upscale, the C-S-H that is composed of LD and HD C-S-H is a single phase. For porous materials, the pore space, which can be infiltrated by either air or solution or both of them, is considered as a porous phase with pore volume V_ϕ and porosity $\phi = V_\phi/V_0$. The wetting phase and no-wetting phase in pores will not be considered here, but discussed specifically in text. Let m denotes the number of solid phases and V_s denotes the total volume of solid phases, it then has $m = n - 1$ and $V_s = \sum_1^m V_i$. The fourth order tensor of elastic moduli, the second order tensor of transport properties and the second order tensor of thermal expansion coefficient of each phase are denoted by $\mathbb{C}_i$, $\boldsymbol{D}_i$ and $\boldsymbol{\alpha}_i$. In the case of isotropy of the solid phases, the tensors can be written as:

$$\mathbb{C}_i = 3K_i\mathbb{K} + 2G_i\mathbb{D}, \quad \boldsymbol{D}_i = D_i\mathbf{I}, \quad \text{and} \quad \boldsymbol{\alpha}_i = \alpha_i\mathbf{I} \tag{C.1}$$

where K_i and G_i are the bulk modulus and shear modulus of the phase i respectively. D_i represents a bulk transport property of the phase i: it can be either electric conductivity or water permeability. $\mathbb{K}_{ijkl} = 1/3 \cdot \delta_{ij}\delta_{kl}$ is the volumetric part of the fourth-order symmetric unit tensor $\mathbb{I}$ and $\mathbb{D} = \mathbb{I} - \mathbb{K}$ is the deviatoric part. $\mathbb{I}$ is defined as $\mathbb{I}_{ijkl} = 1/2 \cdot (\delta_{ik}\delta_{jl} + \delta_{il}\delta_{jk})$ and δ_{ij} stands for Kronecker delta. $\mathbf{I}$ is the second order unit tensor with $\mathbf{I}_{ij} = \delta_{ij}$.

C.2 Concentration

The concentration problem is presented by assuming homogeneous boundary conditions on the RVE [159, 166, 438]. Homogeneous stress and strain boundary conditions correspond respectively, to prescribed surface tractions $\boldsymbol{T}$ and displacements $\boldsymbol{u}$ on the boundary ∂V of the RVE:

$$\text{on} \quad \partial V: \quad \boldsymbol{T} = \boldsymbol{\Sigma} \cdot \boldsymbol{n} \quad \text{and} \quad \boldsymbol{u} = \boldsymbol{E} \cdot \boldsymbol{x} \tag{C.2}$$

where $\boldsymbol{\Sigma}$ is the macroscopic stress tensor and $\boldsymbol{n}$ is the unit outward normal tensor at the boundary. $\boldsymbol{x}$ is the microscopic position vector and $\boldsymbol{E}$ is the macroscopic strain tensor. For the transport problem, the surface flux $\boldsymbol{S}$ and the field vector $\boldsymbol{\mu}$ have the similar equation as eq(C.2):

$$\text{on} \quad \partial V: \quad \boldsymbol{S} = \boldsymbol{Q} \cdot \mathbf{n} \quad \text{and} \quad \boldsymbol{G} = \nabla_x \boldsymbol{\mu} \tag{C.3}$$

where $\boldsymbol{Q}$ is the macroscopic flux tensor and $\boldsymbol{G}$ is the macroscopic potentials tensor.

The macroscopic stress $\boldsymbol{\Sigma}$ and strain $\boldsymbol{E}$ can be expressed as the volume average of the microscopic equilibrated stress field $\boldsymbol{\sigma}(\boldsymbol{x})$ and strain field $\boldsymbol{\varepsilon}(\boldsymbol{x})$, respectively, in the RVE [438]. Taking the same procedure, the macroscopic flux $\boldsymbol{Q}$ and potential $\boldsymbol{G}$ are equal to the volume average of the microscopic equilibrated flux field $\boldsymbol{q}(\boldsymbol{x})$ and potential field $\boldsymbol{g}(\boldsymbol{x})$, respectively, [252, 377].

$$\boldsymbol{\Sigma} = \langle \boldsymbol{\sigma} \rangle_V \quad \text{and} \quad \boldsymbol{E} = \langle \boldsymbol{\varepsilon} \rangle_V \tag{C.4a}$$

$$\boldsymbol{Q} = \langle \boldsymbol{q} \rangle_V \quad \text{and} \quad \boldsymbol{G} = \langle \boldsymbol{g} \rangle_V \tag{C.4b}$$

where $\langle z \rangle_V = 1/V \int_V z(x) dV$ stands for the volume average of quantity z over domain V.

The Hill's lemma can be presented in the following by using the homogeneous boundary conditions eq(C.2) [438]:

$$\langle \boldsymbol{\sigma} : \boldsymbol{\varepsilon} \rangle_V = \langle \boldsymbol{\sigma} \rangle_V : \langle \boldsymbol{\varepsilon} \rangle_V = \boldsymbol{\Sigma} : \boldsymbol{E} \tag{C.5}$$

In the framework of linearity, the fourth-order localization tensors $\mathbb{A}(\boldsymbol{x})$ and $\mathbb{B}(\boldsymbol{x})$ correlate the local strain and stress fields, $\boldsymbol{\sigma}(\boldsymbol{x})$ and $\boldsymbol{\varepsilon}(\boldsymbol{x})$, to the macroscopic strain and stress, $\boldsymbol{E}$ and $\boldsymbol{\Sigma}$, respectively, and the second-order localization tensors $\mathbf{C}(\boldsymbol{x})$ and $\mathbf{D}(\boldsymbol{x})$, correlate the local flux vector and potential fields, $\boldsymbol{q}(\boldsymbol{x})$ and $\boldsymbol{g}(\boldsymbol{x})$, to macroscopic flux and potential, $\boldsymbol{Q}$ and $\boldsymbol{G}$, respectively. They can be expressed as:

$$\boldsymbol{\varepsilon}(\boldsymbol{x}) = \mathbb{A}(\boldsymbol{x}) : \boldsymbol{E} \quad \text{and} \quad \boldsymbol{\sigma}(\boldsymbol{x}) = \mathbb{B}(\boldsymbol{x}) : \boldsymbol{\Sigma} \tag{C.6a}$$

$$\boldsymbol{q}(\boldsymbol{x}) = \mathbf{C}(\boldsymbol{x}) \cdot \boldsymbol{Q} \quad \text{and} \quad \boldsymbol{g}(\boldsymbol{x}) = \mathbf{D}(\boldsymbol{x}) \cdot \boldsymbol{G} \tag{C.6b}$$

The linear localization tensors must obey:

$$\langle \mathbb{A} \rangle_V = \mathbb{I}; \quad \langle \mathbb{B} \rangle_V = \mathbb{I}; \quad \langle \mathbf{C} \rangle_V = \mathbf{I}; \quad \langle \mathbf{D} \rangle_V = \mathbf{I} \tag{C.7}$$

If the heterogeneous material is composed of homogeneous phases, one thus can obtain a linear phase strain

localization tensor as done in [403]:

$$\langle \boldsymbol{\varepsilon} \rangle_{V_i} = \langle \mathbb{A} \rangle_{V_i} : \boldsymbol{E}; \quad \sum_{i=1}^{n} \langle \mathbb{A} \rangle_{V_i} = \mathbb{I} \quad \text{and} \quad \langle \boldsymbol{g} \rangle_{V_i} = \langle \mathbf{D} \rangle_{V_i} \cdot \boldsymbol{G}; \quad \sum_{1=1}^{n} \langle \mathbf{D} \rangle_{V_i} = \mathbf{I} \tag{C.8}$$

Considering the isotropic case, $\langle \mathbb{A} \rangle_{V_i}$ can be simplified to be $\langle \mathbb{A} \rangle_{V_i} = A_i^v \mathbb{K} + A_i^d \mathbb{D}$ with A_i^v and A_i^d the volumetric and deviatoric strain localization coefficients. Considering further simplified case, a spherical inclusion embedded in a reference medium, which is known as an Eshelbian type inclusion [112], the strain localization tensor of phase i can be expressed as [103, 137]:

$$A_i^v = \frac{(1 + \alpha_0(k_i/k_0 - 1))^{-1}}{\sum_i f_i \, (1 + \alpha_0(k_i/k_0 - 1))^{-1}}; \quad A_i^d = \frac{(1 + \beta_0(g_i/g_0 - 1))^{-1}}{\sum_i f_i \, (1 + \beta_0(g_i/g_0 - 1))^{-1}} \tag{C.9}$$

with

$$\alpha_0 = \frac{3k_0}{3k_0 + 4g_0}; \quad \beta_0 = \frac{6\,(k_0 + 2g_0)}{5(3k_0 + 4g_0)} \tag{C.10}$$

where k_0 and g_0 are bulk modulus and shear modulus of the reference medium.

Analogous to the eq(C.9), in the isotropic case, the global potential localization tensor is reduced to $\langle \mathbf{D} \rangle_{V_i} = \mathsf{D}_i^v \mathbf{I}$, and global potential localization tensor of phase i can be expressed as:

$$\mathsf{D}_i^v = \frac{(1 + \frac{1}{3}(D_i/D_0 - 1))^{-1}}{\sum_i f_i \left(1 + \frac{1}{3}(D_i/D_0 - 1)\right)^{-1}} \tag{C.11}$$

As a matter of fact, eq(C.11) has the same formula as the eq(C.9) by setting $\alpha_0 = 1/3$ and replacing k_0, k_i by D_0, D_i in eq(C.9).

C.3 Homogenization

C.3.1 Micro-poro-mechanics

Following the thermo-poro-elasticity, the stress state of a RVE of porous materials is subjected to the homogeneous strain boundary condition of the Hashin type (see eq(C.6a)), the eigenstresses $\boldsymbol{\sigma}^p$ by pore pressure and the eigenstresses $\boldsymbol{\sigma}^T$ by temperature variation. The microscopic constitutive stress equation can be given as:

$$\boldsymbol{\sigma}(\boldsymbol{x}) = \mathbb{C}(\boldsymbol{x}) : \boldsymbol{\varepsilon}(\boldsymbol{x}) + \boldsymbol{\sigma}^P(\boldsymbol{x}) + \boldsymbol{\sigma}^T(\boldsymbol{x}) \tag{C.12}$$

or in the inverse form:

$$\boldsymbol{\varepsilon}(\boldsymbol{x}) = \mathbb{C}^{-1}(\boldsymbol{x}) : \boldsymbol{\sigma}(\boldsymbol{x}) + \boldsymbol{\varepsilon}^P(\boldsymbol{x}) + \boldsymbol{\varepsilon}^T(\boldsymbol{x}) \tag{C.13}$$

where $\mathbb{C}(\boldsymbol{x})$ is the tensor of local elastic moduli which is equal to zero in the pore volume, $\boldsymbol{\sigma}^P(\boldsymbol{x})$ is an eigenstress applied to the pore volume of the material, and $\boldsymbol{\sigma}^T(\boldsymbol{x})$ is an eigenstress applied to the solid phase of the material. Their domains are presented in Table C.1.

The thermal-poro-mechanical problem at hand can be decomposed into three problems (see Figure C.1). In the first problem, only the homogeneous strain boundary condition is considered, and the eigenstresses $\boldsymbol{\sigma}^P(\boldsymbol{x})$ and $\boldsymbol{\sigma}^T(\boldsymbol{x})$ are equal to zero. This case is exactly the drained case for poro-elasticity. The boundary

Table C.1: Decomposition of the problem of a thermo-poro-mechanical loading into three independent problems.

Domains	Problem A	Problem B	Problem C
V_s	$\mathbb{C}(\boldsymbol{x}) : \boldsymbol{\varepsilon}(\boldsymbol{x}) = \mathbb{C}_i(\boldsymbol{x}) : \boldsymbol{\varepsilon}(\boldsymbol{x})$ or $\mathbb{C}(\boldsymbol{x}) = \mathbb{C}_i(\boldsymbol{x})$	0	$\boldsymbol{\sigma}^T(\boldsymbol{x}) = -\mathbb{C}(\boldsymbol{x}) : \boldsymbol{\alpha} T$
V_ϕ	0	$\boldsymbol{\sigma}^P(\boldsymbol{x}) = -P\mathbf{I}$	0

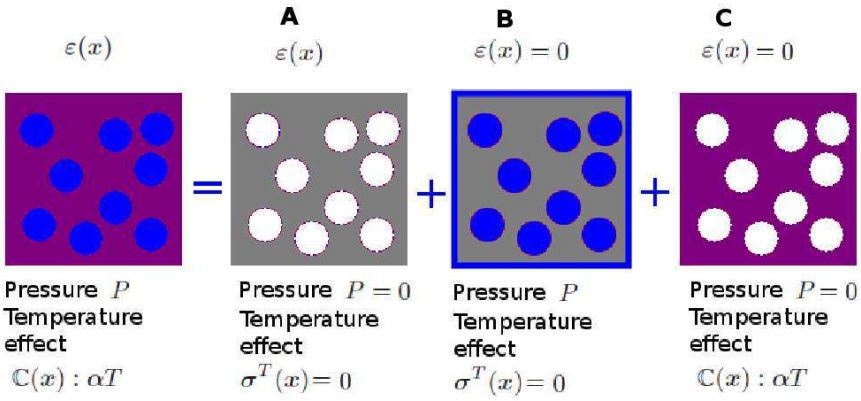

Figure C.1: Decomposition of the problem of a thermo-poro-mechanical loading into three cases.

conditions for the second problem are: the displacement on the boundary of the RVE is equal to zero, and the hydraulic eigenstresses are $\boldsymbol{\sigma}^P(\boldsymbol{x})$. For the last problem, the displacement on the boundary of the RVE is equal to zero and the thermal loading is $\boldsymbol{\sigma}^T(\boldsymbol{x})$. In the following derivation procedures, we introduce the superscripts of $()^A$, $()^B$and $()^C$ to denote the tree problems as done in [137].

C.3.1.1 Problem A: Drained stiffness and Biot coefficients

In the first problem, the regular boundary condition (eq(C.2)a) and the classical strain localization condition of linear continuum micro-mechanics (eq(C.6a)) last two terms in right hand side of eq(C.12) allows to write the local stress equation of state:

$$\boldsymbol{\sigma}^A(\boldsymbol{x}) = \mathbb{C}(\boldsymbol{x}) : \boldsymbol{\varepsilon}^A(\boldsymbol{x}); \quad \boldsymbol{\varepsilon}^A(\boldsymbol{x}) = \mathbb{A}(\boldsymbol{x}) : \boldsymbol{E} \tag{C.14}$$

Using the volume average law as demonstrated in eq(C.4a), viz. $\boldsymbol{\Sigma}^A = \langle \boldsymbol{\sigma}^A \rangle_V$ and combining the eq(C.14), one can obtain the overall effective moduli of the heterogeneous porous material $\mathbb{C}^{hom}$ as:

$$\boldsymbol{\Sigma}^A = \mathbb{C}^{hom} : \boldsymbol{E}; \quad \mathbb{C}^{hom} = \langle \mathbb{C} : \mathbb{A} \rangle_V = \sum_{i=1}^{n} f_i \mathbb{C}_i : \langle \mathbb{A} \rangle_{V_i} \tag{C.15}$$

Let us now consider only the stress equation of solid phases. From the eq(C.14), the average local stress in the solid phase can be expressed as

$$\langle \boldsymbol{\sigma}^A \rangle_{V_s} = \langle \mathbb{C} : \boldsymbol{\varepsilon}^A \rangle_{V_s} = \langle \mathbb{C} : \mathbb{A} \rangle_{V_s} : \boldsymbol{E} \tag{C.16}$$

The principle of eq(C.8) allows us to present the average local strain of the solid phase as $\langle \boldsymbol{\varepsilon}^A \rangle_{V_s} = \langle \mathbb{A} \rangle_{V_s} : \boldsymbol{E}$.

Using this relation and the eq(C.16), one thus deduce the the tensor of effective solid moduli $\mathbb{C}_s^{hom}$ as:

$$\langle \boldsymbol{\sigma}^A \rangle_{V_s} = \mathbb{C}_s^{hom} : \langle \boldsymbol{\varepsilon}^A \rangle_{V_s}; \quad \mathbb{C}_s^{hom} = \langle \mathbb{C} : \mathbb{A} \rangle_{V_s} : \langle \mathbb{A} \rangle_{V_s}^{-1} \tag{C.17}$$

The porosity change is defined as $d\phi = \phi - \phi_0$. In the case of the hydraulic pressure loading $\boldsymbol{\sigma}^P(\boldsymbol{x}) = P\mathbf{I} = \mathbf{0}$ and the thermal loading $\boldsymbol{\sigma}^T(\boldsymbol{x}) = \mathbb{C}(\boldsymbol{x}) : \boldsymbol{\alpha} T = \mathbf{0}$, $(d\phi)^A = \phi \mathbf{I} : \langle \boldsymbol{\varepsilon}^A \rangle_{V_\phi} = \boldsymbol{b}^{hom} : \boldsymbol{E}$, where $\boldsymbol{b}$ is defined as the tensor of effective Biot's coefficient. Substitution of eq(C.14) in the above relation, one can thus have the expression of the effective Biot's coefficient $\boldsymbol{b}^{hom}$:

$$\boldsymbol{b}^{hom} = \phi \mathbf{I} : \langle \mathbb{A} \rangle_{V_\phi} = \mathbf{I} : \left(1 - \sum_{i=1}^{m} f_i \langle \mathbb{A} \rangle_{V_i} \right) \tag{C.18}$$

From eq(C.15)b and the boundary condition shown in the second column of Table (C.1), viz. $\mathbb{C}(\boldsymbol{x}) = \mathbb{C}_i(\boldsymbol{x})$, it deduces $\mathbb{C}^{hom} = (1-\phi)\langle \mathbb{C} : \mathbb{A} \rangle_{V_s}$. Moreover, from eq(C.7), one obtains $\phi_0 \langle \mathbb{A} \rangle_{V_\phi} = \mathbb{I} - (1-\phi_0)\langle \mathbb{A} \rangle_{V_s}$. From these relations mentioned above and eqs(C.17)b and (C.18), the tensor of effective Biot's coefficients can be expressed alternatively as:

$$\left.\begin{aligned} \mathbb{C}^{hom} &= (1-\phi)\langle \mathbb{C} : \mathbb{A} \rangle_{V_s} \\ \mathbb{C}_s^{hom} &= \langle \mathbb{C} : \mathbb{A} \rangle_{V_s} : \langle \mathbb{A} \rangle_{V_s}^{-1} \\ \phi_0 \langle \mathbb{A} \rangle_{V_\phi} &= \mathbb{I} - (1-\phi_0)\langle \mathbb{A} \rangle_{V_s} \end{aligned}\right\} \rightarrow \boldsymbol{b}^{hom} = \mathbf{I} : \left(\mathbb{I} - \mathbb{C}^{hom} : \left(\mathbb{C}_s^{hom} \right)^{-1} \right) \tag{C.19}$$

In the isotropic case, the effective elastic modulus $\mathbb{C}^{hom}$, the effective unjacketed modulus K_s^{hom} and the effective Biot's coefficient can be presented as:

$$\mathbb{C}^{hom} = 3K_d^{hom}\mathbb{K} + 2G^{hom}\mathbb{D} \tag{C.20a}$$

$$K_s^{hom} = \frac{\sum_{i=1}^{m} f_r k_i A_i^v}{\sum_{i=1}^{m} f_i A_i^v} \tag{C.20b}$$

$$b^{hom} = 1 - \sum_{i}^{m} f_i A_i^V = 1 - K_d^{hom}/K_s^{hom} \tag{C.20c}$$

with

$$K_d^{hom} = \sum_{i=1}^{n} f_i k_i A_i^v; \quad G_d^{hom} = \sum_{i=1}^{n} f_i g_i A_i^d \tag{C.21}$$

C.3.1.2 Problem B: Hydraulic loadings and Biot moduli

In the second problem, the RVE subjected to the boundary of zero displacement ($\boldsymbol{E}^B = \langle \boldsymbol{\varepsilon}^B \rangle_V = \mathbf{0}$) and the solid liquid interface is subjected to the eigenstress $\boldsymbol{\sigma}^P$ defined in the third column of Table (C.1). The local stress tensor is given by:

$$\boldsymbol{\sigma}(\boldsymbol{x}) = \mathbb{C}(\boldsymbol{x}) : \boldsymbol{\varepsilon}^B(\boldsymbol{x}) + \boldsymbol{\sigma}^P(\boldsymbol{x}) \tag{C.22}$$

Again, by using the Hill's lemma, eq(C.5), on the stress field of second sub-problem $\boldsymbol{\sigma}^B$ and the strain field of first sub-problem $\boldsymbol{\varepsilon}^B$, the macroscopic stress tensor can be evaluated as:

$$\boldsymbol{E} : \boldsymbol{\Sigma}^B = \langle \boldsymbol{\varepsilon} : \boldsymbol{\sigma}^B \rangle_V = \langle \boldsymbol{\varepsilon}^A : \mathbb{C} : \boldsymbol{\varepsilon}^B \rangle_V + \langle \boldsymbol{\varepsilon}^A : \boldsymbol{\sigma}^P \rangle_V \tag{C.23}$$

The Hill's lemma, eq(C.5), and the concentration relation for boundary condition A, eq(C.14), require the right-hand side of eq(C.23) to be zero, viz. $\langle \boldsymbol{\varepsilon}^A : \mathbb{C} : \boldsymbol{\varepsilon}^B \rangle_V = \langle \boldsymbol{\varepsilon}^A : \boldsymbol{\sigma}^B \rangle_V = \boldsymbol{\Sigma}^A : \langle \boldsymbol{\sigma}^B \rangle_V = 0$. Again, substitution of concentration relation for boundary condition A, eq(C.14), into the second term of the right hand side of eq(C.23) and using the boundary condition presented in the third column of Table (C.1), we can express the tensor of effective Biot's coefficients as:

$$\boldsymbol{\Sigma}^B = \langle \boldsymbol{\sigma}^P : \mathbb{A} \rangle_V = -\phi \mathbf{I} : \langle \mathbb{A} \rangle_{V_\phi} P = -P \boldsymbol{b}^{hom} \tag{C.24}$$

The average local stress in the RVE is $\boldsymbol{\Sigma}^B = \langle \boldsymbol{\sigma}^B \rangle_V = \phi \langle \boldsymbol{\sigma}^B \rangle_{V_\phi} + \sum_{i=1}^m f_i \langle \boldsymbol{\sigma}^B \rangle_{V_i}$. Combining this relation, eqs(C.18) and (C.24) and the condition, $\langle \boldsymbol{\sigma}^B \rangle_{V_\phi} = -P\mathbf{I}$, one obtains:

$$\sum_{i=1}^m f_i \langle \boldsymbol{\sigma}^B \rangle_{V_i} = -P \left(\boldsymbol{b}^{hom} - \phi_0 \mathbf{I} \right) = -P\mathbf{I} : \sum_{i=1}^m f_i \left(\mathbb{I} - \langle \mathbb{A} \rangle_{V_i} \right) \tag{C.25}$$

The average strain over a phase of the solid volume thus can be given by [403]:

$$\langle \boldsymbol{\sigma}^B \rangle_{V_i} = -P\mathbf{I} : \left(\mathbb{I} - \langle \mathbb{A} \rangle_{V_i} \right) \quad \text{in} \quad \mathrm{V_s} \tag{C.26}$$

The variation of the porosity, in this condition, is defined as:

$$(d\phi)^B = \phi \mathbf{I} : \langle \boldsymbol{\varepsilon}^B \rangle_{V_\phi} \tag{C.27}$$

The boundary conditions of this problem require that $\boldsymbol{E}^B = \langle \boldsymbol{\varepsilon}^B \rangle_V = \phi \langle \boldsymbol{\varepsilon}^B \rangle_{V_\phi} + (1-\phi) \langle \boldsymbol{\varepsilon}^B \rangle_{V_s} = \mathbf{0}$. The variation of the porosity, eq(C.27) can be rewritten as:

$$(d\phi)^B = -\mathbf{I} : \sum_{i=1}^m f_i \mathbb{C}_i^{-1} : \langle \boldsymbol{\sigma}^B \rangle_{V_i} \tag{C.28}$$

Substitution of eq(C.26) into eq(C.28), one obtains the effective Biot skeleton modulus N^{hom} in the following form:

$$(d\phi)^B = \frac{P}{N^{hom}}; \quad \frac{1}{N^{hom}} = \mathbf{I} : \sum_{i=1}^m f_i \mathbb{C}_i^{-1} : \left(\mathbf{I} - \mathbf{I} \langle \mathbb{A} \rangle_{V_i} \right) \tag{C.29}$$

In the isotropic case, eq(C.29) is reduced to the more familiar expression [77, 403]:

$$\frac{1}{N^{hom}} = \sum_{i=1}^m \frac{f_i (1 - A_i^v)}{k_i} \tag{C.30}$$

C.3.1.3 Problem C: Thermal loadings

In the problem C, a RVE is subjected to boundary condition of zero displacement ($\boldsymbol{E}^C = \langle \boldsymbol{\varepsilon}^C \rangle_V = \mathbf{0}$), and the system is subjected to the thermal stress $\boldsymbol{\sigma}^T$ defined in the fourth column of Table C.1. The constitutive equation of local stress tensor is then given by:

$$\boldsymbol{\sigma}^C(\boldsymbol{x}) = \mathbb{C}(\boldsymbol{x}) : \boldsymbol{\varepsilon}^C(\boldsymbol{x}) + \boldsymbol{\sigma}^T(\boldsymbol{x}) \tag{C.31}$$

Again, by application of Hill's lemma, eq (C.5), on the stress field of the third sub-problem $\boldsymbol{\sigma}^C$ and the strain field of first sub-problem $\boldsymbol{\varepsilon}^A$, the macroscopic stress tensor for this condition can be expressed as:

$$\boldsymbol{E} : \boldsymbol{\Sigma}^C = \langle \boldsymbol{\varepsilon}^A : \boldsymbol{\sigma}^C \rangle_V = \langle \boldsymbol{\varepsilon}^A : \mathbb{C} : \boldsymbol{\varepsilon}^C \rangle_V + \langle \boldsymbol{\varepsilon}^A : \boldsymbol{\sigma}^T \rangle_V \tag{C.32}$$

Using Hill's lemma and eqC.14, the first term in the right-hand side of eq(C.23) is found to be equal to zero, $\langle \boldsymbol{\varepsilon}^A : \mathbb{C} : \boldsymbol{\varepsilon}^C \rangle_V = \langle \boldsymbol{\sigma}^A : \boldsymbol{\varepsilon}^C \rangle_V = \boldsymbol{\Sigma}^A : \langle \boldsymbol{\varepsilon}^C \rangle_V = 0$. Substitution of eq(C.14) into the second term of the right-hand side of eq(C.32) and using the condition $\boldsymbol{\sigma}^T = -\boldsymbol{k}T$, one obtains the expression of the tensor of effective coefficients $\boldsymbol{k}^{hom}$:

$$\boldsymbol{\Sigma}^C = \langle \boldsymbol{\sigma}^T : \mathbb{A} \rangle_V = -\boldsymbol{k}^{hom} T; \quad \boldsymbol{k}^{hom} = \langle \boldsymbol{k} : \mathbb{A} \rangle_V = \sum_{i=1}^{n} f_i \boldsymbol{k}_i : \langle \mathbb{A} \rangle_{V_i} \tag{C.33}$$

The average local stress in the RVE is $\boldsymbol{\Sigma}^C = \langle \boldsymbol{\sigma}^C \rangle_V = \sum_{i=1}^m f_i \mathbb{C}_i : \langle \boldsymbol{\varepsilon}^C \rangle_{V_i} - T \sum_{i=1}^m f_i \boldsymbol{k}_i$. Combining this relation and eq(C.33), on obtains:

$$\sum_{i=1}^{m} f_i \mathbb{C}_i : \langle \boldsymbol{\varepsilon}^C \rangle_{V_i} = T \sum_{i=1}^{m} f_i \boldsymbol{k}_i : (\mathbb{I} - \langle \mathbb{A} \rangle_{V_i}) \tag{C.34}$$

Note that $\boldsymbol{\alpha} = \mathbb{C}^{-1} : \boldsymbol{k}$, then the average strain in a phase of solid can be evaluated from the above equation obviously, and it has the formula:

$$\langle \boldsymbol{\varepsilon}^C \rangle_{V_r} = \boldsymbol{\alpha}_r : (\mathbb{I} - \langle \mathbb{A} \rangle_{V_r}) T \quad \text{in} \quad V_s \tag{C.35}$$

The boundary conditions of this problem require that $\boldsymbol{E}^C = \langle \boldsymbol{\varepsilon}^C \rangle_V = \phi \langle \boldsymbol{\varepsilon}^C \rangle_{V_\phi} + (1-\phi) \langle \boldsymbol{\varepsilon}^C \rangle_{V_s} = \boldsymbol{0}$. The variation of the porosity is thus given by:

$$(d\phi)^C = -(1-\phi)\mathbf{I} : \langle \boldsymbol{\varepsilon}^C \rangle_{V_s} = \phi \mathbf{I} : \langle \boldsymbol{\varepsilon}^C \rangle_{V_\phi} = -\mathbf{I} : \sum_{i=1}^{m} f_i \langle \boldsymbol{\varepsilon}^C \rangle_{V_i} \tag{C.36}$$

Substitution of eq(C.35) into eq(C.36), one obtains the effective coefficient Q^{hom} as follow:

$$(d\phi)^C = -Q^{hom} T; \quad Q^{hom} = \mathbf{I} : \sum_{i=1}^{m} f_i \boldsymbol{\alpha}_i : (\mathbb{I} - \langle \mathbb{A} \rangle_{V_i}) \tag{C.37}$$

Again, in the isotropic case, the effective coefficient Q^{hom} is then reduced to:

$$Q^{hom} = \sum_{i=1}^{m} f_i \alpha_i (1 - A_i^v) \tag{C.38}$$

C.3.1.4 Macroscopic equations

The overall macroscopic stresses can be summation of the macroscopic stresses of the A, B and C cases, $\boldsymbol{\Sigma} = \boldsymbol{\Sigma}^A + \boldsymbol{\Sigma}^B + \boldsymbol{\Sigma}^C$. Combining eqs(C.15), (C.24) and (C.33), one obtains the equations of macro-poroelasticity:

$$\boldsymbol{\Sigma} = \mathbb{C}^{hom} : \boldsymbol{E} - \boldsymbol{b}^{hom} P - \boldsymbol{k}^{hom} T \tag{C.39}$$

Analogue to eq(C.39), the variation of porosity is summation of the variation of porosity of the A, B and C cases, $d\phi = (d\phi)^A + (d\phi)^B + (d\phi)^C$. From eq(C.18), (C.29) and (C.37), we have:

$$d\phi = \boldsymbol{b}^{hom} : \boldsymbol{E} + \frac{P}{N^{hom}} - Q^{hom} T \tag{C.40}$$

C.3.2 Transport properties

For the transportability of composites with Eshelbian type morphology and in the isotropic case, the overall transportation coefficient can be given by:

$$\boldsymbol{D} = D^{hom}\mathbf{I}; \quad D^{hom} = \sum_{i=1}^{n} f_i D_i \mathsf{D}_i^v \tag{C.41}$$

where D_i is the transport property of solid phase i, while D_i^v is the concentration factor given by eq(C.11).

C.4 Multi-scale porous materials

In this section, we follow the descriptions on the homogenization procedures of porous materials by Ghabezloo [136, 137]. The total porosity of a material with two scale pore volume can be presented as [137]:

$$\phi = \sum_{i=1}^{l} f_i \phi_i^I + \phi^{II} \tag{C.42}$$

where ϕ_i^I is the porosity of phase i in scale I, ϕ^{II} is the overall porosity in scale II, which are corresponding to the active gel pores and capillary pores. For the poroelastic properties of the l porous phases of level I $(\mathbb{C}^I, \boldsymbol{b}_i^I, N_i^I, Q_i^I)$, they can be evaluated by standard homogenization equations aforementioned. Referring to the problem-A, in which a RVE is subjected to the displacement E, zero hydraulic stress and thermal stress as defined in the previous section, and using eqs(C.42) and (C.40), one can obtain the variation of the porosity as:

$$(d\phi)^A = \sum_{i=1}^{l} f_i \left(d\phi_i^I\right)^A + \left(d\phi^{II}\right)^A = -\sum_{i=1}^{l} f_i \boldsymbol{b}_i^I : \langle \boldsymbol{\varepsilon}^A \rangle_{V_i} - \phi_0^{II}\mathbf{I} : \langle \boldsymbol{\varepsilon}^A \rangle_{V_\phi^{II}} \tag{C.43}$$

By using eq(C.8), eq(C.43) can be rewritten as:

$$(d\phi)^A = \sum_{i=1}^{m} f_i \boldsymbol{b}_i^I : \langle \mathbb{A} \rangle_{V_i} : \boldsymbol{E} - \left(\mathbb{I} - \sum_{i=1}^{m} f_i \langle \mathbb{A} \rangle_{V_i} \right) : \boldsymbol{E} \tag{C.44}$$

From the above equation, the homogenized tensor of Biot's coefficients is then obtained as:

$$\boldsymbol{b}^{hom} = -(d\phi)^A \boldsymbol{E}^{-1} = \mathbf{I} - \sum_{i=1}^{m} \left(f_i \langle \mathbb{A} \rangle_{V_i} \left(\mathbf{I} - \boldsymbol{b}_i^I \right) \right) \tag{C.45}$$

If all solid phases are non-porous ($\boldsymbol{b}_i^l = \mathbf{0}$), the eq(C.45) is reducing to eq(C.18). Again, using the isotropic scheme, the Biot coefficients is further reduced to the following expression:

$$b^{hom} = 1 - \sum_{i=1}^{m} \left(f_i A_i^V \left(1 - b_i^I \right) \right) \tag{C.46}$$

By using eqs(C.42) and (C.40), the variation of the porosity for the problem-B can be expressed as:

$$(d\phi)^B = \sum_{i=1}^{l} f_i \left(d\phi_i^I\right)^B + \left(d\phi_i^{II}\right)^B = \sum_{i=1}^{l} f_i \left(-\boldsymbol{b}_i^I : \langle \boldsymbol{\varepsilon}^B \rangle_{V_i} + \frac{P}{N_i^I} \right) - \phi_0^{II}\mathbf{I} : \langle \boldsymbol{\varepsilon}^B \rangle_{V_\phi^{II}} \tag{C.47}$$

Again, for the non-porous materials, i.e, $\boldsymbol{b}_r^I = \mathbf{0}$ and $1/N_r^I = 0$, and using the right-hand side equality of eq(C.28) in (C.47), one obtains the variation of the porosity for the second sub-problem:

$$(d\phi)^B = \sum_{i=1}^{m} f_i \left(\left(\mathbf{1} - \boldsymbol{b}_i^I\right) : \langle \boldsymbol{\varepsilon}^B \rangle_{V_i} + \frac{P}{N_i^l} \right) \tag{C.48}$$

On the other hand, the first homogenization step of each solid phase is then given by:

$$\langle \boldsymbol{\sigma}^B \rangle_{V_i} = \mathbb{C}_i^I : \langle \boldsymbol{\sigma}^B \rangle_{V_i} + P\boldsymbol{b}_i^I, \quad \text{and} \quad \langle \boldsymbol{\sigma}^B \rangle_{V_i} = \left(\mathbb{C}_i^I\right)^{-1} : \left(\langle \boldsymbol{\sigma}^B \rangle_{V_i} - P\boldsymbol{b}_i^I \right) \tag{C.49}$$

The average local stress in the phase i of the solid phase can be evaluated using eq(C.24), the relation of average local stress, $\boldsymbol{\Sigma}^B = \langle \boldsymbol{\sigma}^B \rangle_V = \phi_0 \langle \boldsymbol{\sigma}^B \rangle_{V_\phi} + \sum_{i=1}^m f_i \langle \boldsymbol{\sigma}^B \rangle_{V_i}$ and the term $\boldsymbol{b}^{hom}$ of multi-scale porous material from eq(C.45):

$$\langle \boldsymbol{\sigma}^B \rangle_{V_i} = P \left(1 - \mathbf{I} : \langle \mathbb{A} \rangle_{V_i} + \boldsymbol{b}_i^I : \langle \mathbb{A} \rangle_{V_i} \right) \quad \text{in} \quad V_s \tag{C.50}$$

The relation is reduced to the expression of average local stress of simple porous materials , i.e., eq(C.26), if $\boldsymbol{b}_i^I = \mathbf{0}$. Substitution of eqs(C.50) and (C.49) into eq(C.48), and using the relation $(\mathbf{I} - \boldsymbol{b}_i^I) : (\mathbb{C}_i^I)^{-1} = \mathbf{I} : \left(\mathbb{C}_{si}^I\right)^{-1}$, one obtains:

$$(d\phi)^B = \frac{P}{N^{hom}}; \quad \frac{1}{N^{hom}} = \sum_{i=1}^{m} f_i \left(\mathbf{I} : \left(\mathbb{C}_{si}^I\right)^{-1} : (\mathbb{I} - \langle \mathbb{A} \rangle_{V_i}) : \left(\mathbf{I} - \boldsymbol{b}_i^I\right) + \frac{1}{N_i^I} \right) \tag{C.51}$$

If all solid phases are non-porous materials, i.e, $\boldsymbol{b}_i^I = \mathbf{0}, 1/N_i^I = 0, \mathbb{C}_{si}^I = \mathbb{C}_r$, eq(C.51) is then reduced to eq(C.29). For the isotropic case, eq(C.51) is then expressed as:

$$\frac{1}{N^{hom}} = \sum_{i=1}^{m} f_i \left(\frac{(1 - A_i^V)(1 - b_i^I)}{k_i^I} + \frac{1}{N_i^I} \right) \tag{C.52}$$

The porosity variation for the problem-C is obtained using the eqs(C.42) and (C.40):

$$(d\phi)^C = \sum_{i=1}^{l} f_r \left(d\phi_i^I\right)^C + \left(d\phi_i^{II}\right)^C = \sum_{i=1}^{l} f_i \left(-\boldsymbol{b}_i^I : \langle \boldsymbol{\varepsilon}^C \rangle_{V_i} - Q_i^I T \right) - \phi_0^{II} \mathbf{I} : \langle \boldsymbol{\varepsilon}^C \rangle_{V_\phi^{II}} \tag{C.53}$$

Using the right-hand size equality of eq(C.36) in eq(C.53) and the relation $\boldsymbol{b}_i^I = \mathbf{0}$ and $Q_r^I = 0$ in the non-porous phases, it obtains:

$$(d\phi)^C = \sum_{i=1}^{m} f_i \left(\left(\mathbf{I} - \boldsymbol{b}_i^I\right) : \langle \boldsymbol{\varepsilon}^C \rangle_{V_r} - Q_r^I T \right) \tag{C.54}$$

By using eq(C.39) for the first homogenization step of each solid phase and eq(C.33), and the relation of average local stress, $\langle \boldsymbol{\sigma}^C \rangle_V = \sum_{i=1}^m f_i \mathbb{C}_i : \langle \boldsymbol{\varepsilon}^C \rangle_{V_i} + T \sum_{i=1}^m f_i \boldsymbol{k}_i$; $\langle \boldsymbol{\sigma}^C \rangle_V = \boldsymbol{\Sigma}^C$, the average local strain in phase i of the solid phase is evaluated as:

$$\langle \boldsymbol{\varepsilon}^C \rangle_{V_r} = -\boldsymbol{\alpha}_r^I : (\mathbb{I} - \langle \mathbb{A} \rangle_{V_r}) T \quad \text{in} V_s \tag{C.55}$$

This relation is equivalent to eq(C.35) for simple porous materials. Substitution of eq(C.55) into eq(C.54), we obtain:

$$(d\phi)^C = -Q^{hom} T; \quad Q^{hom} = \sum_{i=1}^{m} f_i \left(\boldsymbol{\alpha}_i^I : (\mathbb{I} - \langle \mathbb{A} \rangle_{V_i}) : \left(\mathbf{I} - \boldsymbol{b}_i^I\right) + Q_i^I \right) \tag{C.56}$$

When all solid phases are non-porous, $\boldsymbol{b}_i^I = \mathbf{0}$ and $Q_i^I = 0$, eq(C.56) is reduced to eq(C.37).

Appendix D

Thermodynamic properties of NaCl+H2O system at subzero temperature

D.1 Gibbs energy description on NaCl+H2O system

The thermodynamic properties of NaCl solution can be derived from Gibbs free energy based principle. However, for strong electrolytes, because of the ions-ions, ions-water interaction, the Gibbs free energy is very difficult to be obtained. The most widely accepted description must be the model by Pitzer and coworkers [299, 303, 304], which can be found elsewhere [8, 15, 16]. In particular, for a univalent-univalent electrolyte with molality m, the excess Gibbs energy G^E can be written as:

$$G^E = n_w RT \left[-4A_\phi \ln(1 + b\sqrt{I}) + 2(m^2 B + m^3 C) \right] \tag{D.1}$$

where

$$A_\phi = 1.400608 \times 10^6 \rho_l^{\frac{1}{2}} (\xi T)^{-\frac{3}{2}} \tag{D.2}$$

is the Debye-Hückel parameter that depends on liquid density ρ_l ($\mathrm{g \cdot cm^{-3}}$) and dielectric permeability of pure water ξ at temperature T(K), n_w is the molarities of one kilogram water, $R = 8.31441$ ($\mathrm{J \cdot K^{-1} \cdot mol^{-1}}$) is the universal gas constant, b is a constant currently assigned a value of 1.2 ($\mathrm{kg^{1/2} \cdot mol^{-1/2}}$) which is independent of temperature and pressure [8, 16], I is the ionic strength ($\mathrm{mol \cdot kg}$), and coefficients B and

C represent binary ion-ion interactions related to the ionic strength [16, 17]:

$$B = \beta^{(0)} + \beta^{(1)} \frac{2[1-(1+\alpha_1\sqrt{I})\exp(-\alpha_1\sqrt{I})]}{\alpha_1^2 I} \tag{D.3a}$$

$$2C = C^{(0)} + 4C^{(1)} \left[6 - \left(6 + 6\alpha_2 I^{1/2} + 3\alpha_2^2 I + \alpha_2^3 I^{3/2}\right)\exp\left(-\alpha_2 I^{1/2}\right)\right] \frac{1}{\alpha_2^4 I^2} \tag{D.3b}$$

where $\beta^{(0)}$ and $\beta^{(1)}$, depending on temperature and pressure, are ion-interaction parameters. α_1 and α_2 are adjustable parameters, which are chosen to be, respectively, 2 ($\mathrm{kg}^{1/2}\cdot\mathrm{mol}^{-1/2}$) and 2.5 ($\mathrm{kg}^{1/2}\cdot\mathrm{mol}^{-1/2}$) for NaCl solution [8, 16, 17]. Akinfiev et al. [8] presented an alternative expression of C, which is related to the ionic strength and includes 12 terms of adjustable parameters that fitted from experiment results. The expression by Akinfiev et al. [8] does not provide the relation of apparent molar volume of the electrolyte at infinite dilution in terms of pressure, although it has less fitting terms.

The ion-interaction terms $\beta^{(i=0,1)}$ and $C^{(i=0,1)}$ for excess Gibbs energy for NaCl solution are given in following forms:

$$\beta^{(0)} = \frac{\mathcal{F}(1,P,T)}{m^0}; \quad \beta^{(1)} = \frac{\mathcal{F}(2,P,T)}{m^0}; \quad C^{(0)} = \frac{\mathcal{F}(3,P,T)}{(m^0)^2}; \quad C^{(1)} = \frac{\mathcal{F}(4,P,T)}{(m^0)^2} \tag{D.4}$$

with

$$\begin{aligned}
\mathcal{F}(i,P,T) = {} & b_{i,1} + b_{i,2}\frac{T}{1000} + b_{i,3}\left(\frac{T}{500}\right)^2 + b_{i,4}\frac{T^0}{T-215} + b_{i,5}\times 10^4\left(\frac{T^0}{T-215}\right)^3 + b_{i,6}\times 10^2\left(\frac{T^0}{T-215}\right)^2 \\
& + 2b_{i,7}\times 10^2\left(\frac{T^0}{T}\right)^2 + b_{i,8}\left(\frac{T}{500}\right)^3 + b_{i,9}\left(\frac{T^0}{650-T}\right)^{1/2} + b_{i,10}\times 10^{-5}\frac{P}{\rho^0} + b_{i,11}2\times 10^{-4}\frac{P}{\rho^0}\frac{T^0}{T-225} \\
& + b_{i,12}\times 10^2\frac{P}{\rho^0}\left(\frac{T^0}{650-T}\right)^3 + b_{i,13}\times 10^{-5}\frac{P}{\rho^0}\frac{T}{500} + b_{i,14}2\times 10^{-4}\frac{P}{\rho^0}\frac{T^0}{650-T} + b_{i,15}\times 10^{-7}\left(\frac{P}{\rho^0}\right)^2 \\
& + b_{i,16}2\times 10^{-6}\left(\frac{P}{\rho^0}\right)^2\frac{T^0}{T-225} + b_{i,17}\left(\frac{P}{\rho^0}\right)^2\left(\frac{T^0}{650-T}\right)^3 + b_{i,18}\times 10^{-7}\left(\frac{P}{\rho^0}\right)^2\frac{T}{500T^0} \\
& + b_{i,19}\times 10^{-7}\left(\frac{P}{\rho^0}\right)^2\left(\frac{T}{500}\right)^2 + b_{i,20}4\times 10^{-2}\frac{P}{\rho^0}\left(\frac{T^0}{T-225}\right)^2 + b_{i,21}\times 10^{-5}\frac{P}{\rho^0}\left(\frac{T}{500T^0}\right)^2 \\
& + b_{i,22}2\times 10^{-8}\left(\frac{P}{\rho^0}\right)^3\frac{T^0}{T-225} + b_{i,23}\times 10^{-2}\left(\frac{P}{\rho^0}\right)^3\left(\frac{T^0}{650-T}\right)^3 + b_{i,24}200\left(\frac{T^0}{650-T}\right)^3
\end{aligned} \tag{D.5}$$

where $\rho_0 = 1$ (g/ml), $T^0 = 1$ K. The parameters $b_{i,j}$ including these in eqs(D.15) and (D.25) are presented in Table D.1

D.2 Properties of supercooled water

The dielectric permeativity ξ of liquid water is given by Kirkwood equation [196], see also [18]:

$$\frac{(\xi-1)(2\xi+1)}{9\xi} = N_A\left[\alpha_{d-p} + g\frac{\mu_{d-p}^2}{3\xi_0 k_b T}\right]\frac{1}{3\mathrm{V}_m} \tag{D.6}$$

Table D.1: Values for parameter $b_{i,j}$. Adopted from Archer (2000) [17].

b_{ij}	i=1	2	3	4	5	6
j=1	0.16975213	-1.79414636	0.017402574	1.23339646	1.74148922	1.64078658
2	0.22591122	5.23254688	-0.11595863	-5.12387550	0.90377494	-0.77918008
3	-0.21148253	-	0.049043291	1.46331147	6.78968430	0.21502726
4	-	-20.65972870	-0.025478459	-20.03181141	5.46196497	-1.01900966
5	-	-	-	-	-13.04039117	-
6	0.05115848	-	-	0.28087799	0.16670784	-
7	-51.6284318	392.33242025	1.21392976	-	-9,26081294	-
8	-	-0.64596432	-0.011436071	-	0.13236058	-
9	0.64068578	-	-	-	-	-
10	-16.20243674	-	-	-	-	-
11	72.26082973	250.62580689	-2.22009679	-	-	-
12	-1.07904472	-	-	-	-	-
13	-	-101.55231544	1.51149396	-	-	-
14	-	-	-15.33930307	-	-	-
15	10.15067387	-	-0.11624695	-	-	-
16	-19.09944846	-104.31579650	-	-	-	-
17	1.11765048	-	0.10312928	-	-	-
18	-10.84847744	-	-	-	-	-
19	-	-	-	-	-	-
20	-	-	-	-	-	-
21	23.63319008	-	-	-	-	-
22	2.59934047	-	-	-	-	-
23	-0.77999327	-	-	-	-	-
24	8.13472440	-	-0.19130871	8.51169963	-	-

Table D.2: Adjustable parameters in eq(D.7). Adopted from Archer (1990) [18].

Parameter b_i	Value	Unit
b_1	-0.04044525	$\mathrm{K \cdot MPa^{-1}}$
b_2	103.6180	$\mathrm{K^{1/2}}$
b_3	75.32165	K
b_4	-23.23778	$\mathrm{K^{1/2}}$
b_5	-3.548184	$\mathrm{K^{1/4}}$
b_6	-1246.311	K
b_6	263307.7	$\mathrm{K^2}$
b_8	-0.6928953	$\mathrm{K \cdot MPa^{-1}}$
b_9	-204.4473	$\mathrm{K^2 \cdot MPa^{-1}}$

with

$$\frac{g-1}{\rho_{d-p}} = \frac{1}{\rho^0_{d-p}}\left[b_1\frac{P_l}{T} + b_2\frac{1}{\sqrt{T}} + b_3\frac{1}{T-215} + b_4\frac{1}{\sqrt{T-215}} + b_5\frac{1}{(T-215)^{1/4}}\right] + \frac{1}{\rho^0_{d-p}}\exp(b_6\frac{1}{T} + b_7\frac{1}{T^2} + b_8P_l\frac{1}{T} + b_9P_l\frac{1}{T^2}) \tag{D.7}$$

In above equations, N_A is Avogadro's constant ($6.0221367\times10^{23}\mathrm{mol}^{-1}$), α_{d-p} is the molecular polarizability ($18.1458392\times10^{-30}\mathrm{m}^3$), V_m the molar volume of water ($18.0153\times10^{-3}\mathrm{kg\cdot mol}^{-1}$), μ_{d-p} is the molecular dipole moment of arbitrary molecule in the fluid ($6.1375776\times10^{-30}\mathrm{C\cdot m}$), g is identified as the Kirkwood correlation factor, $\xi_0 = 8.8541878\times10^{-12}$ ($\mathrm{C^2\cdot J^{-1}\cdot m^{-1}}$) is the dielectric permittivity of vacuum. The adjustable constants $b_i, i = 1\sim9$ are given in Table D.2. Figure D.1(a) shows the variation of dielectric permittivity with temperature (243∼273 K) and pressure (0.1∼87 MPa). In the calculation steps, the density of liquid water is evaluated from the expression by Speedy [372], see Figure (D.1(b)).

The volumetric properties of water at subzero temperature, has been extensively studied for decades [371, 372]. As stated by Mironenko et al, [256], the accuracy of solute apparent molar volume evaluated from density data depends strongly on the adopted value of water molar volume, and the authors estimated

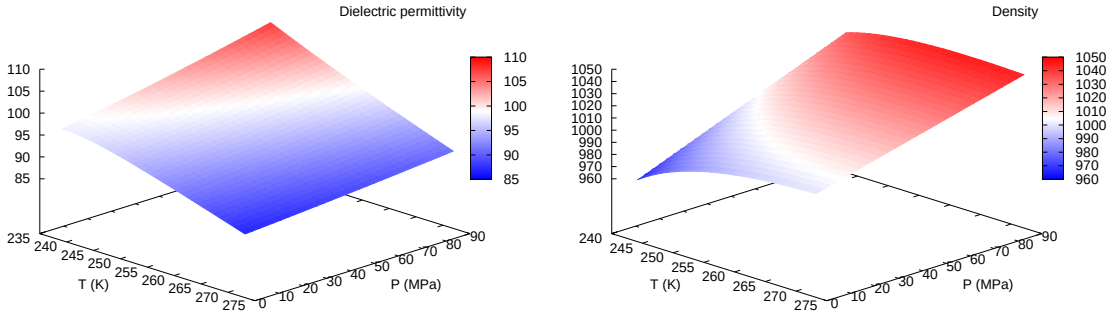

(a) (b)

Figure D.1: Dielectric permittivity (a) and density (b) of water in terms of temperature from 273-240 K and pressure from 0.1-90 MPa.

Table D.3: Values of $B_\alpha^{(n)}$ and C_α in [372].

x	α $(10^{-3}\mathrm{K}^{-1})$	$1/K_l$ $(10^{-11}\mathrm{Pa}^{-1})$	$C_{P,w}$ $(\mathrm{J}\cdot\mathrm{K}^{-1}\cdot\mathrm{mol}^{-1})$
C_x	-0.80	20.0	14.2
$B_x^{(0)}$	1.8021803	4.120	25.952
$B_x^{(1)}$	-0.9416980	-1.130	128.281
$B_x^{(2)}$	0.9055070	77.817	-221.405
$B_x^{(3)}$	-0.0579531	-78.143	196.890
$B_x^{(3)}$	0	54.290	-164.812

that a difference in water density of 50 $\mu\mathrm{g}\cdot\mathrm{cm}^{-3}$ will yield a difference in apparent molar volume of about 0.5 $\mathrm{cm}^3\cdot\mathrm{mol}^{-1}$. Both the temperature and pressure have significant influence on the volumetric properties of water, the water density ρ_w^*, viz $\rho_w^* = \mathsf{M}_w/\mathsf{V}_w$, in terms of pressure and temperature, can be expressed as:

$$\rho_w^* = \rho_s \exp\left[\int_{T_s}^{T} \alpha_w dT + \frac{1}{K_w}(P - P_m)\right] \tag{D.8}$$

where $\rho_s = 920.17$ $(\mathrm{Kg}\cdot\mathrm{m}^{-3})$ was obtained from fitting, α_w and $1/K_w$, are respectively the thermal (volumetric) expansion coefficient and compressibility (reciprocal of bulk modulus) of water, which can be given by [372]:

$$\mathcal{X} = \sum_{i=0}^{N} B_\alpha^{(n)} \left(\frac{T}{227.1} - 1\right)^n + C_\alpha \left(\frac{T}{227.1} - 1\right)^{-1/2} \tag{D.9}$$

$B_\alpha^{(n)}$ and C_α are adjustable parameters given in Table D.3. Note that in eq(D.8), we add the term $P - P_m$ to count the effect of pressure, in addition to the original formula (eq(14) in [372]). The calculated density, which has been used for evaluate the dielectric permittivity of water in previous section, is illustrated in Figure D.1(b).

To evaluate the apparent partial molar volume of solution, the values of Debye-Hückel limiting-law slopes A_v should be calculated firstly, which is evaluated in the form [18, 256]:

$$A_v = 2A_\phi RT\left(3\frac{\partial \ln \xi}{\partial P}\bigg|_T + \frac{\partial \ln \mathsf{V}_w}{\partial P}\bigg|_T\right) \tag{D.10}$$

where ξ is the relative dielectric permittivity, which can be evaluated through the Kirkwood equation, see eq(D.6). The calculated values of Debye-Hückel limiting-law slope A_v, in terms of temperature (240-273 K) and pressure (0.1-90 MPa), are illustrated in Figure D.2(a). The value of A_v at $P = 0.1$ MPa, increases

from about 1.5 to 2.5 as temperature decreases from 273 K to 240 K, which can be verified by data in [8].

The values of Debye-Hückel limiting-law slopes of heat capacity A_c can be evaluated as [18, 256]:

$$A_c = 8RT\frac{\partial A_\phi}{\partial T} + 4RT^2\frac{\partial^2 A_\phi}{\partial T^2} \tag{D.11}$$

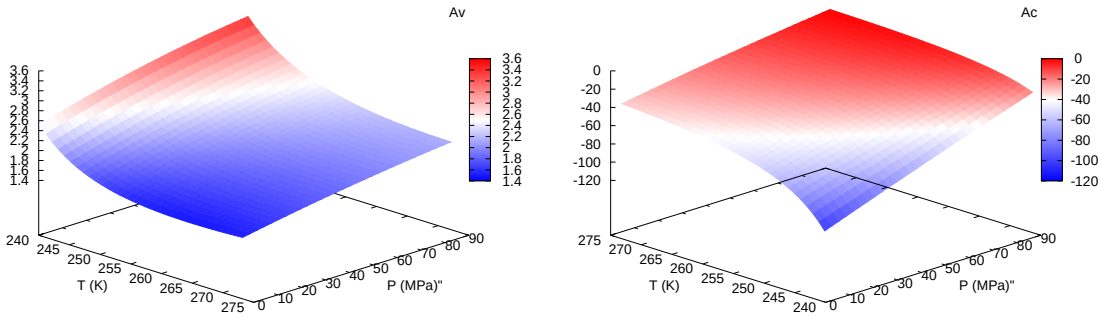

(a) (b)

Figure D.2: The values of Debye-Hückel limiting-law slopes of volume A_v (a) and heat capacity A_c (b) of water in terms of temperature (273-240 K) and pressure (0.1-90 MPa).

Substitution of eq(D.2) into eq(D.11), one obtains the expression of A_c:

$$\begin{aligned} A_c = A_\phi R\left[-\frac{T^2}{\rho^2}\left(\frac{\partial\rho}{\partial T}\right)^2\Big|_P + 2\frac{T^2}{\rho}\frac{\partial^2\rho}{\partial T^2}\Big|_P - 6\frac{T^2}{\xi\rho}\frac{\partial\xi\partial\rho}{\partial T^2}\Big|_P\right] \\ + A_\phi R\left[-6\frac{T^2}{\xi}\frac{\partial^2\xi}{\partial T^2}\Big|_P + 15\frac{T^2}{\xi^2}\left(\frac{\partial\xi}{\partial T}\right)^2\Big|_P - \frac{T}{\rho}\frac{\partial\rho}{\partial T}\Big|_P + 3\frac{T}{\xi}\frac{\partial\xi}{\partial T}\Big|_P + 6\right] \end{aligned} \tag{D.12}$$

Figure D.2(b) shows the variation of A_c with temperature (240-273 K) and pressure (0.1-90 MPa). The values are negative, which are comparable with values in [8, 18].

D.3 Properties of NaCl solution

D.3.1 Volumetric properties

D.3.1.1 Density

The apparent molar volume of the solution with n_r moles of solutes in 1 kilogram water is given by [16, 17]:

$$\begin{aligned} \mathsf{V}_\phi + \frac{\mathsf{V}_w^*}{n_r} = \frac{\mathsf{V}(m_r)}{n_r} + 2A_v\frac{\ln(1+bI^{\frac{1}{2}}) - \ln(1+bI_r^{\frac{1}{2}})}{2b} \\ - 2RT\left[(mB_V(m) - m_rB_V(m_r)) + (m^2C_V(m) - m_r^2C_V(m_r)\right] \end{aligned} \tag{D.13}$$

where V_ϕ is molar volume of electrolyte at infinite dilution, V_w^* is volume of 1 kg of pure water. $\mathsf{V}(m_r)$ is volume of a quantity of solution containing 1 kg of solvent at the given temperature and pressure ($m_r = 6$

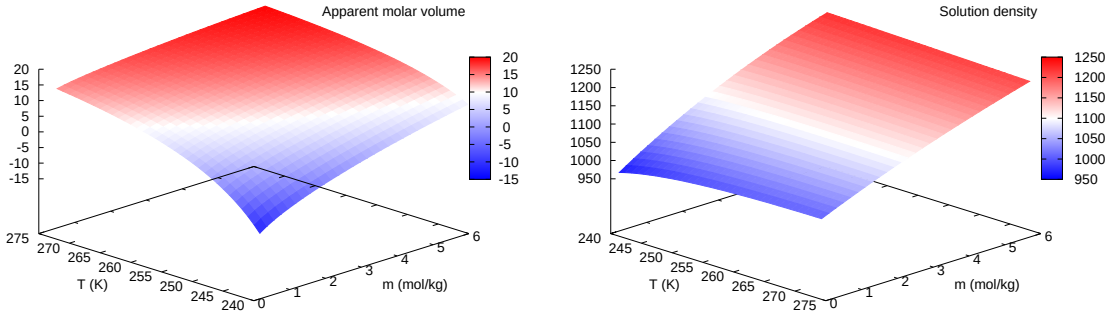

(a) (b)

Figure D.3: Variation of apparent molar volume of NaCl V_ϕ ($\mathrm{ml}\cdot\mathrm{mol}^{-1}$) (a) and total density ρ_l ($\mathrm{kg}\cdot\mathrm{m}^{-3}$) of solution (b) with temperature (273-240 K) and salt concentration (0.2-6 $\mathrm{mol}\cdot\mathrm{kg}^{-1}$) at $P = 0.1$ MPa.

in [16, 17]) ($\mathrm{mol}\cdot\mathrm{kg}^{-1}$). B_V and C_V are adjustable parameters accounting for ion-interaction:

$$B_V = \left.\frac{\partial\beta^{(0)}}{\partial P}\right|_T + 2\left.\frac{\partial\beta^{(1)}}{\partial P}\right|_T \left[1 - \left(1 + \alpha_1 I^{1/2}\right)\exp\left(-\alpha_1 I^{1/2}\right)\right]\frac{1}{\alpha_1^2 I} \tag{D.14a}$$

$$C_V = \left.\frac{\partial C^{(0)}}{\partial P}\right|_T + 4\left.\frac{\partial C^{(1)}}{\partial P}\right|_T \left[6 - \left(6 + 6\alpha_2 I^{1/2} + 3\alpha_2^2 I + \alpha_2^3 I^{3/2}\right)\exp\left(-\alpha_2 I^{1/2}\right)\right]\frac{1}{\alpha_2^4 I^2} \tag{D.14b}$$

The quantity of $V(m_r)$ is related to temperature and pressure:

$$\begin{aligned}\frac{\mathsf{V}_{m_r}}{n_r} = {} & \mathsf{V}^0\left[0.1b_{5,1} + b_{5,2}\times 10^{-4}\frac{T}{3} + b_{5,3}\times 10^{-7}\left(\frac{P+10}{P_0}\right)^{3/2}\frac{T}{300} + b_{5,4}\times 10^{-3}\left(\frac{T}{300}\right)^3\right] \\ & + \mathsf{V}^0\left[b_{5,5}\times 10^{-5}\frac{P}{P_0} + b_{5,6}\times 10^{-5}\frac{T}{3}\frac{P}{P_0} + b_{5,7}\times 10^{-5}\frac{P}{P_0}\left(\frac{T}{300}\right)^2 + b_{5,8}\times 10^{-9}\frac{T}{3}\left(\frac{P}{P_0}\right)^2\right]\end{aligned} \tag{D.15}$$

where, $b_{i=5,j=1\sim 8}$ are adjustable constants, which can be obtained by least square fitting [15–17], $P_0 = 0.1$ (MPa) and $\mathsf{V}^0 = 1.0\times 10^{-3}$ ($\mathrm{m}^3\cdot\mathrm{mol}^{-1}$). The density of solution is then given by:

$$\rho_l = \frac{m\cdot\mathsf{M}_{\mathrm{NaCl}} + 1000}{\mathsf{V}_\phi\cdot m + \mathsf{V}_w^*} \tag{D.16}$$

where $\mathsf{M}_{\mathrm{NaCl}}$ is the molar mass of NaCl (58.5 g/mol). Variations of apparent molar volume of NaCl V_ϕ ($\mathrm{ml}\cdot\mathrm{mol}$) and total liquid density ρ_l ($\mathrm{kg}\cdot\mathrm{m}^3$) with temperature (273-240 K) and NaCl concentrations (0.2-6 $\mathrm{mol}\cdot\mathrm{kg}$) at $P = 0.1$MPa are shown in Figures D.3(a) and D.3(b). Variation of apparent molar volume of NaCl V_ϕ ($\mathrm{ml}\cdot\mathrm{mol}$) and total liquid density ρ_l ($\mathrm{kg}\cdot\mathrm{m}^3$) with pressure (0.1-90 MPa) and NaCl concentration (0.2-6 $\mathrm{mol}\cdot\mathrm{kg}$) at 273.15K are shown in Figures D.4(a) and D.4(b) respectively. The obtained values are close to those given in [17]. From the Figure D.3(a), it can be found that the apparent partial molar volume of NaCl become to be negative when temperature decreases to about -20 ℃, which is consistent with the dat by Tanger and Hegelson [388], and M.V. Mironenko, et al. [256], see Figure (4.5).

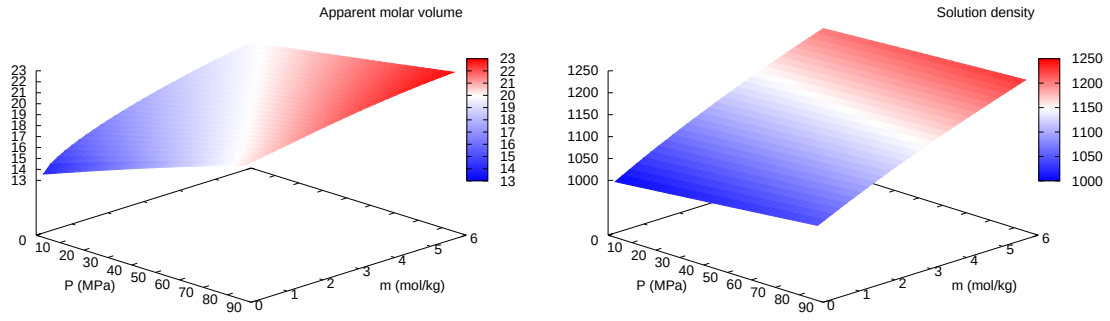

(a) (b)

Figure D.4: Variation of apparent molar volume of NaCl V_ϕ ($\mathrm{ml}\cdot\mathrm{mol}^{-1}$) (a) and total density ρ_l ($\mathrm{kg}\cdot\mathrm{m}^{-3}$) of solution (b) with pressure (0.1-90 MPa) and salt concentration (0.2-6 $\mathrm{mol}\cdot\mathrm{kg}^{-1}$) at $T = 273.15$ K.

D.3.1.2 Compressibility

The compressibility of a solution is defined as (see eqs(B.38) and (B.39)):

$$\frac{1}{K_l} = \frac{1}{\rho_l}\frac{\partial \rho_l}{\partial P} = \frac{1}{K_w} + \sum_i c_i \frac{1}{K_{\phi,i}} \quad \text{with} \quad \frac{1}{K_{\phi,i}} = -\frac{1}{\rho_l}\left(\frac{\mathsf{M}_i}{K_w} + \rho_w^* \frac{\partial \mathsf{V}_{\phi,i}}{\partial P_l}\right) \tag{D.17}$$

The important factor $\partial \mathsf{V}_{\phi,1}/\partial P_l$ can be obtained by differentiating the eq(D.13) to pressure:

$$\begin{aligned}\frac{\partial V_{\phi,i}}{\partial P_l} = \frac{1}{n_r}\frac{\partial V(m_r) - \partial V_w^*}{\partial P} + 2A_K \frac{\ln(1+bI^{\frac{1}{2}}) - \ln(1+bI_r^{\frac{1}{2}})}{2b} \\ - 2RT\left[(mB_K(m) - m_r B_K(m_r)) + (m^2 C_K(m) - m_r^2 C_K(m_r)\right]\end{aligned} \tag{D.18}$$

where A_K, B_K and C_K are adjustable parameters accounting for ion-interactions:

$$A_K = A_\phi RT\left[\frac{2}{\rho_w}\frac{\partial^2 \rho_w}{(\partial P)^2}\bigg|_T - \frac{6}{\xi}\frac{\partial^2 \xi}{(\partial P)^2}\bigg|_T\right] + A_\phi RT\left[-\frac{1}{\rho_w^2}\left(\frac{\partial \rho_w}{\partial P}\right)^2\bigg|_T - 6\frac{1}{\rho_w \xi}\left(\frac{\partial \rho_w \partial \xi}{(\partial P)^2}\right)\bigg|_T + 24\frac{1}{\xi^2}\left(\frac{\partial \xi}{\partial P}\right)^2\bigg|_T\right] \tag{D.19a}$$

$$B_K = \frac{\partial^2 \beta^{(0)}}{(\partial P)^2}\bigg|_T + 2\frac{\partial^2 \beta^{(1)}}{(\partial P)^2}\bigg|_T \left[1 - \left(1 + \alpha_1 I^{1/2}\right)\exp\left(-\alpha_1 I^{1/2}\right)\right]\frac{1}{\alpha_1^2 I} \tag{D.19b}$$

$$C_K = \frac{\partial^2 C^{(0)}}{(\partial P)^2}\bigg|_T + 4\frac{\partial^2 C^{(1)}}{(\partial P)^2}\bigg|_T \left[6 - \left(6 + 6\alpha_2 I^{1/2} + 3\alpha_2^2 I + \alpha_2^3 I^{3/2}\right)\exp\left(-\alpha_2 I^{1/2}\right)\right]\frac{1}{\alpha_2^4 I^2} \tag{D.19c}$$

The variation of compressibility of NaCl solution $1/K_l$ (GPa^{-1}) calculated by eq(D.17) with temperature and salt concentration, and with pressure and salt concentration, are respectively illustrated in Figures D.5(a) and D.5(b). The apparent molar compressibility of NaCl $1/K_\phi$ (GPa^{-1}), calculated by eq(D.17)$_{(2)}$ can be found in Figure D.6.

D.3.1.3 Thermal expansion coefficient

The thermal coefficient of a solution is defined as (see eqs(B.40) and (B.41)):

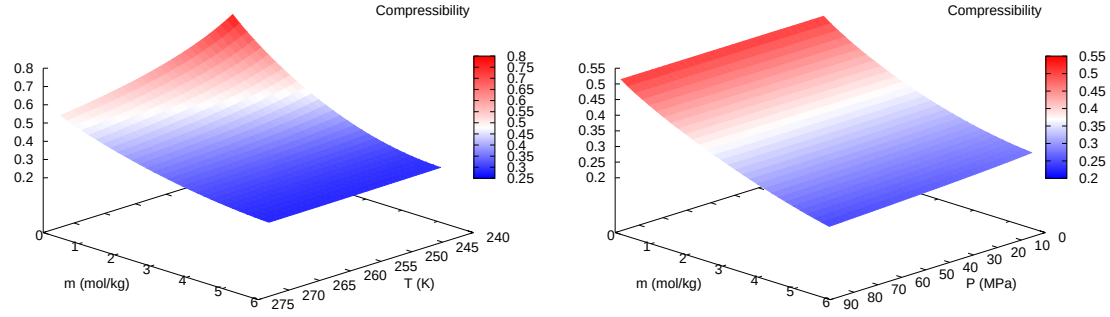

(a) (b)

Figure D.5: Variation of compressibility of NaCl solution $1/K_l$ (GPa^{-1}) with (a) temperature (273-243 K) and salt concentration (0.2-6 mol $\cdot$ kg^{-1}) at $P = 0.1$ MPa, and with (b) pressure (0.1-90 MPa) and salt concentration (0.2-6 mol $\cdot$ kg^{-1}) at $T = 273.15$ K.

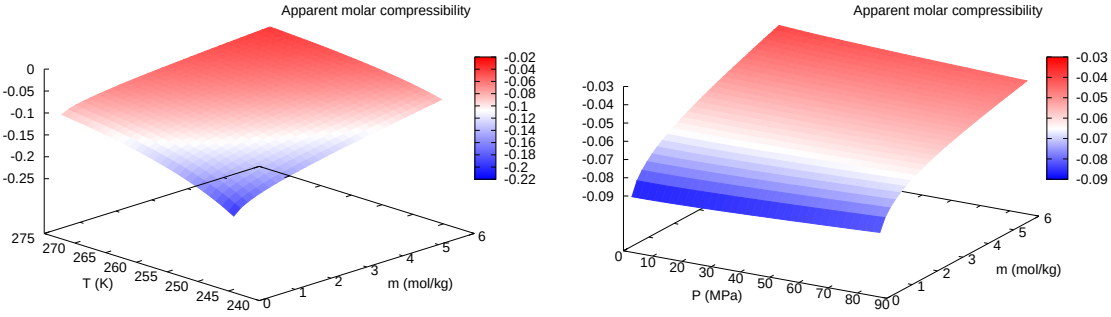

(a) (b)

Figure D.6: Variation of apparent molar compressibility of NaCl $1/K_\phi$ (GPa^{-1}) with (a) temperature (273-243 K) and salt concentration (0.2-6 mol $\cdot$ kg^{-1}) at P=0.1 MPa, and with (b) pressure (0.1-90 MPa) and salt concentration (0.2-6 mol $\cdot$ kg^{-1}) at $T = 273.15$ K.

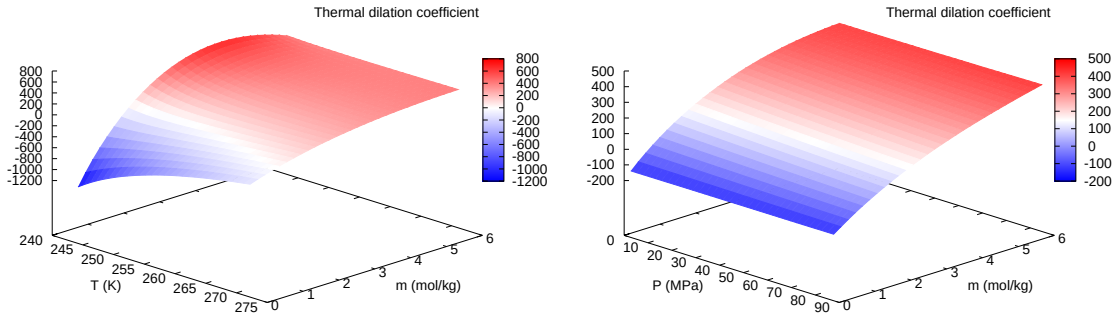

(a) (b)

Figure D.7: Variation of thermal (volumetric) expansion coefficient of NaCl solution $3\alpha_l$ (μm $\cdot$ m^{-1}) with (a) temperature (273-243 K) and salt concentration (0.2-6 mol $\cdot$ kg^{-1}) at $P = 0.1$ MPa, and with (b) pressure (0.1-90 MPa) and salt concentration (0.2-6 mol $\cdot$ kg^{-1}) at $T = 273.15$ K.

$$\alpha_l = -\frac{1}{3}\frac{1}{\rho_l}\frac{\partial \rho_l}{\partial T} = \alpha_w + \sum_i c_i \alpha_{\phi,i} \quad \text{with} \quad \alpha_{\phi,i} = \frac{1}{3}\frac{1}{\rho_l}\left(-\alpha_w \mathsf{M}_i + \rho_w^* \frac{\partial \mathsf{V}_{\phi,i}}{\partial T}\right) \tag{D.20}$$

The important factor $\partial \mathsf{V}_{\phi,1}/\partial T$ can be obtained by the differentiating the eq(D.13) to the variable of temperature in the following form:

$$\begin{aligned}\frac{\partial \mathsf{V}_{\phi,i}}{\partial T} = \frac{1}{n_r}\frac{\partial \mathsf{V}(m_r) - \partial \mathsf{V}_w^*}{\partial T} + 2A_\alpha \frac{\ln(1+bI^{\frac{1}{2}}) - \ln(1+bI_r^{\frac{1}{2}})}{2b} \\ - 2RT\left[(mB_\alpha(m) - m_r B_\alpha(m_r)) + (m^2 C_\alpha(m) - m_r^2 C_\alpha(m_r)\right]\end{aligned} \tag{D.21}$$

where A_α, B_α and C_α are adjustable parameters accounting for ion-interactions:

$$\begin{aligned}A_\alpha = &-\frac{1}{2T}A_v - \frac{RTA_\phi}{\rho_w^2}\frac{(\partial \rho_w)^2}{\partial P \partial T} + 15\frac{RTA_\phi}{\xi^2}\frac{(\partial \xi)^2}{\partial P \partial T} + \frac{2RTA_\phi}{\rho_2}\frac{\partial^2 \rho_2}{\partial T \partial P} - \frac{6RTA_\phi}{\xi}\frac{\partial^2 \xi}{\partial T \partial P} \\ &- 3\frac{RTA_\phi}{\xi \rho_w}\frac{\partial \xi}{\partial P}\frac{\partial \rho_w}{\partial T} - 3\frac{RTA_\phi}{\xi \rho_w}\frac{\partial \xi}{\partial T}\frac{\partial \rho_w}{\partial P}\end{aligned} \tag{D.22a}$$

$$B_\alpha = \frac{\partial^2 \beta^{(0)}}{\partial T \partial P} + \frac{1}{T}\frac{\partial \beta^{(0)}}{\partial P}\bigg|_T + 2\left[\frac{\partial^2 \beta^{(1)}}{\partial T \partial P} + \frac{1}{T}\frac{\partial \beta^{(1)}}{\partial P}\right] \times \left[1 - \left(1 + \alpha_1 I^{1/2}\right)\exp\left(-\alpha_1 I^{1/2}\right)\right]\frac{1}{\alpha_1^2 I} \tag{D.22b}$$

$$C_\alpha = \frac{\partial^2 C^{(0)}}{\partial T \partial P} + \frac{1}{T}\frac{\partial C^{(0)}}{\partial P}\bigg|_T + 4\left[\frac{\partial^2 C^{(1)}}{\partial T \partial P} + \frac{1}{T}\frac{\partial C^{(1)}}{\partial P}\bigg|_T\right] \times \left[6 - \left(6 + 6\alpha_2 I^{1/2} + 3\alpha_2^2 I + \alpha_2^3 I^{3/2}\right)\exp\left(-\alpha_2 I^{1/2}\right)\right]\frac{1}{\alpha_2^4 I^2} \tag{D.22c}$$

The variation of thermal (volumetric) expansion coefficient of NaCl solution $3\alpha_l$ ($\mu\mathrm{m}\cdot\mathrm{m}^{-1}\cdot{}^\circ\mathrm{C}^{-1}$) calculated by eq(D.20) with temperature and salt concentration, and with pressure and salt concentration, are respectively illustrated in Figures D.7(a) and D.7(b). The apparent molar thermal (volumetric) expansion coefficient of NaCl $3\alpha_\phi$ ($\mu\mathrm{m}\cdot\mathrm{m}^{-1}$) calculated by eq(D.20)$_{(2)}$ with temperature and salt concentration, and with pressure and salt concentration, are respectively illustrated in Figures D.8(a) and D.8(b).

D.3.2 Heat capacity

The apparent heat capacity of the solution with n_r moles of solutes in 1 kilogram water is [16, 17]:

$$\begin{aligned}C_{P|\phi} + \frac{c_{P|w}^*}{n_r} = \frac{C_P(m_r)}{n_r} + 2A_c\frac{\ln(1+bI^{\frac{1}{2}}) - \ln(1+bI_r^{\frac{1}{2}})}{2b} \\ - 2RT^2\left[(mB_c(m) - m_r B_c(m_r)) + (m^2 C_c(m) - m_r^2 C_c(m_r)\right]\end{aligned} \tag{D.23}$$

where $C_{P|\phi}$ is molar heat capacity of electrolyte at infinite dilution. $c_{P|w}^*$is the heat capacity of 1 kg of pure water. $C_P(m_r)$ is the heat capacity of a quantity of solution containing 1 kg solvent at the given temperature and pressure, $m_r = 6\mathrm{mol}\cdot\mathrm{kg}^{-1}$ in [16, 17]. B_C and C_C are adjustable parameters accounting for ion-interactions:

$$B_C = \frac{\partial^2 \beta^{(0)}}{\partial T^2}\bigg|_P + \frac{2}{T}\frac{\partial \beta^{(0)}}{\partial T}\bigg|_P + 2\left[\frac{\partial^2 \beta^{(1)}}{\partial T^2}\bigg|_P + \frac{2}{T}\frac{\partial \beta^{(1)}}{\partial T}\bigg|_P\right]\left[1 - \left(1 + \alpha_1 I^{1/2}\right)\exp\left(-\alpha_1 I^{1/2}\right)\right]\frac{1}{\alpha_1^2 I} \tag{D.24a}$$

$$C_C = \frac{\partial^2 C^{(0)}}{\partial T^2}\bigg|_P + \frac{2}{T}\frac{\partial C^{(0)}}{\partial T}\bigg|_P + 4\left[\frac{\partial^2 C^{(1)}}{\partial T^2}\bigg|_P + \frac{2}{T}\frac{\partial C^{(1)}}{\partial T}\bigg|_P\right]\left[6 - \left(6 + 6\alpha_2 I^{1/2} + 3\alpha_2^2 I + \alpha_2^3 I^{3/2}\right)\exp\left(-\alpha_2 I^{1/2}\right)\right]\frac{1}{\alpha_2^4 I^2} \tag{D.24b}$$

When $P = 0.1$ MPa, $C_P(m_r)/n_r$ can be given by the following polynomial [16, 17]:

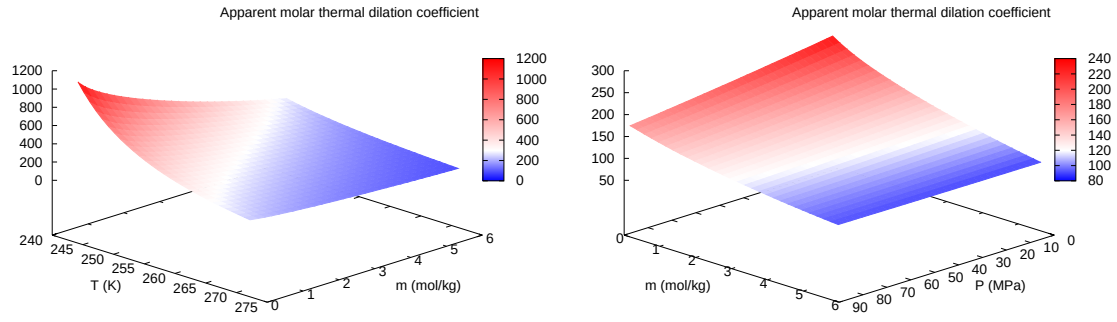

(a) (b)

Figure D.8: Variation of apparent molar thermal (volumetric) expansion coefficient of NaCl solution $3\alpha_\phi$ (μm $\cdot$ m^{-1} $\cdot$ ℃$^{-1}$) with (a) temperature (273-243 K) and salt concentration (0.2-6 mol $\cdot$ kg^{-1}) at $P = 0.1$ MPa, and with (b) pressure (0.1-90 MPa) and salt concentration (0.2-6 mol $\cdot$ kg^{-1}) at $T = 273.15$ K.

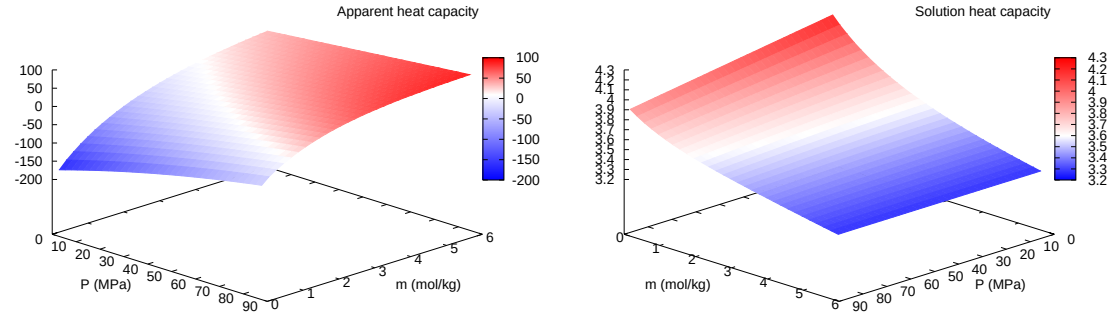

(a) (b)

Figure D.9: Variation of apparent heat capacity of NaCl $C_{P,\phi}$ (J$\cdot$K$^{-1}\cdot$mol^{-1}) (a) and overall heat capacity $C_{P,l}$ (J $\cdot$ K^{-1} $\cdot$ g^{-1}) of solution (b) with temperature (273-240 K) and salt concentration (0.2-6 mol $\cdot$ kg^{-1}) at $P = 0.1$ MPa.

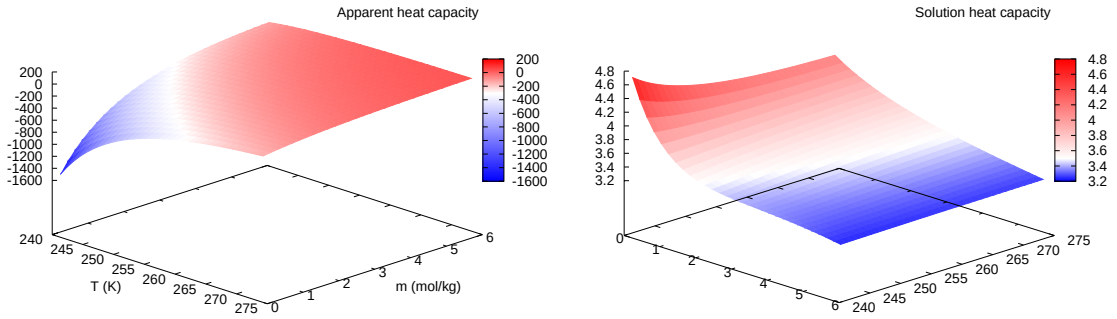

(a) (b)

Figure D.10: Variation of apparent heat capacity of NaCl $C_{P,\phi}$ (J$\cdot$K$^{-1}\cdot$mol^{-1}) (a) and overall heat capacity $C_{P,l}$ (J$\cdot$K$^{-1}\cdot$g^{-1}) of solution (b) in terms of pressure (0.1-90 MPa) and salt concentration (0.2-6 mol$\cdot$kg^{-1}) at $T = 273.15$ K.

$$\frac{C_P(m_r)}{n_r} = \left[b_{6,1} + b_{6,2}\frac{T}{300} + b_{6,3}\left(\frac{T}{300}\right)^2 + b_{6,4}\frac{100}{T}\right] C_P^0 \tag{D.25}$$

where, $C_p^0 = 1.0$ (kJ$\cdot$mol$^{-1}\cdot$K^{-1}), $b_{i=6,j=1\sim4}$ are adjustable constants presented in Table D.1 [15–17]. The overall heat capacity referring to one mass unit of solution can be calculated as:

$$C_{P,l} = \frac{C_{P|\phi}\cdot m + c^*_{P|w}}{m\cdot \mathsf{M}_{\mathrm{NaCl}} + 1000} \tag{D.26}$$

Figures D.9(a) and D.9(b), respectively, show the variation of the apparent molar heat capacity of NaCl solution at infinite dilution $C_{P|\phi}$ (J$\cdot$K$^{-1}\cdot$mol^{-1}) and the variation of the overall heat capacity of solution $C_{P,l}$ (J$\cdot$K$^{-1}\cdot$g^{-1}) with temperature (273-240 K) and salt concentration (0.2-6 mol$\cdot$kg^{-1}) at $P = 0.1$ MPa. Figures D.10(a) and D.10(b), respectively, show the variation of the apparent molar heat capacity of NaCl solution at infinite dilution $C_{P|\phi}$ (J$\cdot$K$^{-1}\cdot$mol^{-1}) and the variation of the overall heat capacity of solution $C_{P,l}$ (J$\cdot$K$^{-1}\cdot$g^{-1}) with pressure (0.1-90 MPa) and salt concentration (0.2-6 mol$\cdot$kg^{-1}) at $T = 273.15$ K.

D.4 Thermal conductivity

Unlike the volumetric property and thermal property of NaCl solution, which are related to the Gibbs free energy [15, 16], the thermal conductivity can not be predicted from the Gibbs energy based formulas. Again, due to the complexity of experiments on the thermal conductivity of solution with temperature, pressure and salt concentration, few data have been published. Ozbek and Phillips [277] applied a semi-empirical model to fit the NaCl solution in range of 0-6 mol$\cdot$kg^{-1}:

$$\begin{aligned}\lambda_l = {} & \lambda_w\left[1 - x_m\left(0.23434 - 7.923\times10^{-4}T + 3.924\times10^{-6}T^2\right)\right] \\ & + \lambda_w\left[x_m^2\left(0.106 - 2\times10^{-4}T + 1.2\times10^{-6}T^2\right)\right]\end{aligned} \tag{D.27}$$

where λ_l is the thermal conductivity of aqueous solution (mW$\cdot$m$^{-1}\cdot$K^{-1}), λ_w is the thermal conductivity of water (mW$\cdot$m$^{-1}\cdot$K^{-1}), T is temperature (K), x_m is the mass fraction of NaCl. Figure D.11(a) illustrates the variation of the thermal conductivity of NaCl solution with the salt concentration and temperature. It can be found that the thermal conductivity of aqueous solution decreases as temperature decreases and as salt concentration increases.

Table D.4: Experimental results for the thermal conductivity of aqueous solution of NaCl at different pressure at 293K (mW$\cdot$m$^{-1}\cdot$K^{-1}). Data from Abdulagatov and Magomedov (1994) [4].

	Pressure (MPa)					
NaCl mass fraction	0.1-2	20	40	60	80	100
2.5%	594	603	611	619	629	639
5%	591	598	607	616	625	633
10%	588	592	600	608	616	624
15%	580	586	593	601	610	617
20%	574	579	585	593	600	605
25%	566	573	578	584	590	597

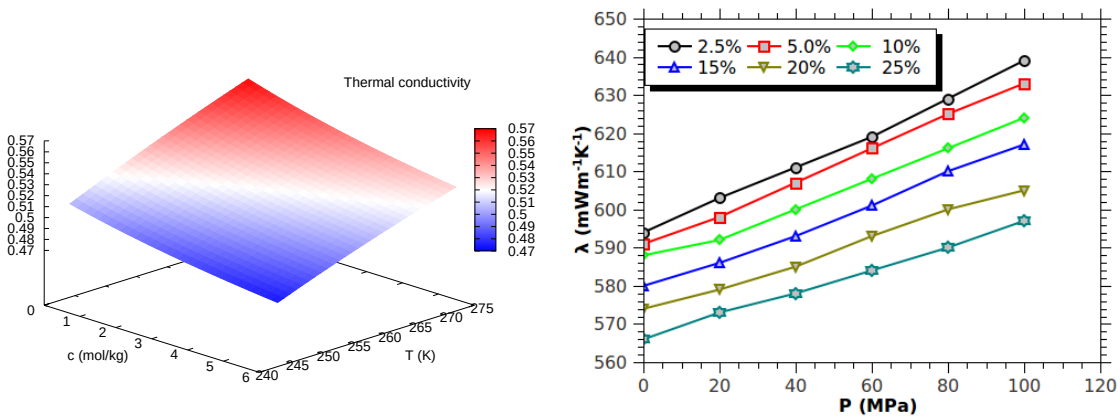

(a) (b)

Figure D.11: (a), Variation of thermal conductivity (λ) of NaCl solution with salt concentration (0.2-6mol $\cdot$ kg^{-1}) and temperature (240-273K) (W $\cdot$ m^{-1} $\cdot$ K^{-1}). (b), Variation of thermal conductivity (λ) of NaCl solution with pressure at 293K (mW $\cdot$ m^{-1} $\cdot$ K^{-1}). Data from Abdulagatov and Magomedov (1994) [4].

The influence of pressure on the thermal conductivity of aqueous solution scan be found in Table D.4 and Figure D.11(b). The slope of the thermal conductivity to the pressure is found to be 0.45 (mW $\cdot$ m^{-1} $\cdot$ K^{-1} $\cdot$ MPa^{-1}) when the mass fraction of NaCl is 2.5%, and it decreases to 0.3 (mW $\cdot$ m^{-1} $\cdot$ K^{-1} $\cdot$ MPa^{-1}) when the mass fraction of NaCl increases to 25%. We take an average value, $\partial\lambda_l/\partial P_l = 0.37$ (mW $\cdot$ m^{-1} $\cdot$ K^{-1} $\cdot$ MPa^{-1}), where the mass fraction of NaCl is about 15%. It thus has:

$$\lambda_l = \lambda_l(P = 0) + 0.37 \times 10^{-4} P_l \quad (\mathrm{W} \cdot \mathrm{m}^{-1} \cdot \mathrm{K}^{-1}) \tag{D.28}$$

It can be concluded that the influence of pressure on the thermal conductivity of aqueous solution is not significant.

Appendix E

Strains of saturated samples

E.1 LVDT verification

The nominal linear displacement of LVDT itself is 0.56 μm/℃. We performed a series of measurements on the displacement of LVDT itself to obtain reliable data. Figure E.1 shows a typical displacement curve of LVDT during freeze-thaw. The freeze-thaw temperature is set in the range of 20∼ −20℃. It can be seen that the slopes of the displacement-temperature curves are 0.5703 and 0.5972 (0.5837 in average) during freezing and thawing respectively. The average values for 6 LVDTs are presented in Table E.1. The obtained values will be used to calculate the strains of cement-based materials subjected to freeze-thaw.

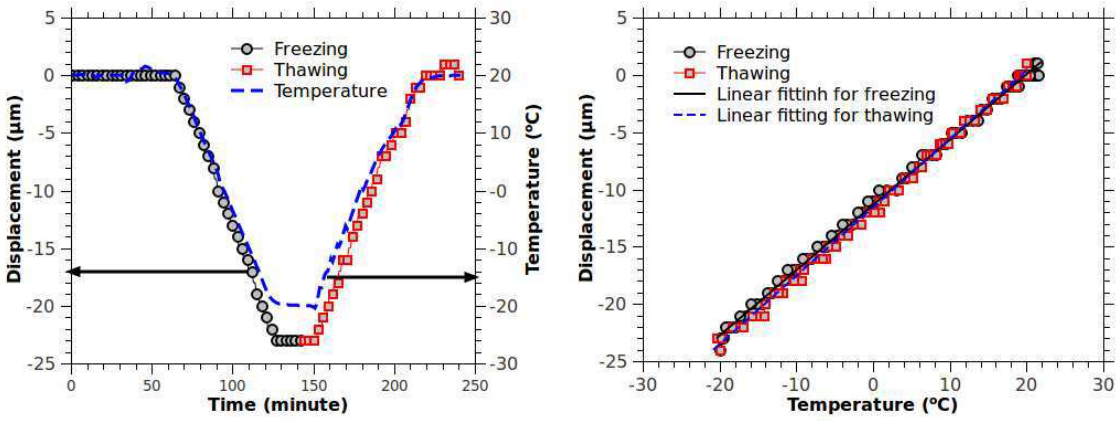

(a) (b)

Figure E.1: Displacement of LVDT (a) in terms of time, (b) in terms of temperature.

Table E.1: The measured displacement – temperature slops of 6 spring LVDTs (Type Microsensor 750).

LVDT Sensor number	1	2	3	4	5	6
Nominal value (μm/°C)	0.56	0.56	0.56	0.56	0.56	0.56
Test 1 (μm/°C)	0.5996	0.5819	0.5601	0.5673	0.5812	0.5602
Test 2 (μm/°C)	0.5962	0.5985	0.5188	0.5601	0.5823	0.5592
Test 3 (μm/°C)	0.5444	0.5837	0.5600	0.5158	0.6266	0.5597
Test 4 (μm/°C)	0.5672	0.5767	0.5628	0.5855	0.6131	0.5672
Test 5 (μm/°C)	0.5926	0.5911	0.5673	0.5533	0.5849	0.5551
Test 6 (μm/°C)	0.5617	0.5899	0.5555	0.5909	0.5932	0.5607
Average (μm/°C)	0.5770	0.5875	0.5541	0.5622	0.5969	0.5637

E.2 Deformations of air entrained cement pastes

Figures E.2 ∼ E.13 show the deformation of cement pastes with different dosage of air voids. Those samples have been initially saturated with NaCl solution from zero∼ 15%. The sample preparation, deformation measurement procedures can be found in section 9.1. The strains presented in Tables E.2 and E.3 are defined in Table 9.3.

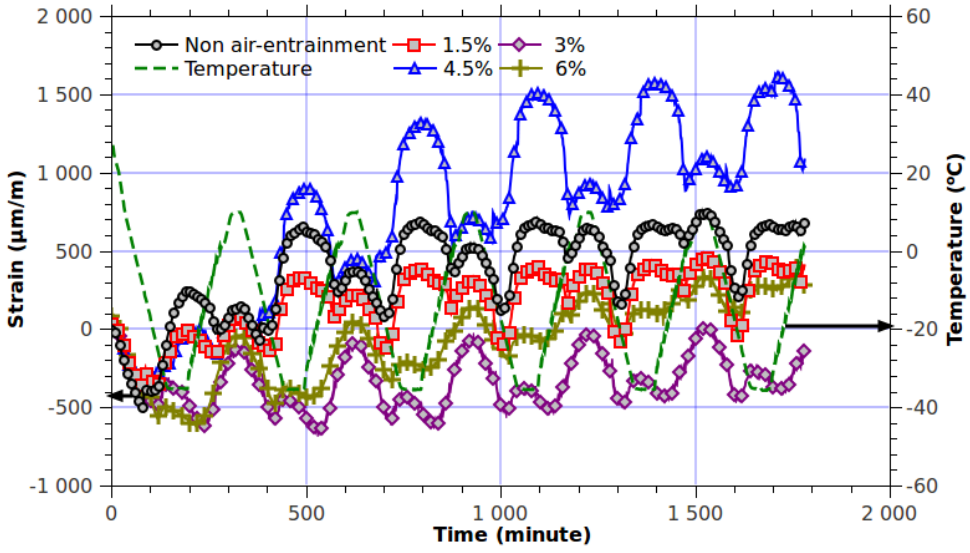

Figure E.2: Deformation of water saturated samples entrained with different dosages of air voids in terms of freeze-thaw time.

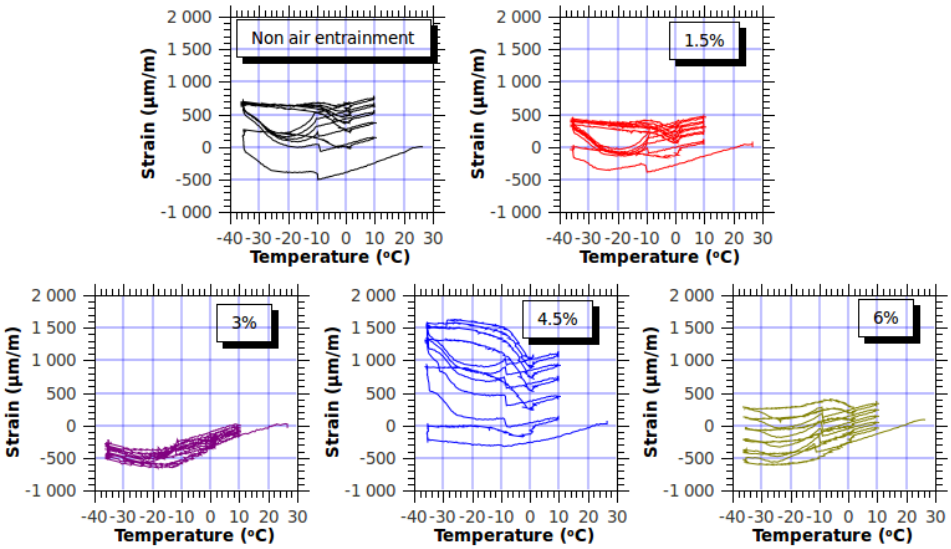

Figure E.3: Deformation of water saturated samples entrained with different dosages of air voids in terms of temperature.

Table E.2: Deformations for air entrained pastes saturated with pure water (1.5% NaCl)[3% NaCl] subjected to freeze-thaw loading.

Sorts	1st cycle	2ed cycle	3rd cycle	4th cycle	5th cycle	6th cycle
	($\times 10^{-6}$)	($\times 10^{-6}$)	($\times 10^{-6}$)	($\times 10^{-6}$)	($\times 10^{-6}$)	($\times 10^{-6}$)
Non air entrained samples						
ε_{th}	−893 (−1200) [−798]	−555 (−997) [−853]	−548 (−982) [−869]	−531 (−973) [−868]	−542 (-) [-]	−560 (-) [-]
ε_{nu}	87 (30) [0]	100 (−78) [0]	67 (−55) [0]	0 (−76) [0]	−51 (-) [-]	−41 (-) [-]
ε_{ex}	263 (−100) [190]	509 (115) [387]	326 (11) [337]	154 (165) [292]	36 (-) [-]	−72 (-) [-]
ε_{pr}	1156 (1300) [988]	1064 (1112) [1240]	874 (993) [1206]	685 (1138) [1160]	578 (-) [-]	488 (-) [-]
ε_{re}	142 (20) [135]	226 (132) [168]	161 (89) [112]	108 (63) [86]	108 (-) [-]	- (-) [-]
ε_{if}	388 (235) [332]	43 (28) [118]	−11 (16) [67]	−10 (-) [-]	0 (-) [-]	- (-) [-]
%1.5 air entrained samples						
ε_{th}	−770 (−590) [−584]	−449 (−347) [−600]	−460 (−334) [−599]	−444 (−353) [−605]	−444 (-) [-]	−460 (-) [-]
ε_{nu}	101 (62) [0]	78 (132) [0]	70 (98) [0]	−41 (58) [0]	−51 (-) [-]	−38 (-) [0]
ε_{ex}	−35 (836) [9]	264 (1418) [79]	155 (1230) [70]	90 (1100) [70]	36 (-) [-]	−28 (-) [-]
ε_{pr}	735 (1426) [593]	713 (1765) [679]	615 (1564) [669]	534 (1463) [675]	480 (-) [-]	432 (-) [-]
ε_{re}	48 (332) [85]	153 (310) [65]	75 (178) [33]	75 (118) [23]	77 (-) [-]	- (-) [-]
ε_{if}	236 (914) [155]	44 (112) [56]	11 (48) [33]	21 (-) [-]	13 (-) [-]	- (-) [-]
%3 air entrained samples						
ε_{th}	−751 (−871) [−786]	−582 (−731) [−747]	−594 (−923) [−730]	−590 (−676) [752]	−649 (-) [-]	−627 (-) [-]
ε_{nu}	85 (100) [0]	86 (167) [0]	25 (133) [0]	44 (77) [0]	66 (-) [-]	40 (-) [-]
ε_{ex}	−455 (−18) [−439]	−340 (283) [−215]	341 (305) [−157]	−299 (248) [−145]	−279 (-) [-]	−281 (-) [-]
ε_{pr}	1206 (853) [347]	922 (356) [532]	935 (1228) [573]	889 (924) [607]	928 (-) [-]	908 (-) [-]
ε_{re}	−154 (42) [−97]	42 (161) [45]	20 (97) [46]	41 (118) [35]	41 (-) [-]	- (-) [-]
ε_{if}	−38 (343) [127]	41 (183) [103]	62 (54) [58]	61 (-) [-]	39 (-) [-]	- (-) [-]
%4.5 air entrained samples						
ε_{th}	−650 (−537) [*]	−408 (−268) [*]	−431 (−281) [*]	−441 (−274) [*]	−420 (-) [-]	−467 (-) [-]
ε_{nu}	0 (100) [0]	59 (196) [0]	137 (428) [0]	175 (439) [0]	114 (-) [-]	101 (-) [-]
ε_{ex}	−36 (750) [261]	813 (1411) [210]	870 (1498) [165]	792 (1510) [164]	648 (-) [-]	531 (-) [-]
ε_{pr}	614 (1287) [*]	1221 (1679) [*]	1201 (1779) [*]	1233 (1784) [*]	1068 (-) [*]	998 (-) [*]
ε_{re}	83 (324) [161]	344 (350) [70]	267 (240) [57]	211 (180) [-]	167 (-) [-]	- (-) [-]
ε_{if}	932 (985)	401 (437)	189 (252)	67 (-)	50 (-)	- (-)
%6 air entrained samples						
ε_{th}	−847 (*) [−945]	−572 (*) [−861]	−573 (*) [−863]	−574 (*) [−854]	−575 (-) [-]	−574 (-) [-]
ε_{nu}	121 (0) [0]	110 (38) [0]	100 (82) [0]	119 (58) [0]	145 (-) [0]	162 (-) [0]
ε_{ex}	−659 (220) [−750]	−331 (717) [−504]	−255 (884) [−513]	−179 (1469) [−501]	−115 (-) [-]	−61 (-) [-]
ε_{pr}	188 (*) [195]	241 (*) [357]	828 (*) [350]	395 (*) [353]	460 (-) [-]	513 (-) [-]
ε_{re}	−124 (303) [−103]	86 (273) [43]	96 (206) [10]	93 (173) [10]	97 (-) [-]	- (-) [-]
ε_{if}	204 (800) [98]	162 (440) [34]	172 (290) [21]	161 (-) [-]	151 (-) [-]	- (-) [-]

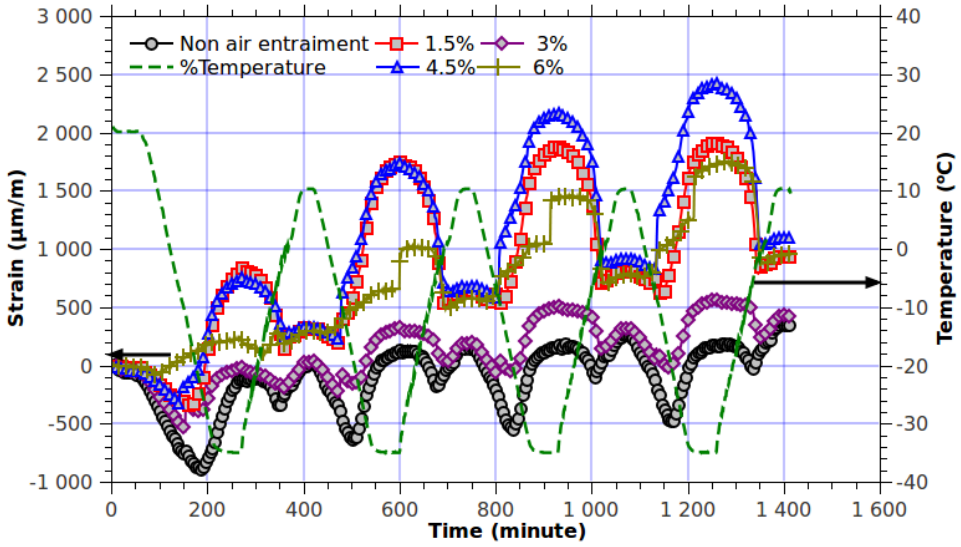

Figure E.4: Deformation of 1.5% NaCl solution saturated samples entrained with different dosages of air voids in terms of freeze-thaw time.

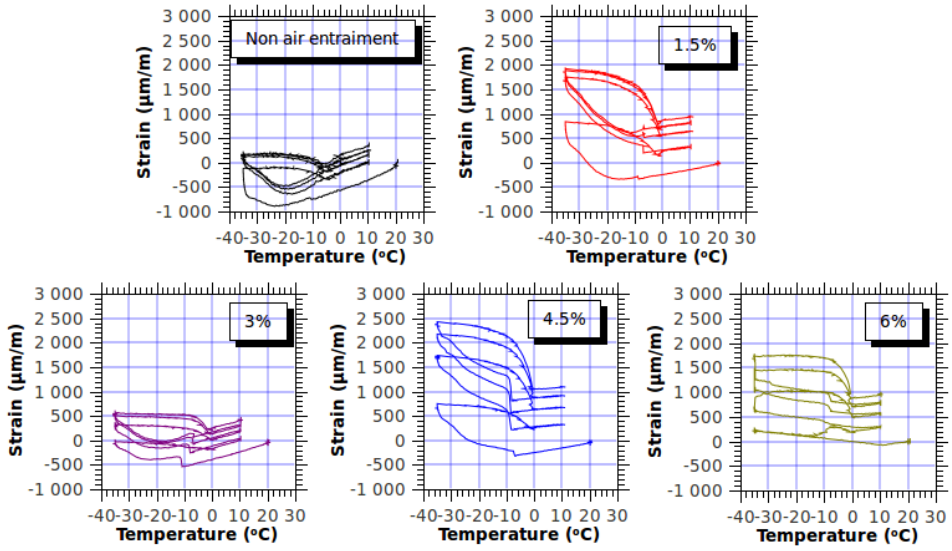

Figure E.5: Deformation of 1.5% NaCl solution saturated samples entrained with different dosages of air voids in terms of temperature.

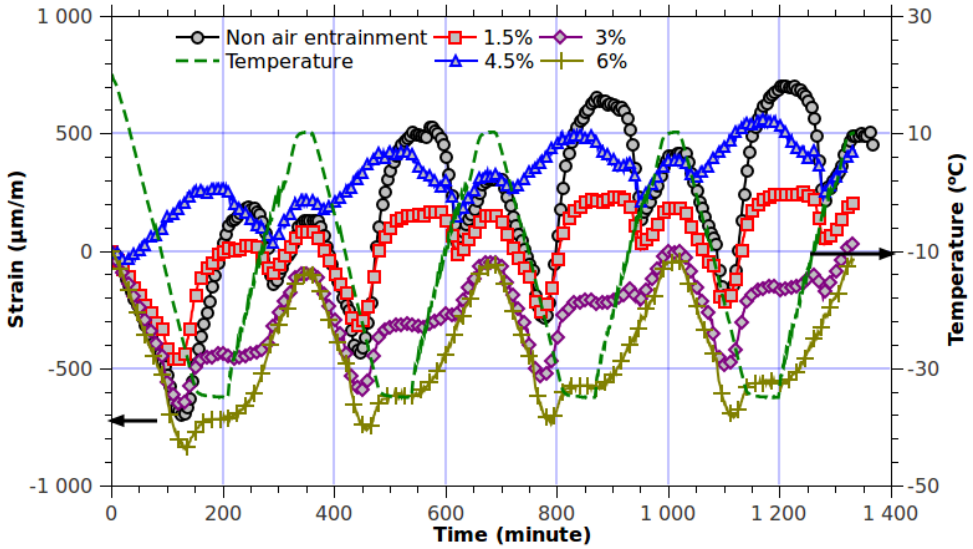

Figure E.6: Deformation of 3% NaCl solution saturated samples entrained with different dosages of air voids in terms of freeze-thaw time.

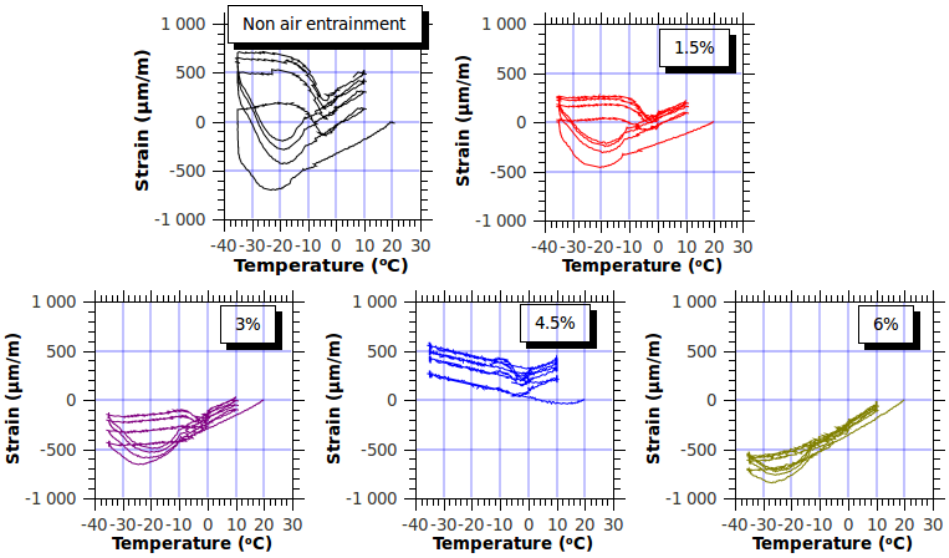

Figure E.7: Deformation of 3% NaCl solution saturated samples entrained with different dosages of air voids in terms of temperature.

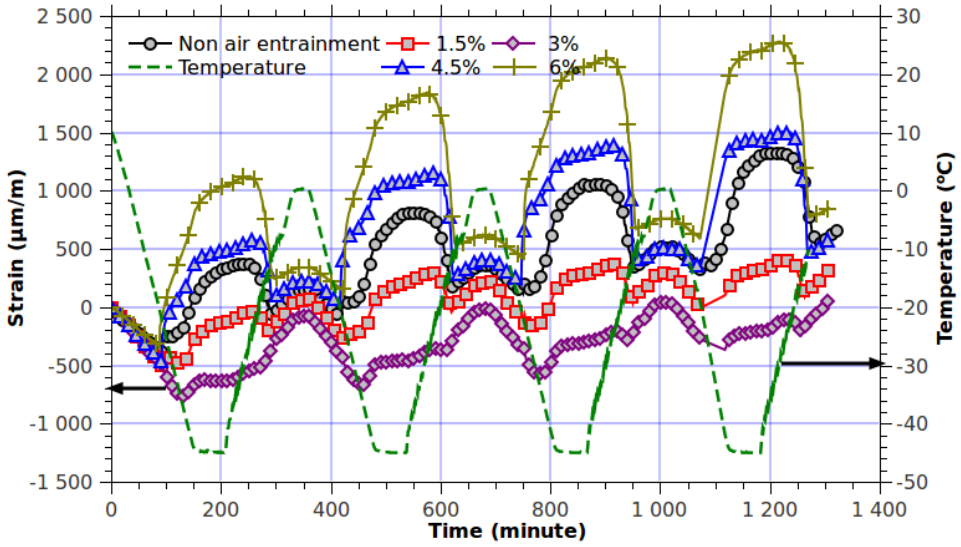

Figure E.8: Deformation of 6% NaCl solution saturated samples entrained with different dosages of air voids in terms of freeze-thaw time.

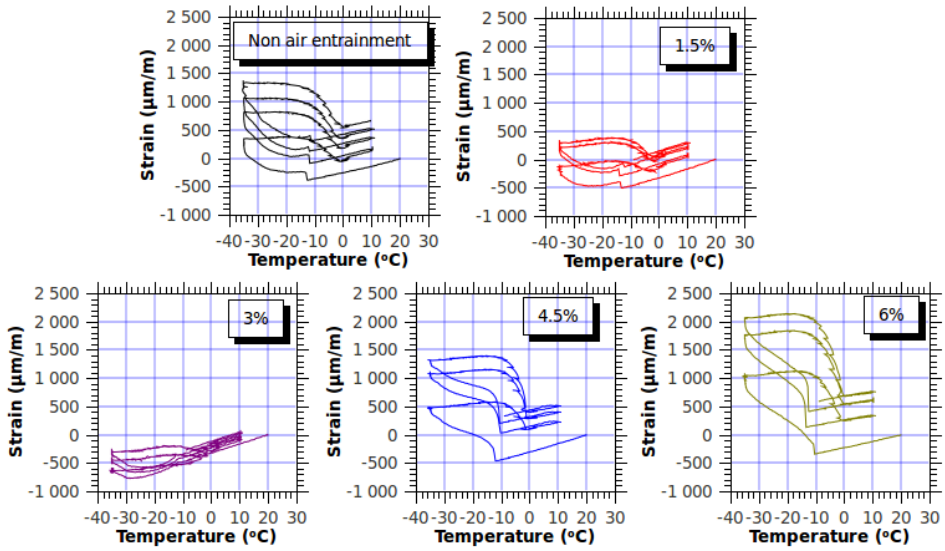

Figure E.9: Deformation of 6% NaCl solution saturated samples entrained with different dosages of air voids in terms of temperature.

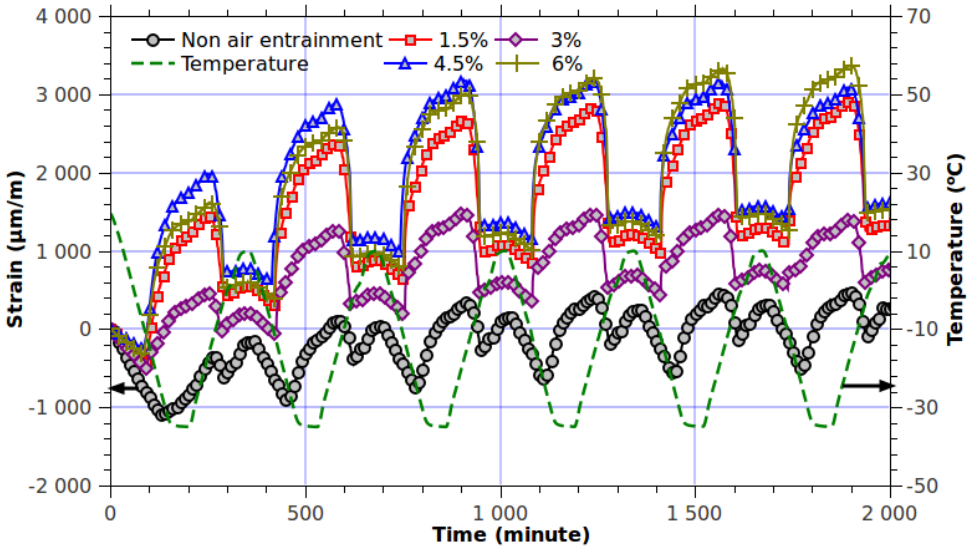

Figure E.10: Deformation of 10% NaCl solution saturated samples entrained with different dosages of air voids in terms of freeze-thaw time.

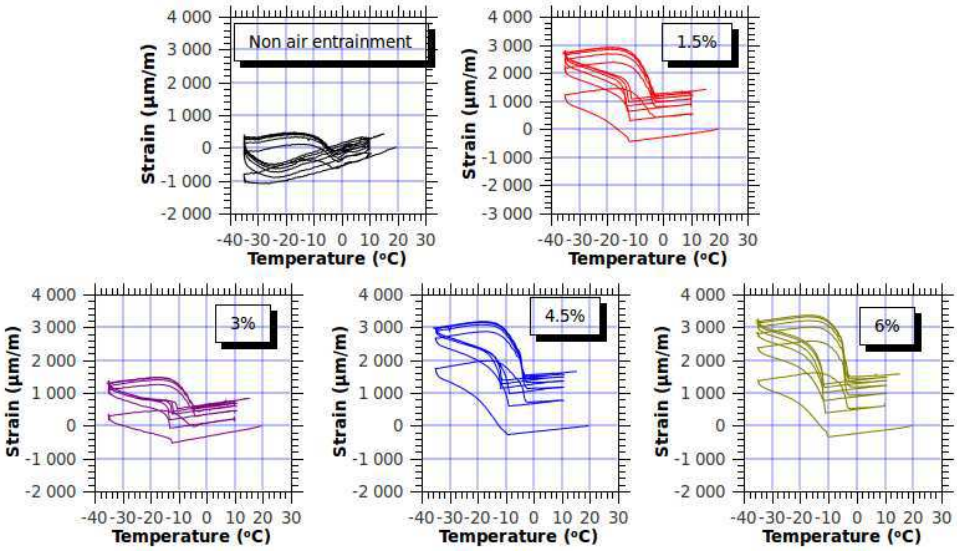

Figure E.11: Deformation of 10% NaCl solution saturated samples entrained with different dosages of air voids in terms of temperature.

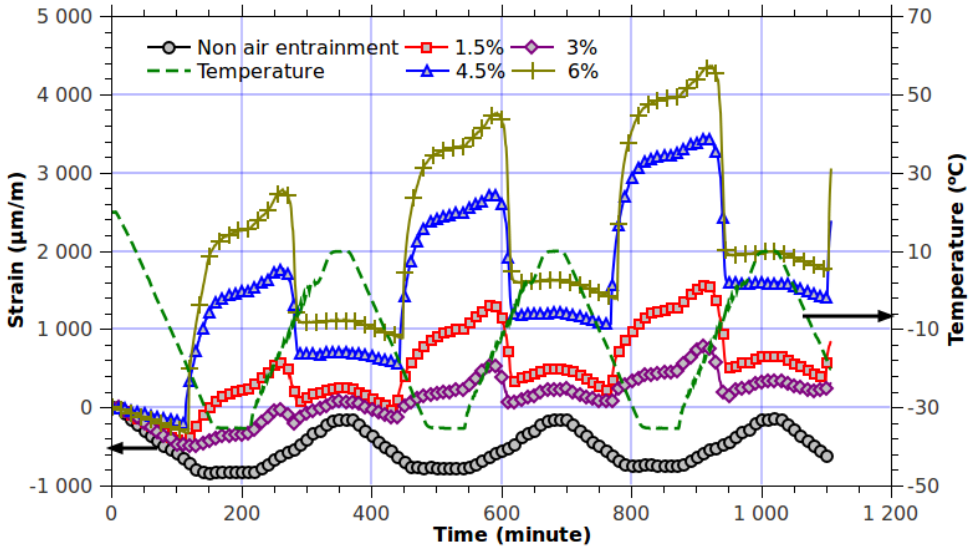

Figure E.12: Deformation of 15% NaCl solution saturated samples entrained with different dosages of air voids in terms of freeze-thaw time.

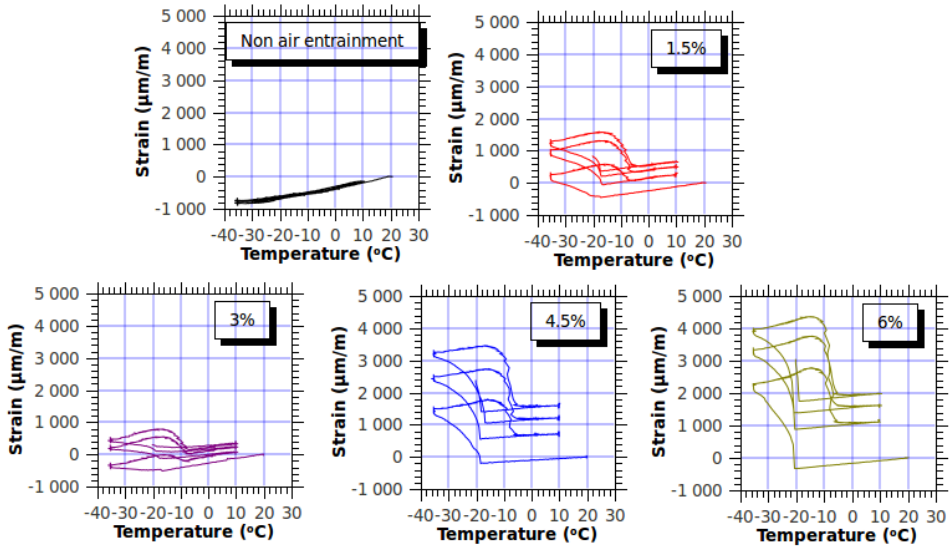

Figure E.13: Deformation of 15% NaCl solution saturated samples entrained with different dosages of air voids in terms of temperature.

Table E.3: Deformations for air entrained pastes saturated with 6% (10%) [15%] NaCl solution subjected to freeze-thaw loading.

Sorts	1^{st} cycle	2^{ed} cycle	3^{rd} cycle	4^{th} cycle	5^{th} cycle	6^{th} cycle
	($\times 10^{-6}$)	($\times 10^{-6}$)	($\times 10^{-6}$)	($\times 10^{-6}$)	($\times 10^{-6}$)	($\times 10^{-6}$)
Non air entrained samples						
ε_{th}	−611(−1385)[−985]	−526(−1211)[−817]	−505(−1229)[−754]	−603(−1239)[−801]	-(−1233)[-]	-(−1264) [-]
ε_{nu}	139(0)[0]	148(0)[0]	80(0)[0]	91(0)[0]	-(0)[-]	-(0)[-]
ε_{ex}	388(−813)[−831]	667(74)[−662]	696(142)[−561]	814(128)[-]	-(73)[-]	-(−51)[-]
ε_{pr}	999(571)[154]	1193(1285)[155]	1201(1369)[190]	1417(1367)[-]	-(1306)[-]	-(1314)[-]
ε_{re}	162(−172)[−160]	210(196)[0]	156(106)[12]	147(108)[-]	-(54)[-]	-(9)[-]
ε_{if}	447(715)[49]	247(265)[36]	266(92)[-]	-(53)[-]	-(31)[-]	-(-)[-]
%1.5 air entrained samples						
ε_{th}	−864(−753)[−679]	−717 (−489) [−535]	−735 (−504) [−520]	−725 (−495) [−511]	- (−496) [-]	- (−505) [-]
ε_{nu}	105(105)[38]	124 (435) [38]	72 (542) [233]	∗ (606) [298]	- (499) [-]	- (446) [-]
ε_{ex}	−33(1445)[229]	232 (1827) [754]	156 (1785) [775]	121 (1751) [-]	- (1683) [-]	- (1600) [-]
ε_{pr}	831(2198)[908]	949 (2317) [1289]	891 (2289) [1295]	846 (2246) [-]	- (2179) [-]	- (2105) [-]
ε_{re}	71(541)[257]	147 (344) [250]	75 (194) [141]	40 (130) [-]	- (95) [-]	- (49) [-]
ε_{if}	270(923)[782]	71 (303) [171]	40 (250) [-]	- (62) [-]	- (12) [-]	- (-) [-]
%3 air entrained samples						
ε_{th}	−877(−871)[−782]	−743 (−558) [−663]	−735 (−551) [−534]	−734 (−541) [−504]	- (−515) [-]	- (−500) [-]
ε_{nu}	0(122)[50]	0 (305) [38]	0 (392) [50]	∗ (329) [28]	- (284) [-]	- (199) [-]
ε_{ex}	−624(460)[−333]	−385 (1048) [148]	−296 (1018) [244]	−251 (870) [-]	- (779) [-]	- (651) [-]
ε_{pr}	253(1331)[449]	358 (1606) [811]	439 (1569) [778]	483 (1411) [-]	- (1294) [-]	- (1151) [-]
ε_{re}	−73(238)[74]	56 (247) [156]	55 (140) [110]	36 (86) [-]	- (64) [-]	- (28) [-]
ε_{if}	166(784)[555]	145 (214) [252]	100 (−8) [-]	- (−5) [-]	- (−64) [-]	- (-) [-]
%4.5 air entrained samples						
ε_{th}	−816(−512)[−408]	−542 (−420) [−346]	−518 (−470) [−411]	−533 (−464) [−500]	- (−460) [-]	- (−403) [-]
ε_{nu}	225(82)[315]	257 (180) [494]	345 (326) [505]	∗ (550) [428]	- (527) [-]	- (417) [-]
ε_{ex}	570(1980)[1478]	928 (2084) [1782]	980 (2005) [2046]	993 (1086) [-]	- (1669) [-]	- (1524) [-]
ε_{pr}	1386(2492)[1886]	1470 (2504) [2149]	1498 (2475) [2457]	1526 (2270) [-]	- (2129) [-]	- (1927) [-]
ε_{re}	224(770)[707]	177 (400) [500]	109 (189) [348]	68 (125) [-]	- (75) [-]	- (51) [-]
ε_{if}	582(886)[1011]	229 (309) [765]	122 (−10) [-]	- (−12) [-]	- (−60) [-]	- (-) [-]
%6 air entrained samples						
ε_{th}	−611(−603)[−450]	−414 (−448) [−350]	−410 (−453) [−365]	−399 (−449) [−381]	- (−432) [-]	- (−433) [-]
ε_{nu}	194(148)[815]	483 (394) [848]	415 (516) [960]	∗ (517) [948]	- (471) [-]	- (527) [-]
ε_{ex}	1120(1611)[2267]	1495 (1985) [2326]	1519 (2027) [2391]	1513 (1979) [-]	- (1948) [-]	- (1893) [-]
ε_{pr}	1731(2214)[2717]	1909 (2433) [2676]	1929 (2480) [2756]	1912 (2428) [-]	- (2380) [-]	- (2326) [-]
ε_{re}	338(593)[1007]	278 (388) [611]	144 (245) [367]	91 (146) [-]	- (98) [-]	- (73) [-]
ε_{if}	713(967)[1066]	302 (430) [676]	138 (197) [-]	- (115) [-]	- (47) [-]	- (-) [-]

Index

List of Symbols and Abbreviations

$\alpha_{d,X}^{hom}, \alpha_{u,X}^{hom}, \alpha_s, \alpha_l, \alpha_c, \alpha_{sk}, \alpha_t, \alpha_i, \alpha_d, \alpha_0, \alpha_{c,m}$ Homogenized thermal expansion coefficient at drained (with subscript d, X and superscript hom) and undrained (with subscript u, X and superscript hom) conditions for material X; Thermal expansion coefficient of solid (with subscript s), liquid (with subscript l), ice crystals (with subscript c) and skeleton (with subscript sk) (K^{-1}); Overall hydration degree (with subscript t) and hydration degree of cement clinkers of compound i in Chapter 6 (-); Measured thermal expansion coefficient (with subscript d) and samples with zero porosity (with subscript 0) (K^{-1}); Hydration degree of cement mortar (-)

β_i Mobility of species i ($\mathrm{m}^2 \cdot \mathrm{s}^{-1} \cdot \mathrm{V}^{-1}$); Length modification coefficient of LVDT in eq(eq:dilation-LVDT) ($\mathrm{m} \cdot {}^{\circ}\mathrm{C}^{-1}$)

$\boldsymbol{\alpha}_{\phi\alpha}, \boldsymbol{\alpha}_{th}$ Partial volumetric thermal dilation coefficient of phase α (with subscript $\phi\alpha$); Tensor of thermal dilation coefficient of solid matrix (with subscript th) (K^{-1})

$\boldsymbol{\epsilon}, \boldsymbol{\epsilon}_{\Delta\rho}, \boldsymbol{\epsilon}_{\mathcal{S}_f}, \boldsymbol{\epsilon}_T, \boldsymbol{\epsilon}_U$ Total freezing strain tensor (no script), freezing strain tensor by density change (with subscript $\Delta\rho$), entropy change (with subscript $\mathcal{S}_f$), temperature change (with subscript T), interfacial energy (with subscript U)

$\boldsymbol{u}$ Displacement

$\boldsymbol{\lambda}, \lambda_l, \lambda_c, \lambda_s$ Heat conductivity tensor (bold form), heat conductivity of liquid (with subscript l), ice crystals (with subscript c) and solid matrix (with subscript s) ($\mathrm{W} \cdot \mathrm{m}^{-2} \cdot \mathrm{K}^{-1}$)

$\boldsymbol{\Sigma}$ Macroscopic stress tensor

$\boldsymbol{v}_l, \boldsymbol{v}_w, \boldsymbol{v}_i$ Velocity of water (with subscript w) and species i (with subscript i) in partial frozen porous system with the velocity of barycentric center of mass (with subscript l), ($\mathrm{m} \cdot \mathrm{s}^{-1}$)

$\boldsymbol{\varepsilon}, \boldsymbol{\varepsilon}^P, \boldsymbol{\varepsilon}^T$ Strain tensor (no script); Strain tensor by pore pressure (with superscript P); Strain tensor by temperature variation (with superscript T)

$\boldsymbol{b}, b, b_\alpha, b_X^{hom}$ Biot's coefficient in tensor form, isotropic from, for phase α and in homogenized from for material X

$\boldsymbol{J}_w, \boldsymbol{J}_i, \boldsymbol{J}_c$ The diffusion flux of of water (with subscript w), species i (with subscript i) in partial frozen porous system ($\mathrm{kg} \cdot \mathrm{m}^{-2} \cdot \mathrm{s}^{-1}$), and conduction current (with subscript c) ($rmA \cdot m^{-2}$)

$\boldsymbol{N}_{\alpha\beta}, N_X^{hom}$ Biot's tangent modulus, with $\alpha\beta \in l, c$ and homogenized Biot's modulus for material X

$\boldsymbol{q}$ Heat flux tensor ($\mathrm{W} \cdot \mathrm{K}^{-1}$)

$\boldsymbol{w}_i, \boldsymbol{w}_l, \boldsymbol{w}_q, \boldsymbol{w}_w, w_i$ Darcean flux tensor of species i (with subscript i); Flux tensor of barycentric center of mass (with subscript l); Flux tensor of water (with subscript w) ($\mathrm{kg} \cdot \mathrm{m}^{-2} \cdot \mathrm{s}^{-1}$); Total current density (with subscript q) ($\mathrm{A} \cdot \mathrm{m}^{-2}$); Adjustable parameters for multi-Gauss fitting (with subscript i) in eqs(8.15) and (8.17) (-)

$\Delta G_{fus}, \Delta G_{hom}^*, \Delta G_{hom,salt}^*$ Gibbs fusion energy at reference pressure P_0 (with subscript fus) ($\mathrm{J} \cdot \mathrm{mol}^{-1}$); Excess Gibbs free energy of an ice embryo with critical size nucleating in pure water (with superscript hom) and in saline solution (with superscript $hom, salt$) homogeneously (J)

ΔH_{fus} Enthalpy change of fusion at current temperature T ($\mathrm{J} \cdot \mathrm{mol}^{-1}$)

$\Delta T, \Delta T_m, \Delta T_f, \Delta T_i$ Depressed temperature by capillary supercooling, depressed melting (with subscript m) and freezing temperature (with subscript f), and width of ith temperature bin T_i (with subscript i) (K)

δ Thickness of unforzen layer (m) or (nm)

$\Delta\alpha$ Thermal expansion coefficient mismatch between epoxy and glass, $\Delta\alpha = \alpha_g - \alpha_e$ in in eq(3.2), (K^{-1})

ΔV_{wc} Molar volume difference between ice and water ($m^3 \cdot mol^{-1}$)

$\dot{\mathcal{E}}$ Total internal energy rate of porous media

$\epsilon_{\text{Total}}, \epsilon_{\text{IF}}, \epsilon_{\text{Tem}}$ Total instantaneous dilation (with subscript Total), by ice nucleation (with subscript IF) and thermal shock (with subscript (Tem))

η_l Viscosity of liquid phase ($Pa \cdot s$)

$\gamma_{cl}, \gamma_{sc}, \gamma_{ls}, \gamma_d, \gamma_i, \gamma_+, \gamma_-, \gamma_\pm$ Surface tension between crystals and liquid (with subscript cl), between crystals and solid wall (with subscript sc), between liquid and solid wall (with subscript ls) ($N \cdot m^{-1}$); Surface tension of dried solid ($N \cdot m^{-1}$); Ionic activity coefficient (with subscript i) (-); Activity coefficient of cation (with subscript +); Activity coefficient of anion (with subscript −); Mean activity coefficient (with subscript ±)

$\kappa, \kappa_{r,0}, \kappa_X^{hom}$ Curvature (no script) (m^{-1}) in eq(2.23), overall permeability of porous materials (no script) in eq(4.18) and section 7.3.1.2, relative permeability (with subscript r), intrinsic permeability (with subscript 0) and homogenized permeability of material X (with subscript X and superscript hom) (m^2)

$\mathbb{A}$ Fourth order Strain localization tensor

$\mathbb{B}$ Fourth order Stress localization tensor

$\mathbb{C}, \mathbb{C}_i, \mathbb{C}^{hom}$ Stiffness tensor (no script); Stiffness tensor of compound i (with subscript i); Homogenized stiffness tensor (with superscript hom)

$\mathbb{D}$ Deviatoric stiffness tensor

$\mathbb{K}$ Volumetric stiffness tensor

$\mathbf{C}$ Second order flux localization tensor

$\mathbf{D}$ Fourth order potential localization tensor

$\mathcal{D}, \mathcal{D}_{sk}, \mathcal{D}_f, \mathcal{D}_{th}$ Total dissipation (no script) ($J \cdot K \cdot s^{-1}$), dissipation of skeleton (with subscript sk), fluid (with subscript f) and heat (with subscript th)

$\mathcal{G}$ Relative diffusion coefficient (-)

$\mathcal{P}, \mathcal{P}_s, \mathcal{P}_w, \mathcal{P}_{def}$ Overall quantities per unit mass of solution (no script) in eq(8.1), the quantities per unit mole of water (with subscript w) and apparent molar quantities of salt (with subscript s); Strain work rate (with subscript def)

$\mathcal{R}$ Cooling rate ($K \cdot s^{-1}$)

$\mathcal{S}, \mathcal{S}_c, \mathcal{S}_c^\circ, \mathcal{S}_f, \mathcal{S}_l, \mathcal{S}_m, \mathcal{S}_{sk}, \mathcal{S}_w, \mathcal{S}_w^\circ$ Overall entropy density (no script); Entropy density of ice (with subscript c) and that at reference state (with subscript c and superscript $\circ$); Fusion entropy density (with subscript f); Entropy density of liquid phase (with subscript l); Entropy density of solid matrix (with subscript m); Entropy density of skeleton (with subscript sk); Entropy density of water (with subscript w); Entropy density of ice (with subscript w) and that at reference state (with subscript w and superscript $\circ$) ($J \cdot m^{-3} \cdot K^{-1}$)

$\mathring{\mathbb{S}}$ Global entropy of porous medium ($J \cdot kg^{-1} \cdot K^{-1}$)

$\mathring{\mathcal{Q}}$ Heat exchange rate

$\mathring{m}_{w \to c}$ Ice formation rate

$\mathring{r}$ Heat source

$\mathsf{C}_{P,w}, \mathsf{C}_{P,c}, \mathsf{C}_f, \mathsf{C}_{P,\phi}, \mathsf{C}^0_{P,m}$ Molar heat capacity of water (with subscript P,w), ice crystals (with subscript P,c) and their difference (with subscript f); Apparent molar heat capacity of salt (with subscript P,ϕ) and these at infinite dilution (with subscript P,m and superscript 0) ($\mathrm{J}\cdot\mathrm{mol}^{-1}\cdot\mathrm{K}^{-1}$)

$\mathsf{M}_w, \mathsf{M}_c, \mathsf{M}_i$ Molar mass of water (with subscript w), ice (with subscript c) and species i (with subscript i) ($\mathrm{kg}\cdot\mathrm{mol}^{-1}$)

$\mathsf{S}_w, \mathsf{S}^\circ_w, \mathsf{S}_c, \mathsf{S}^\circ_c, \mathsf{S}_f$ Molar entropy of water (with subscript w) and that at reference state (with subscript w and superscript $\circ$); Molar entropy of ice crystals (with subscript c) and that at reference state (with subscript c and superscript $\circ$); Molar fusion entropy ($\mathrm{J}\cdot\mathrm{mol}^{-1}\cdot\mathrm{K}^{-1}$)

$\mathsf{V}_w, \mathsf{V}_c, \mathsf{V}_i, \mathsf{V}_{total}, \mathsf{V}_\phi, \mathsf{V}_{\phi,i}, \mathsf{V}^0_m$ Molar volume of water (with subscript w), ice (with subscript c) and species i (with subscript i) ($\mathrm{m}^3\cdot\mathrm{mol}^{-1}$); Total volume of aqueous solution (with subscript *total*); Apparent molar volume of NaCl (with subscript ϕ), species i (with subscript i); And apparent molar volume of electrolyte at infinite dilution (with subscript m and superscript 0) ($\mathrm{m}^3\cdot\mathrm{mol}^{-1}$)

$\mu_w, \mu_c, \mu^\ominus_w, \mu^\ominus_c$ Chemical potential of water (with subscript w) and ice crystals (with subscript c) ($\mathrm{J}\cdot\mathrm{mol}^{-1}$); Chemical potential of bulk water (with subscript w and superscript $\ominus$) and bulk ice crystals (with subscript c and superscript $\ominus$) at reference state ($\mathrm{J}\cdot\mathrm{mol}^{-1}$)

$\phi, \phi_0, \phi_l, \phi_c, \phi_p, \phi_{cap}, \phi_m, \phi_{av}, \phi_{paste}, \phi^{act}, \phi_\delta$ Current Lagrangian porosity (no script); Initial porosity (with subscript 0), partial porosity occupied by liquid phase (with subscript l), partial porosity occupied by ice (with subscript c), percolated critical porosity (with subscript p), capillary porosity (with subscript *cap*), porosity by gravimetric measurement (with subscript m), volume fraction of air voids (with subscript *av*), volume fraction of paste (with subscript *paste*); Active porosity (with superscript *act*); Volume fraction of liquid-like layer (with subscript δ) (-)

Π Osmotic coefficient (-)

Ψ, Ψ_E, Ψ_{sk} Helmholtz free energy density (no script) ($\mathrm{J}\cdot\mathrm{m}^{-3}$); Electric potential (with subscript E) (V); Helmholtz free energy density of skeleton (with subscript sk) ($\mathrm{J}\cdot\mathrm{m}^{-3}$)

$\psi_l, \psi_c, \psi_{sk}$ Helmholtz free energy density of liquid phase (with subscript l), ice crystals (with subscript c), and skeleton (with subscript sk) ($\mathrm{J}\cdot\mathrm{kg}^{-1}$)

$\rho_\alpha, \rho^0_\alpha, \rho_{LD,HD}$ Current (with subscript α) and initial density (with subscript α and superscript 0) of phase α; Density of low density (with subscript LD) and high density (with subscript HD) C-S-H ($\mathrm{kg}\cdot\mathrm{m}^{-3}$)

$\sigma, \sigma_0, \sigma_{gs}, \sigma_s, \sigma_e, \boldsymbol{\sigma}, \boldsymbol{\sigma}^P, \boldsymbol{\sigma}^T$ Separation of two microscopic bodies (no script) (m) or (nm) in eq(2.39), current electric conductivity (no script) and bulk electric conductivity (with subscript 0) in eqs(7.14) to (7.16) and eq(7.22); Stress around the boundary of epoxy (with subscript gs), stress in the glass surface (with subscript g), stress in the epoxy (with subscript e), in eq(3.2) (Pa) or (MPa); Second order stress tensor (in bold form); Eigenstress by pressure (with superscript P); Eigenstress by temperature variation (with superscript T)

τ Tortuosity (-) in eq(4.21), Pore pressure relaxation time in chapter 5

θ Contact angle (π) or ($^\circ$)

φ_α Deformation of phase α

ξ, ξ_r, ξ_0 Surface induced short-range perturbation in eq(2.20) (nm) or (m), dielectric permeability of pure water in eq(D.2) ($\mathrm{F}\cdot\mathrm{m}^{-1}$); Relative permittivity of medium (with subscript r) and the permettivity of free space (with subscript 0) ($\xi_0 = 8.854\times10^{-12}\ \mathrm{C}^2\cdot\mathrm{J}^{-1}\cdot\mathrm{m}^{-1}$)

$A, A_c, A_i, A_k, A^v_{\alpha,X}, A^d_{\alpha,X}, A_\phi, A_x$ Surface area of pore wall (no script); Surface area of ice crystals (with subscript c) ($\mathrm{m}^2\cdot\mathrm{kg}^{-1}$); Constants for Multi-Gauss fitting (with subscript i) in eqs(8.15) and (8.17); An impurity constant (with subscript k) ($\mathrm{m}^{1/2}$); Volumetric (with subscript α, X and superscript v) and deviatric (with subscript α, X and superscript d) localization coeffcicients for phase α in composites X; Concentration based Debye-Hükel constant (with subscript ϕ) ($\mathrm{mol}^{1/2}\cdot\mathrm{kg}^{-1/2}$); Molar fraction based Debye-Hükel constant (with subscript x) (-)

a_i, a_w, a_c Activity of ions (with subscript i), water (with subscript w) and solid solvent (with subscript c) (-)

B, B_i Parameter for short-rang ion-ion interaction in Pitzer's model (no script), Adjustable constants for short-range effects in ionic activity (with subscript i) (-)

$C, C_A, C_f, C_i, C_H, C_{KC}, C_{P,c}, C_{P,l}, C_{P,w}, C_r, C_s, C_\phi$ Parameters for long-rang interaction in Pitzer's model (no script); Constant for conductivity by Archie's law (with subscript A); Heat capacity difference between ice and water (with subscript f); Constants for long-range effects in ionic activity (with subscript i) (-); Constant for permeability by Katz-Thompson (with subscript H) and by Kozeny-Carman equation (with subscript KC); Mass heat capacity of ice crystals (with subscript P, c), liquid phase (with subscript P, l) and water (with subscript P, w) ($\mathrm{J \cdot kg^{-1} \cdot K^{-1}}$); Constant for permeability by Archie's law based on critical pore size (with subscript r); Mass heat capacity of solid matrix (with subscript s); Constant for permeability by Archie's law based on porosity (with subscript ϕ.

c, c_i, c_w, c_i^0 Overall salt concentration (no script); Current concentration of species i (with subscript i) and water (with subscript w); Initial concentration of species i (with subscript i and superscript 0) ($\mathrm{mol/M^3}$)

d, d_i Pore diameter (no script); Characteristic pore diameter by multi-Gauss fitting (with subscript i) (m) or (nm)

$D, D_i, D_0, D_s, \boldsymbol{D}_i$ Diffusivity for general description (no script); Diffusivity of species i or compound i for multi-scale modelling (with subscript i); Bulk diffusivity (with subscript 0) and diffusivity of solid phase (with subscript s) ($\mathrm{m^2 \cdot s^{-1}}$), Conductivity (diffusivity) tensor of compound i (with subscript i in bold form)

e, e_c, e_l, e_s Charge of electron (-1.602×10^{-19}C); Internal energy of ice crystals (with subscript c), liquid solution (with subscript l) and solid skeleton (with subscript s) ($\mathrm{J \cdot kg^{-1}}$)

$E, E_g, E_e, \boldsymbol{E}$ Average local internal energy (no script); Elastic modulus of glass (with subscript g), elastic modulus of epoxy (with subscript e), in eq(3.2), (GPa) or (MPa), Electric field (in bold form) ($\mathrm{V \cdot m^{-1}}$) in section 4.2.2.2; Macro strain tensor (in bold form) in Appendix C

F Specific interfacial potential ($\mathrm{J \cdot m^2}$) in eqs(2.35)→(2.39), Formation factor (-) in eqs(7.14) and (7.18), otherwise the Faraday constant ($\mathrm{C \cdot mol^{-1}}$)

$f_0, f_\theta, f_i^m, f_i^v, f_{LD}, f_{HD}$ Adjustable constant for Multi-Gauss fitting (with subscript 0) in eqs(8.15) and (8.17); Contact angle factor (with subscript θ) (-); mass (with subscript i and superscript m) and volume (with subscript i and superscript v) fraction of compound i in Chapter 6 (-); Volume fraction of low density (with subscript LD) and high density (with subscript HD) C-S-H (-)

$g, g_c, g_i, g_l, g_s, g_{sk}, \boldsymbol{g}$ Shape function for calculating the ice.water saturation degree in eq(8.7);Gibbs free energy density of ice crystals (with subscript c) ($\mathrm{J \cdot kg^{-1}}$); Shear modulus of compounds i (with subscript i) (GPa); Gibbs free energy density of liquid phase (with subscript l), Shear modulus of solid phase (with subscript sk) (GPa); Tensor of potential field

$G, G_i, G_m, G_{sk}, G_X^{hom}, G^E, \boldsymbol{G}$ Shear modulus of porous materials for general description (no script); Shear modulus of compound i (with subscript i); Gibbs free energy density of skeleton (with subscript sk) ($\mathrm{J \cdot kg^{-1}}$); Gibbs free energy density of solid matrix (with subscript m) ($\mathrm{J \cdot kg^{-1}}$); Homogenized drained (with subscript X and superscript hom) shear modulus of material X (GPa); Excess Gibbs free energy when electrolytes mixed with water (with superscript E) ($\mathrm{J \cdot kg^{-1}}$); Tensor of macroscopic potential for flux

$I, I_x, I_c, I_h, \mathbf{I}, \mathbb{I}$ Concentration based (no script) and molar fraction based (with subscript x) ionic strength ($\mathrm{mol^{1/2} \cdot kg^{-1/2}}$); Cubic ice (with subscript c); Hexagonal ice (with subscript h); Second order unit tensor; Fourth order unit tensor

J, J_0 Ice nucleation rate (no script) and the prefactor (with subscript 0) ($\mathrm{s^{-1}}$) or ($\mathrm{m^{-3} \cdot s^{-1}}$)

$K, K_w, K_i, K_l, K_c, K_s, K_X^{hom}, K_{u,X}^{hom}$ Bulk modulus of porous materials for general description (no script); Bulk modulus of compound i (with subscript i); Bulk modulus of water (with subscript w), liquid

solution (with subscript l) and ice crystals (with subscript c); Bulk modulus of solid matrix (with subscript s);Bulk modulus of homogenized drained (with subscript X and superscript hom) and undrained (with subscript u, X and superscript hom) bulk modulus of materials X (GPa)

$k_b, k_s, k_i, k_X^{hom}, \boldsymbol{k}^{hom}, \boldsymbol{k}$ Boltzmann constant (with subscript b) ($\mathrm{J} \cdot \mathrm{K}^{-1}$); Bulk modulus of solid C-S-H (with subscript s) and compound i (with subscript i), (GPa); Thermal parameter of homogenized material X and the tensor form, ($\mathrm{GPa} \cdot \mathrm{K}^{-1}$)

$l, l_{d\Omega,h}$ Distance to air void (no script); Characteristic length of a representative element volume (with subscript $d\Omega$), and characteristic length of heterogeneity of cement paste (m) or (μm)

$L_i, L_i^0, L_{LVDT,i}, \bar{L}$ Current length of ith sample (with subscript i); Initial length of i sample (with subscript i and superscript 0); Length change of ith LVDT (with subscript $LVDT, i$); Spacing factor (μm) or (m)

M(C-S-H), M_0, M_d, M_s Total C-S-H mass; Mass of initial sample (g); Mass of dried sample (g); Mass of vacuum-saturated sample (g)

$m, m_p, m_A, m_i, m_T, m_\alpha$ Constant for permeability (no script) and molality in eq(8.1), for relative conductivity with consideration of percolation (with subscript p) and based on Archie's law (with subscript A), molar concentration of species i (with subscript i) and total concentration (with subscript T) ($\mathrm{mol} \cdot \mathrm{kg}^{-1}$); Mass of phase α (with subscript α) in partial frozen porous system (kg)

$n, n_i, n_w, \boldsymbol{n}$ Percolation exponent (no script) (-); Freezing events occur at temperature T_i with bin width ΔT_i (with subscript i); Molar numbers of water (with subscript w) (molar); Unit outward normal tensor

N_i, N_A Moles per unit area of a single species of monovalent nonvolatile impurities deposited in the film (with subscript i) ($\mathrm{mole} \cdot \mathrm{m}^{-2}$); Avogadro constant ($6.023 \times 10^{23} \mathrm{J}^{-1} \cdot \mathrm{m}^{-1}$)

$P_0, P_{cap}, P_\alpha, P_{max}, P_\alpha^*$ Saturated gas pressure in Chapter 6 and section A.6, otherwise the atmospheric pressure (Pa) or (MPa); Capillary pressure (with subscript cap); Pressure of phase α(with subscript α); Effective pressure of phase α (with subscript α and superscript *); Maximum hydraulic pressure by Power's model (with subscript max) (Pa) or (MPa)

q, q_i Excess net charge (no script), and charge per unit mass of species i (with subscript i) ($\mathrm{C} \cdot \mathrm{kg}^{-1}$) in eqs(4.23) to (4.25)

$Q_X^{hom}, \boldsymbol{Q}$ Effective coefficient for thermal porosity deformation for material X (K^{-1}); Tensor of macroscopic flux

R The gas constant ($8.31441 \mathrm{J} \cdot \mathrm{K}^{-1} \cdot \mathrm{mol}^{-1}$)

$r, r_{eq}, r_k, r_c, r_0,$ Radius of capillary pores (no script), cylindrical ice (with subscript eq), cylindrical pore calculated by Kelvin equation (with subscript k), critical pore (with subscript c), and air voids for Powers' hydraulic model (with subscript 0) (m) or (nm)

$S, S_a, S_w, S_l, S_c, S_{cr}, \boldsymbol{S}$ Specific surface area of porous material (no script) ($\mathrm{m}^2 \cdot \mathrm{g}$); Average specific surface area of sphere (m^{-1}); Water saturation ratio (with subscript w), liquid saturation degree (with subscript l), ice saturation degree (with subscript c) and critical saturation degree (with subscript cr) (-); Tensor of surface flux

s_l, s_c, s_{sk} Entropy density of liquid phase (with subscript l), ice crystals (with subscript c) and skeleton (with subscript sk)($\mathrm{J} \cdot \mathrm{kg}^{-1} \cdot \mathrm{K}^{-1}$)

$T, T_0, \boldsymbol{T}$ Current Kelvin temperature (no script); Freezing/melting temperature for bulk phase at equilibrium (with subscript 0) (K); Tensor of surface traction

t, t_g, t_e Time for cement hydration (no script) (day); Thickness of adsorbed gas for interpretation of nitrogen adsorption/desorption (no script) (nm); Thickness of glass (with subscript g), thickness of epoxy (with subscript e), in eq(3.2), (m)

U Interfacial energy

$V, V_c, V_{cp}, V_{cr}, V_{gel}, V_{HD}, V_{LD}, V_m, V_{mono}, V_{p,i}, V_{r,i}, V_t, V_w$ Current pore volume (no script); Ice volume (with subscript c); Capillary volume fraction (with subscript cp); Volume fraction by chemical reaction (with subscript cr); Volume fraction of C-S-H gel (with subscript gel), low density (with subscript HD) and high density C-S-H (with subscript LD); Volume of the completion monomolecular adsorption (with subscript m); Volume of gas adsorbed when the entire surface is covered by a monolayer (with subscript $mono$) ($m^2 \cdot g^{-1}$); Volume fraction of hydration products (with subscript p, i) and the reactants (with subscript r, i); Total pore volume (with subscript t); Initial water volumetric fraction (with subscript w)

v_g, v_e Poisson ratio of glass (with subscript g), Poisson ratio of epoxy (with subscript e), in eq(3.2), (-)

z_i Valence of species i (-)

A_3S Tricalcium Aluminate

AEA Air entrainment agent

AFM Atomic force microscopy

B-D Brailsford-Major estimation

BJH Barrett-Joyor-Halenda

$C\overline{S}H_2$ Gypsum

C_2S Dicalcium Silicate

C_3S Tricalcium Silicate

C_3AFH_6 Hydrogarnel

C_4AF Tetracalcium Aluminoferrite

C_4AH_{13} or AFm Calcium Aluminate Hydrate

$C_4A\overline{S}H_{12}$ Monosulfate

$C_6A\overline{S}_3H_{32}$ or AFt Calcium Aluminum Sulfate Hydrate)

C-S-H Calcium-Silicate-Hydrate

CH Portlandite

CMA Calcium Magnesium Acetate

CPG Controlled pore glass

CPSD Cumulative pore size distribution

DLVO Derjaguin-Landau-Verwey-Overbeek

DPSD Differenctial pore size distribution

DTG Differential thermalgravimetry

EMT Effective medium theory

ESEM Environment Scanning Electric Microscopy

H H_2O

HD High density

HS Hashin-Stricktman

ITZ Interfacial transition zone

LD Low density

MCM Mobile crystalline material

MIP Mercury intrusion porosimetry

NAD	Nitrogen adsorption/desorption
OPC	Ordinary Portland cement
PSD	Pore size distribution
RVE	Representative volume element
SBA	Santa Barbara Amorphous type material
SCE	Self-consistant scheme
SEM	Scanning Electric Microscopy
TEC	Thermal expansion coefficient
TG	Thermogravimetry
TGA	Thermogravimetric analysis
w/c	Water to cement ratio
Wn	Non-evaporable water